

Integrated Chemical Processes

Edited by
Kai Sundmacher,
Achim Kienle,
Andreas Seidel-Morgenstern

Further Titles of Interest

K. Sundmacher, A. Kienle (Eds.)

Reactive Distillation

Status and Future Directions

2003

ISBN 3-527-30579-3

J. G. Sanchez Marcano, T. T. Tsotsis

Catalytic Membranes and Membrane Reactors

2002

ISBN 3-527-30277-8

T. G. Dobre, J. G. Sanchez Marcano

Chemical Engineering

Modelling, Simulation and Similitude

2005

ISBN 3-527-30607-2

S. Pereira Nunes, K.-V. Peinemann (Eds.)

Membrane Technology

in the Chemical Industry

2001

ISBN 3-527-28458-0

Ullmann's

Processes and Process Engineering

3 Volumes

2004

ISBN 3-527-31096-7

Integrated Chemical Processes

Synthesis, Operation, Analysis, and Control

Edited by

Kai Sundmacher,

Achim Kienle and

Andreas Seidel-Morgenstern



WILEY-VCH Verlag GmbH & Co. KGaA

Prof. Dr.-Ing. Kai Sundmacher

Prof. Dr.-Ing. Achim Kienle

Prof. Dr. Andreas Seidel-Morgenstern

Max Planck Institute for Dynamics of Complex
Technical Systems
Sandtorstr. 1
39106 Magdeburg
Germany

and

Otto-von-Guericke-University
Magdeburg
Universitätsplatz 2
39016 Magdeburg
Germany

All books published by Wiley-VCH are carefully produced. Nevertheless, authors, editors, and publisher do not warrant the information contained in these books, including this book, to be free of errors. Readers are advised to keep in mind that statements, data, illustrations, procedural details or other items may inadvertently be inaccurate.

Library of Congress Card No.: applied for.

British Library Cataloguing-in-Publication Data:

A catalogue record for this book is available from the British Library

Bibliographic information published by

Die Deutsche Bibliothek

Die Deutsche Bibliothek lists this publication in the Deutsche Nationalbibliografie; detailed bibliographic data is available in the Internet at
<http://dnb.ddb.de>

© 2005 WILEY-VCH Verlag GmbH & Co. KGaA,
Weinheim

All rights reserved (including those of translation into other languages). No part of this book may be reproduced in any form – by photoprinting, microfilm, or any other means – nor transmitted or translated into a machine language without written permission from the publishers. Registered names, trademarks, etc. used in this book, even when not specifically marked as such, are not to be considered unprotected by law.

Printed in the Federal Republic of Germany.

Printed on acid-free paper

Typesetting Shiv e-Publishing Technologies Pvt. Ltd.
Bangalore, India

Printing betz-druck GmbH, Darmstadt

Bookbinding Schäffer GmbH i.G., Grünstadt

ISBN-13: 987-3-527-30831-6

ISBN-10: 3-527-30831-8

Contents

Preface XV

Part I Integration of Heat Transfer and Chemical Reactions 1

1 Enhancing Productivity and Thermal Efficiency of High-Temperature Endothermic Processes in Heat-Integrated Fixed-Bed Reactors 3

*Grigorios Kolios, Achim Gritsch,
Bernd Glöckler and Gerhart Eigenberger*

Abstract 3

1.1 Introduction 3

1.2 Heat-Integrated Processes for Endothermic Reactions 4

1.2.1 Optimality Conditions 6

1.2.1.1 Efficiency of Heat Recovery 6

1.2.1.2 Temperature Control 8

1.3 Multifunctional Reactor Concepts 10

1.3.1 Regenerative Processes 12

1.3.1.1 Simultaneous Mode 13

1.3.1.2 Asymmetric Mode 13

1.3.1.3 Symmetric Mode with Side Stream Injection 20

1.3.1.4 Counter-cocurrent Mode 21

1.3.1.5 Overheating During Oxidative Coke Removal 24

1.3.2 Recuperative Processes 27

1.3.2.1 Processes for Large-Scale Applications 29

1.3.2.2 Processes for Small-scale Applications 31

1.4 Conclusions 39

Symbols and Abbreviations 39

References 41

2 Conceptual Design of Internal Reforming in High-Temperature Fuel Cells 45

Peter Heidebrecht and Kai Sundmacher

2.1 Introduction 45

2.2 Technical Background 46

2.3 Modeling 48

2.3.1 Model Derivation 48

2.3.1.1 Anode Channel 49

2.3.1.2	Mixing Rules	52
2.3.1.3	Cathode Channel	53
2.3.1.4	Reaction Kinetics	54
2.3.1.5	Cell Power	55
2.3.2	Conversion Diagram	56
2.4	Applications	58
2.4.1	Comparison of Reforming Concepts	59
2.4.2	Anode Cascade	59
2.4.3	Anode Exhaust Gas Recycling	63
2.5	Summary and Conclusions	65
	Symbols	66
	References	67

3 Instabilities in High-Temperature Fuel Cells due to Combined Heat and Charge Transport 69

Michael Mangold, M Krasnyk, Achim Kienle and Kai Sundmacher

3.1	Introduction	69
3.2	Modeling	70
3.2.1	Model Assumptions	70
3.2.2	Model Equations	70
3.2.3	Simplified Model	72
3.3	Potentiostatic Operation	74
3.3.1	Cell with Infinite Length	74
3.3.2	Cell with Finite Length	76
3.4	Galvanostatic Operation	78
3.5	Conclusions	81
	Symbols	82
	Appendix: Numerical Methods for the Bifurcation Analysis in Section 3.0	83
	References	84

Part II Integration of Separations and Chemical Reactions 85

4 Thermodynamic and Kinetic Effects on the Feasible Products of Reactive Distillation: A-zeo-tropes and A-rheo-tropes 87

Kai Sundmacher, Zhiwen Qi, Yuan-Sheng Huang and Ernst-Ulrich Schlönder

4.1	Introduction	87
4.2	Azeotropes	89
4.2.1	Reactive Condenser and Reboiler	89
4.2.2	Conditions for Singular Points	90
4.2.2.1	Potential Singular Point Surface	90

4.2.2.2	Reaction Kinetic Surface	91
4.2.3	Examples	92
4.2.3.1	Hypothetical Ternary Systems	92
4.2.3.2	Real Ternary System: MTBE-Synthesis	97
4.2.3.3	Real Ternary System with Phase Splitting: Methanol Dehydration	101
4.2.3.4	Real Quaternary System: Isopropyl Acetate Hydrolysis	103
4.2.4	Application of Feasibility Diagram: Column Feasible Split	106
4.2.5	Remarks on Azeotropes	110
4.3	Arheotropes	110
4.3.1	Definition and Conditions	110
4.3.2	Illustrative Examples	111
4.3.2.1	Example 1: Stagnant Sweep Gas	111
4.3.2.2	Example 2: Flowing Sweep Gas	114
4.3.2.3	Example 3: Flowing Sweep Gas with Pervaporation	117
4.3.2.4	Example 4: Reactive Liquid Mixture	119
4.3.3	Remarks on Arheotropes	126
4.4	Kinetic Arheotropes in Reactive Membrane Separation	127
4.4.1	Model Formulation	127
4.4.1.1	Reaction Kinetics and Mass Balances	127
4.4.1.2	Kinetics of Vapor Permeation	129
4.4.2	Residue Curve Maps	130
4.4.2.1	Example 1: Ideal Ternary System	130
4.4.2.2	Example 2: THF Formation	133
4.4.3	Singular Point Analysis	137
4.4.3.1	Approach	137
4.4.3.2	Ideal Ternary System	138
4.4.3.3	THF-System	142
4.4.4	Remarks on Kinetic Arheotropes	144
4.5	Summary and Conclusions	144
	Symbols and Abbreviations	145
	References	147
5	Equilibrium Theory and Nonlinear Waves for Reaction Separation Processes	149
	<i>Achim Kienle and Stefan Grüner</i>	
5.1	Introduction	149
5.2	Theoretical Background	150
5.2.1	Wave Phenomena	150
5.2.2	Mathematical Model	153
5.2.3	Prediction of Wave Patterns	157
5.3	Analysis of Reaction Separation Processes	161

5.3.1	Reactive Distillation	161
5.3.2	Chromatographic Reactors	163
5.3.2.1	Reactions of Type	164
5.3.2.2	Reactions of type	166
5.3.2.3	Binaphthol Separation Problem	168
5.3.3	Extension to Other Processes	171
5.4	Applications	172
5.4.1	New Modes of Operation	172
5.4.2	New Control Strategies	173
5.5	Conclusion	175
	Acknowledgments	177
	Symbols	178
	References	179
6	Simulated Moving-Bed Reactors	183
	<i>Guido Ströhlein, Marco Mazzotti and Massimo Morbidelli</i>	
6.1	Introduction	183
6.2	Continuous Reactive Chromatography	185
6.2.1	Annular Reactive Chromatography	185
6.2.2	Simulated Moving-Bed Reactors	185
6.3	Design Parameters for Simulated Moving-bed Reactors	188
6.4	Modeling Simulated Moving-bed Reactors	195
6.5	Influence of the Stationary Phase Properties on SMBR Efficiency	197
6.6	Conclusion	200
	References	200
7	The Dos and Don'ts of Adsorptive Reactors	203
	<i>David W. Agar</i>	
7.1	Introduction	203
7.1.1	Adsorptive Reactors	203
7.1.2	Multifunctional Reactors	204
7.1.3	Preliminary Evaluation	205
7.2	Reaction Systems	206
7.2.1	The Claus Process	207
7.2.2	Direct Hydrogen Cyanide Synthesis	208
7.2.3	Water-gas Shift Reaction	210
7.2.4	The Deacon Process	211
7.3	Catalyst and Adsorbent	212
7.3.1	The Claus Process	212
7.3.2	Direct Hydrogen Cyanide Synthesis and Water-gas Shift Reaction	214
7.3.3	The Deacon Process	217

7.3.4	Other Adsorptive Catalysts	217
7.4	Reactor and Regeneration	218
7.4.1	Fixed-bed Reactors	218
7.4.2	Fluidized-bed Reactors	219
7.4.3	Pressure Swing Regeneration	220
7.4.4	Temperature Swing Regeneration	221
7.4.5	Reactive Regeneration	221
7.5	Design and Operation	222
7.5.1	Fixed-bed Macrostructuring	222
7.5.2	Pellet Microstructuring	223
7.5.3	Operating Parameter Profiling	224
7.5.4	Heat Effects	227
7.6	Conclusions and Perspectives	228
	Acknowledgments	230
	References	230
8	Reactive Stripping in Structured Catalytic Reactors: Hydrodynamics and Reaction Performance	233
	<i>Tilman J. Schildhauer, Freek Kapteijn, Achim K. Heibel, Archis A. Yawalkar and Jacob A. Moulijn</i>	
8.1	Introduction	233
8.2	Hydrodynamics	236
8.2.1	Flow Patterns	236
8.2.1.1	Monoliths	236
8.2.1.2	Sulzer DX®	240
8.2.1.3	Sulzer katapak-S®	241
8.2.2	Hold-up, Pressure Drop, and Flooding Limits	242
8.2.3	Residence Time Distribution	244
8.2.4	Gas–Liquid Mass Transfer	247
8.2.5	Conclusions	248
8.3	Reactive Experiments	249
8.3.1	Model Reaction	250
8.3.1.1	Kinetics	250
8.3.1.2	Side Reactions	250
8.3.2	Experimental	251
8.3.2.1	Catalysts	251
8.3.2.2	Experimental Set-ups	251
8.3.3	Experimental Results	253
8.3.3.1	Effect of Water Removal	253
8.3.3.2	Co-current versus Countercurrent	254
8.3.3.3	Selectivity	255

8.3.3.4	Acid Excess	257
8.3.4	Conclusions	258
8.4	Comparison of Different Internals	259
8.4.1	Film-flow Monoliths	259
8.4.2	Monoliths versus DX® and katapak-S®	260
8.4.2.1	Activity	260
8.4.2.2	Selectivity	261
8.5	Conclusions and Future Trends	262
	Acknowledgments	263
	Symbols	263
	References	264
9	Reactive Absorption	265
	<i>Eugeny Y. Kenig and Andrzej Górak</i>	
9.1	Introduction	265
9.2	Reactive Absorption Equipment	267
9.3	Modeling Concept	270
9.3.1	General Aspects	270
9.3.2	Equilibrium Stage Model	270
9.3.3	HTU/NTU-concept and Enhancement Factors	271
9.3.4	Rate-based Stage Model	272
9.3.4.1	Balance Equations	273
9.3.4.2	Mass Transfer and Reaction Coupling in the Fluid Film	274
9.4	Model Parameters	276
9.4.1	Thermodynamic Equilibrium	276
9.4.2	Chemical Equilibrium	277
9.4.3	Physical Properties	278
9.4.4	Mass Transport and Fluid Dynamics Properties	280
9.4.5	Reaction Kinetics	280
9.5	Case Studies	282
9.5.1	Absorption of NO _x	283
9.5.1.1	Chemical System	283
9.5.1.2	Process Set-up	284
9.5.1.3	Modeling Peculiarities	284
9.5.1.4	Model Parameters	285
9.5.1.5	Results	286
9.5.2	Coke Gas Purification	286
9.5.2.1	Chemical System	286
9.5.2.2	Process Set-up	289
9.5.2.3	Modeling Peculiarities	290
9.5.2.4	Model Parameters	290

9.5.2.5	Results	291
9.5.2.6	Dynamic Issues	292
9.5.3	CO ₃ Absorption by Aqueous Amine Solutions	295
9.5.3.1	Chemical System	295
9.5.3.2	Process Set-up	296
9.5.3.3	Modeling Peculiarities	296
9.5.3.4	Model Parameters	297
9.5.3.5	Results	298
9.5.4	SO ₂ Absorption into Aqueous NaHCO ₃ /Na ₂ CO ₃ Solutions	299
9.5.4.1	Chemical System	299
9.5.4.2	Process Set-up	300
9.5.4.3	Modeling Peculiarities	301
9.5.4.4	Model Parameters	301
9.5.4.5	Results	302
9.6	Conclusions and Outlook	304
	Acknowledgments	305
	Symbols	305
	References	307

10 Reactive Extraction: Principles and Apparatus Concepts 313

Hans-Jörg Bart

10.1	Introduction	313
10.1.1	Physical Extraction	313
10.1.2	Reactive Extraction	314
10.1.3	Additives	319
10.2	Phase Equilibria	321
10.3	Reactive Mass Transfer	323
10.4	Hydrodynamics	328
10.5	Conclusions	332
	Acknowledgments	333
	References	334

11 Development of Reactive Crystallization Processes 339

*Christianto Wibowo, Vaibhav V. Kelkar,
Ketan D. Samant, Joseph W. Schroer and Ka M. Ng*

11.1	Introduction	339
11.2	Workflow in Process Development	339
11.3	Process Synthesis	341
11.4	Reactive Phase Diagrams	344
11.4.1	Projections and Canonical Coordinates	344
11.4.2	High-Dimensional Phase Diagrams	346

11.5	Kinetic Effects	351
11.5.1	Reactive Crystallization with a Solid Reactant	351
11.6	Asymmetric Transformation of Enantiomers	353
11.6.1	Base Case (BC)	353
11.6.2	Seeded Crystallization (SC)	354
11.6.3	Seeded Crystallization with Racemization (SR)	356
11.7	Conclusions	357
	Acknowledgments	357
	References	357
12	Analysis and Experimental Investigation of Catalytic Membrane Reactors	359
	<i>Andreas Seidel-Morgenstern</i>	
12.1	Introduction	359
12.2	Basic Aspects of Chemical Reaction Engineering	359
12.2.1	Reaction Rates	360
12.2.2	Conversion as a Function of Rate Laws and Feed Composition	361
12.2.3	Selectivity and Yield	364
12.3	Mass Transfer through Membranes	366
12.4	Kinetic Compatibility in Membrane Reactors	368
12.5	Example 1: Product Removal with Membranes ("Extractor")	369
12.5.1	Model Reaction, Procedures and Set-up	370
12.5.2	Reaction Rates	370
12.5.3	Fixed-bed Reactor Experiments	372
12.5.4	Mass Transfer through the Membrane	373
12.5.5	Membrane Reactor Experiments and Modeling	374
12.5.6	Evaluation of the Extractor-type of Membrane Reactor	376
12.6	Example 2: Reactant Dosing with Membranes ("Distributor")	378
12.6.1	Model Reaction, Set-ups and Procedures	380
12.6.1	Reaction Rates	381
12.6.2	Fixed-bed and Membrane Reactor Experiments	382
12.6.3	Theoretical Analysis	383
12.7	Summary and Conclusions	385
	Acknowledgments	386
	References	387

Part III Integration of Mechanical Operations and Chemical Reactions 391**13 Reactive Extrusion for Solvent-Free Processing: Facts and Fantasies 393***Leon P. B. M. Janssen*

Abstract 393

- 13.1 Introduction 393
- 13.2 Advantages and Disadvantages 394
- 13.3 Main Reactions in Extruders 395
- 13.4 Extruder Types 396
- 13.5 Kinetic Considerations 398
- 13.6 Heat Transfer and Thermal Instabilities 401
- 13.7 Instabilities 402
- 13.8 Conclusions 405
- References 406

14 Reactive Comminution 407*Ulrich Hoffmann, Christian Horst and Ulrich Kunz*

- 14.1 Introduction 407
- 14.2 Mechanical Comminution of Solids 408
 - 14.2.1 Reactivity of Mechanically Activated Solids 413
- 14.3 Equipment and Processes 415
 - 14.3.1 Milling Designs 415
 - 14.3.1.1 Crushers 415
 - 14.3.1.2 Cutting Mills 415
 - 14.3.1.3 Roller and Ring-roller Mills 415
 - 14.3.1.4 Disk Attrition Mills 416
 - 14.3.1.5 Grinding Media Mills 416
 - 14.3.1.6 Impact Mills 419
 - 14.3.1.7 Jet Mills 420
 - 14.3.1.8 Pressure and Shear Devices 421
 - 14.3.1.9 Special Milling and Activation Devices 421
 - 14.3.1.10 Dry and Wet Grinding 422
 - 14.3.1.11 Machine Wear 422
 - 14.3.1.12 Energy Efficiency 422
 - 14.3.1.13 Solid Guidance 423
- 14.4 Applications 423
 - 14.4.1 Surface Area Creation 423
 - 14.4.2 Mechanical Activation 424
 - 14.4.2.1 Phase Transitions 424
 - 14.4.2.2 Enhanced Solubility of Minerals 425

14.4.2.3	Surface Cleaning	425
14.4.3	Mechanical Alloying	425
14.4.4	Simultaneous Reaction and Comminution	426
14.4.4.1	Solid–Solid Reactions	426
14.4.4.2	Catalyst Preparation	427
14.4.4.3	Solid–Gas Reactions	428
14.4.4.4	Solid–Liquid Reactions	429
14.4.4.5	Depolymerization Reactions	430
14.5	Conclusions	431
	References	431

15 Reactive Filtration 437

Thomas Rieckmann and Susanne Völker

15.1	Introduction	437
15.2	Separation of Particulates and Catalytic Reaction of Volatiles	438
15.2.1	Flue-gas Treatment	438
15.2.2	Biomass Gasification	440
15.3	Separation of Particulates and Reaction of Solids	441
15.3.1	Diesel Soot Abatement	441
15.3.1.1	Filter Types and Catalyst Performance	443
15.3.1.2	Formal Kinetics and Modeling	445
15.3.2	Filtration Combustion of Solid Fuels	447
15.3.3	Reaction Cyclone	448
15.4	Conclusions	449
	References	450

16 Reaction-Assisted Granulation in Fluidized Beds 453

*Matthias Ihlow, Jörg Drechsler, Markus Henneberg,
Mirko Peglow, Stefan Heinrich and Lothar Mörl*

16.1	Introduction	453
16.1.1	Gas Cleaning	453
16.1.2	Application of the Gas-solid Fluidized Bed	455
16.1.3	Modeling and Experimental Set-up	456
16.2	Modeling	460
16.2.1	Model Assumptions	461
16.2.2	Phase and Reaction Equilibrium	462
16.2.3	Mass and Energy Flows	463
16.2.3.1	Gas Balance	463
16.2.3.2	Suspension Balance	467
16.2.3.3	Gas–Liquid Phase Boundary	471
16.2.3.4	Particle Balance	474

16.2.3.5	Apparatus Wall Balance	477
16.2.3.6	Solution of the Equations	477
16.3	Experiments	479
16.3.1	Fluidized-bed Plant	479
16.3.2	Experiments of Absorption without Granulation of Solid (Reactive Absorption)	481
16.3.2.1	Experimental Realization	481
16.3.2.2	Influence of the Liquid Injection Rate	481
16.3.2.3	Influence of Ca/S Ratio	488
16.3.2.4	Influence of the Gas Inlet Temperature	493
16.3.2.5	Influence of Gas Mass Flow	495
16.3.2.6	Influence of the Particle Diameter	497
16.3.3	Experiments for Reactive Absorption with Overlapped Granulation of Solid	502
16.3.3.4	Experimental Realization	502
16.3.3.2	Batch Experiments	503
16.3.3.3	Continuous Experiments	510
16.3.4	Comparison between Measurement and Simulation	519
16.3.5	Simplified Stationary Balancing	519
16.4	Conclusions	523
	Symbols and Abbreviations	526
	References	529

Index	543
-------	-----

Preface

In the chemical industries, the pretreatment of educts, their chemical conversion into valuable products, and the purification of resulting product mixtures in downstream processes are carried out traditionally in sequentially structured trains of unit operations. In many cases, the performance of this classical chemical process structure can be significantly improved by an integrative coupling of different process units.

The integration of unit operations to form multifunctional processes very often gives rise to synergetic effects which can be technically exploited. By suitable process design, an efficient and environmentally benign process operation can be achieved. Possible advantages of process integration include:

- higher productivity;
- higher selectivity;
- reduced energy consumption;
- improved operational safety; and
- improved ecological harmlessness by avoidance of auxiliary agents and chemical wastes.

Due to the interaction of several process steps in one apparatus, the steady-state and the dynamic operating behavior of an integrated process unit is often much more complex than the behavior of single, non-integrated units. Therefore, suitable methods for the design and control must be developed and applied, ensuring optimal and safe operation of the considered integrated process.

The major objectives of current research activities in this highly interesting domain of chemical engineering are to develop new concepts for process integration, to investigate their efficiency, and to make them available for technical application. The importance of this field is reflected by the increasing number of articles in journals and book contributions that have been published during the past three decades (Fig. 1).

Among these published articles and books, some excellent reviews have appeared which focused on specific aspects of the process integration. Agar and Ruppel [1] were among the first to investigate the whole area of integration of heat-exchanging functions in chemical reactors, whilst Agar [2] later also surveyed other innovative integration concepts in chemical reactor engineering. According to the present editors' knowledge, the first review which covered a broader range of integration concepts including heat exchange, separation and also mechanical unit operations, was published in 1997 by Hoffmann and Sundmacher [3]. The cited works refer to integrated chemical processes as "multifunctional reactors", which is often used as a

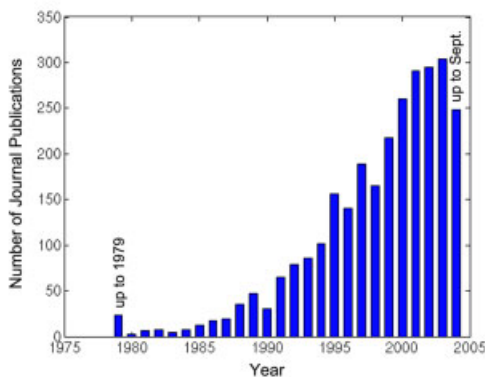


Fig. 1. Journal publications on integrated chemical processes according to the Science Citation Index.

synonym. Multifunctional reactors can be seen as a very important sub-class of the area of “process intensification” which was summarized by Stankiewicz and Moulin [4].

A comprehensive volume covering all aspects of integrated chemical processes including heat exchange, separations and mechanical unit operations is still missing, however, and as a consequence the present book was prepared to fill this gap. The book’s chapters have been authored by leading international experts, and provide overviews on the present state of knowledge and on challenging future issues.

The book is divided into three parts. Part I surveys concepts for heat-integrated chemical reactors, with special focus on coupling reactions and heat transfer in fixed beds and in fuel cells. Part II is dedicated to the conceptual design, control and analysis of chemical processes with integrated separation steps, whilst Part III focuses on how mechanical unit operations can be integrated into chemical reactors.

Part I:

Integration of Heat Transfer and Chemical Reactions

Chapters 1 to 3 discuss two recent and important applications of heat-integrated chemical reactions. Chapter 1, by Kolios et al., is concerned with high-temperature endothermic processes in *heat integrated fixed-bed reactors*. Emphasis is placed on reforming processes, which are widely used for the production of basic chemicals and fuels from fossil feed stocks. These processes require large amounts of heat at temperatures up to 1000 °C. In conventional solutions, only about half of the heat supplied at high temperatures is transferred into the endothermic reaction. Emerging applications such as decentralized hydrogen production for residential and mobile power generation require considerable improvement in specific productivity and thermal efficiency. Therefore, this topic is currently the subject of vivid research activities in industry and academia alike. Chapter 1 also includes an introduction to

the fundamentals of heat-integrated processes, an overview on recent trends in process and apparatus design, and an analysis of the state of the art, with special emphasis on the steam reforming of methane.

The focus in Chapters 2 and 3 is on *high-temperature fuel cells with internal reforming*. In particular, special attention is given to the Molten Carbonate Fuel Cell (MCFC) which is increasingly used for decentralized power generation. In Chapter 2, Heidebrecht and Sundmacher use a simple model of an MCFC to discuss the pros and cons of alternative reforming concepts in high-temperature fuel cells.

The *temperature management in a fuel cell stack* is a key issue in the operation of high-temperature fuel cells. In Chapter 3, prepared by Mangold and colleagues, it is shown that the temperature-dependence of the electrolyte's electrical conductivity is a potential source of instabilities, hot spots, and spatial temperature patterns.

Part II: Integration of Separation Processes and Chemical Reactions

Due to fact that chemical reactions typically do not deliver the desired product alone and that separation processes are always required, a wide range of efforts have long been undertaken to combine these two processes into a single apparatus. Although a comprehensive overview was published recently [5], nine chapters of the present book describe and discuss the possibilities of integrating separation processes and chemical reactions.

In Chapter 4, Sundmacher et al. – in the first contribution – analyze in detail the thermodynamic and kinetic effects relevant to an understanding of *reactive distillation processes*. Although a comprehensive volume on this type of process integration was published in 2003 [6], Chapter 4 focuses on the *a priori* determination of products that can be obtained using such processes.

In exploiting the equilibrium theory, Kienle and Grüner present in Chapter 5 a general analysis of the development and propagation of *nonlinear waves* in reaction separation processes. Besides considering reactive distillation as one example, these authors also analyze reactive chromatography.

In Chapter 6, Morbidelli et al. describe *chromatographic separations combined with chemical reactions*, the focus of their contribution being to present possibilities of performing such processes in a continuous manner.

An analysis of reactors where *adsorbents* are used as a *regenerative source or sink* for one or several of the reactants is discussed systematically by Agar, in Chapter 7.

In cases where reactive distillation cannot be applied because some of the reactants are temperature-sensitive, *reactive stripping* might be an efficient alternative, and the current state of the application of this technology is reviewed by Kapteijn and colleagues in Chapter 8.

Another powerful concept is to combine *absorption processes with chemical reactions*, and a large number of possible concepts for this approach is presented in Chapter 9 by Kenig and Górák.

In addition, *extraction processes* can be performed with reacting species, and several advantages of this technique may be realized compared to conventional consecutive processes, as discussed by Bart in Chapter 10.

Based on a thorough analysis of *reactive crystallization*, Ng and colleagues, in Chapter 11, demonstrate that such integrated processes can also be performed efficiently with solid phases involved.

In the final chapter of Part II, Seidel-Morgenstern presents two examples of how *membrane reactors* might become an alternative to conventional technology.

Part III: Integration of Mechanical Unit Operations and Chemical Reactions

The last four chapters of the book are dedicated to the successful combination of chemical reactions and mechanical process operations. In Chapter 13, Janssen elucidates that *reactive extrusion* has emerged from a scientific curiosity to an industrial process. Nonlinear effects in this process can give rise to instabilities that are of thermal, hydrodynamic, or chemical origin.

In Chapter 14, Hoffmann and colleagues provide a survey on the status and directions of *reactive comminution*. In this type of process integration, mechanical stress exerted in mills is used to enhance the chemical reactions of solids with fluids. Simultaneously, chemical reactions can generate cracks in solid particles and thereby enhance their comminution.

Filtration and chemical reactions can be usefully integrated in order to separate diesel soot particles efficiently from motor exhaust gases, and this is illustrated by Rieckmann and Völker in Chapter 15, together with a series of other examples of reactive filtration processes which are realized in the chemical industries.

In the final chapter, Mörl and coworkers analyze the complex interaction of particle *granulation and/or agglomeration with chemical reactions* in fluidized beds. For the description of the particle property distribution, a population balance approach is recommended which is mathematically challenging but which provides valuable insight into the steady-state and dynamic process operating behavior.

The Book's History, and the Editors' Acknowledgments

The present book is the outcome of the International Max Planck Symposium on Integrated Chemical Processes held in Magdeburg, Germany, on 22–24 March, 2004. At this symposium, renowned scientists met to discuss the current state and future trends in the field of integrated chemical processes. The conference was organized by this book's editors and their colleagues at the Max Planck Institute for Dynamics of Complex Technical Systems, with financial support from the Kompetenznetz Verfahrenstechnik Pro3 e.V. in Germany, which is gratefully acknowledged.

The present editors wish to thank their colleagues Kristin Czyborra, Anett Raasch, and Carolin Apelt for their excellent support in organizing the symposium, and in

collecting the manuscripts which form the basis of this book. Last – but not least – we are thankful to Dr. Hubert Pelc and Rainer Münz from Wiley-VCH for their helpful assistance during the book's preparation.

Magdeburg, Germany
February 2005

Kai Sundmacher, Achim Kienle,
Andreas Seidel-Morgenstern

References

1. D. W. Agar, W. Ruppel, Multifunktionelle Reaktoren für die heterogene Katalyse, *Chem. Ing. Tech.* **1988**, *60*, 731–741.
2. D. W. Agar, Multifunctional Reactors: Old Preconceptions and New Dimensions, *Chem. Eng. Sci.* **1999**, *54*, 1299–1305.
3. U. Hoffmann, K. Sundmacher, Multifunktionale Reaktoren, *Chem.-Ing.-Tech.* **1997**, *69*, 613–622.
4. A. I. Stankiewicz, J. A. Moulin, Process Intensification, *Chem. Eng. Progress*, **2000**, *Jan.*, 22–34.
5. S. Kulprathipanja, (Ed.) *Reactive Separation Processes*, Taylor & Francis, New York, 2002.
6. K. Sundmacher, A. Kienle, (Eds.), *Reactive Distillation, Status and Future Directions*, Wiley-VCH, Weinheim, 2003.

List of Contributors

Editors

Prof. Dr.-Ing. Achim Kienle
Max Planck Institute for Dynamics of
Complex Technical Systems
Sandtorstr. 1
39106 Magdeburg
Germany

and

Otto-von-Guericke-University Magdeburg
Chair for Automation/Modeling
Universitätsplatz 2
39016 Magdeburg
Germany

Prof. Dr.-Ing. Andreas Seidel-Morgenstern
Max Planck Institute for Dynamics of Complex
Technical Systems
Sandtorstr. 1
39106 Magdeburg
Germany

and

Otto-von-Guericke-University Magdeburg
Chair of Chemical Process Engineering
Universitätsplatz 2
39016 Magdeburg
Germany

Prof. Dr.-Ing. Kai Sundmacher
Max Planck Institute for Dynamics of Complex
Technical Systems
Sandtorstr. 1
39106 Magdeburg
Germany

and

Otto-von-Guericke-University Magdeburg
Process Systems Engineering
Universitätsplatz 2
39106 Magdeburg
Germany

Authors

Prof. Dr. David W. Agar
University of Dortmund
Institute of Chemical Reaction Engineering
Department of Biochemical and
Chemical Engineering
Emil-Figge-Str. 70
44227 Dortmund
Germany

Prof. Dr. Hans-Jörg Bart
Technische Universität Kaiserslautern
Lehrstuhl für Thermische
Verfahrenstechnik
Gottlieb-Daimler-Str.
67663 Kaiserslautern
Germany

Jörg Drechsler
AVA – Anhaltinische Verfahrens- und
Anlagentechnik Ingenieurgesellschaft
Henneberg & Partner
Steinfeldstr. 5
39176 Barleben
Germany

Prof. Dr.-Ing. Gerhart Eigenberger
University of Stuttgart
Institute for Chemical Process Engineering
Böblinger Str. 72
70199 Stuttgart
Germany

Bernd Glöckler
University of Stuttgart
Institute for Chemical Process Engineering
Böblinger Str. 72
70199 Stuttgart
Germany

Prof. Dr. Andrzej Górak
University of Dortmund
Department of Biochemical and
Chemical Engineering
Emil-Figge-Str. 70
44227 Dortmund
Germany

Achim Gritsch
University of Stuttgart
Institute for Chemical Process Engineering
Böblinger Str. 72
70199 Stuttgart
Germany

Stefan Grüner
University of Stuttgart
Institute for System Dynamics and
Control Engineering
Pfaffenwaldring 9
70569 Stuttgart
Germany

Achim K. Heibel
Delft University of Technology
Reactor and Catalysis Engineering
Julianalaan 136
2628 BL Delft
The Netherlands

Dr.-Ing. Peter Heidebrecht
Otto-von-Guericke-University Magdeburg
Process Systems Engineering
Universitätsplatz 2
39106 Magdeburg
Germany

Jun.-Prof. Dr.-Ing. Stefan Heinrich
Otto-von-Guericke-University Magdeburg
Institute of Process Equipment and
Environmental Technology
Universitätsplatz 2
39106 Magdeburg
Germany

Dr.-Ing. Markus Henneberg
AVA – Anhaltinische Verfahrens- und Anlagentechnik
Ingenieurgesellschaft Henneberg & Partner
Steinfeldstr. 5
39176 Barleben
Germany

Prof. Dr. Ulrich Hoffmann
Technische Universität Clausthal
Institut für Chemische
Verfahrenstechnik
Leibnizstr. 17
38678 Clausthal-Zellerfeld
Germany

Dr. Christian Horst
Technische Universität Clausthal
Institut für Chemische Verfahrenstechnik
Leibnizstr. 17
38678 Clausthal-Zellerfeld
Germany

Yuan-Sheng Huang
Max Planck Institute for Dynamics of Complex
Technical Systems
Sandtorstr. 1
39106 Magdeburg
Germany

Dr.-Ing. Matthias Ihlow
AVA – Anhaltinische Verfahrens- und
Anlagentechnik
Ingenieurgesellschaft Henneberg & Partner
Steinfeldstr. 5
39176 Barleben
Germany

Prof. Dr. Leon P.B.M. Janssen
University of Groningen
Department of Chemical Engineering
Nijenborgh 4
9747 AG Groningen
The Netherlands

Prof. Dr. Freek Kapteijn
Delft University of Technology
Reactor and Catalysis Engineering
Julianalaan 136
2628 BL Delft
The Netherlands

Vaibhav V. Kelkar
ClearWaterBay Technologies Inc.
20311 Valley Blvd., Suite C
Walnut, CA 91789
USA

Dr. Eugeny Y. Kenig
University of Dortmund
Department of Biochemical and
Chemical Engineering
Emil-Figge-Str. 70
44227 Dortmund
Germany

Prof. Dr.-Ing. Achim Kienle
Max Planck Institute for Dynamics of
Complex Technical Systems
Sandtorstr. 1
39106 Magdeburg
Germany

and

Otto-von-Guericke-University Magdeburg
Chair for Automation/Modeling
Universitätsplatz 2
39016 Magdeburg
Germany

Dr.-Ing. Grigorios Kolios
Christ Pharma & Life Science AG
Hauptstr. 192
4147 Aesch
Switzerland

Mykhaylo Krasnyk
Max Planck Institute for Dynamics of
Complex Technical Systems
Sandtorstr. 1
39106 Magdeburg
Germany

Prof. Dr. Ulrich Kunz
Technische Universität Clausthal
Institut für Chemische Verfahrenstechnik
Leibnizstr. 17
38678 Clausthal-Zellerfeld
Germany

Dr.-Ing. Michael Mangold
Max Planck Institute for Dynamics of
Complex Technical Systems
Sandtorstr. 1
39106 Magdeburg
Germany

Prof. Dr. Marco Mazzotti
Swiss Federal Institute of Technology Zürich
Institut für Verfahrenstechnik
Sonneggstr. 3
8092 Zürich
Switzerland

Prof. Dr. Massimo Morbidelli
Swiss Federal Institute of Technology Zürich
Institut für Chemie- und
Bioingenieurwissenschaften
ETH-Hönggerberg, HCI-F
8093 Zürich
Switzerland

Prof. Dr.-Ing. habil. Dr. h. c. Lothar Mörl
Otto-von-Guericke-University Magdeburg
Faculty of Process and Systems Engineering
Institute of Process Equipment and Environmental
Technology
Universitätsplatz 2
39106 Magdeburg
Germany

Prof. Dr. Jacob A. Moulijn
Delft University of Technology
Reactor and Catalysis Engineering
Julianalaan 136
2628 BL Delft
The Netherlands

Prof. Dr. Ka M. Ng
Hong Kong University of Science and Technology
Department of Chemical Engineering
Clear Water Bay
Kowloon, Hong Kong
China

Mirko Peglow
Fraunhofer Institute for Factory Operation and
Automation IFF Magdeburg
Product Design and Modelling Group
Sandtorstr. 22
39106 Magdeburg
Germany

Dr. Zhiwen Qi
Max Planck Institute for Dynamics of
Complex Technical Systems
Sandtorstr. 1
39106 Magdeburg
Germany

Prof. Dr.-Ing. Thomas Rieckmann
University of Applied Sciences Cologne
Institute of Chemical Engineering and
Plant Design
Betzdorfer Str. 2
50679 Köln
Germany

Dr. Ketan D. Samant
ClearWaterBay Technology Inc.
20311 Valley Blvd., Suite C
Walnut, CA 91789
USA

Dr. Tilman J. Schildhauer
Delft University of Technology
Reactor and Catalysis Engineering
Julianalaan 136
2628 BL Delft
The Netherlands

Prof. Dr.-Ing. Dr. h. c. mult. Ernst-Ulrich
Schlünder (emeritus)
University of Karlsruhe
Institute of Thermal Process Engineering
Kaiserstr. 12
76128 Karlsruhe
Germany

Dr. Joseph W. Schroer
ClearWaterBay Technology Inc.
20311 Valley Blvd., Suite C
Walnut, CA 91789
USA

Prof. Dr.-Ing. Andreas Seidel-Morgenstern
Max Planck Institute for Dynamics of
Complex Technical Systems
Sandtorstr. 1
39106 Magdeburg
Germany

and

Otto-von-Guericke-University Magdeburg
Chair of Chemical Process Engineering
Universitätsplatz 2
39016 Magdeburg
Germany

Guido Ströhlein
Swiss Federal Institute of Technology Zürich
Institut für Chemie- und
Bioingenieurwissenschaften
ETH-Hönggerberg, HCI-F
8093 Zürich
Switzerland

Prof. Dr.-Ing. Kai Sundmacher
Max Planck Institute for Dynamics of
Complex Technical Systems
Sandtorstr. 1
39106 Magdeburg
Germany

and

Otto-von-Guericke-University Magdeburg
Process Systems Engineering
Universitätsplatz 2
39106 Magdeburg
Germany

Dr.-Ing. Susanne Völker
42 Engineering – Chemical Engineering
Consulting Services
von-Behring-Str. 9
34260 Kaufungen
Germany

Dr. Christianto Wibowo
ClearWaterBay Technology Inc.
20311 Valley Blvd., Suite C
Walnut, CA 91789
USA

Dr. Archis A. Yawalkar
Delft University of Technology
Reactor and Catalysis Engineering
Julianalaan 136
2628 BL Delft
The Netherlands

Part I

Integration of Heat Transfer and Chemical Reactions

1

Enhancing Productivity and Thermal Efficiency of High-Temperature Endothermic Processes in Heat-Integrated Fixed-Bed Reactors

Grigorios Kolios, Achim Gritsch, Bernd Glöckler and Gerhart Eigenberger

Abstract

High-temperature endothermic processes (e.g., reforming of hydrocarbons) are widely utilized in the production of basic chemicals and fuels from fossil feedstocks. These processes require large amounts of heat at temperatures up to 1000 °C. In conventional solutions, only about half of the high-temperature heat supplied is transferred into the endothermic reaction. Emerging applications such as decentralized hydrogen production for residential and mobile power generation require considerable improvement in specific productivity and thermal efficiency. Thus, this topic is currently the subject of exciting research activities in industry and academia. This chapter provides an introduction to the fundamentals of heat-integrated processes, an overview on conceptual trends in process and apparatus design, and an analysis of the state of the art, with emphasis on steam reforming of methane.

1.1

Introduction

Endothermic high-temperature processes stand at the beginning of the chemical production chain – for example, syngas is produced mainly through steam reforming of naphtha or natural gas, ethylene and propylene through steam cracking, and styrene through dehydrogenation of ethylbenzene. These processes are usually conducted in large furnaces and belong naturally to the largest fuel consumers. At the same time, they have a significant heat surplus since typically only about 50 % of the heat generated is consumed by the endothermic reaction. In large product- and energy-integrated chemical sites, waste heat can be utilized in subsequent processes. However, rigid thermal coupling throughout the plant imposes constraints regarding the heat balance of individual processes and requires a considerable overhead in order to adjust plant-wide optimal operating conditions. This problem could be significantly relaxed by reducing the surplus of the heat exporters. This is one strong incentive for enhancing the thermal efficiency of endothermic high-temperature processes.

Two emerging trends endorse the concept of heat-integrated processes: first, the production of basic chemicals is moved close to oil and gas wells where crude oil or natural gas is processed in large stand-alone units [1]. Second, fuel cell systems require on-site and on-demand hydrogen production from primary fuels (i.e., natural gas, liquid hydrocarbons or alcohols) [2]. Net heat generation in these processes is equivalent to raw material and energy loss, and is therefore undesirable.

While many publications in the field of heat-integrated processes focus on specific processes such as dehydrogenation of paraffins or hydrogen production [3–5], this chapter is more focused on general conceptual trends in process and apparatus design.

1.2

Heat-Integrated Processes for Endothermic Reactions

The intended purpose of heat-integrated processes for endothermic reactions is illustrated by the example of methane steam reforming for hydrogen generation, which is of high practical relevance [6] and features typical characteristics of the considered process class. The reaction is given by the following stoichiometric equation:



Figure 1.1 shows the heat fluxes required at different process stages for the generation of H_2 equivalent to 1 kW combustion enthalpy based on the lower heating value of hydrogen (LHV, H_2). Typically, the feed composition of the technical process corresponds to a steam-to-carbon molar ratio of $\text{S}:\text{C} = 3:1$. The reaction temperature is determined by chemical equilibrium. The heat consumption of the steam-reforming reaction is equivalent to around 30 % of the lower heating value of the produced hydrogen. The amount of heat required for heating the gaseous feed to reaction tem-

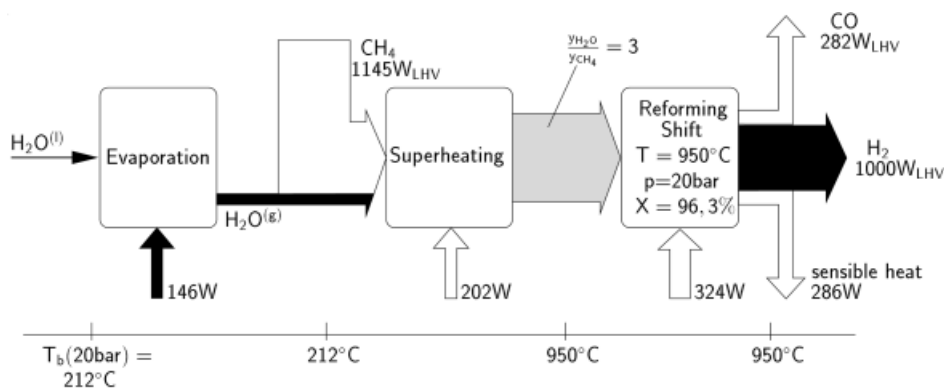


Fig. 1.1. Heat fluxes for hydrogen generation by steam reforming of methane.

perature corresponds to almost 20 % of the heat of combustion. On the other hand, a considerable amount of sensible heat contained in the product stream is usable for feed preheating.

Heat-integrated processes comprise two additional functions besides the main (endothermic) reaction: process heat generation and heat recovery. As shown above, both aspects are equally important, since the heat of reaction and the heat required for feed preheating are in the same range. Figure 1.2 shows, schematically, two different configurations of heat-integrated processes. The process comprises two thermally interconnected reaction stages for the endothermic reaction and for the combustion. Heat exchangers on both sides perform heat recovery by coupling feed preheating with product cooling. In the first configuration (Fig. 1.2(a)) the endothermic reaction mixture and the combustion gas flow countercurrently through all process stages such that the hot effluent from the exothermic reaction is used to heat up the cold feed for the endothermic reaction, and vice versa. In the second configuration (Fig. 1.2(b)), thermal contact between the two process streams is limited to the reaction stage, while heat recovery is separated between the flows of the exothermic and the endothermic reactions.

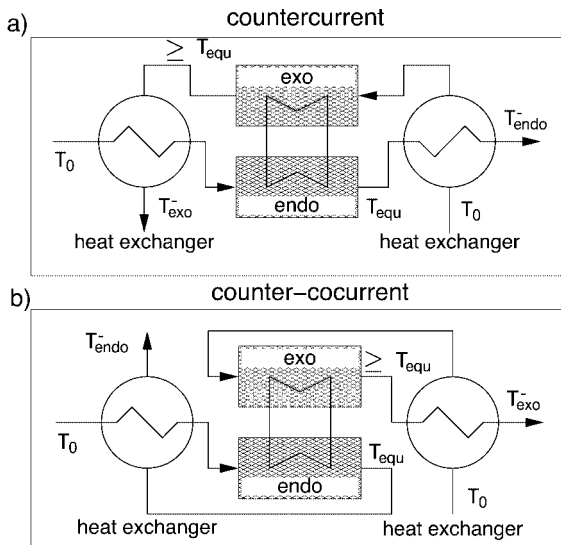


Fig. 1.2. Schematic flow configurations of heat-integrated processes for coupling endothermic and exothermic reactions. (a) Countercurrent flow of process streams. (b) Cocurrent flow of the process streams in the reactor stages and heat recovery in separate circuits.

1.2.1

Optimality Conditions**1.2.1.1 Efficiency of Heat Recovery**

Analysis of the overall heat balance yields basic conditions for optimal heat recovery. The optimizing condition is minimization of heat loss. The feed temperatures of the two process streams, T_0 , and the outlet temperature of the endothermic stage, T_{equ} , are fixed (Fig. 1.2) where T_{equ} is the temperature required for the desired conversion under equilibrium conditions. Obviously, T_{equ} is also a lower limit of the temperature in the combustion stage. The performance of the heat exchangers is given by the mean heat transfer coefficient k_h and the heat exchange area A . Both heat exchangers are assumed to be identical. The mass flow rate of the endothermic mixture and the combustion gas is \dot{M}_{endo} and \dot{M}_{exo} , respectively. Crucial parameters for the efficiency of heat recovery are the heat capacity ratio of the process streams (h) and the number of transfer units of the heat exchangers (NTU):

$$h = \frac{\left(\dot{M} c_p \right)_{endo}}{\left(\dot{M} c_p \right)_{exo}} \quad (1)$$

$$NTU_{endo} = \frac{k_h A}{\left(\dot{M} c_p \right)_{endo}} ; NTU_{exo} = \frac{k_h A}{\left(\dot{M} c_p \right)_{exo}} = \frac{NTU_{endo}}{h} \quad (2)$$

Taking the amount of heat required for bridging the temperature gap ($T_{equ} - T_0$) for the endothermic mixture as a reference, the normalized heat loss is given by the following expression:

$$loss_{norm} = \frac{(T_{endo}^- - T_0) + h (T_{exo}^- - T_0)}{T_{equ} - T_0} \quad (3)$$

A value of $loss_{norm} = 1$ indicates that the total heat loss via the exit streams of the exothermic and the endothermic stage is equal to the amount of heat required to heat up the feed of the endothermic stage about $\Delta T = T_{equ} - T_0$. $loss_{norm}$ can be expressed explicitly as a function of h and NTU_{endo} taking into account the theory of ideal countercurrent heat exchangers [7].

At this point, a distinction is required between the two configurations shown in Fig. 1.2. In the countercurrent configuration the heat capacity fluxes of the heat exchanging streams are generally differing, whereas in the counter-cocurrent configuration they are equal to each other. Hence, we obtain:

$$loss_{norm} = (h-1) \frac{h + e^{\frac{h-1}{h} NTU_{endo}}}{h - e^{-\frac{h-1}{h} NTU_{endo}}} \quad \text{for countercurrent configuration} \quad (4)$$

$$loss_{norm} = \frac{1}{NTU_{endo} + 1} + \frac{h^2}{NTU_{endo} + h} \quad \text{for counter-cocurrent configuration (5)}$$

Figure 1.3 illustrates the dependence of $loss_{norm}$ on h and NTU_{endo} for both configurations.

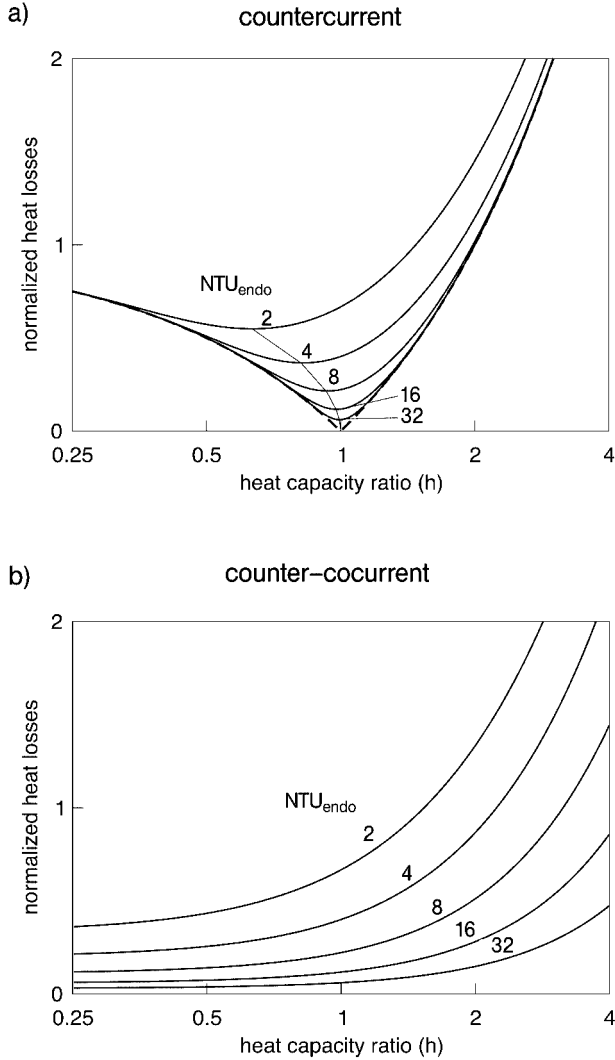


Fig. 1.3. The effect of heat exchanger performance, NTU , and heat capacity ratio, h , on the normalized heat loss for heat-integrated processes in (a) countercurrent and (b) counter-cocurrent flow configuration.

For the countercurrent configuration the optimal heat capacity ratio converges asymptotically to $h = 1$ with increasing NTU values. Even for an ideal heat exchanger ($NTU \rightarrow \infty$), small deviations from the optimal heat capacity ratio cause significant heat losses. On the other hand, heat losses could be minimized with decreasing heat capacity ratio and increasing NTU values for the counter-cocurrent configuration. In this case the heat recovery becomes complete for an ideal heat exchanger ($NTU \rightarrow \infty$) independent of the heat capacity ratio h .

1.2.1.2 Temperature Control

Conventional steam reformers are furnaces containing tubes filled with reforming catalyst. Radiation burners, which are usually installed at the top and the bottom of the furnace, generate the process heat (Fig. 1.4(a)). Figure 1.4(b) shows a schematic lateral temperature profile inside a single reformer tube.

Clearly, in the considered high-temperature processes the process conditions are defined mainly through the thermal stability of the tubes. A considerable temperature difference across the tube wall is required as the driving force for the heat supply to the reforming reaction. The main heat transfer resistances occur at the inner and outer surface of the tube wall.

The impact of heat transfer limitations is illustrated with a generic example describing a best-case scenario (Fig. 1.5). The allowed maximum temperature of the reformer tube is assumed at 950 °C. Hence, the wall temperature and inlet temperature of the reaction gas are set to 950 °C. The reforming reaction is assumed to be instantaneous – that is, at each axial position conversion is set equal to the equilibrium conversion at the respective temperature $X_{equ}(T)$. Dissipative effects (i.e.,

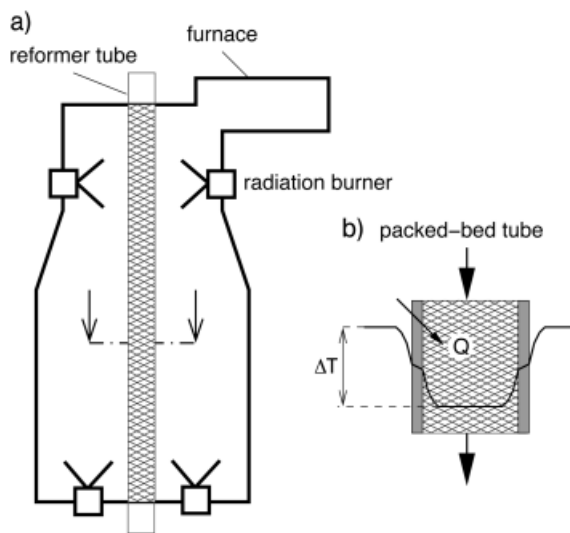


Fig. 1.4. Simplified scheme of an industrial steam reformer furnace. (a) Furnace with radiation burners adapted from [6]. (b) Lateral temperature profile inside a single reformer tube.

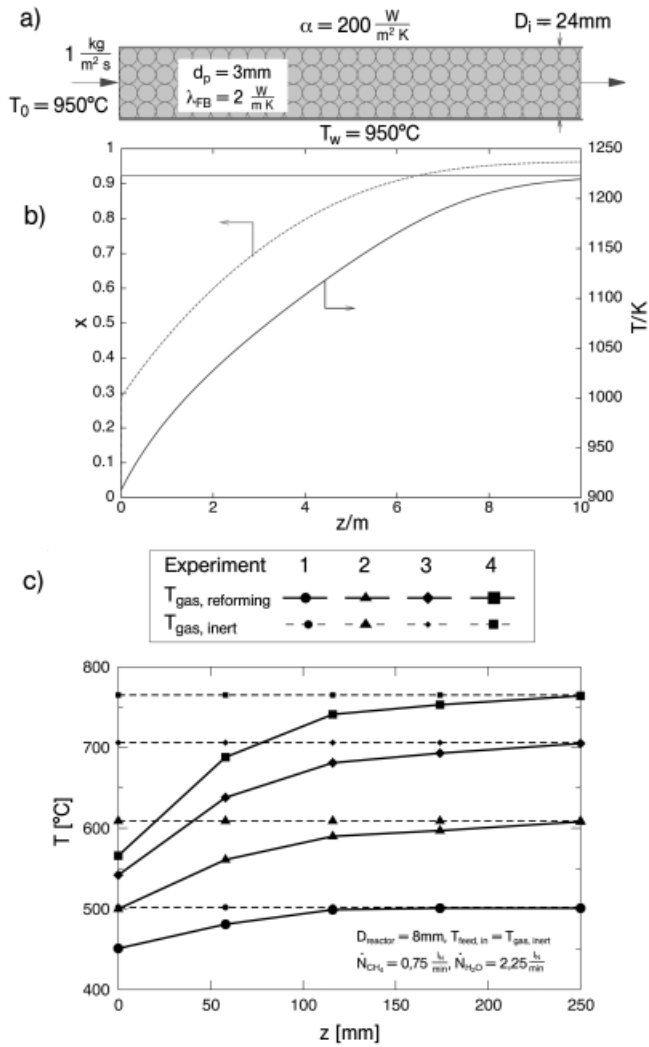


Fig. 1.5. Effect of heat transfer limitation in industrial steam reformers. (a) Scheme of a single catalytic fixed-bed reformer tube with typical heat transfer and operating parameters. (b) Computed temperature profile (solid line) and equilibrium conversion profile (dashed line) in flow direction for a tubular reformer. (c) Measured fixed-bed temperature profiles at different wall temperatures in a tubular reformer ($D_i = 8 \text{ mm}$) filled with spherical catalyst pellets ($d_p = 1.5 \text{ mm}$).

diffusion and heat conduction) are neglected in the axial direction. Finally, we assume a uniform fixed-bed temperature in radial direction. Based on this model the axial temperature profile of the fixed bed is given by the following relationship [8]:

$$\dot{M} c_p \left(1 + |\Delta T_{ad}| \frac{dX_{equ}}{dT} \right) \frac{dT_c}{dz} = \alpha_w \frac{4}{D_i} (T_w - T_c) \quad (6)$$

Figure 1.5(b) shows the axial temperature profile of the packing for a favorable heat transfer coefficient at the tube wall of $\alpha_w = 200 \text{ W/m}^2/\text{K}$ and a small tube diameter of $D_i = 25 \text{ mm}$. The temperature at the inlet cross-section drops immediately to the equilibrium value corresponding to the feed conditions. Further downstream, the temperature increases gradually and approaches asymptotically the wall temperature. A reactor length of approximately 10 m would be necessary in order to reach an equilibrium conversion of 95 %. According to this result, heat transfer limitations between the catalyst packing and the heating tube wall result in poor catalyst utilization. This has been verified experimentally with a laboratory-scale reactor of 8 mm inner diameter (Fig. 1.5(c)). Despite the significantly larger specific heat transfer area of this tube, a temperature drop of up to 200 K has been observed at the entrance to the catalytic bed. Similar behavior – although not especially extreme – is observed with endothermic reactions running under milder conditions. For example, during styrene synthesis in a 2.5-cm tube a temperature difference up to 30 K has been measured between the reactor wall and its center [9]. This heat transfer limitation could be overcome by depositing the catalyst directly on the surface of the tube wall – that is, by using a wall reactor concept. Charlesworth et al. [10] estimated that such a reactor would be two orders of magnitude smaller than a conventional steam reformer.

The above considerations indicate that, independent of implementation details, the space–time yield of endothermic reactions could be significantly enhanced by shifting the reaction site to the heat-exchanging surfaces. This intention has led to the production of a large variety of multifunctional reactor concepts for coupling endothermic and exothermic reactions. In the following section the state of the art in this area will be discussed for selected examples.

1.3

Multifunctional Reactor Concepts

Figure 1.6 contains a classification of multifunctional reactor concepts with integrated heat recovery for coupling endothermic and exothermic reactions [11]. Coupling of methane steam reforming with methane combustion is displayed as a representative example. Equivalent processes can be created based on recuperative heat exchange in a stationary operation mode (left column) or based on regenerative heat exchange in a cyclic operation mode (right column).

The simultaneous mode is the simplest configuration where the feed streams of the endothermic mixture and the combustion gas are mixed and react

simultaneously in the same volume. The amount of oxygen is adjusted to generate sufficient excess heat, in order to compensate non-idealities of heat recovery. The simultaneous mode has been widely applied in technical processes, for example, in autothermal reforming or in oxidative dehydrogenation processes. However, mixing of the process streams imposes substantial constraints to the process conditions, since they must be compatible to the endothermic and to the exothermic subsystem. For example, high-pressure operation, often desirable for steam reforming, would

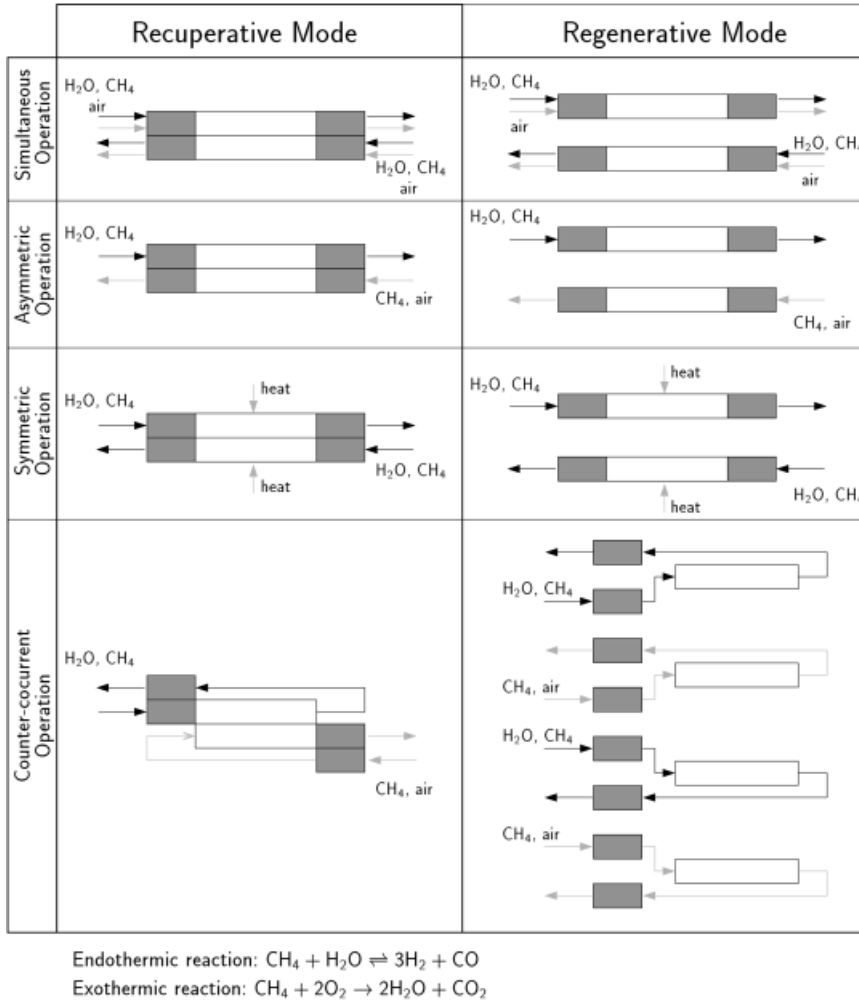


Fig. 1.6. Schematic classification of heat-integrated concepts for the representative example of coupling methane steam reforming and methane combustion.

require pressurization of the combustion air. Finally, dilution of the product by the exhaust gas stream complicates subsequent purification steps.

In the asymmetric mode of operation the endothermic and exothermic reactions take place separately either in different compartments (recuperative mode) or at different time intervals (regenerative mode). The attractiveness of the asymmetric mode is related to the fact that the separation of the process streams allows an individual tuning of the operating conditions for the endothermic and the exothermic subsystem.

The symmetric mode aims at combining the advantages of the simultaneous and the asymmetric mode: only the endothermic reaction takes place in the main reactor. The process heat is added through a hot, inert side stream (e.g., the effluent gas of an external combustion chamber). The side stream can be distributed along the reactor in order to adjust a specific temperature profile.

The counter-cocurrent concept features a modular design: it provides separate heat exchanger loops for heat recovery within the endothermic mixture and the combustion gas. Cocurrent flow of exothermic and endothermic process streams is principally favorable with respect to the controllability of heat release.

As indicated by this schematic representation, different configurations vary with respect to the degree of coupling between the process streams. The strongest coupling occurs in the simultaneous mode, where chemical and thermal interaction occurs between the process streams. In contrast to this, the counter-cocurrent concept features only thermal interaction between the process streams localized in the reactor stage.

As stated earlier in Section 1.2.1.1, equality of the heat capacity fluxes in the heat recovery sections is a crucial condition for efficient heat recovery. This condition is inherently fulfilled by the simultaneous and the counter-cocurrent concept. In the asymmetric concept the flow rates of the process streams must be adjusted accordingly. The requirement of equal heat capacity fluxes cannot be fulfilled in the symmetric concept due to the continuous side stream addition. However, besides these structural properties the design details are decisive for their specific performance and efficiency of individual solutions.

1.3.1

Regenerative Processes

Surprisingly, the majority of advanced heat-integrated reactor concepts employ a cyclic mode of operation with regenerative heat exchange. They have been proposed mainly for syngas and olefin production. Their potential field of application is in large chemical and petrochemical processes, where a compact reactor could replace a complex network of reactors and heat exchangers. The following survey reflects the classification introduced in Fig. 1.6.

1.3.1.1 Simultaneous Mode

A pioneering report on the simultaneous concept with integrated heat recovery proposes a reverse-flow mode of operation for syngas production from natural gas [12]. The process is implemented in an adiabatic fixed-bed reactor with inert end zones and a catalytically active section in the middle. The experiments confirm the feasibility of the concept. The results of this investigation, together with those of subsequent studies [13, 14], indicate that local excess temperatures up to 1500 °C are the major problem of this concept. One reason for this is the tendency for the reaction zones of combustion and reforming to separate from each other. Due to a preferential adsorption of oxygen on the catalyst surface, total oxidation of hydrocarbons is favored [15]. Steam reforming and the water-gas-shift reaction take off after complete depletion of oxygen. Additionally, ignition of homogeneous combustion is unavoidable if the temperature exceeds 600 °C. Coke formation in the heat-exchange zones has been identified as an additional reason for the temperature runaway. De Groot et al. [13] show that the major source of coke in the upstream section is methane cracking and the Boudouard equilibrium in the downstream section. The sudden ignition of accumulated coke may lead to extreme local temperature peaks.

1.3.1.2 Asymmetric Mode

The CATOFIN process developed by ABB-Lummus for dehydrogenation of C3–C4 paraffins [16, 17] can be considered as the prototype process of coupling endothermic and exothermic reactions. Figure 1.7 shows the process scheme in schematic form. Each cycle includes the production phase and two regeneration steps. The heat consumption of the endothermic reaction during the production phase is taken from the heat stored in the fixed bed. The thermal reservoir is restored by a superheated air purge during the second phase. In addition to convective heating, heat is generated through the combustion of carbonaceous deposits. Finally, hydrogen is passed over the fixed bed in order to convert the catalyst back to its reduced, active form, and this produces additional heat. A similar concept has been proposed for

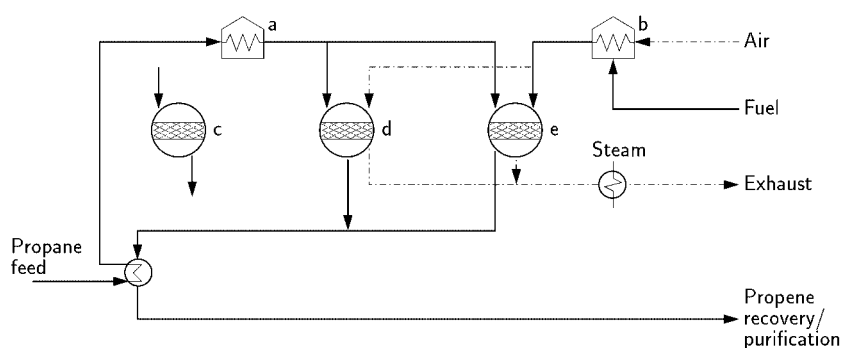


Fig. 1.7. CATOFIN process: dehydrogenation of propane adapted from Ullmann [54]. (a) charge heater; (b) air heater; (c) purge step; (d) production step; (e) regeneration step.

styrene synthesis [18]. The attraction of this concept results from the simplicity of the reactor – a simple adiabatic fixed-bed type – and the process-integrated regeneration of the catalyst – that is, the removal of carbonaceous deposits. Both, cocurrent flow and countercurrent flow have been investigated. The authors concluded that the reverse-flow mode is superior with regard to selectivity because the endothermic reaction runs along an increasing temperature profile. However, at a low air-to-hydrocarbon ratio the yield of the cocurrent-flow mode is higher than in the reverse-flow mode. This is due to a wrong-way phenomenon caused by coupling the endothermic reaction with countercurrent heat exchange.

Figure 1.8 illustrates the operating behavior of the reverse-flow CATOFIN process in the limit of equal heat capacities during reaction and regeneration cycle ($h = 1$). The inlet temperature of the regeneration gas is set approximately $|\Delta T_{ad}|$ above the inlet temperature of the endothermic reaction feed. In the periodic steady state, only two narrow zones close to both reactor ends contribute considerably to the conversion, while the major part of the fixed bed cools down to a temperature level well

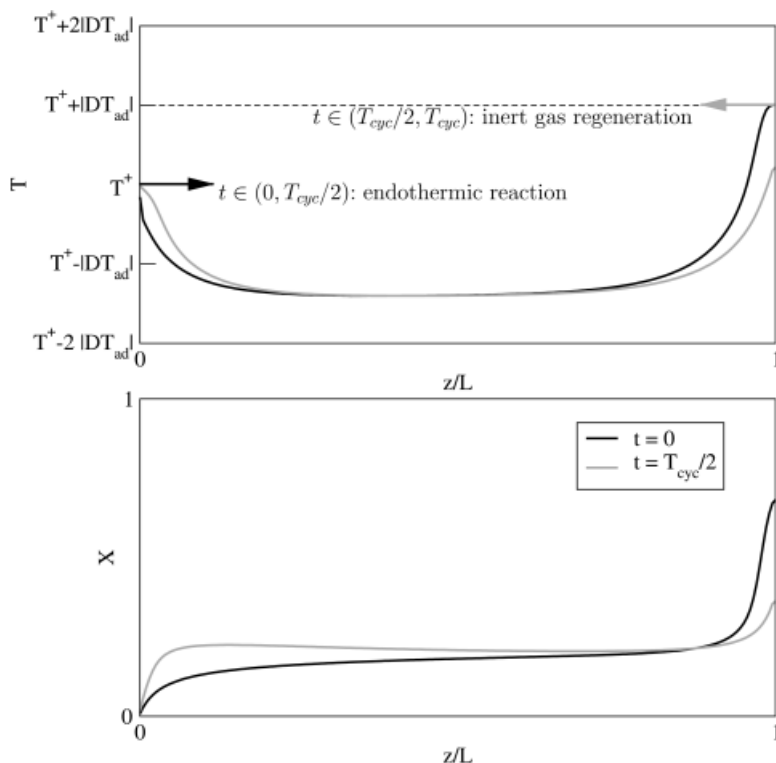


Fig. 1.8. Reverse-flow CATOFIN process at equal heat capacity fluxes during production and regeneration cycle: periodic temperature profiles (top) and conversion profiles (bottom) at the end of the endothermic semicycle ($t = t_{cyc}/2$) and the regeneration cycle ($t = 0$).

below the adiabatic temperature drop of the endothermic reaction. The accumulation of heat consumption of the endothermic reaction in the fixed bed is the reverse analogy to the accumulation of heat of weakly exothermic reactions in autothermal reactors [19]. This counter-intuitive effect indicates the complexity of coupling chemical reactions with countercurrent heat exchange.

The asymmetric reverse-flow operation mode as proposed by Levenspiel [20] is a straightforward extension of the CATOFIN process in order to integrate heat generation and heat recovery in the reactor. Its application in syngas production has been studied theoretically in a series of papers by Kulkarni and Duduković [21, 22]. This study demonstrates the feasibility of coupling methane steam reforming with methane combustion, but it also reveals the susceptibility of the process to severe overheating. Operation with preheated feed during the exothermic semicycle is proposed as a remedy.

A detailed analysis of an asymmetric process coupling styrene synthesis through dehydrogenation of ethylbenzene with combustion of hydrogen has been presented in [23]. Figure 1.9 shows typical periodic steady-state conditions of the process. One

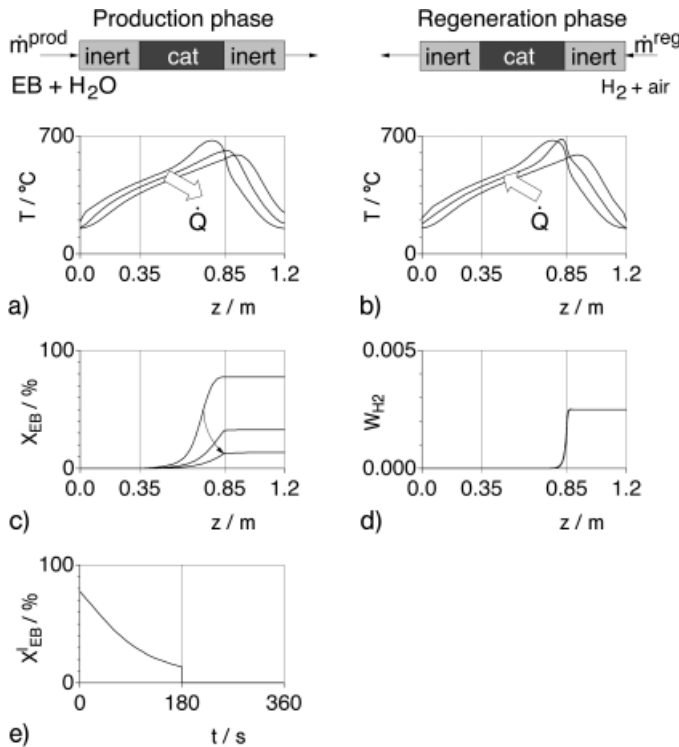


Fig. 1.9. Coupling of dehydrogenation of ethylbenzene to styrene and hydrogen combustion in a catalytic fixed-bed reverse flow reactor [9]. (a, b) Fixed-bed temperature profiles during production and regeneration cycle.

(c) Ethylbenzene conversion during production cycle. (d) Hydrogen weight fraction during regeneration cycle. (e) Ethylbenzene conversion during one period.

finding of this study is the importance of structuring the fixed bed in catalytic and inert sections. In particular, a sufficient length of the right inert zone is decisive for the establishment of a sufficient temperature level in the catalytic part. However, heat release within a narrow zone at the right end of the catalytic section implies inefficient heat storage. The initial temperature profile of the endothermic semicycle enables indeed high conversion at a high selectivity, but subsequently the temperature peak is shifted into the right inert section and becomes useless.

The major conclusions from the above-described studies are consistent: in the asymmetric mode of operation the reaction zones of the exothermic and endothermic reactions inherently repel each other, leading either to an extreme maximum temperature or to poor performance. A noncontinuous heat supply and production during every other semicycle cause obviously strong fluctuations of operation. Moreover, reasonable states of operation are attainable only with an excess of gas during the exothermic semicycle. This contradicts the condition of equal heat capacities for optimal heat recovery (see Section 1.2.1.1). For example, the heat loss in the case displayed in Fig. 1.9 is equal to the heat demand of the endothermic reaction. Different strategies have been assessed with regard to their potential to reduce hotspots during the exothermic semicycle and to improve thermal efficiency.

Latent heat storage

It is clear that temperature oscillations during heating–cooling cycles depend on the fixed-bed heat capacity. Figure 1.10 shows a simplified picture of the effect of phase change on the effective heat capacity of pure substances. Considerable amounts of

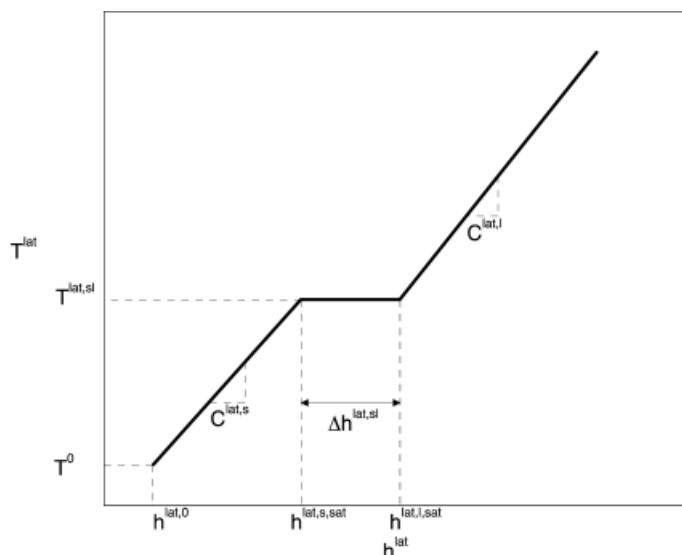


Fig. 1.10. Temperature plotted versus specific enthalpy of a pure substance undergoing phase changes (melting, solidifying).

heat can be stored at a constant temperature level at the melting point. The principle of latent heat storage is discussed in detail in Ref. [24]. Figure 1.11 illustrates the effect of adding aluminum-filled pellets to the catalytic fixed bed in the reverse-flow reactor for styrene synthesis. The melting temperature of aluminum (664 °C) is compatible with the operating temperature of the styrene catalyst. The amount of heat required for melting aluminum would be sufficient to heat-up the same amount of solid metal by approximately 400 K. In Fig. 1.11. the diagrams on the left-hand side show the conditions during the production cycle in the periodic steady

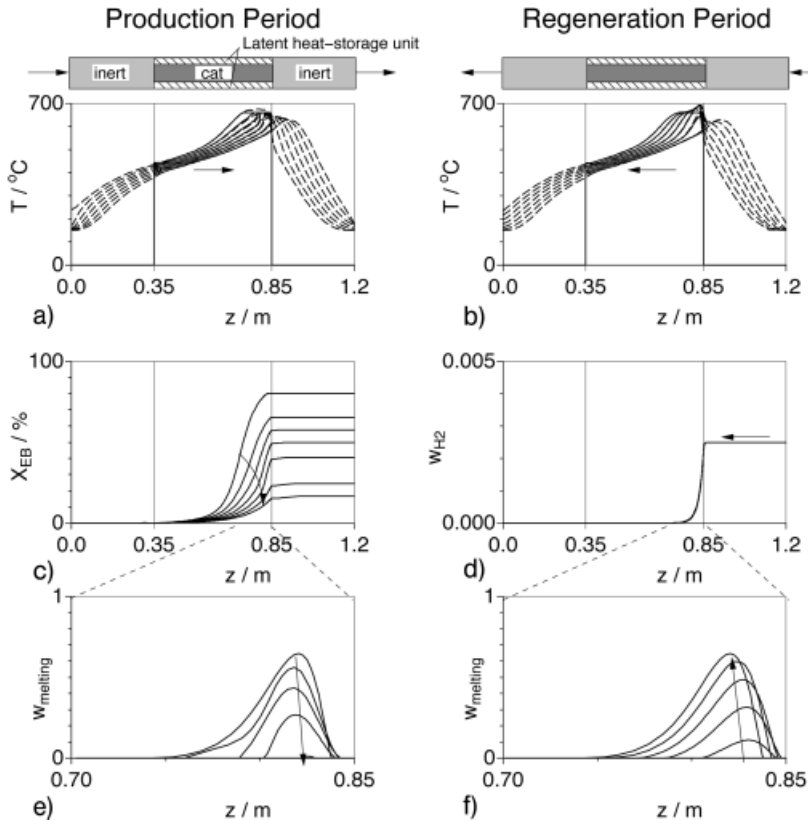


Fig. 1.11. Coupling of dehydrogenation of ethylbenzene to styrene and hydrogen combustion in a catalytic fixed-bed reverse-flow reactor with a mixed bed of catalytic pellets and aluminum powder (50:50) [23]. (a, b) Temperature profile of the latent heat storage (solid line) and of the fixed bed (dashed line) during production and regeneration periods. (c) Ethylbenzene conversion during the production cycle. (d) Hydrogen weight fraction during the regeneration cycle. (e, f) Molten fraction of the latent heat storage during production and regeneration period.

state. At the start of the endothermic semicycle, part of the aluminum has been molten and a temperature plateau has formed close to the right end of the catalytic zone. During the endothermic semicycle the fraction of molten aluminum shrinks. However, the maximum temperature remains at a constant level over a significant part of the semicycle, preventing a fast drop of the conversion profile. During the subsequent exothermic semicycle aluminum is melted again, absorbing a significant amount of the heat of combustion. It thus reduces overheating of the catalyst. Figure 1.12 shows the effect of latent heat storage on maximum temperature and conversion during a cycle in the periodic steady state. It becomes clear that the installation of heat storage has a beneficial effect on reactor performance, but it does not completely solve the problem of conversion fluctuations and suboptimal heat recovery. The major problem remains – the heat of combustion is stored within a narrow zone close to the right boundary of the catalytic section. It travels during the production phase into the inert section and becomes useless for dehydrogenation reaction.

Distributed heat release

The concepts discussed so far indicate that the major challenge in asymmetric operation is correct adjustment of the loci of heat release and heat consumption. A reactor concept aiming at an optimum distribution of the process heat has been proposed [25, 26] for coupling methane steam reforming and methane combustion. The primary task in this context is to define a favorable initial state and to assess the distribution of heat extraction from the fixed bed during the endothermic semicycle. An optimal initial state features cold ends and an extended temperature plateau in the catalytic part of the fixed bed. The downstream heat transfer zone is inert, in order to avoid any back-reaction (Fig. 1.13).

Taking into account the fact that methane steam reforming is a rapid reaction and that the local conversion is determined mainly by the catalyst temperature ($X_{ref} = X_{ref}(T)$), the evolution of the temperature profile can be estimated through a simplified procedure based on geometric considerations. It can be shown, that

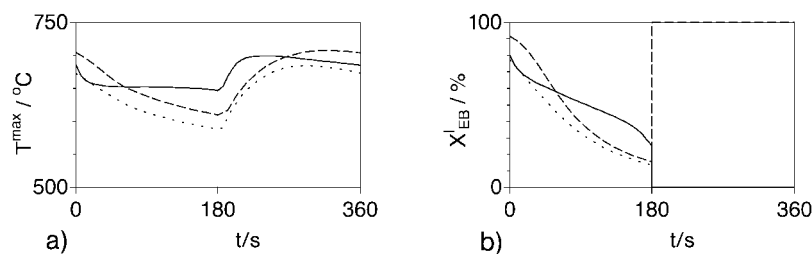


Fig. 1.12. Maximum temperature (a) and ethylbenzene conversion (b) during one production cycle for a fixed bed of uniform heat capacity (dotted line), for a structured fixed-bed with inert end sections of higher heat capacity (dashed line), and for latent heat storage inside the catalytic section (solid line) [9].

equilibrium-limited endothermic reactions lead to a sharp, traveling heat transfer zone if cold feed enters a uniformly preheated catalytic fixed bed [25]. The heat transfer zone and the reaction zone can therefore be approximated by step functions propagating through the fixed bed in flow direction. The heat transfer zones at the left and the right end of the profile propagate with the velocity of a thermal wave, w_{therm} , which depends on the heat capacity flux of the gas stream and the heat capacity of the solid phase:

$$w_{therm} = \frac{(\dot{m} \cdot c_p)_g}{\rho c} = \frac{v^0 (\rho \cdot c_p)_g}{\rho c} \quad (7)$$

In the reaction zone, superposition of convective cooling and heat consumption through the endothermic reaction leads to an accelerated cooling of the fixed bed. The ratio of the propagation velocity of the reaction front (w_{endo}) and the thermal front can be estimated as follows:

$$\frac{w_{endo}}{w_{therm}} \approx 1 + |\Delta T_{ad}| \frac{X_{ref}(T_{max}) - X_{ref}(T_{low})}{T_{max} - T_{low}} \quad (8)$$

For the example of methane steam reforming, Eq. (8) yields an acceleration factor of 4. Accordingly, the axial displacement of the reaction zone is a multiple of the axial displacement of thermal fronts. The difference of the axial displacement between the reaction front and the thermal front determines the axial profile of heat demand during the subsequent exothermic semicycle. Efficient heat recovery requires equal heat capacities of the process streams during both semicycles. The initial state can be restored by discrete heat sources distributed at equal distances along the catalytic part of the reactor. Each point source initiates a thermal wave that covers the distance to the next heating point (Fig. 1.13, right). This concept features

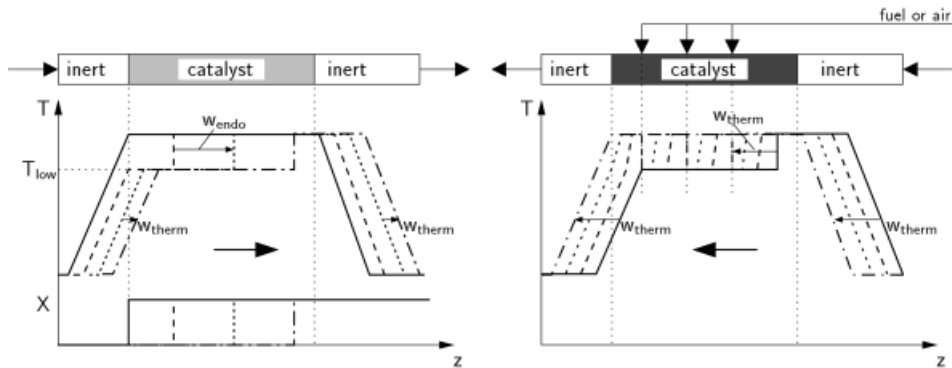


Fig. 1.13. Schematic picture of the evolution of temperature profiles in a reverse-flow reactor with distributed side feed during production (left) and regeneration cycles (right) [25].

optimal characteristics in several respects: The conversion of the endothermic reaction is determined by the temperature plateau in the catalytic part and can be maintained at a constant level throughout the complete endothermic semicycle. The heat capacities of the process gases during the production and the regeneration step can be adjusted properly in order to achieve optimal heat recovery.

The concept has been implemented in a laboratory-scale set-up. A sketch of the reactor is shown in Fig. 1.14 (left). Point-wise heat generation at well-defined positions along the fixed bed is accomplished with a special gas distributor which is located in the central reactor axis and has openings at four axial positions. The distributor is activated during the exothermic semicycle. Air is supplied to the reactor through the openings and burns part of the fuel contained in the main stream. The combustion reaction is almost instantaneous and represents approximately a point heat source. This configuration prevents direct contact of oxygen with the catalytic fixed bed and protects the catalyst against oxidation. Moreover, uncontrolled combustion of carbonaceous deposits and its detrimental consequences can be excluded. Nevertheless, catalyst decoking is ensured by mild, endothermic reactions, for example, gasification or hydrogenation. The right-hand part of Fig. 1.14 shows the temperature profiles at the end of consecutive endothermic and exothermic semicycles in periodic steady-state operation. The length of the production and regeneration cycle was set to 3 minutes. During the production cycle a mean methane conversion higher than 98 % could be attained. Despite insufficient insulation and a high wall-to-volume ratio of the laboratory set-up, a production capacity of $1.5 \text{ kW}_{\text{LHV},\text{H}_2} \text{ L}^{-1}$ was achieved with a thermal efficiency of approximately 70 % – that is, the heat loss is in the order of 40 % of the heat uptake for the reforming reaction.

1.3.1.3 Symmetric Mode with Side Stream Injection

Side stream injection provides a flexible basis for new process variants. A derivate of this concept is the symmetric process: Shifting the combustion into an external combustion chamber and feeding the hot effluent gases to the main reactor enables a continuous heat supply to the endothermic reaction, and continuous production. The endothermic reaction mixture is fed in periodically changing directions to the reactor, and this leads to symmetric conditions during both semicycles. The advantage over the simultaneous mode is the exclusion of direct contact and of undesirable side reactions of the endothermic reaction mixture with oxygen. The symmetric process is particularly suitable for mole-number-increasing reactions since dilution of the reaction mixture with inert gases may shift the chemical equilibrium towards higher conversion. Accordingly, the symmetric process has been applied to styrene synthesis [23, 27]. Side feed can be added either through a single or multiple ports. Distributed side feeding provides additional control variables, such as periodic activation of the side ports [27]. This can be utilized for optimizing the shape of the temperature profile with respect to product selectivity. However, improved controllability and variability of the symmetric process goes along with a significantly increased complexity of the reactor design. Fine-structured inlet manifolds and static mixers are required in order to achieve a uniform distribution of the side feed over the reac-

The most suitable variant comprises the following sequence of steps: combustion in forward flow direction–dehydrogenation forward–combustion backward–dehydrogenation backward. Model-based analysis reveals the importance of matching the kinetics of the endothermic and exothermic reactions in order to establish the desired temperature profile. Therefore, axial structuring of the fixed bed is crucial. An optimized reactor design (Fig. 1.16) comprises inert heat transfer sections at both ends of the reactor in order to avoid back-reaction. Adjacent to the end zones, sections of low catalytic activity are provided where the combustion mainly takes place, whilst the central section is filled with highly active dehydrogenation catalyst. Additionally, a mixture of propane and less reactive methane can be used as fuel, in order to adjust the temperature level in the central part of the reactor. The reaction zones of combustion and dehydrogenation are separated from each other. Considerably higher flow rates during the exothermic phases ($\dot{M}_{exo} : \dot{M}_{endo} = O(10)$) are required for carrying the heat of combustion into the dehydrogenation zones. The conversion of the dehydrogenation reaction is uniform over the entire period of the production cycles. The heat loss due to incomplete heat recovery in the case shown is approximately 90 % of the generated heat, and is thus a multiple of the heat utilized by dehydrogenation.

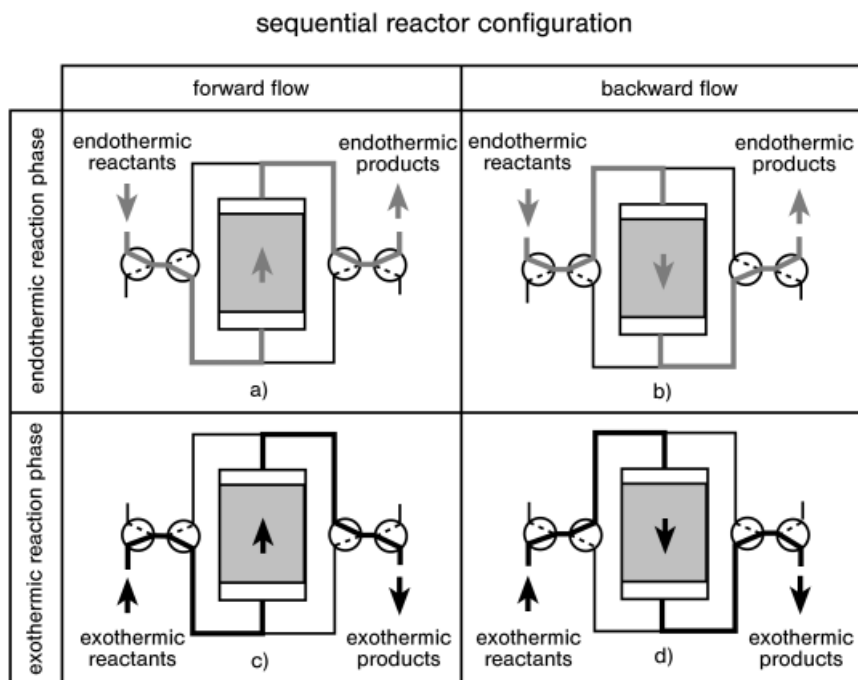


Fig. 1.15. Coupling of propane dehydrogenation and methane combustion in a four-step catalytic fixed-bed process [28].

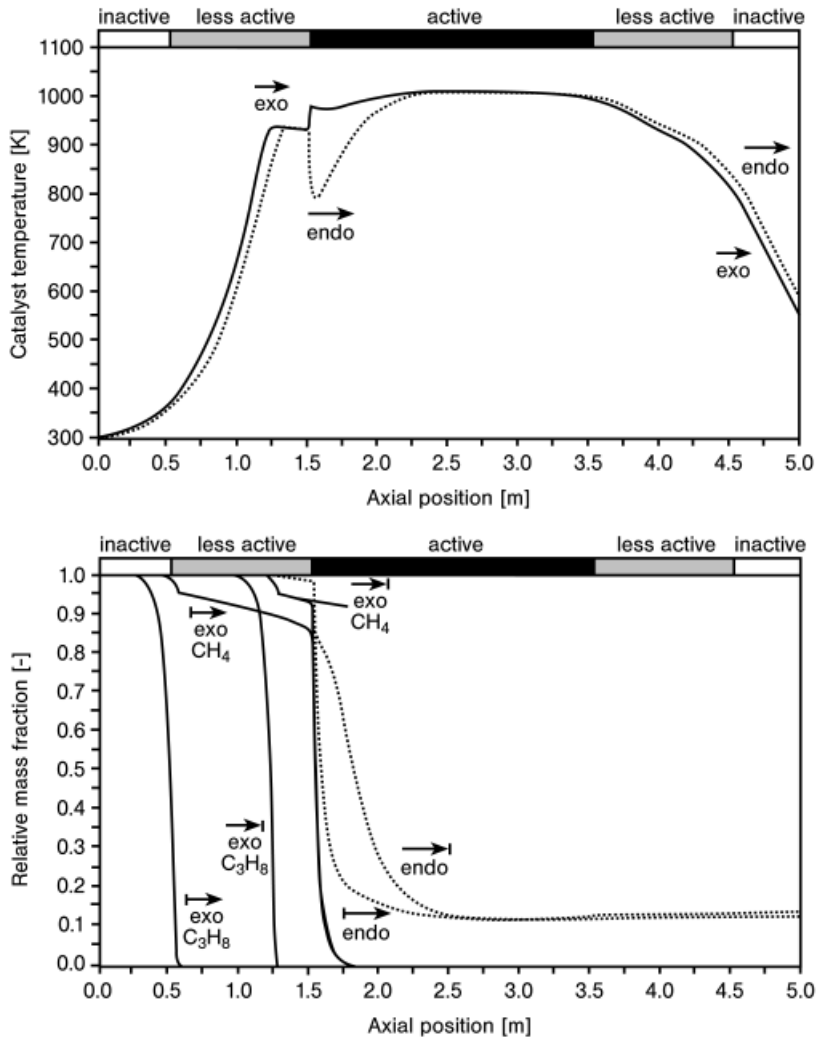


Fig. 1.16. Four-step propane dehydrogenation process [28]: Temperature profiles (top) and mass fraction profiles (bottom) at the end of the first two steps (1- exo, 2- endo). The end profiles of the subsequent steps are mirror images of the profiles shown.

This study also addresses the detrimental effect of carbonaceous deposits formed during the dehydrogenation steps. The ignition of accumulated coke during the subsequent regeneration step can lead to extreme local temperature peaks that are able to deactivate the catalyst or even to destroy the reactor. The phenomenon of temperature excursion during the exothermic gas–solid reactions has been analyzed by Niesen and Watzenberger [29] and Salden [30], and will be discussed briefly in the following section.

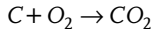
1.3.1.5 Overheating During Oxidative Coke Removal

Regenerative processes for hydrocarbon processing include oxidative coke removal as an integral part of the process cycle in order to sustain a high catalytic activity. However, the results of both experimental and theoretical studies agree that oxidative coke removal may lead to severe, uncontrollable temperature excursions [13, 14, 28]. This phenomenon is elucidated in the following text in order to identify the reasons for this critical behavior, as well as to suggest possible remedies, based upon an analysis given in Ref. [30].

We assume a fixed-bed of semi-infinite axial extension with a uniform initial temperature T_{fb}^0 and coke loading q_B^0 . We further neglect dispersive effects and assume that coke combustion is an instantaneous reaction. Passing a gas stream with inlet temperature T^+ and inlet oxygen concentration $c_{O_2}^+$ at a flow rate v^0 through the fixed-bed, typically two stationary traveling fronts are formed (Fig. 1.17). The propagation velocity of the thermal front w_{therm} depends on the heat capacity of the gas and the fixed bed (Eq. (7)). The propagation velocity of the reaction front is given by the following expression

$$w_R = \frac{c_{O_2}^0}{q_B^0} v^0 \quad (9)$$

resulting from the stoichiometry of complete coke combustion:



Hence, w_{therm} and w_R are independent of each other. The effective temperature rise depends on the ratio of w_{therm} and w_R and can be estimated based on the following simplified considerations.

In a quasi-homogeneous model, the evolution of the temperature T_{fb} , the coke loading q_B , and the oxygen concentration c_{O_2} are given by the following set of equations:

$$(\rho c) \frac{\partial T_{fb}}{\partial t} = -(\rho c_p)_g v \frac{\partial T_{fb}}{\partial z} + (-\Delta H_R) r \quad T_{fb}(z=0, t) = T^+; \quad T_{fb}(z, t=0) = T_{fb}^0 \quad (10)$$

$$\frac{\partial q_B}{\partial t} = -r \quad q_B(z, t=0) = q_B^0 \quad (11)$$

$$0 = -v^0 \frac{\partial c_{O_2}}{\partial z} - r \quad c_{O_2}(z=0, t) = c_{O_2}^+ \quad (12)$$

Transformation of the above system into moving coordinates $\tau = t$; $\xi = z - w_{therm} t$ yields:

$$(\rho c) \frac{\partial T_{fb}}{\partial \tau} = (-\Delta H_R) r \quad T_{fb}(\xi, \tau=0) = T_{fb}^0 \quad (13)$$

$$\frac{\partial q_B}{\partial \tau} = w_{therm} \frac{\partial q_B}{\partial \zeta} - r \quad q_B(\zeta, \tau = 0) = q_B^0; \quad q_B(\zeta \rightarrow \infty, \tau) = q_B^\infty \quad (14)$$

$$0 = -v^0 \frac{\partial c_{O2}}{\partial \zeta} - r \quad c_{O2}(\zeta = 0, \tau) = c_{O2}^+ \quad (15)$$

Additionally, the constant pattern assumption implies the following conditions:

$$\frac{\partial T_{fb}}{\partial \tau} = - (w_R - w_{therm}) \frac{\partial T_{fb}}{\partial \zeta} \quad (16)$$

$$\frac{\partial q_B}{\partial \tau} = - (w_R - w_{therm}) \frac{\partial q_B}{\partial \zeta} \quad (17)$$

Eq. (17) inserted in Eq. (14) yields:

$$- (w_R - w_{therm}) \frac{\partial q_B}{\partial \zeta} = w_{therm} \frac{\partial q_B}{\partial \zeta} - r \quad (18)$$

$$\Rightarrow r = w_R \frac{\partial q_B}{\partial \zeta} \quad (19)$$

Combining Eqs. (13), (16), and (19) leads to:

$$- (\rho c) (w_R - w_{therm}) \frac{\partial T_{fb}}{\partial \zeta} = (-\Delta H_R) w_R \frac{\partial q_B}{\partial \zeta} \quad (20)$$

$$\Rightarrow \frac{dT_{fb}}{dq_B} = - \frac{w_R}{w_R - w_{therm}} \cdot \frac{(-\Delta H_R)}{(\rho c)} \quad (21)$$

Here, we must discriminate between two cases:

1. Reaction front faster than thermal front ($w_R > w_{therm}$):

$$\Delta T = T_{fb}^0 - T_{max} = - \frac{w_R}{w_R - w_{therm}} \cdot \frac{(-\Delta H_R)}{(\rho c)} \cdot q_B^0 = - \frac{w_{therm}}{w_R - w_{therm}} \cdot \frac{(-\Delta H_R)}{(\rho c_p)_g} \cdot c_{O2}^+ \quad (22)$$

$$\Rightarrow \Delta T_{eff} = \frac{1}{\frac{(\rho c)}{q_B^0} - \frac{(\rho c_p)_g}{c_{O2}^+}} \cdot (-\Delta H_R) \quad (23)$$

This case, displayed in Fig. 1.17(c), occurs at high inlet oxygen concentrations or small initial coke loading – that is, the combustion is limited by the amount of coke. The heat generation by reaction exceeds the heat consumption for heating

up the cold gas stream. For $w_R \gg w_{therm}$ the effective temperature rise approaches asymptotically the value

$$\Delta T_{ad}^s = \frac{q_B^0(-\Delta H_R)}{\rho c}$$

that can be interpreted as the adiabatic temperature rise of the solid phase.

2. Reaction front slower than thermal front ($w_R < w_{therm}$):

$$\Delta T = T^+ - T_{max} = \frac{w_R}{w_R - w_{therm}} \cdot \frac{(-\Delta H_R)}{(\rho c)} \cdot q_B^0 = \frac{w_{therm}}{w_R - w_{therm}} \cdot \frac{(-\Delta H_R)}{(\rho c_p)_g} \cdot c_{O_2}^+ \quad (24)$$

$$\Rightarrow \Delta T_{eff} = \frac{1}{\frac{(\rho c_p)_g}{c_{O_2}^+} - \frac{(\rho c)}{q_B^0}} \cdot (-\Delta H_R) \quad (25)$$

This case, displayed in Fig. 1.17(d), occurs at a low inlet oxygen concentration or a high initial coke loading – that is, the combustion is oxygen-limited. The heat of combustion is carried away downstream by convection. For $w_R \ll w_{therm}$ the effective temperature rise approaches asymptotically the value

$$\Delta T_{ad}^g = \frac{c_{O_2}^+(-\Delta H_R)}{(\rho c_p)_g}$$

which can be interpreted as the adiabatic temperature rise of the gas phase.

Figure 1.18 displays the effective temperature rise during oxidative coke removal as a function of the oxygen molar fraction of the regeneration gas according to Eqs. (23) and (25), respectively. The adiabatic temperature rise of the shown case is 38 K. However, ΔT_{eff} can be much higher and tends to infinity at the limit of $w_R \rightarrow w_{therm}$. This can be explained as follows: when the velocities of the thermal front and the reaction front are equal, the heat of combustion accumulates in a narrow zone which may lead to extremely high local temperatures. This conclusion has been verified theoretically through detailed simulations [30].

The above considerations hold under the condition that the ignition temperature of coke combustion is lower than T_{fb}^0 in the coke-limited regime, or lower than T^+ in the oxygen-limited regime. However, in the considered heat-integrated processes the feed temperature T^+ is generally far below the ignition temperature. The fatal aspect in this scenario is that coke regeneration is carried out “carefully” – that is, with a low oxygen concentration. Oxygen deficiency leads to incomplete coke removal according to the following condition:

$$w_R = w_{therm} = \frac{c_{O_2}^+}{q_B^0 - q_B^r} \cdot v^0 \quad (26)$$

In this way, the reaction front is synchronized inevitably with the thermal front, leading to the observed temperature excursions (Fig. 1.19).

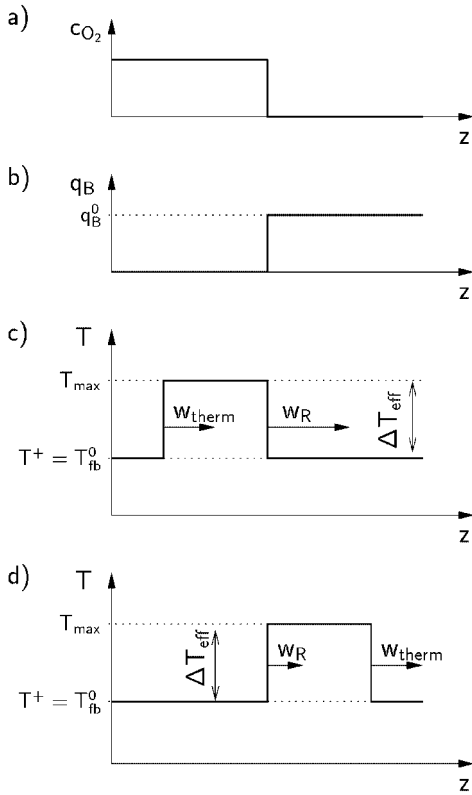


Fig. 1.17. Schematic picture of front propagation during oxidative coke removal. (a) Oxygen concentration in the regeneration gas, e.g., air. (b) Coke loading of the solid phase. (c) Front propagation of the thermal front (velocity w_{therm}) and the reaction front (w_R) with preceding reaction front. (d) Front propagation with preceding thermal front (special case: $T^+ = T_{fb}^0$).

Hence, in order to prevent overheating it is not simply the amount of coke that matters; rather, it is also necessary to avoid synchronization of the thermal and combustion fronts. This can be achieved by correctly adjusting the oxygen inlet concentration, in order to carry out regeneration in the coke-limited regime.

1.3.2

Recuperative Processes

The activities of heat-integrated processes with recuperative heat exchange are mainly devoted to the conversion of primary fuels (hydrocarbons or alcohols) to hydrogen, with few exceptions – for example, investigations on the dehydrogenation of light alkanes in Schmidt's group [3]. The practical relevance and vitality of

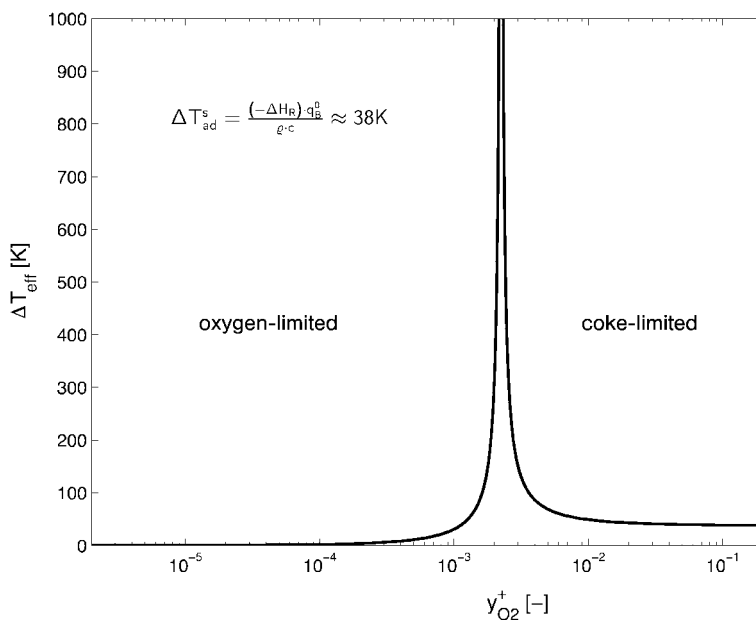


Fig. 1.18. Effective temperature rise during oxidative coke removal as a function of the oxygen mole fraction of the regeneration feed gas.

research on heat-integrated fuel processors can be estimated from the number of established companies and start-ups active in this area [31]. Two major trends prevail: One focusing on optimization of existing concepts and one aiming at novel concepts based on micro-reactors.

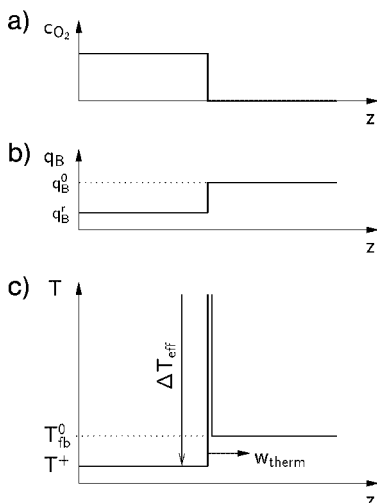


Fig. 1.19. Front propagation during oxidative coke removal with low inlet temperature. (a) Oxygen concentration in the regeneration gas. (b) Coke loading of the solid phase. (c) Development of temperature excursion in the propagating reaction zone.

1.3.2.1 Processes for Large-Scale Applications

Processes developed on the basis of conventional reforming technology are designed for large-scale hydrogen production, for example in chemical plants, power plants or hydrogen filling stations. Optimized designs aim at reduction of waste heat generation at a level that renders steam export obsolete.

ICI developed a two-stage process comprising a gas-heated tubular fixed-bed reformer (GHR) interconnected with an autothermal reformer for industrial syngas generation [32, 33]. The term autothermal reforming (ATR) is used for the simultaneous coupling of reforming and oxidation. Figure 1.20 shows a scheme of this combined process. About 25 % of the hydrocarbon is converted in the GHR, with the product stream being redirected into a concentric tube before leaving the GHR. The gas is cooled down through countercurrent heat exchange with fresh gas, before entering the ATR stage where conversion is completed. The hot syngas from the ATR passes through the GHR supplying additional heat to the steam-reforming process.

The Haldor Topsøe Convection Reformer (HTCR) has been developed for the production of hydrogen from hydrocarbons without steam generation. The elementary unit of the reformer consists of two concentric tubes (Fig. 1.21). The annular space

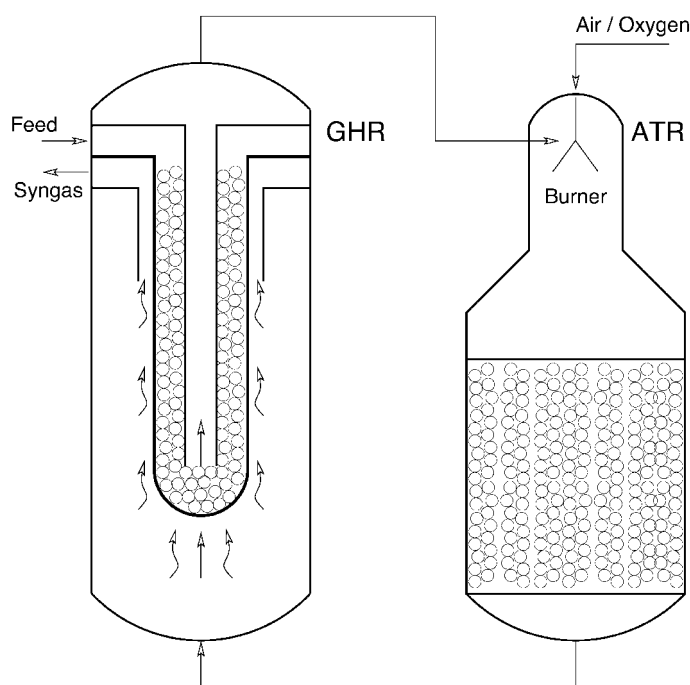


Fig. 1.20. Autothermal syngas generation by combining simultaneous autothermal reforming in an air/oxygen-fired fixed-bed reactor (ATR) and steam reforming in a gas-heated tubular fixed-bed reactor (GHR) [32, 33].

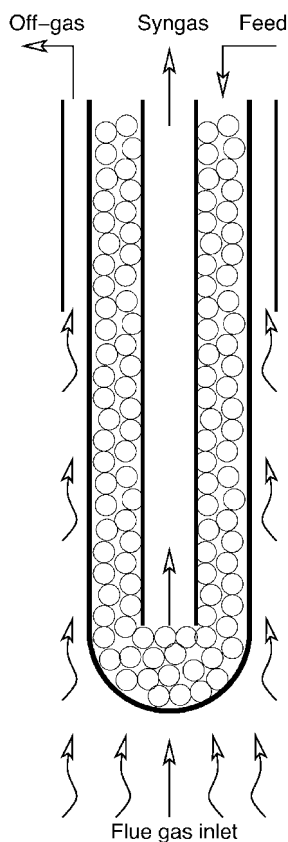


Fig. 1.21. Schematic set-up of the heat-integrated HTCR process for industrial syngas production by steam reforming of natural gas.

between the two tubes is filled with catalyst. Feed gas enters the outer tube at one end, while the other end is closed. In this way, countercurrent heat exchange is attained between the product stream in the inner tube and fresh gas in the annular space. A bundle of these modules is inserted into a furnace, where the combustion of fresh gas and off-gas from the hydrogen purification unit produces the process heat. The hot flue gas is conducted upwards and supplies heat to the reforming process, for overheating of the reaction mixture and for steam generation. In this way, the HTCR process enables almost complete recovery of the sensible heat of the process gases. According to technical data presented by the manufacturer, the HTCR process has an overall thermal efficiency of $\eta = LHV_{H_2^{prod}} / LHV_{CH_4^*} = 72\%$ with zero steam export.

A concept with a higher degree of heat integration is described in Ref. [34]. The concept has been derived from the FLOX burner (FLOX = flameless oxidation in the gas phase) [35]. This combustion regime can be attained with highly preheated fresh air in combination with intensive recirculation in the combustion chamber, and features extremely low emissions. Fresh air preheating is accomplished in the FLOX burner through countercurrent heat exchange with the hot flue gases in an

integrated heat exchanger. Thus, heat recovery is inherently included in the FLOX burner. In the FLOX reformer the reforming modules consisting of two concentric tubes, similar to those of the HTCR- and ICI-GHR design, which hang in the combustion chamber. Steam generation, reforming and water-gas-shift reaction are integrated in every module. Figure 1.22 shows a scheme of the heat management of this concept. The two heat recovery loops of the reforming and combustion gas are almost completely separated from each other. The heat content of the reforming gas is utilized for vaporizing the liquid water and the water-gas shift stage for CO-removal is cooled by the produced steam. The sensible heat of the flue gas is utilized for preheating the fresh air superheating the methane/steam mixture. The FLOX-reformer design is modular with a capacity of $50\text{--}250 \text{ Nm}^3 \text{ H}_2 \text{ h}^{-1}$. Thermal efficiency exceeds 80 %.

1.3.2.2 Processes for Small-scale Applications

Nowadays, the most common small-scale application of hydrogen is the use in residential or mobile fuel cell systems. Special requirements of this application are compact design, integrated CO-removal, high energetic efficiency, quick start-up and fast transient behavior. The proposed solutions comprise unit-operation-based concepts as well as multifunctional, micro-structured reactors.

A gasoline processing system has been developed by Daimler Chrysler [36] based on ATR. Catalytic ATR is extremely rapid, and provides the potential for a very compact process. The specific productivity of the ATR is about $15 \text{ kW}_{\text{LHV, gasoline}} \text{ L}^{-1}$. The fuel is sprayed into a preheated air stream. The ATR-product stream enters a high-temperature shift reactor (HTS), in order to convert CO. Both ATR and HTS are designed as adiabatic metallic monolith reactors, which are coated with different noble metal catalysts for reforming and water-gas shift reactions. The operation temperature of the ATR is above 750°C , while the HTS operates at about 450°C . Therefore, it is recommended that the two units are interconnected with a heat exchanger, in order to recover the heat of the ATR product stream for preheating the ATR feed (Fig. 1.23). The behavior of the coupled system has been analyzed in Ref. [37].

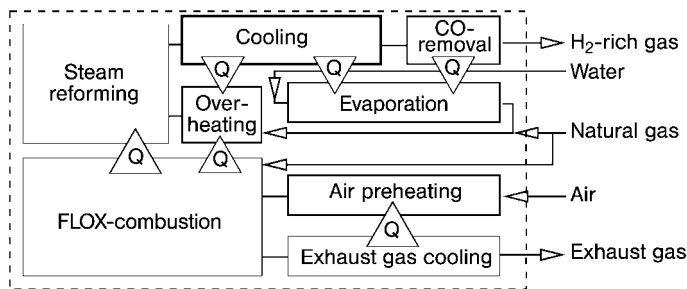


Fig. 1.22. Flowsheet of the FLOX-reformer. The triangles indicate the exchanged heat fluxes between different stages of the process [34].

One major conclusion of this study is that integrated heat recovery reduces the sensitivity of the process against fluctuations of the operating parameters, and thus enhances the feasible operation range. The effect of heat recovery during a load change is illustrated in Fig. 1.24. The stationary temperature profiles are shown at gasoline loads equivalent to 3 and 33 kW_{LHV} of gasoline. The temperature profile at the inlet of the ATR is dominated by the fast oxidation, while steam reforming of gasoline takes off further downstream. At high load, the temperature maximum could exceed the allowed limit. In contrast, if heat generation falls below a certain threshold, the heat losses become dominant and the reactor extinguishes. Heat recovery stabilizes the operating conditions in the following way: At high load the efficiency of heat recovery declines and the inlet to the ATR stage drops. This compensates partially the temperature rise in the combustion zone of ATR and limits the peak temperature. At low load the efficiency of heat recovery improves, and hence the inlet temperature of the ATR increases. This stabilizes the ignited state. Experimental studies confirm that integrated heat recovery enables a loading variation of 1:10 and contributes to a fast and smooth transient behavior.

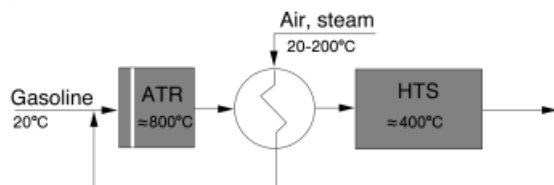


Fig. 1.23. Flowsheet for a heat-integrated system of an autothermal gasoline reformer (ATR) and a high-temperature shift stage (HTS) interconnected with a heat exchanger [37].

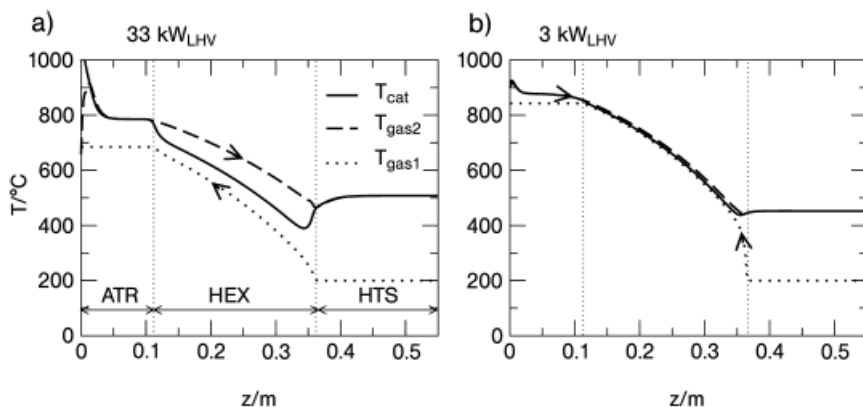


Fig. 1.24. Steady-state, axial temperature profiles for the gasoline reformer in Figure 1.21. (a) High load: 33 kW_{LHV}; (b) low load: 3 kW_{LHV}.

The progress in micro-reactor technology provides the background for the development of compact fuel processors and peripheral components of fuel cell systems.

Published performance data [38–42] indicate the high development status already reached: Volume-specific productivity values up to $750 \text{ l}_N\text{H}_2/\text{lit.}/\text{h} \equiv 2,3 \text{ kW}_{\text{LHV},\text{H}_2}/\text{lit.}$ and overall thermal efficiency values from 80 to 90 % have been reported for gas generation processes including feed preheating, gas generation and purification. Unfortunately, no further details are available about reactor design and the process conditions except for very few of them.

The Integrated Fuel Processor (IFP)

This was developed by Ballard Power [40], and is a multifunctional reactor including the evaporation of a methanol/water mixture, autothermal methanol reforming and preferential oxidation (PrOx) for CO removal. The device consists of a stack of identical, structured plates which divide its volume in two compartments with micro-structured rectangular channels. These plates are made from aluminum and copper, thus ensuring high thermal conductivity for a uniform temperature over the entire reactor volume. A schematic picture of a single plate is shown in Fig. 1.25. Liquid methanol/water mixture enters the first compartment and evaporates when heated by the exothermic PrOx reaction, which takes place on the other side of the plate. The reactants are mixed with air and enter the porous section of the plates where the reforming reaction takes place as the reaction gases cross the plates. In the second chamber, secondary air is added and the reaction products pass over a PrOx-catalyst while exchanging heat with the first chamber. The temperature of the reactor is adjusted to 280 °C. Proof-of-concept experiments with the IFP gave an extremely high productivity of $2.5 \text{ m}_N^3 \text{ H}_2/\text{lit.}/\text{h} \equiv 7.5 \text{ kW}_{\text{LHV},\text{H}_2}/\text{lit.}$ A special powder-metallurgical fabrication method allows for producing impermeable and porous areas on the plate as required for the flow distribution, embossing the surface structure and impregnating with reforming catalyst (Cu/ZnO) in one step. The plates are piled to a stack and joined by sintering. However, the IFP-design is not suitable for high-temperature applications such as gasoline or methane processors. Furthermore, the above-mentioned autothermal reforming processes are charged with the inherent shortcomings of the simultaneous mode with regard to product dilution and pressure limitations. Therefore, the focus is set on high-temperature steam reforming. The potential of catalytic plate reactors with narrow channels regarding controllability, productivity and efficiency has been demonstrated in detailed theoretical studies by Zafir and Gavrilidis [43]. One crucial task in implementing the concept is the development of fabrication techniques for catalytic activation of the plates and for assembling a stack. The solution of choice would be to coat the plates before joining them to a stack. However, the conditions required by the common joint methods – soldering or diffusion bonding – would damage the catalyst, whilst the alternative of laser welding is too expensive. Therefore, although coating the completely assembled reactor is often employed as the only viable solution, this is extremely difficult to control [44] and is a clear restriction of the adequacy of micro-fabricated reactors for specific applications. Moreover, the suggestion of “the smaller the better” is not

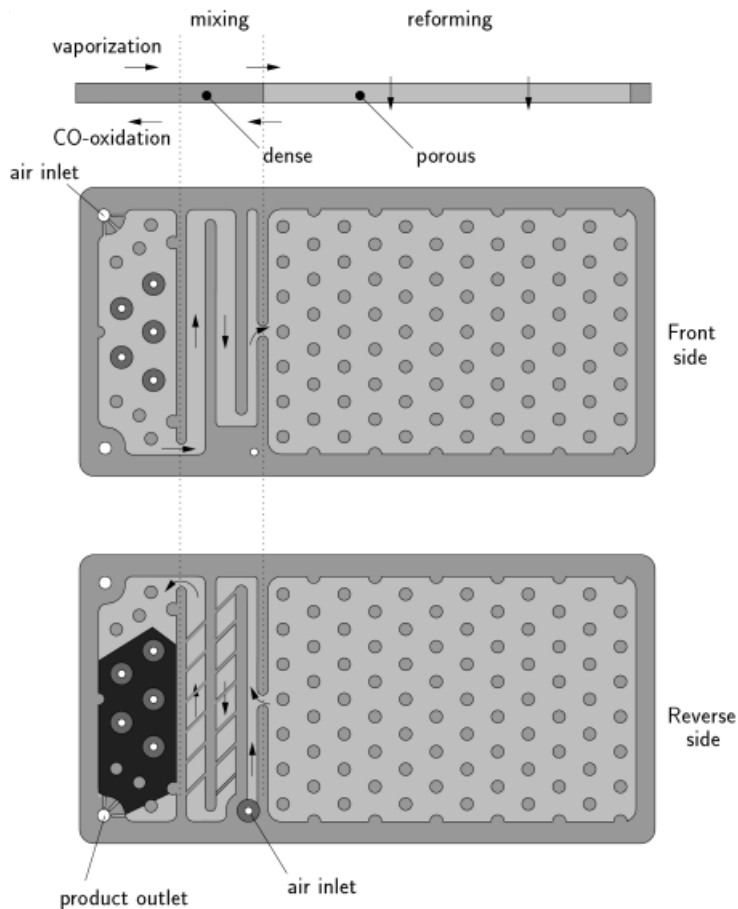


Fig. 1.25. Schematic diagram of a single plate of the Integrated Fuel Processor (IFP) [40]. Top = flow scheme; center = view to the front side; bottom = view to the reverse side.

generally true in the context of processes with integrated heat recovery. Decreasing the channel width allows a given heat transfer area to be installed in shorter devices. This enhances the influence of heat conductivity and tends to equalize temperature gradients; thus, it is an advantage for temperature control in the reaction stage. However, the same effect considerably affects the efficiency of heat recovery in the heat exchanger sections [45]. Therefore, it is not recommended that attention be focused exclusively on minimization of the hydraulic diameter and the size of the devices.

Another important aspect is optimization of the process parameters. The challenge here is to control catalytic combustion, in order to attain overlapping of the combustion and reforming reaction over a sufficient interval [46]. The operating conditions are mainly determined by the fuel composition and the heat exchange

mode between the process streams. In low-temperature processes (e.g., methanol reforming) or in processes without feed preheating, hydrogen is required to stabilize the ignited state of the catalytic combustion [47, 48]. However, the presence of hydrogen is extremely critical at high temperatures due to the ignition of homogeneous combustion. The use of less-reactive pure methane is recommended in this case, in order to avoid runaway [49]. Additionally, countercurrent flow of the reforming and the combustion gas gives rise to separation of the reaction zones and to runaway of the combustion reaction. A considerable excess of the combustion gas flow rate against the reforming gas flow rate is required in order to stabilize reasonable operating conditions at the cost of a lower thermal efficiency [45]. Overlapping of the reaction zones could be enforced either through distributed side-feeding of air or fuel or through cocurrent flow of combustion and reforming gas stream in the catalytic part of the reactor [50].

A comprehensive concept including process and apparatus design has been developed based on the folded plate reactor design [51]. Comparable concepts are known from the Boreskov Institute of Catalysis [52]. The body of the reactor consists of a folded sheet of metal that divides its volume in two chambers, forming channels with rectangular cross-sections (Fig. 1.26). By applying this technique, the channel width can be adjusted individually at each side, depending on the respective heat of reaction and reaction kinetics: narrow channels (as small as 1 mm) are indicated for fast reactions, whereas wide channels (up to 10 mm) allow for the installation of sufficient amounts of catalyst for slow reactions. An important feature of the folded-sheet design is that all channels are accessible from the side over the entire reactor length. In this way, it is possible to distribute the feed at arbitrary positions, in order to specifically control the operating conditions. The frontal ends can be sealed (e.g., with silicon rubber) if they are permanently exposed to low temperatures; otherwise, welding or high-temperature soldering is used which ensures thermal stability up to 900 °C. In this way, the two chambers can be separated from each other with a minimum number of joints, and this reduces potential failure sources. The channels are filled with structured spacers; these play an important role in the reactor concept as they support the reactor walls, provide the mechanical stability to the

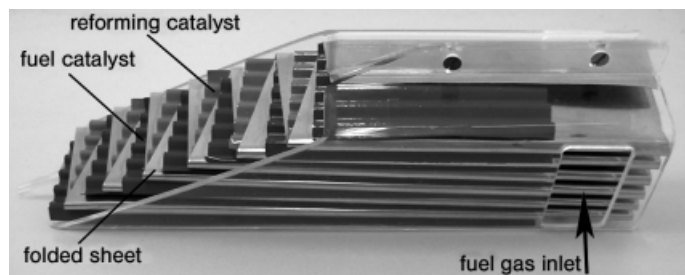


Fig. 1.26. Model of the folded sheet reactor with corrugated, catalyst-coated spacers.

reactor structure, and contribute to the improvement of the heat exchange through planar contact to the reactor wall. Spacers with crossing passages can be used as static mixers downstream of the injection ports in order to distribute the feed uniformly over the depth of each channel; finally, the spacers can be coated with catalyst. In this way, it is possible to adjust the axial structure of the channels in order to attain optimal implementation of multiple functions. The gas inlet and outlet ports are integrated in shells, forming the reactor casing. They are assembled together by two longitudinal weld seams, and the casing can also be reinforced to enhance the rigidity of the device. Two prototype reactors have been developed – one for low-temperature methanol steam reforming, and one for high-temperature methane steam reforming based on the folded-sheet reactor concept.

Methanol steam reforming

The concept has been developed to the stage of a bench-scale prototype for $3m_N^3/h$ hydrogen [53]. The complete hydrogen generation process including evaporation of methanol and water, superheating, reforming, water-gas shift combined with product cooling, are integrated in this device. Heat supply is controlled by distributed side-feeding of fuel (hydrogen) at five stages along the reactor. The experiments showed a good methanol conversion ($X > 90\%$) with moderate CO formation ($y_{CO} \sim 2\%$) and excellent dynamics upon load changes.

However, the distribution of the fuel in the depth of the channels required a complex capillary distributor with tiny exit nozzles. The particular device, although optimal with regard to the uniformity of gas distribution, seems not to be an adequate technical solution.

Methane steam reforming

The counter-cocurrent reformer concept including two countercurrent heat exchangers and a cocurrent reaction section (Fig. 1.27(a)) was considered in order to attain optimal conditions for kinetic control of the combustion [8]. It is well known that cocurrent cooling is generally favorable in preventing runaway of highly exothermic reactions. In the particular case, chemical cooling is provided by the reforming reaction.

The conditions in the reaction section are of primary interest for the entire process. Experiments have been conducted with superheated feed streams using a three-channel model reactor in order to analyze the coupling of methane reforming and methane combustion in the cocurrent mode. Figure 1.27(c) shows a sketch of the configuration representing an elementary unit of the folded sheet reactor with a combustion channel of full-height in the middle and two reforming channels of half of full-height, one on each side. Heat losses to the surroundings have been partially compensated by an electrically heated insulation. The diagrams show the temperature profile (Fig. 1.27(b)) and the performance data of the reactor (Fig. 1.27(d)) depending on the fuel concentration in the steady state. The most important result is that the cooling effect of the reforming reaction effectively prevents runaway of combustion. Hence, it is possible to achieve complete conversion under moderate

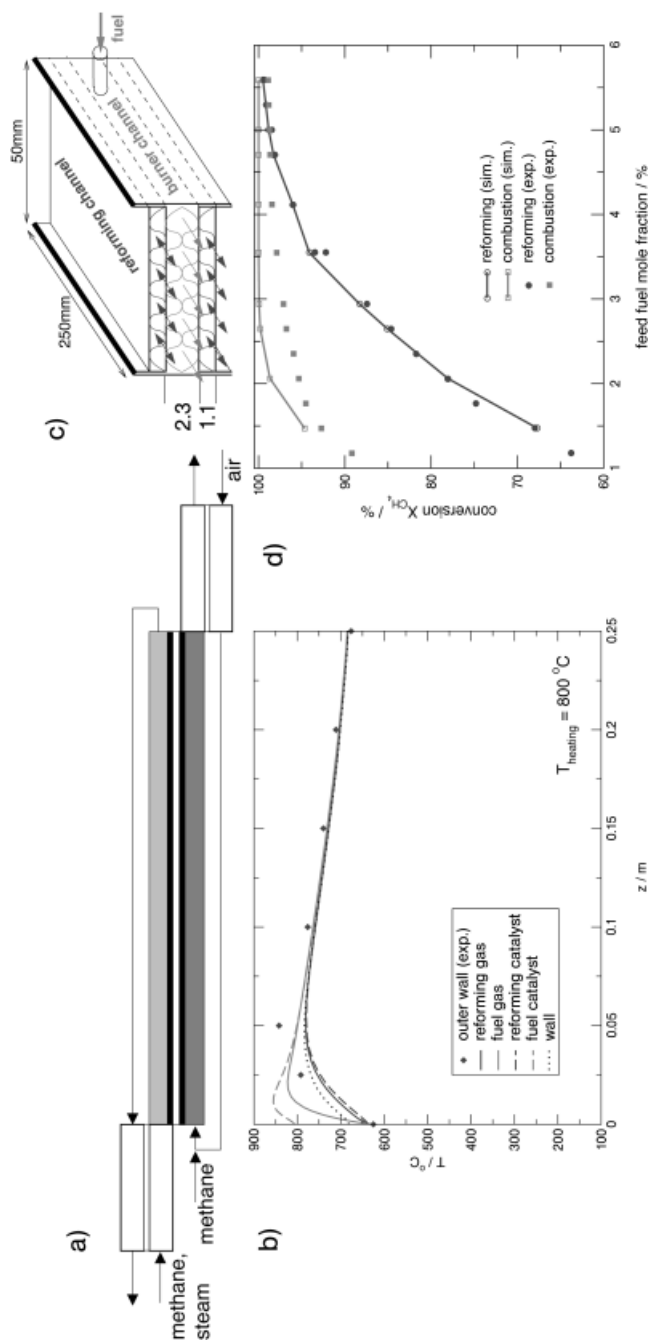


Fig. 1.27. Methane steam reformer with cocurrent flow in the reaction zone. reactor for coupling of steam reforming and combustion. (d) Simulated and (a) Flow scheme. (b) Simulated and measured temperature profiles in the measured methane conversion depending on fuel feed concentration of the combustion reaction. (c) Sketch of the three-channel

conditions. Furthermore, the generated excess heat can be varied through proper adjustment of the amount of fuel added. This defines the temperature difference between the exit and inlet which is the driving force for heat recovery in the subsequent heat exchange sections. Experiments conducted with the three-channel reactor proved that the efficiency of thermal coupling of combustion and reforming could be increased far beyond the common values of the state-of-the-art processes. Indeed, up to 85 % of the generated heat can be utilized by the reforming reaction despite the heat losses of the experimental set-up. Figure 1.28 shows schematically the general reactor design, along with simulated temperature and conversion profiles. The additional side stream feeding port enables to control the temperature in the reforming stage at varying loads. According to the simulation results, 90 % of the released heat of combustion is expected to be taken up by the reforming reaction. The specific production capacity is estimated as $2.5 \text{ m}_N^3 \text{ H}_2/\text{h}/\text{Liter}_{\text{reactor}}$.

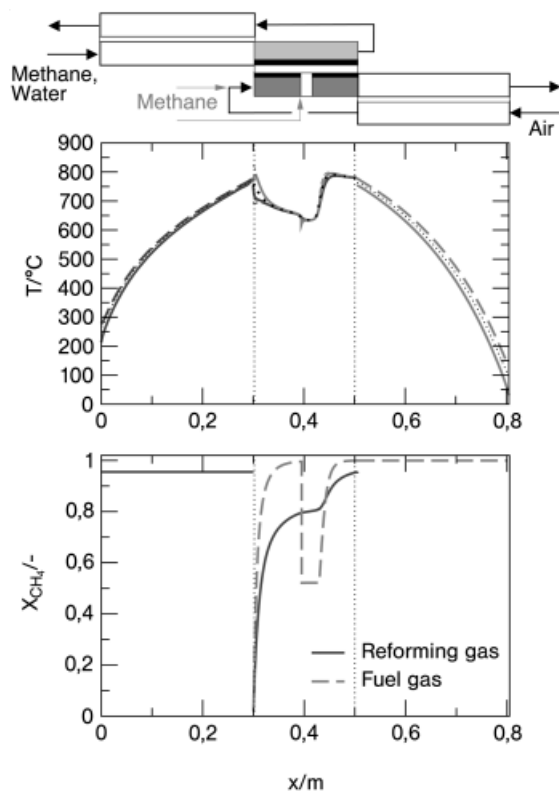


Fig. 1.28. Integrated, autothermal methane reformer with cocurrent flow in the reaction zone and countercurrent heat recovery. Simulated steady-state temperature and conversion profiles.

Experimental proof-of-concept with a bench-scale reactor (production capacity of $3.3 \text{ m}_N^3 \text{ H}_2/\text{h}$) is the subject of ongoing investigations.

1.4

Conclusions

The coupling of high-temperature endothermic and exothermic reactions in multi-functional devices with integrated heat recovery is gaining increasing interest, driven in particular by the developing hydrogen technology. Conventional concepts are not suitable to meet the demands on specific performance, thermal efficiency and autonomy of the process. Two routes are currently being pursued towards novel solutions employing either regenerative or recuperative heat exchange for heat coupling and heat recovery.

Regenerative processes based on the reverse-flow reactor concept are preferred in large-scale applications due to their simple and scalable reactor design. Compact recuperative concepts based on the wall reactor concept provide the best potential for small-scale applications. Apart from these general features, correct structuring of the catalytic and fluid-dynamic properties of the reactor is essential for an optimal design. Distributed feeding of combustion air or fuel ensures optimal heat transfer from the exothermic to the endothermic part. An integrated approach combining apparatus design and process development is indicated for optimal implementation of novel solutions.

With regard to fuel processors for hydrogen production, autothermal reforming processes have initially approached the technological and economical targets for technical implementation, though their applicability is limited due to principal shortcomings of the concept. Properly designed steam reforming processes may possibly compete with autothermal reformers with regard to space-time yield and heat recovery, while offering high flexibility in terms of operating conditions. They may, therefore, be utilized in a wide spectrum of applications.

Symbols and Abbreviations

A	area, m^2
c	specific heat capacity of the solid phase, $\text{J kg}^{-1} \text{K}^{-1}$
c_p	specific heat capacity of the gas phase, $\text{J kg}^{-1} \text{K}^{-1}$
c_j	concentration of component j , mol m^{-3}
D_i	inner diameter, m
h	heat capacity ratio
h	specific enthalpy, J mol^{-1}
k_h	heat transfer coefficient, $\text{W m}^{-2} \text{K}^{-1}$
$loss_{norm}$	normalized heat losses
\dot{M}	mass flux, kg s^{-1}
\dot{N}	molar flux, mol s^{-1}
NTU	number of transfer units

p	pressure, bar
q_B	coke loading, mol m ⁻³
r	reaction rate, mol m ⁻³ s ⁻¹
t	time, s
T	temperature, K
v^0	superficial gas velocity, m s ⁻¹
$w_{i\text{therm}}$	thermal front propagation velocity, m s ⁻¹
$w_{\text{endo/exo/R}}$	reaction front propagation velocity, m s ⁻¹
X	conversion of reaction
y_j	molar fraction of the component j
z	axial coordinate, m

Greek letters

α_w	heat transfer coefficient, W m ⁻² K ⁻¹
ΔH_R	heat of reaction, kJ mol ⁻¹
ΔT	temperature difference, K
ΔT_{ad}	adiabatic temperature rise, K
ΔT_{eff}	effective temperature rise, K
λ	axial heat conductivity, W m ⁻¹ K ⁻¹
ρ	density, kg m ⁻³
τ	time in transformed system of coordinates, s
ζ	spatial coordinate in transformed system, m

Indices

0, +	inlet or initial conditions
–	outlet conditions
c	fixed-bed catalyst
cyc	cycle
equ	equilibrium conditions
endo	endothermic reaction
exo	exothermic reaction
fb	fixed-bed
g	gas phase
l	liquid phase
lat	latent heat storage
low	lower value
max	maximum value
prod	production cycle
reg	regeneration cycle
ref	steam reforming
s	solid phase
w	separating wall

Acronyms

ATR	Autothermal Reformer
GHR	Gas-Heated Reformer
HTS	High-Temperature Shift Stage
LHV	Lower Heating Value
PrOx	Preferential Oxidation

References

1. Horizon 2015: *Perspectives for the European Chemical Industry. A study by the European Chemical Industry Council* (www.cefig.org), 2004.
2. J. Larminie, A. Dicks, *Fuel Cell Systems Explained*. 2nd edn., Wiley, 2003.
3. K. Venkataraman, J. M. Redenius, L. D. Schmidt, Millisecond Catalytic Wall Reactors: Dehydrogenation of Ethane. *Chem. Eng. Sci.*, **2002**, 57, 2335–2343.
4. K. Venkataraman, E. C. Wanat, L. D. Schmidt, Steam Reforming of Methane and Water Gas Shift in Short Contact Time Reactors. *AIChE J.*, **2003**, 49, 1277–1284.
5. M. Zafir, A. Gavrilidis, Modeling of a catalytic plate reactor for dehydrogenation-combustion coupling. *Chem. Eng. Sci.*, **2001**, 56, 2671–2683.
6. P. Häussinger, Ullmann's Encyclopedia of Industrial Chemistry. *Hydrogen*, 1989, Vol. A13, VCH Verlagsgesellschaft, Weinheim, 311 ff.
7. E. U. Schlünder, *Introduction into heat transfer*, Vieweg, Braunschweig, 3rd edn, 1981.
8. G. Kolios, B. Glöckler, A. Gritsch, et al., Heat-Integrated Reactor Concepts for Hydrogen Production by Methane Steam Reforming. *Accepted for Publication in Fuel Cells*, 2004.
9. G. Kolios, Zur autothermen Führung der Styrolsynthese mit periodischem Wechsel der Strömungsrichtung. Nr. 501, VDI-Fortschrittsberichte, Reihe 3, VDI-Verlag, Düsseldorf, 1997.
10. R. Charlesworth, A. Gough, C. Ramshaw, Combustion and steam reforming of methane on thin layer catalysts for use in catalytic plate reactors. *Fourth UK/National Conference on Heat Transfer, Institution of Mechanical Engineers*, 26–27 September 1995, pp. 85–89.
11. G. Kolios, J. Frauhammer, G. Eigenberger, Autothermal Fixed-Bed Reactor Concepts. *Chem. Eng. Sci.*, **2000**, 55, 5945–5967.
12. R. F. Blanks, T. S. Wittrig, D. A. Peterson, Bidirectional adiabatic synthesis gas generator. *Chem. Eng. Sci.*, **1990**, 45, 2407–2413.
13. A. M. De Groote, G. F. Froment, Synthesis Gas Production from Natural Gas in a Fixed-Bed Reactor with Reversed Flow. *Can. J. Chem. Eng.*, **1996**, 74, 735–742.
14. K. Gosiewski, Simulations of non-stationary reactors for the catalytic conversion of methane to synthesis gas. *Chem. Eng. Sci.*, **2001**, 56, 1501–1510.
15. G. Voser, J. Frauhammer, Modeling steady state and ignition during catalytic methane oxidation in a monolith reactor. *Chem. Eng. Sci.*, **2000**, 55, 2271–2286.
16. R. G. Craig, T. J. Delaney, J. M. Duffalo, *Catalytic dehydrogenation performance of the catofin process*. DeWitt Petrochemical Review, Houston 1990.
17. C. Ercan, R. J. Gartside, Reactor Performance and Stability in an Alternating Reaction-Reheat Paraffin Dehydrogenation System. *Can. J. Chem. Eng.*, **1996**, 74, 626–637.

18. T. N. Haynes, C. Georgakis, H. S. Caram, The application of reverse flow reactors to endothermic reactions. *Chem. Eng. Sci.*, **1992**, 47, 2927–2932.
19. Yu. Sh. Matros, *Catalytic processes under unsteady-state conditions. Studies in surface science and catalysis*. 1989, vol. 43, Reversal of the reaction mixture flow in the fixed catalyst bed. Amsterdam: Elsevier.
20. O. Levenspiel, Chemical Engineer's Grand Adventure. *Chem. Eng. Sci.*, **1988**, 43, 1427–1435.
21. M. S. Kulkarni, M. P. Duduković, A bidirectional fixed-bed reactor for coupling exothermic and endothermic reactions. *AIChE J.*, **1996**, 42, 2897–2910.
22. M. S. Kulkarni, M. P. Duduković, Periodic operation of asymmetric bidirectional fixed-bed reactors with temperature limitations. *Ind. Eng. Chem. Res.*, **1998**, 37, 770–781.
23. G. Kolios, G. Eigenberger, Styrene synthesis in a reverse-flow reactor. *Chem. Eng. Sci.*, **1999**, 54, 2637–2646.
24. W. R. Humphries, E. I. Griggs, A design handbook for phase change thermal control and energy storage devices. *NASA Technical paper*, 1074, Washington DC, 1977.
25. B. Glöckler, G. Kolios, G. Eigenberger, Analysis of a novel reverse-flow reactor concept for autothermal methane steam reforming. *Chem. Eng. Sci.*, **2003**, 58, 593–601.
26. B. Glöckler, A. Gritsch, A. Morillo, et al., Autothermal reactor concepts for endothermic fixed-bed reactions. *Chem. Eng. Res. Des.*, **2004**, 82 (A2), 148–159.
27. J. D. Snyder, B. Subramaniam, A novel flow strategy for ethylbenzene dehydrogenation in a packed-bed reactor. *Chem. Eng. Sci.*, **1994**, 49, 5585–5601.
28. M. van Sint Annaland, *A novel reverse flow reactor coupling endothermic and exothermic reactions*. PhD thesis, Twente University, Enschede, The Netherlands, 2000.
29. U. Nieken, O. Watzenberger, Periodic operation of the Deacon process. *Chem. Eng. Sci.*, **1999**, 54, 2619–2626.
30. A. Salden, *Adsorption/Incineration Process for Waste Gas Purification*. Ph.D. thesis, University of Stuttgart, Germany. 2002, Logos Verlag Berlin.
31. www.fuelcelltoday.com: Knowledge Bank.
32. E. H. Stitt, P. E. J. Abbott, B. J. Cromarty, et al., Emerging Trends in Syngas and Hydrogen. Presented at CatCon2000, 12–13 June, 2000, Houston, TX, USA.
33. E. H. Stitt, Multifunctional Reactors? 'Up to a Point Lord Copper'. *Chem. Eng. Res. Des.*, **2004**, 82 (A2), 129–139.
34. H. P. Schmidt, J. A. Wünnig, FLOX• Steam Reforming for PEM Fuel Cell Systems. 59th "Congresso ATI", Genua, 2004.
35. J. Wünnig, Flammenlose Oxidation von Brennstoff mit hochvorgewärmter Luft *Chem.-Ing.-Tech.*, **1991**, 63, 1243–1245.
36. A. Docter, G. Konrad, A. Lamm, Reformer für Benzin und benzinähnliche Kraftstoffe. *VDI – Berichte*, **2000**, 84, 399–411.
37. S. Springmann, *Kinetische Grundlagen und dynamische Simulation der autothermen Kraftstoffreformierung*. PhD thesis, University of Stuttgart, Germany. 2003, Logos Verlag Berlin.
38. P. S. Chintawar, B. Bowers, C. O'Brien, et al., Advanced High Efficiency Quick Start Fuel Processor for Transportation Applications. *Progress Report for Hydrogen, Fuel Cells, and Infrastructure Technologies Program*. U.S. Department of Energy; 2003.
39. N. Edwards, S. R. Ellis, J. C. Frost, et al., On-board hydrogen generation for transport applications: the HotSpot• methanol processor. *J. Power Sources*, **1998**, 71, 123–128.
40. M. Schuessler, M. Portscher, U. Limbeck, Monolithic integrated fuel processor for the conversion of liquid methanol. *Catalysis Today*, **2003**, 79–80, 511–520.

41. M. Krumpelt, T. R. Krause, J. D. Carter, et al., Fuel processing for fuel cell systems in transportation and portable power applications. *Catalysis Today*, **2002**, 77, 3–16.
42. S. Ahmed, R. Ahluwalia, S. H. D. Lee, Quick-Starting Fuel Processors – A Feasibility Study. *Progress Report for Hydrogen, Fuel Cells, and Infrastructure Technologies Program*. U.S. Department of Energy; 2003.
43. M. Zafir, A. Gavrilidis, Catalytic combustion assisted methane steam reforming in a catalytic plate reactor. *Chem. Eng. Sci.*, **2003**, 58, 3947–3960.
44. A. L. Dicks, S. L. Jones, R. Judd, et al., Assessment of advanced catalyst performance and fabrication options for a compact steam reformer. *Technical report: ETSU F/02/00180/REP*, U.S. Department of Trade and Industry; 2001.
45. J. Frauhammer, *Ein neues Gegenstrom-Reaktorkonzept für endotherme Hochtemperaturreaktionen*. PhD thesis, University of Stuttgart, Germany. 2003, VDI Verlag, Düsseldorf.
46. G. Kolios, J. Frauhammer, G. Eigenberger, A simplified procedure for the optimal design of autothermal reactors for endothermic high-temperature reactions. *Chem. Eng. Sci.*, **2001**, 56, 351–357.
47. Z. R. Ismagilov, V. V. Pushkarev, O. Yu. Podyacheva, et al., A catalytic heat-exchanging tubular reactor for combining of high-temperature exothermic and endothermic reactions. *Chem. Eng J.*, **2001**, 82, 355–360.
48. F. A. Robbins, H. Zhu, G. S. Jackson, Transient modeling of combined catalytic combustion/CH₄ steam reforming. *Catalysis Today*, **2003**, 83, 141–156.
49. A. Gritsch, G. Kolios, G. Eigenberger, Reaktorkonzepte zur autothermen Führung endothermer Hochtemperaturreaktionen. *Chem.-Ing.-Tech.*, **2004**, 76, 722–725.
50. G. Kolios, J. Frauhammer, G. Eigenberger, Efficient reactor concepts for coupling of endothermic and exothermic reactions. *Chem. Eng. Sci.*, **2002**, 57, 1505–1510.
51. G. Friedrich, G. Gaiser, G. Eigenberger, et al., *Kompakter Reaktor für katalytische Reaktionen mit integriertem Wärmerücktausch*. European Patent, EP 0 885 653 B1, 2003.
52. V. A. Kirillov, N. A. Kuzin, A. V. Kulikov, et al., Thermally coupled catalytic reactor for steam reforming of methane and liquid hydrocarbons. *Theor. Found. Chem. Eng.*, **2003**, 37, 1–9.
53. A. Morillo, A. Freund, C. Merten, Concept and design of a novel compact reactor for autothermal steam reforming with integrated evaporation and CO cleanup. *Ind. Eng. Chem. Res.*, **2004**, 43, 4624–4634.
54. R. Killpack, Ullmann's Encyclopedia of Industrial Chemistry. Propene, 1989, Vol. A22, VCH Verlagsgesellschaft, Weinheim, 217 ff.

2

Conceptual Design of Internal Reforming in High-Temperature Fuel Cells

Peter Heidebrecht and Kai Sundmacher

2.1

Introduction

The storage and production of fuels for fuel cells is currently under investigation by numerous research and development groups worldwide. Its impact on the electric efficiency and profitability of any type of fuel cell system is probably as important as the fuel cell design itself. Among the many proposed and investigated variants to supply hydrogen for the electrochemical oxidation process, the steam reforming concept has emerged as one of the most promising. A fuel which can either easily be stored or is available at the fuel cell site – for example gasoline, diesel fuel or natural gas – undergoes a reaction with water vapor to produce hydrogen and several byproducts. Often, this reforming product must be cleaned up before being fed into the fuel cell.

The key issue with reforming is the supply of heat to the endothermic process and the demand for high temperatures in order to obtain high reaction rates and favorable chemical equilibria. Whilst for low-temperature fuel cells this heat must be provided by external sources (e.g., the direct oxidation of a part of the feed gas), high-temperature fuel cells such as the Solid Oxide Fuel Cell (SOFC) and Molten Carbonate Fuel Cell (MCFC) can act as a heat source for the reforming process. This idea leads to a direct internal reforming (DIR) concept in which the endothermic reforming process is integrated into the fuel cell where the exothermic electrochemical reactions occur. The interactions of both processes are based on their mass and energy coupling. The use of mathematical models is probably the best way to gain a deeper understanding of the interactions of in-situ reforming and electrochemical oxidation.

Some research groups working on the modeling of MCFC include the reforming reactions in their process models in different ways. He and Chen [1] and Yoshiba et al. [2] only consider the water–gas shift reaction in a spatially distributed anode channel. Due to its high rate, they assume the shift reaction to be in chemical equilibrium. Lukas and Lee [3] and Park et al. [4] also describe the water–gas shift reaction in equilibrium, but in addition they include the steam reforming reaction of methane as an irreversible reaction with a finite reaction rate. In particular, Park

et al. focus on the effect of an indirect reforming unit in the stack. Although all of these models consider the influence of non-electrochemical reactions inside the fuel cell, none of them is suitable to easily and intuitively explain their impact on the system. This is mostly due to the complexity of these detailed models.

Advanced flow sheet configurations for MCFC have been investigated by Fellows [5] and Kortbeek and Ottervanger [6]. These authors propose more complex configurations, for example the use of some fuel cells primarily for reforming and others for energy production in one single stack. These configurations can be evaluated by using sophisticated models, but this does not improve the intuitive understanding of the interaction of reforming and electrochemical reactions. Therefore, a rather simple model is required that describes the basics of a DIR-MCFC in a physically meaningful way, but is also easy to apply.

In this chapter, we focus on the MCFC with internal reforming. After a brief technical introduction of this type of fuel cell, a model is presented that describes the interaction of the reforming reaction and the electrochemical oxidation reaction inside the MCFC with a set of only two ordinary differential equations (ODE) and some algebraic equations (AE). A diagram is introduced which allows the simulation results to be displayed in an easily interpretable way. Finally, the usefulness of the model and its accompanying diagram are demonstrated in several applications.

2.2

Technical Background

The working principle of the MCFC is illustrated in Fig. 2.1. The anode is fed with a preheated mixture of desulfurized natural gas and steam at a steam:carbon (S/C) ratio of about 2.5. This feed is converted via steam reforming into a hydrogen-rich gas mixture at the reformer catalyst, which is placed inside the anode channel. Carbon monoxide is the byproduct of this reforming reaction. Simultaneously, the water-gas shift reaction transforms carbon monoxide into carbon dioxide and another hydrogen molecule:

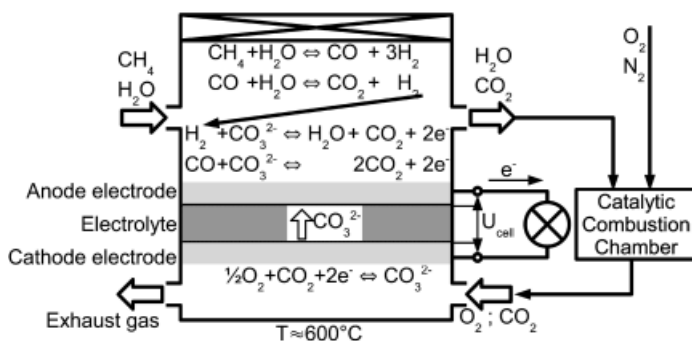


Fig. 2.1. Working principle of the Molten Carbonate Fuel Cell (MCFC) with direct internal reforming (DIR).



The equilibrium limitations of these two reforming reactions are overcome by continuous removal of hydrogen and carbon monoxide which are directly oxidized electrochemically at the anodic electrode. There, these components react with carbonate ions from the electrolyte to produce carbon dioxide, water and electrons according to the following stoichiometric relationships:



In addition to mass integration, the reforming process, Eqs. (1) and (2), which overall is endothermic, is energetically coupled to the exothermic oxidation reactions, Eqs. (3) and (4). Thus, the heat required for the generation of hydrogen is provided.

The anode exhaust gas is mixed with air, and the nonoxidized components are totally oxidized in a catalytic combustion chamber. Because air is fed in excess, the exhaust gas from the burner still contains a significant amount of oxygen. This gas is then fed to the cathode channel where the electrochemical reduction of oxygen takes place. There, new carbonate ions are produced from carbon dioxide and oxygen according to the backward direction of the following cathode reaction:



The carbonate ions are transported towards the anode electrode through the electrolyte, which is an eutectic carbonate melt. The cathodic exhaust gas leaves the fuel cell and, due to its high temperature of about 500 °C, it can be used for subsequent steam generation, for additional production of electric energy via a micro turbine or for other purposes.

In addition to hydrogen possibly being formed directly inside the anode channel, it can also be produced by other reforming steps. Figure 2.2 shows the three basic

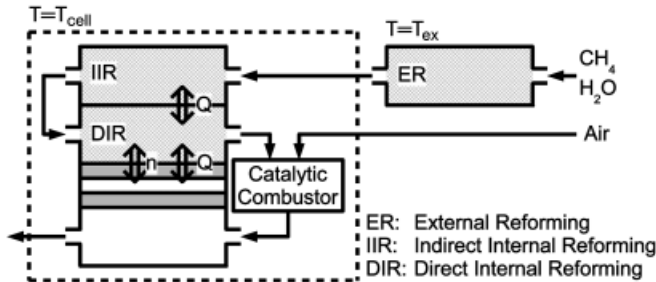


Fig. 2.2. Reforming concepts for high-temperature fuel cells.

reforming concepts for high-temperature fuel cells. External reforming (ER) occurs in a separate vessel outside the cell stack. Any arbitrary temperature can be applied, but high temperatures require external heating. For temperatures well below the cell temperature, the cell exhaust gas can be used to supply the required reaction heat to the ER process. The main advantage of ER is that it can be designed and operated independently of the conditions of the fuel cell itself.

The indirect internal reformer (IIR) is situated within the cell stack in separate reforming channels, where only the reforming reaction takes place. This concept features energetic coupling with the exothermic oxidation process. The main advantage is that no external heat exchanger is required, as the separator plate between IIR and anode channel fulfills this function. The IIR can be seen as an external reformer operating at fuel cell temperature.

Direct mass and energy coupling of the reforming and electrochemical processes are a unique feature of the direct internal reforming (DIR) concept. There, not only heat is exchanged between the two processes, but the products of the reforming reactions are also continuously removed by the oxidation reactions. This is a highly integrated concept which offers the chance for high system efficiency, but it requires sophisticated system design in order to work properly.

2.3

Modeling

A tool is required for the evaluation of possible combinations of different reforming concepts, and for the analysis of various flow sheet options such as gas recycling, cell cascading, and side feeding. This tool should be:

- physically meaningful in order to allow for an intuitive understanding of its results;
- flexible;
- fast to solve, as the task here is not a detailed and exact prediction of the cell behavior, but the conceptual design of a DIR-MCFC; and
- easy to illustrate and to be interpreted.

In this section, a mathematical model is introduced which fulfills these requirements. First, the complete model equations are given and their derivation is briefly indicated. In the second part, an accompanying diagram to this model is introduced, in which the simulation results can be displayed.

2.3.1

Model Derivation

The steady-state anode model is derived from a dynamic, spatially two-dimensional description of a single cross-flow MCFC in terms of dimensionless variables [7, 8] under the following assumptions:

- The system is at steady state.
- An infinite cathode gas recycle ratio is applied; this leads to a spatially concentrated composition and temperature of the cathode gas.

- The cell is isothermal. Temperature is a system parameter that can be set arbitrarily. Nevertheless, temperature effects on equilibria and reaction kinetics are still considered.
- The reaction system is simplified. The two reforming reactions (Eqs. (1) and (2)) are combined in a single reaction.



- Electrochemical carbon monoxide oxidation (Eq. (3)) is neglected.
- Mass transport resistance within the electrode pores is neglected.
- Potentiostatic operating mode is applied – that is, the cell voltage is taken as an input parameter.
- The ion transport resistance in the electrolyte perpendicular to the cell plain is negligible. Moreover, it is assumed that no ion conduction occurs along the cell plain. Thus, the electrolyte has identical electric potentials at the anode and cathode electrode, but these are locally distributed.
- The possibility of an anode gas recycling is considered.

In the following section, the component mass balances in the anode channel, some mixing rules, the equations for the cathode gas composition, the kinetics of the reforming and the electrochemical reactions and finally the equations for the fuel cell power are provided.

2.3.1.1 Anode Channel

The governing equations – that is, mainly the component and the total mass balances in the anode channels – are provided here in dimensionless form. The five ordinary differential equations (ODE) with respect to the spatial coordinate describe the development of the five unknowns in one single anode channel, namely the mole fractions, χ_i , with $i = \{\text{CH}_4, \text{H}_2\text{O}, \text{H}_2, \text{CO}_2\}$, as well as the molar flow density inside the anode channel, γ . Here, the Damköhler numbers, Da_j , are the dimensionless reaction rate constant of the reforming and the oxidation reaction, respectively, the r_j are the corresponding dimensionless reaction rates, and the v_{ij} are the stoichiometric coefficients:

$$\gamma \frac{d\chi_i}{d\zeta} = \sum_{j=\text{ref}, \text{ox}} (v_{i,j} - \chi_i \bar{v}_j) Da_j r_j \quad (7)$$

$$\frac{d\gamma}{d\zeta} = \sum_{j=\text{ref}, \text{ox}} \bar{v}_j Da_j r_j \quad (8)$$

The mole fractions and the total molar flow rate at the anode channel inlet, $\chi_{i,\text{in}}$ and Γ_{in} , serve as initial conditions:

The Damköhler numbers for the reforming and the oxidation reaction,

$$\chi_i(\zeta = 0) = \chi_{i,\text{in}} \quad (9)$$

$$\gamma(\zeta = 0) = \Gamma_{\text{in}} \quad (10)$$

Da_{ox} and Da_{red} , can not only be used to adjust finite reaction rate constants of both reactions in the simulation, but each of these reactions can be eliminated by setting the specific Damköhler number to zero. Thus, it is possible to simulate a pure reforming channel ($Da_{ox} = 0$) or an anode channel without direct internal reforming ($Da_{ref} = 0$).

To reduce the number of ODE even further, a physically motivated transformation is applied. The idea is that for a given composition of the feed gas (CH_4/H_2O -mixture, characterized by the S/C ratio), the composition of the gas at any point in the anode channel or in any of the reforming units is described by only two states: the extent of the reforming reaction, assigned ξ_{ref} , and the extent of the oxidation reaction, assigned ξ_{ox} . These variables are made dimensionless and normalized to unity, so they can be interpreted as follows:

$\xi_{ref} = 0 \Leftrightarrow$ gas is not reformed ... $\xi_{ref} = 1 \Leftrightarrow$ gas is completely reformed

$\xi_{ox} = 0 \Leftrightarrow$ gas is not oxidized ... $\xi_{ox} = 1 \Leftrightarrow$ gas is completely oxidized

Note that the extent of oxidation reaction is identical to the well-known fuel utilization, relating the rate of electrochemical fuel consumption to the fuel feed rate. Usually, a high fuel utilization is desirable.

The mole fraction of any component in the anode gas channel, χ_i , can be described as a function of the two extents of reactions, ξ_j :

$$\chi_i = \frac{\chi_{i,feed} + \sum_{j=ref,ox} \nu_{i,j} \cdot \xi_j \xi_{j,max}}{1 + \sum_{j=ref,ox} \bar{\nu}_j \cdot \xi_j \xi_{j,max}} \quad (11)$$

where the feed mole fractions are fixed by the S/C ratio:

$$\chi_{CH_4,feed} = \frac{1}{1+S/C}$$

$$\chi_{H_2O,feed} = \frac{S/C}{1+S/C}$$

The maximum possible extents of reactions

$$\xi_{ref,max} = \frac{1}{1+S/C}$$

$$\xi_{ox,max} = \frac{4}{1+S/C}$$

are used to normalize the extents of reaction. Via Eq. (11), the spatial derivative of the mole fraction in the component mass balance, Eq. (7), is replaced by the derivative of the extent of reaction:

$$\begin{aligned}
\frac{d\chi_i}{d\zeta} &= \sum_{j=\text{ref},\text{ox}} \left(\nu_{i,j} - \chi_i \bar{\nu}_j \right) \cdot \frac{d\xi_j}{d\zeta} \xi_{j,\text{max}} \cdot \left(1 + \sum_j \bar{\nu}_j \xi_j \xi_{j,\text{max}} \right)^{-1} \\
&= \sum_{j=\text{ref},\text{ox}} \left(\nu_{i,j} - \chi_i \bar{\nu}_j \right) \cdot \frac{Da_j r_j}{\gamma}
\end{aligned} \tag{12}$$

Rearranging Eq. (12) yields a set of ODE for the extents of the reforming and the oxidation reactions:

$$\frac{d\xi_j}{d\zeta} = \frac{Da_j r_j}{\gamma \cdot \xi_{j,\text{max}}} \cdot \left(1 + \sum_{j=\text{ref},\text{ox}} \bar{\nu}_j \xi_j \xi_{j,\text{max}} \right) \tag{13}$$

Inserting Eq. (13) into the total mass balance, Eq. (8), yields

$$\frac{d\gamma}{d\zeta} = \gamma \cdot \frac{\sum_{j=\text{ref},\text{ox}} \bar{\nu}_j \frac{d\xi_j}{d\zeta} \xi_{j,\text{max}}}{1 + \sum_{j=\text{ref},\text{ox}} \bar{\nu}_j \xi_j \xi_{j,\text{max}}} \tag{14}$$

The numerator on the right-hand side of Eq. (14) is the spatial derivative of the denominator. Thus, with

$$f = 1 + \sum_{j=\text{ref},\text{ox}} \bar{\nu}_j \xi_j \xi_{j,\text{max}} \tag{15}$$

we can rewrite Eq. (14) as

$$\frac{1}{\gamma} \frac{d\gamma}{d\zeta} = \frac{1}{f} \frac{df}{d\zeta} \tag{16}$$

Considering the initial condition of the total mass balance (Eq. 10), the solution of this ODE reads as follows:

$$\gamma = \Gamma_{in} \cdot \frac{1 + \sum_{j=\text{ref},\text{ox}} \bar{\nu}_j \xi_j \xi_{j,\text{max}}}{1 + \sum_{j=\text{ref},\text{ox}} \bar{\nu}_j \xi_{j,\text{in}} \xi_{j,\text{max}}} \tag{17}$$

Equations (14) and (17) can be simplified by introducing a corrected molar flow marked with a tilde, $\tilde{\Gamma}$. The molar flow of the gas may change due to two reasons: first, the adding of another flow to this gas stream or the removal of a part of the gas; and second, the change in total mole numbers due to chemical reactions. The correction eliminates the second effect:

$$\Gamma_{in} = \tilde{\Gamma}_{in} \cdot \left(1 + \sum_{j=\text{ref},\text{ox}} \bar{\nu}_j \cdot \xi_{j,\text{in}} \xi_{j,\text{max}} \right) \tag{18}$$

Thus, we receive for the molar flow density inside the anode channel:

$$\gamma = \tilde{\Gamma}_{in} \cdot \left(1 + \sum_{j=ref,ox} \bar{\nu}_j \xi_j \xi_{j,max} \right) \quad (19)$$

With Eq. (19), the final form of the component mass balance in terms of extents of reactions is obtained:

$$\frac{d\xi_j}{d\zeta} = \frac{Da_j r_j}{\tilde{\Gamma}_{in}} \cdot \frac{1}{\xi_{j,max}} \quad (20)$$

This is the main equation of the model, describing the progress of the reforming and the oxidation process along the spatial coordinate, ζ .

The initial conditions are given by the extents of reaction at the anode channel inlet:

$$\xi_j(\zeta = 0) = \xi_{j,in} \quad (21)$$

2.3.1.2 Mixing Rules

In one of the examples in the later sections of this chapter, an anode gas recycle is applied. Figure 2.3 shows such a configuration, together with the assigned variable names.

To calculate the required initial conditions for Eq. (20) and the molar flow into the anode channel, namely $\xi_{j,in}$ and $\tilde{\Gamma}$, some mixing rules are required. They result from the total and the component balances at the mixing point at the channel inlet:

$$\Gamma_{in} = \Gamma_0 + \Gamma_{back} \quad (22)$$

$$\Gamma_{in} \cdot \chi_{i,in} = \Gamma_0 \cdot \chi_{i,0} + \Gamma_{back} \cdot \chi_{i,back} \quad (23)$$

The mole fractions in Eq. (23) can be described by the extents of reaction (Eq. (11)):

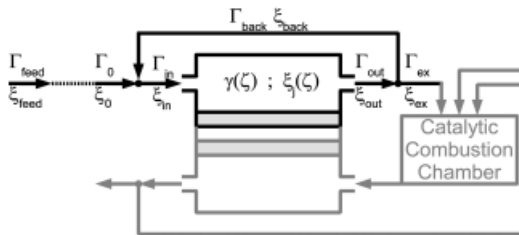


Fig. 2.3. Flow scheme and assigned variables of the steady-state anode model.

$$\begin{aligned}
& \Gamma_{in} \cdot \frac{\chi_{i,feed} + \sum_{j=ref,ox} \nu_{i,j} \xi_{j,in} \xi_{j,max}}{1 + \sum_{j=ref,ox} \bar{\nu}_j \xi_{j,in} \xi_{j,max}} \\
&= \Gamma_0 \cdot \frac{\chi_{i,feed} + \sum_{j=ref,ox} \nu_{i,j} \xi_{j,0} \xi_{j,max}}{1 + \sum_{j=ref,ox} \bar{\nu}_j \xi_{j,0} \xi_{j,max}} + \Gamma_{back} \cdot \frac{\chi_{i,feed} + \sum_{j=ref,ox} \nu_{i,j} \xi_{j,back} \xi_{j,max}}{1 + \sum_{j=ref,ox} \bar{\nu}_j \xi_{j,back} \xi_{j,max}} \quad (24)
\end{aligned}$$

Replacing the real molar flows by corrected molar flows, according to Eq. (17), yields:

$$\begin{aligned}
& \sum_{j=ref,ox} \nu_{i,j} (\tilde{\Gamma}_{in} \cdot \xi_{j,in} - \tilde{\Gamma}_0 \cdot \xi_{j,0} - \tilde{\Gamma}_{back} \cdot \xi_{j,back}) \xi_{j,max} \\
&+ (\tilde{\Gamma}_{in} - \tilde{\Gamma}_0 - \tilde{\Gamma}_{back}) \cdot \chi_{i,feed} = 0 \quad (25)
\end{aligned}$$

Because this equation must be fulfilled for any feed composition, $\chi_{i,feed}$, two equations follow:

$$\tilde{\Gamma}_{in} = \tilde{\Gamma}_0 + \tilde{\Gamma}_{back} \quad (26)$$

$$\xi_{j,in} = \frac{\tilde{\Gamma}_0 \cdot \xi_{j,0} + \tilde{\Gamma}_{back} \cdot \xi_{j,back}}{\tilde{\Gamma}_0 + \tilde{\Gamma}_{back}} \quad (27)$$

While the first of these two equations describes the addition of molar flows, the second is a lever rule applied to the extents of reaction at the mixing point.

2.3.1.3 Cathode Channel

For the calculation of the electrochemical reaction rates the cathode gas composition is required. Considering the MCFC as a black box, the anode feed gas is completely oxidized with air which is fed into the catalytic combustion chamber, either electrochemically or in an ordinary combustion reaction. With this, the amount and composition of the exhaust gas is independent of the electric cell performance and can be calculated directly from the conditions of the anode feed and the air feed. According to the assumption of spatially concentrated conditions inside the cathode channel, the exhaust conditions correspond to the conditions in the cathode gas channel. Thus, the cathode gas composition is determined from a combustion calculus.

The amount of air which is fed into the combustion chamber depends on the anode feed conditions and a given air number according to:

$$\Gamma_{air} = \frac{\lambda_{air}}{\chi_{O_2,air}} \cdot \Gamma_{feed} \cdot 2\chi_{CH_4,feed} \quad (28)$$

The total mass balance of the combustion yields the cathode outlet flow rate:

$$\Gamma_c = \Gamma_{feed} + \Gamma_{air} \quad (29)$$

The component mass balances deliver the molar fractions of the cathode gas as:

$$\chi_{CO_2,c} = \frac{\Gamma_{feed} \cdot \chi_{CH_4,feed}}{\Gamma_c} \quad (30)$$

$$\chi_{H_2O,c} = \frac{\Gamma_{feed} \cdot (\chi_{H_2O,feed} + 2\chi_{CH_4,feed})}{\Gamma_c} \quad (31)$$

$$\chi_{O_2,c} = \frac{\Gamma_{air} \cdot \chi_{O_2,air} - \Gamma_{feed} \cdot 2\chi_{CH_4,feed}}{\Gamma_c} \quad (32)$$

$$\chi_{N_2,c} = \frac{\Gamma_{air} \cdot \chi_{N_2,air}}{\Gamma_c} \quad (33)$$

There are no further components present in the cathode gas.

2.3.1.4 Reaction Kinetics

In addition to the two ODE for the extents of reactions, reaction kinetics are required. The reaction rate expressions describe reversible kinetics with a temperature-dependent equilibrium constant. The temperature dependence of the reaction rate constant is assumed to obey Arrhenius' law. However, for the proposed methodology this is of minor importance since isothermal cell operation is assumed.

Primarily, the reforming reaction rate depends on the anode gas composition according to the following power law kinetics:

$$\begin{aligned} r_{ref}(\xi, \vartheta) &= k_{ref}(\vartheta) \cdot \left\{ r_{ref}^+(\xi) - \frac{r_{ref}^-(\xi)}{K_{eq,ref}(\vartheta)} \right\} \\ &= \exp \left(Arr_{ref} \left(\frac{1}{\vartheta_{ref}^0} - \frac{1}{\vartheta} \right) \right) \cdot \left\{ \chi_{CH_4} \chi_{H_2O}^2 - \frac{\chi_{CO_2} \chi_{H_2}^4}{K_{eq,ref}(\vartheta)} \right\} \end{aligned} \quad (34)$$

The oxidation rate depends not only on the gas composition and the temperature parameter, but also on the electric potential difference between the electronically conductive part of the anode electrode and the ionically conductive electrolyte. Defining the electric potential of the solid part of the anode electrode as zero potential, the reaction rate depends on the electric potential in the electrolyte, ϕ_e . On the other hand, the reduction reaction rate depends on the electric potential difference at the cathode electrode, which is the difference between the given cell voltage, U_{cell} , and the electrolyte potential, ϕ_e . The equilibrium constants are determined by the

temperature-dependent open circuit voltages, $\Delta\phi_{ox,0}$ and $\Delta\phi_{red,0}$. Applying Butler–Volmer reaction kinetics, we receive:

$$\begin{aligned} r_{ox}(\xi, \vartheta, \phi_e) &= k_{ox}(\vartheta, \phi_e) \cdot \left\{ r_{ox}^+(\xi) - \frac{r_{ox}^-(\xi)}{K_{eq,ox}(\vartheta, \phi_e)} \right\} \\ &= \exp\left(Arr_{ox} \left(\frac{1}{\vartheta_{ox}^0} - \frac{1}{\vartheta} \right) \right) \cdot \exp\left(\frac{-\phi_e - \Delta\phi_{ox,0}(\vartheta)}{\vartheta} \right) \\ &\quad \cdot \left\{ \chi_{H_2} - \chi_{H_2O} \cdot \chi_{CO_2} \cdot \exp\left(-2 \cdot \frac{-\phi_e - \Delta\phi_{ox,0}(\vartheta)}{\vartheta} \right) \right\} \end{aligned} \quad (35)$$

$$\begin{aligned} r_{red}(\xi, \vartheta, U_{cell}, \phi_e) &= k_{ox}(\vartheta, U_{cell}, \phi_e) \cdot \left\{ r_{red}^+(\xi) - \frac{r_{red}^-(\xi)}{K_{eq,red}(\vartheta, U_{cell}, \phi_e)} \right\} \\ &= \exp\left(Arr_{red} \left(\frac{1}{\vartheta_{red}^0} - \frac{1}{\vartheta} \right) \right) \cdot \exp\left(2.5 \cdot \frac{U_{cell} - \phi_e - \Delta\phi_{red,0}(\vartheta)}{\vartheta} \right) \\ &\quad \cdot \left\{ \chi_{CO_2,c}^{-2} - \chi_{O_2,c}^{0.75} \cdot \chi_{CO_2,c}^{-0.5} \cdot \exp\left(-3 \cdot \frac{U_{cell} - \phi_e - \Delta\phi_{red,0}(\vartheta)}{\vartheta} \right) \right\} \end{aligned} \quad (36)$$

For the reduction reaction, Eq. (36), the reaction orders correspond to the superoxide reaction mechanism [9].

Since Eqs. (35) and (36) contain three unknowns (r_{ox} , r_{red} and ϕ_e), a steady-state charge balance is needed as an additional governing equation. It states that the current density produced at the anode electrode must be equal to the current density produced at the cathode electrode at any given point in the channel:

$$Da_{ox} \cdot r_{ox} = Da_{red} \cdot (-r_{red}) \quad (37)$$

In order to obtain the desired oxidation reaction rate (which is required in Eq. (20)), Eqs. (35) to (37) have to be solved for r_{ox} .

2.3.1.5 Cell Power

In the following illustrative examples, the electric DC power output of the cell is required in order to determine the performance of the cell. It is defined as the product of the change of the extent of the oxidation reaction, corresponding to the fuel utilization in this cell, with the given cell voltage.

$$P_{el} = \Delta\xi_{ox} \cdot U_{cell} \quad (38)$$

2.3.2

Conversion Diagram

With only two locally distributed states in the model, it is possible to illustrate all results in a phase diagram. In this diagram, the space coordinate is eliminated by plotting one state versus the second. Figure 2.4 shows the extent of the reforming reaction on the horizontal axis and the extent of oxidation reaction on the vertical axis.

Because the mole fraction of any component may not be negative, certain restrictions for physically reasonable states have to be considered in this conversion diagram. Due to these restrictions, all attainable states must be situated within a triangle, as illustrated in Fig. 2.4. In this figure it is also indicated that, for a given temperature and cell voltage, the reaction rates at every point within the attainable region are defined. A positive reforming rate means that the gas state moves to the right, while a positive oxidation rate causes an upwards move of the state. Together, both reaction rates form a vector indicating in which direction the state moves along the spatial coordinate.

All reactions are considered to be reversible, so the gas composition can reach equilibrium for one or both reactions in the anode channel. In Fig. 2.5, several equilibrium lines of the reforming reaction are displayed for different temperatures. On these lines, the rate of the reforming reaction equals zero.

The reforming equilibrium lines start from the right-hand bottom corner and end in the right-hand upper corner of the attainable region. How far they move to the left depends only on the given temperature. In general, low temperatures lead to a low equilibrium conversion of the reforming reaction; thus, the equilibrium curve reaches far to the left. For increasing temperature, the equilibrium line is shifted to the right – that is, towards higher equilibrium–reforming conversions.

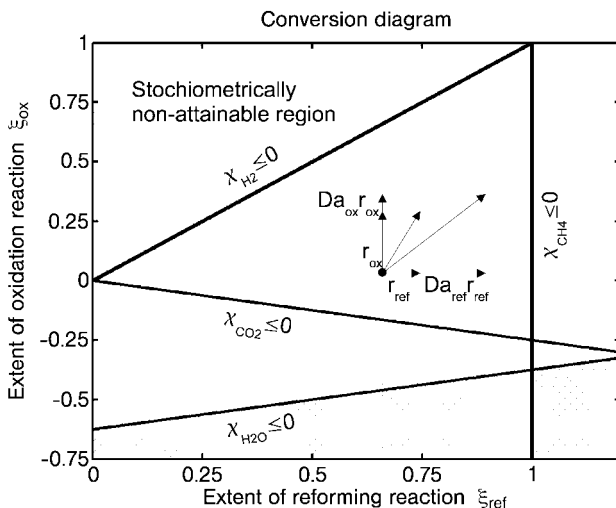


Fig. 2.4. The conversion diagram, stoichiometrically attainable region and reaction rate vector.

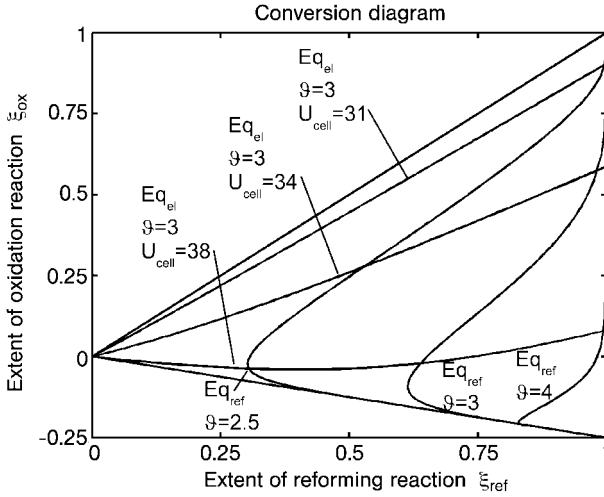


Fig. 2.5. Equilibrium lines of the reforming reaction (Eq_{ref}) at various temperatures and equilibrium lines of the oxidation reaction (Eq_{ox}) at constant temperature and various cell voltages. The dimensionless numbers correspond to the following values:
 $\theta = \{2.5, 3, 4\} \triangleq \{470^\circ\text{C}, 620^\circ\text{C}, 920^\circ\text{C}\}$
 $U_{cell} = \{31, 34, 38\} \triangleq \{796\text{mV}, 873\text{mV}, 976\text{mV}\}$

All oxidation equilibrium lines start at the diagram's origin and end somewhere at the right-hand boundary line. On each equilibrium line, the oxidation process comes to a halt. Their course depends on the given parameters of temperature and cell voltage. The three exemplary lines in Fig. 2.5 are at constant temperature, but varying cell voltage. The line approaches the diagonal for low cell voltage, which means that the electrochemical reaction reaches its equilibrium only at very low hydrogen contents in the gas. For high cell voltage, the equilibrium is at low extents of the oxidation reaction.

Due to their characteristic course, there is always one unique intersection point of both curves for any given temperature and voltage. At this intersection point, both reaction rates become zero. Once the gas has reached it, both reactions stop and the gas composition does not change anymore along the spatial coordinate, unless the temperature or the cell voltage is changed. Thus, this is a stationary point. Because the reactions always run towards their equilibrium, this stationary point is an attractor.

Two exemplary trajectories are shown in Fig. 2.6. The boundary condition of the first simulation is that both extents of reaction are zero; this means that upon entering the channel the gas has not undergone reforming or oxidation reactions. Within the channel, the reforming reaction starts and as soon as there is a significant amount of hydrogen available, the oxidation reaction rate also increases. Thus, the trajectory moves from the origin to the right and then starts to move upwards as

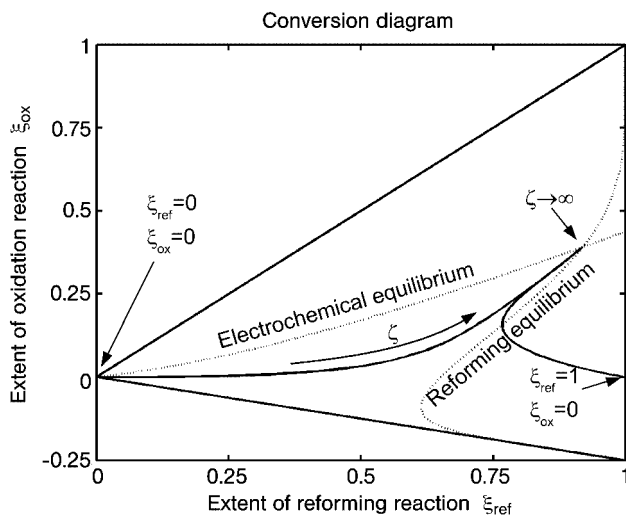


Fig. 2.6. Conversion diagram with two exemplary trajectories for identical temperature and cell voltage, but with different inlet conditions. Both end up in the same attractor, which is the intersecting point of the reforming and the oxidation equilibrium lines.

well. For an infinite channel length, the trajectory ends in the attractor point. The same holds true for a different inlet condition. Assume that a completely reformed gas enters the anode channel. Then, the inlet condition is situated beyond the equilibrium line of the reforming reaction, so the reforming will run backwards. Because the gas contains large amounts of hydrogen, the oxidation can start at once, so the trajectory goes up and left at first. At a certain point, the equilibrium line of the reforming process is reached. Here, only the oxidation reaction takes place, further consuming hydrogen from the gas mixture. This helps to overcome the reforming equilibrium line, so after this point the reforming reaction moves in forward direction again, now producing hydrogen instead of consuming it. For infinite channel length, the same attractor point is reached as in the first example.

2.4 Applications

The steady-state anode model can be applied for various purposes. In the following section, three applications are demonstrated, namely:

- A comparison of different combinations of reforming concepts.
- An evaluation of the benefit of a fuel cell cascade.
- An evaluation of a fuel cell operated with an anode exhaust gas recycle.

2.4.1

Comparison of Reforming Concepts

As indicated in Fig. 2.2, three different reforming concepts are available for high-temperature fuel cells. The steady-state anode model presented above allows a comparison of various combinations of reforming concepts. First, a system without a reforming catalyst inside the anode channel is considered – that is, a fuel cell without DIR. Three alternatives for fuel gas treatment are discussed:

- Low-temperature ER which can easily be heated by the cell's hot exhaust gas.
- IIR where the reforming temperature equals that of the cell.
- High-temperature ER which requires additional external heating.

In this application, all three reforming units are considered to be infinitely long, and thus equilibrium is reached in each unit. The effluent of the reforming unit is fed into the anode channel where only hydrogen oxidation takes place ($Da_{ref} = 0$).

The resulting trajectories are plotted in Fig. 2.7. Low-temperature ER and IIR produce anode fuel gases which are reformed to an extent of 30 % and 65 %, respectively. The subsequent fuel cell process can reach fuel utilizations of 20 % and 60 %, respectively. This fuel utilization is not satisfying because a large proportion of the fuel cannot be utilized for electric energy production. Only high-temperature ER offers the possibility to reach high fuel utilization, but its drawback is the need for extra heating, which certainly decreases the overall system efficiency. Thus, none of these alternatives is satisfying.

The situation changes significantly if DIR is applied. Figure 2.8 shows that, independent of the gas pre-treatment, high fuel utilizations can be reached with DIR, because all trajectories end in a single point being close to the right upper corner. Here, an additional drawback of the high-temperature ER is revealed: As the cell temperature is lower than the reforming temperature, the anode inlet condition is beyond the equilibrium line of the reforming reaction, and thus the reforming runs to the backward direction in the first part of the channel, spoiling the high conversion degree of reforming. The same attractor point, being reached by these three configurations with gas pre-treatment before the anode channel, can be reached by a system without any pre-treatment, where the fresh gas is directly fed into the anode channel (trajectory “DIR only”; Fig. 2.8).

These considerations clearly show the advantage of the DIR concept. Independent of the pre-treatment of the feed gas, the application of DIR always leads to a high degree of fuel utilization. As shown here, the steady-state anode model and the representation of its solutions in the conversion diagram are useful tools for evaluation and comparison of different process configurations.

2.4.2

Anode Cascade

Various authors consider appropriate flow sheets for fuel cell systems. Fellows [5] proposes to employ a cascade of fuel cells, operating at different cell voltages, to increase the overall electric power output. According to this concept the exhaust gas

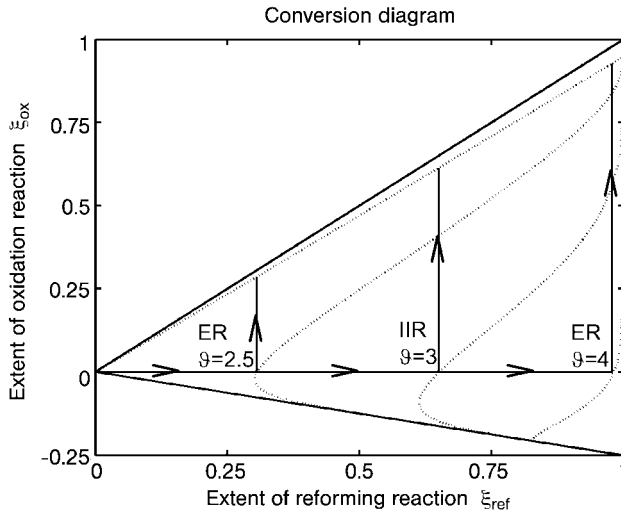


Fig. 2.7. Conversion diagram with trajectories for different reforming configurations without DIR.

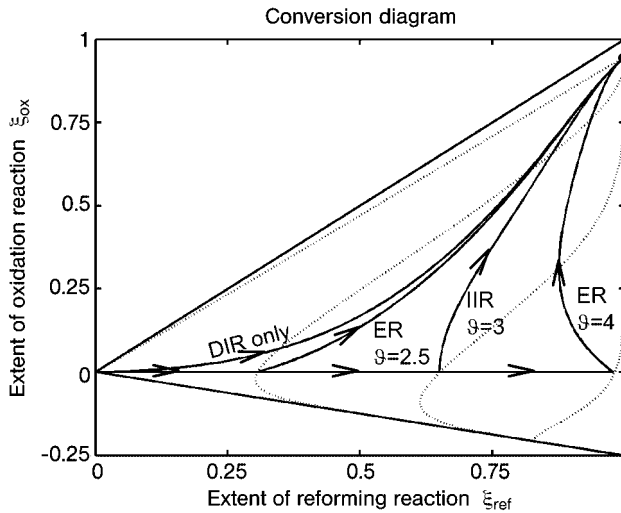


Fig. 2.8. Conversion diagram with trajectories for different reforming configurations based on DIR. High degrees of fuel utilization are attainable (cf. Fig. 2.7).

of the first cell's anode compartment is fed into a second cell, and so on (Fig. 2.9). The cascade considered here consists of two cells. Both cells together have the same size as the single cell used as a reference process for comparison.

With regard to the electric connections of the cascade, two different configurations are possible (Fig. 2.10). One possibility is that each cell is operated at its own cell voltage ($U_{cell,1}$ and $U_{cell,2}$) with an independent cell current ($I_{cell,1}$ and $I_{cell,2}$). Then, both cells require a separate electrical converter and they are connected as parallel current sources (Fig. 2.10(a)). The alternative is a configuration where the individual cell voltages differ, while the same cell current runs through both cells (Fig. 2.10(b)). This series connection requires only one electrical converter, and thus it requires less hardware installation. On the other hand, the equality condition of both cell currents reduces the number of degrees of freedom for the operation of this cell. Both electric configurations are analyzed in the following section.

All three systems – that is, the single cell and the two cell cascades in either configuration – are simulated with the steady-state anode model. They are optimized to yield an optimum of electric power at a given feed rate. The optimization variables are the cell voltage for the single cell system, and both cell voltages plus the size of the first cell for both cascade configurations.

Figure 2.11 shows the resulting trajectories for the two-cell cascade in parallel configuration in comparison to the single cell. The electric power output is illustrated by the rectangles on the left of the vertical axis. Their area is the product of the cell voltage and the differences of oxidation conversion over each cell. From the values in Tab. 2.1 it can be seen that the electric power output of the cascade configuration exceeds that of the single cell by 4.6 %.

The trajectory for the series connection is shown in Fig. 2.12. The differences of oxidation conversion over both cells are equal, so that the condition of equal cell currents

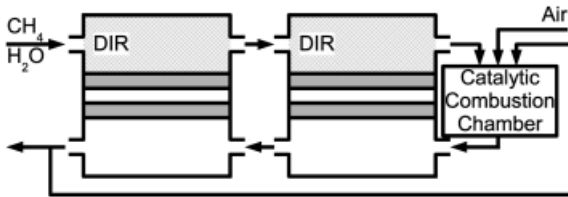


Fig. 2.9. Flow sheet of a fuel cell cascade.

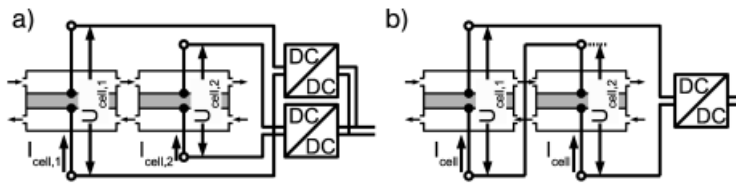


Fig. 2.10. Alternative electric configurations of a fuel cell cascade. a) Parallel cascade with independent cell voltage and cell current of each cell; b) series cascade with independent cell voltage and equal cell current.

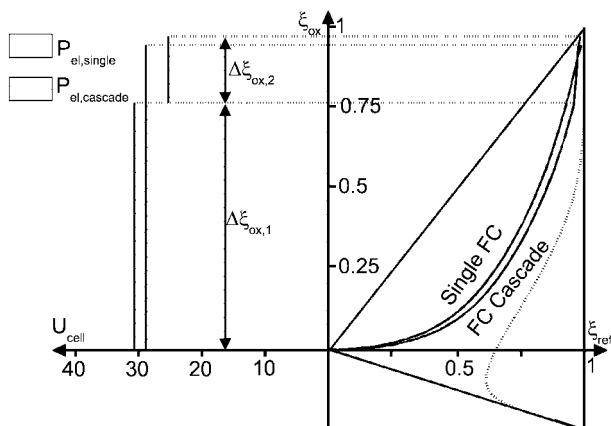


Fig. 2.11. Conversion diagram with a trajectory for a single cell and a trajectory for a fuel cell cascade in electric parallel configuration. Cell voltages are optimized for maximum electric power output. For quantitative results, see Tab. 2.1.

in both cells is fulfilled. This condition leads to a smaller increase of electric power, nevertheless the increase of the overall power output by 3.7 % is still significant.

According to these calculations, the option of applying fuel cell cascades in order to increase the electric power output and thereby increase the system efficiency is an interesting option. From an economical point of view, the additional hardware installations which are necessary for such a system stand against this configuration, at least for small systems. For large systems – for example in the Megawatt class –

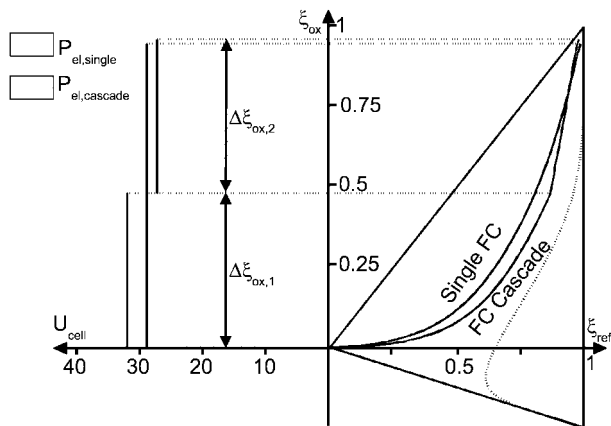


Fig. 2.12. Conversion diagram with a trajectory for a single cell and a trajectory for a fuel cell cascade in electric series configuration. Cell voltages are optimized for maximum electric power output. For quantitative results, see Tab. 2.1.

Table 2.1. Optimization results of the single cell and both two-cell cascades.

	Length [ζ]	Voltage [U_{cell}]	Extent of oxidation reaction [$\Delta\xi_{ox}$]	Electric power [P_{el}]
Single	1.0	28.83	0.947	27.30
Parallel cascade				
One-cell	0.674	30.81	0.683	21.04
Two-cell	0.326	27.00	0.278	7.51
Total	1.0	–	0.961	28.55 (+4.6%)
Series cascade				
One-cell	0.508	31.84	0.480	15.28
Two-cell	0.492	27.20	0.480	13.06
Total	1.0	–	0.960	28.34 (+3.7%)

this might be profitable. The benefit of the steady-state anode model in this case goes beyond illustration and intuitive understanding, it can also serve as a tool for a first quantitative system design, and it allows rough economic calculations.

2.4.3

Anode Exhaust Gas Recycling

In the open literature, one can find the proposal to recycle part of the anode exhaust gas back towards the anode inlet [5, 6], as shown in Fig. 2.3. Especially for pure DIR systems, this has certain advantages: If fresh feed gas is fed into the anode channel, only low hydrogen contents will be present at the inlet, and consequently the electrode will not be used in this region. This can be amended by recycling a part of the exhaust, which still contains some hydrogen, back to the inlet.

Define the recycle flow via a recycle ratio, R , according to:

$$R = \frac{\tilde{\Gamma}_{feed}}{\tilde{\Gamma}_{back}} \quad (39)$$

Then, the mixing rules (Eqs. (26) and (27)) simplify to

$$\tilde{\Gamma}_{in} = (1 + R) \cdot \tilde{\Gamma}_{feed} \quad (40)$$

$$\xi_{j,in} = \frac{\xi_{j,0} + R \cdot \xi_{j,back}}{1 + R} \quad (41)$$

where the initial condition is identical to Eq. (10):

$$\xi_j(\zeta = 0) = \xi_{j,in} \quad (42)$$

and the extent of reaction of the recycle stream is equal to the conditions at the channel outlet:

$$\xi_{j,out} = \xi_j(\zeta = 1) \quad (43)$$

Figure 2.13 shows the trajectory of a single cell without ($R = 0$) and with anode gas recycling ($R = 0.3$). Both are operated at their individual optimal cell voltage, so that the electric power output is maximized. While the inlet condition of the system without recycle is at the origin, the inlet condition of the recycle system is calculated via the lever rule (Eq. (27)) from the conditions of the feed gas and the anode exhaust gas. Because the exhaust gas composition is unknown, one has first to guess the outlet condition and then calculate the inlet condition and integrate along the channel to obtain a new value for the outlet condition. For the correct solution, the guessed and simulated values must be equal. This can be achieved by an error minimization algorithm or by iterative insertion of the latest simulated value as a new guess for the exhaust condition.

The electric power output of the recycle system is always lower than would be obtained from the system without recycling. This is because back-mixing always leads to a deterioration in reactor performance in systems with a positive reaction order with respect to the educts. Thus, the higher the recycling ratio is, the lower the electric power output becomes. Moreover, the conversion diagram can be used for explaining the role of anode gas recycling. For DIR systems with unreformed feed, the trajectories are usually bent to the left-hand side. This means that the inlet condition of a recycle system can only lie within the bent of the corresponding no-recycle

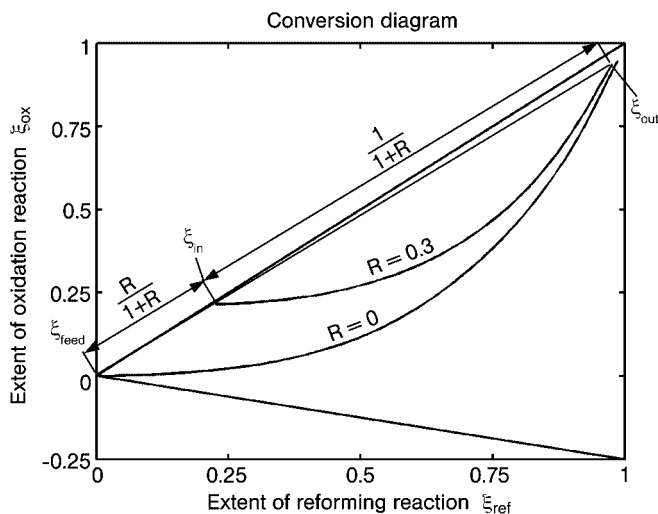


Fig. 2.13. Conversion diagram with trajectories for systems without and with anode gas recycling.

system. Consequently, the trajectory lies closer to the main diagonal. In this region, lower cell voltages must be applied to achieve comparable oxidation rates and therefore reach high fuel utilizations. In this way, the electric power output of the cell is decreased.

Although this result shows the disadvantage of anode gas recycling, it has benefits that may compensate for the loss in power output. This is due to the fact that feeding fresh gas into a DIR-channel without any gas recycling leads to high reforming reaction rates at the inlet. Consequently, the temperature falls sharply, leading to strong temperature gradients. This can be avoided by the recycling of anode exhaust gas, which leads to a homogenization of the temperature profile.

2.5

Summary and Conclusions

High-temperature fuel cells such as the Molten Carbonate Fuel Cell (MCFC) or the Solid Oxide Fuel Cell (SOFC) offer the possibility of integrating the endothermic reforming process and the exothermic electrochemical oxidation process inside the cell. In addition to heat integration, mass integration of both processes helps to overcome equilibrium limitations of the reforming reactions. Thereby, process integration allows for high degrees of fuel utilization and high efficiency of fuel cell systems.

The interaction of these two processes can be described by a simple isothermal model, which is based on balances of mass and charge. The model describes the extent of the reforming and oxidation reactions along the anode channel. The essential simulation results can easily be displayed in a conversion diagram which is a phase diagram of the two dynamic state variables, namely the extents of two reactions.

In this chapter, three applications of this model are demonstrated. The comparison of different reforming concepts reveals the advantages of direct internal reforming (DIR) in the anode channel of the fuel cell. Moreover, with the help of the proposed model, the benefit of fuel cell cascades can be demonstrated and they can be compared to single cells. Results indicate that a considerable power increase can be expected, but the additional hardware required might offset any benefit in the case of smaller systems. The third application demonstrates that anode gas recycle can be simulated with this model, but it also reveals its limitations, as temperature effects are not considered.

This shows that the basic features of DIR, although a highly integrated and complex process concept, can be analyzed using simple process models. In particular, these simple models are helpful for preliminary process design.

Symbols

All variables are dimensionless.

Latin symbols

Arr_j	Arrhenius number of reaction j
Da_j	Damköhler number of reaction j
k_j	Arrhenius term of reaction j
K_j	equilibrium constant of reaction j
r_j	reaction rate of reaction j
P_{el}	electric power
R	anode gas recycle ratio
U_{cell}	cell voltage

Greek symbols

γ	molar flow density (in the anode channel)
Γ	molar flow (outside any channel)
$\tilde{\Gamma}$	corrected molar flow
ζ	spatial coordinate
ϑ	temperature
λ_{air}	air number
$\nu_{i,j}$	stoichiometric coefficient of component i in reaction j
$\bar{\nu}_j$	sum of stoichiometric coefficients of reaction j
ξ_j	extent of reaction j
$\xi_{j,max}$	normalization factor for ξ_j
ϕ_e	electric potential in the electrolyte
$\Delta\phi_{j,0}$	standard equilibrium potential difference of reaction j
χ_i	mole fraction of component i

Indices

Subscripts

0	standard condition
air	air (fed into the catalytic combustion chamber)
back	anode gas recycle
c	cathode
e	electrolyte
ex	exhaust gas
feed	system feed
i	component index
in	anode channel inlet
j	reaction index
max	see above, $\xi_{j,max}$
out	anode channel outlet
ox	oxidation reaction
red	reduction reaction
ref	reforming reaction

Superscripts

+	forward reaction direction
−	backward reaction direction
0	equilibrium

Values of dimensionless model parameters

	Da_j	Arr_j	Equilibrium	Feed	Air/Others
Reforming	25	84.4	$K_{eq,ref} = \exp\left(26.22 - \frac{75.83}{T}\right)$	$S/C = 2.5$	$\lambda_{air} = 2.2$
Oxidation	5	21.6	$\Delta\phi_{ox,0} = 28.26 - 19.84 \cdot T$	$\Gamma_{feed} = 1$	$\chi_{O_2,air} = 0.21$
Reduction	0.3	31.2	$\Delta\phi_{red,0} = 78.00 - 23.06 \cdot T$		

References

1. W. He, Q. Chen, *Journal of Power Sources*, **1998**, 73, 182–192.
2. F. Yoshida, N. Ono, Y. Izaki, et al., *Journal of Power Sources*, **1998**, 71, 328–336.
3. M. D. Lukas, K. Y. Lee, H. Ghezal-Ayagh, *Control Engineering Practice*, **2002**, 10, 197–206.
4. H.-K. Park, Y.-R. Lee, M.-H. Kim, et al., *Journal of Power Sources*, **2002**, 104, 140–147.
5. R. Fellows, *Journal of Power Sources*, **1998**, 71, 281–287.
6. P. J. Kortbeek, R. Ottervanger, *Journal of Power Sources*, **1998**, 71, 223–225.
7. P. Heidebrecht, K. Sundmacher, *Chemical Engineering Science*, **2003**, 58, 1029–1036.
8. P. Heidebrecht, K. Sundmacher, *Fuel Cells*, **2002**, No. 3-4, 166–180.
9. J. A. Prins-Jansen, K. Hemmes, J. H. W. de Wit, *Electrochimica Acta*, **1997**, 42, 3585–3600.

3

Instabilities in High-Temperature Fuel Cells due to Combined Heat and Charge Transport

Michael Mangold, M Krasnyk, Achim Kienle and Kai Sundmacher

3.1

Introduction

Fuel cells are characterized by the combined transport of mass, heat, and electrical charge. Especially in the case of high-temperature fuel cells, the control of the temperature inside the fuel cell stack is a key issue for the process operation. Because the stacks are very sensitive to thermal stress, great care must be taken in order to avoid strong temperature gradients and local over-heating. A number of potential sources of hot-spot formation are known from classical fixed-bed reactors: Creeping reaction fronts, caused, e.g., by a drop of the inlet temperature or by a catalyst deactivation, lead to an over-adiabatic temperature rise [10]. The coupling of exothermic and endothermic reactions, e.g., the coupling of exothermic electrochemical reactions and endothermic internal reforming reactions, is another possible reason for high temperature peaks [5]. In this chapter, it is shown that there may be an additional source of hot-spot formation only present in fuel cells and, to our knowledge, not yet reported in the open literature. This new source is the temperature-dependent conductivity of the electrolyte that is used to transport charge from one electrode to the other and to close the electrical circuit internally. The charge transport occurs by migration, diffusion, and convection of ions. The mobility of the ions and hence the conductivity of the electrolyte increases with increasing temperature [3, 9, 11]. This property may be a potential source of instability: A local temperature rise reduces the resistance of the electrolyte and increases the local current density. Due to ohmic losses and reactive heat production, this raises the local temperature further and finally may lead to the formation of a hot spot.

It is the objective of this chapter to study this effect by a model-based analysis. The spatially distributed model used here will be derived in the next section. In a first step, the steady-state behavior of the model will be investigated by a phase plane analysis for the case of potentiostatic operation of the cell. In the second step, numerical bifurcation analysis of the model will be used to study the technically more interesting case of galvanostatic operation.

3.2

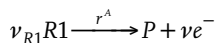
Modeling

3.2.1

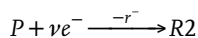
Model Assumptions

The analysis of instabilities in high-temperature fuel cells is based on a spatially distributed model derived in this section. A countercurrent fuel cell as shown in Fig. 3.1 is considered. The main model assumptions are:

- The model is one-dimensional in space with space coordinate η . Gradients in the direction of the gas flow are considered.
- As electrodes and electrolyte are in very close contact, they are assumed to have the same temperature Θ^S . The anode and cathode gas channels have a finite heat transfer to the solid part with temperatures Θ^A and Θ^C , respectively.
- As the electrolyte in the fuel cell typically is a very thin layer, charge transport in η direction is neglected in the electrolyte.
- A simple anodic reaction



and a cathodic reaction



are considered. $R1$ and $R2$ are gaseous components in the anode and the cathode, P is an ionic species responsible for the charge transport in the electrolyte. Reversible kinetics of the Butler–Volmer type are used to describe the reaction rates.

- The capacity of the anodic and cathodic double layers is neglected, as the charging and discharging of the double layers is generally assumed to be a very fast process compared to the other processes in the cell.
- A full model of the charge transport in the electrolyte would require the detailed description of the ionic transport processes inside the electrolyte. However, for the orientating study pursued in this contribution, it seems more appropriate to choose a simpler model that is able to describe the temperature dependence of the electrolyte qualitatively. The temperature dependence of diffusion coefficients in molten electrolytes can be described by an Arrhenius function [1]. Therefore, the temperature dependence of the conductivity is assumed to be of an Arrhenius type, as suggested in [6].

3.2.2

Model Equations

Mass, energy, and charge balances lead to the following system of dimensionless model equations:

Anode mass balance for component $R1$:

$$\frac{\partial x_{R1}}{\partial \tau} = -v^A \frac{\partial x_{R1}}{\partial \eta} - \beta^A i (1 - x_{R1}) \quad x_{R1}(0, \tau) = 1 \quad (1)$$

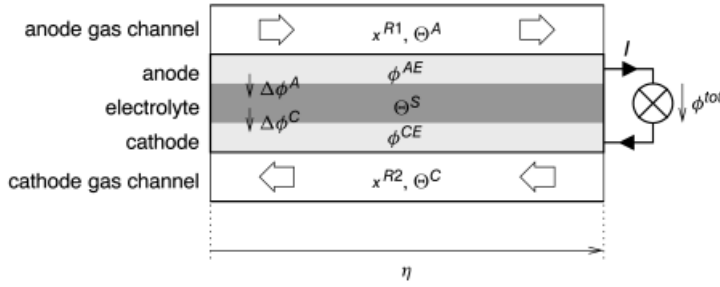


Fig. 3.1. Sketch of the considered fuel cell.

Energy balance for the anode gas channel:

$$\frac{\partial \Theta^A}{\partial \tau} = -v^A \frac{\partial \Theta^A}{\partial \eta} + Bi^A \frac{1}{\varepsilon} (\Theta^S - \Theta^A) \quad \Theta^A(0, \tau) = 0 \quad (2)$$

Cathode mass balance for component $R2$:

$$\frac{\partial x_{R2}}{\partial \tau} = v^C \frac{\partial x_{R2}}{\partial \eta} + \beta^C i (1 - x_{R2}) \quad x_{R2}(1, \tau) = 0 \quad (3)$$

Energy balance for the cathode gas channel:

$$\frac{\partial \Theta^C}{\partial \tau} = v^C \frac{\partial \Theta^C}{\partial \eta} + Bi^C \frac{1}{\varepsilon} (\Theta^S - \Theta^C) + \beta^C i (\Theta^S - \Theta^C) \quad \Theta^C(1, \tau) = 0 \quad (4)$$

Energy balance for the solid parts of the cell consisting of electrodes and electrolyte:

$$\begin{aligned} \frac{\partial \Theta^S}{\partial \tau} = & \frac{\partial^2 \Theta^S}{\partial \eta^2} + \left(B - (\varphi^{CE} - \varphi^{AE}) \right) i + \kappa^E \left(\left(\frac{\partial \varphi^{AE}}{\partial \eta} \right)^2 + \left(\frac{\partial \varphi^{CE}}{\partial \eta} \right)^2 \right) \\ & + \left(\frac{Bi^S}{2} + \varepsilon \beta^S i \right) (\Theta^A - \Theta^S) + \frac{Bi^S}{2} (\Theta^C - \Theta^S) \end{aligned} \quad (5)$$

$$\left. \frac{\partial \Theta^S}{\partial \eta} \right|_{0, \tau} = Bi^B \Theta^S(0, \tau) \quad \left. \frac{\partial \Theta^S}{\partial \eta} \right|_{1, \tau} = -Bi^B \Theta^S(1, \tau)$$

Voltage drop in the electrolyte, $\psi^\kappa \exp\left(\gamma^\kappa \frac{\Theta^S}{1+\Theta^S}\right)$ being the electrolyte conductivity:

$$i = \psi^\kappa \exp\left(\gamma^\kappa \frac{\Theta^S}{1+\Theta^S}\right) (\Delta\varphi^A + \Delta\varphi^C - (\varphi^{CE} - \varphi^{AE})) \quad (6)$$

Anodic reaction kinetics:

$$i = \psi^A \exp\left(\gamma^A \frac{\Theta^S}{1+\Theta^S}\right) \left\{ \exp\left(-\left(1-\beta^A\right)\gamma^* \frac{\Delta\varphi^A}{1+\Theta^S}\right) x_{R1} - K_{eq}^A \exp\left(\beta^A \gamma^* \frac{\Delta\varphi^A}{1+\Theta^S}\right) \right\} \quad (7)$$

Cathodic reaction kinetics:

$$i = \psi^C \exp\left(\gamma^C \frac{\Theta^S}{1+\Theta^S}\right) \left\{ \exp\left(-\left(1-\beta^C\right)\gamma^* \frac{\Delta\varphi^C}{1+\Theta^S}\right) - K_{eq}^C \exp\left(\beta^C \gamma^* \frac{\Delta\varphi^C}{1+\Theta^S}\right) x_{R2} \right\} \quad (8)$$

Electrical potential in the anode:

$$\kappa^E \frac{\partial^2 \varphi^{AE}}{\partial \eta^2} = i \quad \varphi^{AE}(0, \tau) = \varphi_0^{AE} \quad \frac{\partial \varphi^{AE}}{\partial \eta} \Big|_{1, \tau} = 0 \quad (9)$$

Electrical potential in the cathode:

$$-\kappa^E \frac{\partial^2 \varphi^{CE}}{\partial \eta^2} = i \quad \kappa^E \frac{\partial \varphi^{CE}}{\partial \eta} \Big|_{0, \tau} = I \quad \frac{\partial \varphi^{CE}}{\partial \eta} \Big|_{1, \tau} = 0 \quad (10)$$

3.2.3

Simplified Model

For the further analysis of the system, some additional simplifying assumptions are made:

- A high flow rate in the gas channels and a low fuel utilization are assumed. In this case, the temperature and the composition in the gas channels are approximately constant and identical to the inlet conditions. Therefore, the mass and energy balances (1, 2, 3, 4) are no longer needed, and the reaction kinetics (7, 8) can be simplified to zero-order kinetics.
- As the electrodes are typically made of highly conducting material, it seems justified to assume infinite conductivity of them, i.e. $\kappa^E \rightarrow \infty$. Under this assumption, the potentials φ^{AE} and φ^{CE} become space-independent, $\varphi^{tot} = \varphi^{CE} - \varphi^{AE}$ being the total cell voltage. The anode potential is identical to the reference

potential φ_0^{AE} , the cathode potential is given implicitly by the over-all charge balance $I = \int_0^1 i \, d\eta$.

- The enthalpy flux caused by mass transport from the gas channels to the electrodes is considered negligible.

Using Θ instead of Θ^S for the solid temperature, the resulting simplified system of model equations reads:

$$\frac{\partial \Theta}{\partial \tau} = \frac{\partial^2 \Theta}{\partial \eta^2} + (B - \varphi^{tot})i - Bi^S \Theta \quad (11)$$

$$\left. \frac{\partial \Theta}{\partial \eta} \right|_{0,\tau} = Bi^B \Theta(0,\tau) \quad \left. \frac{\partial \Theta}{\partial \eta} \right|_{1,\tau} = -Bi^B \Theta(1,\tau)$$

$$i = \psi^A \exp\left(\gamma^A \frac{\Theta}{1+\Theta}\right) \left\{ \exp\left(-\left(1-\beta^A\right)\gamma^* \frac{\Delta\varphi^A}{1+\Theta}\right) - K_{eq}^A \exp\left(\beta^A \gamma^* \frac{\Delta\varphi^A}{1+\Theta}\right) \right\} \quad (12)$$

$$i = \psi^C \exp\left(\gamma^C \frac{\Theta}{1+\Theta}\right) \left\{ \exp\left(-\left(1-\beta^C\right)\gamma^* \frac{\Delta\varphi^C}{1+\Theta}\right) - K_{eq}^C \exp\left(\beta^C \gamma^* \frac{\Delta\varphi^C}{1+\Theta}\right) \right\} \quad (13)$$

$$i = \psi^K \exp\left(\gamma^K \frac{\Theta}{1+\Theta}\right) (\Delta\varphi^A + \Delta\varphi^C - \varphi^{tot}) \quad (14)$$

$$I = \int_0^1 i \, d\eta \quad (15)$$

The values of the dimensionless parameters in Eqs. (11–15) used in the simulations and considered as realistic for high-temperature fuel cells are listed in Tab. 3.1. The system (11–15) is underdetermined, until one additional correlation for the cell current I and the cell voltage φ^{tot} are added to the model equations. This additional correlation may be to set the cell current to a constant value (galvanostatic operation), to set the cell voltage to a constant value (potentiostatic operation), or to relate the cell current to the cell voltage by some external load. From the viewpoint of mathematical analysis, the potentiostatic operation is the most convenient mode of operation, because in this case the partial differential Eq. (11) and the algebraic Eqs. (12–14) can be solved for the unknowns Θ , $\Delta\varphi^A$, $\Delta\varphi^C$, and i . The integral Eq. (15) is an explicit equation for the cell current I in potentiostatic operation. As I does not appear in any other equation, (15) does not have to be included in the analysis in this case. The situation is more complicated in the case of galvanostatic operation, because then the algebraic Eqs. (12–14) and the integral Eq. (15) form a set of implicit equations for the unknowns $\Delta\varphi^A$, $\Delta\varphi^C$, i , and φ^{tot} . The modes of galvanostatic and potentiostatic operation will be investigated in the following sections.

Table 3.1. Parameter values used in the simulations, if not given differently in the text.

$$B = 0.9328$$

$$\psi^A = \psi^C = 7.385 \cdot 10^4$$

$$\gamma^A = \gamma^C = 15.04$$

$$\gamma^* = 32$$

$$\psi^K = 4.86 \cdot 10^3$$

$$Bi^S = 6480$$

$$Bi^B = 1.08$$

3.3

Potentiostatic Operation

This section treats the steady-state behavior of the cell for the case of fixed cell voltage. In the first part, a cell of infinite length is considered. This reduces the problem to the analysis of two ordinary differential equations in space describing the stationary energy balance. The second part deals with a fuel cell of finite length and includes the boundary conditions of Eq. (11) in the investigation.

3.3.1

Cell with Infinite Length

In the steady-state case, the energy balance (11) can be transformed to two first-order differential equations in space:

$$\frac{d\Theta}{d\eta} = \Theta_p \quad (16)$$

$$\frac{d\Theta_p}{d\eta} = (\varphi^{tot} - B) i + Bi^S \Theta \quad (17)$$

The newly introduced variable Θ_p is the spatial temperature gradient. As the cell voltage φ^{tot} is given, the steady-state system is completed by the three implicit algebraic correlations (12–14) for the unknowns $\Delta\varphi^A$, $\Delta\varphi^C$, and i . The solution of the steady-state system can be visualized in a phase diagram, where Θ_p is plotted against Θ . The result for the parameter values listed in Tab. 3.1 is shown in Fig. 3.2.

An equilibrium point of (16, 17), where $\frac{d\Theta}{d\eta} = \frac{d\Theta_p}{d\eta} = 0$, corresponds to a solution with a spatially constant temperature profile and to a single solution point in the phase plane. In the example shown in Fig. 3.2 two classes of equilibrium points exist. The equilibria are either saddle points or marginally stable focuses, as follows directly from the Jacobian

$$J = \begin{pmatrix} 0 & 1 \\ Bi^S + (\varphi^{tot} - B) \frac{\partial i}{\partial \Theta} & 0 \end{pmatrix} \quad (18)$$

The other trajectories shown in Fig. 3.2 belong to spatially inhomogeneous solutions. They can also be grouped into two categories. The first group are solutions coming from and going towards infinity with a single temperature maximum or temperature minimum on the Θ -axis. An example is the solution “I” in Fig. 3.2. Solutions of this type exist, if one of the equilibria is a saddle point. The second category are closed trajectories around a focus point and hence exist, if there is a focus among the equilibria. Solution “II” in Fig. 3.2 belongs to this category. The closed trajectories correspond to periodic solutions in space: When moving along the space coordinate, the temperature oscillates between a minimum – the utter left point of the closed trajectory – and a maximum – the trajectory’s utter right point.

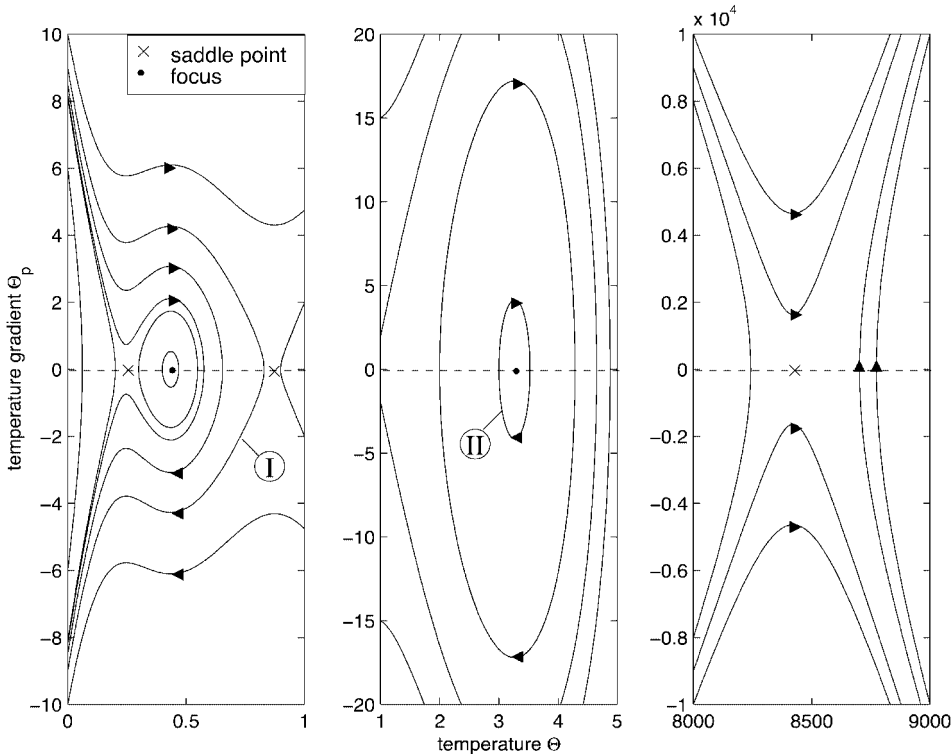


Fig. 3.2. Steady-state solutions of an infinite length system for potentiostatic operation; $\varphi^{tot} = 0.425$; other parameters as in Tab. 3.1.

The number and type of equilibrium points of the system depends on the values of the model parameters and can be determined conveniently by a bifurcation analysis. Figure 3.3 shows the solution dependency on the model parameters γ^κ and φ^{tot} . In region “I”, the only existing equilibrium is a saddle point and hence no closed trajectories exist. Closed trajectories and pattern solutions exist in the shaded area in Fig. 3.3. The boundary of the shaded area is given by the locus of saddle-node bifurcations, where a saddle point and a focus coincide. The shaded region can be sub-divided into four areas of qualitatively different behavior. In regions “II”, “III”, and “V”, two saddle points and one focus exist. In region “IV”, three saddle points and two focuses are found. It can be seen from Fig. 3.3 that the interval of cell voltages, for which pattern solution are possible, becomes larger, if the value of γ^κ increases, i.e., if there is stronger temperature dependence of the electrolyte’s electrical conductivity.

3.3.2

Cell with Finite Length

The steady-state solutions of the finite length system are the subset of solutions of the infinite length system that fulfills the boundary conditions given in (11). In a phase diagram, the left and right boundary condition are straight lines with slope Bi^B and $-Bi^B$, respectively, as is shown in Fig. 3.4. Steady-state solutions of the finite length system always start on the upper dashed line that defines the left boundary

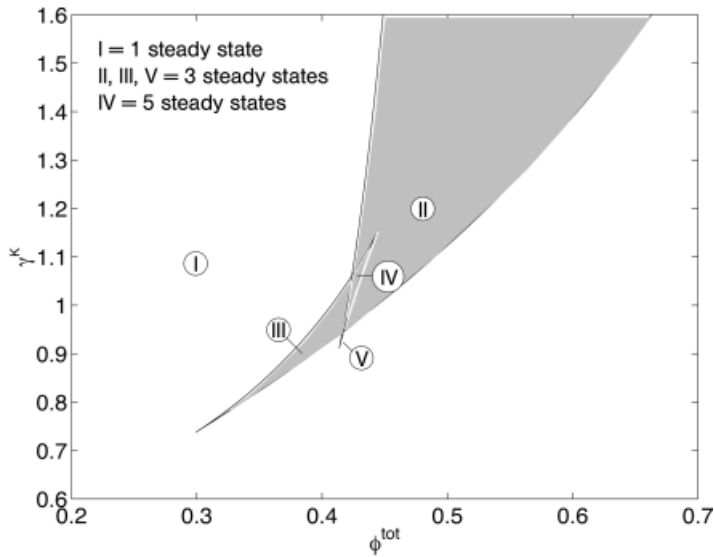


Fig. 3.3. Saddle node bifurcations of an infinite length system in the γ^κ – φ^{tot} plane; parameters as in Tab. 3.1; the shaded region marks the area of existence of pattern solutions.

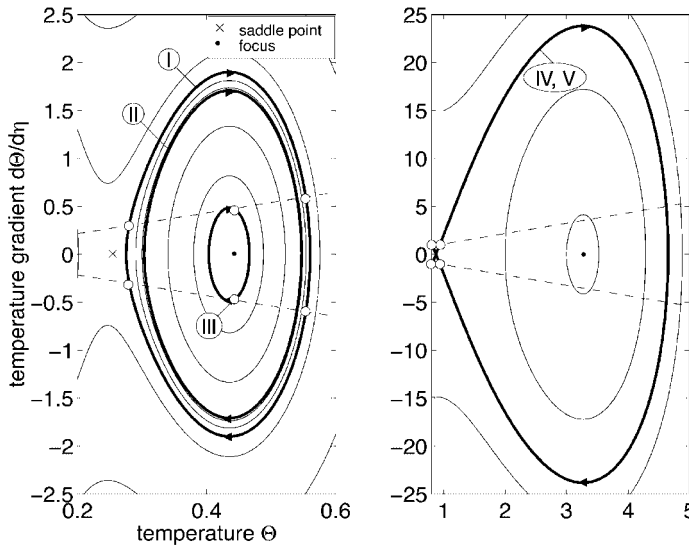


Fig. 3.4. Steady-state solutions of a finite-length system for potentiostatic operation; $\varphi^{tot} = 0.425$; other parameters as in Tab. 3.1; dashed lines are points fulfilling the boundary conditions; circles on the trajectories mark boundary points of the solutions.

condition. They follow one of the solution trajectories of the infinite-length system and end on the lower dashed line defining the right boundary condition. The distance in space covered the trajectory by while moving from the starting point to the end point must be equal to the length of the system. On a closed trajectory, a solution may take several turns before reaching the right boundary point, provided that the system is long enough. A pattern solution may be asymmetric with respect to the center of the considered space interval, if the corresponding closed trajectory intersects the dashed boundary lines several times.

In the example shown in Fig. 3.4, five coexisting solutions are found, the spatial temperature profiles of which are depicted in Fig. 3.5. The solutions I, II, and III are symmetric pattern solutions and run on three different closed trajectories of the infinite length system. In contrast, the solutions IV and V exist on the same closed trajectory and differ only by the starting and end points on the boundary lines. Because the starting and end points are asymmetric with respect to the Θ -axis, the solutions IV and V also are asymmetric. It should be noted that this asymmetric solution exists, although the model equations are perfectly symmetric.

One purpose of the investigation of the potentiostatic operation is to motivate the numerical results obtained for the galvanostatic operation mode and presented in the next section. Furthermore, the described phase plane analysis does not provide any information on the stability of the found solutions. The stability analysis will be included in the numerical studies of Section 3.4.

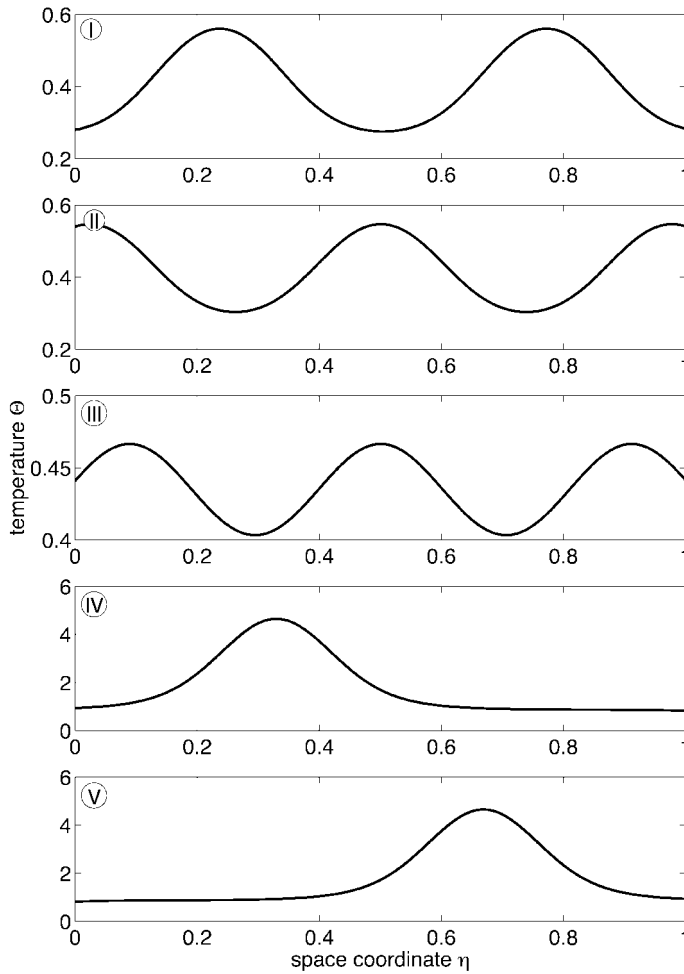


Fig. 3.5. Spatial temperature profiles of the solutions I–V in Fig. 3.4.

3.4

Galvanostatic Operation

In contrast to classical chemical reactors, a fuel cell provides the possibility to control the reaction rate directly from outside by setting the cell current, because the local cell current density and the local reaction rate are related by a constant factor. This operation of a fuel cell at constant cell current is more important than the potentiostatic operation from a technical point of view, as fuel cells typically are characterized by current–voltage plots. Because the integral Eq. (15) has to be included in the analysis, the investigation of the galvanostatic operation is more difficult and requires numerical methods. In the following, numerical bifurcation

analysis is applied to the spatially discretized system (11–15). Details on the numerical methods are given in the Appendix.

Figure 3.6 shows codimension-1 singularities in a parameter plane spanned by the activation energy of the anodic reaction γ^A and the activation energy of the electrolyte conductivity γ^K , when the total cell current I is used as the bifurcation parameter. Hysteresis and isola varieties are found. The nonlinear behavior becomes increasingly complicated for increasing values of γ^K . Steady-state multiplicities even exist for rather small values of γ^K , but vanish if the electrolyte's conductivity is temperature-independent, i.e., $\gamma^K = 0$. This confirms that the multiple steady states are caused not by the electrochemical reaction alone, but by the combination of reaction and varying electrical conductivity.

One-parameter continuations for a fixed value of γ^A and increasing values of γ^K are shown in Fig. 3.7 (a)–(f). In Fig. 3.7 (a), all steady-state solutions are stable and unique. When going from the conditions of Fig. 3.7 (a) to those of Fig. 3.7 (b), the lowest line of isola varieties in Fig. 3.6 is crossed. Therefore, Fig. 3.7 (b) contains an additional isolated branch of solutions. Increasing γ^K to the value used in Fig. 3.7 (c) leads to the generation of a hysteresis, as a line of hysteresis varieties is crossed in Fig. 3.6. More isolas and hystereses are created when the value of γ^K is increased further, as can be seen in Fig. 3.7 (c)–(f). Finally, up to seven coexisting steady states are found in Fig. 3.7 (f). Figure 3.8 shows the spatial temperature profiles of the seven states. Although the temperature maxima and minima of the coexisting solutions vary strongly, the total cell voltages of the different solutions are found to

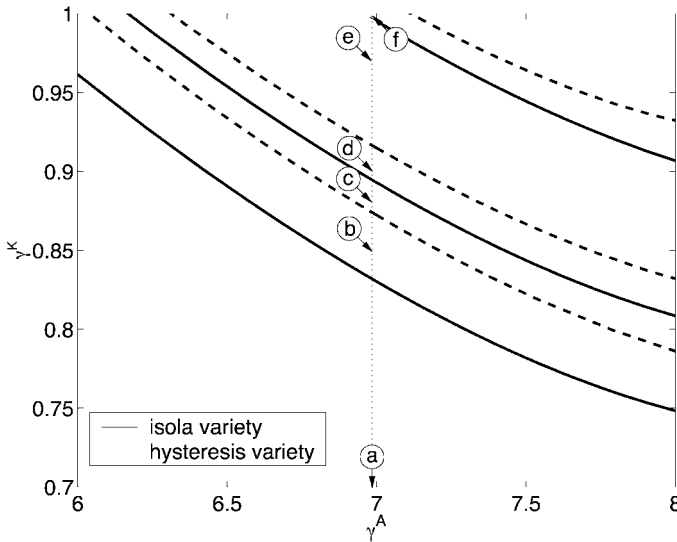


Fig. 3.6. Codimension-1 singularities of a finite length system for the case of galvanostatic operation (I is the bifurcation parameter); (a)–(f) point to the parameter values of γ^K and γ^A used in the one-parameter continuation of Fig. 3.7.

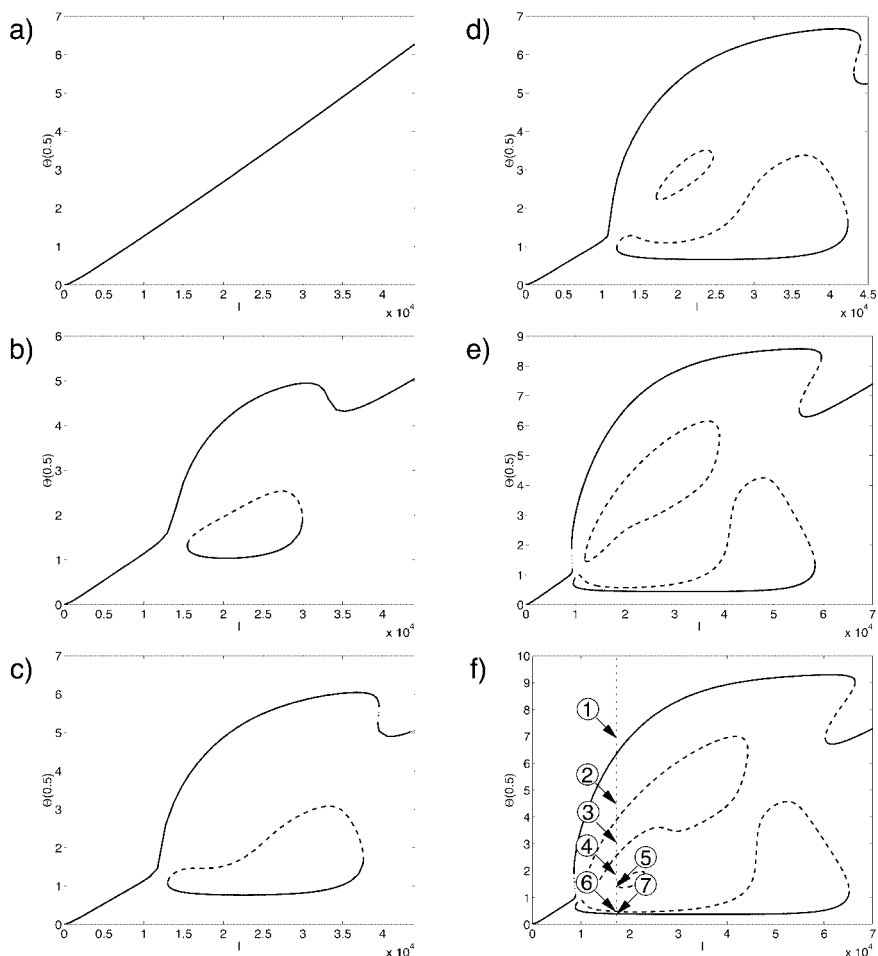


Fig. 3.7. One-parameter continuation of steady states with continuation parameter I ; solid lines = stable solutions; dashed lines = unstable solutions; $\gamma^A = \gamma^C = 7$, (a) $\gamma^k = 0.5$, (b) $\gamma^k = 0.85$, (c) $\gamma^k = 0.88$, (d) $\gamma^k = 0.9$, (e) $\gamma^k = 0.97$, (f) $\gamma^k = 1$.

be very close to each other. This means that for a given cell current, almost the same electrical power may be achieved at quite different temperature levels. The temperature profiles of the two stable solutions (1) and (7) are very inconvenient for the practical operation. They are characterized by high temperature peaks and strong temperature gradients, and would probably damage the cell. The shape of the temperature profile has much better properties in the case of the unstable solutions (4) and (5). Therefore, it may be interesting to operate the cell at an unstable steady state by using feedback control.

3.5

Conclusions

Temperature measurements and avoidance of local over-temperatures and steep temperature gradients are a key issue for the operation of high-temperature fuel cells. The results of this contribution show that the temperature dependence of the electrolyte's conductivity may have a strong influence on the spatial temperature field in a cell, and lead to hot spots. The physical reason for this behavior is that the conductivity of the ion-conducting electrolyte increases with increasing temperature. Therefore, a local temperature disturbance has a destabilizing effect on the fuel cell: A temperature increase at one point leads to a higher conductivity and hence to a higher current density at this point; this results in a stronger local heat production due to the exothermic electrochemical reaction that increases the temperature further. If the total cell current is kept constant, an increase of the current density at one point must be balanced by a reduced current density at another point. This explains the formation of spatial patterns in galvanostatic operation found in this contribution. The temperature dependence of the electrolyte usually is not very strong. However, one of the main results of these studies was that, in combination with the nonlinear properties of the electrochemical reactions, the electrolyte nevertheless can cause hot spots as well as channels of high current density that do not exist in the case of temperature-independent conductivity.

The occurrence of hot spots must be avoided during the practical operation of high-temperature fuel cells. This can be done in different ways: One possibility is to keep the total cell current and the average current density low. However, this solution is unsatisfactory, because future fuel cell research must aim at intensifying the process of power generation and the power density. Figure 3.8 may point to another, more efficient solution: For the same cell current, different, possibly unstable

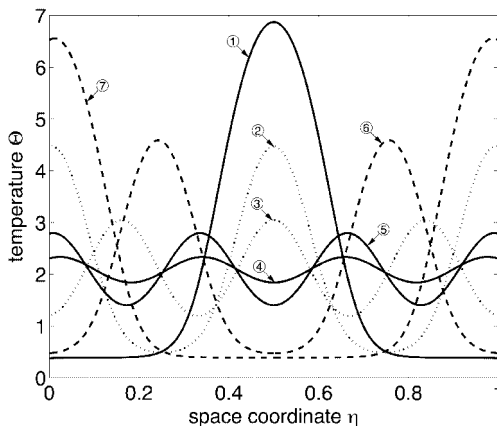


Fig. 3.8. Coexisting spatial temperature profiles under the conditions of Fig. 3.7 (f), $I = 20000$; (1), (7) = stable solutions, (2)–(6) = unstable solutions.

pattern solution may coexist that differ strongly in their maximum temperatures. In this case, a safe operation of the cell is possible, if the system is brought into the operation mode with the smallest temperature gradients by a suitable control.

Finally, it may be worthwhile comparing the nonlinear behavior of fuel cells with that of classical chemical reactors. For classical chemical reactors, two groups of mechanisms are mainly known to be responsible for multiplicities and instabilities. The first group are auto-catalytic and self-inhibitory effects in isothermal systems. The second group are nonlinear temperature dependencies of the reaction rates in non-isothermal systems. The nonlinear effects in fuel cells caused by a varying electrical conductivity can also be grouped into the two categories. Effects belonging to the first category were found for PEMFCs in experiments and simulations [8]. Multiplicities in PEMFCs can be caused by the humidity dependency of the membrane's electrical conductivity. Because water as the product of the electrochemical reaction improves the conductivity and hence accelerates the reaction, this can be considered as an autocatalytic effect. The effects studied in this contribution are thermokinetic and belong to the second category: The heat generated by the reaction increases the conductivity and the local reaction rate.

Symbols

Latin symbols

B	heat of reaction
Bi	Biot number
K_{eq}	equilibrium constant
i	current density
I	cell current
v	flow velocity
x	molar fraction

Greek symbols

β	mass transfer coefficient
γ	Arrhenius number
ε	ratio thermal capacity gas/solid
η	space coordinate
Θ	temperature
κ	conductivity
τ	time coordinate
φ	electrical potential
$\Delta\varphi^{A/C}$	potential difference anode/cathode
ψ	pre-exponential factor

Sub- and superscripts

A	anode	κ	electrolyte
AE	anode electrode		
C	cathode		
CE	cathode electrode		
E	electrode		
S	solid		

Appendix: Numerical Methods for the Bifurcation Analysis in Section 3.0

The system (11–15) is discretized using a finite-volume method with an equidistant grid of 200 grid points. In the steady-state case, this leads to a system of algebraic equations

$$\mathbf{0} = \mathbf{f}(\mathbf{x}), \quad \mathbf{f}, \mathbf{x} \in \mathfrak{R}^n \quad (19)$$

In order to determine limit points and higher order singularities, additional equations are needed. As proposed in [7], the augmented system

$$\frac{\partial \mathbf{f}}{\partial \mathbf{x}} \mathbf{v} - \beta \mathbf{r} = \mathbf{0} \quad (20)$$

$$\mathbf{r}^T \frac{\partial \mathbf{f}}{\partial \mathbf{x}} - \gamma \mathbf{v} = \mathbf{0} \quad (21)$$

$$\|\mathbf{v}\| = 1 \quad (22)$$

$$\|\mathbf{r}\| = 1 \quad (23)$$

and the turning point condition

$$\mathbf{r}^T \frac{\partial \mathbf{f}}{\partial \mathbf{x}} \mathbf{v} = 0 \quad (24)$$

are used here. The condition for a hysteresis variety

$$\mathbf{r}^T \frac{\partial}{\partial \mathbf{x}} \left(\frac{\partial \mathbf{f}}{\partial \mathbf{x}} \mathbf{v} \right) \mathbf{v} = 0 \quad (25)$$

and the condition for an isola variety with continuation parameter p

$$\mathbf{r}^T \frac{\partial \mathbf{f}}{\partial p} = 0 \quad (26)$$

are taken from [2]. A one-parameter pseudo arc length continuation algorithm [4] is applied to (19) in order to trace steady-state solutions in one parameter. The same algorithm is used to trace limit points in two parameters, if applied to (19–24), or to trace hysteresis varieties or isola varieties if applied to (19–24) in combination with (25) or (26), respectively.

References

1. J. Bockris, A. Reddy, 1998, *Modern Electrochemistry: Ionics*. New York: Plenum Press.
2. M. Golubitsky, D. Schaeffer, 1985, *Singularities and Groups in Bifurcation Theory*. New York: Springer.
3. K. Huang, S. Tichy, J. Goodenough, Superior perovskite oxide-ion conductor; strontium and magnesium-doped LaGaO₃: I, phase relationships and electrical properties. *J. Am. Ceram. Soc.*, **1998**, 81, 2565–2575.
4. H. Keller, 1977, Numerical solution of bifurcation and nonlinear eigenvalue problems. In: P. Rabinowitz (Ed.), *Application of Bifurcation Theory*, New York: Academic Press.
5. G. Kolios, J. Frauhammer, G. Eigenberger, Efficient reactor concepts for coupling of endothermic and exothermic reactions. *Chem. Engng. Sci.*, **2002**, 57, 1505–1510.
6. G. Kortüm, 1966, *Lehrbuch der Elektrochemie*. Weinheim: Verlag Chemie.
7. P. Kunkel, 1991, Augmented systems for generalised turning points. In: R. Seydel (Ed.) *Proc. of Bifurcation and Chaos: Analysis, Algorithms, Applications*. International Series of Numerical Mathematics, Vol. 97, pp. 231–236. Basel: Birkhäuser Verlag.
8. J. Moxley, S. Tulyani, J. Benziger, Steady-state multiplicity in the autohumidification polymer electrolyte membrane fuel cell. *Chem. Engng. Sci.*, **2003**, 58, 4705–4708.
9. B. Steele, A. Heinzel, Materials for fuel-cell technologies. *Nature*, **2001**, 414, 345–352.
10. E. Wicke, D. Vortmeyer, Zündzonen heterogener Reaktionen in gasdurchmischten Körnerschichten. *Zeitschrift für Elektrochemie*, **1959**, 63, 145–152.
11. Y. Ye, L. Rikho-Struckmann, B. Munder, et al., Feasibility of an electro-chemical membrane reactor for partial oxidation of n-butane to maleic anhydride. *Ind. Eng. Chem. Res.*, **2004**, 43, 4551–4558.

Part II

Integration of Separations and Chemical Reactions

4

Thermodynamic and Kinetic Effects on the Feasible Products of Reactive Distillation: A-zeo-tropes and A-rheo-tropes

Kai Sundmacher, Zhiwen Qi, Yuan-Sheng Huang and Ernst-Ulrich Schlönder

4.1 Introduction

Today, there is an increasing interest in the theoretical study and the practical application of integrated reactive separation processes such as reactive distillation columns [1–3] or membrane-assisted reactors [37]. However, to date there is no general method available for designing such processes. For practical applications, it is important to be able to evaluate quickly whether a certain reactive separation process is a suitable candidate to reach certain targets. Therefore, feasibility analysis tools being based on minimal thermodynamic and kinetic information of the considered system are valuable.

For traditional distillation process design, residue curve maps (RCMs) were successfully established to predict the feasible splits and products of countercurrent columns. The stable nodes in a RCM represent possible top and bottom products. During the past decade, this methodology was also regarded suitable for reactive distillation processes. Therefore, RCMs of batch reactive reboilers (as depicted in Fig. 4.1) were extensively investigated. In particular, the effect of the chemical reaction kinetics has been intensively studied for both homogeneous systems [4–9] and heterogeneous systems [10–12]. More recently, Chadda et al. [13] have shown that the stable nodes of the considered batch reactive reboiler yields the composition of feasible bottom products of a countercurrent column, but these nodes cannot be used to determine the column's top products. These authors elaborated a new design methodology being based on two flash cascades – a vapor-fed flash cascade and a liquid-fed flash cascade (see Fig. 4.1) – the stable nodes of which represent the feasible top and bottom products of a fully reactive countercurrent distillation column.

As an alternative method, Qi et al. [14] proposed to use a reactive condenser (see Fig. 4.1) to predict possible top products of a countercurrent reactive distillation column. The feasibility analyses of the reactive condenser and the reactive reboiler are analogous to the flash-cascade approach. The latter authors used transformed

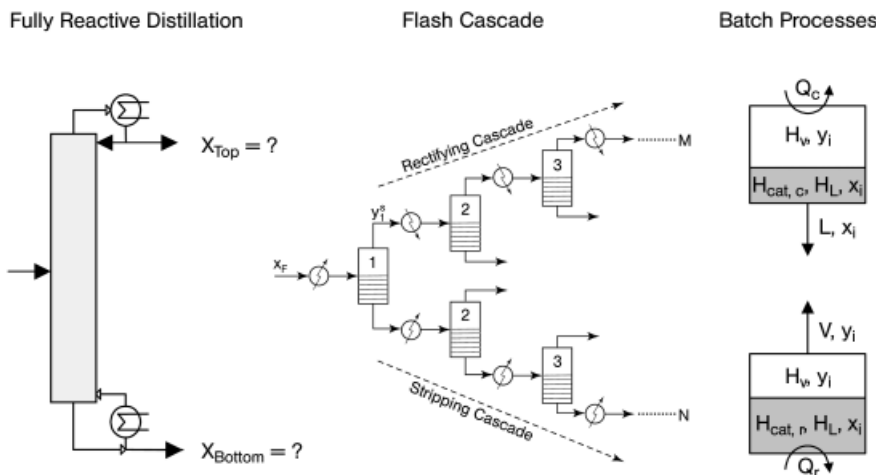


Fig. 4.1. Flash cascades [13] and batch processes (reactive condenser/reactive reboiler, [14]) being used to predict the top and bottom products of a countercurrent reactive distillation column.

variables to formulate a condition for the existence of nonreactive azeotropes, kinetic azeotropes and reactive azeotropes, as formerly discussed extensively by Doherty and his coworkers [15–18]. Qi et al. [14] also presented a mathematical method to predict the locus curve of all possible singular points, the so-called potential singular point surface (PSPS). The location of the PSPS in the phase diagram:

- depends only on reaction stoichiometry and physical thermodynamics;
- is valid for the reactive reboiler and the reactive condenser;
- is independent on the reaction rate expression; and
- is valid for equilibrium-controlled as well as for kinetically controlled reactions.

Azeotropes represent phase equilibrium-controlled singular points of a phase diagram. The classical concept of azeotropy is not suitable to describe and to analyze mass transfer-controlled processes. Mass transfer-controlled singular points in non-reactive systems were investigated first by Schlünder [19], who termed such points as “pseudo-azeotropes” [19]. More recently, Huang et al. [20] studied reactive membrane separation and proposed the term “A-rheo-trope” for the singular points obtained in this mass transfer-controlled process. In translation, this term means that “... the liquid composition is not changing with flux”. However, also for mass transfer-controlled processes, one can formulate a potential singular point surface in analogy to the PSPS of phase equilibrium-controlled systems. Qi and Sundmacher [21] investigated the influence of mass transfer on the feasible products of countercurrent reactive pervaporation by using the PSPS. Huang et al. [20] generalized this approach for reactive membrane separation processes.

In correspondence to the just-given introduction to the state of the art of feasible product analysis of reactive distillation and reactive membrane separation processes, the following three major sections of this chapter are structured as follows:

- Section 4.2 is focused on phase equilibrium-controlled vapor–liquid systems with kinetically or equilibrium-controlled chemical reactions. The feasible products are kinetic azeotropes or reactive azeotropes, respectively.
- Section 4.3 elucidates the role of vapor–liquid mass transfer resistances on the feasible products of nonreactive or reactive separation processes. The latter are considered under chemical equilibrium conditions (i.e., they are very fast reactions). The feasible products are denoted as arheotropes.
- Section 4.4 extends the proposed methodology to reactive membrane separation systems being controlled by vapor–liquid mass transfer and finite chemical reaction kinetics, simultaneously. For this general case the term “kinetic arheotrope” is introduced for the singular points obtained in phase diagrams.

4.2

Azeotropes

4.2.1

Reactive Condenser and Reboiler

A reactive condenser (see above) and a reactive reboiler (see below) are depicted on the right-hand side of Fig. 4.1. Reactive reboilers were widely studied as the most simple case of a batch reactive distillation process [6–12]. In both batch processes, the chemical reaction is considered to be enhanced by a catalyst with constant hold-up $H_{cat,c}$ in the condenser and constant hold-up $H_{cat,r}$ in the reboiler. The liquid phase itself can be either homogeneous or heterogeneous – that is, it can split into two liquid subphases. In general, the catalyst activity in the two liquid phases can be different [10–12]. Moreover, phase equilibrium is established between the liquid phase and the vapor phase, i.e., $y_i = y_i(\mathbf{x})$, and also between the liquid subphases arising from a possible phase splitting $x'_i = x'_i(\mathbf{x}'')$. The following single reversible chemical reaction is considered in the liquid phases:



where ν_i is the stoichiometric coefficient of components i ($\nu_i < 0$ for reactants, $\nu_i > 0$ for products). The summation of ν_i yields ν_T . The reaction rate is expressed as

$$r^{phase} = k_f^{phase} \mathfrak{R}^{phase}(\mathbf{x}^{phase}) \quad (2)$$

with k_f as the rate constant of the forward reaction at boiling temperature and \mathfrak{R} as the normalized reaction rate.

The dimensionless mass balances for the reactive condenser and the reactive reboiler are obtained as [14]:

Condenser:

$$\frac{dy_i}{d\xi} = -(x_i - y_i) + (v_i - v_T y_i) Da_c \Theta \quad i = 1, \dots, NC \quad (3)$$

Reboiler:

$$\frac{dx_i}{d\zeta} = (x_i - y_i) + (v_i - v_T x_i) Da_r \Theta \quad i = 1, \dots, NC \quad (4)$$

where $d\xi = (L/Hv) dt$, $d\zeta = (V/H_L) dt$, $k_{f,ref}$ is rate constant at fixed reference conditions. The condenser and reboiler Damköhler numbers are in turn defined as $Da_c = H_{cat,c} k_{f,ref} / L_0$ and $Da_r = H_{cat,r} k_{f,ref} / V_0$. The cooling policy $L = L_0 = \text{constant}$ and the heating policy $V = V_0 = \text{constant}$ were applied for the reactive condenser and the reactive reboiler, respectively. The overall reaction term Θ is given by

$$\Theta = \frac{k_f'}{k_{f,ref}} \beta \Re'(x') + \frac{k_f''}{k_{f,ref}} (1 - \beta) \Re''(x'') \quad (5)$$

which represents the overall reaction driving force in the two liquid phases. In Eq. (5), k_f' and k_f'' refer to the corresponding liquid phases.

In Eqs. (3) and (4), the vapor phase mole fractions y_i and the liquid phase mole fractions x_i have to fulfil the vapor–liquid–liquid equilibrium conditions in case of heterogeneous liquid mixtures, and the vapor–liquid equilibrium conditions in homogeneous mixtures. For the latter case, the reaction term Θ in Eq. (5) simplifies to

$$\Theta = \frac{k_f}{k_{f,ref}} \Re(\mathbf{x}). \quad (6)$$

4.2.2

Conditions for Singular Points

4.2.2.1 Potential Singular Point Surface

The right-hand side of Eqs. (3) and (4) consist each of two terms. The first term represents the effect of distillation (separation vector), and the second the effect of the chemical reaction (reaction vector). For nonreactive systems only the separation vector plays a role. For kinetically controlled systems, both vectors can dominate the system behavior, depending on the value of Da . For $Da \rightarrow \infty$, the liquid mixture approaches chemical equilibrium.

As condition for a singular point, the composition remains unchanged. For the reactive condenser, the vapor phase composition y_i does not change in time, i.e.,

$(dy_i/d\xi) = 0$. In analogous manner, for the reactive reboiler $(dx_i/d\xi) = 0$ defines the singular point. Thus, the following singularity conditions are obtained from Eqs. (3) and (4):

Condenser:

$$0 = -(x_i - y_i) + (v_i - v_T y_i) Da_c \Theta \quad i = 1, \dots, NC - 1, \quad (7)$$

Reboiler:

$$0 = (x_i - y_i) + (v_i - v_T x_i) Da_r \Theta \quad i = 1, \dots, NC - 1, \quad (8)$$

where $Da_{c,r} \in (0, \infty)$ for the kinetically controlled system and $Da_{c,r} = 0$ for the nonre-active case. The NC th component mole fraction is calculated from the summation of mole fractions to unity. Applying Eq. (7) to an arbitrary reference component k and eliminating the term $Da_c \Theta$ leads to:

$$\frac{x_i - y_i}{v_i - v_T y_i} = \frac{x_k - y_k}{v_k - v_T y_k} \quad i = 1, \dots, NC - 2. \quad (9)$$

Rearranging Eq. (9) produces the following rate-independent conditions for the singular points of the reactive condenser:

$$X_i = Y_i \quad i = 1, \dots, NC - 2 \quad (10)$$

with X_i and Y_i as the transformed liquid and vapor mole fractions:

$$X_i \equiv \frac{v_k x_i - v_i x_k}{v_k - v_T x_k} \quad \text{and} \quad Y_i \equiv \frac{v_k y_i - v_i y_k}{v_k - v_T y_k} \quad i = 1, \dots, NC - 2. \quad (11a,b)$$

Starting from Eqs. (8), it can be easily shown that Eqs. (10) are also valid for the singular points of the reactive reboiler.

Equations (10) are the general rate-independent conditions for all singular points of the reactive condenser and the reactive reboiler for systems with homogeneous or with heterogeneous liquid phase. This is also true for multi-reaction systems if one uses generalized definitions for X_i and Y_i as proposed by Ung and Doherty [17]. Generally, in a $(NC-1)$ dimensional composition space with NR chemical reactions, $(NC-NR-1)$ rate-independent conditions, $X_i - Y_i = 0$, fix the *Potential Singular Point Surface* (PSPS). For a single-reaction system the PSPS is a curve.

4.2.2.2 Reaction Kinetic Surface

To fix the singular points, additional NR conditions are needed. For $NR = 1$ – that is, a single-reaction system – there is exactly one additional governing equation which is simply Eq. (7) (condenser) or Eq. (8) (reboiler) with $i = k$, where k is the reference

component among the system components. This additional equation can be simplified for different reaction conditions, as listed in Tab. 4.1. For $NR > 1$, each kinetic equation represents a $(NC-1)$ dimensional rate-dependent hypersurface. Singular points are common points (intersection points or tangential points) of the PSPS with this reaction kinetic surface. Possible singular points are pure components, nonreactive azeotropes ($Da = 0$), kinetic azeotropes ($0 < Da < \infty$), and reactive azeotropes ($Da \rightarrow \infty$).

4.2.3

Examples

4.2.3.1 Hypothetical Ternary Systems

In the first considered hypothetical ternary systems, the single chemical reaction



is assumed to take place in the liquid phase. Thus, there is one rate-independent condition for the existence of singular points. Using C as reference component, the PSPS is given by:

$$X_A = Y_A \quad (13)$$

with the transformed variables

$$X_A = \frac{x_A + x_C}{1 + x_C} \text{ and } Y_A = \frac{y_A + y_C}{1 + y_C}. \quad (14a, b)$$

Assuming constant relative volatilities α_{ij} of the components, the vapor–liquid equilibrium is given by:

$$y_i = \frac{\alpha_{ik} x_i}{\sum_{j=1}^{NC} \alpha_{jk} x_j}. \quad (15)$$

Table 4.1. Steady-state conditions of reactive condenser and reactive reboiler.

	Reactive condenser	Reactive reboiler
Non-reactive case ($Da = 0$)	$x_i - y_i = 0$	$x_i - y_i = 0$
Kinetically controlled case ($0 < Da < \infty$)	$-(x_i - y_i) + (v_i - v_T y_i) Da_c \Theta = 0$	$(x_i - y_i) + (v_i - v_T x_i) Da_r \Theta = 0$
Chemical equilibrium- controlled case ($Da \rightarrow \infty$)	$(v_i - v_T y_i) \Theta = 0$	$(v_i - v_T x_i) \Theta = 0$

Two volatility sequences are considered:

Example 1: $\alpha_{AC} = 0.2$, $\alpha_{BC} = 3$, i.e., the reaction product C is intermediate boiler.

Example 2: $\alpha_{AC} = 5$, $\alpha_{BC} = 3$, i.e., the reaction product is high boiler.

Consequently, Eq. (13) can be written as quadratic form in terms of the liquid mole fractions x_A and x_B :

$$\frac{(x_A - 1/2)^2}{\alpha_{BC} - 1} - \frac{(x_B - 1/2)^2}{\alpha_{AC} - 1} = \frac{\alpha_{AC} - \alpha_{BC}}{4(\alpha_{AC} - 1)(\alpha_{BC} - 1)}. \quad (16)$$

Depending on the values of the relative volatilities α_{AC} and α_{BC} , the shape of the PSPS is fixed:

$$(\alpha_{BC} - 1) \cdot (\alpha_{AC} - 1) \begin{cases} < 0 & \text{ellipse} \\ = 0 & \text{parabola} \\ > 0 & \text{hyperbola} \end{cases} \quad (17)$$

The ellipse and hyperbola types are shown in Fig. 4.2(a) and (b), respectively. The PSPS goes through all-pure component vertices and the stoichiometric pole π of $x = (1, 1)$ since $\nu_T = -1$. For the ellipse type (example 1; Fig. 4.2(a)), the PSPS does not move into the triangle but rather intersects with the chemical equilibrium surface only at the pure components A and B. Consequently, there exists no reactive azeotrope, and all azeotropes are located outside the triangle. A reactive azeotrope (RA = a non-pure component intersection of the PSPS with the chemical equilibrium surface) is located, if C is the highest boiler (example 2; Fig. 4.2(b)). This is in agreement with the general conclusion reached by Barbosa and Doherty [16] that reactive azeotropes can exist only if the volatilities of the reactants are either all higher or all lower than the volatilities of the products.

For example 1, the singular points of the considered reactive condenser are collected in one diagram in Fig. 4.3(a), while Fig. 4.3(b) shows analogous singular points for the reactive reboiler. In both systems, as mentioned earlier, all singular points are located on the same ellipse-shaped PSPS. In general, the location and stability of the singular points of the reboiler and condenser are different for the same Damköhler number. For process design purposes the stable nodes at positive Damköhler numbers are of major interest. These points are collected and depicted in a feasibility diagram (Fig. 4.3(c)), which illustrates the changing of possible column products with respect to the Damköhler number. For the here-considered system, pure A can be the only top product and pure B can be the only bottom product.

For example 2, Figs. 4.4(a) and (b) show the bifurcations of all singular points with respect to the Damköhler numbers of the reactive condenser and the reactive reboiler, respectively. As can be seen from the feasibility diagram in Fig. 4.4(c), at Damköhler numbers $Da_c > 0.830$, two possible condenser products – that is, the top products of a fully reactive distillation column, are predicted. The kinetic azeotrope in the reactive reboiler is always the possible bottom product of a column.

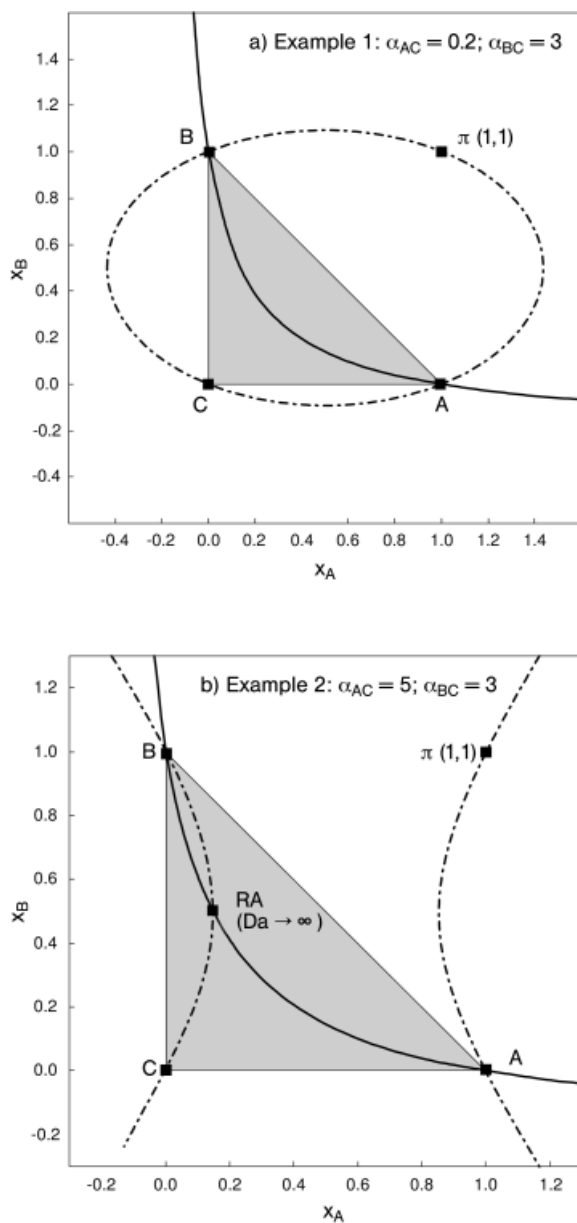


Fig. 4.2. Potential singular point surfaces (dashed-dotted curve) for an ideal ternary system with single reaction $A + B \rightleftharpoons C$. (a) Ellipse-type system; (b) hyperbola-type system. RA = reactive azeotrope; solid curve = chemical equilibrium surface.

If the liquid mixture is extremely non-ideal, liquid phase splitting will occur. Here, we first consider the hypothetical ternary system. The physical properties are adopted from Ung and Doherty [17] and Qi et al. [10]. The catalyst is assumed to have equal activity in the two liquid phases. The corresponding PSPS is depicted in Fig. 4.5, together with the liquid–liquid envelope and the chemical equilibrium surface. The PSPS passes through the vertices of pure A, B, C, and the stoichiometric pole π . The shape of the PSPS is affected significantly by the liquid phase non-idealities. As a result, there are three binary nonreactive azeotropes located on

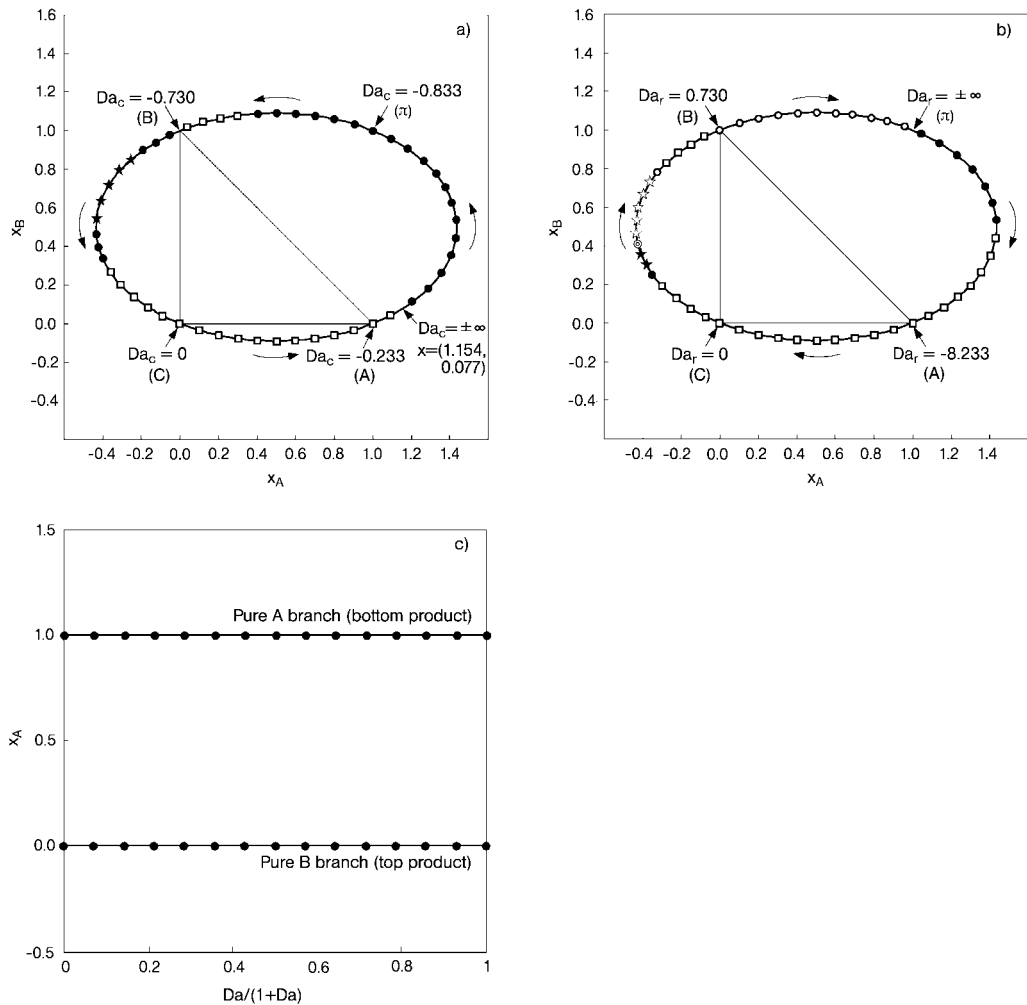


Fig. 4.3. Bifurcation diagrams for reactive condenser (a) and for reactive reboiler (b), and feasibility diagram (c) for ellipse-type system.

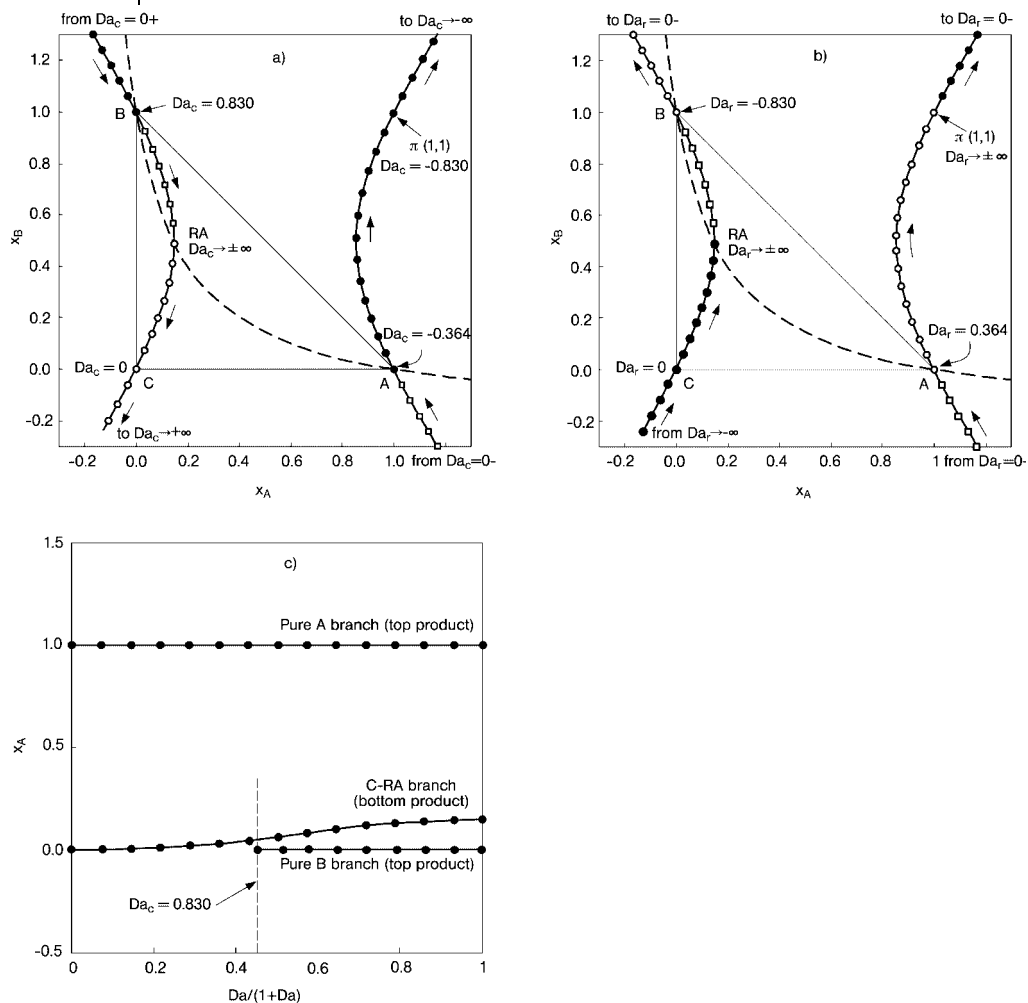


Fig. 4.4. Bifurcation diagrams for reactive condenser (a) and for reactive reboiler (b), and feasibility diagram (c) for hyperbola-type system. Dashed curve = chemical equilibrium surface.

the triangle edges and one ternary heterogeneous nonreactive azeotrope inside the triangle. As most interesting feature, one branch of the PSPS is an ellipse-shaped isola moving through the A-vertex and the nonreactive azeotropes (AB, AC and ABC-azeotropes). This PSPS branch also contains a ternary heterogeneous reactive azeotrope at the intersection with the chemical equilibrium surface inside the liquid–liquid region. Between components B and C, the PSPS evolves from the hyperbola-type PSPS of the ideal system as depicted in Fig. 4.2(b).

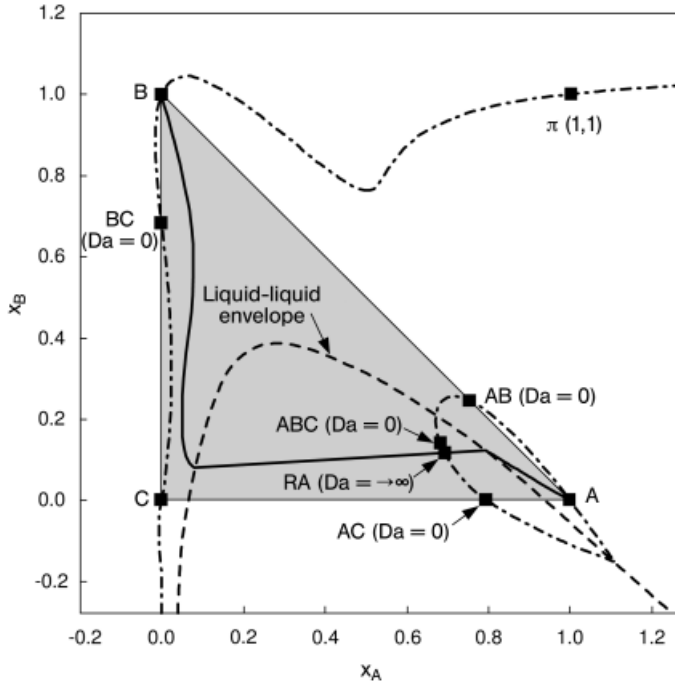


Fig. 4.5. Potential singular point surface (dashed-dotted curve) for a ternary system with phase splitting behavior and the single reaction $A + B \rightleftharpoons C$. RA = reactive azeotrope; solid curve = chemical equilibrium surface.

4.2.3.2 Real Ternary System: MTBE-Synthesis

MTBE (Methyl.-tert.-butylether) is produced by reacting isobutene and methanol (MeOH) in the liquid phase:



Venimadhavan et al. [4, 7] studied the effect of the reaction kinetics on the singular point bifurcations of this system in a reactive reboiler. These authors reported one kinetic pinch point at $Da_r = 0.166$. Below, we describe the PSPS and locate the singular points by intersecting the PSPS with the kinetic surfaces. The VLE parameters and the kinetics are taken from Venimadhavan et al. [4].

For the considered reaction system, MTBE is taken as the reference component and MeOH is chosen as independent component. Then, the PSPS is described by

$$X_{\text{MeOH}} = Y_{\text{MeOH}} \quad (19)$$

with the transformed variables

$$X_{MeOH} = \frac{x_{MeOH} + x_{MTBE}}{1 + x_{MTBE}} \quad (20)$$

and

$$Y_{MeOH} = \frac{y_{MeOH} + y_{MTBE}}{1 + y_{MTBE}}. \quad (21)$$

Figure 4.6 illustrates the PSPS and the chemical equilibrium surface. The PSPS has a hyperbola-type shape and passes through all pure component vertices and the stoichiometric pole π . It intersects the isobutene-MeOH edge and the MeOH-MTBE edge at two points, which are nonreactive binary azeotropes. From Fig. 4.6 one can also see that there exists no reactive azeotrope in this system. All the bifurcation branches and the pure component vertices, as discussed by Venimadhavan et al. [7], are located on the PSPS.

In Fig. 4.7, the PSPS is depicted together with the kinetic surfaces at four selected reboiler Damköhler numbers. At nonreactive conditions (i.e., $Da_r = 0$; Fig. 4.7(a)),

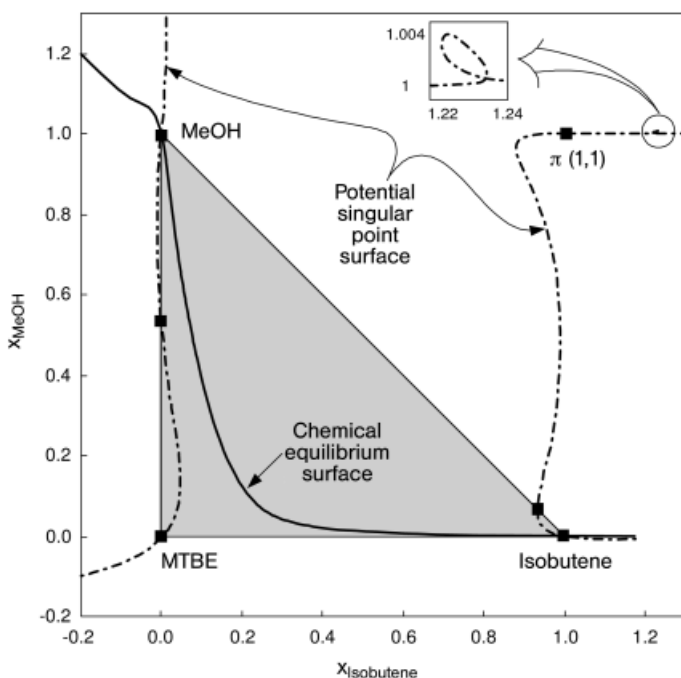


Fig. 4.6. Potential singular point surface and chemical equilibrium surface for MTBE synthesis at 8.11×10^5 Pa.

one part of the kinetic surface is the line $x_{\text{MeOH}} = 0$ which intersects the PSPS at the pure isobutene vertex (saddle point, \square) and the pure MTBE vertex (stable node, \bullet). Another part of the kinetic surface intersects the PSPS at the isobutene-MeOH azeotrope (unstable node, \circ), the MeOH-MTBE azeotrope (saddle point) and the pure MeOH vertex (stable node).

At increasing Da_r -numbers, the isobutene-MeOH azeotrope moves out of the composition triangle, while the MeOH-MTBE azeotrope moves into the triangle (Fig. 4.7(b)). The latter point meets the stable node coming from the MTBE-vertex at a Damköhler number of $Da_r = 0.166$. At this Da_r -number the PSPS and the kinetic surface have a common tangent point (kinetic tangent pinch), as shown in

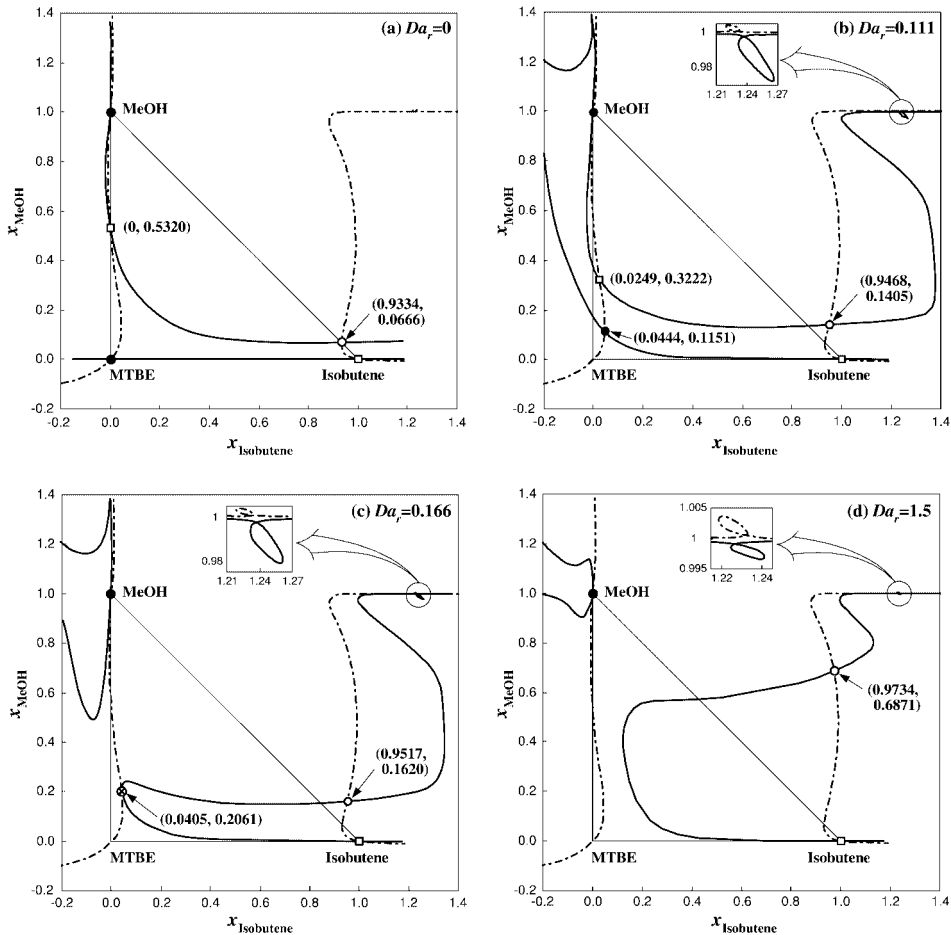


Fig. 4.7. Reactive reboiler. Intersections of potential singular point surface with reaction kinetic surfaces at four different Damköhler numbers Da_r ; MTBE synthesis at 8.11×10^5 Pa.

Fig. 4.7(c). For $Da_r > 0.166$ (Fig. 4.7(d)), only three singular points remain in the system: pure MeOH which is a stable node at any Damköhler number; pure isobutene which is a saddle point at any Damköhler number; and the above-mentioned unstable node which is located outside the triangle.

As can be seen from Fig. 4.7, the kinetic tangent pinch point at the critical Damköhler number $Da_r = 0.166$ has an important role for the topology of the maps. This is also reflected by the feasibility diagrams given in Fig. 4.8(a–c). In Fig. 4.8(c), the stable node branch at positive Damköhler numbers are collected from the singular point analyses of the reactive condenser (Fig. 4.8(a)) and the reactive reboiler

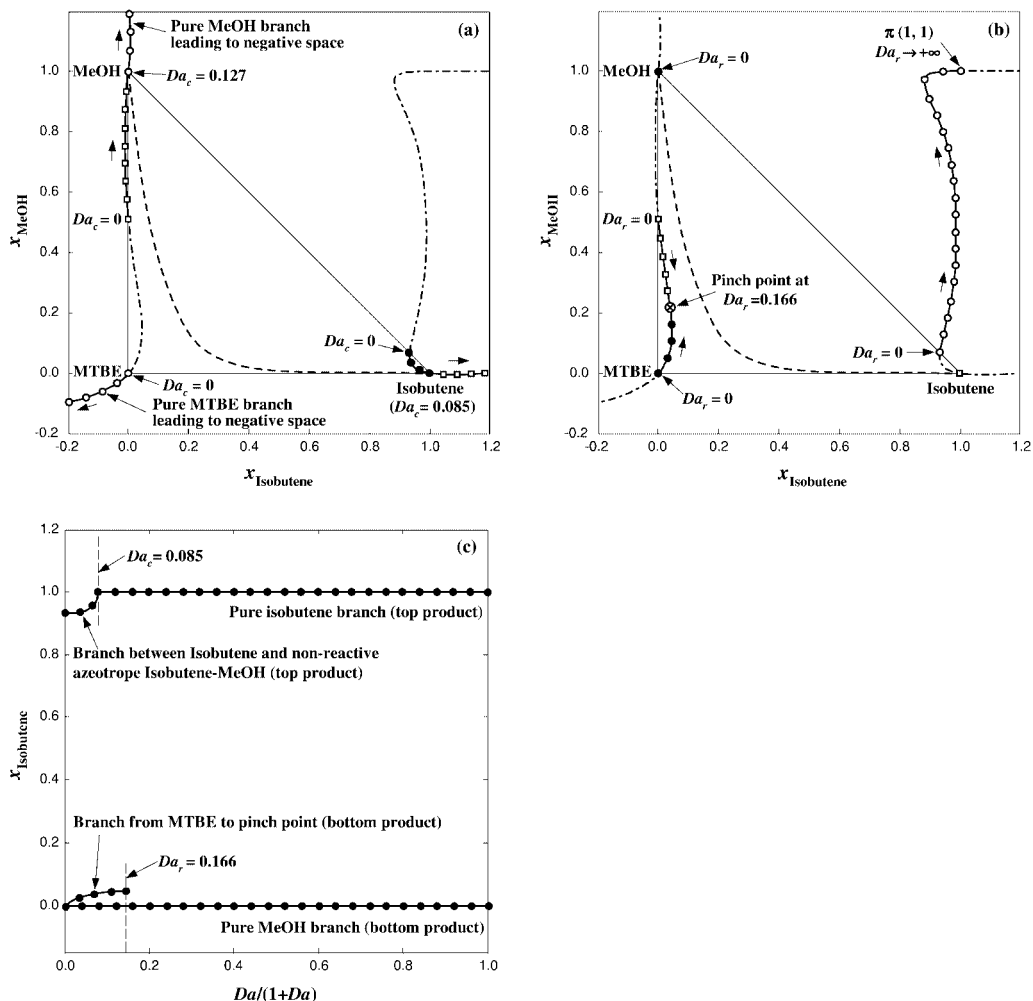


Fig. 4.8. Bifurcation diagrams for reactive condenser (a) and for reactive reboiler (b), and feasibility diagram (c) for MTBE synthesis

at 8.11×10^5 Pa. Dashed curve = chemical equilibrium surface.

(Fig. 4.8(b)). At Damköhler numbers $Da_c > 0.085$ and $Da_r > 0.166$, pure isobutene and pure MeOH are feasible top and bottom products, respectively. At $Da_r < 0.166$, both pure MeOH and a kinetic azeotrope (i.e., the mixture on the branch from MTBE to the pinch point) are possible bottom products, while another kinetic azeotrope (i.e., the mixture on the branch between isobutene and the nonreactive azeotrope isobutene-MeOH) is the possible top product.

4.2.3.3 Real Ternary System with Phase Splitting: Methanol Dehydration

Dimethyl ether (DME) can be produced by dehydration of methanol using alumina as solid catalyst. The main reaction is given by



Nisoli et al. [22] have studied the attainable regions for this reaction system with simultaneous distillative separation. These authors found an immiscible region between water and DME, which shrinks as the pressure increases. The PSPS of this system was calculated based on the VLE parameters given in the studies of Nisoli et al. [22]. Water was chosen as the reference component and DME as independent variable to represent the system:

$$X_{\text{DME}} = Y_{\text{DME}} \quad (23)$$

with the transformed variables

$$X_{\text{DME}} = x_{\text{DME}} - x_{\text{H}_2\text{O}} \quad (24)$$

$$Y_{\text{DME}} = y_{\text{DME}} - y_{\text{H}_2\text{O}}. \quad (25)$$

Figure 4.9(a) and (b) illustrate the system behavior at a total pressure of 15 atm and 8 atm, respectively. As can be seen from the location of the PSPS, this system has similar features as the ideal system example 1 which has an ellipse-shaped PSPS (see Fig. 4.2(a)), as discussed above. Due to the boiling sequence of the reaction components, the PSPS is fully located outside the physically relevant composition space and, as a consequence, no reactive azeotrope can appear. It is worth noting that inside the phase-splitting region, the PSPS of the real heterogeneous system and the PSPS of the pseudohomogeneous system are different. However, this does not affect the feasible top and bottom products of a fully reactive distillation column.

When the pressure decreases, the chemical equilibrium line intersects the liquid-liquid envelope within the physically relevant composition space. Consequently, the chemical equilibrium line coincides with one of the tie lines with the phase-splitting region (see the enlarged region of Fig. 4.9(b)).

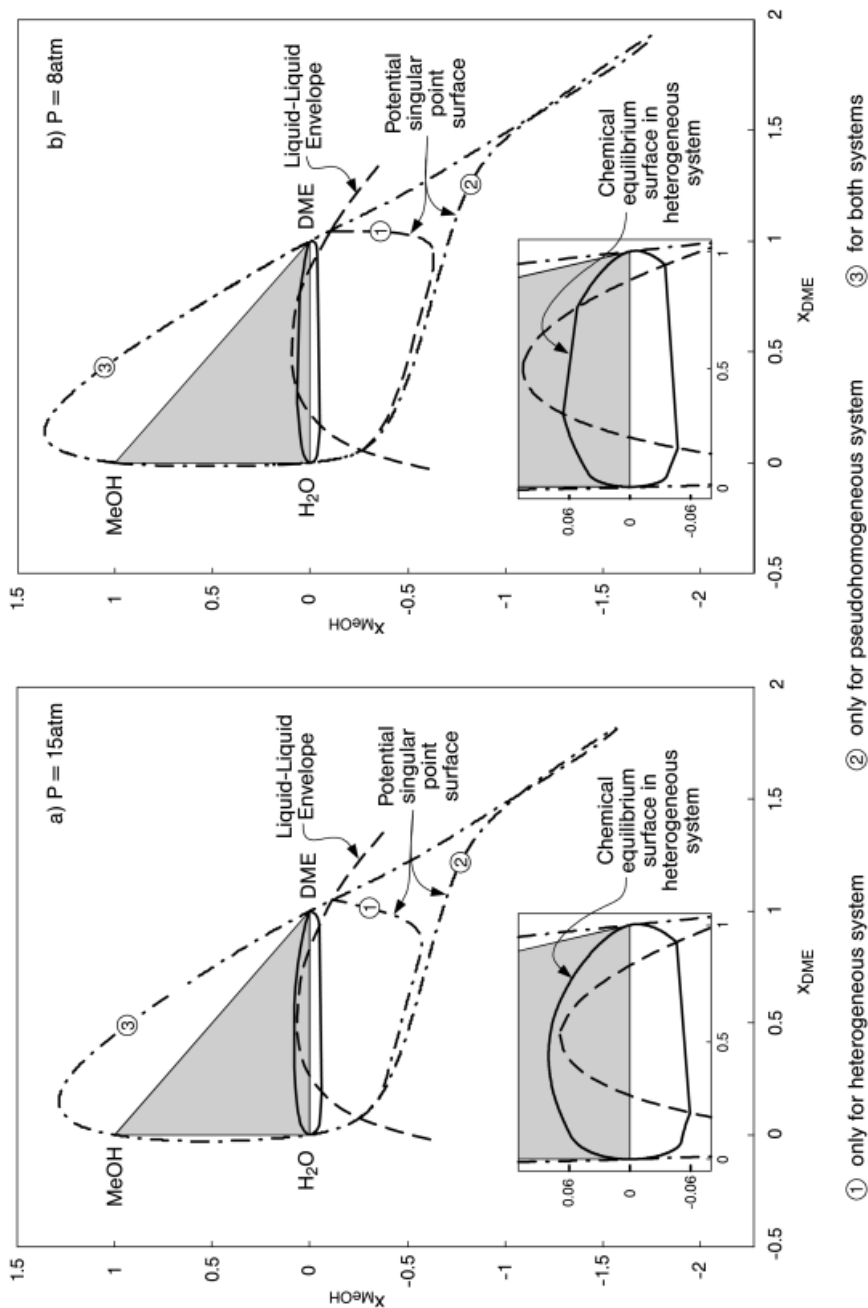


Fig. 4.9. Potential singular point surface, liquid-liquid envelope and chemical equilibrium surface for methanol dehydration at two different pressures.

4.2.3.4 Real Quaternary System: Isopropyl Acetate Hydrolysis

The hydrolysis of isopropyl acetate (IPOAc) to acetic acid (HOAc) and isopropanol (IPA) is a reversible reaction:



For this system, Venimadhavan et al. [7] have studied the bifurcation of the singular points in a reactive reboiler, while Chadda et al. [13] demonstrated the flash-cascade approach. In the present investigation, the same thermodynamic properties and kinetic expression were used (see Tab. 4 in Ref. [7]).

Since there is only one chemical reaction in this quaternary system, there are two rate-independent conditions for the singular points. IPOAc is taken as reference component, and HOAc and IPA are used to represent the PSPS:

$$X_{\text{HOAc}} = Y_{\text{HOAc}} \text{ and } X_{\text{IPA}} = Y_{\text{IPA}} \quad (27\text{a}, \text{b})$$

with the following transformed variables definitions:

$$X_{\text{HOAc}} = x_{\text{HOAc}} + x_{\text{IPOAc}} \text{ and } Y_{\text{HOAc}} = y_{\text{HOAc}} + y_{\text{IPOAc}} \quad (28\text{a}, \text{b})$$

$$X_{\text{IPA}} = x_{\text{IPA}} + x_{\text{IPOAc}} \text{ and } Y_{\text{IPA}} = y_{\text{IPA}} + y_{\text{IPOAc}}. \quad (29\text{a}, \text{b})$$

The surfaces described by Eqs. (27a) and (27b) in the three-dimensional composition space intersect with each other and yield the PSPS as curves given in Fig. 4.10(a). The PSPS contain several branches, three of which pass through the pure components HOAc, IPOAc and water, and are located outside the composition space but are not depicted. The branch passing through the IPA-vertex locates four nonreactive azeotropes – that is, IPA-IPOAc, IPOAc-Water, IPA-IPOAc-Water, and IPA-Water. This branch also contains the reactive azeotrope. The PSPS is also displayed in the transformed composition space (Fig. 4.10(b)).

The corresponding feasibility diagrams are given in Fig. 4.11, which collects the stable nodes obtained from the intersection of the PSPS and the kinetic surfaces of the reactive condenser and the reactive reboiler. Note that the diagram in Fig. 4.11(a) is given in terms of the transformed liquid phase mole fractions X_i because these variables allow a geometric illustration of feasible splits, as outlined in the next section. There are two branches where potential bottom products are located – the pure HOAc branch at any Damköhler number, and the pure IPA branch at $1.22 < Da < 1$ (Fig. 4.11(b)). Only the branch between the nonreactive azeotrope IPA-IPOAc-Water and the reactive azeotrope contains potential top products. As a consequence, there are two possible feed regions yielding two different bottom products (Fig. 4.11(a): region I for pure IPA, region II for pure HOAc).

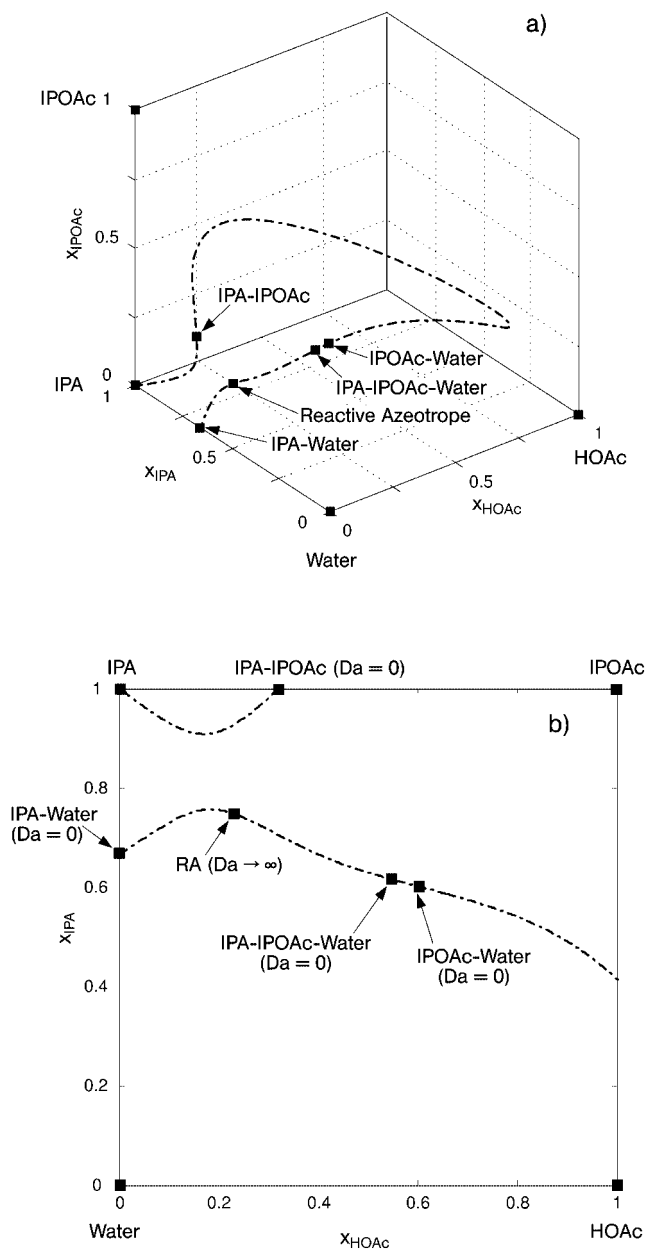


Fig. 4.10. Potential singular point surface for isopropyl acetate (IPOAc) reaction system at 1.01×10^5 Pa. (a) Liquid phase composition space in mole fractions x_i ; (b) representation in transformed composition space.

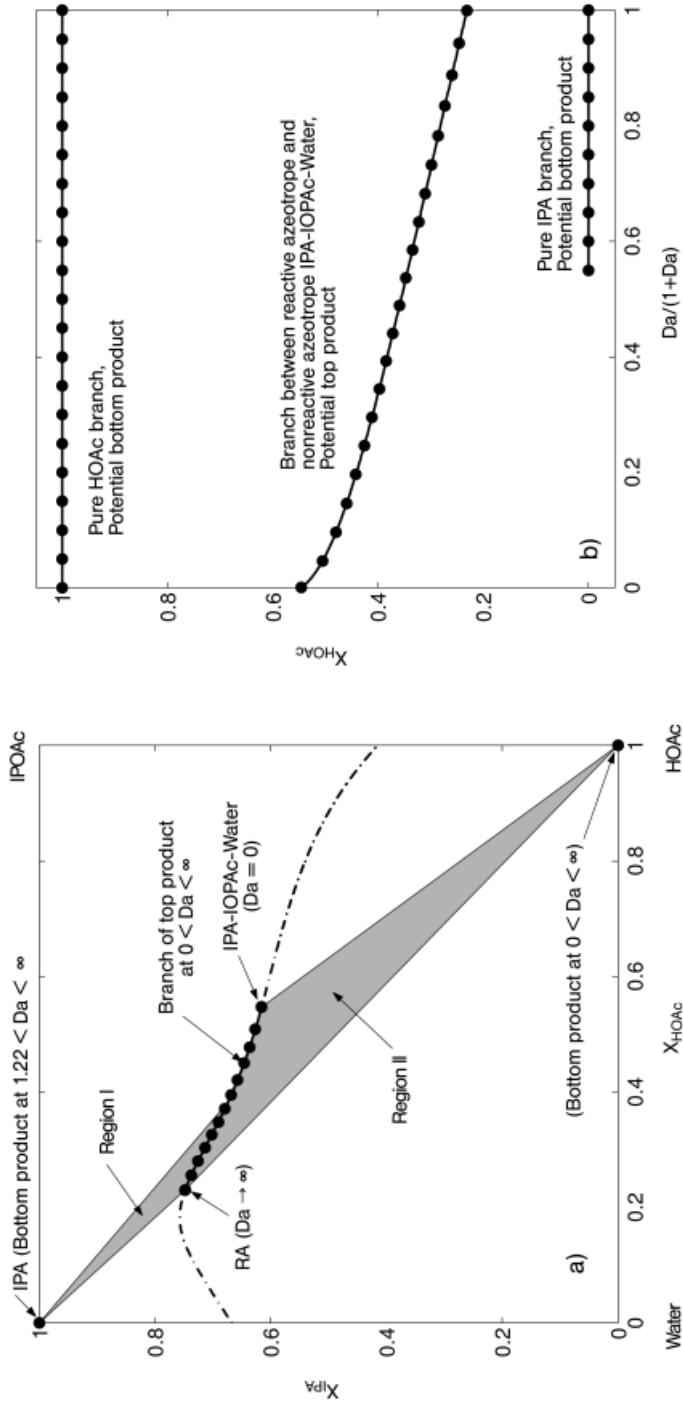


Fig. 4.11. Feasibility diagrams for isopropyl acetate (IPOAc) reaction system at 1.01×10^5 Pa.

4.2.4

Application of Feasibility Diagram: Column Feasible Split

Based on Fig. 4.11(a), a feasible split of a single-feed fully reactive distillation column at specified feed composition can be predicted. First, the operating equations are derived in terms of the transformed mole fractions. The assumption of constant molar overflow (CMO) is applied and the general equilibrium stage approach is taken. The stage index $j = 1$ indicates the reactive condenser and the index $j = NT$ the reactive reboiler. For a general stage j , the component mass balances is given by:

$$L_{j-1}x_{i,j-1} + V_{j+1}y_{i,j+1} - L_jx_{i,j} - V_jy_{i,j} + v_i Da \Re_j = 0. \quad (30)$$

which can be rewritten in terms of transformed variables [14]:

$$\tilde{L}_{j-1}X_{i,j-1} + \tilde{V}_{j+1}Y_{i,j+1} - \tilde{L}_jX_{i,j} - \tilde{V}_jY_{i,j} = 0 \quad (31)$$

with definitions

$$\tilde{L}_j = L_j \left[1 - (v_T / v_k) x_{k,j} \right], \quad (32a)$$

$$\tilde{V}_j = V_j \left[1 - (v_T / v_k) y_{k,j} \right], \quad (32b)$$

$$X_{i,j} = \frac{x_{i,j} - (v_i / v_k) x_{k,j}}{1 - (v_T / v_k) x_{k,j}} = \frac{v_k x_{i,j} - v_i x_{k,j}}{v_k - v_T x_{k,j}}, \quad (32c)$$

$$Y_{i,j} = \frac{y_{i,j} - (v_i / v_k) y_{k,j}}{1 - (v_T / v_k) y_{k,j}} = \frac{v_k y_{i,j} - v_i y_{k,j}}{v_k - v_T y_{k,j}}. \quad (32d)$$

For the reactive condenser and the reactive reboiler, the mass balances are given by:

$$\tilde{V}_2 Y_{i,2} - \tilde{L}_1 X_{i,D} - \tilde{F}_D X_{i,D} = 0 \quad (38)$$

$$\tilde{L}_{NT-1} X_{i,NT-1} - \tilde{V}_{NT} Y_{i,NT} - \tilde{F}_B X_{i,B} = 0 \quad (39)$$

with $\tilde{F}_D = F_D \left[1 - (v_T / v_k) x_{k,D} \right]$ and $\tilde{F}_B = F_B \left[1 - (v_T / v_k) x_{k,B} \right]$.

The corresponding operating lines for the rectifying and stripping section are
Rectifying:

$$Y_{i,j+1} = \frac{\tilde{R}}{1+\tilde{R}} X_{i,j} + \frac{1}{1+\tilde{R}} X_{i,D} \quad i = 1, \dots, NC - 2 \quad (40)$$

Stripping:

$$X_{i,j-1} = \frac{\tilde{s}}{1+\tilde{s}} Y_{i,j} + \frac{1}{1+\tilde{s}} X_{i,B} \quad i = 1, \dots, NC - 2 \quad (41)$$

where $\tilde{R} = \tilde{L}_2 / \tilde{F}_D$ and $\tilde{s} = \tilde{V}_{NT} / \tilde{F}_B$.

The total mass balances for the column are:

$$\tilde{F}_F X_{i,F} = \tilde{F}_D X_{i,D} + \tilde{F}_B X_{i,B} \quad i = 1, \dots, NC - 2 \quad (42)$$

$$\tilde{F}_F = \tilde{F}_D + \tilde{F}_B \quad (43)$$

with the definition $\tilde{F}_F = F_F [1 - (v_T / v_k) x_{k,F}]$.

From Eqs. (42) and (43) one obtains

$$\frac{\tilde{F}_D}{\tilde{F}_B} = \frac{X_{i,B} - X_{i,F}}{X_{i,F} - X_{i,D}} \quad i = 1, \dots, NC - 2 \quad (44)$$

which can be rewritten as

$$\frac{s}{1+R} \frac{[1 - (v_T / v_k) x_{k,D}]}{[1 - (v_T / v_k) x_{k,B}]} = \frac{X_{i,B} - X_{i,F}}{X_{i,F} - X_{i,D}} \quad i = 1, \dots, NC - 2 \quad (45)$$

where $s/(1+R) = F_D/F_B$ according to the CMO assumption.

Equation (44) can also be used to obtain a direct relationship between the feed, distillate and bottom compositions, i.e.,

$$\frac{X_{1,B} - X_{1,F}}{X_{1,F} - X_{1,D}} = \frac{X_{i,B} - X_{i,F}}{X_{i,F} - X_{i,D}} \quad i = 1, \dots, NC - 2. \quad (46)$$

Since the form of the transformed mass balances and the operating equations for the kinetically controlled reactive distillation are identical to the corresponding equations for conventional countercurrent distillation, we therefore can apply the same

procedure for designing a reactive distillation column based on the transformed variables. The main idea is to use the feasibility diagram to determine the reflux and reboil ratios, and the Damköhler number. Moreover, the operating equations can be used to determine the stage numbers and the feed position. The whole procedure consists of the following five steps:

1. For the given system determine the PSPS and the singular points by intersecting the PSPS with the kinetic surfaces for the reactive condenser and the reactive reboiler.
2. Collect the stable nodes along the singular point branches and display them in feasibility diagrams.
3. For a given feed composition X_F , specify a desired potential bottom product X_B (or top product X_D). Then, find the top product X_D (or bottom product X_B) from the overall mass balance that is a straight line, on which X_B , X_F , and X_D are located (Eq. (46)). According to X_D (or X_B) one can determine the corresponding Da -number.
4. Select a reflux ratio R and determine the corresponding reboil ratio s from Eq. (45).
5. Calculate the operating equations for the rectifying section and the stripping section starting from the determined X_D and X_B , until they intersect with each other. During the calculation, the VLE (or VLLE) and the reaction rate will be based on the mole fractions. The molar and transformed variables are transformed to each other. The total stage number and the feed position for the reactive distillation column are fixed. If no intersection can be found, select a new reflux ratio r and repeat steps 4 to 5. In case that no intersection can be found, a feasible split is not possible for the single-feed reactive distillation column with constant Damköhler number.

Now, the algorithm given above is briefly demonstrated for IPOAc-synthesis. Steps 1 and 2 were already carried out above and the feasibility diagrams are shown in Fig. 4.11. For the given X_{F1} (Fig. 4.12(a)), pure HOAc is chosen as the bottom product. As a result, the top product $X_D = (0.425, 0.656)$ is determined by extrapolating the straight line between X_B and X_{F1} and by intersecting it with the PSPS. (One can get the same X_D from Eq. (46).) From the feasibility diagram (Fig. 4.11(b)), we obtain the Damköhler number corresponding to X_D , i.e., $Da = 0.33$. Choosing $r = 0.7$, one obtains $s = 3.884$ from Eq. (45). Starting from X_B and X_D we solve the operating equations stage by stage and plot the composition of each stage in Fig. 4.12(a) until the rectifying and the stripping section intersect. Counting the stage numbers yields the total stage number ($NT = 30$) and the feed stage ($N_f = 15$). To check the correctness of this split, we simulated the reactive distillation column using the equilibrium-stage model with the obtained configurations. As can be seen from Fig. 4.12(a), the simulated profiles are in good agreement with the designed ones. For detailed comparison, the compositions are listed in Tab. 4.2.

Figure 4.12(b) illustrates the feasible split for the feed composition X_{F2} . Pure HOAc is chosen as the bottom product and the corresponding Damköhler number is $Da = 5.68$. The predicted split and the simulation results are compared in Fig. 4.8(b) and Tab. 4.2.

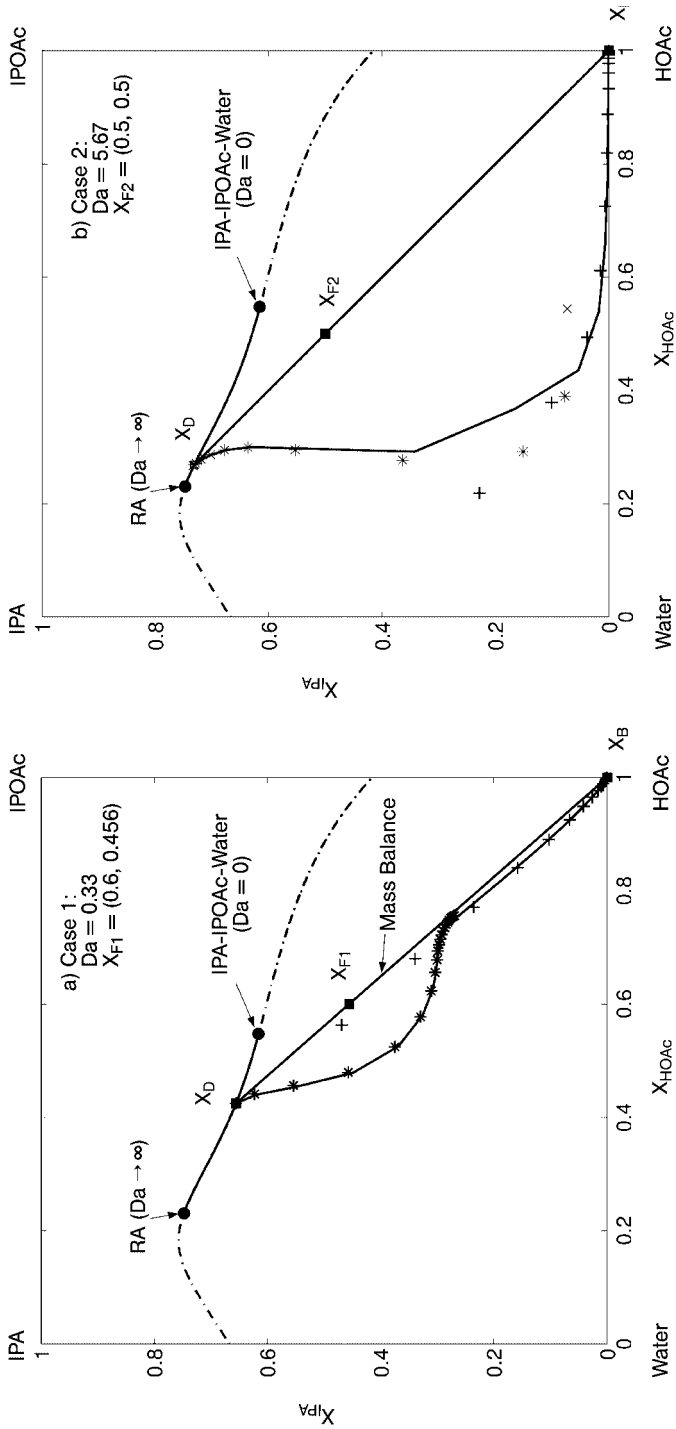


Fig. 4.12. Design diagrams for isopropyl acetate (IPOAc) reactive distillation column and comparison with simulation results (solid curves: simulated column profile; markers: * = stage composition for column rectifying section; + = stage composition for column stripping section).

Table 4.2. Comparison of mole fractions predicted from the feasible split algorithm and from the simulation.

	Da = 0.33		Da = 5.67	
	Feasible split prediction	Simulation*	Feasible split prediction	Simulation**
<i>Distillate</i>				
HOAC	0.0193	0.0193	0.0464	0.0443
IPA	0.2498	0.2497	0.5089	0.5065
IPOAc	0.4057	0.4057	0.2223	0.2247
Water	0.3252	0.3253	0.2223	0.2245
<i>Bottom</i>				
HOAC	1.0	0.99943	1.0	0.99956
IPA	0.0	0.00003	0.0	0.0
IPOAc	0.0	0.00013	0.0	0.0
Water	0.0	0.00041	0.0	0.00044

* $NT = 30$; $Nf = 15$, $r = 0.7$, $s = 3.884$ ** $NT = 25$; $Nf = 9$, $r = 5.0$, $s = 13.0$

4.2.5

Remarks on Azeotropes

The possible singular points in vapor–liquid phase equilibrium-controlled reactive separation systems are pure components and azeotropes. Depending on the regime of the chemical reaction, these are nonreactive azeotropes ($Da = 0$), kinetic azeotropes ($0 < Da < \infty$), or reactive azeotropes ($Da \rightarrow \infty$). Only the stable singular points are potential top and bottom products of a countercurrent nonreactive/reactive distillation column. The collection of the potential products in a feasibility diagram is the basis for designing single-feed, fully nonreactive or fully reactive distillation columns. The proposed design method is simple to use, and can be geometrically interpreted for ternary and quaternary systems.

4.3

Arheotropes

4.3.1

Definition and Conditions

The definition of, and the necessary conditions for, the existence of an arheotrope are based on the material balances of a batch distillation process in the presence of a stagnant or flowing sweep gas (Fig. 4.13). Let us first consider a nonreactive liquid mixture. In this case, the component and total mass balances are given by:

$$\frac{dH_i}{dt} = -n_i \quad (47)$$

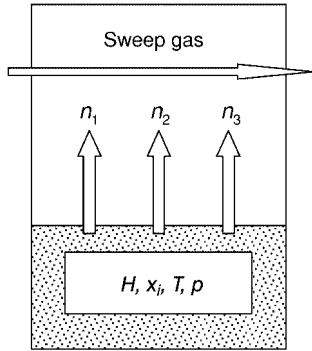


Fig. 4.13. Open batch distillation with sweep gas flow.

$$\frac{dH}{dt} = -n_T \quad (48)$$

where H is the liquid hold-up and n_T is the escaping total vapor flux. Combining Eqs. (47) and (48) yields:

$$\frac{dx_i}{d \ln H} = \chi_i - x_i \quad i = 1, \dots, NC - 1 \quad (49)$$

with the relative flux $\chi_i = n_i/n_T$. Nonreactive *arheotropes* are steady-state solutions of Eqs. (49) i.e.,

$$0 = \chi_i - x_i \quad i = 1, \dots, NC - 1. \quad (50)$$

As a special case, if the relative flux χ_i equals the vapor phase bulk composition y_i being in equilibrium with the liquid bulk phase composition x_i , then we speak of a nonreactive *azeotrope*. Thus, the azeotropic case can be seen as a limiting case of the *arheotropic* case.

4.3.2

Illustrative Examples

4.3.2.1 Example 1: Stagnant Sweep Gas

The first example illustrates the behavior of a binary mixture in an open-batch distillery with a stagnant sweep gas. Figure 4.14 shows the historical set-up from 1977 [19, 23–29]. The still was heated by a Bunsen burner, while the condenser was installed in the form of a watchglass cooled by evaporation of water due to natural convection.

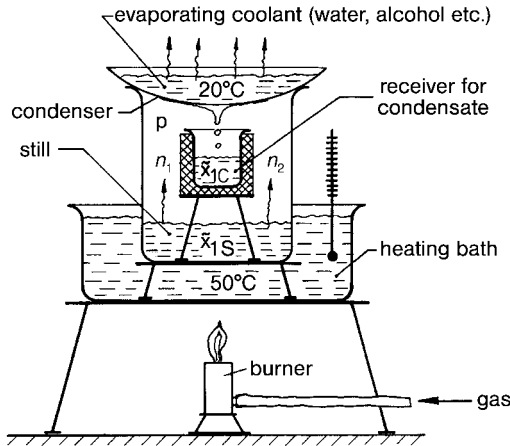


Fig. 4.14. Bench-scale batch distillery, beaker still and watchglass condenser.

When operating this distillation unit below the boiling temperature, the vapor space is partly filled with ambient air; the watchglass must not perfectly seal the still.

The concentrations at the condenser $x_{j,C}$ are identical to the relative fluxes χ_j because of total condensation of the vapor escaping from the liquid surface. Schlünder [19] derived the following relationship between mole fractions of liquid in the still, $x_{j,S}$, and the mole fractions of the condensed liquid in the receiver, $x_{j,C}$:

$$\frac{1 - K_{2C} + (K_{2C} - K_{1C})x_{1C}}{1 - K_{2S} + (K_{2S} - K_{1S})x_{1S}} = \left[\frac{K_{1C}x_{1C} - x_{1C}}{K_{1S}x_{1S} - x_{1S}} \right]^{\left[\frac{k_{13}}{k_{23}} - \left(\frac{k_{13}}{k_{23}} - 1 \right) x_{1C} \right]} \quad (51)$$

Equation (51) is based on the Stefan–Maxwell equations describing the mass transport in the gas phase.

To illustrate the system behavior, the ternary mixture 1 = iso-propanol, 2 = water, and 3 = air is considered here. In order to obtain an algebraic solution, both the diffusivities of iso-propanol in air and iso-propanol in water vapor were assumed to be approximately the same, which is not far from reality. The liquid phase mass transfer resistance was negligibly small, as will be shown below. The phase equilibrium constants $K_{j,C}$ and $K_{j,S}$ were calculated with activity coefficients from van Laar's equation. Water vapor diffuses 2.7-fold faster in the inert gas air than iso-propanol. The ratio of the respective mass transfer coefficients k_{j3} equals the ratio of the respective diffusivities to the power of 2/3rd according to standard convective mass transfer equations $Sh = f(Re, Sc)$.

Figure 4.15 shows the calculated residue curves according to Eq. (51) at various temperatures in the still, while the temperature at the condenser was kept constant by evaporation of water due to natural convection. The azeotropic concentration of this mixture ($x_1 = 62$ mol%) in practical terms does not vary much with pressure and temperature. The azeotropic iso-propanol content at 50 °C is as low as 38 % and will not decrease much further at even lower still temperatures. The minimum azeotro-

pic concentration is reached, if the Stefan–Maxwell equation approaches Fick’s law of diffusion. As the still temperature approaches the normal boiling point, the arheotrope reaches the azeotrope at 62 mol% propanol concentration. This is due to that fact that convective Stefan flux totally overrides the diffusion effect. Figure 4.16 shows the experimental verification of Eq. (56).

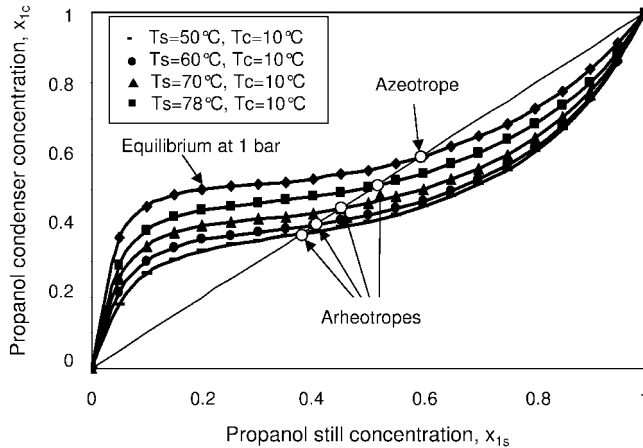


Fig. 4.15. Residue curves for iso-propanol (1)–water (2) mixtures at various still temperatures. $k_{13}/k_{23} = 0.5$. Air is the third component (3).

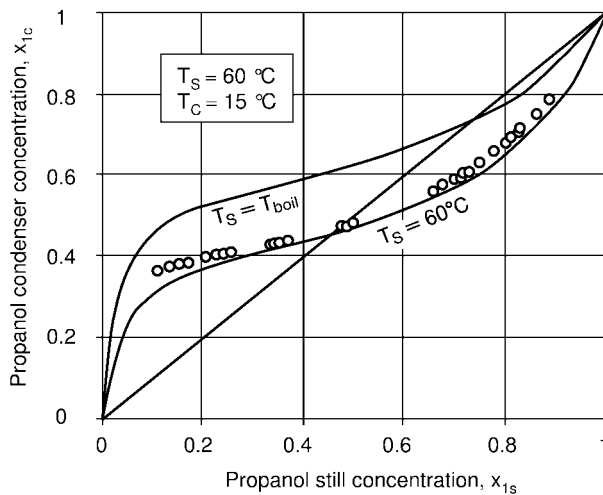


Fig. 4.16. Experimental data for iso-propanol and water mixture, $T_s = 60\text{ °C}$, $T_c = 15\text{ °C}$ [29].

4.3.2.2 Example 2: Flowing Sweep Gas

This example illustrates the distillation of a binary mixture in an open-batch distillery with flowing sweep gas, as shown in Fig. 4.17. The vapor emerging from the batch distillery is carried away by the sweep gas flow, thus keeping the partial vapor pressures above the gas–liquid interface at a constant value, depending on the magnitude of the sweep gas flow rate.

We consider a nonreacting mixture such as iso-propanol (1) and water (2), evaporating into ambient air at constant temperature. Assuming the physical equilibrium condition (VLE) at the vapor–liquid interface and applying the Stefan–Maxwell-flux equations to the liquid phase and linear flux equations to the air-diluted gas phase, we derive the following expression for the relative flux χ_1 :

$$\chi_1(x_1) = \frac{p(x_1)}{2} \left(\sqrt{1 - \frac{4q(x_1)}{p(x_1)^2}} - 1 \right) \quad (52)$$

with

$$-p(x_1) = \frac{1 + (1 - K_{gas}/\alpha_{12})(x_1 - K_{liq}) - K_{liq}(Y_{1,in}/K_1 + Y_{2,in}/K_2 K_{gas}/\alpha_{12})}{(K_{liq} - 1)(1 - K_{gas}/\alpha_{12})} \quad (53a)$$

$$q(x_1) = \frac{x_1 - Y_{1,in}K_{liq}/K_1}{(K_{liq} - 1)(1 - K_{gas}/\alpha_{12})}. \quad (53b)$$

Here, five dimensionless groups appear:

- K_1 and K_2 are the equilibrium constants for the components 1 and 2, while α_{12} is the relative volatility of iso-propanol versus water vapor.
- The gas phase kinetic separation factor K_{gas} is defined as:

$$K_{gas} \equiv \frac{NTU_1}{1 + NTU_1} \frac{1 + NTU_2}{NTU_2} \quad (54)$$

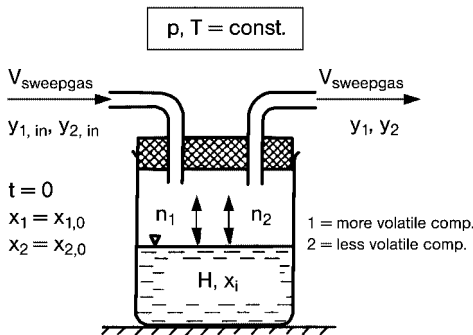


Fig. 4.17. Batch distillation with flowing sweep gas and free gas–liquid interface.

- The liquid phase kinetic separation factor K_{liq} is defined as:

$$K_{liq} \equiv \exp\left(-\frac{u_{liq}}{k_{liq}}\right) \quad (55)$$

- The number of transfer units NTU_i is defined as:

$$NTU_i \equiv \frac{Ak_{gas,i}}{V_{sweepgas}} \quad (56)$$

where $V_{sweepgas}$ is the volumetric sweep gas flow rate, A is the gas–liquid interface area and $k_{gas,i}$ are the gas side mass transfer coefficients. u_{liq} represents the velocity at which the liquid level moves down towards the bottom of the distillery during the evaporation process. The latter quantity is identical with the velocity of the net flux, also named as the Stefan flux. k_{liq} is the liquid side mass transfer coefficient.

It can be shown that the dimensionless group K_{liq} is directly proportional to difference between the relative flux χ_i and the liquid bulk concentration x_i :

$$K_{liq} = \frac{\chi_i - x_i}{\chi_i - x_{i,Ph}} \quad (57)$$

which means: If the evaporation velocity u_{liq} is much higher than the liquid phase mass transfer coefficient k_{liq} , then K_{liq} tends towards zero and the distillation process is nonselective – that is, this is the case of flash evaporation. If u_{liq} is much lower than k_{liq} then $x_{i,Ph}$ at the interface becomes equal to the bulk concentration x_i .

Figure 4.18 shows the function $\chi_1(x_1)$ – both predicted and measured – for the binary mixture of iso-propanol and water for various sweep gas inlet humidities, thus exhibiting various arheotropic compositions. For zero air humidity there is only one unstable arheotrope at 50 mol% of iso-propanol. For 7.2 g H₂O kg⁻¹ air, which corresponds to a typical winter climate (in Germany), we obtain two arheotropes – an unstable one at 58 mol% and a stable one at 90 mol%.

For 16.1 g H₂O kg⁻¹ air, which corresponds to a typical summer climate, no arheotropes appear at all. Within those two regimes where $\chi_1 > 1$ (i.e., $\chi_2 < 0$), evaporation of water reverses into condensation. Because of the low evaporation rate at 30 °C the liquid phase mass transfer resistance is negligibly small.

Figure 4.19 illustrates the effect of liquid phase mass transfer, represented by the dimensionless group K_{liq} (see Eqs. (55) and (57)). If the evaporation velocity is in the same order of magnitude as the liquid phase mass transfer coefficient, then the selectivity of the evaporation process vanishes though the relative volatility as well as the gas phase mass transfer coefficients remain unchanged.

It might be worth drawing attention to the fact that the liquid phase and the gas phase mass transfer resistances affect the distillation process in different ways. Because we consider a binary mixture, the liquid phase mass transfer resistance

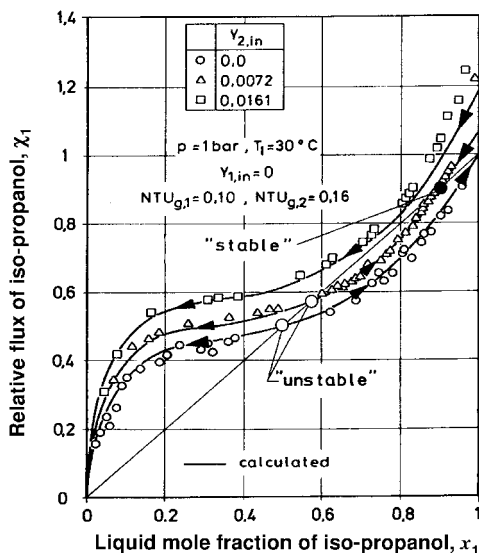


Fig. 4.18. Experimental data for the residue curves of the mixture iso-propanol (1)–water (2) according to Eq. (52) for low NTU -values and various sweep gas inlet humidities $\tilde{Y}_{2,in}$ and moderate evaporation rates ($K_{liq} = 0.9999$) [32].

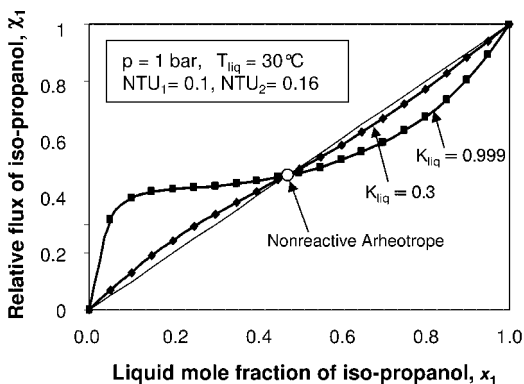


Fig. 4.19. Residue curves of the mixture iso-propanol (1)–water (2) (conditions as in Fig. 4.18), showing the effect of liquid phase mass transfer resistances.

cannot change arheotropic compositions, but it can reduce the selectivity of the distillation process even down to zero. On the other hand, the gas phase mass transfer resistances do change arheotropic compositions but will not reduce the selectivity. This behavior becomes obvious immediately from Eqs (53a) and (53b). The two dimensionless groups K_{gas} and K_{liq} appear in an asymmetric form. In this case – and

in other cases where net fluxes appear – it does not make sense to combine the individual mass transfer resistances to an “overall transfer mass transfer resistance”.

In order to get a feeling under which condition the liquid phase mass transfer becomes rate-controlling and thus reduces the selectivity of an open distillation process, we should make a rough approximation about the order of magnitude of the mass transfer coefficients and the evaporation velocities. Under ambient conditions, the magnitude of gas phase diffusivities is about $\delta_{gas} \approx 10^{-5} \text{ m}^2 \text{ s}^{-1}$, while the value for liquid phase diffusivities is about $\delta_{liq} \approx 10^{-9} \text{ m}^2 \text{ s}^{-1}$. The magnitude of the thickness of the viscous sublayers in the gas phase is about 10^{-3} m , and in the liquid phase is about 10^{-5} m . Therefore, the magnitude of the mass transfer coefficients is in the order of $k_{gas} \approx 10^{-2} \text{ m s}^{-1}$ for the gas phase and $k_{liq} \approx 10^{-4} \text{ m s}^{-1}$ for the liquid phase.

The evaporation velocity at ambient pressure and, say, 60°C , which corresponds to a mole fraction in the sweep gas of about 30 % water vapor, is about $u_{liq} = 10^{-5} \text{ m s}^{-1}$. This results in $K_{liq} = 0.904$ which is rather close to 1, so that the effect of the liquid phase mass transfer resistance on the selectivity of an open distillation process with a free gas–liquid interface in most cases can be ignored. If, however, k_{liq} becomes very small (as in the pervaporation process described in the next example), K_{liq} might become very small and thus reduce the selectivity of the open distillation process practically down to zero.

4.3.2.3 Example 3: Flowing Sweep Gas with Pervaporation

This example illustrates the distillation of a binary mixture in an open-batch distillery with flowing sweep gas and pervaporation by having a porous plate floating on top of the liquid hold up, as shown in Fig. 4.20. The porous plate was made from inert sintered metal with various pore sizes between 100 and $1 \text{ m}\mu$, and had a thickness of 1 mm. The porosity was 40 % and the tortuosity factor was about 2. This results in an effective liquid phase mass transfer coefficient of about $k_{liq} = 2 \times 10^{-7} \text{ m s}^{-1}$, which results in $K_{liq} = 1.9 \times 10^{-22}$. Therefore, one would expect the distillation process to be nonselective – that is, $S_1 = \chi_1 - x_1 = 0$.

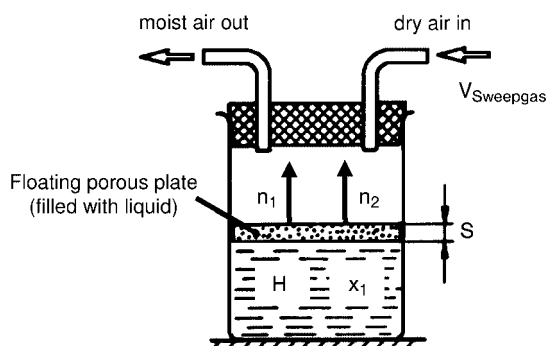


Fig. 4.20. Open batch distillation with flowing sweep gas and a floating porous plate on the gas–liquid interface.

Figure 4.21 shows the selectivity S_1 as a function of the iso-propanol concentration at various pore diameters d_p . The gas phase-controlled azeotrope was chosen to be at 50 mol% iso-propanol. Surprisingly, on the left-hand side the azeotrope S_1 showed almost the same magnitude as the one for a free interface, provided that the pore diameters were not too small, while on the right-hand side the selectivity was absolutely zero, as to be expected. The reason for this unexpected phenomenon is as follows.

On the left-hand side of Fig. 4.21, iso-propanol escapes preferentially. Therefore, water accumulates at the surface of the plate. This causes a two-fold instability:

- The surface tension at the surface increases during evaporation, thus giving rise to the onset of Marangoni convection.
- The density at the surface increases during evaporation thus giving rise to the onset of Bénard convection.

Both types of convection stimulate a vivid internal fluid circulation within the porous plate, thereby reducing the liquid phase mass transfer resistance almost down to zero. This circulation becomes suppressed by friction force if the pore diameters are sufficiently small.

On the right-hand side of Fig. 4.21 the situation is just the opposite; density and surface tension gradients are stable so that there is no internal fluid circulation. A mathematical analysis of this phenomenon has been provided in Ref. [31].

In order to prove the hypothesis as well as the mathematical simulation, the following experiment was performed. A watchglass was filled with iso-propanol and a blotting paper, soaked with water, was placed on top, thus floating on the water. The iso-propanol was dyed with methylene blue. After a few minutes, the blue

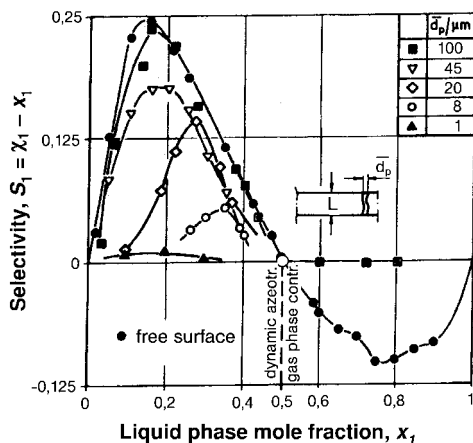


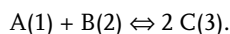
Fig. 4.21. Experimental data of the selectivity $S_1 = \chi_1 - x_1$ in a pervaporation distillation process of the mixture iso-propanol (1)–water (2). Sintered metal plate, thickness $L = 1$ mm. Pore diameters between 100 and 1 μm . [31].

Marangoni cells could be observed on the surface of the blotting paper (Fig. 4.22, right). Alternatively, the positions of the two liquids were reversed, with the blue water underneath and the pale propanol soaked in the blotting paper, whereupon no Marangoni cells appeared (see Fig. 4.22, left).

From this example it can be concluded that any kind of analysis of multiphase transport phenomena in porous media should also include a stability check.

4.3.2.4 Example 4: Reactive Liquid Mixture

This example considers distillation of a reacting ternary mixture in an open batch distillery with flowing sweep gas. From this example, one can see the determination of “reactive azeotropes” and “reactive arheotropes”. The considered hypothetical reaction is



In the following, component A is numbered as 1, component B as 2, and component C as 3. At chemical equilibrium conditions, the following relationship holds:

$$x_1 x_2 - \frac{x_3^2}{K_{eq}} = 0 \quad (58)$$

with the chemical equilibrium constant $K_{eq} = 2$.

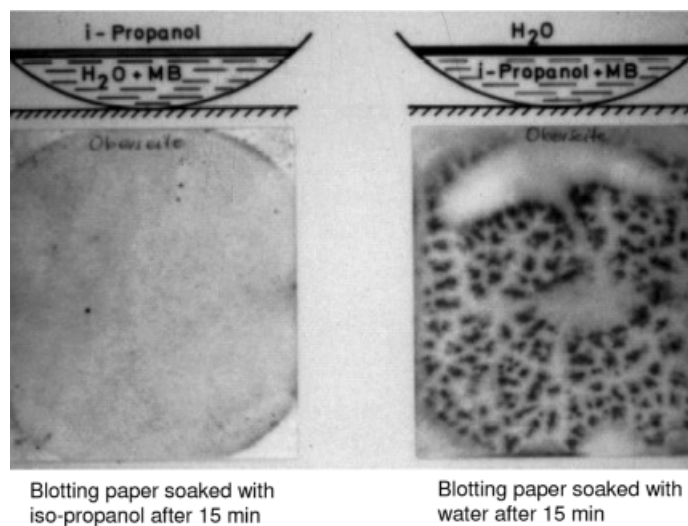


Fig. 4.22. Experimental proof for the onset of Marangoni convection for the mixture iso-propanol–water exposed to ambient air. Left-hand side: water below and propanol on top in the blotting paper: stable; right-hand side: propanol below and water on top in the blotting paper: unstable.

The relative volatilities are assumed to be $\alpha_{13} = 5$ and $\alpha_{23} = 3$, and gas phase mass transfer coefficients are $k_{1,gas} = 0.5 \text{ m s}^{-1}$ and $k_{2,gas} = 1.0 \text{ m s}^{-1}$. The flow rate per unit interface area of the sweep gas is chosen between $G = 0.001$ to 0.4 m s^{-1} , which results in either high or low gas phase NTU_i -values. Presupposing that the vapor mole fractions are low, i.e. $y_i \ll 1$, one can say that:

a) The Stefan flux is negligible in the gas phase (but not in the liquid phase!).

b) Vapor mole fractions y_i are practically equal to the molar sweep gas loadings \tilde{Y}_i . Material balances of the liquid phase for the nonreacting mixture are:

$$\frac{dx_i}{d \ln H} = \chi_i - x_i \quad i = 1, 2, 3 \quad (59)$$

For the gas phase, the mass balances are:

$$\tilde{Y}_{i,in} = 0 \quad i = 1, 2, 3 \quad (60)$$

$$n_i = n_{sweepgas} \tilde{Y}_i \quad i = 1, 2, 3 \quad (61)$$

$$n_T = n_{sweepgas} \sum_{j=1}^3 \tilde{Y}_j \quad (62)$$

$$\chi_i = \frac{n_i}{n_T} = \frac{\tilde{Y}_i}{\sum_{j=1}^3 \tilde{Y}_j} \quad i = 1, 2, 3 \quad (63)$$

Gas phase mass transfer fluxes (Stefan flux in the gas phase is negligible as long as the vapor phase mole fractions are below say 20 %, which means either moderate temperatures and/or high sweep gas flow rates) are:

$$n_i = A_{ph} \rho_{gas} k_{i,gas} (\tilde{Y}_{i,ph} - \tilde{Y}_i) \quad i = 1, 2, 3 \quad (64)$$

$$\tilde{Y}_i = \frac{NTU_i}{1 + NTU_i} \tilde{Y}_{i,ph} \quad i = 1, 2, 3 \quad (65)$$

with

$$NTU_i = \frac{k_{i,gas} A_{ph}}{V_{sweepgas}} = \frac{k_{i,gas}}{G} \quad i = 1, 2, 3. \quad (66)$$

Liquid phase mass transfer fluxes (Stefan flux not negligible) fulfil the relationship

$$\frac{\chi_i - x_i}{\chi_i - x_{i,Ph}} = K_{liq} \quad i = 1, 2, 3, \quad (67)$$

where K_{liq} is defined as in Eq. (55).

Phase equilibrium at the interface is expressed as follows:

$$\tilde{Y}_{i,Ph} = K_i x_{i,Ph} \quad i = 1, 2, 3 \quad (68)$$

$$\tilde{Y}_i = \frac{NTU_i}{1 + NTU_i} K_i x_{i,Ph} \quad i = 1, 2, 3 \quad (69)$$

Introducing

$$K_{gas,23} = \frac{NTU_2}{1 + NTU_2} \frac{1 + NTU_3}{NTU_3} \text{ and } K_{gas,13} = \frac{NTU_1}{1 + NTU_1} \frac{1 + NTU_3}{NTU_3} \quad (70)$$

and

$$\alpha_{23} = \frac{K_2}{K_3} \text{ and } \alpha_{13} = \frac{K_1}{K_3} \quad (71)$$

one obtains

$$\frac{\tilde{Y}_2}{\tilde{Y}_3} = \frac{\chi_2}{\chi_3} = K_{gas,23} \alpha_{23} \frac{x_{2,Ph}}{x_{3,Ph}} \text{ and } \frac{\tilde{Y}_1}{\tilde{Y}_3} = \frac{\chi_1}{\chi_3} = K_{gas,13} \alpha_{13} \frac{x_{1,Ph}}{x_{3,Ph}}. \quad (72)$$

After further rearrangement, one obtains

$$\frac{\chi_2 / x_{2,Ph}}{\chi_3 / x_{3,Ph}} = \alpha_{23}^* \text{ and } \frac{\chi_1 / x_{1,Ph}}{\chi_3 / x_{3,Ph}} = \alpha_{13}^* \quad (73)$$

where $\alpha_{23}^* = K_{gas,23} \alpha_{23}$ and $\alpha_{13}^* = K_{gas,13} \alpha_{13}$.

Substituting the liquid interface concentrations $x_{i,Ph}$ by the liquid bulk concentrations x_i using Eq. (67) gives

$$\frac{\chi_1}{\chi_3} = \alpha_{13}^* \frac{(K_{liq} - 1) \chi_1 + x_1}{(K_{liq} - 1) \chi_3 + x_3} \text{ and } \frac{\chi_2}{\chi_3} = \alpha_{23}^* \frac{(K_{liq} - 1) \chi_2 + x_2}{(K_{liq} - 1) \chi_3 + x_3} \quad (74)$$

Rearranging and introducing the following abbreviations

$$\varepsilon_{13} = (K_{liq} - 1)(1 - \alpha_{13}^*) \text{ and } \varepsilon_{23} = (K_{liq} - 1)(1 - \alpha_{23}^*) \quad (75)$$

one obtains

$$\frac{\chi_1/x_1}{\chi_3/x_3} = \alpha_{13}^* \frac{1}{1 + \varepsilon_{13}\chi_3/x_3} \text{ and } \frac{\chi_2/x_2}{\chi_3/x_3} = \alpha_{23}^* \frac{1}{1 + \varepsilon_{23}\chi_3/x_3} \quad (76)$$

From the material balance of the liquid phase according to Eq. (59) follows

$$\frac{\chi_1/x_1}{\chi_3/x_3} = \alpha_{13}^* \frac{1}{1 + \varepsilon_{13}\chi_3/x_3} \text{ and } \frac{\chi_2/x_2}{\chi_3/x_3} = \frac{d \ln x_2 + d \ln H}{d \ln x_3 + d \ln H} \quad (77)$$

Then Eqs. (76) and (77) lead to

$$\frac{d \ln x_1 + d \ln H}{d \ln x_3 + d \ln H} = \alpha_{13}^* \frac{d \ln H}{\varepsilon_{13}(d \ln x_3 + d \ln H) + d \ln H} \quad (78a)$$

$$\frac{d \ln x_2 + d \ln H}{d \ln x_3 + d \ln H} = \alpha_{23}^* \frac{d \ln H}{\varepsilon_{23}(d \ln x_3 + d \ln H) + d \ln H} \quad (78b)$$

or explicitly in H as function of the concentrations x_i :

$$(d \ln H)^2 + p_{13}(d \ln H) + q_{13} = 0 \quad (79a)$$

$$(d \ln H)^2 + p_{23}(d \ln H) + q_{23} = 0 \quad (79b)$$

with

$$p_{13} = \frac{(1 + \varepsilon_{13}) \frac{dx_1}{x_1} + (\varepsilon_{13} - \alpha_{13}^*) \frac{dx_3}{x_3}}{1 + \varepsilon_{13} - \alpha_{13}^*} \quad (80a)$$

$$p_{23} = \frac{(1 + \varepsilon_{23}) \frac{dx_2}{x_2} + (\varepsilon_{23} - \alpha_{23}^*) \frac{dx_3}{x_3}}{1 + \varepsilon_{23} - \alpha_{23}^*} \quad (80b)$$

$$q_{13} = \frac{\varepsilon_{13}}{1 + \varepsilon_{13} - \alpha_{13}^*} \frac{dx_1}{x_1} \frac{dx_3}{x_3} \quad (80c)$$

$$q_{23} = \frac{\varepsilon_{23}}{1 + \varepsilon_{23} - \alpha_{23}^*} \frac{dx_2}{x_2} \frac{dx_3}{x_3} \quad (80d)$$

Eventually, elimination of the hold-up H results in a final equation, which allows the calculation of residue curves for the nonreacting mixtures by stepwise integration:

$$p_{13} \left(1 \pm \sqrt{1 - \frac{4q_{13}}{p_{13}^2}} \right) - p_{23} \left(1 \pm \sqrt{1 - \frac{4q_{23}}{p_{23}^2}} \right) = 0 \quad (81)$$

From these four solutions, only the one with positive signs are physically meaningful. This is a rigorous solution including both liquid phase and gas phase mass transfer resistances. It can be applied also to non-ideal mixtures when calculating the relative volatilities α_{ij} from appropriate VLE-equations.

Equation (81) can also be used to predict the existence of reactive arheotropes provided that the mixture is in permanent chemical equilibrium – that is, the Damköhler number is sufficiently large. The condition which must be fulfilled has been given by Frey and Stichlmair [30], who concluded that the slope of the nonreacting residue curve must coincide with the slope of the stoichiometric lines of the chemical reaction, given by the stoichiometric coefficients v_i .

$$\left[\frac{dx_2}{dx_1} \right]_{phy} = \left[\frac{dx_2}{dx_1} \right]_{chem} \quad (82)$$

Inserting Eq. (82) into Eq. (81) gives the qualifying Eq. (83) to predict the locus curve $x_{2,az} = F_{phy}(x_{1,az})$ at which possible reactive arheotropes can be found (i.e., the potential singular point surface, PSPS). The second curve is given by the equation describing the chemical equilibrium $x_{2,az} = F_{Chem}(x_{1,az})$.

$$p_{13,az} = \frac{(1 + \varepsilon_{13}) \frac{1}{x_{1,az}} - (\varepsilon_{13} - \alpha_{13}^*) \frac{1}{x_{3,az}} \left(1 + \left[\frac{dx_2}{dx_1} \right]_{chem} \right)}{1 + \varepsilon_{13} - \alpha_{13}^*} dx_1 \quad (83a)$$

$$p_{23,az} = \frac{(1 + \varepsilon_{23}) \frac{1}{x_{2,az}} \left[\frac{dx_2}{dx_1} \right]_{chem} - (\varepsilon_{23} - \alpha_{23}^*) \frac{1}{x_{3,az}} \left(1 + \left[\frac{dx_2}{dx_1} \right]_{chem} \right)}{1 + \varepsilon_{13} - \alpha_{13}^*} dx_1 \quad (83b)$$

$$q_{13,az} = - \frac{\varepsilon_{13}}{1 + \varepsilon_{13} - \alpha_{13}^*} \frac{1}{x_{1,az} x_{3,az}} \left(1 + \left[\frac{dx_2}{dx_1} \right]_{chem} \right) dx_1^2 \quad (83c)$$

$$q_{23,az} = -\frac{\varepsilon_{23}}{1 + \varepsilon_{23} - \alpha_{23}^*} \frac{1}{x_{2,az} x_{3,az}} \left[\frac{dx_2}{dx_1} \right]_{Chem} \left(1 + \left[\frac{dx_2}{dx_1} \right]_{Chem} \right) dx_1^2 \quad (83d)$$

If the ratio of the evaporation velocity to the liquid phase mass transfer velocity w_{liq}/k_{liq} tends towards zero (i.e., $K_{liq} = 1$), then Eq. (81) reduces to:

$$\left(\frac{1}{1 - \alpha_{13}^*} \frac{1}{x_1} + \Omega \frac{1}{x_3} \right) dx_1 = \left(\frac{1}{1 - \alpha_{23}^*} \frac{1}{x_2} - \Omega \frac{1}{x_3} \right) dx_2 \quad (84)$$

where $\Omega = \frac{\alpha_{13}^*}{1 - \alpha_{13}^*} - \frac{\alpha_{23}^*}{1 - \alpha_{23}^*}$, while Eq. (82) can be reduced to

$$\left(\frac{1}{1 - \alpha_{13}^*} \frac{1}{x_{1,az}} + \Omega \frac{1}{x_{3,az}} \right) = \left(\frac{1}{1 - \alpha_{23}^*} \frac{1}{x_{2,az}} - \Omega \frac{1}{x_{3,az}} \right) \left[\frac{dx_2}{dx_1} \right]_{Chem} \quad (85)$$

For the reaction $A + B \rightleftharpoons 2C$, let x_1 be the independent variable, while x_2 is the dependent one; thus, the slope of the stoichiometric lines is $(dx_2/dx_1)_{Chem} = 1$.

Figure 4.23 shows the curves according to Eq. (83) and Eq. (85) for various sweep gas flow rates G and vanishing liquid phase mass transfer resistance (i.e., $K_{liq} = 1$). The points of intersection with the chemical equilibrium line mark the concentrations at which reactive azeotropes exist. As can be seen, the reactive azeotrope

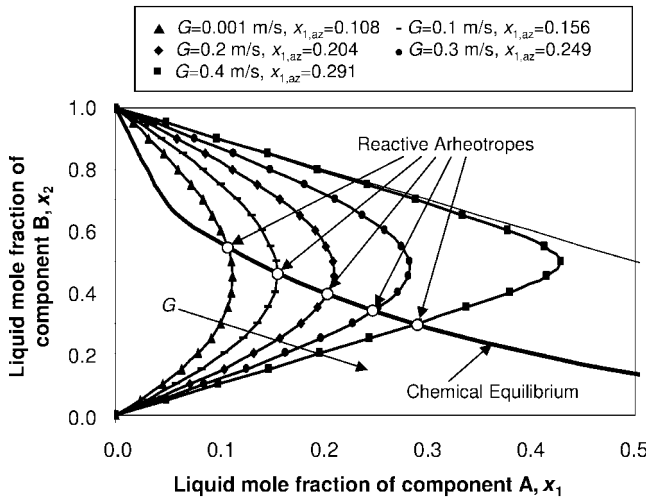


Fig. 4.23. Reactive azeotropes for the reaction $A + B \rightleftharpoons 2C$ at various sweep gas flow rates G ($Da \rightarrow \infty$, $\alpha_{13} = 5$, $\alpha_{23} = 3$, $k_{1,gas} = 0.5 \text{ cm s}^{-1}$, $k_{2,gas} = 1 \text{ cm s}^{-1}$).

composition $x_{1,az}$ is shifted to larger values as the sweep gas flow rate G is increased. Note that the interface vapor concentrations are in equilibrium with the liquid phase bulk concentrations.

Figure 4.24 shows the reactive arheotrope trajectories according to Eq. (83) for various amounts of the liquid phase mass transfer resistance – that is, for various values of K_{liq} and a low sweep gas flow rate G (at large NTU_i -values). As a result, the reactive arheotropic composition $x_{1,az}$ is shifted to larger values as the liquid phase mass transfer resistance becomes more important – that is, as the value of K_{liq} decreases. Note that the interface liquid concentrations are in equilibrium with the vapor phase bulk concentrations. Therefore, gas phase mass transfer resistances cannot have any influence on the position of the reactive arheotrope compositions. On the other hand, liquid phase mass transfer resistances do have an effect, though the value of all binary k_{liq} have been set equal. Again, this effect results from the competition between the diffusion fluxes and the Stefan flux in the liquid phase.

This gives rise to a warning: In feasibility studies for an open batch distillation process certain assumptions are made as to the heating policy (see e.g. Ref. [7]). Since the ratio of the evaporation velocity to the liquid phase mass transfer coefficient u_{liq}/k_{liq} also depends on the “heating policy”, one must ensure that this ratio is sufficiently low; otherwise the composition of the reactive arheotrope will also depend on the “heating policy.”

Figure 4.25 shows the reactive arheotrope trajectories according to Eq. (83) for various amounts of the liquid phase mass transfer resistance – that is, for various values of K_{liq} and larger sweep gas flow rates $G = V_{sweepgas}/A_{ph}$. With increasing sweep gas flow rate the effect of the liquid phase mass transfer resistance vanishes, and at $G = 0.4 \text{ m s}^{-1}$ the reactive arheotropic composition $x_{1,az}$ is practically not affected at all.

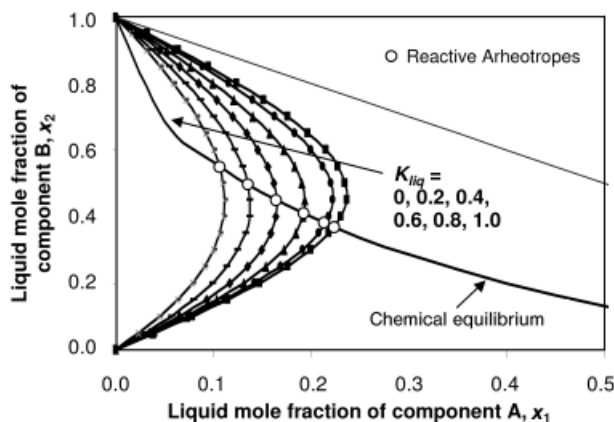


Fig. 4.24. Reactive arheotropes for the reaction $A + B \rightleftharpoons 2 C$ at various liquid phase mass transfer resistances K_{liq} (low sweep gas flow rate G , $Da \rightarrow \infty$, $\alpha_{13} = 5$, $\alpha_{23} = 3$, $k_{1,gas} = 0.5 \text{ cm s}^{-1}$, $k_{2,gas} = 1 \text{ cm s}^{-1}$).

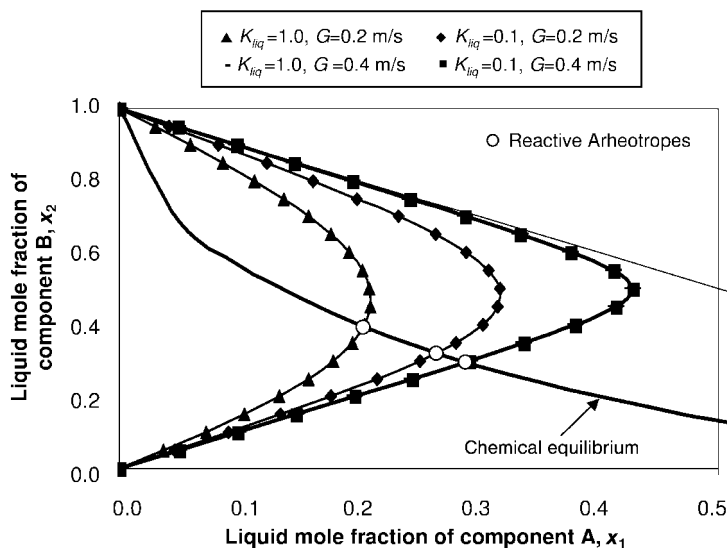


Fig. 4.25. Reactive azeotropes for the reaction $A + B \rightleftharpoons 2C$ at various liquid phase mass transfer resistances K_{liq} (large sweep gas flow rate G , $Da \rightarrow \infty$, $\alpha_{13} = 5$, $\alpha_{23} = 3$, $k_{1,gas} = 0.5 \text{ cm s}^{-1}$, $k_{2,gas} = 1 \text{ cm s}^{-1}$).

4.3.3

Remarks on Azeotropes

The aim of this section is to show that in an open batch distillation process both gas-phase and liquid-phase mass transfer resistances have a remarkable effect on the compositions at which nonreactive azeotropes and reactive azeotropes appear.

Both mass transfer resistances are interconnected in a rather complex manner. The structure of these interconnections was made visible by the presentation of analytical solutions which could be easily handled on a spreadsheet calculation tool, even for much more complicated VLE equations with variable relative volatilities and chemical equilibrium equations of any complexity because no integration procedure is necessary, but just finding roots.

Both mass transfer resistances – as can be seen from the analytical solutions – act in a different way and cannot be combined to a so-called “overall transfer resistance”. The introduction of such a lumped parameter will hide essential physical effects, evoked by these two resistances separately.

Eventually, there is an essential difference between batch distillation processes and column distillation processes. Whilst in most adiabatic column distillation processes Stefan fluxes are usually very small (unless inert gases are present, as in hydrogenation or oxidation processes), the batch distillation process just lives from

the existence of the Stefan flux. However, this difference can only be ignored as long as the mass transfer resistances are negligible.

4.4

Kinetic Arheotropes in Reactive Membrane Separation

The possible products of a reactive membrane separation process are influenced by the mass transfer characteristics of the applied membranes. In the following section it is shown how the concepts and tools, being developed for reactive vapor-liquid separation, can also be used to analyze the feasibility of membrane separators.

4.4.1

Model Formulation

Here, a batch membrane separator is considered, as depicted in Fig. 4.26(a). The difference between this process and the reactive reboiler which was considered in Section 4.2 is that a membrane is introduced above the vapor phase. For the further analysis, the following assumptions are made:

- The membrane holds the major mass transfer resistance; thus, the liquid phase and the retentate vapor bulk phase are assumed to be in phase equilibrium.
- Vacuum is applied on the permeate side of the membrane.
- The chemical reaction takes place at boiling temperature in the reactive hold-up H_r of the liquid phase.
- A vapor permeation process is considered; that is, the membrane is placed above the vapor-liquid interface.
- Accumulations of components within the retentate vapor phase or within the membrane body are neglected.

It should be noted that the equivalent continuously operated process of the batch reactive membrane process is the membrane reactor depicted in Fig. 4.26(b). Here, the spatial coordinate z replaces the time coordinate of the batch process. Feasibility analysis has the task of estimating the retentate composition which is attainable at infinite reactor length.

4.4.1.1 Reaction Kinetics and Mass Balances

The chemical reaction taking place in the liquid phase is represented by Eq. (1), and the mass balance can be formulated as [20]

$$\frac{dx_i}{d\xi} = \left(x_i - \frac{n_i}{n_T} \right) + Da \left(v_i - v_T x_i \right) \frac{H_r}{H_{r,0}} \frac{n_{T,0}}{n_T} \frac{k_f}{k_{f,ref}} \Re \quad i = 1, \dots, NC - 1 \quad (86)$$

where $d\xi = (n_T/H)dt$, H_r is the hold-up in which the reaction proceeds, n_i the component mass flux through the membrane area, and $n_T = \sum_{i=1}^{NC} n_i$ the total mass

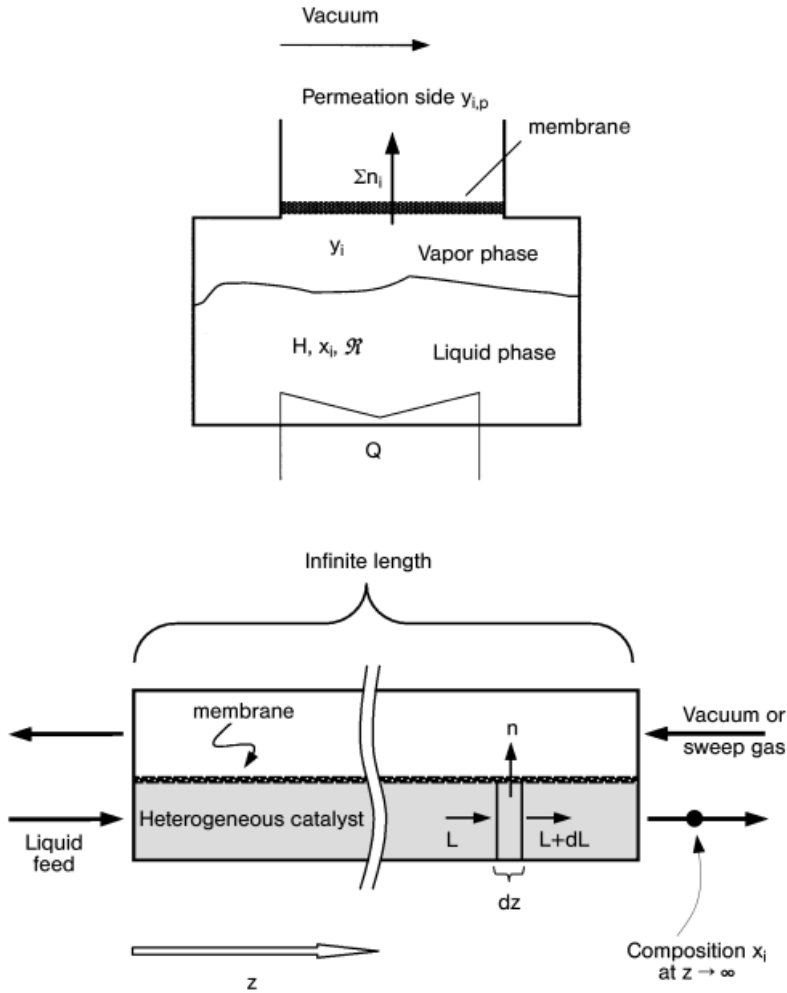


Fig. 4.26. (a) Batch reactive membrane separation process;
(b) equivalent continuous reactive membrane separation process.

flux. The Damköhler number Da is defined as the ratio of the characteristic reaction rate ($H_{r,0} \times k_{f,ref}$) and the characteristic escaping total flux $n_{T,0}$

$$Da \equiv \frac{H_{r,0} k_{f,ref}}{n_{T,0}} \quad (87)$$

To study the autonomous dynamic behavior, two suitable heating strategies can be assumed:

- $n_T/n_{T,0} = H_r/H_{r,0}$, if the chemical reaction takes place as a homogeneous reaction in the whole liquid bulk phase;

- $n_T = n_{T,0} = \text{constant}$, if the chemical reaction takes place in a solid catalyst phase of which the molar hold-up is constant during the process ($H_r = H_{r,0} = \text{constant}$).

At both strategies, the reaction kinetic effect is characterized by a single parameter (i.e., Damköhler number Da), and Eq. (86) can be rewritten as

$$\frac{dx_i}{d\xi} = \left(x_i - \frac{n_i}{n_T} \right) + Da \left(v_i - v_T x_i \right) \frac{k_f}{k_{f,ref}} \Re \quad i = 1, \dots, NC - 1 \quad (88)$$

4.4.1.2 Kinetics of Vapor Permeation

In a partial pressure-driven vapor permeation process, the NC -dimensional vector of mass fluxes through the porous membrane can be expressed as [33]:

$$(n) = \frac{S}{RT} [k] (\gamma p - \gamma_p p_p) \quad (89)$$

where $[k]$ is the $NC \times NC$ -dimensional matrix of effective binary mass transfer coefficients k_{ij} , S is the effective permeation area, γp and p_p denote the vector of mole fractions and the total pressure on the membrane permeate side, respectively. If vacuum is applied on the permeate side, the partial pressures of the diffusing components on the permeate side are negligible ($p_p \rightarrow 0$). For the subsequent process analysis, it is useful to formulate Eq. (89) in terms of dimensionless mass transfer coefficients κ_{ij} which are the ratios of the effective mass transfer coefficients k_{ij} related to a reference one. Here, the first main diagonal element k_{11} is taken as reference:

$$(n) = \frac{Sp}{RT} k_{11} [\kappa] (\gamma) \quad \text{with } \kappa_{ij} \equiv \frac{k_{ij}}{k_{11}}. \quad (90)$$

In general, all elements of the mass transfer matrix depend on the process variables, and in particular on the vapor phase composition. The mass transfer mechanisms in membranes can be rather complicated. However, for the conceptual analysis of the considered membrane process, it is not advantageous to go into the details of mass transport. Therefore, in the following the effective binary mass transfer coefficients k_{ij} are assumed to be constants.

Three cases can be distinguished concerning the mathematical structure of the matrix $[k]$:

1. Scalar $[k]$ if the membrane is nonselective, i.e., it has no separation effect on the components, and therefore $[k]$ in Eq. (90) is an identity matrix.
2. Diagonal $[k]$ if the permeating components are only driven by their own partial pressure differences; this case is valid, for example, for a Knudsen-membrane.

3. Nondiagonal $[k]$ if the permeating components interact with each other within the membrane; this will be the case for example if bulk diffusion and/or competitive adsorption effects are involved.

Despite the fact that the matrix elements can be positive or negative, $[k]$ must be positive definite because of the constraints imposed by the second law of thermodynamics.

4.4.2

Residue Curve Maps

4.4.2.1 Example 1: Ideal Ternary System

In this example, the effect of a selective membrane on the ternary mixture undergoing a reversible chemical reaction in ideal liquid phase is considered:



The dimensionless rate of the chemical reaction is given as:

$$\Re = x_B x_C - \frac{x_A}{K_{eq}}. \quad (92)$$

The relative volatilities are $\alpha_{BA} = 5$ and $\alpha_{CA} = 3$, and the chemical equilibrium constant $K_{eq} = 5$.

Figure 4.27 shows residue curve maps for the reactive reboiler at three different Damköhler numbers. In the nonreactive case ($Da = 0$; Fig. 4.27(a)), the map topology is structured by one unstable node (pure B), one saddle point (pure C), and one stable node (pure A). Since pure A is the only stable node of nonreactive distillation, this is the feasible bottom product to be expected in a continuous distillation process.

In a kinetically controlled chemical reaction ($Da = 1$; Fig. 4.27(b)), the stable node moves from the pure A vertex into the composition triangle. In an equilibrium-controlled chemical reaction ($Da \rightarrow \infty$; Fig. 4.27(c)), the reaction approaches its chemical equilibrium, and therefore the stable node is located on the equilibrium surface.

In analogous manner, residue curve maps of the reactive membrane separation process can be predicted. First, a diagonal $[\kappa]$ -matrix is considered with $\kappa_{CC} = 5$ and $\kappa_{BB} = 1$ – that is, the undesired byproduct C permeates preferentially through the membrane, while A and B are assumed to have the same mass transfer coefficients. Figure 4.28(a) illustrates the effect of the membrane at nonreactive conditions. The trajectories move from pure C to pure A, while in nonreactive distillation (Fig. 4.27(a)) they move from pure B to pure A. Thus, by application of a C-selective membrane, the C vertex becomes an unstable node, while the B vertex becomes a saddle point. This is due to the fact that the membrane changes the effective volatilities (i.e., the products $x_{ii} \alpha_{iA}$) of the reaction system such that $\kappa_{CC} \alpha_{CA} > \kappa_{BB} \alpha_{BA}$.

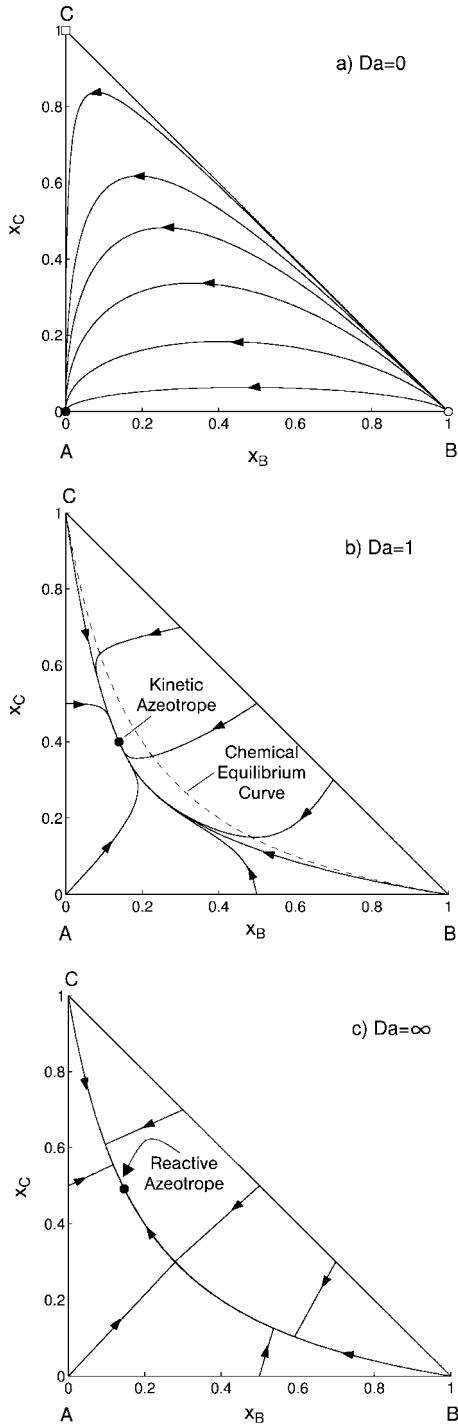


Fig. 4.27. Residue curve maps for reactive distillation; $B + C \rightleftharpoons A$; $K_{eq} = 5$; $\alpha_{BA} = 5.0$; $\alpha_{CA} = 3.0$. (a) $Da = 0$; (b) $Da = 1$; (c) $Da \rightarrow \infty$.

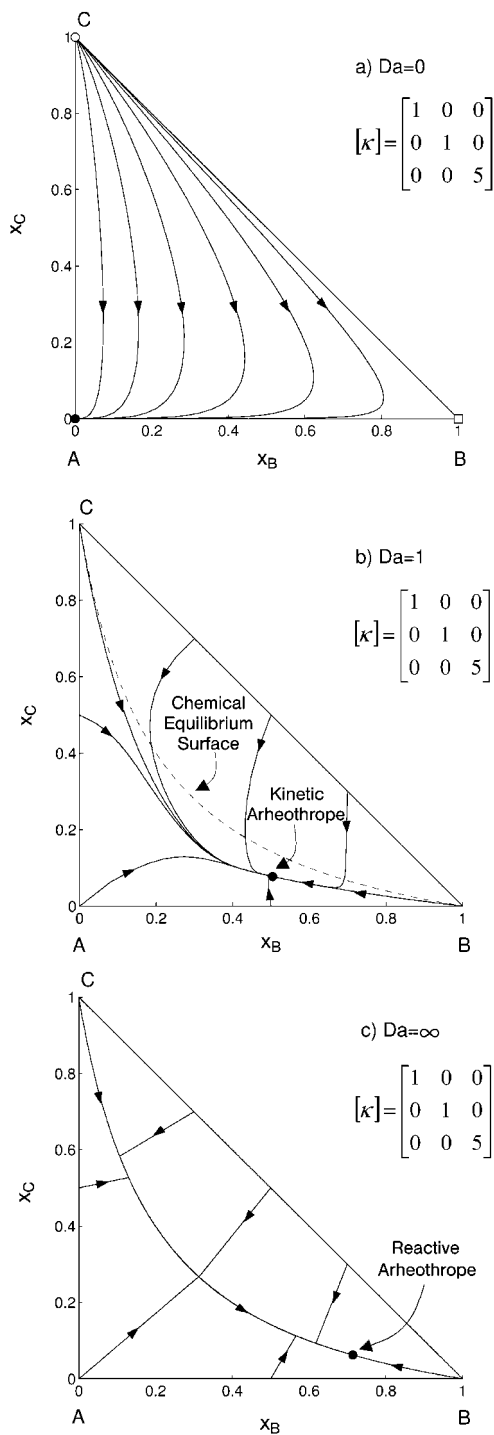


Fig. 4.28. Residue curve maps for reactive membrane separation; $B + C \rightleftharpoons A$; $K_{eq} = 5$; $\alpha_{BA} = 5.0$, $\alpha_{CA} = 3.0$; membrane: diagonal $[\kappa]$ -matrix.

At kinetically controlled reactive conditions ($Da = 1$), Fig. 4.28(b) shows that the stable node moves into the composition triangle, as in reactive distillation (Fig. 4.27(b)). This point is termed the “kinetic arheotrope” because its location in the phase diagram depends on the membrane mass transfer resistances and also on the rate of chemical reaction. The kinetic arheotrope moves towards the B vertex with increasing C-selectivity of the membrane. At infinite Damköhler number, the system is chemical equilibrium-controlled (Fig. 4.28(c)), and therefore the arheotrope is located exactly on the chemical equilibrium curve. In this limiting case, it is called a “reactive arheotrope”.

4.4.2.2 Example 2: THF Formation

1,4-Butanediol (1,4-BD) can be decomposed heterogeneously to tetrahydrofuran (THF) and water:



Limbeck et al. [34] have studied the kinetics of this irreversible reaction at macroporous acidic ion exchange resins as catalysts. In this reaction, the byproduct water has a significant affinity with the catalyst, and thus severely inhibits the catalytic reaction. Therefore, these authors proposed the following rate expression:

$$r = \eta a_{H_2O} \frac{k_f K_{S,BD} a_{BD}}{1 + K_{S,BD} a_{BD}} = \frac{1}{1 + K_{S,H_2O} \sqrt{a_{H_2O}}} \frac{k_f K_{S,BD} a_{BD}}{1 + K_{S,BD} a_{BD}} \quad (94)$$

where $K_{S,BD}$ and K_{S,H_2O} are the sorption constants of 1,4-BD and water respectively, and η is the water inhibition factor. The temperature dependencies of k_f , $K_{S,BD}$ and K_{S,H_2O} are as follows:

$$\frac{k_f}{k_{f,ref}} = \exp\left(\frac{-18282.42}{T/[K]}\right) / \exp\left(\frac{-18282.42}{404.2}\right) \quad (95)$$

$$K_{S,BD} = 6.29 \times 10^{-2} \times \exp\left(\frac{1335.1}{T/[K]}\right) \quad (96a)$$

$$K_{S,H_2O} = 2.43 \times \exp\left(\frac{764.97}{T/[K]}\right) \quad (96b)$$

The boiling point of THF at 5 atm (404.2 K) is chosen as the reference temperature. The liquid phase activity coefficients were calculated using the Wilson equation [35].

Since water is the byproduct, and also has an undesired inhibitory effect on catalyst activity, it must be separated efficiently from the reaction mixture. To achieve this, both conventional reactive distillation and reactive membrane separation are considered as process alternatives. In the latter process, a Knudsen-membrane is applied. Consequently, the mass transfer matrix $[\kappa]$ has a diagonal structure and the diagonal elements are the Knudsen-selectivities – that is, the square-roots of the ratios of the molecular weights M_i :

$$[\kappa] = \begin{bmatrix} 1 & 0 & 0 \\ 0 & \sqrt{M_{BD}/M_{THF}} & 0 \\ 0 & 0 & \sqrt{M_{BD}/M_{H_2O}} \end{bmatrix} = \begin{bmatrix} 1 & 0 & 0 \\ 0 & 1.1 & 0 \\ 0 & 0 & 2.5 \end{bmatrix} \quad (97)$$

Thus, water will pass preferentially through the Knudsen-membrane.

Residue curve maps of the THF system were predicted for reactive distillation at different reaction conditions (Fig. 4.29). The topology of the map at nonreactive conditions ($Da = 0$) is structured by a binary azeotrope (unstable node) between water and THF. Pure water and pure THF are saddle nodes, while the 1,4-BD vertex is a stable node.

At $Da = 0.4$ (Fig. 4.29(b)), the two saddle points from the pure vertices move into the composition triangle. The stable node from the 1,4-BD vertex moves to the kinetic azeotrope at $x = (0.0328, 0.6935)$. Pure water and pure THF now become stable nodes. The unstable node between water and THF remains unmoved, and forms two separatrices with the two saddle points. Thereby, the whole composition space is divided into three subspaces which have each a stable node, namely pure water, pure THF and the kinetic azeotrope.

At $Da \rightarrow \infty$ (Fig. 4.29(c)), only pure water and pure THF remain stable nodes. The residue curves first are dominated by the reaction stoichiometry and approach the chemical equilibrium surface, and then converge to the water vertex or to the THF vertex. When starting from pure 1,4-BD, the undesired byproduct of water will be the final product in the distillation still.

The effect of a Knudsen-membrane on process behavior is illustrated in Fig. 4.30(a), which is valid at nonreactive conditions. Compared to Fig. 4.29(a), the unstable node on the THF-water edge is moved closer to the water vertex by application of the Knudsen-membrane, while the two saddle points and stable node are not affected.

At $Da = 0.4$ (Fig. 4.30(b)), the residue curve map is structured by one unstable node, two saddle points, and three stable nodes (as in Fig. 4.29(b)), but the locations of the two saddle points and the stable node are changed. In particular, the kinetic azeotrope at $x = (0.2313, 0.2520)$ is located closer to the THF vertex than the kinetic azeotrope at $x = (0.0328, 0.6935)$.

Similar to the reactive distillation process, at $Da \rightarrow \infty$ the composition space is again divided into two subspaces which have either pure THF or pure water as attractors (Fig. 4.30(c)). However, as a very important feature of the reactive membrane

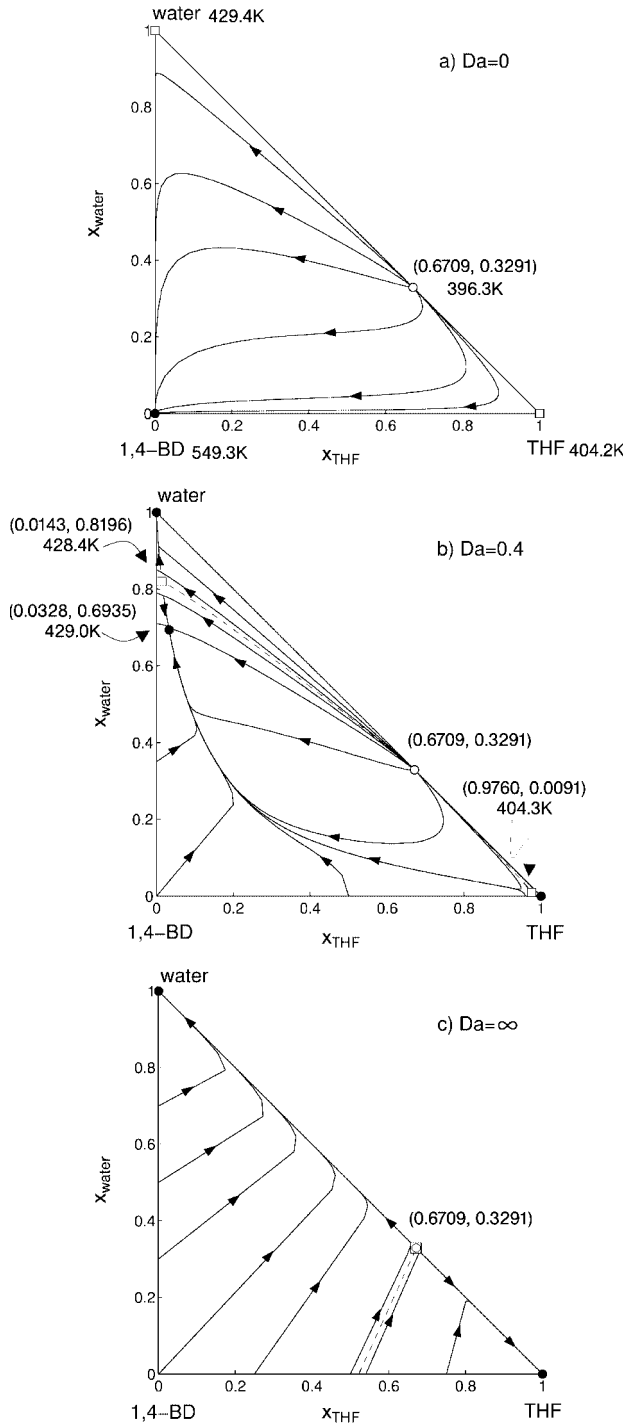


Fig. 4.29. Residue curve maps for reactive distillation; 1,4-BD \rightarrow THF + Water; $p = 5$ atm. (a) $Da = 0$; (b) $Da = 0.4$; (c) $Da \rightarrow \infty$.

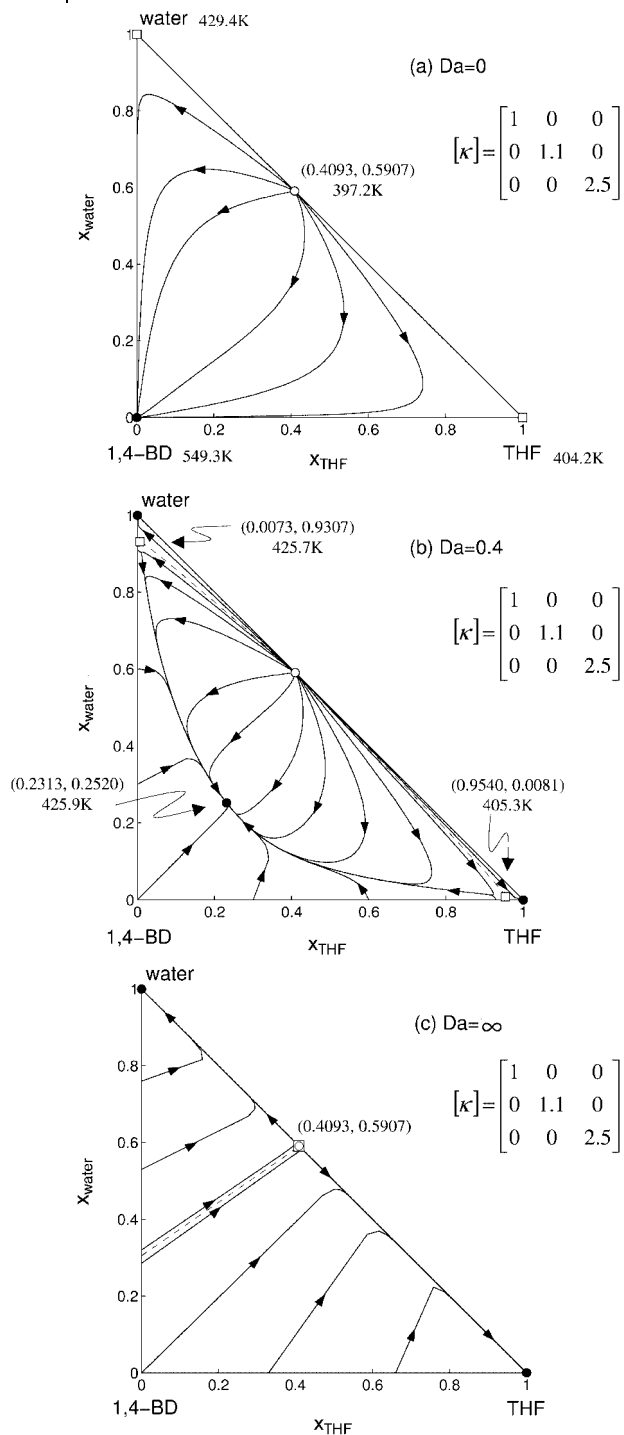


Fig. 4.30. Residue curve maps for reactive membrane separation; 1,4-BD \rightarrow THF + Water; $p = 5$ atm; Knudsen-membrane. (a) $Da = 0$; (b) $Da = 0.4$; (c) $Da \rightarrow \infty$.

separation process, when starting with pure 1,4-BD it is possible to attain pure THF as the desired product. This is not possible with conventional reactive distillation.

4.4.3

Singular Point Analysis

4.4.3.1 Approach

The locations of the singular points in reactive membrane separation processes depend on both the separation effects (distillation/membrane separation) and the reaction effect. Singular points can be generally obtained as steady-state solutions of Eq. (88):

$$0 = \left(x_i - \frac{n_i}{n_T} \right) + Da \left(v_i - v_T x_i \right) \frac{k_f}{k_{f,ref}} \Re \quad i = 1, \dots, NC - 1 \quad (98)$$

Four important cases can be distinguished:

1. *Nonreactive distillation*: $Da = 0$ and $[k]$ is a scalar matrix. Then, Eq. (98) simplifies to the classical condition of a nonreactive azeotrope:

$$x_i = y_i, \quad i = 1 \dots NC - 1 \quad (99)$$

2. *Reactive distillation*: $Da \neq 0$ and $[k]$ is a scalar matrix. This case was intensively studied by Qi et al. [14], who analyzed the existence and location of reactive and kinetic azeotropes.

3. *Nonreactive membrane separation*: $Da = 0$ and $[k]$ is a non-scalar matrix. Then, the condition for a nonreactive arheotrope (Eq. (50)) is recovered:

$$x_i = \frac{n_i}{n_T}; \quad i = 1, \dots, NC - 1 \quad (100)$$

4. *Reactive membrane separation*: $[k]$ -matrix is a non-scalar matrix. This case was intensively studied by Huang et al. [20] ("*kinetic arheotrope*").

Similar to reactive distillation (as discussed in Section 4.2.2.1), the concept of the PSPS is useful to analyze the singular points of a reactive membrane separation process. By introducing the new transformed variables

$$X_i = \frac{v_k x_i - v_i x_k}{v_k - v_T x_k} \quad \text{and} \quad Y_i = \frac{v_k n_i - v_i n_k}{v_k n_T - v_T n_k} \quad (101a,b)$$

the condition for reactive/kinetic arheotropes can be simply expressed as:

$$X_i = Y_i, \quad i = 1, \dots, NC - 2 \quad (101c)$$

The transformed vapor composition variable Y_i can be expanded for the different possible structures of the mass transfer matrix:

$$Y_i = \frac{\nu_k \sum_{j=1}^{NC} \kappa_{ij} Y_j - \nu_i \sum_{j=1}^{NC} \kappa_{kj} Y_j}{\nu_k \sum_{i=1}^{NC} \sum_{j=1}^{NC} \kappa_{ij} Y_j - \nu_T \sum_{j=1}^{NC} \kappa_{kj} Y_j} \text{ for nondiagonal } [\kappa] \quad (102a)$$

$$Y_i = \frac{\nu_k \kappa_{ii} Y_i - \nu_i \kappa_{kk} Y_k}{\nu_k \sum_{i=1}^{NC} (\kappa_{ii} Y_i) - \nu_T \kappa_{kk} Y_k} \text{ for diagonal } [\kappa] \quad (102b)$$

$$Y_i = \frac{\nu_k Y_i - \nu_i Y_k}{\nu_k - \nu_T Y_k} \text{ for scalar } [\kappa] \quad (102c)$$

4.4.3.2 Ideal Ternary System

PSPS of reactive membrane separation with diagonal $[\kappa]$ -matrix

For the ideal ternary system discussed in Section 4.4.2.1, the PSPS is the same as for the reactive distillation example in Section 4.2.3.1 (see Fig. 4.4(b)) if one changes the vertices. It is worth mentioning, that the reactive reboiler is just a special case of the reactive membrane separation process with a scalar $[k]$. Now, the question arises how the PSPS and the branch of stable singular points will be influenced by a membrane having a diagonal mass transfer matrix. In Fig. 4.31 the PSPS are presented for different κ_{CC} -values. The solid lines represent the different branches of stable nodes. Clearly, there exists a critical value, $\kappa_{CC,crit} = 5/3$, above which the PSPS is turned from the C-vertex towards the B-vertex. At the intersections of the PSPS with the chemical equilibrium surface ($Da \rightarrow \infty$), reactive azeotropes are located. They move towards the B-vertex with increasing C-selectivity of the membrane – that is, increasing κ_{CC} -value. Above a certain value, the reactive azeotrope coincides with the pure B-vertex and at this point the PSPS is tangential to the chemical equilibrium surface.

Generalization

For a more generalized analysis of the qualitative influence of membranes on the singular points, the reactive membrane separation process is now considered with a nondiagonal $[\kappa]$ -matrix. The condition for a kinetic azeotropes is given by

$$X_B = Y_B \Rightarrow \frac{(-x_B - x_A)}{(-1 - x_A)} = \frac{(-n_B - n_A)}{(-n_T - n_A)} \quad (103)$$

It is easy to show that Eq. (103) can be cast into the following quadratic form:

$$(x)^T [A](x) + (b)^T (x) + c = 0 \quad (104)$$

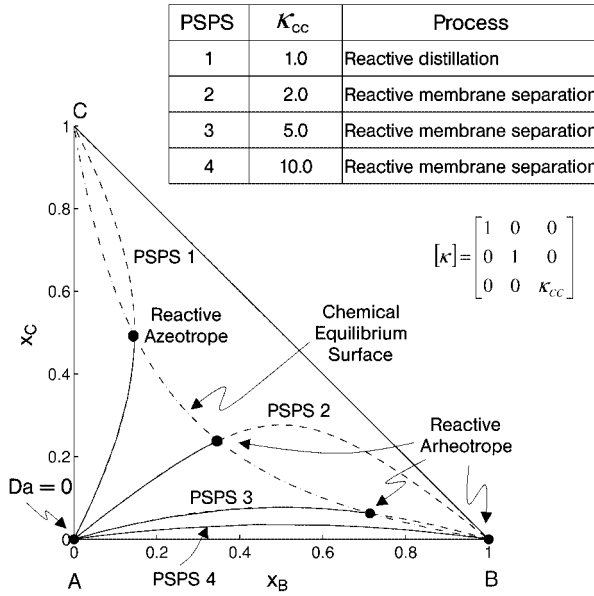


Fig. 4.31. Potential singular point surfaces and stable node bifurcation behavior of reactive membrane separation at different mass transfer conditions; $B + C \rightleftharpoons A$; $K_{eq} = 5$; $\alpha_{BA} = 5.0$, $\alpha_{CA} = 3.0$.

with

$$[A] = \begin{bmatrix} a_1 & \frac{a_2}{2} \\ \frac{a_2}{2} & a_3 \end{bmatrix} \quad (105a)$$

$$(b)^T = (a_4, a_5) \quad (105b)$$

$$c = a_6 \quad (105c)$$

where

$$a_1 = -1 - \kappa_{BA} + \kappa_{AB}\alpha_{BA} + \kappa_{BB}\alpha_{BA} \quad (106a)$$

$$a_2 = -\kappa_{BA} + \kappa_{CA} - \kappa_{AB}\alpha_{BA} - \kappa_{CB}\alpha_{BA} + \kappa_{AC}\alpha_{CA} + \kappa_{BC}\alpha_{CA} \quad (106b)$$

$$a_3 = 1 + \kappa_{CA} - \kappa_{AC}\alpha_{CA} - \kappa_{CC}\alpha_{CA} \quad (106c)$$

$$a_4 = 1 + 2 \cdot \kappa_{BA} - \kappa_{CA} - \kappa_{BB}\alpha_{BA} + \kappa_{CB}\alpha_{BA} \quad (106d)$$

$$a_5 = -1 + \kappa_{BA} - 2 \cdot \kappa_{CA} - \kappa_{BC}\alpha_{CA} + \kappa_{CC}\alpha_{CA} \quad (106e)$$

$$a_6 = -\kappa_{BA} + \kappa_{CA} \quad (106f)$$

In the composition triangle, Eq. (104) describes a second-order surface the shape of which is fixed by the signs of the eigenvalues λ_1 and λ_2 of the symmetric matrix $[A]$. The following cases can be distinguished:

$$\begin{aligned} \lambda_1 \lambda_2 < 0 & \Rightarrow \text{hyperbolic system} \\ \lambda_1 \lambda_2 > 0 & \Rightarrow \text{elliptic system} \\ \lambda_1 = 0 \text{ or } \lambda_2 = 0 & \Rightarrow \text{parabolic system} \end{aligned} \quad (107)$$

For the special case with a diagonal $[\kappa]$, Eqs. (116a–f) can be reduced to

$$a_1 = -1 + \kappa_{BB}\alpha_{BA}, a_2 = 0 \quad (108a,b)$$

$$a_3 = 1 - \kappa_{CC}\alpha_{CA}, a_4 = -a_1 \quad (108c,d)$$

$$a_5 = -a_3, a_6 = 0 \quad (108e,f)$$

In this case, the shape of the PSPS can be classified as follows:

$$\begin{aligned} (-1 + \kappa_{BB}\alpha_{BA})(1 - \kappa_{CC}\alpha_{CA}) < 0 & \Rightarrow \text{hyperbolic system} \\ (-1 + \kappa_{BB}\alpha_{BA})(1 - \kappa_{CC}\alpha_{CA}) > 0 & \Rightarrow \text{elliptic system} \\ (-1 + \kappa_{BB}\alpha_{BA}) = 0 \text{ or } (1 - \kappa_{CC}\alpha_{CA}) = 0 & \Rightarrow \text{parabolic system} \end{aligned} \quad (109)$$

For the case of a scalar $[\kappa]$, the reader is referred to Section 4.2.3.1 (Eqs. (16) and (17)).

Influence of membranes on singular points

A ternary system with a hyperbola-type PSPS is used to investigate the influence of membrane permeation (Fig. 4.32). The applied parameters (α_{iA} and κ_{ij}) and the corresponding eigenvalues of the matrix $[A]$ are summarized in Tab. 4.3. For comparison, again the PSPS for the reactive distillation process is given in Fig. 4.32(a). The effect of a selective membrane with a diagonal $[\kappa]$ -matrix is illustrated in Fig. 4.32(b, d).

The PSPS changes into an ellipse if an incorrect membrane, which preferentially retains the byproduct C, is applied (Fig. 4.32(c)). In this case, the pure C vertex is the only stable node of the system, which means that the only feasible product is the pure byproduct C at reactive and also at nonreactive conditions.

The effect of a nondiagonal $[\kappa]$ -matrix is illustrated in Fig. 4.32(d). Off-diagonal elements might appear if molecular interactions between the permeating species are involved. As an example, here the interaction of A and C is embodied into the $[\kappa]$ -matrix by assuming $\kappa_{AC} = 0.5$ and $\kappa_{CA} = 0.5$. All other parameters are the same as in Fig. 4.32(b). As can be seen, the horizontal hyperbola is slightly rotated and deformed. As a result, a binary mixture on the A-B-edge, instead of pure A, is the stable node at nonreactive conditions. Moreover, pure B is achievable at $Da \rightarrow \infty$, which cannot be attained in the absence of A–C-interactions at the given parameter settings (cf. Fig. 4.32(b)).

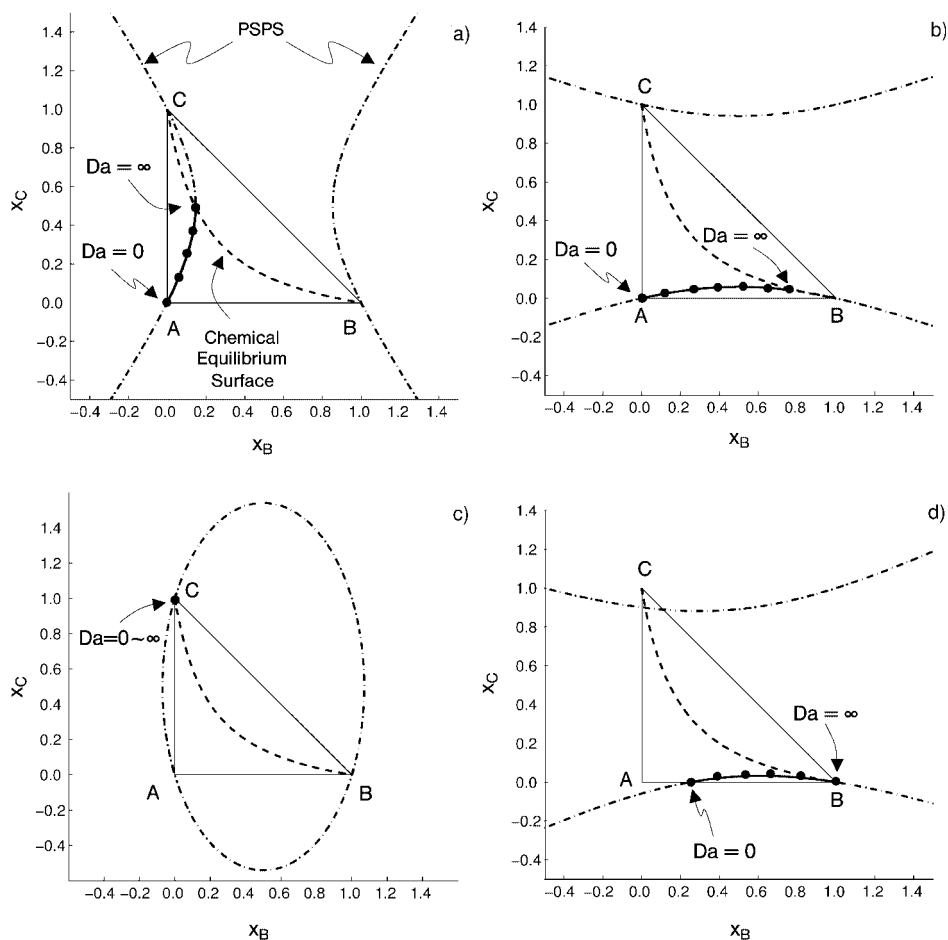


Fig. 4.32. Potential singular point surfaces and stable node bifurcation behavior for an intrinsically hyperbolic system; $B + C \leftrightarrow A$; $K_{eq} = 5$ (for parameters, see Tab. 4.3).

Table 4.3. Parameters used for the potential singular point surfaces presented in Fig. 4.32.

Fig.	Parameters		Eigenvalues of [A]		PSPS	Physical meaning
	Volatilities	[κ]	λ_1	λ_2		
32a	$\alpha_{BA} = 3.0$ $\alpha_{CA} = 2.0$	Scalar $\begin{bmatrix} 1 & 0 & 0 \\ 0 & 1 & 0 \\ 0 & 0 & 1 \end{bmatrix}$	2	-1	Vertical hyperbola	Intrinsic hyperbolic system, (membrane without any separation effect, corresponds to reactive distillation)
32b	$\alpha_{BA} = 3.0$ $\alpha_{CA} = 2.0$	Diagonal $\begin{bmatrix} 1 & 0 & 0 \\ 0 & 1 & 0 \\ 0 & 0 & 5 \end{bmatrix}$	2	-9	Horizontal hyperbola	Selective membrane which preferentially transfers C
32c	$\alpha_{BA} = 3.0$ $\alpha_{CA} = 2.0$	Diagonal $\begin{bmatrix} 1 & 0 & 0 \\ 0 & 1 & 0 \\ 0 & 0 & 0.2 \end{bmatrix}$	2	0.6	Ellipse	(incorrect) Membrane creates a stable node at the undesired byproduct C, membrane causes change to elliptic system
32d	$\alpha_{BA} = 3.0$ $\alpha_{CA} = 2.0$	Non-diagonal $\begin{bmatrix} 1 & 0 & 0.5 \\ 0 & 1 & 0 \\ 0.5 & 0 & 5 \end{bmatrix}$	2.05	-9.55	Rotated and deformed hyperbola	Interaction of A and C in selective membrane creates non-reactive binary azeotrope at A-B edge

4.4.3.3 THF-System

Figure 4.33 illustrates the PSPS and bifurcation behavior of a simple batch reactive distillation process. Qualitatively, the surface of potential singular points is shaped in the form of a hyperbola due to the boiling sequence of the involved components. Along the left-hand part of the PSPS, the stable node branch and the saddle point branch 1 coming from the water vertex, meet each other at the kinetic tangent pinch point $x = (0.0246, 0.7462)$ at the critical Damköhler number $Da = 0.414$. The right-hand part of the PSPS is the saddle point branch 2, which runs from pure THF to the binary azeotrope between THF and water.

Figure 4.34 shows the PSPS for the reactive membrane separation process with application of a Knudsen-membrane. In comparison with reactive distillation, the membrane turns the vertical hyperbola into a horizontal hyperbola. In particular, the membrane shifts the stable node branch towards the THF-vertex such that THF-rich products can be attained in the considered Knudsen-membrane reactor.

Because the boiling temperature of 1,4-BD is much higher than of the two reaction products and the reaction is irreversible, the bifurcation behavior is only affected by the mass transfer coefficient ratio $\kappa_{water}/\kappa_{THF}$, if κ_{BD} is not extremely high or low. There exists a critical value of $\kappa_{water}/\kappa_{THF} = 2.1$, above which the stable node branch approaches the THF-vertex.

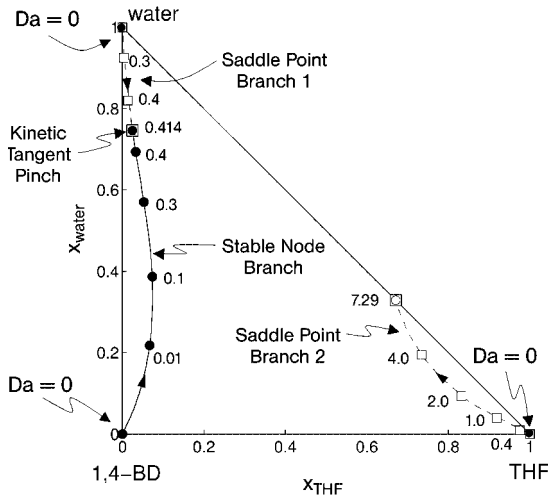


Fig. 4.33. Potential singular point surface and bifurcation behavior for reactive distillation; 1,4-BD \rightarrow THF + Water; $p = 5$ atm.

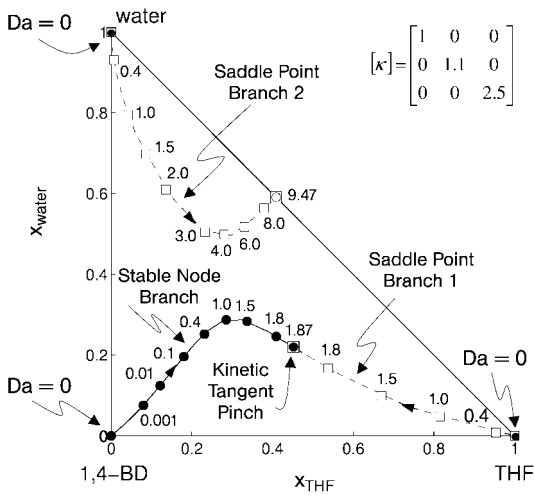


Fig. 4.34. Potential singular point surface and bifurcation behavior of reactive membrane separation using a Knudsen-membrane; 1,4-BD \rightarrow THF + Water; $p = 5$ atm.

4.4.4

Remarks on Kinetic Arheotropes

As demonstrated by means of residue curve analysis, selective mass transfer through a membrane has a significant effect on the location of the singular points of a batch reactive separation process. The singular points are shifted, and thereby the topology of the residue curve maps can change dramatically. Depending on the structure of the matrix of effective membrane mass transfer coefficients, the attainable product compositions are shifted to a desired or to an undesired direction.

A singular point of reactive membrane separation should be denoted as *kinetic arheotrope* because it is a process phenomenon rather than a thermodynamic phenomenon. The condition for arheotropy can be elegantly expressed in terms of new transformed variables, which are a generalized formulation of the transformed composition variables first introduced to analyze reactive azeotropes.

4.5

Summary and Conclusions

The determination of feasible products is very important for conceptual process design and for the evaluation of competing process variants. In this chapter, methods have been discussed to identify feasible products as singular points of residue curve maps (RCM). RCM-analysis is a tool which is well established for nonreactive and reactive distillation processes. Here, it is shown how RCM can also be used for reactive membrane separation processes.

While in the past the focus has been on phase equilibrium-controlled processes, today there is an increasing interest in predicting the effects of interfacial mass transfer resistances on the productivity and selectivity of integrated chemical processes. As has been shown in recent research investigations, mass transfer-controlled processes can be treated in a similar manner as thermodynamically controlled processes. In both categories, all possible products are located on potential singular point curves (PSPS), the location of which in the phase diagram depends on the vapor–liquid equilibria (VLE), the reaction stoichiometry, and the mass transfer kinetics of the considered process. Once the PSPS is fixed, feasible products can be found as stable intersection points of the PSPS with a kinetic curve, the location of which is governed by chemical reaction kinetics. The intensity of the chemical reaction is expressed in terms of the Damköhler number, Da . As special limiting cases, $Da = 0$ corresponds to a nonreactive operation, while $Da = \infty$ corresponds to a chemical equilibrium-controlled operation.

In order to denote singular points, a clear terminology is needed. The well-known term *a-zeo-trope* should only be used for phase equilibrium-controlled singular points, whilst the newer term, *a-rheo-trope*, is proposed for mass transfer-controlled processes. Translated, the latter term means that “*the composition is not changing with flux*”. The different types of azeotropes and arheotropes, together with the names of those investigators who were the first to deal with these singular points, are summarized in Tab. 4.4.

Table 4.4. Classification of singular points in reactive distillation and reactive membrane separation processes.

Separation Reaction	Phase equilibrium-controlled separation: Distillation	Mass transfer-controlled separation: Membrane Permeation
	$[\kappa] = \begin{bmatrix} 1 & 0 & 0 \\ 0 & 1 & 0 \\ 0 & 0 & 1 \end{bmatrix}$	$[\kappa] = \begin{bmatrix} 1 & \kappa_{AB} & \kappa_{AC} \\ \kappa_{BA} & \kappa_{BB} & \kappa_{BC} \\ \kappa_{CA} & \kappa_{CB} & \kappa_{CC} \end{bmatrix}$
No reaction: $Da = 0$	Azeotrope First introduced by Wade and Merriman [36]	Arheotrope First introduced as “Pseudo-azeotrope” by Schlünder [19]
Kinetically controlled reaction: $Da \in (0, \infty)$	Kinetic azeotrope First studied by Venimadhavan et al. [4]	Kinetic arheotrope Huang et al. [20]
Chemical equilibrium- controlled reaction: $Da \rightarrow \infty$	Reactive azeotrope First introduced by Barbosa and Doherty [15]	Reactive arheotrope Huang et al. [20]

Symbols and Abbreviations

A_i	liquid phase activity of component i
A_{ph}	interfacial area, m ²
Da, D	Damköhler number, $D = Da/(1+Da)$
F	molar flow rate, mol s ⁻¹
G	flow rate per unit interface area, m s ⁻¹
H	molar liquid hold-up in vessel, mol
H_{cat}	molar catalyst hold-up in vessel, mol(<i>cat</i>)
$IPOAc$	isopropylacetate
k_f	forward reaction rate constant, s ⁻¹
k	mass transfer coefficient, m s ⁻¹
$[k]$	matrix of binary effective mass transfer coefficients
k_{ij}	effective binary mass transfer coefficient of pair i - j , m s ⁻¹
$K_{S,i}$	sorption constant of component i at solid catalyst
K_{eq}	chemical equilibrium constant
K_i	phase equilibrium constant of component i
L, V	liquid flow rate, vapor flow rate, mol s ⁻¹
M_i	molecular weight of component i , kg mol ⁻¹
n_i	mass flux of component i , mol s ⁻¹
NC	total number of components
NR	number of chemical reactions

NT	number of stages
NTU	number of gas phase transfer units
p	total pressure, Pa
$PSPS$	potential singular point surface
r	rate of reaction, $\text{mol mol}(\text{cat})^{-1} \cdot \text{s}^{-1}$
R	reflux ratio
RA	reactive azeotrope
RCM	residue curve map
s	reboil ratio
S	effective permeation area, m^2
S_i	mass transfer selectivity of component i
u	velocity, Eq. (60)
V	volumetric flow rate, $\text{m}^3 \text{s}^{-1}$
x	vector of liquid phase mole fractions
x_i	liquid phase mole fraction of component i
X_i	transformed liquid phase mole fraction of component i
y_i	vapor phase mole fraction of component i
Y_i	transformed vapor phase mole fraction of component i
\tilde{Y}_i	sweep gas loading of component i
□	saddle point
●	stable node
○	unstable node

Greek letters

α_{ij}	relative volatility between components i and j
χ	relative flux, $\chi_i = N_i / N_T$
γ	liquid phase activity coefficient
δ	diffusivity, $\text{m}^2 \text{s}^{-1}$
ξ	dimensionless time
Θ	dimensionless reaction term
κ_{ij}	dimensionless binary mass transfer coefficient between components i and j
λ	eigenvalue of matrix $[A]$
ν_i	stoichiometric coefficient of component i
π	pole of stoichiometric lines
χ_i	relative mass flux of component i
ρ	density, kmol m^{-3}

Superscripts and subscripts

'/'	extract phase/raffinate phase
0	initial state
B, D, F	at bottom, distillate, feed of column
c, r	reactive condenser, reactive reboiler

eq	chemical equilibrium
gas, liq	gas phase, liquid phase
k	reference component
P	permeation side
Ph	interphase
Phase	active liquid phase
Ref	at reference temperature
T	total
THF	tetrahydrofuran

References

1. R. Taylor, R. Krishna, *Chem. Eng. Sci.*, **2000**, *55*, 5183–5229.
2. M. F. Malone, M. F. Doherty, *Ind. Eng. Chem. Res.*, **2000**, *39*, 3953–3957.
3. K. Sundmacher, A. Kienle, *Reactive Distillation – Status and Future Directions*. Weinheim: Wiley-VCH, 2003.
4. G. Venimadhavan, G. Buzad, M. F. Doherty, et al., *AIChE J.*, **1994**, *40*, 1814–1824.
5. E. Rev, *Ind. Eng. Chem. Res.*, **1994**, *33*, 2174–2179.
6. C. Thiel, K. Sundmacher, U. Hoffmann, *Chem. Eng. Sci.*, **1997**, *52*, 993–1005.
7. G. Venimadhavan, M. F. Doherty, M. F. Malone, *AIChE J.*, **1999**, *45*, 546–556.
8. W. Song, G. Venimadhavan, J. M. Manning, et al., *Ind. Eng. Chem. Res.*, **1998**, *37*, 1917.
9. W. Song, R. S. Huss, M. F. Doherty, et al., *Nature*, **1997**, *388*, 561–563.
10. Z. Qi, A. Kolah, K. Sundmacher, *Chem. Eng. Sci.*, **2002**, *57*, 163–168.
11. Z. Qi, K. Sundmacher, *Comp. & Chem. Eng.*, **2002**, *26*, 1459–1471.
12. F. Steyer, Z. Qi, K. Sundmacher, *Chem. Eng. Sci.*, **2002**, *57*, 1511–1520.
13. N. Chadda, M. F. Malone, M. F. Doherty, *AIChE J.*, **2001**, *47*, 590–601.
14. Z. Qi, D. Flockerzi, K. Sundmacher, *AIChE J.*, **2004**, *50*, 2866–2876.
15. D. Barbosa, M. F. Doherty, *Proc. Royal Soc. London*, **1987**, *A413*, 459–464.
16. D. Barbosa, M. F. Doherty, *Chem. Eng. Sci.*, **1988**, *43*, 529–540.
17. S. Ung, M. F. Doherty, *Chem. Eng. Sci.*, **1995**, *50*, 23–48.
18. S. Ung, M. F. Doherty, *AIChE J.*, **1995**, *41*, 2382–2392.
19. E. U. Schlünder, *Verfahrenstechnik*, **1977**, *11*, 682–686.
20. Y. S. Huang, K. Sundmacher, Z. Qi, et al., *Chem. Eng. Sci.*, **2004**, *59*, 2863–2879.
21. Z. Qi, K. Sundmacher, *Sep. & Purif. Tech.*, **2004**, *34*, 201–211.
22. Nisoli, M. F. Malone, M. F. Doherty, *AIChE J.*, **1997**, *43*, 374–387.
23. E. U. Schlünder, *Chem. Ing. Tech.*, **1978**, *50*, 749–754.
24. E. U. Schlünder, *Int. Chem. Engng.*, **1979**, *19*, 373–379.
25. E. U. Schlünder, *Proc. 3rd Int. Drying Symp.* 1982, *2*, 315–325 and 325–336.
26. E. U. Schlünder, *Chem. Ing. Tech.*, **1983**, *55*, 301–303.
27. D. Fullarton, E. U. Schlünder, *Chem. Ing. Tech.*, **1986**, *58*, 398–400.
28. D. Fullarton, E. U. Schlünder, *Chem. Eng. Process.*, **1986**, *20*, 255–263.
29. D. Fullarton, E. U. Schlünder, *Chem. Eng. Process.*, **1986**, *20*, 265–270.
30. T. Frey, J. Stichlmair, *Chem. Ing. Tech.*, **1998**, *70*, 1373–1380.
31. J. Schwarzbach, M. Nilles, E. U. Schlünder, *Chem. Eng. Process.*, **1987**, *22*, 163–175.
32. Th. Riede, E. U. Schlünder, *Chem. Eng. Process.*, **1990**, *27*, 83–93.
33. R. Krishna, J. A. Wesselingh, *Chem. Eng. Sci.*, **1997**, *52*, 861–911.

34. U. Limbeck, C. Altwicker, U. Kunz, et al., *Chem. Eng. Sci.*, **2001**, 56, 2171–2178.
35. J. Gmehling, U. Onken, Vapour-Liquid Equilibrium Data Collection, Chemistry Data Series. *Frankfurt am Main, DECHEMA*. 1977, Part 1, 2, 5.
36. J. Wade, R. W. Merriman, *J. Chem. Soc. Trans.*, **1911**, 99, 997–1011.
37. A. Seidel-Morgenstern, Analysis and Experimental Investigation of Catalytic Membrane Reactors, in: K. Sundmacher, A. Kienle, A. Seidel-Morgenstern: *Integrated Chemical Processes*, Weinheim: Wiley-VCH, 2005, Chapter 12.

5

Equilibrium Theory and Nonlinear Waves for Reaction Separation Processes

Achim Kienle and Stefan Grüner

5.1

Introduction

In this chapter, unifying concepts for analyzing and understanding the dynamics of integrated reaction separation processes with rapid chemical reactions are introduced. The text is based on some recent studies [11–13], and extends the concepts introduced earlier for reactive distillation processes [23] to other integrated reaction separation processes. The class of processes to be considered is rather broad. It includes reaction processes where simultaneous separation is used to enhance a reaction, for example, by shifting inherent equilibrium limitations. Various process examples of this kind are provided in this book. The chapter also includes separation processes with potentially reactive mixtures. In this case, a chemical reaction can be either an unwanted side effect or it can be used directly to achieve a certain separation, which is not possible under nonreactive conditions (see e.g. Ref. [10]). The latter represents a reaction-enhanced separation.

In all cases the dynamics is governed by propagating concentration fronts and pulses, so-called nonlinear waves. It has been shown that equilibrium theory [33, 34] provides a general framework for predicting the various wave patterns of reaction separation processes. Nonreactive separation processes are also included as a limiting case. The procedures are based on simple graphical methods and thereby provide an easy understanding of the process dynamics. This knowledge can be used for improving process operation and process control in various ways.

The outline of this chapter is as follows: First, some basic wave phenomena for separation, as well as integrated reaction separation processes, are illustrated. Afterwards, a simple mathematical model is introduced, which applies to a large class of separation as well as integrated reaction separation processes. In the limit of reaction equilibrium the model represents a system of quasilinear first-order partial differential equations. For the prediction of wave solutions of such systems an almost complete theory exists [33, 34, 38], which is summarized in a second step. Subsequently, application of this theory to different integrated reaction separation processes is illustrated. The emphasis is placed on reactive distillation and reactive chromatography, but applications to other reaction separation processes are also

briefly discussed. It is shown that different processes share many common features on the conceptual level. Finally, the usefulness of theoretical insights for improved process operation and improved process control is demonstrated. In particular, a new advanced operational strategy for simulated moving-bed chromatographic processes is discussed, and some advanced strategies for model-based measurement and model-based control. The latter are based on low-order dynamic models which can be obtained directly from the wave analysis.

5.2

Theoretical Background

5.2.1

Wave Phenomena

The dynamic behavior of many separation, as well as integrated reaction separation processes, is governed by traveling concentration fronts and pulses. To illustrate the basic phenomena let us first focus on a simple nonreactive fixed-bed chromatographic process as illustrated in Fig. 5.1. The process is isothermal – that is, the temperature is constant along the column; heat effects are neglected. The adsorption follows the competitive Langmuir isotherm. For such a system the transient profiles during the loading of an initially clean bed as illustrated in Fig. 5.1(a) consists of N_s constant pattern waves, which travel with constant velocity and shape in the direction of the fluid flow towards the outlet of the column. Therein, N_s is the number of solutes which adsorb on the solid phase. In the present case the mixture contains two solutes. Corresponding concentration fronts of different components will travel jointly, such as front s_1 in Fig. 5.1(a). Further, it can be shown that different concentration fronts will – except in singular cases – always travel with different propagation velocities, such as fronts s_1 and s_2 in Fig. 5.1(a). In particular, the velocities of different wave fronts will increase in the direction of the fluid flow (i.e., $w(s_2) > w(s_1)$), so that the fronts will not overtake each other.

A different type of behavior is observed during the regeneration of a totally loaded bed with pure solvent, as illustrated in Fig. 5.1(b). This asymmetry in the dynamics is due to the nonlinearity of the system and will not arise in linear systems. During regeneration the wave pattern consists of N_s dispersive waves, which spread as they travel downstream in the direction of the fluid flow. The spreading is due to the fact that each concentration within a certain wave front travels with different velocity. In particular, the traveling velocity is monotonically increasing with increasing concentration. This is in contrast to the previous case, where all concentration values within a certain front travel with the same velocity. Nevertheless, as in the previous case, different waves will always have different velocities, which will increase in the direction of the fluid flow – that is, the foremost concentration of front r_1 can not overtake the last concentration of front r_2 . In contrast to this, corresponding concentrations of different components at any given value of z will travel with the same velocity.

The third scenario in Fig. 5.1(c) shows the evolution of a feed pulse in a totally regenerated bed. This can be viewed as a combination of a stepwise increase and a

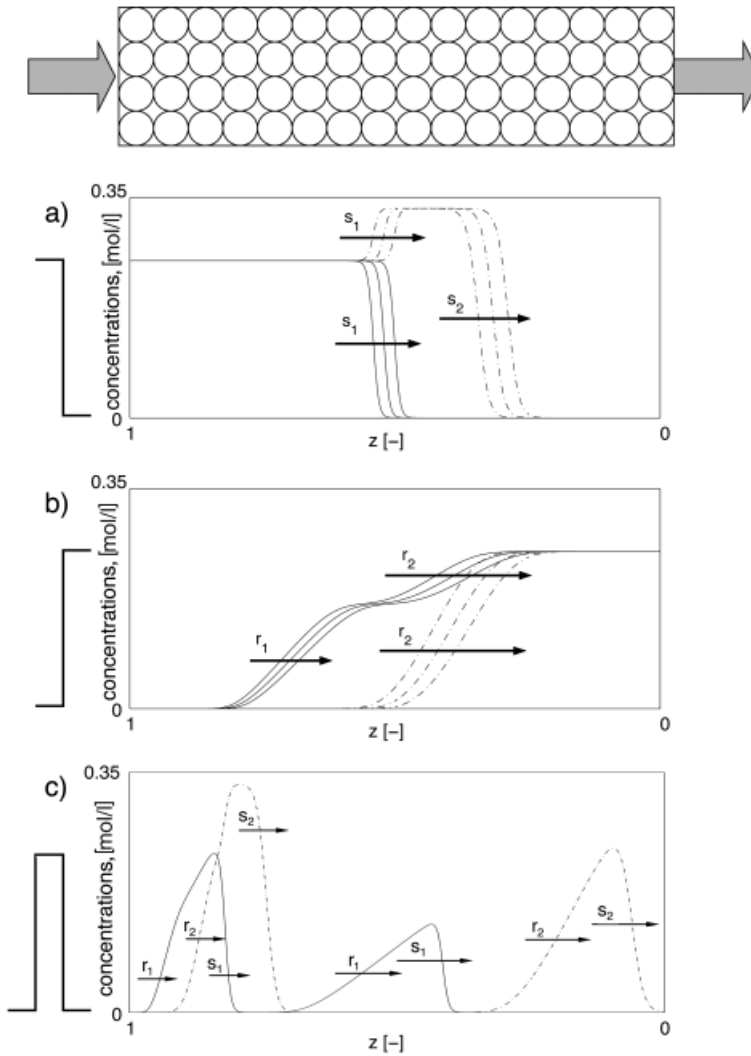


Fig. 5.1. Dynamic behavior in two-solute chromatography (a) Loading of an initially unloaded bed, (b) purging of an initially loaded bed with pure solvent; (c) column response to a feed pulse. The solid lines represent the solute with the higher affinity to the solid phase.

stepwise decrease of the feed concentration and therefore represents the combination of the two scenarios illustrated in Fig. 5.1(a) and (b). Consequently, the pulse will be resolved into two constant pattern waves s_1 , s_2 in the front, and two spreading waves r_1 , r_2 in the rear. According to the general rules of elementary wave interactions [34], the fast spreading wave r_2 will overtake the slow constant pattern wave s_1 , and two separate pulses of the two components are formed. The pulse of the component with

the higher affinity to the solid phase is always behind. For a detailed discussion of the wave dynamics of nonreactive chromatographic processes the reader is referred to Refs. [16, 33, 34].

The same principles apply to moving-bed chromatographic processes [34]. Important differences between fixed-bed and moving-bed chromatographic processes are the following:

- In fixed-bed chromatographic processes only a trivial steady state is possible, i.e. the bed is totally loaded or is totally regenerated. Hence, fixed-bed chromatographic processes are usually operated dynamically. In contrast to this, in moving-bed chromatographic processes nontrivial steady states are possible, which is therefore the preferred mode of operation.
- In fixed-bed chromatographic processes waves can only travel in the direction of the fluid flow, whereas in moving-bed chromatographic processes they may travel either in the direction of the fluid phase or in the direction of the solid phase.

This can be rationalized in the following way. In a moving-bed chromatographic process the solid phase moves in the opposite direction to the fluid phase. Hence, the wave velocity in a moving-bed process is the difference between the wave velocity in a corresponding fixed-bed process and the velocity of the solid flow. Depending on the velocity of the solid flow and the wave velocities, the fronts will either move in the direction of the solid phase or in the direction of the fluid phase toward the inlet of the solid or the fluid phase where they are stopped by the repelling influence of the system boundaries and a steady state is established. If the absolute values of the wave and the solid velocity are equal, a balanced wave is obtained. Because the wave velocities of different wave fronts are different at steady state, at most one concentration front can stand at the middle of the column section whereas the others are at the system boundaries, where they can overlap.

The same principles apply to distillation processes as illustrated in in Fig. 5.2, and to other countercurrent separation processes [18, 20, 30, 40].

In continuous distillation, as in moving-bed chromatography, steady state is the preferred mode of operation. The steady-state concentration profiles consist of $N_c - 1$ concentration fronts in each column section, where N_c is the number of components. At steady state, at most one of these concentration fronts is balanced in the middle of each column section. The other fronts are located at the system boundaries where they can overlap. After some disturbance, depending on its magnitude and sign, some of the fronts will start moving until they are stopped by the repelling influence of the system boundaries and a new steady state is established. This is illustrated in Fig. 5.2 for a pure rectifying column, which serves for the separation of the light boiling component methanol from a mixture of methanol, ethanol, and 1-propanol. For moderately nonideal mixtures all wave fronts in a distillation column will be of the constant pattern wave type, as illustrated in Fig. 5.2. For highly nonideal mixtures additional wave fronts and/or combined wave fronts are possible [20]. The latter consist of spreading parts and constant pattern parts. In contrast to the chromatographic processes considered above the temperature along a distillation column is no longer constant, even if heat effects are negligible. Because the temp-

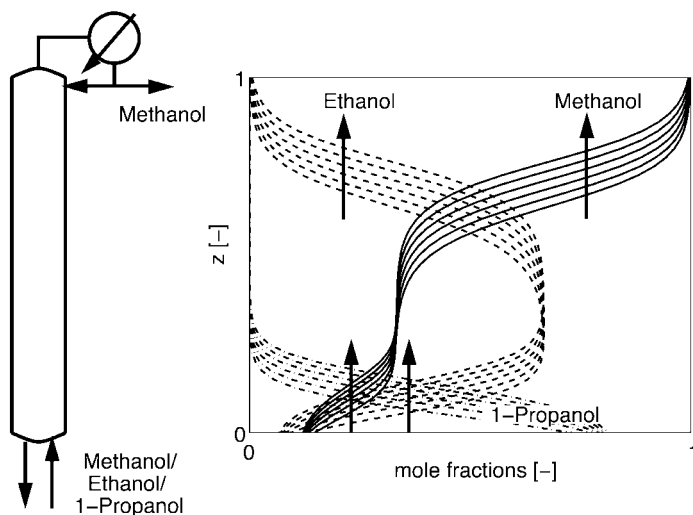


Fig. 5.2. Dynamic transient behavior of a rectifying column for the separation of methanol from a mixture of methanol, ethanol, and 1-propanol after a stepwise increase in reflux at the top of the column.

erature in a distillation is essentially the boiling point temperature of the mixture, it will also change with concentration. Hence, wave propagation of concentration fronts is also reflected in the propagation of corresponding temperature fronts. Since online temperature measurement is usually much cheaper, quicker and reliable than online concentration measurement, it provides a good way of monitoring and controlling the front dynamics in distillation columns. A detailed analysis of traveling wave fronts in distillation was given in Refs. [17, 20, 21, 29, 30].

Similar patterns of behavior can be observed in reactive distillation columns or other integrated reaction separation processes with fast reversible reactions [11, 23] as illustrated in Fig. 5.3 for a pure rectifying column with a ternary mixture and a reaction of type $2B \rightleftharpoons A + C$ taking place in the liquid phase. However, due to the reaction equilibrium the profiles consist of a single concentration front, which is clearly different from the nonreactive problem illustrated in Fig. 5.2.

In the remainder of the chapter, wave dynamics in integrated reaction separation processes will be studied in more detail. The analysis is based on a simple mathematical model, which will be discussed in the following section.

5.2.2

Mathematical Model

The following is based on a simple model system, as illustrated in Fig. 5.4. The system consists of two homogeneous phases which exchange mass across a phase boundary and have convective transport in countercurrent direction. In addition,

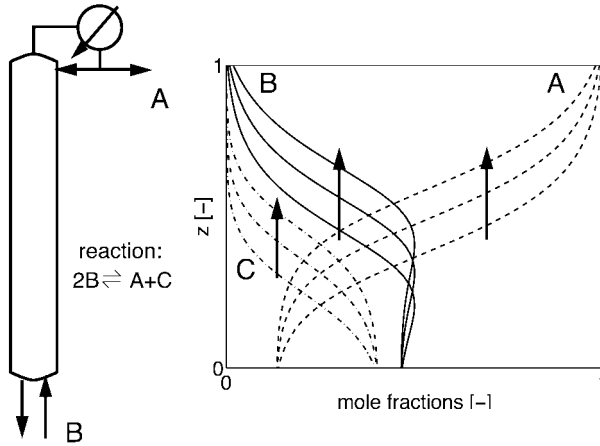


Fig. 5.3. Dynamic transient behavior of a rectifying column with a fast chemical reaction of type $2B \rightleftharpoons A + C$ after a decrease in reflux at the top.

chemical reactions may take place. This system represents an elementary building block of almost any integrated reaction separation process. Fixed-bed processes are also included for vanishing convective velocity of the corresponding phase. In the remainder, emphasis is placed especially on distillation and chromatographic processes with chemical reaction. In distillation, phase (') corresponds to the liquid, and phase (") to the vapor phase. For chromatographic processes, phase (') is the fluid and phase (") the solid phase.

Assuming

- negligible energy effects;
- negligible axial dispersion;
- constant hold-ups and flow rates, and
- constant pressure,

the model equations follow from the material balances. If for example chemical reactions take place in phase (') the model equations have the following form:

$$\begin{aligned}
 \frac{\partial \mathbf{x}}{\partial t} - \frac{\partial \mathbf{x}}{\partial z} &= -\mathbf{j}(\mathbf{x}, \mathbf{y}) + \underbrace{\mathbf{v}\mathbf{r}(\mathbf{x})}_{\text{reaction}}, & \mathbf{x}(z=1) &= \mathbf{x}_{in}, \\
 \underbrace{\alpha \frac{\partial \mathbf{y}}{\partial t}}_{\text{accumulation}} + \underbrace{\beta \frac{\partial \mathbf{y}}{\partial z}}_{\text{convection}} &= \underbrace{\mathbf{j}(\mathbf{x}, \mathbf{y})}_{\text{transfer}}, & \mathbf{y}(z=0) &= \mathbf{y}_{in},
 \end{aligned} \tag{1}$$

$$\mathbf{x}, \mathbf{y}, \mathbf{j} \in \mathbb{R}^N, \quad \mathbf{r} \in \mathbb{R}^{N_r}.$$

An analogous treatment is possible if chemical reactions take place in phase ("), or even in both phases by adding suitable reaction terms in the corresponding model equations.

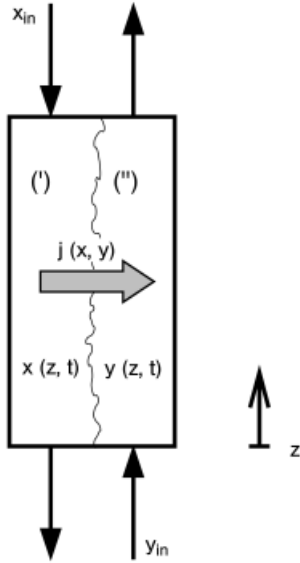


Fig. 5.4. A single section of an integrated reaction separation process.

In this formulation, N is the number of independent components, N_r the number of independent reactions, z and t are dimensionless space and time according to

$$z = \frac{\bar{z}}{l}, \quad t = \frac{\bar{t}v'}{l}. \quad (2)$$

x and y are some suitable concentration measures. In (reactive) distillation, for example, mole fractions are used. Then j and r are dimensionless transfer and reaction rates, α is the ratio of the molar hold-ups in both phases and β is the ratio of the molar flow rates in both phases. Due to the summation condition for mole fractions only $N_c - 1$ components are independent, i.e., $N = N_c - 1$.

In contrast to this, in (reactive) chromatography usually mass or molar concentrations are used. Then, j and r are the corresponding rates of change of these quantities, and α and β are the ratios of the volumetric hold-ups and the volumetric flow rates in both phases. N is equal to N_s , the number of solutes. For the details, we refer to Ref. [11].

Assuming thermodynamic equilibrium between phase (') and ('), the two-phase model in Eq. (1) can be further simplified. The resulting pseudohomogeneous model is obtained from the sum of the balances of both phases according to

$$\frac{\partial}{\partial t} (\alpha y(x) + x) + \frac{\partial}{\partial z} (\beta y(x) - x) = v r(x). \quad (3)$$

Therein, $y(x)$ represents the equilibrium relation for the composition of phase ($''$), which is in general a function of the composition of phase ($'$).

In the nonreactive case, r is equal to zero and Eq. (3) reduces to a homogeneous system of first-order quasilinear partial differential equations

$$\frac{\partial}{\partial t}(\alpha y(x) + x) + \frac{\partial}{\partial z}(\beta y(x) - x) = 0. \quad (4)$$

For this type of equation an almost complete mathematical theory exists which is based on the method of characteristics [33, 34, 38]. This theory has been applied to distillation processes [17, 20, 29] and to chromatographic processes [33, 34] among others. An alternative approach based on physical insight has also been proposed [16]. The main results will be summarized in the next section.

In the reactive case, r is not equal to zero. Then, Eq. (3) represents a nonhomogeneous system of first-order quasilinear partial differential equations and the theory is becoming more involved. However, the chemical reactions are often rather fast, so that chemical equilibrium in addition to phase equilibrium can be assumed. The chemical equilibrium conditions represent N_r algebraic constraints which reduce the dynamic degrees of freedom of the system in Eq. (3) to $N - N_r$. In the limit of reaction equilibrium the kinetic rate expressions for the reaction rates become indeterminate and must be eliminated from the balance equations (Eq. (3)). Since the model Eqs. (3) are linear in the reaction rates, this is always possible. Following the ideas in Ref. [41], this is achieved by choosing the first N_r equations of Eq. (3) as reference. The reference equations are solved for the unknown reaction rates and afterwards substituted into the remaining $N - N_r$ equations.

The procedure leads to the following reduced set of equations

$$\frac{\partial}{\partial t}(\alpha Y + X) + \frac{\partial}{\partial z}(\beta Y - X) = 0 \quad (5)$$

with transformed concentration variables according to

$$X = x^{II} - v^{II} (v^I)^{-1} x^I, \quad Y = y^{II} - v^{II} (v^I)^{-1} y^I, \quad (6)$$

$$X, Y, x^{II}, y^{II} \in R^{N-N_r}, \quad x^I, y^I \in R^{N_r}.$$

Therein, x^I, y^I represent the concentrations corresponding to the N_r reference equations and x^{II}, y^{II} the concentrations corresponding to the remaining $N - N_r$ equations. Accordingly, the matrix of stoichiometric coefficients is split into two parts v^I, v^{II} . For the details, the reader is referred to Ref. [13].

Transformed concentration variables were first introduced by Doherty and co-workers [2, 41] for the steady-state design of reactive distillation processes. In the

more general framework considered here, it is readily seen that they also apply to the corresponding dynamic problem and to other integrated reaction separation processes such as chromatographic reactors

From this, the following important conclusions can be drawn:

- Using the transformed variables the reactive problem (Eq. (5)) is completely equivalent to a nonreactive problem (Eq. (4)) of reduced dimension. Hence, in the limit of chemical equilibrium the dynamic behavior of reaction separation processes is equivalent to the dynamic behavior of nonreactive processes.
- All methods available for the nonreactive problem (Eq. (4)) can also be applied to the reactive problem in transformed concentration variables (Eq. (5)).
- On the conceptual level considered here, different processes have similar properties. Methods developed for a specific class of integrated reaction separation processes can also be applied to other processes within the framework outlined above.

Finally, it should be noted that the above treatment is only valid for *constant flow rates*. For processes without solvent (e.g., reactive distillation processes), this assumption is only valid for equimolar reactions. For equimolar reactions the definition of transformed concentration variables introduced by Ung and Doherty [41] reduces to the definition in Eq. (6). For processes with solvent, (e.g., reactive chromatographic processes), the assumption of constant flow rates is also valid in good approximation, if the concentration of the solvent is high compared to the other reacting species. This is also true if one of the reactants is used simultaneously as a solvent, as in many applications of reactive chromatography (see e.g. Refs. [1, 28]).

In contrast to the steady-state case treated by Ung and Doherty [41], additional dynamic phenomena may arise for *variable flow rates*, as will be discussed in the conclusion section.

5.2.3

Prediction of Wave Patterns

The wave and pulse patterns of nonreactive separation processes, as well as the integrated reaction separation processes illustrated above, can be easily predicted with some simple graphical procedures derived from Eqs. (4) and (5). The behavior crucially depends on the equilibrium function $y(x)$ in the nonreactive case, and on the transformed equilibrium function $Y(X)$ in the reactive case. In addition to phase equilibrium, the latter also includes chemical equilibrium. An explicit calculation of the transformed equilibrium function and its derivatives is only possible in special cases. However, in Ref. [13] a numerical calculation procedure is given, which applies to any number of components, any number of reactions, and any type of phase and reaction equilibrium.

In the scalar case (i.e., $N = 1$), wave solutions are easily constructed with the equilibrium diagram $y(x)$ or $Y(X)$. According to the above considerations, typical scalar problems are: a binary nonreactive distillation process, a ternary reactive distillation process with a single chemical reaction, a reactive distillation process with N_c components and $N_c - 2$ chemical reactions, or a chromatographic reactor with N_s solutes

and $N_s - 1$ chemical reactions. In nonreactive distillation, the equilibrium diagram $y(x)$ represents the well-known McCabe Thiele diagram, whilst in nonreactive chromatography, $y(x)$ represents the image of the adsorption isotherm. In the reactive case, similar diagrams can be drawn for the transformed equilibrium function $Y(X)$. Examples are provided in the next section.

In this diagram, constant boundary conditions are represented by two points. In Fig. 5.5., the boundary conditions are indicated by bullets. They must lie on the equilibrium line, since simultaneous phase and reaction equilibrium is assumed. Any wave solution is represented by a time invariant line connecting both boundary points. The image of a constant pattern wave is a straight line, whereas the image of a spreading wave is represented by the corresponding line segment of the equilibrium line. (It should be noted that constant pattern wave solutions of the continuously distributed equilibrium models in Eqs. (4) and (5) are discontinuities or so-called “shock waves”. Any mass transfer resistance, axial dispersion or discretization of the underlying PDEs will result in constant pattern waves with finite slope.) The wave type is easily determined with the following right-hand-rule. (If y , x are mole or mass fractions required then they are the mole or mass fraction of the component with the higher affinity to phase (“).) The wave is a constant pattern wave if the equilibrium curve lies on the right as we proceed along the straight line connecting the two boundary points in the direction of phase (“) (see Fig. 5.5(a)). Since in nonreactive distillation the concentration of the light-boiling component always decreases in the direction of the liquid phase, all waves are constant pattern waves for moderately nonideal mixtures, with an equilibrium diagram as in Fig. 5.5(a). Otherwise, they are spreading waves as illustrated in Fig. 5.5(b). Examples of spreading waves are desorption fronts in chromatographic processes, as illustrated above. For a constant pattern wave, each concentration moves with the same velocity, which depends only on the quotient of the concentration differences across the wave according to

$$w = \frac{\beta\Lambda - 1}{\alpha\Lambda + 1}, \quad \text{with} \quad \Lambda = \frac{\Delta y}{\Delta x}. \quad (7)$$

For a spreading wave, each concentration moves with a different velocity, which now depends on the slope of the equilibrium curve:

$$w(x) = \frac{\beta\lambda - 1}{\alpha\lambda + 1}, \quad \text{with} \quad \lambda = \frac{dy}{dx}(x). \quad (8)$$

For nonconvex equilibrium functions, combined wave solutions are possible which consist in parts of spreading waves and in others of constant pattern waves. In the equilibrium diagram combined wave solutions represent the convex hull of the equilibrium line, as illustrated in Fig. 5.5(c).

For fixed-bed processes, the boundary conditions are given by the feed concentration and the initial loading of the bed. For countercurrent processes with two

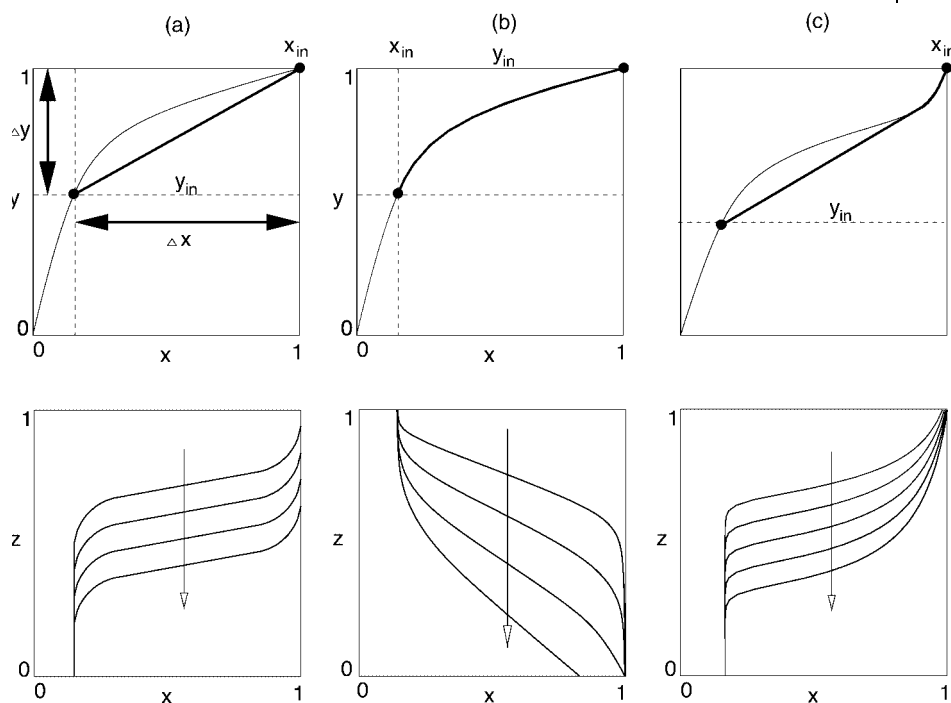


Fig. 5.5. Construction of wave solutions in the scalar case.
(a) Constant pattern wave; (b) spreading wave; (c) combined wave solution.

independent feeds, the boundary conditions are given by the respective feed concentrations. In distillation, the boundary conditions are not independent. In a rectifying column a condenser at the top relates the input concentration of the liquid with the output concentration of the vapor. In a stripping column, a reboiler, relates the input concentration of the vapor with the output concentration of the liquid. Limiting concentrations at the top of a rectifying column are given by the unstable node of the corresponding distillation region – that is, the lightest boiling component or the lightest boiling azeotrope. At the bottom of a stripping column limiting concentrations are given by the stable node of the corresponding distillation region – that is, the heaviest boiling component or the heaviest boiling azeotrope.

In the multidimensional case (i.e. $N > 1$), wave solutions are constructed in the phase space of the concentrations x_i , also called the hodograph space. For simplicity, the procedure will be demonstrated for a two-dimensional problem (i.e. $N = 2$). However, the same concepts apply to higher dimensional problems [16, 34, 38].

Let us first focus on a nonreactive system with constant separation factors. Typical examples are distillation processes with constant relative volatilities or adsorption processes described by competitive Langmuir isotherms. For nonreactive systems with constant separation factors, the constant pattern waves and spreading waves are

straight lines in the hodograph space, as illustrated in Fig. 5.6. They do not depend on the operating conditions. They are given by the right eigenvectors of the Jacobian matrix of the equilibrium function $\frac{\partial y}{\partial x}$.

Constant boundary conditions represent points in this hodograph space. Any wave solution can be constructed from the path grid of the eigenvectors by connecting the boundary points by a suitable sequence of wave solution (i.e., line segments in Fig. 5.6). If we follow the direction of phase (') – that is, the direction of the liquid phase in a distillation column or the direction of the fluid phase in a chromatographic column the wave velocity must increase from wave to wave. The procedure is illustrated in Fig. 5.6 for the scenarios illustrated previously in Fig. 5.1. The paths of the slow waves belonging to the smaller eigenvalues are indicated by the dotted lines. The boundary condition at the inlet of the fluid phase during the loading in Fig. 5.1(a) is indicated by the abbreviation BC, and the initial condition of the bed by IC. Boundary and initial conditions are exchanged for the regeneration of the totally loaded bed that was illustrated in Fig. 5.1(b). The pulse injection illustrated in Fig. 5.1(c) represents a loading step followed by a regeneration step, as outlined above. The image of this cycle in the hodograph space is represented by the closed loop between BC and IC. As the pulse pattern evolves, it is resolved into two separate pulses of the two solutes lying on the straight lines adjacent to the initial condition IC in Fig. 5.6.

Additional complexity will arise for nonreactive systems with more complicated sorption isotherms or systems with integrated chemical reactions. For these types of mixtures, spreading waves and shock waves are usually curved lines in the hodograph space and therefore will not coincide. Spreading waves follow from the eigenvectors of the phase equilibrium and do not depend on the operating conditions. In contrast to this, shock waves follow from the global material balances across the shock and will therefore depend on the operating conditions. However, as proposed in Ref. [16] the shock curves can be approximated by the eigenvectors to gain at least a qualitative picture. The reason for this is that the shock wave curves and the eigenvectors are always tangential at the starting point.

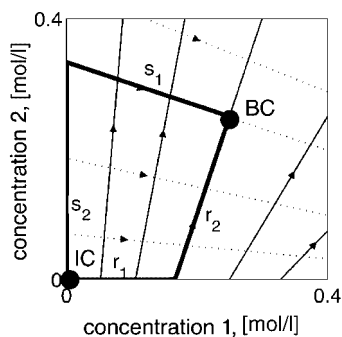


Fig. 5.6. Construction of wave solutions in the hodograph space corresponding to the scenario in Fig. 5.1.

New phenomena compared to nonreactive Langmuir systems are the same as in the binary case – that is, the existence of combined waves due to the occurrence of inflection points of the equilibrium functions $y(x)$ or $Y(X)$ and limitations on feasible product composition due to adsorptivity reversal similar to azeotropic distillation. Nonreactive examples for the latter were treated in Refs. [6 – 8], reactive examples will be discussed in the next section.

5.3

Analysis of Reaction Separation Processes

In this section the methods developed in the previous section will be applied to analyze the dynamic behavior of integrated reaction separation processes. Emphasis is placed on reactive distillation and reactive chromatography. Finally, possible applications to other integrated reaction separation processes including membrane reactors and sorption-enhanced reaction processes will be briefly discussed. More details about reactive distillation processes were provided in Ref. [39]. For chromatographic reactors the reader should refer to Chapter 6 of this book, for sorption-enhanced reaction processes to Chapter 7, and for membrane reactors to Chapter 12.

5.3.1

Reactive Distillation

Let us first consider a reaction of type



taking place in the liquid phase of a fully reactive distillation column. In the remainder component A has index 1', component B has index 2' and component C has index 3'. Then chemical equilibrium of the reaction in Eq. (9) is given by

$$K = \frac{x_2 x_3}{x_1^2}. \quad (10)$$

Further, an ideal vapor liquid equilibrium is assumed with constant relative volatilities according to

$$y_i = \frac{\alpha_i x_i}{1 + \sum_{k=1}^{N_C-1} (\alpha_k - 1) x_k}, \quad i = 1, \dots, N_C - 1. \quad (11)$$

According to the previous section, the dynamic degrees of freedom of the system in chemical equilibrium is equal to one corresponding to a binary nonreactive system.

If reactant A is taken as the reference component, the following definition of the transformed concentration variables apply

$$X = x_2 + \frac{x_1}{2}, \quad Y = y_2 + \frac{y_1}{2}. \quad (12)$$

Hence, pure product C has a value of zero and pure product B a value of one of the transformed concentration variable. The equilibrium composition of pure reactant A has a value of 0.5.

The transformed equilibrium function $Y(X)$ which is required for the construction of wave solutions is obtained by elimination of the original concentration variables x_i , y_i from Eqs. (10) – (12). The properties of the transformed equilibrium function of this system have been discussed in detail [4, 5, 11], and a short summary will be given. In the remainder of this section $Y(X)$ is illustrated in Fig. 5.7 for three different cases. In Fig. 5.7(a), component A is the intermediate-boiling component, in Fig. 5.7(b) it is the heavy-boiling component, and in Fig. 5.7(c) it is the light-boiling component. The first case corresponds to a zeotropic binary nonreactive system, the second to a binary nonreactive system with an azeotrope with temperature minimum, and the third to a binary nonreactive system with an azeotrope with temperature maximum. Since an ideal vapor liquid equilibrium was assumed, the azeotropic points in Figs. 5.7(b) and (c) are so-called “reactive azeotropes”, where reaction and distillation compensate each other [3]. As in a nonreactive column, these azeotropes cannot be crossed at steady state in a fully reactive column. It is worth noting that the qualitative features do not depend on the specific values of the equilibrium constant K and the relative volatilities α_i [4, 5].

The corresponding wave patterns of the transformed concentration variable X for a reactive distillation column are shown in Fig. 5.8. Here, a single feed with pure reactant A is introduced in the middle of the column. As in the nonreactive binary case, the composition profiles consist of a single front in each column section,

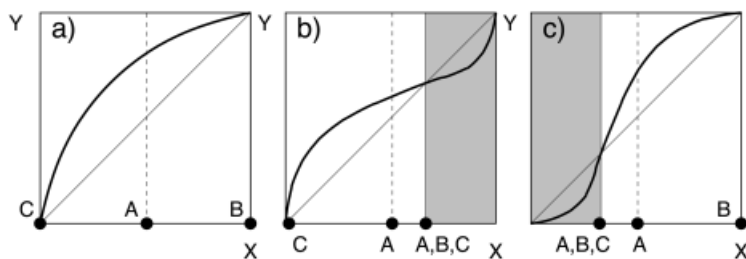


Fig. 5.7. Transformed equilibrium function of a reactive distillation process with a reaction of type $2A \rightleftharpoons B + C$ and a mixture with constant relative volatilities (schematic)
(a) Reactant A has intermediate volatility, (b) reactant A has highest volatility, (c) reactant A has lowest volatility.

which moves up or down depending on the internal flow rate ratio of the corresponding column section. If reactant *A* has intermediate volatility (see Fig. 5.8(a)), the concentration profiles will tend to pure *C* at the bottom and pure *B* at the top. If reactant *A* has the highest volatility (see Fig. 5.8(b)), only pure *C* can be obtained at the bottom and always a mixture of all three components at the top, no matter how long the column. The reverse situation is observed if reactant *A* has the lowest volatility (see Fig. 5.8(c)). Then, only pure *B* can be obtained at the top of the column, whereas a mixture of all three components is always obtained at the bottom of the column, irrespective of column length. Total conversion is only possible in the first case, where reactant *A* has intermediate volatility and is therefore trapped in the middle of the column.

The profiles of the mole fractions x_i are easily calculated from the transformed concentration variable by solving Eqs. (10) and (12) for given *X*. Some characteristic profiles of the mole fractions corresponding to the rectifying section in Fig. 5.8(a) were shown in Fig. 5.3. For the other cases, the reader is referred to Ref. [11]

In summary, we find that the transformed equilibrium function provides useful insight not only into the steady-state behavior but also in to the transient behavior. This was illustrated here with a very simple example. However, an application to more complicated examples is straightforward, as shown in Ref. [13].

5.3.2

Chromatographic Reactors

In this section, applications to chromatographic reactors will be discussed. As in the previous section, the initial focus is on a reaction of type $2A \rightleftharpoons B + C$ taking place in

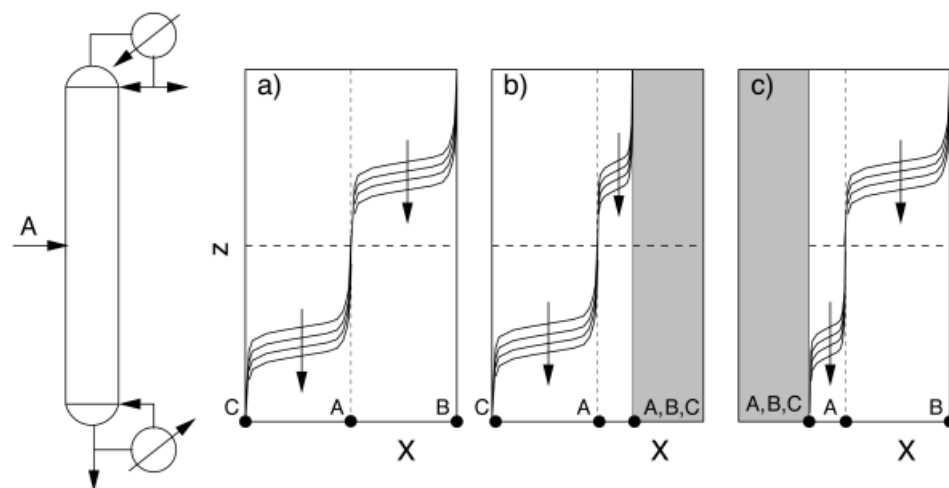


Fig. 5.8. Front patterns in a reactive distillation column corresponding to Fig. 5.7 (schematic) (a) Reactant *A* has intermediate volatility, (b) reactant *A* has highest volatility, (c) reactant *A* has lowest volatility.

the liquid or solid phase of the chromatographic reactor. It is shown that, in both cases, similar patterns of behavior can be observed as in reactive distillation. In particular, it is shown that total conversion is limited by reactive azeotropy if the reactant has highest or lowest affinity to the solid phase, no matter how long the column is. The results do not depend on the feed concentration. Total conversion is only possible if the reactant has intermediate affinity to the solid phase.

Following this, a reaction of type $A \rightleftharpoons B + C$ is considered. Many esterification and ester hydrolysis reaction, can be brought to this form. The analysis reveals that, for the latter reaction, total conversion is always possible provided that the feed concentration is sufficiently low. In contrast to this, limitations will arise for high feed concentrations similar to the previous case – that is, if the reactant has highest or lowest affinity to the solid phase. It is worth noting that these results are consistent with experimental observations [28].

Finally, a multireaction system will also be considered. The example is related to the separation of binaphthol enantiomers, and was reported by Morbidelli, Mazzotti and co-workers in some detail [1]. Separation of the enantiomers is even possible with an achiral stationary phase due to dimerization reactions taking place in the fluid phase.

5.3.2.1 Reactions of Type $2A \rightleftharpoons B + C$

In analogy to the previous section, let us first consider a reaction of type



taking place in the fluid phase of a chromatographic reactor. As before, component A has index $1'$, component B has index $2'$, and component C has index $3'$. Instead of mole fractions x_i , molar concentrations c_i will be used for the description of the system. Then, the reaction equilibrium is given in analogy to Eq. (10) by

$$K = \frac{c_2 c_3}{c_1^2}. \quad (14)$$

Phase equilibrium is described by the multicomponent competitive Langmuir isotherm according to

$$q_i = \frac{\alpha_i c_i}{N_s \left(1 + \sum_{k=1} b_k c_k \right)}, \quad i = 1, \dots, N_s. \quad (15)$$

Since all three components are adsorbed independently on to the solid phase, the number of dynamic degrees of freedom in chemical equilibrium is now equal to two. This corresponds to a nonreactive, two-solute chromatographic process. If

reactant A is taken as the reference component, then the following definition of the transformed concentration variables apply

$$C_1 = c_2 + \frac{c_1}{2}, \quad C_2 = c_3 + \frac{c_1}{2}, \quad (16)$$

$$Q_1 = q_2 + \frac{q_1}{2}, \quad Q_2 = q_3 + \frac{q_1}{2}. \quad (17)$$

The construction of wave solutions for this two-dimensional system is made most conveniently in the hodograph space of the transformed concentration variables C_1 , C_2 , as explained previously. For this purpose the pathgrid of eigenvectors of the Jacobian of the transformed equilibrium function $\mathbf{Q}(\mathbf{C})$ must be calculated. The procedure is described in more detail in Refs. [11, 13], and the results are illustrated schematically in Fig. 5.9. In analogy to Fig. 5.8, three different cases are considered. In the first case in Fig. 5.9(a), reactant A has intermediate affinity to the solid phase, whereas in Fig. 5.9(b) it has highest and in Fig. 5.9(c) it has lowest affinity to the solid phase. In this representation the x-axis represents pure product B and the y-axis pure product C. Equilibrium concentrations corresponding to pure reactant A lie on the bisection line. As in the previous section on reactive distillation, limitations on feasible products occur if reactant A has highest or lowest affinity to the solid phase. These limitations are represented by a line of reactive azeotropy, which is the boundary of the shaded regions in Fig. 5.9. If A has highest affinity to the solid phase, the line of reactive azeotropy is always below the feed line, as in Fig. 5.9(b). However, it is always above the feed line if reactant A has the lowest affinity to the solid phase.

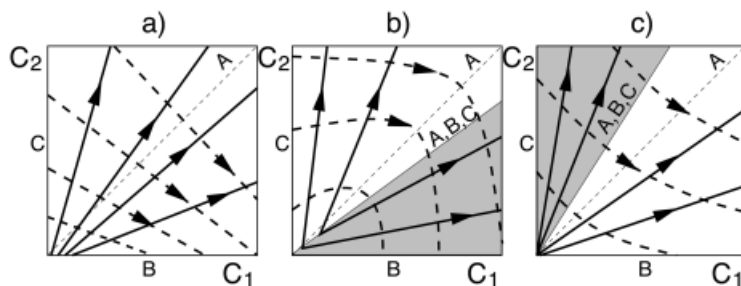


Fig. 5.9. Pathgrid of the eigenvectors of the transformed equilibrium function of a reactive chromatographic process with a reaction of type $2A \rightleftharpoons B + C$ in the liquid phase and a mixture with competitive multicomponent Langmuir isotherms (schematic)
 (a) Reactant A has intermediate affinity to the solid phase,
 (b) reactant A has highest affinity to the solid phase, (c) reactant A has lowest affinity to the solid phase.

Again, these structural results do not depend on specific values of the equilibrium constant K and the parameters of the Langmuir isotherm a_i , b_i , as was shown in the appendix of Ref. [11]. Further, it was shown that the same patterns of behavior will arise if the chemical reaction is taking place in the solid phase instead of the fluid phase. The latter is of particular interest in applications where the adsorbent acts simultaneously as a catalyst. Practical examples will be discussed in the next section; the interested reader is also referred to Chapter 6 of this book. In this context it is worth noting that the structural properties in Fig. 5.9 depend crucially on the stoichiometry of the system, which will be also discussed in the next section.

According to Fig. 5.9, the following patterns of behavior can be predicted for a fixed-bed chromatographic reactor with a pulse injection of pure reactant A. As in nonreactive two-solute chromatography, the final pulse pattern will consist of two pulses. In the first case, where reactant A has intermediate affinity to the solid phase, two separate pulses of product B and C will be obtained provided that the column is long enough to allow total separation of the pulses. Only in this case is total conversion of reactant A possible. In contrast to this, in Fig. 5.9(b), where reactant A has highest affinity to the solid phase, only pure product C can be obtained whereas the other pulse lies on the line of reactive azeotropy which is the upper boundary of the shaded region in Fig. 5.9(b). Consequently, the other pulse will always contain a mixture of all three components, no matter how long the column. Since A has highest affinity to the solid phase the latter pulse will always be behind the first one. The reverse situation can be observed in Fig. 5.9(c). Here, only pure product B can be obtained, whereas the other pulse will always contain a mixture of all three components. As A has lowest affinity to the solid phase in Fig. 5.9(c), the latter pulse will always be in front of the pulse of pure B. The corresponding pulse patterns are illustrated in Fig. 5.10.

Similar limitations can be observed during the steady-state operation of a moving-bed chromatographic reactor, or during cyclic operation of a simulated moving-bed reactor [11].

5.3.2.2 Reactions of type $A \rightleftharpoons B + C$

Many practical applications deal with a reaction of type $A \rightleftharpoons B + C$ rather than $2A \rightleftharpoons B + C$. Typical examples, which can be brought to this form are esterification [25, 26] and ester hydrolysis reactions [9, 28]. In general the reaction mechanism is



In the forward direction the ester is formed, and in the reverse direction it is hydrolyzed. For esterification, the alcohol can be used as a solvent as described for methyl acetate synthesis [26]. For ester hydrolysis, water can be used as a solvent, as described for hydrolysis of methyl formate, ethyl formate, methyl acetate and ethyl acetate [28]. Usually, the solvent is taken in large excess and it can be assumed in good approximation that its concentration is constant. For constant alcohol

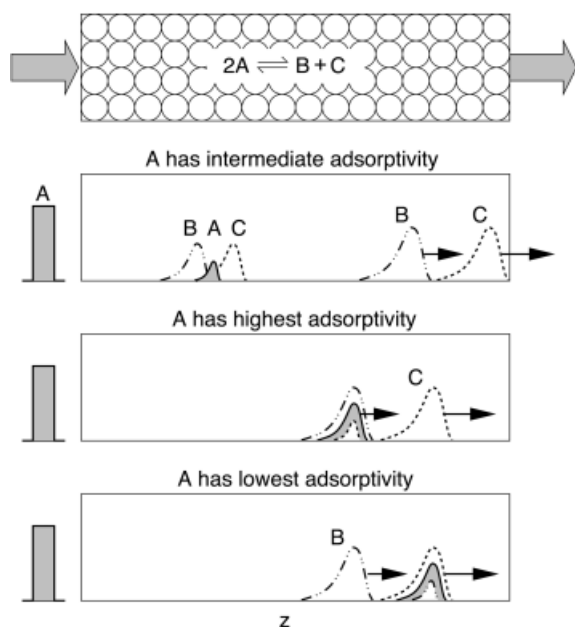


Fig. 5.10. Pulse patterns in a fixed-bed chromatographic reactor corresponding to Fig. 5.9 (schematic) (a) Reactant A has intermediate adsorptivity; (b) reactant A has highest adsorptivity; (c) reactant A has lowest adsorptivity.

concentration the following shorthand notation of Eq. (18) is introduced for the esterification reaction:



For constant water concentration an analogous shorthand notation can be introduced for the hydrolysis reaction:



If component A has again index 1', component B index 2', and component C index 3' the reaction equilibrium follows now from

$$K = \frac{c_2 c_3}{c_1} \quad (21)$$

if the chemical reaction takes place in the fluid phase and

$$K = \frac{q_2 q_3}{q_1} \quad (22)$$

if the reaction takes place in the solid phase. The constant solvent concentration is taken into account in the equilibrium constant K . The definition of the transformed concentration variables is now

$$C_1 = c_2 + c_1, \quad C_2 = c_3 + c_1, \quad (23)$$

$$Q_1 = q_2 + q_1, \quad Q_2 = q_3 + q_1, \quad (24)$$

due to the modified stoichiometry. With this modified definition and the modified reaction equilibrium as in Eqs. (21) or (22), respectively, a similar analysis is possible, as in the previous section [12]. The results are illustrated schematically in Fig. 5.11, in analogy to Fig. 5.9.

Compared to Fig. 5.9 the line of reactive azeotropy is now shifted to higher concentrations for the cases in Fig. 5.11(b) and (c). Consequently, for a sufficiently low feed concentration, total conversion with pure products B and C is possible in all three cases. Theoretical limitations only occur for high feed concentration. In many practical applications the theoretical limitation illustrated in Fig. 5.11b, c is beyond the solubility limit of the reactants, and has then no practical significance.

5.3.2.3 Binaphthol Separation Problem

In this section, the application of equilibrium theory is illustrated for a fairly complex multireaction system. The problem to be considered is that of the separation of binaphthol enantiomers through using achiral chromatography. This problem was studied by Baciocchi et al. [1] among others, who in particular made the following experimental observations. When a pulse with a racemic composition of enantiomers was injected on to the column, no separation occurred. However in all cases

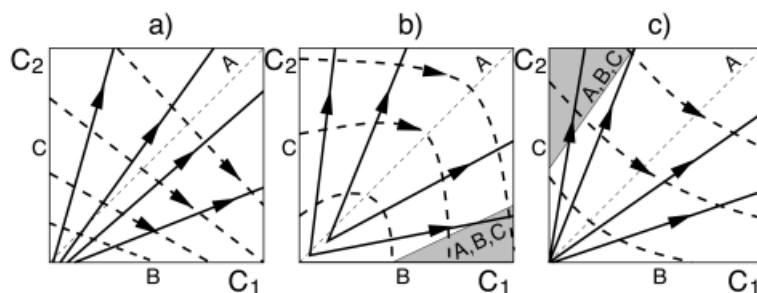


Fig. 5.11. Pathgrid of the eigenvectors of the transformed equilibrium function of a reactive chromatographic process with a reaction of type $A \rightleftharpoons B + C$ in the liquid phase and a mixture with competitive multicomponent Langmuir isotherms (schematic)
 (a) Reactant A has intermediate affinity to the solid phase;
 (b) reactant A has highest affinity to the solid phase,
 (c) reactant A has lowest affinity to the solid phase.

where a non-racemic mixture was injected, the pulse split into a first fraction with pure excess enantiomer and a second fraction with almost racemic composition. This was rather surprising, since the selectivity of an achiral stationary phase is the same for both enantiomers. This separation effect could be explained by the presence of dimerization reactions. According to Ref. [1], we shall denote the enantiomers as S and R ; these can build three different dimers according to



Dimers RR and SS are termed homochiral dimers, whereas the mixed dimer RS is termed a heterochiral dimer. A fraction of pure enantiomer is always a mixture of the monomer and the corresponding homochiral dimer, but it does not contain any heterochiral dimer. It was shown, that the separation of the excess enantiomer of a non-racemic feed mixture is the combination of two effects [31], the difference in reaction equilibrium constants of the homo- and heterochiral dimerization reaction and the difference in the adsorptivity of the homo- and heterochiral dimers.

The above experimental observations were reproduced with numerical simulation [1]. The model was based on the following assumptions:

- (i) Phase equilibrium was assumed between the solid and fluid phases and modeled with the competitive Bi-Langmuir adsorption isotherm. Using the notation introduced in this chapter, the adsorption isotherm reads

$$q_i = \frac{h_i c_i}{G} + \frac{a_i c_i}{B}, \quad i = R, S, RR, SS, RS, \quad (28)$$

with

$$G = 1 + g_1(c_R + c_S) + g_2(c_{RR} + c_{SS}) + g_3 c_{RS},$$

$$B = 1 + b_1(c_R + c_S) + b_2(c_{RR} + c_{SS}) + b_3 c_{RS}.$$

Equal selectivity was assumed between all monomers and homochiral dimers and a large difference in selectivity between homo- and heterochiral dimers.

- (ii) Further, it was assumed that the dimerization reactions take only place in the liquid phase. The reactions are rather fast, and therefore reaction equilibrium was assumed. The equilibrium constants of the homo- and the heterochiral dimerization are related by

$$K_{hetero} = 2K_{homo}. \quad (29)$$

With simultaneous phase and reaction equilibrium the system has only two dynamic degrees of freedom (five solutes – three chemical equilibria) and therefore corresponds again to a nonreactive system with two solutes. If the dimers are taken as reference components the following definition of the transformed concentration variables is found from Eq. (6)

$$C_R = c_R + 2c_{RR} + c_{RS}, \quad C_S = c_S + 2c_{SS} + c_{RS}, \quad (30)$$

$$Q_R = q_R + 2q_{RR} + q_{RS}, \quad Q_S = q_S + 2q_{SS} + q_{RS}. \quad (31)$$

which is consistent with the model formulation in Ref. [1]. For the prediction of wave solutions the pathgrid of the eigenvectors of the transformed equilibrium function $Q(C)$ is calculated using methods described in the appendix of Ref. [13]. The results are illustrated in Fig. 5.12 in the right diagram. For comparison, the pathgrid of a nonreactive Langmuirian system with two solutes is shown on the left.

For the reactive system the x-axis corresponds to pure R enantiomer containing only homochiral RR dimer, and the y-axis corresponds to pure S enantiomer containing only homochiral SS dimer. Racemic concentrations line on the bisection line. A mixture with excess R enantiomer lies in the lower half-plane and a mixture with excess S enantiomer lies in the upper half-plane.

Although both diagrams appear similar at first glance, there are some important differences. In particular, in the reactive system all solid lines intersect at the origin. The dotted lines are parallel and change their orientation at the bisection line. Furthermore, the pathgrid of the reactive system is symmetric with respect to the bisection line due to the fact that both enantiomers behave the same. This topology has important implications for the construction of wave solutions as discussed in detail in Ref. [13].

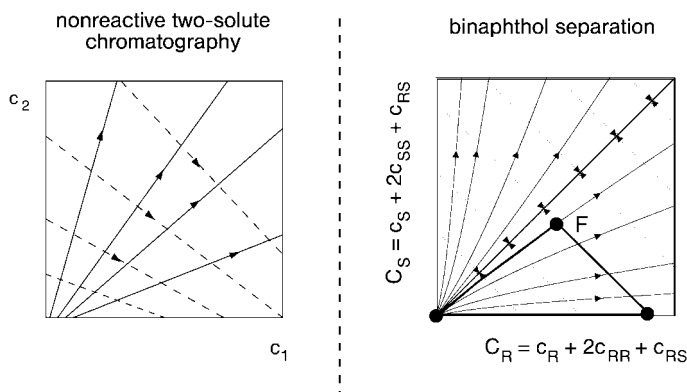


Fig. 5.12. Pathgrid of a nonreactive two-solute chromatographic system compared to the reactive binaphthol system.

Let us consider for example a pulse injection of a non-racemic mixture on an initially clean bed. Again, the pulse can be decomposed into a stepwise increase followed by a stepwise decrease of the feed concentration. The corresponding wave solution is illustrated in Fig. 5.12 with the thick solid line. Due to the topology of the pathgrid any pulse pattern through the origin forms a triangle. In contrast to this the corresponding wave solution in the nonreactive case always forms a quadrangle. Hence, in the nonreactive case the solution consists of four waves which split into two pulses, as described in the theory section. In contrast to this in the reactive case in Fig. 5.12(b) the solution consists of only three waves. These will be resolved into a first fraction of pure excess enantiomer, corresponding to the piece along the ordinate in Fig. 5.12, and a second piece with almost racemic composition corresponding to the piece along the wave curve through the origin in Fig. 5.12(b). The corresponding chromatogram is illustrated in Fig. 5.13. Due to the special topology in Fig. 5.12 both fractions will never separate, no matter how long the column.

A similar separation effect can be achieved for a racemic feed if the bed is preloaded with one of the enantiomers. In this case, any pulse pattern in Fig. 5.12 forms a quadrangle, and consequently, a separation of the two fractions is possible. A detailed discussion is provided in Ref. [13].

5.3.3

Extension to Other Processes

The theory presented above also applies to other integrated reaction separation processes which fall into the class of systems illustrated in Fig. 5.1. Typical examples are sorption-enhanced gas phase reactions (as described in Chapter 7) or membrane reactors (as described in Chapter 12).

As in reactive distillation and reactive chromatography, many sorption-enhanced reaction processes are controlled by phase equilibrium in addition to reaction equilibrium. The situation is different for membrane reactors, where phase equilibrium between the phases adjacent to the membrane is often trivial and the process is

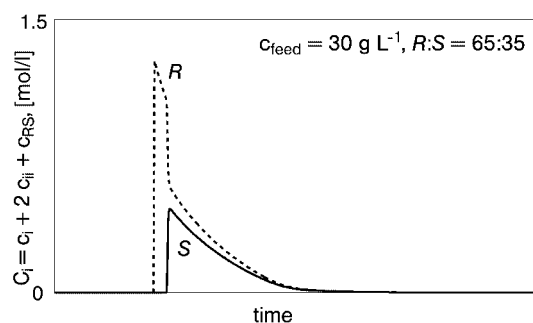


Fig. 5.13. A typical chromatogram for the binaphthol separation problem if a nonracemic feed pulse is injected to a clean bed.

dominated by the finite transport velocity across the membrane. Hence, the assumption of phase equilibrium leading to a pseudohomogeneous model as in Eqs. (3) and (5) is not valid, and a more general two-phase model of the type in Eq. (1) with finite transport velocity across the membrane must be considered. Using the ideas introduced in Chapter, equilibrium theory can also be applied to processes with non-negligible transfer resistance between both phases. Application to membrane reactors is discussed in Ref. [13].

5.4 Applications

In this section, possible applications of the theory presented in the previous section are highlighted. It was shown that the equilibrium theory and nonlinear waves provide a simple means for understanding the dynamic behavior of many integrated processes. It thereby often directly guides the way to improved process operation and improved process control. Several examples will be discussed subsequently.

5.4.1 New Modes of Operation

A new advanced operation strategy for simulated moving-bed (SMB) chromatographic processes is illustrated in Fig. 5.14. This makes direct use of traveling wave phenomena.

SMB processes use cyclic switching of the inlets and outlets to simulate a counter-current flow between the solid and liquid phases. They are used for continuous separation of fine and speciality chemicals (e.g., pharmaceuticals) Figure 5.14 illustrates a comparison between the standard mode of operation with a constant feed concentration during the switching interval (solid line) and a new type of operation with periodic modulation of the feed concentration (dashed line) called *ModiCon* [36, 37]. The concentration profiles in Fig. 5.14 are shown in the middle of the switching interval. In this example, *ModiCon* uses a feed of pure solvent in the first half of the switching interval corresponding to a zero concentration of the mixture to be separated and a double concentration in the second half of the switching interval. Hence, the total amount of feed is the same in both cases. From Fig. 5.14 it is clear that the way in which the feed is supplied makes a big difference. In Fig. 5.14 the product purity at the raffinate is increased for *ModiCon*, while productivity and solvent consumption are the same as in the standard mode of operation. In contrast, productivity and solvent consumption can be improved if the same product purity is chosen as in the conventional mode of operation [37]. For a practical benchmark problem an improvement in productivity of more than 100% and a solvent reduction of about 50% compared to the standard mode of operation was found [35]. This effect was seen to be directly related to nonlinear wave propagation of the concentration fronts in Fig. 5.14 during the switching intervals [36]. From the analysis it was concluded that a decrease in feed concentration in the first half of the interval and an increase in the second half of the interval is advantageous for systems with favorable

adsorption isotherms. The reverse strategy must be applied to systems with unfavorable adsorption isotherms.

The illustration in Fig. 5.14 is for a simple nonreactive process. However, according to the theory developed above we can expect similar results for SMB processes with fast chemical reactions.

5.4.2

New Control Strategies

Insights from nonlinear wave theory can also be used for designing new control strategies. A major problem in controlling product purities in separation as well as integrated reaction separation processes is often the lack of a cheap, reliable and fast online concentration measurement. This problem can be solved in two different ways: (i) through simple inferential control, or (ii) model-based measurement.

In the first case, product purities are controlled indirectly by controlling front positions. In distillation columns the front positions are easily controlled with cheap, reliable and fast online temperature measurements on sensitive trays inside the column [27]. A similar procedure was recently proposed for moving-bed chromatographic processes with UV rather than temperature measurement [37]. However, the performance of such an approach is usually limited. Exact product specifications cannot be guaranteed because of this indirect approach. Furthermore, in combined reaction separation processes the relationship between the measured variable and the variable to be controlled is often non-unique, which may lead to severe operational problems as shown for reactive distillation processes [23]. It was concluded that these problems could be overcome if in addition some direct or indirect measure of conversion is taken into account.

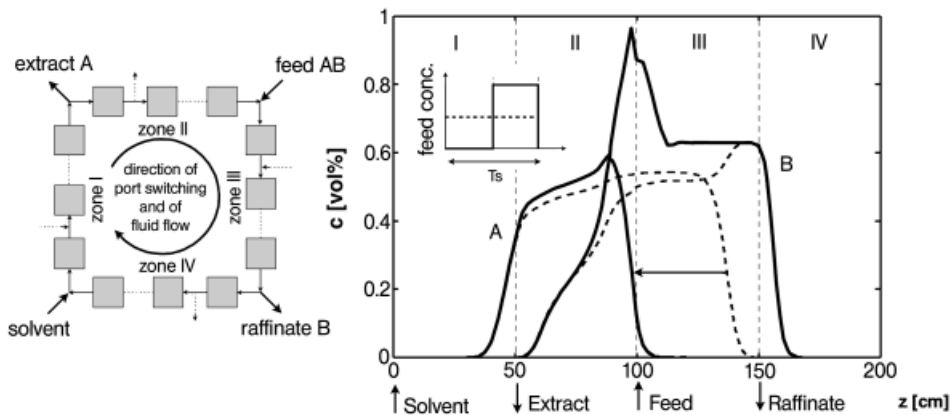


Fig. 5.14. Simulated moving-bed chromatographic processes with periodic variation of the feed concentration (ModiCon).

In the second case, product purities are estimated online from available measurement information by using model-based measurement techniques. Model-based measurement relies on a suitable process model which computes the unmeasurable internal state variables from the given inputs of the plant. Due to model deviations and unmeasured disturbances, the model predictions will diverge from the true plant behavior unless some suitable dynamic model correction is applied. A very simple and intuitive procedure for designing such a model correction based on physical insight from wave propagation dynamics was proposed for reactive and nonreactive distillation processes [14]. A similar approach for moving-bed chromatographic processes was also discussed [37].

Finally, nonlinear wave can also be used for nonlinear model reduction for applications in advanced, nonlinear model-based control. Successful applications were reported for nonreactive distillation processes with moderately nonideal mixtures [21]. For this class of mixtures the column dynamics is entirely governed by constant pattern waves, as explained above. The approach is based on a wave function which can be used for the approximation of the concentration profiles inside the column. The wave function can be derived from analytical solutions of the corresponding wave equations for some simple limiting cases. It is given by

$$x_i(z, s^{(1)}, \dots, s^{(N_c-1)}) = x_i^{(1)} + \sum_{k=1}^{N_c-1} \frac{x_i^{(k+1)} - x_i^{(k)}}{1 + \exp\left\{-\rho^{(k)}(z - s^{(k)})\right\}}. \quad (32)$$

Each term under the sum represents a single constant pattern wave, as illustrated in Fig. 5.15. Therein, $s^{(k)}$ represents the position, $\rho^{(k)}$ the slope and $x_i^{(k)}$, $x_i^{(k+1)}$ the

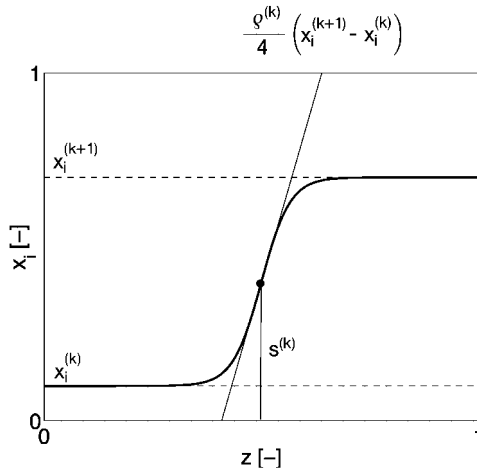


Fig. 5.15. A single constant pattern wave.

pinches on the left and on the right of front number k . The slopes and pinch compositions can be calculated from the physical properties and operating conditions. The $N_c - 1$ front positions are the only unknown variables in this function. A low-order dynamic model of a distillation column is obtained by substituting the wave function into the integral material balances of the column section.

A comparison of the steady-state profiles predicted by the wave model and those predicted by a rigorous tray-by-tray column model is shown in Fig. 5.16 for a coupled column system which serves for the separation of a mixture of methanol, ethanol, and 1-propanol. The approximation by the wave model in Fig. 5.16 is fairly good, although the reduction of the system order is considerable. The state variables of the rigorous model are the concentration and temperatures on each column tray. In contrast to this the state variables of the wave model are only the front positions.

It is not only the steady-state behavior that is reproduced quite nicely by the wave model, but also the dynamic transient behavior, as illustrated in Fig. 5.17 with the time plots of the product concentrations after a stepwise change of the feed flow rate of $\pm 10\%$.

Wave models were successfully used for the design of a supervisory control system for automatic start-up of the coupled column system shown in Fig. 5.15 [19] and for model-based measurement and online optimization of distillation columns using nonlinear model predictive control [15]. The approach was also extended to reactive distillation processes by using transformed concentration variables [22]. However, in reactive – as in nonreactive – distillation, the approach applies only to processes with constant pattern waves, which must be checked first.

5.5

Conclusion

In this chapter it was shown that equilibrium theory, which was first developed for nonreactive chromatographic and nonreactive distillation processes is readily extended to many integrated reaction separation processes with fast reversible reactions. The theory provides an easy understanding of the dynamics of these processes and therefore has many useful applications in process control. Further, the theory nicely predicts inherent limitations of integrated reaction separation processes, which may not be obvious from first glance. It emphasizes fundamental features, which are common to many of these processes.

The analysis presented in this chapter was based on three crucial assumptions. Namely, mass transfer and reaction kinetics were neglected. Further, constant flow rates were assumed. Although these assumptions are valid in many applications, an extension to finite mass transfer and reaction kinetics as well as variable flow rates seems challenging for future research in this field. As indicated in the last section, finite mass transfer and reaction kinetics may affect the feasible products of integrated reaction separation processes quite significantly. Strong impact can therefore also be expected for the dynamic behavior. The same applies to variable convective flow rates due to nonequimolar reactions. While this effect is not too important

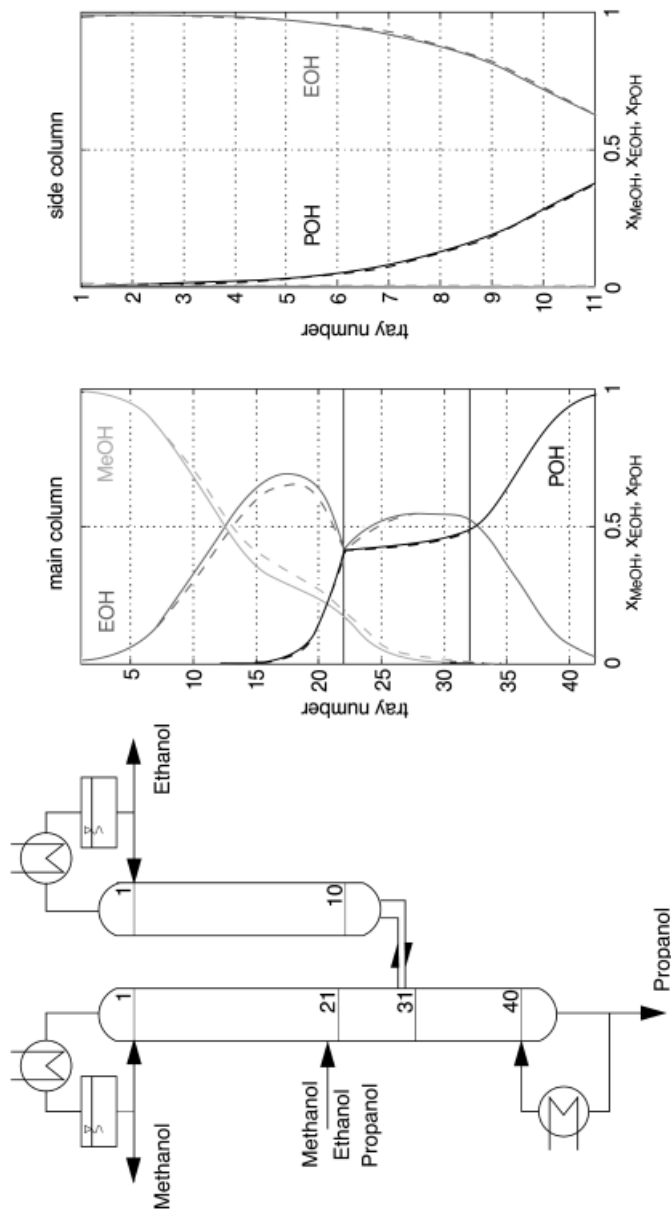


Fig. 5.16. Comparison of steady-state concentration profiles in a coupled column system predicted by a rigorous model from first principles (dashed line) and a low-order model based on the wave approach (solid line).

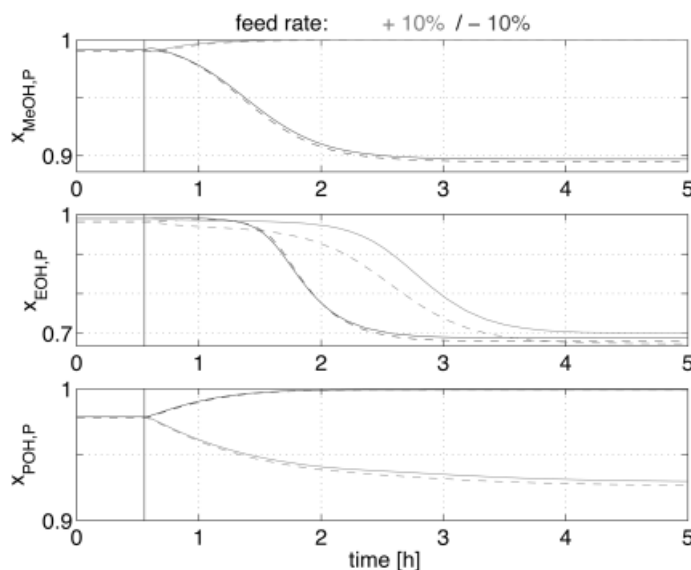


Fig. 5.17. Comparison of a rigorous model from first principles (dashed line) and a low-order model based on the wave approach (solid line) for the coupled column system in Fig. 5.16. Time plots of the product concentrations after a step change of the feed rate of $\pm 10\%$.

for the steady-state behavior [2, 42], it is of major significance for the dynamics of these processes. The reason is, that variable flow rates will directly affect the characteristic velocities. Hence they will change not only the propagation velocity of the wave fronts but possibly also the wave types. Similar phenomena can be observed in nonreactive chromatography [32, 24] and nonreactive distillation [29] with variable convective flow rates due to a non-negligible transport across the phase boundary. Previous studies on the steady-state design of reactive distillation processes have suggested the use of an extended definition of the transformed variables, where variable flow rates are taken into account by some suitable scaling [42]. However, an extension to the dynamic problem considered here is less obvious and requires further investigation. This is not surprising, because in the non-reactive case studies cited above the mathematical treatment for variable flow rates is quite involved.

Acknowledgments

The authors thank all students and colleagues at Stuttgart University, MPI Magdeburg and Magdeburg University who were involved in this research. The financial support of DFG (Deutsche Forschungsgemeinschaft) within the joint research projects SFB 412 on Computer Aided Modeling and Simulation of Chemical Processes for Process Analysis, Synthesis and Operation and FOR 447 on Membrane Enhanced Reaction is greatly acknowledged.

Symbols

a_i, b_i	parameters of the Langmuir isotherm
c_i	molar concentration in the fluid phase [kmol/m ³]
C_i	transformed concentration variable of the fluid phase [kmol/m ³]
j_i	mass transfer rate
K_i	chemical equilibrium constant [–]
l	length [m]
N	dimension of general concentration vectors x, y
N_c	number of components
N_s	number of solutes
N_r	number of reactions
q_i	molar concentration in the solid phase [kmol/m ³]
Q_i	transformed concentration variable of the solid phase [kmol/m ³]
r_j	dimensionless reaction rate [–]
\bar{t}	time [s]
t	dimensionless time [–]
v	convective velocity [m/s]
w	wave velocity [–]
x_i	in general: concentration of phase (')
	in distillation: mole fraction of the liquid phase [–]
X_i	in general: transformed concentration of phase (')
	in distillation: transformed mole fraction of the liquid phase [–]
y_i	in general: concentration of phase (")
	in distillation: mole fraction of the vapor phase [–]
Y_i	in general: transformed concentration variable of phase (")
	in distillation: transformed mole fraction the vapor phase [–]
\bar{z}	spatial coordinate [m]
z	dimensionless spatial coordinate [–]

Greek Letters

α	ratio of hold-ups in phases (") and (') [–]
α_i	constant relative volatility [–]
β	ratio of the convective flow rates in phases (") and (') [–]
ν_{ij}	stoichiometric coefficients [–]

Sub- and superscripts

i, k	species
j	reaction
in	input
'	Phase (')
"	Phase (")

References

1. R. Baciocchi, G. Zenoni, M. Mazzotti, et al., Separation of binaphthol enantiomers through achiral chromatography. *J. Chromatogr. A.*, **2002**, 944, 225–240.
2. D. Barbosa and M. F. Doherty, A new set of composition variables for the representation of reactive phase diagrams. *Proc. R. Soc. Lond.*, **1987**, A413, 459–464.
3. D. Barbosa and M. F. Doherty, Theory of phase diagrams and azeotropic conditions for two-phase reactive systems. *Proc. R. Soc. Lond.*, **1987**, A413, 443–458.
4. D. Barbosa and M. F. Doherty, The influence of equilibrium chemical reactions on vapor-liquid phase diagrams. *Chem. Engng. Sci.*, **1988**, 43, 529–540.
5. D. Barbosa and M. F. Doherty, The simple distillation of homogeneous reactive mixtures. *Chem. Engng. Sci.*, **1988**, 43, 541–550.
6. D. Basmadjian and P. Coroyannakis, Equilibrium-theory revisited – Isothermal fixed-bed sorption of binary systems. 1. Solutes obeying the Langmuir isotherm. *Chem. Engng. Sci.*, **1987**, 42, 1723–1735.
7. D. Basmadjian, P. Coroyannakis, C. Karayannopoulos, Equilibrium-theory revisited – Isothermal fixed-bed sorption of binary systems. 2. Non-Langmuir solutes with type I parent isotherms – Azeotropic systems. *Chem. Engng. Sci.*, **1987**, 42, 1737–1752.
8. D. Basmadjian, P. Coroyannakis, C. Karayannopoulos, Equilibrium-theory revisited – Isothermal fixed-bed sorption of binary systems. 3. Solutes with type I, type II and IV parent isotherms – Phaseseparation phenomena. *Chem. Engng. Sci.*, **1987**, 42, 1753–1764.
9. T. Falk and A. Seidel-Morgenstern, Comparison between a fixed-bed reactor and a chromatographic reactor. *Chem. Engng. Sci.*, **1999**, 54, 1479–1485.
10. V. Gaikar and M. Sharma, Separations through reactions and other novel strategies. *Sep. Purif. Meth.*, **1989**, 18, 111–176.
11. S. Grüner and A. Kienle, Equilibrium theory and nonlinear waves for reactive distillation columns and chromatographic reactors. *Chem. Engng. Sci.*, **2004**, 59, 901–918.
12. S. Grüner, A. Kienle, P. T. Mai, et al., Analysis of ester hydrolysis reactions in a chromatographic reactor using equilibrium theory, 2004. International Symposium on Preparative and Industrial Chromatography and Allied Techniques, SPICA 2004, October 17–20, Aachen, Germany.
13. S. Grüner, M. Mangold, A. Kienle, Dynamics of reaction separation processes in the limit of chemical equilibrium, 2004. Submitted for publication to *AIChE J.*
14. S. Grüner, K. D. Mohl, A. Kienle, et al., Nonlinear control of an industrial reactive distillation column. *Contr. Engng. Practice*, **2003**, 11, 915–925.
15. S. Grüner, S. Schwarzkopf, I. Uslu, et al., Nonlinear model predictive control of multicomponent distillation columns using wave models. Proceedings, 7th International Symposium on Advanced Control of Chemical Processes. Vol. 1, pp. 231–236, January 2004, Hong Kong, China.
16. F. G. Helfferich and G. Klein, *Multicomponent Chromatography. Theory of Interference*. M. Dekker, New York, 1970.
17. Y.-L. Hwang, On the nonlinear wave theory for dynamics of binary distillation columns. *AIChE J.*, **1995**, 41, 190–194.
18. Y.-L. Hwang, Wave propagation in mass-transfer processes: From chromatography to distillation. *Ind. Engng. Chem. Res.*, **1995**, 34, 2849–2864.

19. A. Itigin, J. Raisch, T. Moor, et al., A two-level hybrid control strategy for the start-up of a coupled distillation plant, 2003. Proceedings European Control Conference ECC, Cambridge, UK.
20. A. Kienle, *Nichtlineare Wellenphänomene und Stabilität stationärer Zustände in Destillationskolonnen*. VDI Fortschritts-Berichte Nr. 3/506. VDI-Verlag, Düsseldorf, 1997.
21. A. Kienle, Low-order dynamic models for ideal multicomponent distillation processes using nonlinear wave propagation theory. *Chem. Engng. Sci.*, **2000**, 55, 1817–1828.
22. A. Kienle, Nonlinear model reduction for nonreactive and reactive distillation processes using nonlinear wave propagation theory. In: *SPC-2000, Third Symposium on Process Control*, pp. 72–78, Ploiesti, Romania, 2000.
23. A. Kienle and W. Marquardt, Nonlinear dynamics and control of reactive distillation processes. In: K. Sundmacher and A. Kienle, (Eds), *Reactive Distillation – Status and Future Directions*, pp. 241–281. Wiley-VCH, Weinheim, 2003.
24. M. LeVan, C. A. Costa, A. E. Rodrigues, et al., Fixed-bed adsorption of gases – Effect of velocity variations on transition types. *AIChE J.*, **1988**, 34, 996–1005.
25. F. Lode, G. Francesconi, M. Houmard, et al., Synthesis of methylacetate in a simulated moving-bed reactor: Experiments and modeling. *AIChE J.*, **2003**, 49, 1516–1524.
26. F. Lode, M. Houmard, C. Migliorini, et al., Continuous reactive chromatography. *Chem. Engng. Sci.*, **2001**, 56, 269–291.
27. W. L. Luyben, B. D. Tyreus, M. L. Luyben, *Plantwide Process Control*. McGraw-Hill, New York, 1998.
28. P. T. Mai, T. D. Vu, K. X. Mai, et al., Analysis of heterogeneously catalyzed ester hydrolysis performed in a chromatographic reactor and in a reaction calorimeter. *Ind. Engng. Chem. Res.*, **2004**, 43, 4691–4702.
29. W. Marquardt, *Nichtlineare Wellenausbreitung – ein Weg zu reduzierten Modellen von Stofftrennprozessen*. VDI Fortschrittsberichte Nr. 8/161. VDI-Verlag, Düsseldorf, 1988.
30. W. Marquardt, Traveling waves in chemical processes. *Int. Chem. Engng.*, **1990**, 30, 585–606.
31. R.-M. Nicoud, J.-N. Jaubert, I. Rupprecht, et al., Enantiomeric enrichment of non-racemic mixtures of binaphthol with non-chiral packings. *Chirality*, **1996**, 8, 234–243.
32. D. L. Peterson and F. Helfferich, Towards a generalized theory of gas chromatography at high solute concentrations. *J. Phys. Chem.*, **1969**, 65, 1283–1293.
33. H.-K. Rhee, R. Aris, N. R. Amundson, *First-Order Partial Differential Equations: Volume I – Theory and Application of Single Equations*. Prentice-Hall, New Jersey, 1986.
34. H.-K. Rhee, R. Aris, N. R. Amundson, *First-Order Partial Differential Equations: Volume II – Theory and Application of Hyperbolic Systems of Quasilinear Equations*. Prentice-Hall, New Jersey, 1989.
35. H. Schramm, M. Kaspereit, A. Kienle, et al., Improving simulated moving bed processes by cyclic modulation of the feed concentration. *Chem. Engng. Technol.*, **2002**, 25, 1151–1155.
36. H. Schramm, M. Kaspereit, A. Kienle, et al., Improved operation of simulated moving bed process through cyclic modulation of feed flow and feed concentration. *Chem. Engng. Sci.*, **2003**, 58, 5217–5227.
37. H. Schramm, M. Kaspereit, A. Kienle, et al., Simulated moving bed process with cyclic modulation of the feed concentration. *J. Chromatogr. A*, **2003**, 1006, 77–86.

38. J. Smoller, *Shock Waves and Reaction-Diffusion Equations*. 2nd ed., Springer, New York, 1994.
39. K. Sundmacher and A. Kienle, *Reactive Distillation – Status and Future Trends*. Wiley-VCH, Weinheim, 2003.
40. D. Tondeur and M. Bailly, Unifying concepts in non-linear unsteady processes. Part II: Multicomponent waves, competition and diffusion. *Chem. Eng. Process.*, **1987**, 22, 91–105.
41. S. Ung and M. F. Doherty, Calculation of residue curve maps for mixtures with multiple equilibrium chemical reactions. *Ind. Engng. Chem. Res.*, **1995**, 34, 3195–3202.
42. S. Ung and M. F. Doherty, Synthesis of reactive distillation systems with multiple equilibrium chemical reactions. *Ind. Engng. Chem. Res.*, **1995**, 34, 2555–2565.

6 Simulated Moving-Bed Reactors

Guido Ströhlein, Marco Mazzotti and Massimo Morbidelli

6.1 Introduction

Hybrid processes have attracted an increasing amount of attention in the past due to their potential for making significant improvements in process efficiency. Research in this area is to a large extent committed to integrated processes, where two or more conventional process units are combined into a single apparatus. Typically, this involves the integration of a chemical reaction into another unit operation such as distillation, absorption, adsorption, extraction, filtration, and heat transfer. In the case of reactor-separator processes, the additional degrees of freedom in the unit design offer the possibility to tailor concentration profiles inside the unit in order to achieve higher selectivities and higher yields. Especially in the scope of equilibrium-limited reactions, integrated reactor-separator processes can increase performance substantially because they allow an equilibrium-limited yield to be overcome, but due to the same operating conditions for reaction and separation, the field of application is limited.

Reactive chromatography belongs to the category of reactor-separator processes, and it is especially attractive as alternative to reactive distillation if the components involved are nonvolatile or heat-sensitive, as are often encountered in biotechnology.

The principle of reactive chromatography can be easily explained using a simple reversible reaction of type $A \leftrightarrow B + C$. Looking at a single chromatographic column filled with a stationary phase which serves as a selective adsorbent and as a heterogeneous catalyst, the development of a pulse of A injected into the continuous eluent stream is shown in Fig. 6.1.

It is assumed that C has the lowest affinity to the stationary phase, while A has an intermediate, and B a high affinity. These differences in affinity lead to different migration velocities in the column. As soon as A enters the column, its decomposition is catalyzed by the stationary phase and yields B and C. Since C is the least retained component, and hence has the highest migration velocity, it travels ahead of A, whilst B – being the most strongly retained component – stays behind A. Due to this spatial separation of the products from the reactant, the driving force at the reaction locus is kept high and the reaction can ideally be driven to complete conversion; thus, the two pure products peaks can be collected at the outlet. It is worth noting

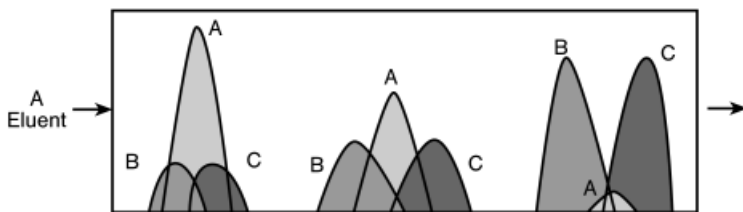


Fig. 6.1. Development of a pulse of reactant A along the column length with a stationary phase catalyzing the reaction $A \rightleftharpoons B + C$.

that the adsorptivity of the reactant has not to be necessarily intermediate between those of the two products, but this leads to the highest efficiency of the chromatographic reactor. For reactions involving more than one reactant, one has to ensure that each of the reactant species is available at the reaction locus; hence, they all must have very similar adsorptivities. For reactions with two reactants, this problem of reactant availability can be solved easily by using one of them as the eluent.

The advantages of reactive chromatography in comparison to conventional reactor-separator sequences have been shown experimentally for various reactions. An overview has been given by Lode et al. [1]. Recently, new contributions have been made concerning the partial oxidation of methane to methanol [2], MTBE synthesis [3], lactosucrose production [4], methyl acetate synthesis [5] and a regioselective enzymatic esterification [6]. Also, by using simulated moving-bed reactor (SMBR) modeling it has been shown that genetic algorithms can be very useful in the optimization of these complex units [7].

For all these types of reactions, the design of the stationary phase plays a crucial role in process efficiency. The optimal balance must be found between the competing stationary phase properties of sorption selectivity, sorption capacity and catalytic activity. A large majority of the stationary phases used in reactive chromatography are commercially available alumina, zeolites, immobilized enzymes, ion-exchange resins or a mixture of pellets having either adsorptive or catalytic properties. Recently, more attention has been given to ion-exchange resins specifically tailored to the reaction implemented in a chromatographic reactor [8]. The main variables which can be changed in order to improve the stationary phase are the distribution and the amount of functional groups, the chemistry of the functional groups, and the pellet morphology.

Due to the low efficiency of chromatographic processes operated in the batch mode – that is, a high eluent requirement, a high product dilution, and inefficient use of the stationary phase volume – reactive chromatography has been transformed successfully into a continuous process using mature technologies originated from purely separative continuous chromatography such as simulated-moving-bed and annular chromatography reactors.

6.2

Continuous Reactive Chromatography

Analogous to purely separative chromatography, continuous reactive chromatographic processes are based on the idea of moving the solid phase co-currently or countercurrently to the liquid. The most well-known co-current process is probably annular chromatographic technology. Different implementations of countercurrent processes have been proposed, including a true countercurrent set-up where the solid phase is continuously moved. The movement of solid particles obviously imposes severe technical problems due to the particle abrasion and fluid flow inhomogeneity. In order to overcome these problems, simulated moving-bed technology emerged in the early 1960s [9], since when it has been successfully operated in industry for a variety of separation problems, and particularly in the area of isomer and chiral separation.

6.2.1

Annular Reactive Chromatography

In annular reactive chromatography, the solid phase is enclosed between two concentrically arranged cylinders which rotate around their common axis. The eluent is fed from the top of the unit and is equally distributed over the perimeter. The reacting species are introduced at a single stationary point and their migration along the solid bed occurs through a vertical and a horizontal velocity. Light components, which are components with a low affinity to the solid phase, travel more with the liquid than with solid phase, and therefore they exhibit a high vertical and a low horizontal velocity. Instead, heavy components are transported preferentially with the solid phase and migrate with a higher horizontal and lower vertical velocity. The mechanism of reaction and separation is analogous to that for a single batch column. The species produced can then be collected as pure fractions at different angles compared to the feed port, as shown in Fig. 6.2 for a reaction $A \leftrightarrow B + C$ and affinities as in Chapter 1. Annular chromatography is therefore especially favorable for cases involving several reactions and multiple required products, though its major drawback is a low efficiency, which is comparable to that of batch operation.

Several examples of these applications were summarized previously [1], and more recently the use of annular chromatography for the synthesis of triacetin has been reported [10].

6.2.2

Simulated Moving-Bed Reactors

The typical configuration for a true countercurrent (TCC) chromatographic reactor is shown in Fig. 6.3 for a reaction of type $A \leftrightarrow B + C$.

The unit is divided into four sections, each one fulfilling a specific task. The central sections 2 and 3 are supposed to separate B and C from A, and B from C, respectively, so that they can be withdrawn purely in the extract and raffinate stream.

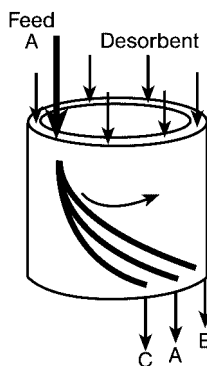


Fig. 6.2. Annular chromatographic reactor containing a stationary phase catalyzing the reaction $A \rightleftharpoons B + C$.

In section 1, the solid phase is regenerated so that it can be recycled to section 4, while in the latter section the eluent is depleted of C and can then be fed back to the unit in section 1.

The reactant A is introduced in the unit with the feed, is then transported with the liquid phase into section 3, adsorbs there and travels with the resin also in section 2. On the one hand, the liquid and solid flow rates in the central sections must be adjusted in a way that A is kept long enough in the central sections in order to react completely, but on the other hand they are constrained by the movement of B and C. For a constant solid flow rate, the liquid flow in section 2 should be high enough to wash out the light component C, but small enough to let the heavy component B reach the extract port, and vice versa for section 3. The determination of flow rates in sections 1 and 4 is comparatively easy, as only one component is present and hence only a lower and an upper constraint, respectively, has to be fulfilled. A typical concentration profile for a TCC unit is shown in Fig. 6.4.

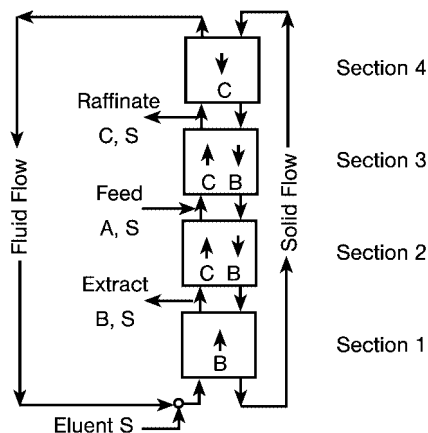


Fig. 6.3. True countercurrent (TCC) chromatographic reactor containing a stationary phase catalyzing the reaction $A \rightleftharpoons B + C$.

The practical implementation of the TCC reactor imposes several technical problems (as discussed earlier), and consequently the simulated moving-bed (SMB) technology emerged. Movement of the solid is simulated by periodically switching the inlet and outlet ports in the direction of the liquid flow, as shown in Fig. 6.5.

In the SMB technology, four sections can again be identified and the tasks as described for the TCC unit remain the same. The SMB is theoretically equivalent to a TCC set-up if the number of columns in every section is infinite. In practice, two

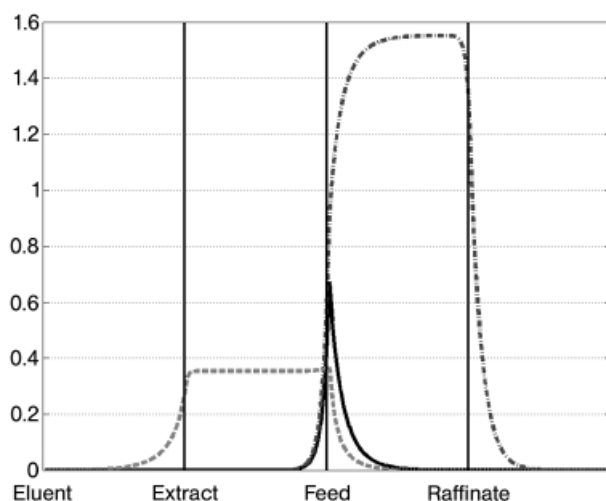


Fig. 6.4. Concentration profiles inside a true countercurrent (TCC) unit for the reaction: $A \rightleftharpoons B + C$. Dashed line = component B; dash-dotted line = component C; solid line = component A.

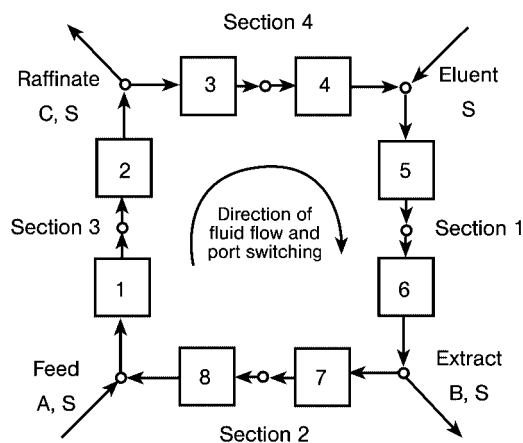


Fig. 6.5. Simulated moving-bed reactor containing a stationary phase catalyzing the reaction $A \rightleftharpoons B + C$.

columns per sections (as shown in Fig. 6.3) are often considered enough to simulate the solid flow.

For certain systems, modifications of the set-up shown in Fig. 6.5 may be advantageous, for example if the light product C is hardly adsorbed onto the solid phase, then section 4 can be omitted (open-loop SMB).

For the production of higher-fructose syrup, Hashimoto and co-workers proposed a three-section SMB containing two different kinds of columns [11]: first, separation columns included in the simulated solid-phase movement, which are filled with a stationary phase possessing only adsorptive properties, and second, reaction columns filled with a heterogeneous catalyst which remain stationary relative to the outlet ports, as shown in Fig. 6.6.

Such a configuration is especially useful if the conditions for the reaction such as temperature and residence time are significantly different from those for separation.

6.3

Design Parameters for Simulated Moving-bed Reactors

Although well-defined design strategies exist for the optimal operation of a purely separative SMB [12], nothing comparable is available for the SMBR, although some similarities between the two units can be exploited in order to provide guidelines for the design of the latter system.

Numerical optimization of SMB units is state-of-the-art [13], and a good starting point is obtained using the analytical solution of the equilibrium theory model for a TCC unit.

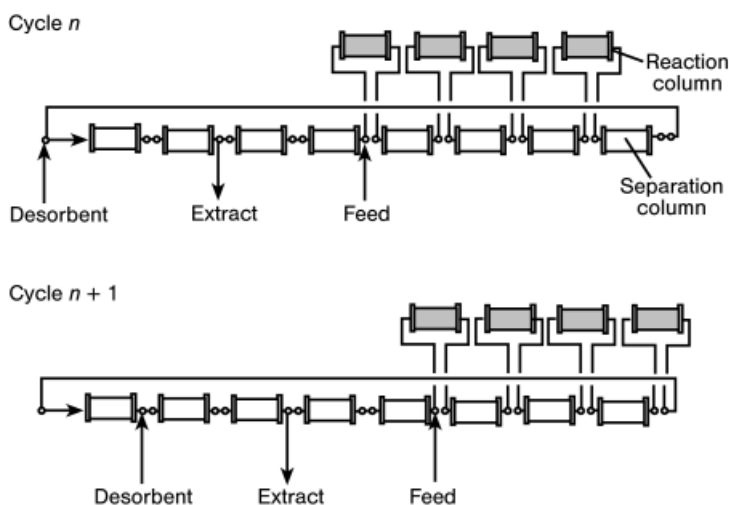


Fig. 6.6. Three-section simulated moving-bed reactor with stationary reaction columns.

This approach is based on the similarity between a TCC and a SMB unit, such that the flow rates in a TCC can be converted easily to the equivalent ones in a SMB unit. In the frame of equilibrium theory – that is, a model assuming one-dimensional flow – adsorption equilibrium between solid and liquid phase and neglecting axial dispersion, the following mass balances are obtained for each component i in every section j of a TCC unit:

$$\frac{\partial}{\partial \tau} [\varepsilon^* \cdot c_i + (1 - \varepsilon^*) \cdot q_i] + (1 - \varepsilon_p) \cdot \frac{\partial}{\partial z} [m_j \cdot c_i - q_i] = 0$$

$$\tau = \frac{t \cdot Q_s}{V_{unit}}$$

$$z = \frac{x}{L}$$

$$m_j = \frac{Q_j - \varepsilon_p \cdot Q_s}{(1 - \varepsilon_p) \cdot Q_s}$$

where τ and z , the dimensionless time and space coordinate respectively, are calculated from the volumetric solid flow rate Q_s , the unit volume V_{unit} , and the column length L . The porosities ε^* and ε_p indicate the overall bed void fraction and the particle porosity, c_i and q_i the liquid and solid concentration, respectively, and Q_j the volumetric liquid flow rate in section j . The main design parameter m_j represents the ratio of the effective volumetric liquid flow rate to the volumetric solid flow rate in the j^{th} section. For linear isotherms and some specific nonlinear isotherms, an analytical solution is available which yields constraints for the m_j -values in order to obtain complete separation [12, 14]. While for m_1 and m_4 only a lower and an upper boundary, respectively, apply, the solution for m_2 and m_3 yields intervals which are dependent on each other. These are usually represented in a plot depicting the m_2 – m_3 plane, as shown for example in Fig. 6.7 for a Langmuir isotherm.

Under the prerequisite, that the inequalities for m_1 and m_4 are fulfilled, the region of complete separation is confined by the triangle b-w-a, outside which either only a pure raffinate or extract stream or no pure outlet can be obtained. This can be seen by considering that, starting from an operation point inside the triangle, as the m_3 value increases the heavy component moves closer to the raffinate outlet and above a certain value pollutes it, whilst a decreasing m_2 value allows the light component to approach the extract outlet. It can easily be shown, that the vertex of the triangle is the optimal point of operation because the difference between m_3 – m_2 , which is proportional to the feed flow rate, has its maximum there, leading to minimal eluent requirement and maximal yield [15]. It is worth noting, that the triangular region of complete separation reduces to a right-angled triangle if the isotherms are linear.

For the SMBR, only an analytical solution which also relies on equilibrium theory for linear isotherms and an irreversible – as well as a reversible reaction – of type A reacting to B and C is available in the literature [16].

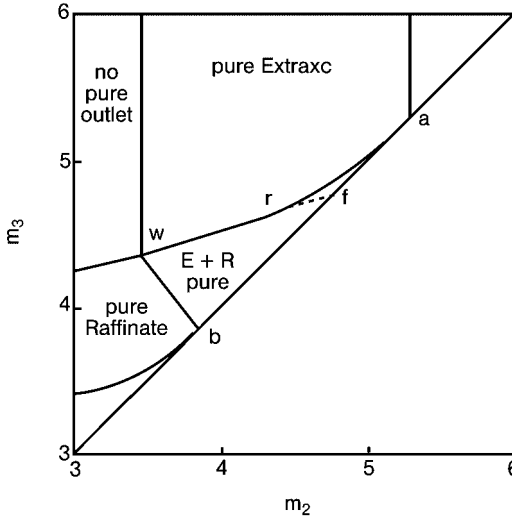


Fig. 6.7. Simulated moving-bed operating region for complete separation.

The mass balance resulting is very similar to the one discussed above, but a term incorporating the reaction is added, yielding a non-homogeneous PDE:

$$\frac{\partial}{\partial \tau} [\varepsilon^* \cdot c_i + (1 - \varepsilon^*) \cdot q_i] + (1 - \varepsilon_p) \cdot \frac{\partial}{\partial z} [m_j \cdot c_i - q_i] = v_i \cdot Da_j \cdot f(\vec{c}_i)$$

$$Da_j = \frac{k_R \cdot L_j}{u_s}$$

with v_i being the stoichiometric coefficient and $f(c_i)$ representing the dependence of the reaction rate on all compositions. The Damköhler number in section j , Da_j , is defined as the ratio between the residence time in the solid phase and the characteristic time for the reaction, and is calculated from the velocity of the solid phase u_s , the length of section j L_j and the reaction rate constant k_R . Using the linear isotherm

$$q_i = H_i \cdot c_i$$

with H_i being the Henry coefficient of component i , it can be assumed without loss of generality, that B is the heaviest product and C the lightest, hence

$$H_B > H_A > H_C$$

For the optimal design of the reactive SMBR, not only the conditions for the separation of B and C have to be fulfilled, but some additional constraints have also to be

imposed in order to account for the decomposition of A. As discussed above for the purely separative case, the operating region in the m_2 – m_3 plane turns into a right-angled triangle (see Fig. 6.8), where the solid lines constituting the triangle boundaries are given by the Henry coefficients of the products B and C.

Due to the presence of A, the triangle itself is subdivided into three regions. In subregion I, the m_2 value is too high to allow A to enter section 2, and hence the reaction takes place only in section 3 (Fig. 6.9, left). For subregion II instead, the low m_2 value allows A to enter section 2, but due to the low m_3 values, section 3 is void of component A (Fig. 6.9, center). Only in subregion 3, can the reactant enter both sections, and this leads to the highest solid-phase productivity (Fig. 6.9, right).

For an irreversible reaction of the type $A \rightarrow B + C$, iso-conversion lines show the region of operating points, where a certain conversion can be obtained (Fig. 6.10). The feasible region of operating conditions for the SMBR can then be obtained as the intersection between the separation triangle and the region below the iso-conversion line corresponding to the desired value.

In Fig. 6.10, the iso-conversion lines are plotted for a model system with $H_A = 1$, $H_B = 1.5$, and $H_C = 0.5$. With increasing conversion, the vertex of the operation region moves closer to the diagonal, which implies a smaller difference $m_3 - m_2$ and hence less productivity. The Damköhler number has a similar impact on the operating region, as shown in Fig. 6.11.

Thus, for example, for a reduced residence time of A in sections 2 and 3, the productivity must be decreased in order to ensure the desired conversion of 95 %.

In some cases, the adsorptivity of the reactant and of one of the products – that is, H_A and H_C – are very similar. The 99 % conversion line for a model system with three different H_A values is shown in Fig. 6.12.

With reducing H_A , the iso-conversion line moves towards the origin. At a certain point, it is no longer enclosed in the separation triangle and only the region inter-

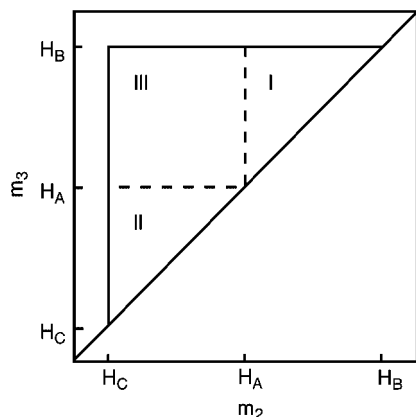


Fig. 6.8. Simulated moving-bed reactor operating region for linear isotherms and an irreversible reaction $A \rightarrow B + C$.

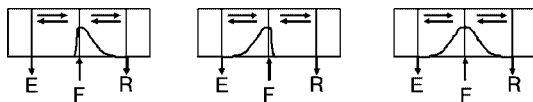


Fig. 6.9. Concentration profiles of reactant A in subregions I, II and III, respectively. Solid line = concentration profile of A; E, F, R denoting extract, feed and raffinate, respectively.

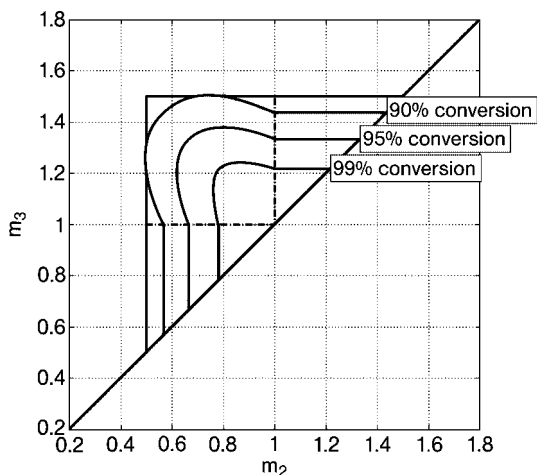


Fig. 6.10. Iso-conversion lines for an irreversible reaction $A \rightarrow B + C$; $H_A = 1$; $H_B = 1.5$; $H_C = 0.5$; $Da_2 = Da_3 = 1$.

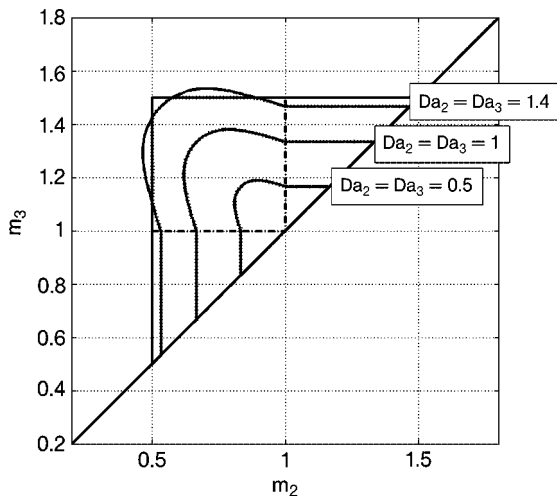


Fig. 6.11. Iso-conversion lines for 95 % conversion and different Damköhler numbers. $H_A = 1$; $H_B = 1.5$; $H_C = 0.5$.

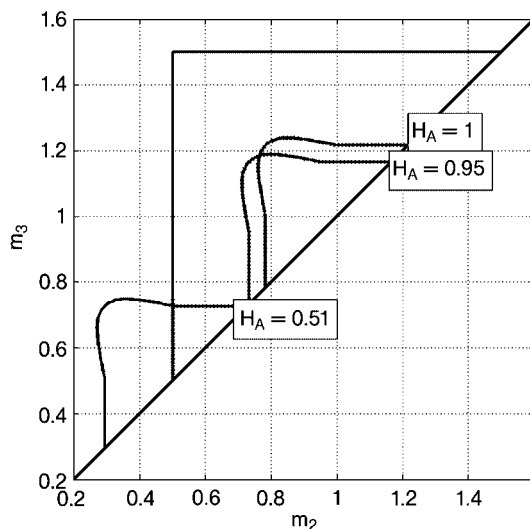


Fig. 6.12. Influence of H_A on iso-conversion lines at 99 % for an irreversible reaction. $H_B = 1.5$; $H_C = 0.5$; $Da_2 = Da_3 = 1$.

secting with the separation triangle guarantees the desired conversion and complete separation of B and C. For $H_A = 0.51$, that is very close to H_C , the optimal point of operation is situated on the left boundary of the separation triangle and clearly closer to the diagonal, hence with low productivity. This is due to the fact that the separation of C and A in section 3 becomes very difficult because they migrate with very similar velocities. The obvious measure for H_C would be to increase the residence time in section 3 (i.e., that is Da_3) in order to ensure the desired conversion also at high throughputs. The resulting operating regions are shown in Fig. 6.13, where the increase in the Da_3 value is obtained by increasing the length of the corresponding section.

The vertex of the operating region moves upwards on the left boundary of the triangle, and therefore a higher throughput is possible, as expected.

For a reversible reaction $A \leftrightarrow B + C$, the presence of chemical equilibrium imposes a further constraint on the operating region, as illustrated in Fig. 6.14, where the effect of the equilibrium constant value on the operating parameter region for a conversion of 90 % is shown.

It is seen that for an increasing equilibrium constant, the operating region for the reversible reaction approaches that for the irreversible reaction, as would be expected. Decreasing equilibrium constants move the optimal point of operation closer to the diagonal, hence reducing productivity.

In the case of an irreversible reaction, the reactant feed concentration has no impact on the operating region, but in the reversible case an increasing reactant feed concentration reduces the operating region (Fig. 6.15).

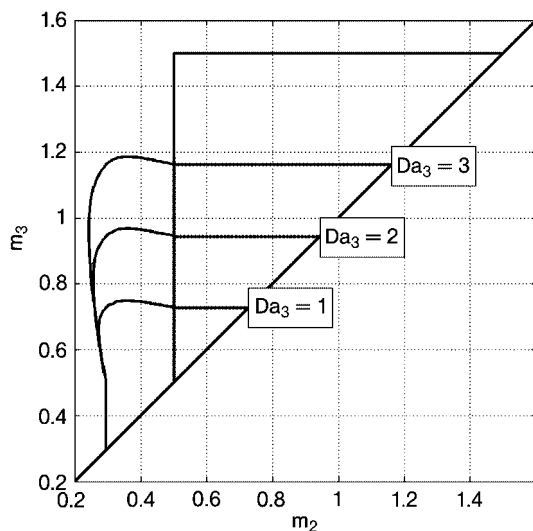


Fig. 6.13. Influence of Da_3 on the operating regions for an irreversible reaction at 99 % conversion. $H_A = 0.51$; $H_B = 1.5$; $H_C = 0.5$; $Da_2 = 1$.

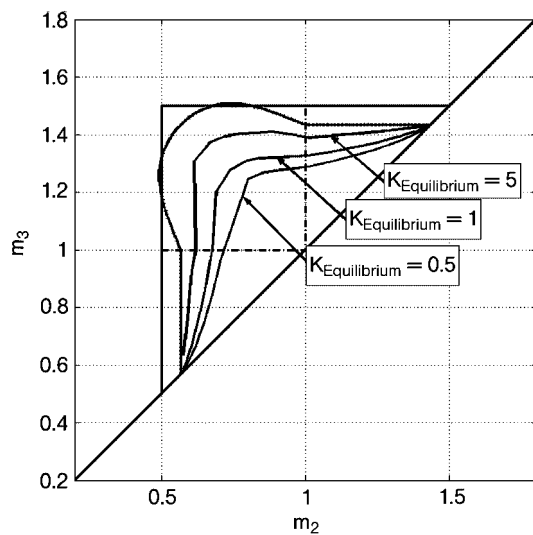


Fig. 6.14. Influence of the equilibrium constant value on iso-conversion lines at 90 %. $H_A = 1$; $H_B = 1.5$; $H_C = 0.5$; $Da_2 = Da_3 = 1$; $c_A^{\text{Feed}} = 1 \text{ g L}^{-1}$.

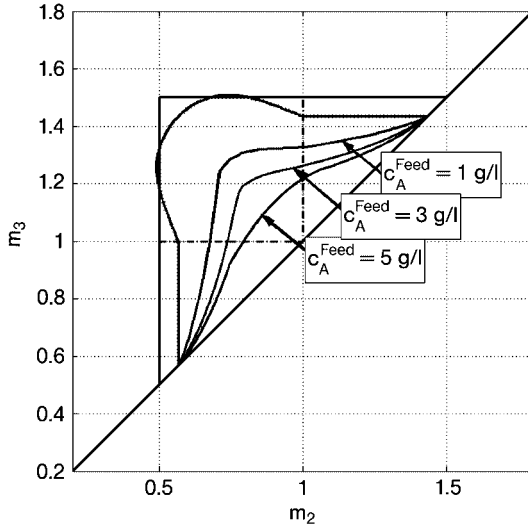


Fig. 6.15. Influence of reactant feed concentration on iso-conversion lines at 90 %. $H_A = 1$; $H_B = 1.5$; $H_C = 0.5$; $Da_2 = Da_3 = 1$; $K_{\text{Equilibrium}} = 1$.

Since the unit productivity is given by the product of the reactant feed concentration and the feed flow rate, the competing effect of an increasing reactant feed concentration and a decreasing feed flow rate, that is a decreasing difference $m_3 - m_2$, leads to a problem of optimization.

The impact of the Damköhler numbers and the value of H_A on the operating region is the same as discussed previously for the irreversible system. More details on this subject can be found in Ref. [16].

6.4

Modeling Simulated Moving-bed Reactors

The necessary degree of detail in the rigorous modeling of reactive chromatography in order to obtain good agreement between simulation and experiment depends of course on the considered system. For most systems, the following model has proved to be detailed enough in order to catch all important system properties.

The mass balance for a single column taking into account axial dispersion and mass transfer kinetics, as well as a change in fluid velocity because of the density change due to the reaction, yields:

$$\varepsilon^* \cdot \frac{\partial c_i}{\partial t} + \frac{\partial(u \cdot c_i)}{\partial z} = \varepsilon_b \cdot D_{ef} \cdot \frac{\partial^2 c_i}{\partial z^2} - (1 - \varepsilon^*) \cdot \left(\frac{\partial q_i}{\partial t} - v_i \cdot k_R \cdot f(\bar{c}_i) \right)$$

with u being the superficial fluid velocity and D_{ef} the effective axial dispersion coefficient. The mass balance for the solid phase, assuming a linear driving force for the mass transfer and a heterogeneously catalyzed reaction, gives:

$$\frac{\partial q_i}{\partial t} = k_m (q_i^{\text{eq}} - q_i) + \nu_i r$$

with q_i^{eq} being the equilibrium concentration given by the adsorption isotherm. The most commonly used equilibrium isotherms are certainly the so-called Langmuirian ones. The thermodynamically consistent Langmuir isotherm for a system with N components and an inert eluent is given by

$$q_i^{\text{eq}} = \frac{N \cdot K_i \cdot c_i}{1 + \sum_{j=1}^N K_j \cdot c_j}$$

with N being the saturation capacity and K_i the selectivity of component i . In practice, a saturation capacity N_i which is different for every component is often used in order to empirically improve accuracy. If the eluent is strongly adsorbable and all adsorption sites on the resin are saturated, the sum of $K_j \cdot c_j$ becomes large with respect to 1 and the stoichiometric adsorption isotherm is frequently used:

$$q_i^{\text{eq}} = \frac{N \cdot K_i \cdot c_i}{\sum_{j=1}^N K_j \cdot c_j}$$

For a higher accuracy of the isotherm, the activities in the liquid phase instead of the concentrations can be used. If a thermodynamic model for the computation of the solid-phase activities exists, the equilibrium concentration c_i and q_i can also be calculated from the condition of equal activity, as was done for example for the esterification of acetic acid on Amberlyst 15 using the Flory–Huggins activity model for the solid phase and a UNIFAC model for the liquid phase [17].

More details about isotherm models can be found in Ref. [18].

The reaction rate equations used in SMBR modeling are commonly of the power law type, and relate the reaction rate r_i of component i to its stoichiometric coefficient ν_i , to the reaction rate constant k_R , and to the solid-phase concentrations of the reactants and the products, q_R and q_P , respectively:

$$r_i = \nu_i \cdot k_R \cdot \left(\frac{\sum_j q_{R,j}^{\alpha_j} - \sum_m q_{P,m}^{\beta_m}}{K_{\text{Eq}}} \right)$$

with K_{Eq} being the reaction equilibrium constant and α_j and β_m empirical exponents for the reactants and the products, respectively. It is worth noting that α_j and β_m are identical with the stoichiometric coefficients if the stoichiometric equation represents the true mechanism of the reaction. The Arrhenius equation relates the reaction rate constant to the activation energy E and the temperature T :

$$k_R = k_{R,0} \cdot \exp\left(\frac{-E}{R \cdot T}\right)$$

In certain cases, the assumption of a pseudo-homogeneous catalytic mechanism might be valid [19], and the reaction rate equation would depend only on the concentrations in the liquid phase.

For a complete model of a SMBR unit, the model above describing a single-batch column can simply be repeated for each column in the unit, whilst adding the changes along the fluid path due to the inlet and outlet ports as well as the switching procedure [16].

6.5

Influence of the Stationary Phase Properties on SMBR Efficiency

In the following section, an example is discussed to illustrate how the most important stationary phase properties – namely, sorption selectivity, sorption capacity, and catalytic activity – affect the SMBR performance.

For this, the reaction of methanol and acetic acid to methyl acetate and water using the sulfonic ion-exchange resin Amberlyst 15 as a heterogeneous catalyst was chosen as a model system. Methanol was used as eluent. Several modifications of the original resin were obtained by removing a fraction of the sulfonic groups from the polymeric backbone. This partial desulfonation leads to a lower ion-exchange capacity, and whilst the original Amberlyst 15 has an ion-exchange capacity of 5 mEq $\text{H}^+ \text{g}^{-1}$ resin, the modified resins have capacities of 3.4, 2.4, 1.2, and 0.9 mEq $\text{H}^+ \text{g}^{-1}$ resin, respectively. For these different resins, extensive measurements were carried out in order to determine the adsorption and catalytic properties.

Using a Flory–Huggins and a UNIFAC model for the calculation of the solid- and liquid-phase activities, respectively, it was possible to determine the adsorptive properties as a function of the ion-exchange capacity of the resin [20].

A detailed SMBR model was used in order to optimize the unit with the objective function of minimal eluent requirement under the constraints of full conversion and complete product separation. Due to the reduced cost of these resins, the cost of this process is in fact controlled by the cost of the solvent recovery from the extract and raffinate streams.

The major motivation for investigating the desulfonated resins was the concept that a reduced concentration of sulfonic groups leads to a less-acidic resin and therefore to a lower adsorptivity of water which will in turn facilitate the resin regeneration in section 1 of the SMBR; hence, less eluent is needed per unit product. On the other hand, nonpolar components such as methyl acetate have better access to the

polymeric backbone and can adsorb more easily. The difference in adsorptivity between the two products methyl acetate and water is thus reduced, which complicates the separation of the two products, and so has a negative impact on the eluent requirement. Certainly, the catalytic activity of the resin reduces with a decreasing concentration of sulfonic groups, and so the residence time of the reactants must be increased in order to attain full conversion. The expected impact of these three competing contributions to the eluent requirement per unit product is illustrated qualitatively in Fig. 6.16.

In the particular case under examination here, using the flow rates in sections I to IV and the switching time as decision variables, the optimization yielded an optimal resin capacity of 4.3 mEq g^{-1} , assuming a molar fraction of 100 % acetic acid in the feed stream, as shown in Fig. 6.17.

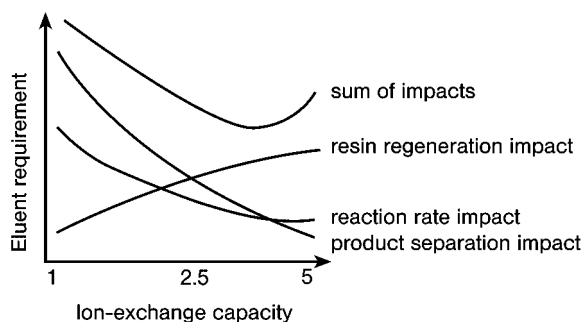


Fig. 6.16. Qualitative impact of changing ion-exchange capacities on eluent requirement.

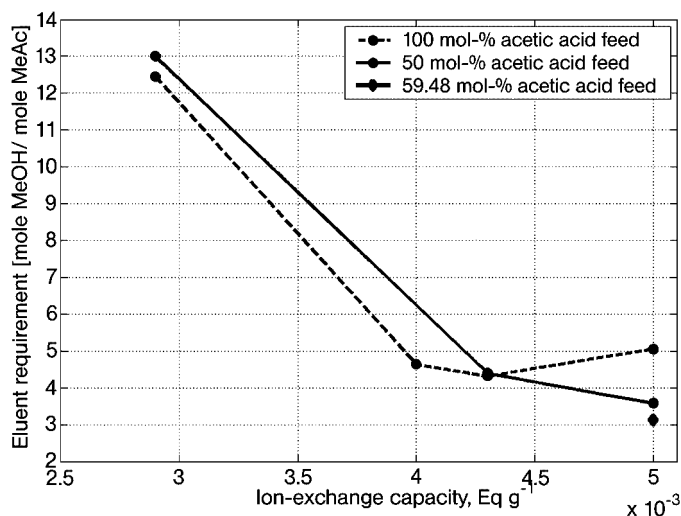


Fig. 6.17. Optimal ion-exchange capacity and feed concentration with respect to eluent requirement; segmentation 3-2-3-2.

For a stoichiometric feed concentration of acetic acid instead, the optimal resin capacity was calculated as 5 mEq g⁻¹, which is the original Amberlyst 15 resin. Further optimization, including also the feed concentration of acetic acid as a decision variable, yielded an eluent requirement of ca. 3 mol methanol per mol methyl acetate for a 5 mEq g⁻¹ resin and 60:40 acetic acid:methanol feed stream (Fig. 6.17).

The steep increase of the eluent requirement with decreasing resin capacity can be investigated in more detail by analyzing the key adsorptive and reaction parameters.

The key reaction parameter is clearly the reaction rate constant, which increases linearly with the ion-exchange capacity of the resin. Higher reaction rates clearly enhance SMBR efficiency and reduce eluent requirement.

As mentioned above, in each section of the SMBR, a specific task must be fulfilled and certain binary selectivities can be chosen as key adsorption parameters to explain the separation behavior in each section. In section I, the heavy product (water) must be desorbed by the eluent (methanol) from the ion-exchange resin, and therefore a low selectivity between water and methanol is desirable in order to reduce the methanol flow rate in this section as much as possible. In section IV, the light component (methyl acetate) is removed from the eluent stream, and consequently a low-selectivity methanol/methyl acetate is advantageous. In sections II and III, the products water and methyl acetate are separated and a high-selectivity water/methyl acetate is therefore beneficial. The selectivity of acetic acid to methyl acetate and the water/acetic acid selectivity should also be high in order to permit an easy separation of acetic acid from the products – which in turn allows the residence time of acetic acid to be increased and the conversion to be raised.

The influence of the ion-exchange capacity on these key binary selectivities is shown graphically in Fig. 6.18.

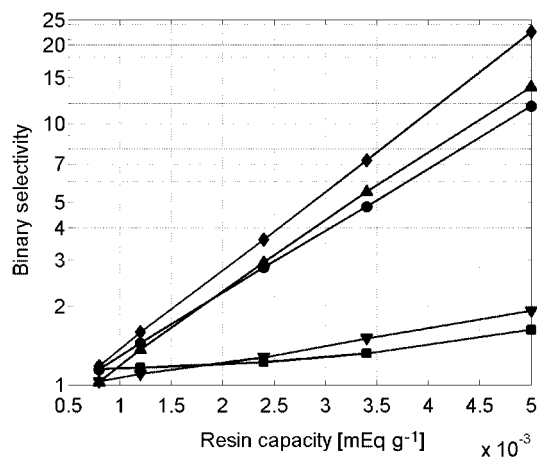


Fig. 6.18. Calculated binary selectivities as a function of ion-exchange capacity of the resin. ▼ = water/methanol; ◆ = water/methyl acetate; ■ = acetic acid/methyl acetate; ▲ = water/acetic acid; ● = methanol/methyl acetate.

While the selectivity of water/methanol is reduced slightly, and of methanol/methyl acetate strongly, with decreasing resin capacity, the key selectivities of water/methyl acetate and water/acetic acid decrease sharply as the resin capacity decreases.

The positive impact of easier resin and solvent regeneration in sections I and IV at lower resin capacities is, according to Fig. 6.17, clearly dominated by the negative impact of the strongly decreasing key selectivities in sections II and III.

6.6

Conclusion

The feasibility of combining chemical reaction and adsorption separation in a single unit has been discussed in this chapter. In particular, two units allowing continuous operation have been considered, namely annular reactive chromatography and simulated moving-bed reactors.

The first of these units is less efficient, but is very convenient for collecting multiple products, whereas the second unit has a higher efficiency due to the countercurrent movement of solid and liquid phase, but allows only two fractions to be collected. The use of approximate (equilibrium theory) and detailed models provides a reasonable approach to the optimal design of these complex units.

Several experimental systems have been outlined in which SMBR seems to represent a potentially competitive technology. In some cases (which have not been discussed here), initial analyses have been conducted at the laboratory pilot unit level, and the results have demonstrated good understanding of the behavior of these units, as well as their reliability. However, significant industrial use of SMBR units that which would identify them as an established technology (as with purely separative SMB) has not yet been reported, at least in the open literature. Nonetheless, it is expected that in future SMBRs will become increasingly competitive as improved functionalized resins are developed, including those with a tailored distribution of reactive and adsorptive groups along the particle diameter.

References

1. F. Lode, M. Houmard, C. Migliorini, et al., Continuous reactive chromatography. *Chem. Engng. Sci.*, **2001**, 56 (2), 269–291.
2. M. C. Bjorklund and R. W. Carr, Enhanced methanol yields from the direct partial oxidation of methane in a simulated countercurrent moving bed chromatographic reactor. *Indust. Engng. Chem. Res.*, **2002**, 41 (25), 6528–6536.
3. Z. Y. Zhang, K. Hidajat, A. K. Ray, Application of simulated countercurrent moving-bed chromatographic reactor for MTBE synthesis. *Indust. Engng. Chem. Res.*, **2001**, 40 (23), 5305–5316.
4. M. Kawase, A. Pilgrim, T. Araki, et al., Lactosucrose production using a simulated moving bed reactor. *Chem. Engng. Sci.*, **2001**, 56 (2), 453–458.
5. F. Lode, G. Francesconi, M. Mazzotti, et al., Synthesis of methylacetate in a simulated moving-bed reactor: Experiments and modeling. *AIChE J.*, **2003**, 49 (6), 1516–1524.
6. J. P. Meissner and G. Carta, Continuous regioselective enzymatic esterification in a simulated moving

- bed reactor. *Indust. Engng. Chem. Res.*, **2002**, 41 (19), 4722–4732.
7. Z. Y. Zhang, K. Hidayat, A. K. Ray, Multiobjective optimization of simulated countercurrent moving bed chromatographic reactor (SCMCR) for MTBE synthesis. *Indust. Engng. Chem. Res.*, **2002**, 41 (13), 3213–3232.
 8. G. Ströhlein, F. Lode, M. Mazzotti, et al., 2004, Design of Stationary Phase Properties for Optimal Performance of Reactive Simulated-Moving-Bed Chromatography. *Chem. Engng. Sci.*, in press.
 9. D. B. Broughton and C. G. Gerhold, 1961, Continuous sorption process employing fixed bed of sorbent and moving inlets and outlets, U.S. Patent 2,985,589.
 10. F. Lang, 2003, A continuous annular chromatographic reactor, PhD Thesis, ETH Zurich, Switzerland.
 11. K. Hashimoto, S. Adachi, H. Noujima, et al., A new process combining adsorption and enzyme reaction for producing higher-fructose syrup. *Biotechnol. Bioeng.*, **1983**, 25, 2371–2393.
 12. M. Mazzotti, G. Storti, M. Morbidelli, Optimal operation of simulated moving bed units for nonlinear chromatographic separations. *J. Chromatogr. A*, **1997**, 769 (1), 3–24.
 13. Z. Zhang, M. Mazzotti, M. Morbidelli, Multiobjective optimization of simulated moving bed and Varicol processes using a genetic algorithm. *J. Chromatogr. A*, **2003**, 989 (1), 95–108.
 14. C. Migliorini, M. Mazzotti, M. Morbidelli, Robust design of countercurrent adsorption separation processes: 5. Nonconstant selectivity. *AIChE J.*, **2000**, 46 (7), 1384–1399.
 15. G. Storti, M. Masi, S. Carra, et al., Optimal design of multicomponent countercurrent adsorption separation processes involving nonlinear equilibria. *Chem. Engng. Sci.*, **1989**, 44 (6), 1329–1345.
 16. F. Lode, M. Mazzotti, M. Morbidelli, Comparing true countercurrent and Simulated Moving-Bed chromatographic reactors. *AIChE J.*, **2003**, 49 (4), 977–990.
 17. M. Mazzotti, B. Neri, D. Gelosa, et al., Dynamics of a chromatographic reactor: esterification catalyzed by acidic resins. *Indust. Engng. Chem. Res.*, **1997**, 36, 3163–3172.
 18. G. Guiochon, S. Golshan-Shirazi, A. M. Katti, 1994, *Fundamentals of preparative and nonlinear chromatography*. Boston, Academic Press.
 19. W. Yu, K. Hidayat, A. K. Ray, Determination of adsorption and kinetic parameters for methyl acetate esterification and hydrolysis reaction catalyzed by Amberlyst 15. *Appl. Catal. A*, **2004**, 260 (2), 191–205.
 20. F. Lode, S. Freitas, M. Mazzotti, M. Morbidelli, 2004, Sorptive and catalytic properties of partially sulfonated resins. *Ind. Eng. Chem. Res.*, **2004**, 43 (11), 2658–2668.

7

The Dos and Don'ts of Adsorptive Reactors

David W. Agar

7.1

Introduction

7.1.1

Adsorptive Reactors

In adsorptive reactors an adsorbent is employed as a regenerative source or sink for one or more of the reacting species, thus enabling a modification of the concentration conditions within the reactor to enhance its performance. In a simple reversible reaction, for instance, the local adsorption of a reaction (by)product in a fixed bed comprised of catalyst and adsorbent serves to displace the equilibrium composition to higher conversions than would otherwise be attained (Fig. 7.1). Due to the progressive exhaustion of the adsorbent capacity, one observes two distinct reaction fronts: (i) a stationary equilibrium-limited purely catalytic reaction zone in the vicinity of the reactor inlet; and (ii) a dynamic downstream zone corresponding to the location of the adsorptive breakthrough front. It can be appreciated that neither of these fronts is especially sharp due to the decelerating reaction kinetics when approaching equilibrium on one hand and the protracted interaction between adsorption and reaction on the other hand. The almost quantitative conversions which can thus be achieved are of course of limited duration – sooner or later the propagating adsorptive reaction zone reaches the end of the reactor necessitating regeneration of the adsorbent after which the adsorptive–reaction cycle can be commenced anew.

Although most attention has been devoted to the task of equilibrium displacement through the (by)product removal just described [1], the incorporation of adsorption in chemical reactors can also be used to enrich reactants, either as an alternative technique to shift equilibria or to ensure complete conversion in irreversible reactions by providing local excess of one reactant [2]. In addition, adsorption can be exploited to sequester labile intermediates [3], thus avoiding unwanted consecutive reactions, or to intensify heat and mass transfer processes by enhancing local gradients [4], through acting as a local heat source for endothermic reactions, for example (Fig. 7.2).

7.1.2

Multifunctional Reactors

The term adsorptive or, more broadly, sorptively enhanced reactor [1] conventionally refers to heterogeneously catalyzed gas phase reactors in which only a single component is adsorbed macroscopically. Chromatographic reactors, on the other hand, involve liquid-phase systems with either homogeneous or heterogeneous catalysis and preferential rather than exclusive adsorption phenomena [5]. Although fundamental distinctions exist in the applications, configurations, modes of regeneration and the importance of heat effects, for example, the principles and underlying design equations of adsorptive and chromatographic reactors are identical. The adsorptive reactor is also closely related to the reverse-flow reactor, with its regenerative storage of heat rather than mass in a fixed bed, and to the membrane reactor, in

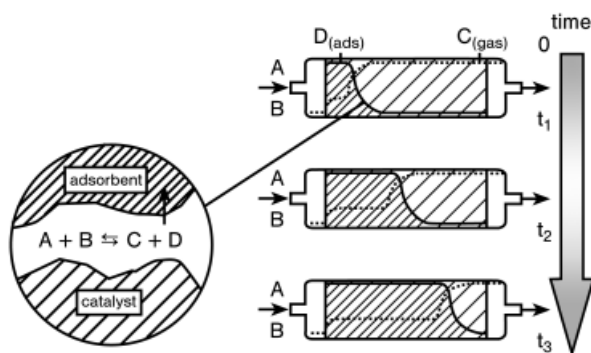


Fig. 7.1. Principle of an adsorptive reactor for enhancing conversion of an equilibrium-limited reaction.

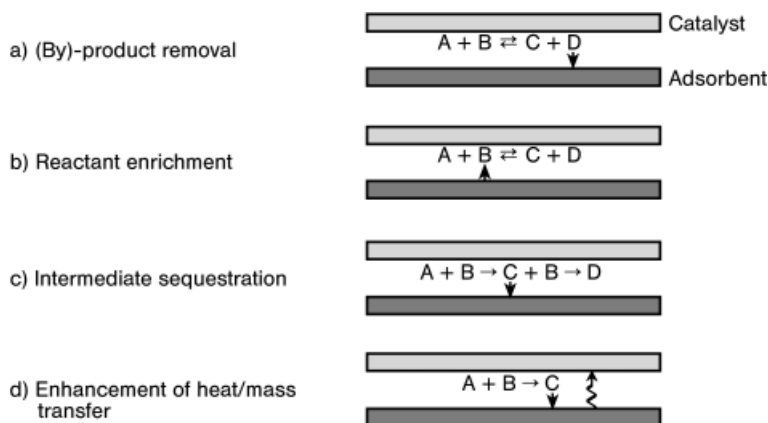


Fig. 7.2. Objectives of adsorptive reactors.

which specific components are recuperatively added to or withdrawn from the reaction medium along the length of the reactor. The latter relationship is similar to that between a countercurrent heat exchanger reactor and the asymptotic limit of a reverse flow reactor at short cycle times [6]. These analogies become apparent when one compares the concentration profile in an adsorptive reactor concept for the denitrification of flue gas with the temperature profile for a reverse flow reactor [7] or with a catalytic membrane reactor for the same purpose [8] (Fig. 7.3). Despite their various similarities, each class of reactor nevertheless exhibits its own strengths and weaknesses, as can be illustrated by a comparison of adsorptive and membrane reactors (Tab. 7.1).

7.1.3

Preliminary Evaluation

At first sight, adsorption and reaction are well-matched functionalities for integrated chemical processes. Their compatibility extends over a wide temperature range, and their respective kinetics are usually rapid enough so as not to constrain either process, whereas the permeation rate in membrane reactors commonly lags behind that of the catalytic reaction [9]. The phase slippage observed in extractive processes [10], for example, is absent and the choice of the adsorbent offers a powerful degree of freedom in the selective manipulation of concentration profiles that lies at the heart of all multifunctional reactor operation [11]. Furthermore, in contrast to reactive distillation, the effective independence of concentration and temperature profiles

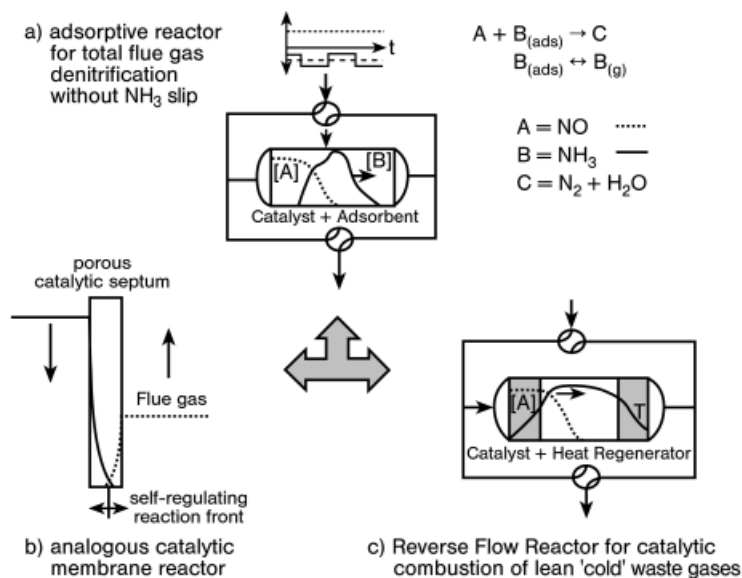
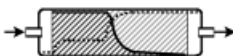
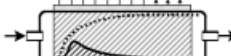


Fig. 7.3. Analogies between adsorptive, membrane and reverse-flow reactors for flue gas denitrification and oxidative catalytic waste gas treatment.

Table 7.1. The pros and cons of adsorptive and membrane reactors.

 <p>Adsorptive reactors</p> <ul style="list-style-type: none"> ↳ discontinuous operation ↳ adsorption rapid ↳ capacity vs. selectivity ↳ thermal regeneration ↳ no unwanted catalytic activity ↳ flushing ↳ cycle time 	 <p>Membrane reactors</p> <ul style="list-style-type: none"> ↳ continuous operation ↳ permeation sluggish ↳ permeability vs. permselectivity ↳ thermal driving force not feasible ↳ no unwanted catalytic activity ↳ sealing ↳ operating life
---	--

should also facilitate process integration. However, the need for periodic adsorbent regeneration in an expedient manner that does not adversely effect overall performance, together with the inherently discontinuous operation this entails, represent less favorable aspects of adsorptive reactors, as do the need for large adsorptive capacities to provide reasonable cycle times, distortions introduced by the accompanying unsteady-state heat effects and the tendency to enhance unwanted side reactions, especially of the adsorbate with its high retention times within the reactor.

7.2

Reaction Systems

Closer inspection reveals that this somewhat superficial and largely self-evident evaluation is by no means exhaustive, and concrete experimental studies on adsorptive reactors expose both additional pitfalls and benefits that are often specific for a particular reaction system and decisive for the success or otherwise of adsorptive reactor concepts. Before illustrating this point with the help of four examples with which the author is personally acquainted – the Claus reaction, the direct hydrogen cyanide synthesis from ammonia and carbon monoxide and, to a lesser extent, the water-gas shift reaction and the Deacon process – it is worthwhile briefly reviewing other reaction systems for which the potential of adsorptive reactors has been examined (Tab. 7.2).

Three groups – those of Alpay, Rodrigues and Sircar – deserve special mention for their considerable contributions to the development of adsorptive reactors over the past decade [1, 25–29]. The emphasis on the challenge of insitu CO_2 capture in connection with hydrogen production and the predominance of pressure swing regeneration concepts is also noteworthy. The preference for the adsorption of simple stable molecules is explained by the fact that the adsorptive capacities tend to be higher and the susceptibility for the adsorbate to undergo reaction lower. The modeling studies carried out are mostly concerned with the numerical solution of conventional, and usually isothermal, reactor design equations which have been expanded to include an

Table 7.2. Reaction systems studied for adsorptive reactors.
The adsorbed species is underlined in the reaction equations.

[12] $\text{CO} + 2\text{H}_2 \rightleftharpoons \text{CH}_3\text{OH}$	[18] $\text{VOC} + \text{O}_2 \rightarrow \text{CO}_2 + \text{H}_2\text{O}$
[2] $2\text{NH}_3 + 2\text{NO} + \frac{1}{2}\text{O}_2 \rightarrow 2\text{N}_2 + 3\text{H}_2\text{O}$	[19] $2\text{HCl} + \frac{1}{2}\text{O}_2 \rightleftharpoons \text{Cl}_2 + \text{H}_2\text{O}$
[13] $\text{CO} + \frac{1}{2}\text{O}_2 \rightleftharpoons \text{CO}_2$	[20] $\text{CH}_2\text{:CHCH}_2\text{CH}_3 \rightleftharpoons \text{CH}_2\text{:CHCH:CH}_2 + \text{H}_2$
[14] $\text{C}_6\text{H}_{12} \rightleftharpoons \text{C}_6\text{H}_6 + \text{H}_2$	[21] $\text{NH}_3 + 2\text{CO} \rightleftharpoons \text{HCN} + \text{CO}_2 + \text{H}_2$
[15] $2\text{CH}_4 + \text{O}_2 \rightarrow \text{C}_2\text{H}_2 + 2\text{H}_2\text{O}$	[22] $2\text{H}_2\text{S} + \text{SO}_2 \rightleftharpoons \frac{3}{8}\text{S}_8 + \text{H}_2\text{O}$
[16] $\text{CO} + \text{H}_2\text{O} \rightleftharpoons \text{CO}_2 + \text{H}_2$	[23] $\text{C}_6\text{H}_{11}\text{CH}_3 \rightleftharpoons \text{C}_6\text{H}_5\text{CH}_3 + 3\text{H}_2$
[1] $\text{CO}_2 + \text{H}_2 \rightleftharpoons \text{CO} + \text{H}_2\text{O}$	[24] $2\text{C}_3\text{H}_6 \rightleftharpoons \text{C}_2\text{H}_4 + \text{CH}_2\text{CH}=\text{CHCH}_3$
[17] $\text{CH}_4 + 2\text{H}_2\text{O} \rightleftharpoons \text{CO}_2 + 4\text{H}_2$	

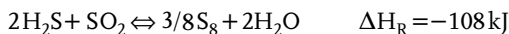
adsorptive term. Details of adsorbent regeneration and overall cycle performance are seldom addressed, and asymptotic analytical solutions corresponding to those for reverse flow reactor operation remain to be derived. Many nominally adsorptive reactors actually involve gas–solid reactions rather than adsorption, which exhibit different behavior due to the independence between “adsorbate” loading and “adsorptive” partial pressure. Understandably, for a technology still to achieve a technical breakthrough, investigations have concentrated on the development of suitable adsorbents and the demonstration of the fundamental feasibilities of various concepts.

7.2.1

The Claus Process

The study of adsorptive reactors for the Claus process represents a departure from most previous studies in that the equilibrium position is already well on the product side, with a conversion of 93 % being achievable for isothermal operation of gas with 10 mol % H_2S without additional measures [30]. The need to attain conversions in excess of 99.5 % to ensure that the residual sulfur emissions meet environmental specifications [31] nevertheless makes the reaction system an interesting candidate for adsorptive equilibrium displacement.

The (simplified) reaction equation:



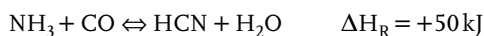
reveals the greater sensitivity of the equilibrium composition, as reflected in the law of mass action, to the removal of the water of reaction rather than the interstage or in-situ condensation of sulfur traditionally practiced, in the cold-bed adsorption (CBA) “Sulfreen” process for example. The withdrawal of water within the reactor thus has the potential to reduce the number of reaction stages required without the complications of sulfur condensation within the reactor – catalytic deactivation for instance – and perhaps obviate the need for a costly treatment of the tail gases that would otherwise be necessary. The adsorptive removal of water can be carried out above the sulfur dew point of typically 230 °C or so, thus inverting the sequence in which the products would normally condense (Fig. 7.4).

A simple tandem reverse-flow reactor scheme has been proposed for this purpose [11] (Fig. 7.5). By condensing the sulfur formed in the reactor outlet and reheating the residual anhydrous inert gas stream, one obtains a thermally efficient integration of the elutive adsorbent regeneration into the reactor operation. The arrangement depicted represents an “adsorptive” equivalent to the reverse-flow reactor with removal of a hot side-stream [6].

7.2.2

Direct Hydrogen Cyanide Synthesis

The second reaction used to illustrate various features of adsorptive reactors is the direct synthesis of hydrogen cyanide from ammonia and carbon monoxide:



This overall reaction is already carried out industrially via the intermediate formamide (HCONH_2) which, together with the use of disparate operating conditions (high pressures and mild temperatures for formamide synthesis, vacuum and high temperatures for its decomposition), overcomes the unfavorable thermodynamics of

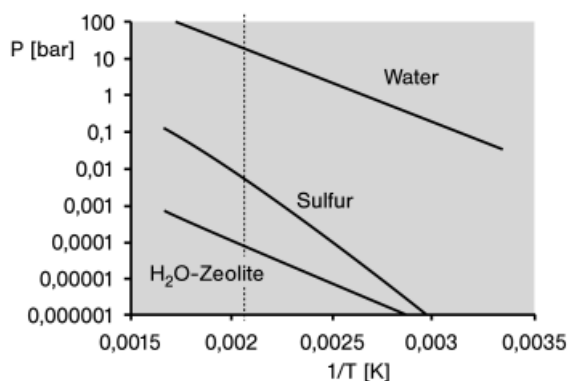


Fig. 7.4. Comparison of sulfur and water vapor dew points with an adsorptive separation of water vapor on 3A zeolite (the dotted line indicates the Clausius reaction temperature).

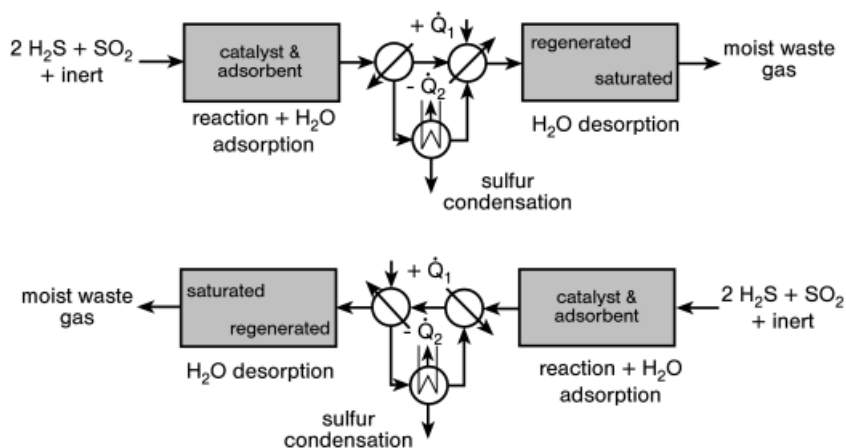


Fig. 7.5. Tandem reactor concept for single-stage, high-conversion Claus process with integrated elutive regeneration.

the direct reaction (equilibrium conversion $< 3\%$) (Fig. 7.6). The disadvantageous equilibrium position for a simpler single-stage process cannot be ameliorated to any real extent by using other techniques for enhancing product formation, such as excess of one reactant, or operation at other temperatures and pressures. Unfortunately, at the temperatures at which known catalysts are active for this reaction ($> 400\text{ }^{\circ}\text{C}$), the adsorption of the water of reaction is no longer an option. It is thus necessary to reformulate the adsorptive reaction problem by introducing a secondary reaction, for example the water-gas shift reaction [30]:



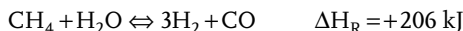
which also takes place on the catalysts used (mixed iron and chromium oxides). By supplying additional carbon monoxide one can thus reactively consume the water of reaction and the equilibrium position of the supplementary reaction, and thus indirectly the main reaction too, can be displaced to higher conversions by incorporation of CO_2 adsorption, which is feasible at the prevailing reaction temperatures. In actual fact, the exact mechanism of HCN synthesis, which may result from a direct reaction between one molecule of ammonia and two molecules of carbon monoxide, is not known, but so long as carbon dioxide adsorption can be exploited to shift the equilibrium position of the overall reaction this is immaterial.

In addition to the much higher temperatures needed, this reaction is also more challenging than the Claus process with respect to the greater demands placed on adsorbent selectivity in the presence of another weak(er) acid (HCN) and the importance of an unwanted side-reaction ($2\text{CO} \rightleftharpoons \text{C} + \text{CO}_2$ $\Delta H_{\text{R}} = -172 \text{ kJ}$) which is also encouraged by CO_2 removal.

7.2.3

Water-gas Shift Reaction

The removal of carbon dioxide from the product gases of methane steam reforming and the subsequent shift reaction:



in the context of hydrogen generation remains very much the “holy grail” of adsorptive reactor research, especially in light of the renewed interest that this process has attracted in connection with fuel cell applications. Traditionally, hydrogen production is increased by the thermally extravagant technique of using three to four times the stoichiometric amount of steam. Even so, the unfavorable equilibrium of the water-gas shift reaction makes it necessary to employ two reaction stages operated at different temperatures (450 and 250 °C) and the residual levels of around 3000 ppmV CO must still be reduced to the < 100 ppmV specified using the catalytic processes of methanation or preferential oxidation, in which almost perfect catalytic selectivities are required to prevent unwanted hydrogen consumption under the

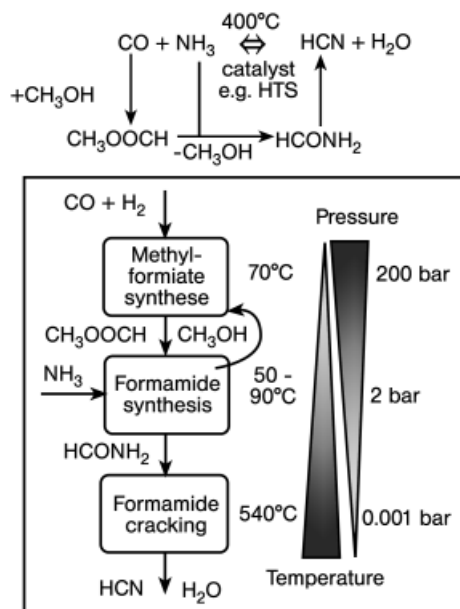


Fig. 7.6. Scheme for the direct and indirect synthesis of hydrogen cyanide from ammonia and carbon monoxide.

prevailing concentration conditions – that is, in the presence of a large excess of the competing reactants carbon dioxide and hydrogen respectively [32] (Fig. 7.7).

An adsorptive reactor with integrated carbon dioxide removal has the potential to achieve the desired hydrogen product purity in a single reaction step and at one temperature level (Fig. 7.7) – a dramatic simplification of the conventional technology used in ammonia synthesis gas production for example. The task of CO_2 capture is rendered more difficult than in the case of HCN synthesis by the need to avoid the uptake of the reactant steam. Despite extensive research, most studies in this area have largely foundered on two issues: (i) the necessity for thermal regeneration with large temperature swings to release the tightly bound carbon dioxide from the mostly chemically based CO_2 scavengers; and (ii) the need to reconcile the often-conflicting demands on the “adsorbent” for consistently rapid adsorption kinetics and high adsorptive capacities, in order to ensure compact reactors and reasonable cycle times.

The use of an adsorptive reactor operation with reactant enrichment, in which adsorption is used to maintain a high level of excess steam within the catalytic reaction zone, has attracted comparatively little attention.

7.2.4

The Deacon Process

The Deacon process for the heterogeneously catalyzed oxidation of hydrogen chloride to chlorine at around 350°C represents an energetically and possibly

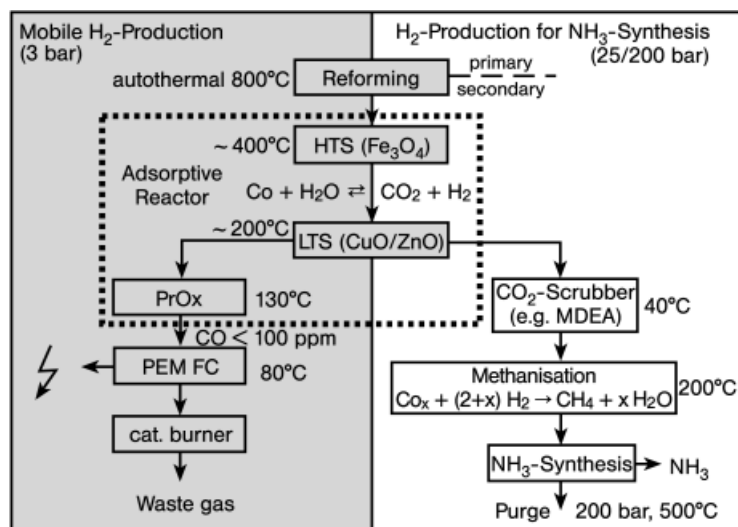
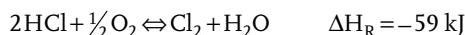
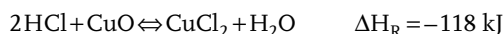


Fig. 7.7. Flowsheet for the production of hydrogen from methane for ammonia synthesis and fuel cell applications indicating the potential for rationalization using an adsorptive reactor.

economically advantageous alternative to electrolysis for internally recycling chlorine in integrated chemical plant complexes [19]. The equilibrium limitation of conversion at a maximum value of around 85 % entails a complicated downstream processing with corrosion-resistant materials to separate off chlorine and recycle unconverted hydrogen chloride. By resolving the net reaction:



into two constituent partial reactions: an “adsorptive” chlorination of the copper oxide-based catalyst and its subsequent oxidative “regeneration”:



one can overcome the equilibrium restriction achieving complete conversions and thus simplify both product recovery and corrosion problems. Once again, the actual reaction mechanism is almost certainly more complicated, involving basic oxychlorides and cupric-cuprous transitions, but this is of only limited relevance for the adsorptive reactor concept.

This unsteady-state Deacon process clearly involves gas–solid reaction rather than true adsorption, and differs from the previous examples in that the product is formed in the chemical regeneration step. Even so, adsorption plays a crucial role in this process, which can also be used to illustrate the challenges of integrating the catalytic and “adsorptive” functionalities within a single pellet, with the demands that this places on both the active solid-phase components and its support material, and the need to adapt both “catalyst” and reactor to multifunctional reactor operation. Furthermore, the questions that arise concerning thermal integration between the exo- and endothermic half-cycles and the usefulness of partial loading and regeneration strategies in optimizing the overall process performance are of general validity for adsorptive reactors.

7.3

Catalyst and Adsorbent

7.3.1

The Claus Process

Initial experimentation aimed at demonstrating the principle feasibility of the appealingly simple adsorptive Claus process concept described in the previous section yielded promising results indicating excellent harmonization between the catalytic and adsorptive processes for a commercial titanium oxide-based catalyst and a 3A zeolite adsorbent, respectively [30]. The amounts of water vapor adsorbed

at the reaction temperature (c. 10 wt%) are modest, but sufficient to ensure reasonable cycle times of 10 min or longer, and the more or less linear isotherm facilitates the elutive regeneration process envisaged. Molecular sieve phenomena guarantee that only water – the smallest molecule present – is taken up by the adsorbent to any extent. Catalytic selectivities were also adequate to prevent adsorptive distortions in the concentration profiles inducing undesirable side reactions, such as the formation of carbonyl sulfide with the “inert” CO_2 present in the feedstock ($\text{CO}_2 + \text{H}_2\text{S} \rightleftharpoons \text{COS} + \text{H}_2\text{O}$).

Less welcome were the discrepancies introduced by the different rates and capacities for the adsorption of the reactants hydrogen sulfide and sulfur dioxide on the catalyst, which were brought to light by the apparent contradiction between an almost complete conversion of the hydrogen sulfide over a period of almost an hour and a less than perfect value of around 95 % for sulfur dioxide, despite the exact stoichiometry of the adsorptive reactor feed [33]. Further investigations led to the hypothesis that this behavior results from chromatographic separation of the reactants on the catalyst (Fig. 7.8). In retrospect perhaps this is not surprising when one considers that sulfation of this catalyst a well-known phenomenon. This represents a fundamental dilemma for adsorptive reactors: catalytic adsorption is a prerequisite for the reaction to take place, but under the inherently unsteady-state conditions unavoidable differences in reactant adsorption on the catalyst mean that deviations from the stoichiometric ratios arise that can actually hinder conversion. The fact that this flaw so clearly exposed by the Claus reaction and has not been reported elsewhere is no accident; it is due to the importance of only slight deviations from

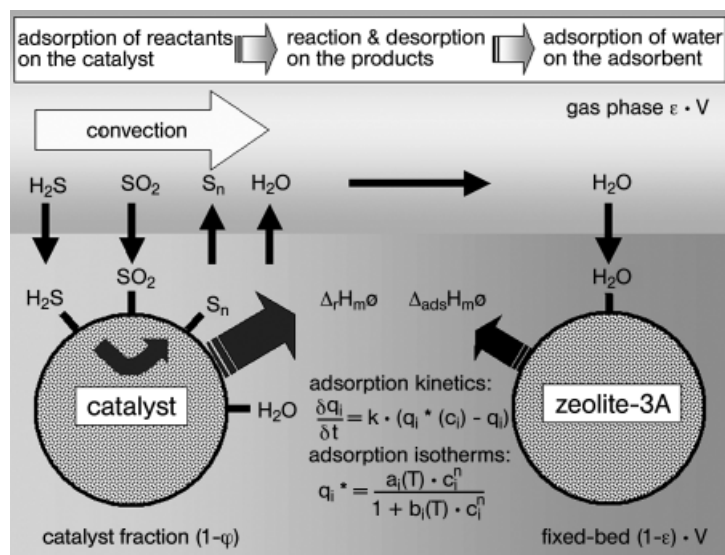


Fig. 7.8. Adsorption of reactants and products on catalyst and adsorbent in the adsorptive Claus process.

stoichiometric compositions at the extremely high conversions being sought. Although countermeasures are available (see Section 7.5.1), the apparently paradoxical fact that catalytic adsorption can be bad for adsorptive reactors needs to be more widely appreciated.

7.3.2

Direct Hydrogen Cyanide Synthesis and Water-gas Shift Reaction

In the case of the direct HCN synthesis and water-gas shift reactions, the temperature range of interest for adsorptive reactor operation (i.e., $> 350^\circ\text{C}$) lies at the upper limit at which chemisorption be used effectively. If the temperatures are much higher, one is forced to use gas–solid reactions to attain reasonably high “adsorptive” capacities at the cost of a more demanding regeneration procedure. Whereas the partial pressure over an adsorbent depends on both its temperature and the adsorbate loading, the dissociation pressure above a decomposing solid is a function of the temperature alone (Fig. 7.9). A reduction in the partial pressure of the adsorptive at a given temperature will thus merely result in a diminished loading for an adsorbent but the complete breakdown of a solid compound with which it was previously in equilibrium, and vice versa, leading to the development of completely different breakthrough front structures.

A modified hydrotalcite adsorbent (magnesium aluminum hydroxycarbonate $\text{Al}_2\text{Mg}_6(\text{OH})_{16}\text{CO}_3 \cdot 4\text{H}_2\text{O}$) doped with potassium carbonate to enhance its alkalinity has been proposed for carbon dioxide capture at temperatures of around 400°C [34, 35]. By preparing this material according to a published recipe [36], we were able to demonstrate that the kinetics of CO_2 adsorption are adequate to keep pace with the rate of the water-gas shift reaction. A major drawback is, however, the extremely low loading capacity of $< 2\text{ wt}\%$. Although we only achieved around half of the published values for the commercial product, even these would be incapable of providing cycle times of more than a few minutes at the space times characteristic

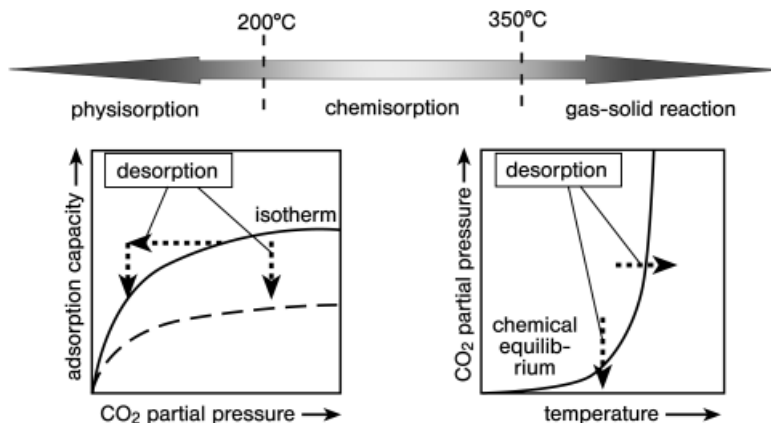
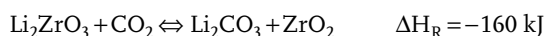


Fig. 7.9. Comparison of adsorption and gas–solid reaction.

of catalytic reactors. As a consequence, the adsorptive reactor concept becomes unwieldy due to the large amounts of adsorbent required. For example, in the case of a typical 50-kW automotive fuel cell application, a cycle time of 20 min would necessitate the use of around 35 L of the hydrotalcite adsorbent! [37]. As thermal regeneration processes are relatively slow due to the high thermal inertia of the fixed bed and the reactor construction, rapid cycling processes are not an option.

The selectivity of modified hydrotalcite material for carbon dioxide with respect to water vapor (an important prerequisite for the water-gas shift reaction) was good, but it adsorbed large quantities of HCN, even though carbon dioxide is the more acidic component, making it wholly unsuitable for the direct HCN synthesis, especially as it subsequently proved impossible to recover the adsorbed HCN as such [21].

Moving on to gas–solid reactions for CO₂ capture, magnesium oxide can be rejected due to the lability of the corresponding carbonate and the greater stability of its hydroxide, while the old chestnut of calcium oxide requires temperatures in excess of 750 °C to regenerate the carbonate (Fig. 7.10). There are, nevertheless, other solid materials which can form carbonates in the temperature window of interest and be regenerated at lower temperatures of around 600 °C, for example lithium zirconate [38] which can theoretically adsorb 22.3 wt% CO₂:



Our own studies with lithium zirconate have demonstrated the critical importance of the ratio between the lithium salts and zirconia used in its preparation [21]. Further, it appears that the reaction is strongly inhibited by the superficial formation of solid products curtailing capacity and impairing kinetics to the point where characteristic adsorption times are measured in hours rather than the seconds necessary. Very slow rates of CO₂ adsorption can also be observed in the early published data on lithium zirconate and, while some progress has been made [39], developing a

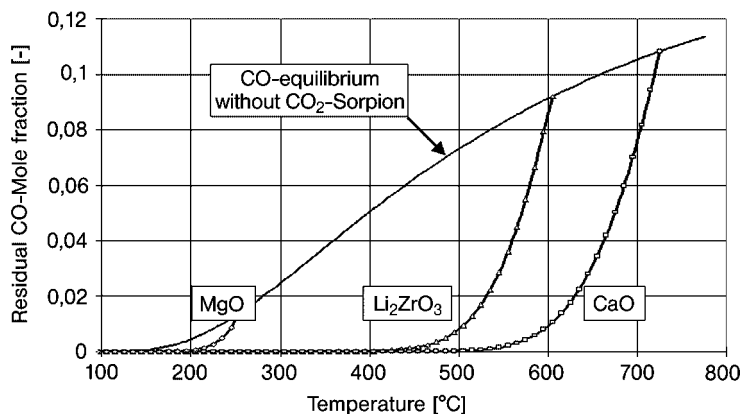


Fig. 7.10. Temperature ranges for carbon dioxide adsorbents in the water-gas shift reaction.

suitable method of preparation to provide rapid kinetics represents a research project in its own right.

To summarize, no panacea is presently visible on the horizon for high-temperature CO₂ capture: all adsorbents proposed to date suffer from either low capacities, slow adsorption rates, poor selectivities, or impractical regeneration procedures. The catalyst also exhibits its share of problems. The high-temperature shift catalyst, which also proved to be a promising candidate for the direct HCN synthesis, deactivates when exposed to a severely reducing environment for too long a period (Fig. 7.11) [21]. The adsorptive removal of carbon dioxide from the reaction medium modifies the prevailing redox conditions in this direction, and thus exacerbates the loss of activity. Finally, it proved impossible to suppress the undesirable Boudouard reaction, in which carbon monoxide disproportionates to carbon dioxide and coke, kinetically. This reaction is of course also encouraged by insitu adsorptive CO₂ removal and leads to both loss of feedstock and catalytic deactivation through coking.

Whilst the enhancement of unwanted side reactions through excessive distortion of the concentration profiles is an effect that has been reported elsewhere (e.g., in reactive distillation [40] or the formation of acetylenes in membrane reactors for the dehydrogenation of alkanes to olefins [41]), the possible negative feedback of adsorption on catalytic activity through the reaction medium composition has attracted less attention. As with the chromatographic distortions introduced by the Claus catalyst, the underlying problem arises because the catalyst is being operated under unsteady-state conditions. One could modify the catalyst to compensate for this, but the optimal activity over the course of the whole cycle would be comprised as a consequence.

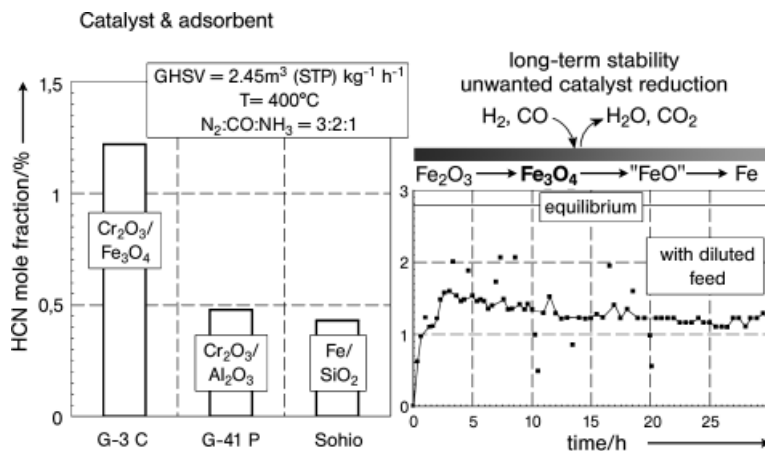


Fig. 7.11. Catalytic activities and deactivation in the adsorptive direct synthesis of hydrogen cyanide due to unfavorable redox conditions.

7.3.3

The Deacon Process

The active phase of the Deacon catalyst is usually assumed to be a complex melt of copper or chromium and alkaline metal chlorides under reaction conditions, which is distributed within the pore network of an inert carrier [42]. Such supported liquid-phase catalysts (SLPC) are eminently suitable for “adsorbing” large amounts of the reacting components as sorption takes place in a bulk phase and is not restricted to only a limited number of suitable surface sites. The periodic expansion and contraction of the melt as a result of (de)sorption imposes considerable strains on the carrier structure; hence, special mechanically robust support materials are needed to withstand such strains and prevent the catalyst crumbling away and disintegrating after a few cycles. In addition, even when it is immobilized on the carrier, the melt is extremely aggressive and resistant materials must be used for reactor construction. Due to the volatility of some of the chlorides present the temperature must be maintained below 400 °C, which limits the scope for accelerating the rate-limiting oxidative regeneration step by increasing the temperature [19]. For the unsteady-state adsorptive Deacon process the catalyst composition had to be modified to reduce volatility and enhance the oxidative of the reaction phase.

The most critical problem to be solved was that of unwanted HCl adsorption (!) on the catalyst carrier, since this resulted in the liberation of unconverted HCl in the regeneration phase and the resulting adsorptive HCl “slip” contaminated the chlorine product, thus nullifying the intended simplification of downstream processing. The use of non-oxide ceramics (e.g., silicon carbide) as supports, which were also expedient by virtue of their greater mechanical strength, suppressed HCl adsorption on the carrier to negligible levels and thus avoided the difficulties described.

7.3.4

Other Adsorptive Catalysts

In view of the shortcomings of catalysts and adsorbents that have been reviewed in this section, it seems amazing that several catalyst systems exist where adsorptive phenomena are exploited, albeit often unconsciously. In the area of automotive exhaust treatment, for example, the three-way catalyst incorporates ceria as an oxygen storage medium to help alleviate short-term deviations from the critical lambda value [43]. More recently, NO_x storage catalysts containing barium carbonate have been developed for diesel and lean-burn engines, in which NO is catalytically oxidized and stored as barium nitrate within the catalyst to await subsequent destruction in a periodic catalytic reduction phase under rich conditions [44]. It is interesting to note that surface inhibition effects similar to those conjectured for lithium zirconate have also been encountered in such systems [45].

The inherent ability of selective catalytic reduction (SCR) catalysts for stack gas denitrification to store ammonia adsorptively can be exploited with appropriate control algorithms to damp out the influence of fluctuations in the amount of gas and level of nitrogen oxides being treated. Moreover, it also forms the basis of the adsorptive reactor concept for the total denitrification of flue gases without ammonia

slip referred to in Section 7.1.2. The inclusion of grains of hydride-forming alloys, such as LaNi_5 in hydrogenation catalysts for slurry reactors, has been proposed as means of preventing local hydrogen deficiencies due to poor hydrodynamics adversely affecting selectivity in multistep hydrogenations [46]. This is analogous to the oxygen storage function of ceria in the three-way catalyst. Finally, the widespread “spillover” phenomena [47] between supports and active sites can also be considered as instances of adsorptive catalysis in the broadest sense of the term.

What these successful and sometimes serendipitous applications of adsorptive catalysts have in common are the low concentrations of reactants and short “cycle times”, which mean that relatively small amounts of material have to be adsorbed. The integration of the adsorptive functionality does not therefore really interfere with the catalytic activity. The objective is primarily to ensure high performance in the presence of the fluctuating concentrations and flows that often characterize end-of-pipe treatment stages.

7.4

Reactor and Regeneration

A variety of fixed- and fluidized-bed reactors configurations can be used as adsorptive reactors (Fig. 7.12).

7.4.1

Fixed-bed Reactors

Adsorptive reactor configuration is mainly dictated by the cycle time, which in turn is determined by the adsorptive capacity. For high-capacity systems, with cycle times of 10 min or longer, simple multiple fixed-bed arrangements suffice, in which individual reactors are periodically taken off-line and regenerated when performance deteriorates due to adsorbent exhaustion. The total number of beds is designed to ensure continuous operation, and the ratio of the number of reactors in the productive and regenerative phases depends on their relative duration, together with any intermediate purging steps that may be necessary. For shorter cycle times of just a few minutes, one can employ rotating-bed arrangements in which the catalyst and adsorbent pass through separate reactive and regenerative zones. In terms of their design equations, these two configurations are virtually indistinguishable, and the analogies even extend down to operational features – for example, the need for a flushing period for periodically switched fixed-beds has its counterpart in the unavoidable slight leakages between the zones in rotating beds.

For even shorter cycle times the use of mixed fixed-bed systems demands a greater mechanical complexity. An example of this is the Pulsar rapid cycle pressure swing adsorption technology developed by QuestAir [48], which has been applied to adsorptive oxygen enrichment and hydrogen purification. For such high-frequency operation an especially low-dispersion adsorbent is mounted on compact rotors which are integrated into hybrid compressor/vacuum pump equipment with precisely synchronized switching valve arrangements.

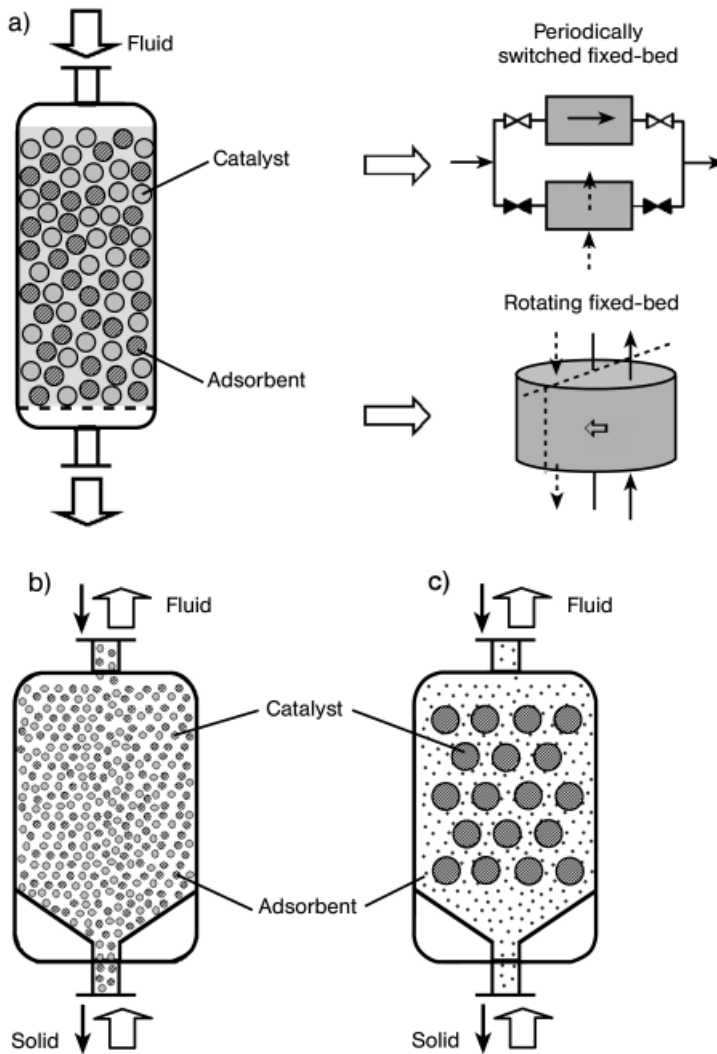


Fig. 7.12. Adsorptive reactor designs. a) Fixed-beds; b) moving beds and c) fluidized beds.

7.4.2

Fluidized-bed Reactors

Alternatively, one can resort to the use of moving- or fluidized-bed systems in which the adsorbent, and sometimes also the catalyst, is continuously withdrawn from the reactor to undergo an external regeneration. Ideally, one tries to achieve countercurrent adsorbent flow pattern to optimize utilization of the adsorptive capacity. The major problems of such arrangements are those of solids handling (e.g., gas-tight

introduction and removal of solids to and from the reactor), prevention of blockages, abrasion, and electrostatic phenomena. The challenges are greater still when the adsorbent and catalyst constitute distinct solid phases which must be classified, for example on the basis of particle size, or function independently as mobile and stationary phases. One of the very first adsorptive reactors – the gas–solid–solid-trickle flow reactor proposed for methanol synthesis [12] – belongs to this category, as does a fluidized-bed configuration for the unsteady-state Deacon process [49]. The extra mechanical demands placed on the adsorbent and catalyst, in addition to the chemical and physical criteria described in the preceding section, usually make the realization of such adsorptive reactors a less attractive option.

The simulated moving-bed (SMB) reactor arrangements [5], that are so popular for chromatographic reactors, in which the movement of adsorbent and catalyst is achieved by progressively switching inlet and outlet ports along a sequence of four or more fixed beds, plays a less central role for adsorptive reactors. One reason for this is that SMB operation implicitly involves the use of elutive regeneration (see Section 7.4.3), which is inappropriate for many adsorptive reactors. Another reason is the tighter adsorptive selectivity, which makes multistage operation less attractive.

In view of the extensive number of publications on the subject of adsorptive reactors (see Tab. 7.2), the neglect with which regeneration processes have been treated is surprising and short-sighted, since it is this section of the cycle and its expedient integration in the overall process that often holds the key to success.

Four basic regenerative procedures – or hybrids thereof – can be used in conjunction with adsorptive reactor operation: pressure swing, temperature swing, elution, and reaction.

7.4.3

Pressure Swing Regeneration

Pressure swing processes can draw on the considerable experience available with separation technology in this area, provide rapid regeneration, and also lend themselves to situations in which the reaction is carried out under pressure, as the work that otherwise must be invested in compression or evacuation may become a critical factor. Fixed-bed systems must be designed to ensure that the pressure drop does not impede the efficacy of regeneration, and multi-step depressurization–pressurization cycles with inert and product purges can often be employed to advantage (Fig. 7.13) [1]. Elutive processes are similar in that adsorbent regeneration is carried out by a drop in partial rather than absolute pressure. Their main disadvantage is the often large amount of sweep gas comprising inert eluent and the adsorptive that arises in the regeneration, and which may require further processing. For this reason, elutive processes are of interest when a valueless byproduct such as water vapor or carbon dioxide is being desorbed and when an inert eluent is available within the process, as for example in the case of the Claus process (see Section 7.2.1).

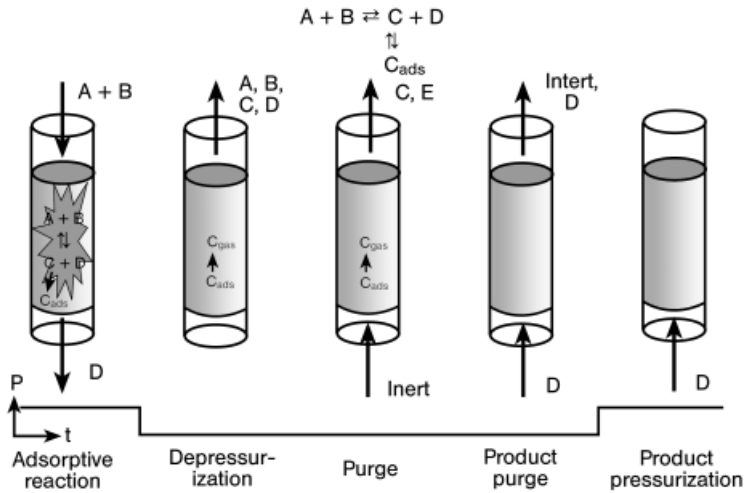


Fig. 7.13. Schematic sequence of pressure swing operation for an adsorptive reactor (from Ref. [1]).

7.4.4

Temperature Swing Regeneration

Temperature swing regeneration is usually much slower than the pressure swing or elutive processes due to the need to overcome the thermal inertia of the reactor system and the limitations imposed on introducing heat into it. Furthermore, at the intermediate temperatures used in adsorptive reactors, high-temperature heat sources, not always available within the process itself, are required. This means that thermal regeneration is largely confined to adsorptive reactors with long cycle times, with process internal heat sources or fluidized beds. Many of the temperature swing processes proposed for CO₂ capture fail to meet these basic criteria. Microwave heating [50] mitigates the unwanted effects of temperature gradients and enables a degree of fractionation through the controlled desorption process, but requires special designs to give uniform penetration and introduce large amounts of heat. Electric swing processes which have been proposed in connection with CO₂ sequestration remain an interesting, but as yet unproven, technology [51].

7.4.5

Reactive Regeneration

The suitability of regenerating the adsorbent by reactive means can only be judged on a case-by-case basis. With some adsorptive reactors – for example, for the total denitrification of flue gases or the unsteady-state Deacon process – the reactive regeneration is the object of the exercise. The prerequisite that the adsorbate does not undergo further reaction and is adsorbed in reasonable amounts at moderate temperatures means that the molecules being adsorbed tend to be small and stable, and thus do not lend themselves to reactive regeneration.

Displacement desorption, in which the adsorbate is driven off by a more strongly adsorbing species, entails an additional regeneration cycle to desorb the expelling agent and can thus only be justified for recovery of a high-value adsorbed intermediate.

7.5

Design and Operation

The performance of adsorptive (and indeed almost all multifunctional) reactors benefits from an expedient nonuniform distribution and integration of the functionalities at various levels. Simply combining given proportions of catalyst and adsorbent in a fixed-bed reactor seldom realizes the full potential available [52]. The objective may be to maximize utilization of adsorbent capacity or to optimize catalyst productivity. Although these aims need not be mutually exclusive, they often give rise to different strategies.

It is possible to distinguish between macrostructuring of the fixed-bed, microstructuring of the catalyst or adsorbent pellets and profiling of various operating parameters over the course of the cycle. Whereas the first two techniques are fixed by the design of the adsorptive reactor, the last is more flexible, as it can be adjusted to reflect the progress of the operating cycle.

7.5.1

Fixed-bed Macrostructuring

Macrostructuring measures are a well-known concept for the suppression of hot-spots by local dilution of catalyst in multitubular reactors, for example [53]. It is also intuitively obvious that the need for adsorption to enhance an equilibrium reaction is much lower at the front end of the reactor, where kinetics rather than equilibrium are decisive, than downstream. The converse, however is not true: in the outlet of such an adsorptive reactor both catalyst and adsorbent are required for maximal conversion. By a judicious selection of the ratio between the two, one can ameliorate the front broadening effects that arise in the reactor outlet.

In some instances it is even beneficial to segregate the fixed bed into a series of alternating catalytic and adsorptive zones – for example, when there is a need periodically to remove and replace a deactivating catalyst for external regeneration purposes. More subtly, such a partial de-integration of the catalytic and adsorptive functionalities can be used to solve problems with adsorption on the catalyst, as encountered in the adsorptive reactor for the Claus process. In the mode of operation described by Hashimoto [54] (Fig. 7.14), the adsorptive elements are switched so as to simulate a countercurrent flow to the reaction medium, whilst the reactors remain “stationary”. The catalyst is thus operated under steady-state conditions and, following an initial start-up phase, attains adsorptive equilibrium. The differences in the rates and amounts of hydrogen sulfide and sulfur dioxide adsorbed onto the Claus catalyst thus become immaterial for reactor operation with this configuration.

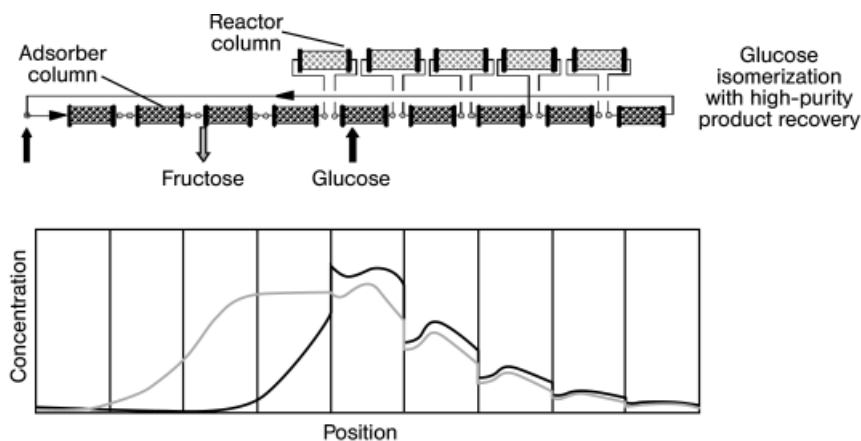


Fig. 7.14. Operation of a simulated moving-bed reactor for glucose isomerization using steady-state reaction stages according to Hashimoto [54].

7.5.2

Pellet Microstructuring

At the other extreme, it may well be advantageous to integrate the adsorbent and catalyst into a single hybrid pellet (Fig. 7.15). As with macrostructuring, the localized microstructuring of activity within catalyst pellets is hardly unknown, and has been proposed for both the optimal usage of active components [55] or for extending catalyst lifetimes in the presence of certain deactivation phenomena [56]. The primary benefit of microstructuring in adsorptive reactors would seem to be in avoiding unnecessary interparticulate gradients, which might otherwise constrain both the rate of reaction and the degree of adsorbent utilization [57] (Fig. 7.16). The closeness of catalytic and adsorptive sites in hybrid catalyst-adsorbent pellets means that diffusive mass transfer imposes little or no limitations on the overall process. Simulations of the adsorptive removal of water from the Claus reaction system or the desorptive introduction of water in the water-gas shift reaction have demonstrated that the integration of the functionalities into a single pellet can result in modest improvements in the cycle times under otherwise identical conditions (Fig. 7.17). The dramatic protraction of cycle times at high values of the Thiele modulus indicates the positive effects of overcoming internal diffusive resistances, but are, unfortunately, of little relevance for practical purposes.

It should be noted that similar results could be achieved by reducing the size of distinct catalyst and adsorbent particles in a “conventional” mixed fixed bed, insofar as pressure drop considerations do not militate against such an approach. The precise structuring of the catalytic activity and adsorptive capacity within the pellet can also be shown to be much less important than their integration, the reason being that a hybrid pellet at any given location in the fixed bed is exposed to a range of concentration conditions over the course of the cycle. Thus, it is next to impossible to

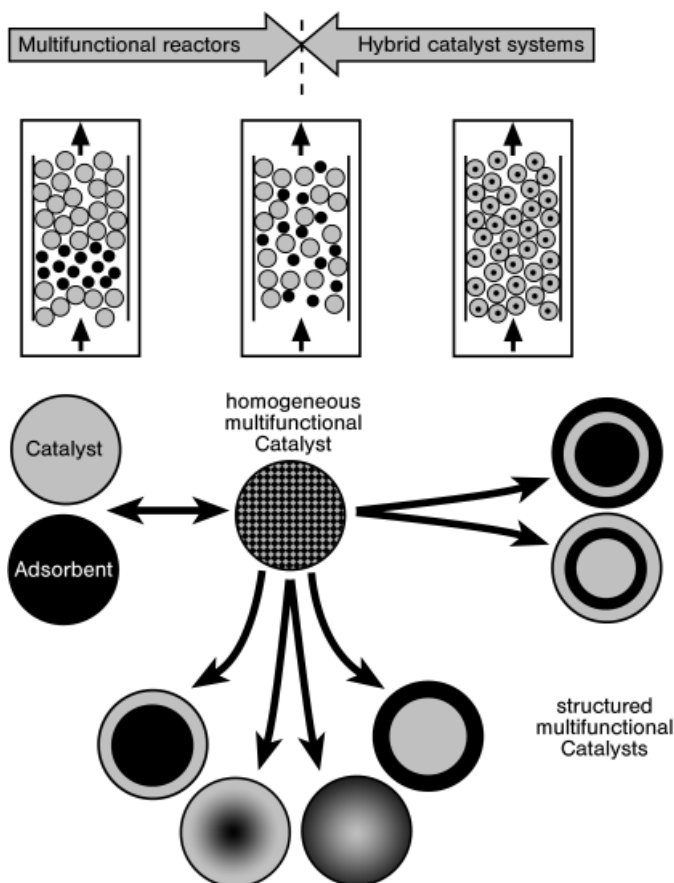


Fig. 7.15. Macro- and microstructuring of catalytic and adsorptive functionalities.

devise a structured distribution of the functionalities which yields an optimal performance at all stages of the process. The exploitation of microstructured hybrid pellets as an additional degree of freedom in the design of adsorptive reactors would thus seem destined to play, if any, a secondary role – and then only in conjunction with macrostructuring of the fixed-bed or parameter profiling. In view of the technical challenges and questionable economics associated with the preparation of such multifunctional adsorptive catalysts, this can perhaps be considered a mixed blessing.

7.5.3

Operating Parameter Profiling

Optimization of the pressure levels and the duration of inert and product sweeps in pressure swing adsorptive reactors was referred to in Section 7.4.3. One can,

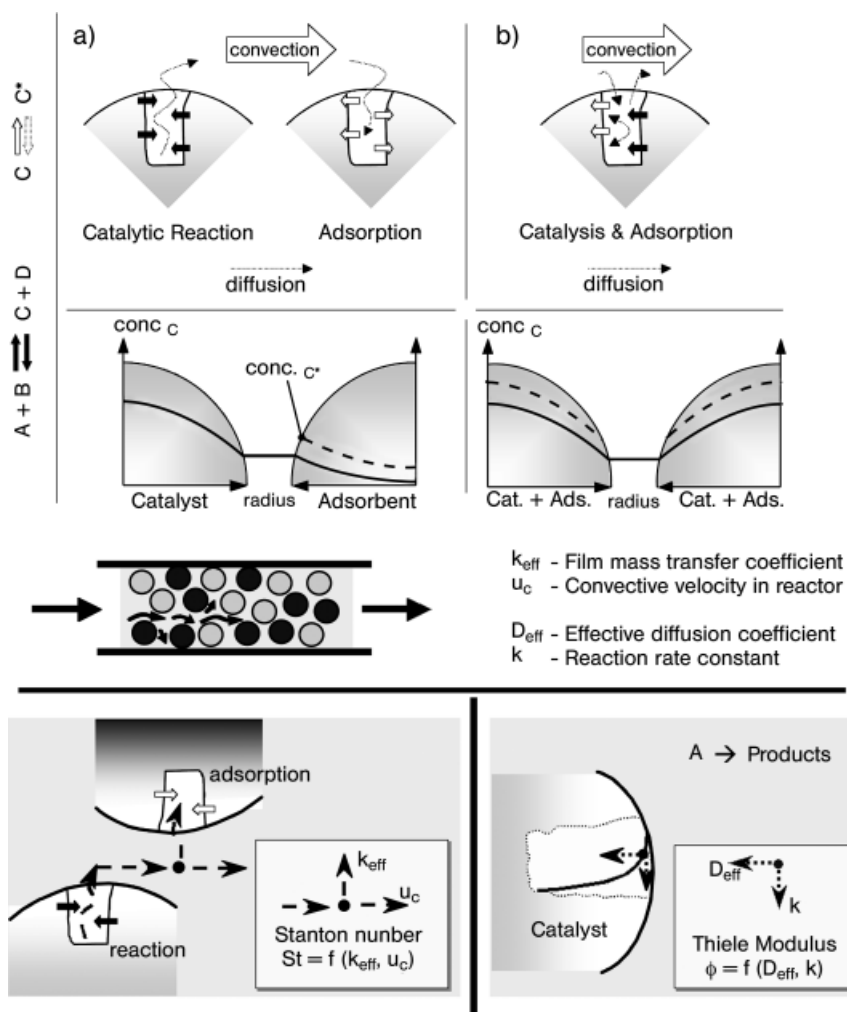


Fig. 7.16. Mass transfer intensification in a) distinct and b) catalyst hybrid adsorbent pellets together with the pertinent design parameters.

however, also vary the values of the pressure – and indeed a variety of other operating parameters such as temperatures and flow rates – continuously over the course of the reactive cycle to enhance performance, to ensure sharper breakthrough fronts and thus greater adsorbent utilization, for example. This technique, with its daunting array of possibilities, has been somewhat neglected, a notable exception being recent studies of Xiu et al. [28], which demonstrated that the cycle time for CO_2 capture in a steam reforming system could be extended eight-fold by employing an appropriate temperature profile along the adsorptive reactor (Fig. 7.18). It can

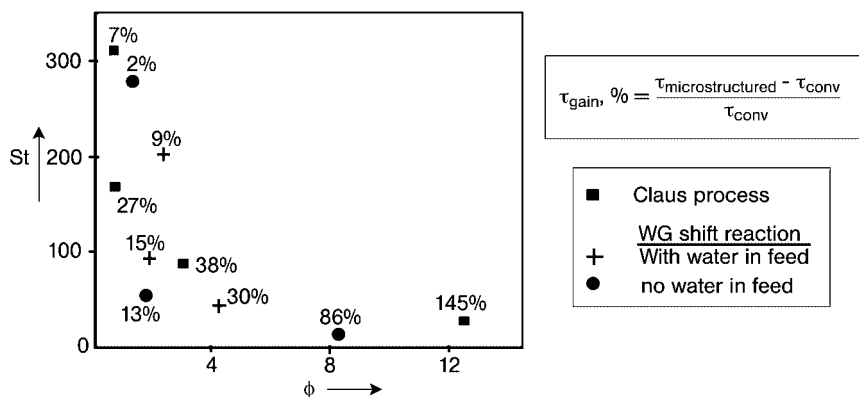


Fig. 7.17. Extension of cycle times (τ) due to microstructuring of hybrid catalyst-adsorbent pellets for the Claus and water-gas shift reactions compared to the use of comparable distinct catalyst and adsorbent pellets as a function of the Thiele modulus (ϕ) and Stanton number (St) [52]. In the water-gas shift reaction preloaded adsorbent is used to enhance the level of excess steam both with and without an additional steam supply in the reactor inlet.

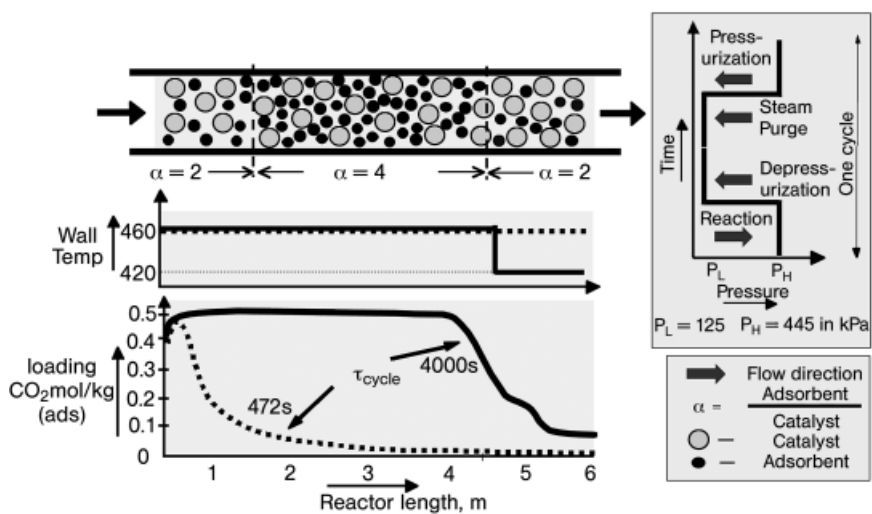


Fig. 7.18. Adsorptive reactor with fixed-bed macrostructuring and temperature profiling for steam reforming of methane according to Xiu et al. [28].

also be appreciated that manipulating process parameters according to the prevailing phase of the adsorptive reactor cycle may well be a key to unlock the potential of the less flexible macro- and microstructuring measures.

At this point it should also be noted that few investigations have been devoted to the temperature profiles arising in adsorptive reactors, let alone their manipulation to enhance process performance. Despite the often considerable heat effects present, isothermal operation is commonly assumed, and the efficient thermal integration of temperature swing regeneration processes tend to be treated superficially, if at all. To some extent this neglect can be justified by the fact that the thermal response times – especially in laboratory- or bench-scale equipment in which most studies have been conducted – are often an order of magnitude larger than the adsorptive cycle times, so that the temperature changes over a single cycle are often minimal [33]. Nevertheless, the cumulative effect over several cycles will not be negligible. For example, model calculations for the unsteady-state Deacon process revealed that a co-current regeneration process was superior in its ability to remove the heat from the fixed bed. This prevented temperatures drifting up from cycle to cycle due to the exothermic nature of the overall reaction, albeit with the penalty of a less efficient utilization of the chlorine storage capacity of the (hybrid) catalyst system [58]. In view of the difficulties involved with alternative methods of heat removal for this extremely corrosive system, the requirements of maintaining the reactor temperature assume a higher priority than the optimal use of the adsorbent.

7.5.4

Heat Effects

From such considerations it is only a small step to the idea of trying to exploit the heat effects arising in adsorptive reactors, as has in fact already been done in the form of so-called “chemical” heat pumps, in which adsorption–desorption processes at different temperature levels are used to either obtain high-grade or recover low-grade heat [59]. A more chemically oriented application of this principle has been proposed by Yongsunthon and Alpay [23], who used the heat of adsorption of toluene on a 10X zeolite (-95 kJ mol^{-1}) to supply some of the endothermic heat of reaction needed to produce toluene from methylcyclohexane ($+202 \text{ kJ mol}^{-1}$). A related concept of desorptive reactor cooling, in which the desorption of an inert material from a previously loaded adsorbent in a mixed fixed bed with catalyst provides efficient and intensive regenerative cooling for an exothermic reaction, has also been developed (Fig. 7.19) [60]. The cycle times achieved are in the practically relevant range of the order of 10 min or more, and can be extended using macrostructuring and adjusting the residual level of inert in the feed stream in analogy to the techniques described earlier in this section.

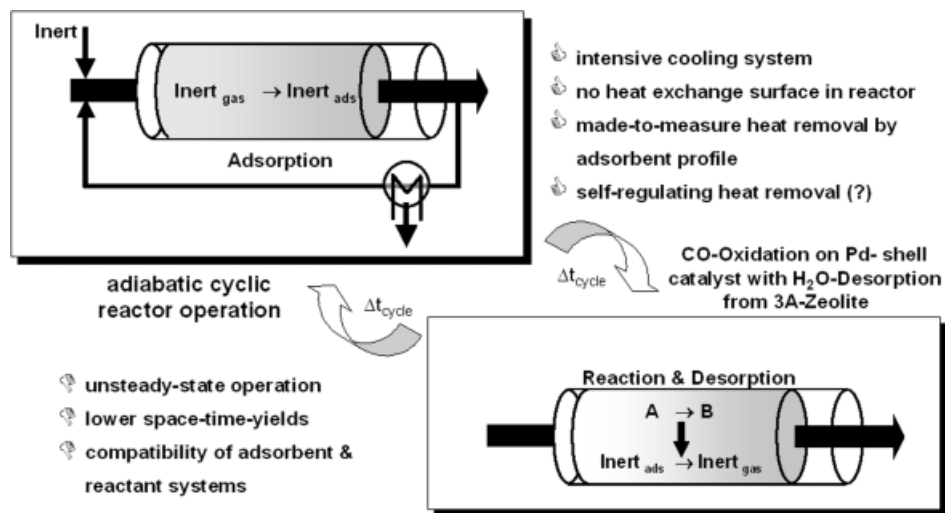


Fig. 7.19. Principle of desorptive cooling for an exothermic chemical reaction.

7.6

Conclusions and Perspectives

The preceding review of various aspects of adsorptive reactors has hopefully provided some insights as to why this apparently so promising technology has yet to fulfil its potential. The often conflicting (and sometimes incompatible) demands placed on catalyst and adsorbent, the enhancement of unwanted side reactions or catalyst deactivation, and the difficulties of an expedient adsorbent regeneration with realistic overall cycle times can quickly disillusion those trying to harness this particular type of multifunctional reactor.

It is instructive to compare the example of the seemingly more feasible Claus process with the less tractable direct HCN synthesis. The major difference lies in the much poorer selectivity of both catalyst and adsorbents at the higher temperatures (400 °C rather than 250 °C) in the latter case, which would seem to indicate that adsorptive reactors function better at lower temperatures. The ability to use a process gas stream for elutive regeneration and to overcome problems due to distortive reactant adsorbent on the catalyst using the partial de-integration described in Section 7.5.1 are further points favoring the use of adsorptive reactors in the first instance.

It should also always be borne in mind, that process integration inherently entails a loss of degrees of freedom (Fig. 7.20), and the designer of a multifunctional reactor must always seek additional design variables, which might enable them to better harmonize the demands of the two underlying operations. The multiscale architecture of the process and the structured distribution of the functionalities within it must be analyzed in the context of the process synthesis if this objective is to be realized [61].

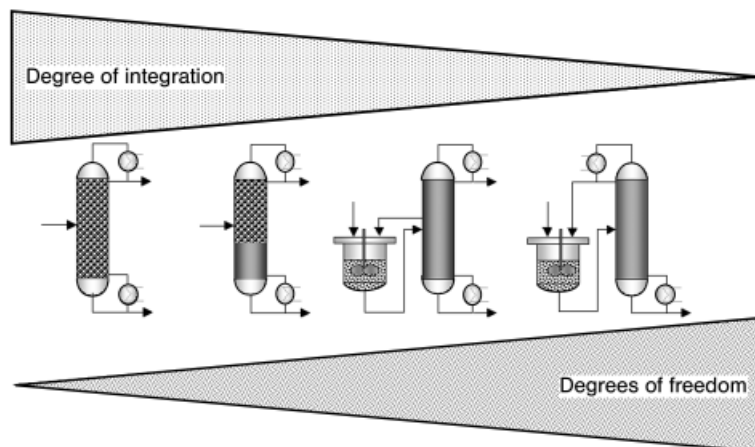


Fig. 7.20. Process integration and degrees of freedom in multifunctional reactor design.

Some generalized qualitative guidance which can be derived from the work presented is as follows:

- use selective adsorbents with a “macroscopic” capacity
- make sure that adsorption is rapid and follows a favorable isotherm
- structure adsorptive and reactive functionalities within the reactor and the catalyst
- profile operating parameters both spatially and chronologically
- integrate the regeneration process expediently in the overall operation
- avoid high-temperature operation
- suppress excessive “catalytic” adsorption
- ensure that unwanted side reactions are not enhanced more than the main reaction
- seek alternatives to thermal regeneration
- eschew solids handling operations

Some of these criteria help to explain the greater success of chromatographic reactors over adsorptive reactors for the gas phase reactions described here. They also point to a niche (if somewhat trivial) application of adsorptive reactors in end-of-pipe environmental processes, in which low concentrations of a gas-borne pollutant are adsorbed from waste gas over a long period before being destroyed by catalytic oxidation in a high-temperature regeneration step utilizing the heat liberated by combustion by means of a gas recycle.

Whilst the development of new adsorbents on monolithic [62] or fibrous supports [63] to cut pressure drops, of high-capacity metal organic frameworks (MOFs) [64], or of highly selective molecularly imprinted polymers (MIPs) [65], is certainly beneficial for the realization of novel adsorptive reactive concepts, the serendipity of catalytic chemistry and the accompanying adsorption process remains the crucial factor for the success or otherwise of an adsorptive reactor. Thus, although a healthy degree of skepticism is appropriate when assessing the suitability of an adsorptive

reactor for a given reaction engineering task it should never be rejected out of hand, especially in light of the plethora of design options available.

Acknowledgments

The author would like to express his gratitude to the members of the research group for integrated separation processes at the university of Dortmund for their assistance with much of the work presented, to the German research foundation (DFG) for their financial support of the work on adsorptive and structured multifunctional reactors, to the participants of the international symposia on multifunctional reactors (ISMR) and for their diverse contributions to this review, and to the organizers of the International Max Planck Symposium on "Integrated chemical processes" for providing an appropriate forum for sharing these reflections on adsorptive reactors with a wider audience.

References

1. B. T. Carvill, J. R. Hufton, M. Amand, et al., *AIChE J.*, **1996**, 42, 2765–2772.
2. D. W. Agar, W. Ruppel, *Chem. Engng. Sci.*, **1988**, 43, 2079–2085.
3. A. L. Tonkovich, R. W. Carr, R. Aris, *Science*, **1993**, 262 (10), 221–223.
4. I. Yongsunthon, E. Alpay, *Chem. Engng. Sci.*, **1999**, 54, 2647–2657.
5. A. Seidel-Morgenstern, Chromatographic Reactor, in: *Catalysis from A to Z*, 164, 2nd completely revised and enlarged edition, B. Cornils, W. A. Herrmann, R. Schlögl, C.-H. Wong, (Eds.), Wiley-VCH, Weinheim, 2003.
6. U. Nieken, G. Kolios, and G. Eigenberger, *AIChE J.*, **1995**, 41, 1915–1925.
7. Yu. Matros, *Stud. Surf. Sci. & Catal.*, **1985**, 22, 1–364.
8. H. J. Slood, G. F. Versteeg, W. P. M. Van Swaaij, *Chem. Engng. Sci.*, **1990**, 45, 2415–2421.
9. K. R. Westerterp, *Chem. Engng. Sci.*, **1992**, 47, 2195–2206.
10. H.-J. Bart, *Reactive extraction*, Springer, Heidelberg, 2001.
11. D. W. Agar, *Chem. Engng. Sci.*, **1999**, 54, 1299–1305.
12. M. Kuczynski, M. H. Oyevaar, R. T. Pieters, et al., *Chem. Engng. Sci.*, **1987**, 42, 1887–1898.
13. G. G. Vaporciyan, R. H. Kadlec, *AIChE J.*, **1989**, 35, 831–844.
14. S. Goto, T. Tagawa, T. Oomiya, *Kagaku-kogaku-ronbunshu (Chem. Engng. Essays)*, **1993**, 19, 978–993.
15. Y. Jiang, I. V. Yentekakis, C. G. Vayenas, *Science*, **1994**, 264, 1563.
16. D. Harrison, C. Han, *Chem. Engng. Sci.*, **1994**, 49, 5875–5883.
17. S. S. Kurdyumov, A. R. Brun-Tsekovoi, A. I. Rozenthal, *Petr. Chem.*, **1996**, 36, 139–143.
18. A. N. Zagoruiko, O. V. Kostenko, A. S. Noskov, *Chem. Engng. Sci.*, **1996**, 51, 2989–2994.
19. D. W. Agar, O. Watzenberger, A. Hagemeyer, in: *Proceedings of R'97 meeting Recovery, Recycling Re-integration*, Geneva, 1997, 4, IV.45–IV.50.
20. J. Sheikh, L. S. Kershenbaum, E. Alpay, *Chem. Engng. Sci.*, **2001**, 56, 1511–1516.
21. Chr. Dittrich, *Fortschritt-Berichte VDI Reihe 3*, 748, VDI-Verlag, Duesseldorf, 2002.
22. M. P. Elsner, M. Menge, C. Müller, et al., *Catalysis Today*, **2003**, 79–80, 487–494.
23. I. Yongsunthon, E. Alpay, *Chem. Engng. Sci.*, **1998**, 53, 691–696.

24. V. G. Gomes, K. W. K. Yee, *Chem. Engng. Sci.*, **2002**, 57, 3838–3850.
25. E. Alpay, D. Chatsiriwech, L. S. Kershenbaum, et al., *Chem. Engng. Sci.*, **1994**, 49, 5845–5864.
26. Y. Ding, E. Alpay, *Chem. Engng. Sci.*, **2000**, 55, 3929–3940.
27. J. M. Loureiro, A. E. Rodrigues, Adsorptive Reactors, in: *Adsorption: Science and Technology*, pp. 223–238, A. E. Rodrigues, M. D. LeVan, D. Tondeur, (Eds.), Kluwer Academic Pub., Dordrecht, Holland, 1989.
28. G.-H. Xiu, P. Li, A. E. Rodrigues, *Chem. Engng. Sci.*, **2003**, 58, 3425–3437.
29. J. R. Hufton, S. Mayorga, S. Sircar, *AIChE J.*, **1999**, 45, 248–256.
30. M. P. Elsner, Chr. Dittrich, D. W. Agar, *Chem. Engng. Sci.*, **2002**, 57, 1607–1619.
31. T. A. Luft Specification, Germany, No. 2.5.1, 1986.
32. F. Joensen, J. R. Rostrup-Nielsen *J. Power Sources*, **2002**, 105, 195–201.
33. M. P. Elsner, *Experimentelle und modellbasierte Studien zur Bewertung des adsorptiven Reaktorkonzeptes am Beispiel der Claus-Reaktion*, Logos Verlag, Berlin, 2004.
34. Z. Yong, V. Mata, A. E. Rodrigues, *Separation and Purification Technology*, **2002**, 26, 195–205.
35. Y. Ding, E. Alpay, *Chem. Engng. Sci.*, **2000**, 55, 3461–3474.
36. S. G. Mayorga, J. R. Hufton, S. Sircar, et al., *Sorption enhanced reaction process for production of hydrogen – Phase 1, final report*, U.S. dept. of energy #DE-FC36-95G010059, 1997.
37. C. Müller, D. W. Agar, *Chem.-Ing.-Tech.*, **2000**, 72, 982–983.
38. K. Nakagawa, T. Ohashi, *J. Electrochem. Soc.*, **1998**, 145, 1344–1346.
39. R. Xiong, J. Ida, Y. S. Lin, *Chem. Engng. Sci.*, **2003**, 58, 4377–4385.
40. Z. Zhiwen Qi, K. Sundmacher, E. Stein, et al., *Separation and Purification Technology*, **2002**, 26, 147–163
41. Y. C. Yen, Styrene from Ethylbenzene using membrane reactors in *PEP Review* 91-3-4, SRI Consulting, Menlo Park, 1993.
42. J. Villadsen, H. Livbjerg, *Catal. Rev.-Sci. Eng.*, **1978**, 20, 203.
43. B. Engler, E. S. J. Lox, Environmental catalysis, in: *Handbook of heterogeneous catalysis*, 4, p. 1581, G. Ertl, H. Knözinger, J. Weitkamp, (Eds.), Wiley-VCH, Weinheim, 1997.
44. W. S. Epling, L. E. Campbell, A. Yezerets, et al., *Catalysis Rev.*, **2004**, 46, 63–245.
45. U. Tuttlies, V. Schmeisser, G. Eigenberger, *Topics in Catalysis*, **2004**, 30–31, 187–192.
46. E. D. Snijder, G. F. Versteeg, W. P. M. van Swaaij, *Chem. Engng. Sci.*, **1992**, 47, 3809–3816.
47. G. M. Pajonk, Section 5.3.2 Spillover Effects, in: *Handbook of Heterogeneous Catalysis*, 3, p. 1064–1077, G. Ertl, H. Knözinger, J. Weitkamp, (Eds.), Wiley-VCH, Weinheim, 1997.
48. B. G. Keefer, D. G. Doman, *US Patent* 2000. 6 051 050 from 18.04.2000.
49. M. Mortensen, R. G. Minet, T. T. Tsotsis, et al., *Chem. Engng. Sci.*, **1999**, 54, 2131–2139.
50. D. Bathen, *Separation and Purification Technology*, **2003**, 33, 163–177.
51. R. R. Judkins, T. D. Burchell, *US Patent* 1999, 5 972 077 from 26.10.1999.
52. W. Dietrich, M. Grünwald, D. W. Agar, *Chem. Eng. J.*, **2005**, in print.
53. R. Krishna, S. T. Sie, *Chem. Engng. Sci.*, **1994**, 49, 4029–4065.
54. K. Hashimoto, S. Adachi, H. Noujima, Y. Ueda, *Biotechnology and Bioengineering*, **1983**, 25, 2371–2393.
55. M. Morbidelli, A. Gavrilidis, A. Varma, *Catalyst Design: Optimal Distribution of Catalyst in Pellets, Reactors and Membranes*, Cambridge University Press, Cambridge, 2001.
56. E. R. Becker, J. Wie, *J. Catalysis*, **1977**, 46, 372–381.
57. M. Gruenewald, D. W. Agar, *Chem. Engng. Sci.*, **2004**, 59, 5519–5526.
58. F. Ziegler, *Int. J. Thermal Sci.*, **1999**, 38, 191–208.

59. U. Niesen, O. Watzenberger, *Chem. Engng. Sci.*, **1999**, 54, 2619–2626.
60. M. Gruenewald, D. W. Agar, *Ind. Eng. Chem. Res.*, **2004**, 43, 4773–4779.
61. G. Schembecker, S. Tlatlik, *Chem. Eng. Processing*, **2003**, 42, 179–189.
62. T. Ito, H. Kanesaka, T. Ikeda, *Zeolites*, **1996**, 16, 220.
63. M. Suzuki, *Carbon*, **1994**, 32, 577–586.
64. J. L. C. Rowsell, O. M. Yaghi, *Microporous and Mesoporous Materials*, **2004**, 73, 3–14.
65. O. Brüggemann, K. Haupt, L. Ye, E. Yilmaz, et al., *J. Chromatogr. A*, **2000**, 889, 15–24.

8

**Reactive Stripping in Structured Catalytic Reactors:
Hydrodynamics and Reaction Performance**

*Tilman J. Schildhauer, Freek Kapteijn, Achim K. Heibel,
Archis A. Yawalkar and Jacob A. Moulijn*

8.1

Introduction

In the field of integrated processes, reactive separations are prominently present due to the high degree of synergy to be achieved in many processes [1, 2]. Reactive separations can have positive effects on the conversion, as well as on the selectivity in a process.

In the case of equilibrium-limited reactions, the combination of reaction and separation in one (multifunctional) apparatus allows equilibrium limitations to be overcome by removing one or more products from the phase in which the reaction takes place. If a catalyst is present in a process, in-situ removal of an inhibiting product, which strongly adsorbs onto the catalyst surface, will lead to a higher catalyst activity and lifetime.

In separations limited by azeotrope formation under nonreactive conditions, the addition of a reaction (that is, usually adding catalyst) constantly changes the concentrations such that the separation continues beyond the azeotrope. In processes with coupled products (enantiomers, *ortho-/meta-/para*-substitution), the in-situ removal of the desired product will favor the reaction towards this product, and will therefore strongly increase the selectivity.

Sometimes, the thermal effects that occur anyway during phase changes might be exploited for an improved temperature control, for example cooling by solvent evaporation in exothermic processes.

The best-known and (commercially) most successful example of combining reaction and separation is the reactive distillation. Reactive distillation has been investigated widely [3, 4; see also Chapters 3, 4, and 5] and is applied to many processes [5]. However, the integration of more than one functionality in an apparatus leads to a loss in degrees of freedom. For a successful integration, the feasible window of operation concerning process conditions such as pressure and temperature must coincide for the reaction, the separation and the apparatus (Fig. 8.1).

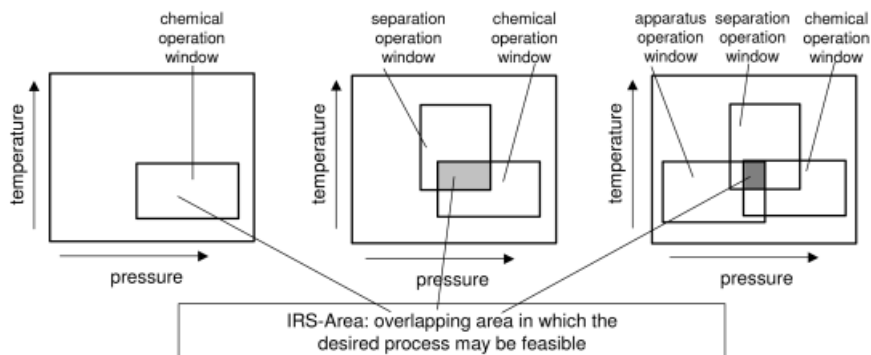


Fig. 8.1. Superposition of operation windows (schematic, for two parameters only). (From Ref. [6].)

For a number of processes, reactive distillation is not possible, as some of the reactants are destroyed or degraded in side reactions by heating them up to boiling temperature. Examples of such processes are the Knoevenagel-condensation of aldehydes or ketones with components of high CH-acidity, the production of enamines or carbonic acid amides, or the esterification of fatty acids with fatty alcohols to fatty esters [7].

In such processes, the creation of a permanent gas phase by means of an (inert) gas allows a low-boiling compound (often water) to be stripped from the liquid phase at temperatures lower than the reactant boiling points.

This so-called “reactive stripping” offers not only a greater freedom in the choice of pressure and temperature, but also in the concentrations and feeding points of the liquid reactants. Usually, the separation of the stripped compound(s) from the strip gas can be achieved in a simple condenser, permitting an easy recycle of the strip gas. The liquids and the strip gas only have to be heated up to the temperature, which is optimal for the desired reaction. Especially when boiling points are high, reactive stripping can be more energy efficient than reactive distillation, but not if full conversion in one pass is desired (Fig. 8.2). The Sinopec/Lummus bisphenol-A process is a commercial example of reactive stripping [8].

In a number of petrochemical processes, a gas (hydrogen) is present as reactant. In hydrodesulfurization (HDS), hydrocracking (HC), and hydrodenitrogenation (HDN), the reaction products H_2S and ammonia, respectively, are known to decrease the catalyst activity, but are partly transferred to the gas phase. Therefore, also these processes profit from reactive stripping.

Several investigations of these petrochemical processes address the question of co-current versus countercurrent operation [1, 9, 10]. Whereas reactive distillation is a countercurrent operation by definition, in HDS, HC and HDN countercurrent operation is favorable because the gas–liquid equilibrium (GLE) of H_2S and ammonia lies to high extent on the gas side. However, this cannot be generalized. As shown in Fig. 8.3, an internal loop can occur if the gas flow, which stripped the

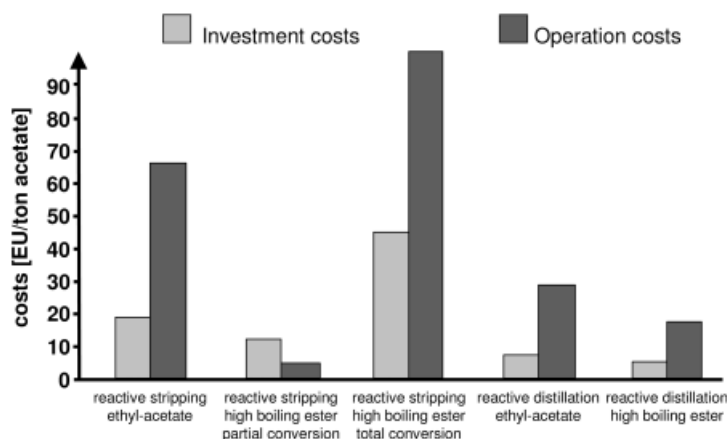


Fig. 8.2. Production costs for a high-boiling ester for various flowsheet options. (From Ref. [6].)

undesired product, comes into contact with fresh liquid reactant entering the reactor free of the undesired product. In this case, the undesired product will be (re)absorbed by the liquid, thus increasing the overall hold-up of the undesired product in the reactor.

In many cases, neither full conversion nor complete separation of the undesired product will be achieved in one pass through the apparatus. The recycled liquid contains a certain (low) concentration of the undesired product when entering the reactor (Fig. 8.4). Readsorption of the undesired product will then be negligible.

Nonetheless, the possibility of an internal loop should be checked carefully in some preliminary simple modeling work. If countercurrent operation is less favorable, a cross-flow-type operation could be chosen, where the reactor is divided into

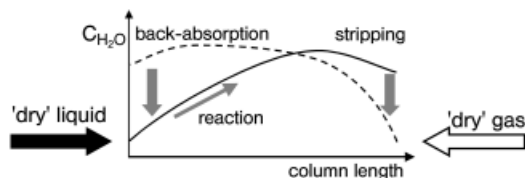


Fig. 8.3. Concentration profile of water for the gas and the liquid phase. The arrows indicate mass transfer by stripping and readsorption and water production by reaction.

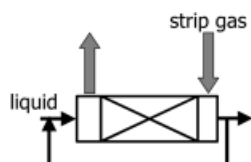


Fig. 8.4. Schematic flowsheet for a countercurrent reactive stripping process with liquid recycle.

several parts each being operated in co-current mode, but with individual gas streams for each part (Fig. 8.5).

In principle, any catalyst bed used for reactive distillation or trickle bed operation can also be applied in reactive stripping. The performance will depend mainly on the optimal ratio between catalyst hold-up, the gas–liquid and the liquid–solid interface. However, recycling of the strip gas flow makes a low pressure drop (and therefore a high voidage) especially beneficial. In countercurrent operation, flooding – a well-known problem – must be avoided. The present studies have focused on structured catalyst supports, developed for either reactive distillation or reactive stripping, with a particular emphasis being placed on the use of so-called film-flow monoliths.

8.2

Hydrodynamics

In this section of the studies, the flow patterns of two-phase flow in the investigated packings (monoliths, Sulzer DX®, and Sulzer katapak S®) are discussed. Further, the resulting residence time distribution (RTD), flooding limits, and mass transfer behavior are compared.

8.2.1

Flow Patterns

8.2.1.1 Monoliths

Monolithic catalyst carriers are state-of-the-art in exhaust gas cleaning, for example in automobiles, DeNO_x or removal of VOCs. To minimize diffusion length and to increase the geometric surface area, monoliths with small-diameter channels have been developed which can be produced easily by extrusion, followed by calcination. In the past few years the application of monoliths in gas–liquid operation has been investigated intensively [10–13].

As shown in Fig. 8.6, several typical flow patterns can be found in the monolith channels, depending on gas–liquid ratio, flow rates, viscosity, surface tension, and channel diameter. All of these flow patterns show a very low static hold-up, but only two are regular and allow stable operation: the so-called Taylor-flow and the film-flow regime.

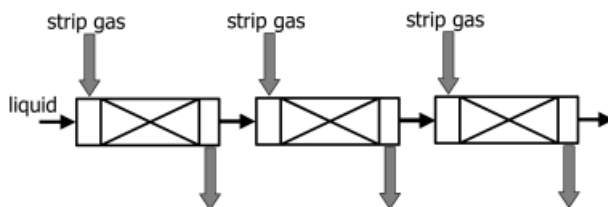


Fig. 8.5. Schematic flowsheet for a co-current/cross-flow reactive stripping process.

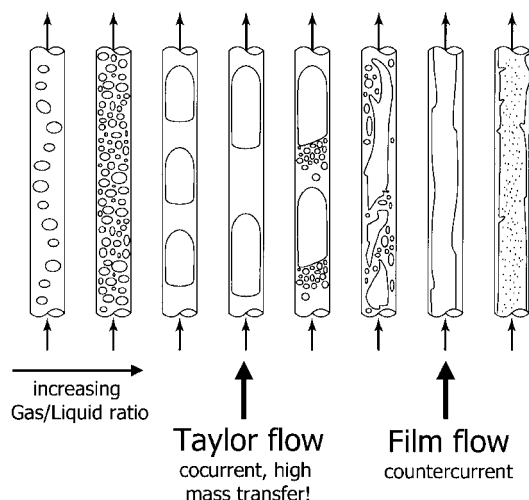


Fig. 8.6. Gas–liquid flow patterns in capillaries.

Taylor-flow or bubble train-flow regimes are characterized by gas bubbles, which are separated from the channel wall by a very thin liquid film, and from each other by a liquid slug. At flow rates of industrial interest, this regime is achieved with typical organic fluids or water in monolith channels smaller than 2 mm. Typical geometric surface areas are between 1200 and 4000 m² m⁻³. Due to the thin liquid films between the bubbles and the wall on the one hand, and a strong internal recirculation of the liquid slug and exchange between the slugs and the films during the moving of the slugs and bubbles along the channel on the other hand, mass transfer in this regime is extraordinarily high and is accompanied with a low pressure drop. Gas and liquid are fed co-currently into the reactor by a spray nozzle for the liquid and free gas suction, or together through a special set of static mixers to form a foamy layer on top of the monoliths. The low pressure drop permits having, if necessary, a high recirculation rate of gas as well as liquid. Figure 8.7 shows a set-up using monoliths in Taylor-flow regime where the heat of reaction is removed by an external heat exchanger. Meanwhile, Akzo Nobel runs a commercial process applying the Taylor-flow regime, namely the hydrogenation of anthraquinone.

In monolithic catalyst carriers with wider channels, the liquid forms a film on the channel walls, whereas in the core of the channel a continuous gas phase exists. As shown by Lebens [10], countercurrent gas–liquid operation is now possible, and shows certain advantages over the countercurrent trickle bed operation. Typical channel diameters are 3–5 mm, and the geometric surface areas are between 550 and 1000 m² m⁻³. Below the flooding point, almost no hydrodynamic interaction between the gas and liquid can be observed; for example, the RTD is the same for both co-current and countercurrent operation. Apart from some surface waves, the film flow is completely laminar.

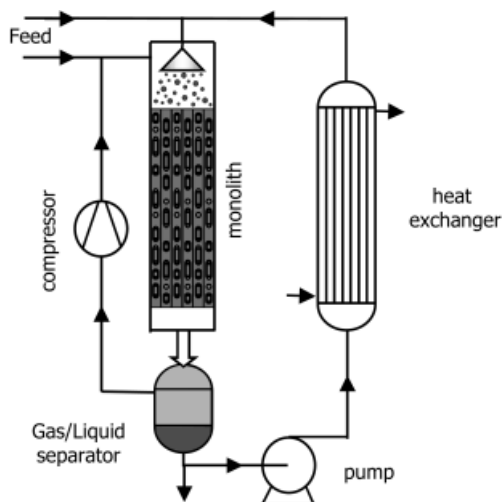


Fig. 8.7. Schematic flowsheet for a co-current monolithic loop reactor. (From Ref. [14].)

In collaboration with the University of Wageningen, magnetic resonance imaging (MRI) was used to visualize the film flow in the monoliths [15]. As shown in Fig. 8.8, liquid (water) was fed onto a complete piece of monolith from which four channels then were prolonged for measurement. In Fig. 8.9, the liquid is represented as light areas in the corners of the four channels. Clearly, the channel walls are not uniformly irrigated. In the corners, the gas–liquid interface is shaped like an arc, whereas between the pockets, only a thin liquid film remains ($\sim 70\ \mu\text{m}$). This retraction of the film into the corners can be attributed to the high surface tension of the liquid used (water). Additionally, the liquid pockets of one channel have different sizes, and this leads to channel scale maldistribution.

In order to improve the channel wall irrigation, modified channel geometries have been developed. Figure 8.10 shows the top view of different monoliths and the corresponding MRI-picture of one channel. The cell density for all three samples is 25 cells per square inch (cpsi); the diameter is 43 mm. Some details of the monoliths

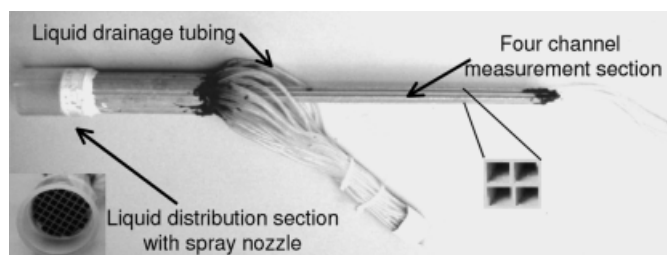


Fig. 8.8. Detail of the experimental set-up used for MRI-visualization of the liquid flow in four monolith channels.

investigated are listed in Tab. 8.1. On the left side, a clear corner flow can be observed for the square channel. For the internally finned monoliths (IFM, center), the situation improves in that a larger part of the wall is irrigated. Monoliths with strongly rounded channel corners (MRC) achieve the best distribution of liquid, with the film thickness being very constant and the walls almost completely wetted. As shown in Sections 8.2.2, 8.2.3, and 8.2.4, these different channel geometries also have an impact on RTD, mass transfer, and flooding behavior.

In order to improve the flooding behavior at the point where two pieces of monolith are stacked on each other, it was suggested [17] that short pieces of monoliths

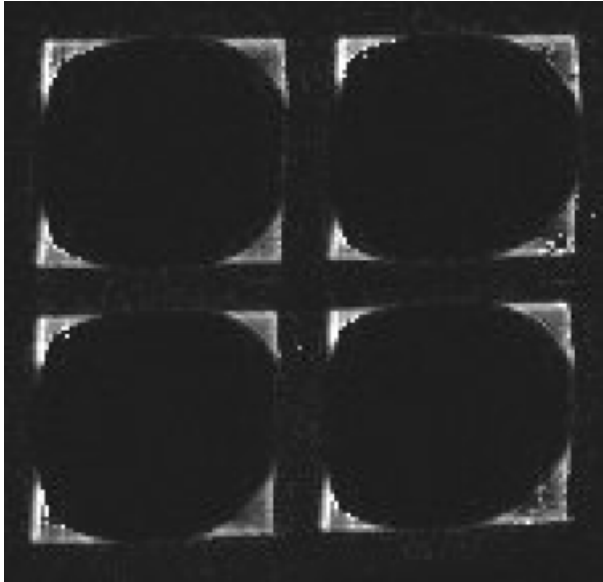


Fig. 8.9. MRI-visualization of the liquid flow in four monolith channels ($u_{LS} = 0.03 \text{ m s}^{-1}$; no forced gas flow, 25 cpsi monolith).

Table 8.1. Geometric details of the monoliths investigated.

Cell density [cells in ⁻²]	25	25	25	25	50
Shape	Square (SQ)	Rounded 1 (RC)	Rounded 2 (MRC)	Finned (IFM)	Square
Void fraction - ε [%]	65	63	59	73	68
Surface/volume ratio - a [m ² m ⁻³]	640	591	546	1040	920
Hydraulic diameter - $d_{hydraulic}$ [mm]	4.07	4.29	4.31	2.81	2.96
Corner radius - r_{corner} [mm]	–	0.74	1.35	–	–
Number of full channels	44	44	44	44	88

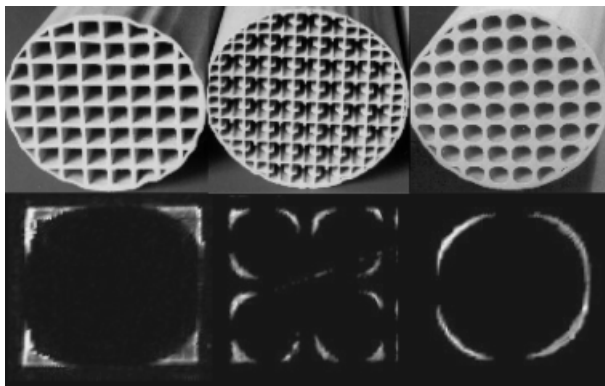


Fig. 8.10. Top view of different monolith types and the corresponding MRI-visualization of the liquid flow in one channel. Left: 25 cps square channels (SQ); center: 25 cps internally finned (IFM); right: 25 cps more rounded corners (MRC).

with wider channels be stacked between the standard monoliths (Fig. 8.11). In consequence, the laminar film flowing down the monolith channels is disturbed and remixed at these stacking points, and this has a positive influence on the liquid side mass transfer and RTD.

8.2.1.2 Sulzer DX®

These packings are built up from corrugated sheets of wire gauze (Fig. 8.12). Liquid forms a thin film that is spread over the complete wire gauze by capillary forces. At the location where two corrugated sheets touch, the liquid films are partly remixed.

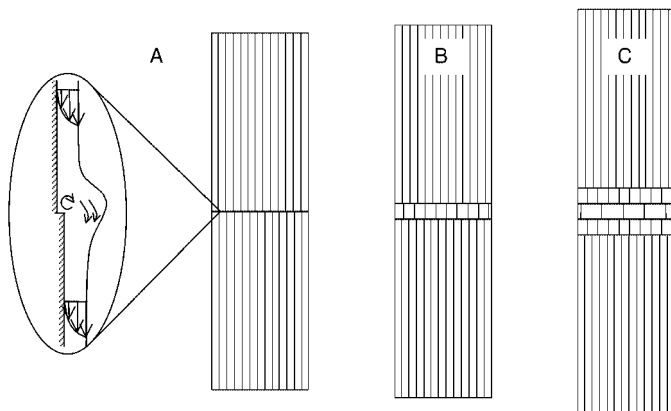


Fig. 8.11. Stacking of monoliths for extension of flooding limits, residence time distribution (RTD) and mass transfer by remixing the laminar layers. Short pieces with a higher hydraulic diameter, turned through 45°, are stacked between longer monoliths with a small hydraulic diameter. (From Ref. [23].)

The 5 cm-long packings are stacked with an axial 90° turn against each other, and this again leads to a complete mixing of the liquid films. Due to their high voidage (ca. 80 %) and high surface area ($900 \text{ m}^2 \text{ m}^{-3}$), these packings are often applied for vacuum distillation. For the application in reactive stripping, the wire gauze is coated with catalyst.

8.2.1.3 Sulzer katapak-S®

Sulzer katapak-S® were developed for use in reactive distillation, though their use for trickle bed operations [18, 19] and as catalyst carrier in bubble flow columns [20] has also been investigated. Like DX, these packings consist of corrugated sheets made from wire gauze. Every second channel between the corrugated sheets is closed to form a “tea bag” which is filled with catalyst particles (Fig. 8.13). Therefore, voidage (ca. 40 %) and surface area ($440 \text{ m}^2 \text{ m}^{-3}$) are approximately half of those for the DX.

Due to capillary forces, pure liquid phase flow is found in the catalyst bags, and this leads also to a high static hold-up. At low liquid loadings, only a very thin film is formed on the wire gauze in the open channels that is spread by the gas flow. At liquid flow rates, beyond the so-called loading point, liquid flows through the open channels also as bypassing rivulets. If the liquid flow rates become even higher, the flooding limits are reached.

Generally, liquid–solid mass transfer and surface reaction on the catalyst are dominant in the catalyst bag, whereas the open channels serve for the gas–liquid mass transfer. As in DX-packings, the liquid film is partly remixed at the connecting knots between the two corrugated sheets. Even more importantly, the packings are turned by 90° against each other every 20 cm. At this point, partial flooding occurs, and consequently the liquid from the open channels and the tea bags is remixed to a high extent. As shown in Sections 8.2.3 and 8.2.4, these two different mixing patterns have a strong influence on RTD and gas–liquid mass transfer.

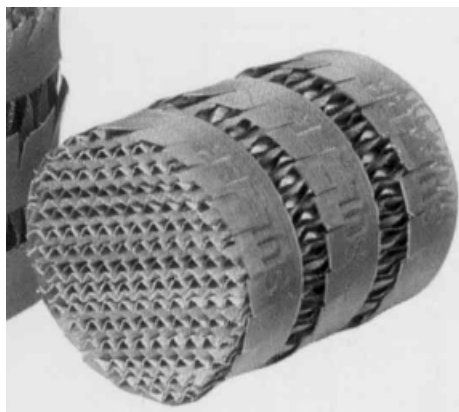


Fig. 8.12. One element of Sulzer DX® packing.

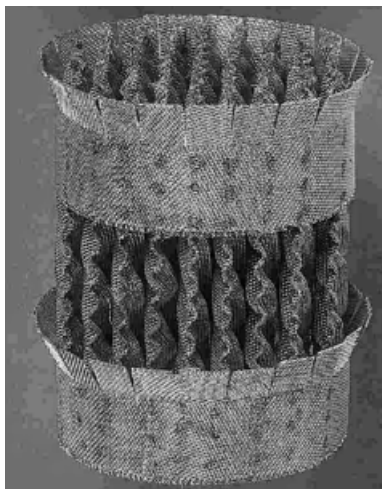


Fig. 8.13. One element of Sulzer katalapak-S® packing.

8.2.2

Hold-up, Pressure Drop, and Flooding Limits

Magnetic resonance imaging permitted direct observation of the liquid hold-up in monolith channels in a noninvasive manner. As shown in Fig. 8.14, the film thickness – and therefore the wetting of the channel wall and the liquid hold-up – increase nonlinearly with the flow rate. This is in agreement with a hydrodynamic model, based on the Navier–Stokes equations for laminar flow and full-slip assumption at the gas–liquid interface. Even at superficial velocities of 4 cm s^{-1} , the liquid occupies not more than 15 % of the free channel cross-sectional area. This relates to about 10 % of the total reactor volume. Van Baten, Ellenberger and Krishna [21] measured the liquid hold-up of katalapak-S®. Due to the capillary forces, the liquid almost completely fills the volume between the catalyst particles in the “tea bags” (about 20 % of the total reactor volume) even at liquid flow rates of 0.2 cm s^{-1} (Fig. 8.15). The formation of films and rivulets in the open channels of the structure cause the further slight increase of the hold-up.

Experiments to measure pressure drop and flooding limits were performed in a set-up accommodating monoliths with diameters of 43 mm (Fig. 8.16), while the length of the monoliths varied up to total length of 1 meter. The liquid was distributed by a nozzle; the gas was introduced in countercurrent mode via mass flow controllers in the system. At the outlet of the monolith, a special device was mounted (Fig. 8.17), which improved draining of the monolith. The pressure drop along the column was measured using differential pressure transmitters. All experiments were performed at room temperature and atmospheric pressure.

Typically, the pressure drop increases for a given liquid velocity slowly with increasing gas flow rates. Between 100 and 300 Pa m^{-1} , the pressure drop

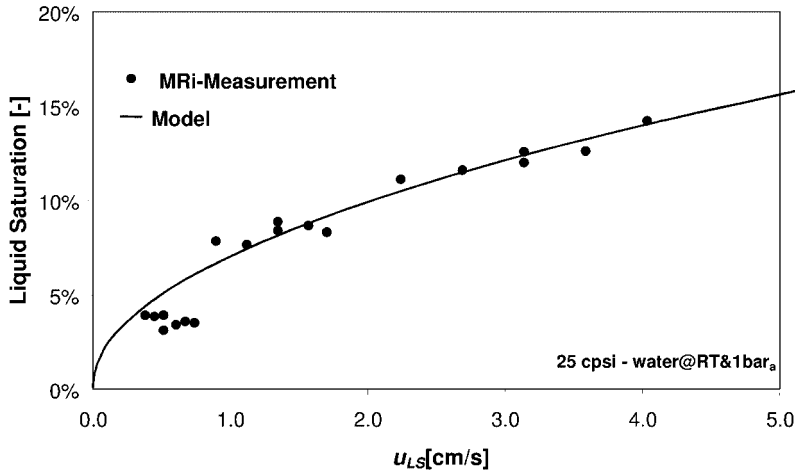


Fig. 8.14. Liquid hold-up in monolith channels: comparison of modeling result with data obtained from MRI-experiments for liquid flow visualization.

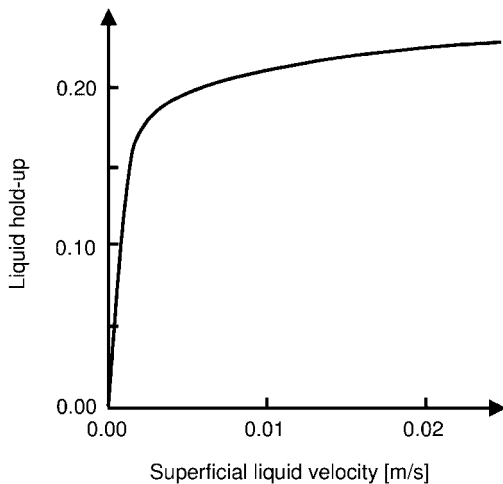


Fig. 8.15. Experimentally determined liquid hold-up in katapak-S® packing. (From Ref. [21].)

rises strongly, and the flooding starts. These curves appear similar to those for katapak-S®, except that the onset of flooding occurs at pressure drops of about 800–1000 Pa m⁻¹ [22]. For comparison, Fig. 8.18 shows the (more or less coinciding) flooding points for 25 cpsl monoliths with square channels ($d_{\text{hydraulic}} = 4$ mm), katapak-S® ($d_{\text{hydraulic}} = 6.4$ mm) and Montz multipak ($d_{\text{hydraulic}} = 7$ mm).

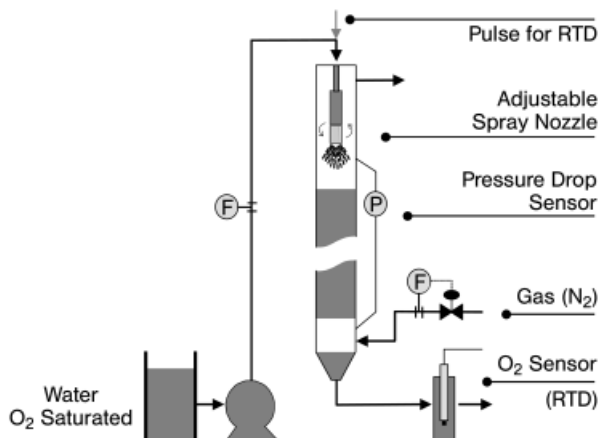


Fig. 8.16. Schematic flowsheet for the experimental determination of pressure drop, flooding limits, residence time distribution (RTD), and mass transfer.

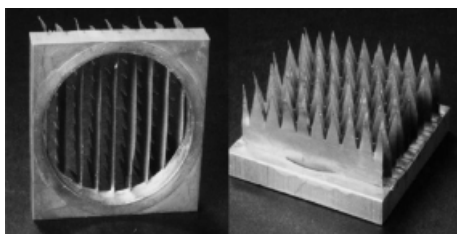


Fig. 8.17. Outlet device for improved draining of monoliths by optimized droplet formation.

Flooding in monoliths starts at the outlet, the inlet, or where two pieces of monoliths are stacked. At these points, the laminar film is disturbed. Droplets or waves might fill the cross-sectional area and are transported upwards by the gas. It was proposed to add at these critical points short pieces of monoliths with a larger channel diameter in order to avoid the onset of flooding by widening the cross-sectional area (Figs. 8.11 and 8.19(a)). As shown in Fig. 8.19(b), the flooding limits are shifted towards higher gas flow rates. In this way, countercurrent operation is possible even in 200-cpsi monoliths ($d_{\text{hydraulic}} = 1.25 \text{ mm}$).

8.2.3

Residence Time Distribution

The liquid RTD in monoliths was measured in the set-up described above (see Fig. 8.16). Monoliths with a length of 50–100 cm were used for these experiments, and an additional length of 1 cm was investigated to take into account the effects of the tracer injection, liquid distribution, and collection section on residence time.

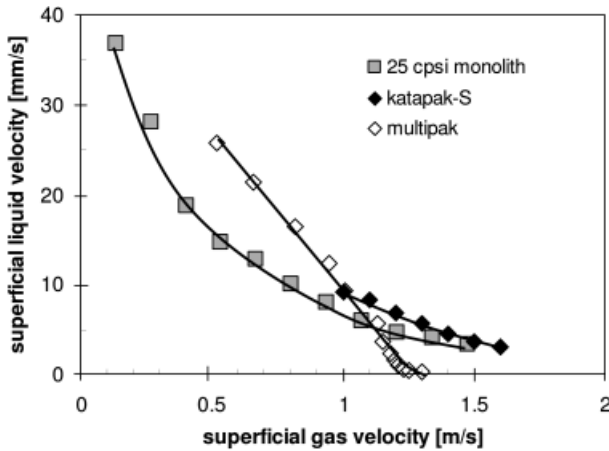


Fig. 8.18. Experimentally determined flooding limits (water/air) for different packings. (Data for katapak from Ref. [22]; data for Multipak from Ref. [27].)

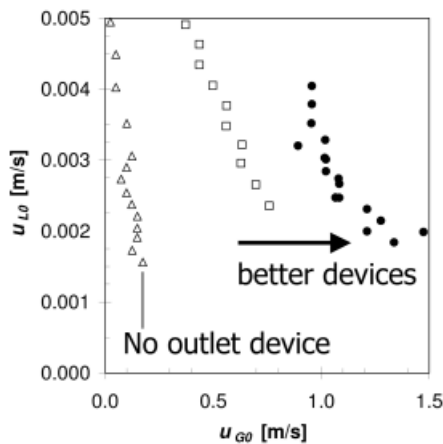
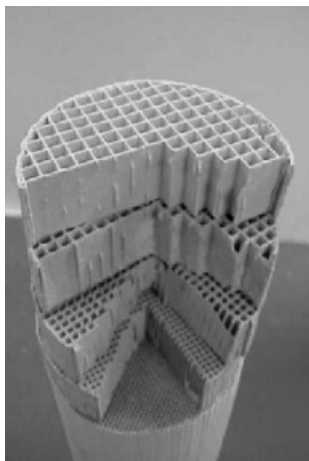


Fig. 8.19. (a) Improved monolith stacking at the reactor inlet and outlet. (b) Flooding limits of 50 cpsi monolith ($d_{\text{hydraulic}} = 3 \text{ mm}$) in countercurrent operation for different gas flow rates.

The liquid (tap water) was pumped through the tracer injection fitting, where a determined tracer volume was injected. Before entering the spray nozzle, the liquid flow was monitored for the dye concentration using an optical flow cell. The liquid passed the channels of the monolith and was collected with a small stirred vessel (mixing-cup). From this mixing cup the liquid was led on to a second probe, which measured the dye concentration by spectroscopy. The absorption of light is related to the concentration of the tracer by the Beer–Lambert law.

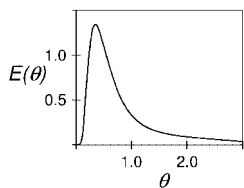


Fig. 8.20. Experimental dimensionless RTD for a finned monolith (IFM) of 75 cm length. (From Ref. [10].)

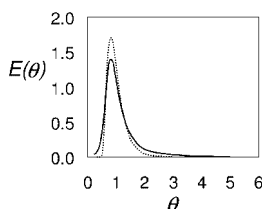


Fig. 8.21. Experimental dimensionless RTD for a continuous monolith of 100 cm length (RC, full line) and stacked monoliths (50 cpsi/25 cpsi, length 100 cm, dotted line).

Each experiment was repeated at least four times, and good reproducibility was found between the different experiments. Air was used as medium for the gas phase, but it transpired that gas flow has almost no influence on the liquid RTD.

Figure 8.20 shows the dimensionless RTD for a finned monolith (IFM) of 75 cm length (from Ref. [10]). Typical for all film-flow monoliths are the high peaks at times earlier than the mean residence time, as well as the very long tailing. Both phenomena can be explained with the character of the laminar flow. The fastest liquid can be found at the film surface in the corners, as here the distance to the channel wall is maximal. This causes the early breakthrough, whereas the tailing represents the liquid flowing with very small velocity next to the wall. In round-channel geometries, the breakthrough comes later than in square geometries, because the maximum film thickness is lower. However, as the channel wall is nearly completely wetted in round geometries, the tailing increases [24].

The stacking of monoliths (see Fig. 8.11) remixes the liquid film each time, and thus, the difference between slow- and fast-flowing liquid layers should decrease. Figure 8.21 shows the not deconvoluted RTD curves for a 100 cm-long continuous monolith (25 cpsi, round channels) and a set of four pieces of 21 cm length (50 cpsi, square channels) with five pieces of 3 cm length (25 cpsi) stacked before, after, and in between the longer ones. The effect of the stacking on the early peak is not as strong. Nonetheless, in the stacked case no dye emerges before half of the mean residence time, whereas the breakthrough starts at one-fourth of the residence time in the continuous monolith. More evident is the cutting of the tail. In the stacked case, the tail ends at about $\theta = 2.5$, whereas in the continuous monolith the tail persists until $\theta = 4.5$. As a consequence, the number of tanks in series describing the standard deviation of the system with the continuous monolith is about 3.3 compared to 9.6 in the stacked case.

The RTD of katapak-S® has been measured by Moritz and Hasse (Fig. 8.22). Below the load point, a narrow distribution with a pronounced tail is observed which can be attributed to stagnant zones present at low liquid loads. Around the load point, the continuous flow through the catalyst-filled bag causes a narrow distribution without any tailing, whereas the bypassing flows occurring beyond the load

point strongly broadens the RTD. The mean residence times of packings with catalyst-filled bags are comparatively higher than those of monoliths due to the higher liquid hold-up [25].

8.2.4

Gas–Liquid Mass Transfer

In the above-described set-up (Fig. 8.16), the physical absorption of oxygen in water was used to measure the gas to liquid mass transfer. Thin-film fluorescence quenching-based sensors were installed to determine the oxygen concentration at the inlet and exit of the reactor. From the measured oxygen concentrations, the mass transfer coefficient was calculated based on the reactor-based liquid velocity:

$$k_L a_l = \frac{u_{LS}}{l} \cdot \ln \left(\frac{c_{in}}{c_{out}} \right) \quad (1)$$

To separate liquid distribution, entrance and collection effects, a short monolith piece was measured and deduced for the determination of the $k_L a$ -value of the considered monolith section in developed laminar film regime. Figure 8.23 shows some results for monoliths of different channel geometry and diameter. In general, a slight increase of the mass transfer performance with liquid velocity is found. This can be related to a large amount to the increase in gas–liquid interface area for higher flows.

Two basic trends can be determined. By comparing the 25 cpsi monoliths, channel rounding clearly leads to better mass transfer performance. The slightly rounded channels (RC) show a small increase, but a significant improvement is found for the more rounded channels (MRC). As expected, a higher S/V ratio or cell density also

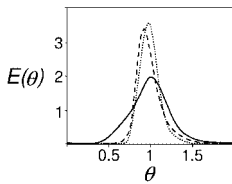


Fig. 8.22. Experimental dimensionless RTD for katapak-S® packing (from Ref. [22]): far below loading point (dashed line); at loading point (dotted line); beyond loading point (full line).

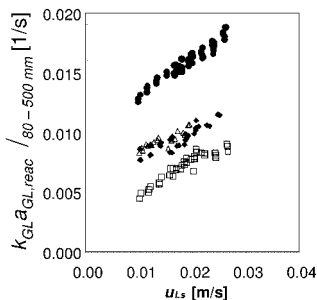


Fig. 8.23. Experimental gas–liquid mass transfer coefficients for fully developed laminar flow (monolith section from 80–500 mm) \square = 25 cpsi square channels; \triangle = 50 cpsi square channels; \blacklozenge = 25 cpsi rounded corners (RC); \bullet = 25 cpsi more rounded corners (MRC).

leads to a better mass transfer performance. Even though the S/V ratio for the MRC monoliths is significant less (60 %), a better performance is found compared to the 50 cpsi square monoliths. This clearly indicates the importance of channel shape in fully developed laminar flow.

However, the mass transfer coefficients found are clearly lower than those reported for distillation packings [26, 27]. This can be explained by the flow patterns in distillation packings, where the films constantly are disturbed and remixed, and therefore a completely developed laminar profile is never present. The mass transport is dominated by convection, not diffusion. It would be expected that remixing of the film layers, as accomplished by the stacking of monoliths (see Section 8.2.3) improves not only the RTD but also the mass transfer performance of monoliths.

To compare the mass transfer behavior under realistic stripping conditions, a set of experiments was carried out at elevated temperatures and pressures. In a 2 m-long column (diameter 5 cm), nitrogen was brought into contact with a mixture of ca. 14 mol% ester (octyl-hexanoate) and 86 mol% cumene, enriched with 2000–2500 ppm water, which was representative for the reactive experiments in these studies.

First, the effects of gas and liquid flows, co-current versus countercurrent operation, pressure and temperature were checked. As expected, based on the influence of these parameters on the vapor pressure or the vapor–liquid equilibrium (VLE), the fraction of water stripped by the nitrogen increases with increasing gas flows, decreasing liquid flows, lower pressures and higher temperatures. Countercurrent operation is more efficient than co-current operation, because the liquid phase at the inlet was already enriched with the compound which was to be separated.

In a second set of experiments, different monolith types – Sulzer DX®-packings and katapak-S® – were tested under varying gas flow rates in countercurrent operation. The scatter of the data points in Fig. 8.24 was caused by the slightly changing water concentrations in the organic liquid.

Nonetheless, certain trends can be identified from these results. At low gas flow rates, the GLE is far to the liquid side, and therefore all monoliths and packings show low apparent stripping efficiency. The situation is inversed at high gas flow rates: now, most of the water can be stripped, and the differences in mass transfer performance again are not clearly visible. In the middle range, the expected advantage of structured packings over monoliths can be observed, but no difference was seen between the different monoliths. This is most probably due to the entrance effects (the better mass transfer of the developing film is equal for all channel geometries) and the less-pronounced corner flow of the organic liquid, which has a low surface tension.

8.2.5

Conclusions

The very particular flow patterns investigated explain to a large extent the differences observed between monoliths and distillation packings. The generally low pressure drop of monoliths and DX-packings can be attributed to the high voidage and large

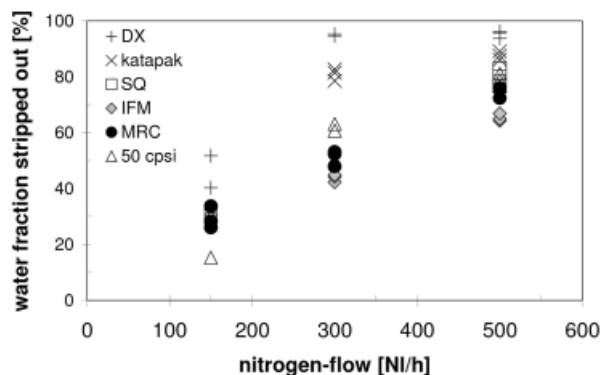


Fig. 8.24. Performance of water stripping from a 14 % ester/cumene mixture for different type of packings, depending on the nitrogen flow (2 m column length, 5 cm diameter, 160 °C, 5 bar_{abs}, liquid flow 25 kg h⁻¹, water contents 2000–2500 ppm).

hydrodynamic diameter, whereas the katapak-S® gains from the separation of gas flow and liquid-filled channels due to capillary forces in the catalyst-filled bags. The onset of flooding occurs at similar conditions for all packings; however, the ongoing development of improved monolith stacking and inlet/draining devices shifts the flooding limits for monoliths towards higher capacities and smaller hydrodynamic diameters.

The fully laminar flow regime in long monoliths leads to high early peaks and very long tailing in the RTD and fair mass transfer performance, whereas continuous remixing of the fluid due to the corrugations and the 90° turn of stacked distillation packings (DX, katapak-S®, but also Montz Multipak or katapak-SP®) reveals a narrower RTD and higher mass transfer rates. Rounded monolith channels have a better mass transfer and RTD than squared channels. However, an even larger improvement is expected (and was shown for RTD at low liquid loads) by remixing the laminar layers in stacked monoliths. On the other hand, straight-channel monoliths with fully developed laminar flow may have an advantage in gas–liquid contacting of highly viscous fluids (for example polymers) or in liquid–liquid processes. Compared to corrugated packings, the straight flow in continuous monoliths permits smaller hydrodynamic diameters, and therefore higher geometric surface areas.

8.3

Reactive Experiments

The feasibility of using catalyst-coated film-flow monoliths for reactive stripping applications was demonstrated successfully by a set of reactive experiments in a pilot-scale reactor [28].

The following sections introduce the kinetics and the side reactions of the chosen model reaction, the catalyst and the set-up used for the experiments, and outline the main results that are valid, independent of the type of packing used.

8.3.1

Model Reaction

As shown by Schembecker and Tlatlik [6], the production of a high-boiling ester is a promising system for reactive stripping application. The esterification of hexanoic acid with 1-octanol was studied as model reaction. The reaction runs very slowly without additional catalyst, and can be catalyzed by solid acids such as Amberlyst® or zeolites. Water, besides the octyl-hexanoate one of the reaction products, strongly inhibits the activity of the catalyst and lowers the maximally obtainable conversion of this equilibrium-limited reaction. In two side reactions, di-octyl-ether and octene are formed. As discussed later, the stripping of the water influences not only the activity, but also the selectivity. Therefore, this particular reaction is an illustrative example for the production of a high-boiling ester rather than a process of direct industrial interest.

8.3.1.1 Kinetics

The kinetics of the esterification of 1-octanol with hexanoic acid on zeolite BEA was studied by Nijhuis et al. [29]. For the acid, a first-order behavior was found, whereas the alcohol showed a negative reaction order of -1 . From the data, an Eley–Rideal mechanism was concluded. The acid adsorbs onto the surface of the catalyst and reacts with an alcohol. The adsorption of water, alcohol, ester or ether inhibits the reaction. Hoek [30] found that the adsorption constant of water is more than one order of magnitude higher than those of the other compounds. The rate law given by Nijhuis et al. [29] also includes the equilibrium limitation:

$$r_{\text{ester}} = \frac{k_1 \cdot k_3 \cdot c_{\text{acid}} \cdot c_{\text{catalyst}} \left(1 - \frac{c_{\text{ester}} \cdot c_{\text{water}}}{K_{\text{eq}} \cdot c_{\text{alcohol}} \cdot c_{\text{acid}}} \right)}{\left(1 + \left\{ \frac{k_1 \cdot c_{\text{acid}}}{k_3 \cdot c_{\text{alcohol}}} \right\} + K_{\text{ester}} \cdot c_{\text{ester}} + K_{\text{alcohol}} \cdot c_{\text{alcohol}} + K_{\text{water}} \cdot c_{\text{water}} \right)} \quad (2)$$

8.3.1.2 Side Reactions

As mentioned earlier, two side reactions are present. Octene is formed to a low extent ($<2\%$), and this might occur by dehydration of the 1-octanol or by splitting of an ester. Due to the small amounts, neither the mechanism of octene formation was further investigated, nor the principally possible isomerization of octene and subsequent formation of secondary esters or ethers.

The etherification of two 1-octanol molecules to di-octyl-ether is more important. Nijhuis et al. [29] suggested a dual-site mechanism and a second-order reaction for the alcohol:

$$r_{\text{ether}} = \frac{k_4 \cdot K_{\text{alcohol}}^2 \cdot c_{\text{alcohol}}^2 \cdot c_{\text{catalyst}}}{\left(1 + \left\{ \frac{k_1 \cdot c_{\text{acid}}}{k_3 \cdot c_{\text{alcohol}}} \right\} + K_{\text{ester}} \cdot c_{\text{ester}} + K_{\text{alcohol}} \cdot c_{\text{alcohol}} + K_{\text{water}} \cdot c_{\text{water}} \right)^2} \quad (3)$$

Under the experimental conditions chosen, no equilibrium limitation for this reaction was observed. The values for all kinetic parameters are presented in Tab. 8.2.

8.3.2

Experimental

8.3.2.1 Catalysts

Any (solid) acid can catalyze this esterification (e.g., Nafion® or Amberlyst®), though zeolite BEA turned out to be most active. Before coating, the monoliths were fired at 1000 °C. Following the procedure described in Ref. [31], a slurry of BEA-powder, colloidal silica and a small amount of surfactant in water was prepared. The double quantity of water was used to obtain very thin (but uniform and stable) catalyst layers in the wide channels. The monoliths were dipped into the slurry, dried and calcined. To increase the catalyst hold-up, they were again coated, dried and calcined. An ion exchange with ammonium nitrate solution and subsequent calcination was carried out to guarantee obtaining the H-BEA form. Using this method, 22–26 g of catalyst could typically be coated onto a piece of monolith (43 mm diameter, 50 cm long). Higher catalyst hold-ups can be achieved by repeating the coating procedure several times.

The coating of wire gauze DX-packings is also described in Ref. [31], and in this way a catalyst hold-up of 17 g in 50 cm of packing was achieved. The catalyst bags of the katapak-S® were filled with a sieve fraction (250–500 µm) of ground H-BEA extrudates, and this resulted in ca. 66–67 g catalyst in 50 cm of packing.

8.3.2.2 Experimental Set-ups

Most of the experiments were carried out in a pilot-scale reactor (Fig. 8.25). For each experiment, four pieces of coated monoliths were stacked carefully in line and mounted in a 2 m- high heated column of 50 mm diameter. The preheated liquid feed was distributed via a spray nozzle. After each pass, the liquid was collected in the liquid-supply vessel and was circulated continuously through the reactor (batch-recycle mode). The preheated countercurrent nitrogen stream was fed after one pass to a condenser to separate the liquid, and then vented. The condensables were collected in a phase separator, from where the water could be tapped off, whilst the

Table 8.2. Kinetic parameters for the reaction rate expressions of esterification/etherification of hexanoic acid and 1-octanol (as determined by Ref. [29]; K_{water}^* from Ref. [30]).

Parameter	Value	Units
k_1	0.020	$\text{l g}_{\text{cat}}^{-1} \text{min}^{-1}$
K_{alcohol}	9.2	l mol^{-1}
k_3	0.046	$\text{l g}_{\text{cat}}^{-1} \text{min}^{-1}$
k_4	0.00051	$\text{mol g}_{\text{cat}}^{-1} \text{min}^{-1}$
K_{ester}	7.5	l mol^{-1}
K_{water}^*	600	l mol^{-1}
K_{eq}	16	–

organics were sent back to the liquid vessel via an overflow. During the experiments liquid samples were taken from the liquid inlet to the reactor and from the reactor outlet. Samples were analyzed using gas chromatography (GC) and a Karl Fischer coulombmeter (KF) to determine concentrations and water contents. Herein, the conversion measured at the reactor inlet for a certain time point is referred to as “reactor inlet conversion”. The difference in conversion between the reactor inlet and outlet samples at the same time point will be called “per (single) pass conversion”.

For reactive stripping experiments, ca. 13 L of liquid was used containing cumene as solvent, tetradecane as internal standard, and ca. 12 mol% each of hexanoic acid and octanol-1. For the experiments with elevated acid concentrations, these values were 20 mol% and 11 mol%, respectively. All experiments were carried out at 160 °C and 5 bar absolute pressure.

The total BEA catalyst amount in the reactor ranged from 91 to 103 g for the different monolith sets. The mass balances for the experiments were in the range of 99 % to 101 %. The water balances for the reported experiments were in the range of 97 % to 101 %, thus giving sufficient confidence in the results of GC- and KF-analyses. Flooding of the column was never observed.

For the experiments with increased water content or suppressed water removal, a 5 cm-long piece of coated monolith was mounted in a 500-mL autoclave. All liquid concentrations, operation conditions and catalyst hold-up were the same as in the pilot-scale plant. To maintain a gradient-less operation, a turbine-type stirrer recirculated the liquid very rapidly through the monolith channels. During the experiments, liquid samples were taken from the reactor and analyzed as described above.

For the activity test, stirred glass flasks (50 mL) were run under atmospheric pressure and reflux conditions. The solvent (cumene) boils at 160 °C, and the vapor enters the cooler above the glass flask, from where the condensates flow back. Treatment of the samples, all liquid concentrations and catalyst hold-up were similar to those in the pilot-scale plant and in the autoclave.

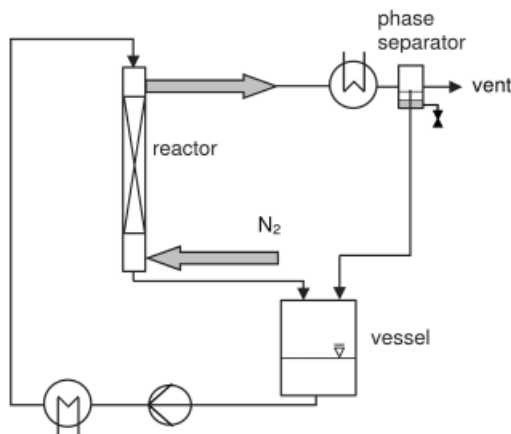


Fig. 8.25. Schematic flowsheet for pilot-scale reactive stripping experiments in countercurrent mode.

8.3.3

Experimental Results

In this section, only general findings will be discussed which are valid for all packings investigated. Differences between the monolith types or between distillation packings and monoliths, which can be explained by the different flow patterns, are discussed in Section 8.4.

Figure 8.26 shows the initial reaction rates, measured for the original BEA powder, for BEA-extrudates (ca. 12 mm long, 1.5 mm diameter), milled extrudates, samples from BEA coating and from coating of DX-packings. It is clearly visible, that all initial rates (with exception of that for the DX-coating) are practically equal. It can be concluded that internal (pore) diffusion limitation plays no role. Also, the coating procedure seems to have no negative impact on the activity in the case of monoliths. For the coating of the DX-packings, slight deactivation can be assumed, as the DX-packings had already been used and recalcined several times.

8.3.3.1 Effect of Water Removal

The conversion of hexanoic acid as a function of time for the three different experiments is plotted in Fig. 8.27. For orientation, the maximally obtainable conversion if no water is removed from the mixture is also plotted (79 % under the chosen conditions). The lowest curve shows a blank experiment where the liquid flows over uncoated monoliths and reacts homogeneously. The second curve represents an experiment in the autoclave where the water removal is suppressed. The comparison of these two curves indicates that, without decreasing the water contents, the catalytic activity of the BEA cannot be used efficiently. The third (highest) curve proves the effect of reactive stripping. The reaction runs much faster and easily continues beyond the equilibrium.

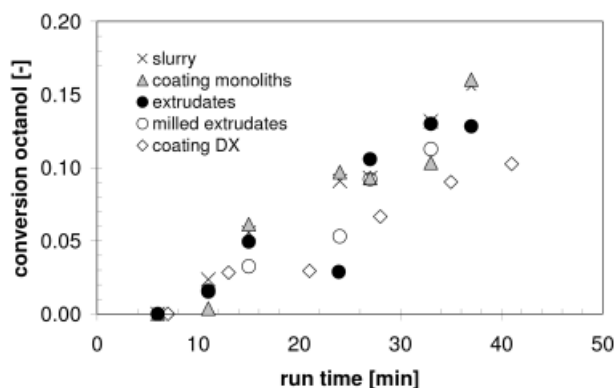


Fig. 8.26. Initial rates for different zeolite BEA-based catalysts, measured in open round-bottomed glass flask reactors (160 mg catalyst, 160 °C, atmospheric pressure).

8.3.3.2 Co-current versus Countercurrent

Due to an always high water contents at the reactor inlet, the eventual internal water loop (as described in Fig. 8.3) should not be a problem. However, if co-current and countercurrent operation is compared (Fig. 8.28), a clear difference between these two operation modes is found only for the water concentrations, whereas the gain in space-time yield is limited to around 10 %. This can be attributed to the high recirculation rate of the liquid, whereas in both experiments the gas phase was vented after one pass. Therefore, the gas-liquid operation was of the cross-flow-type rather than pure co-current or countercurrent. To identify the effect of pure co-current or countercurrent operation, the gas phase should also be recycled.

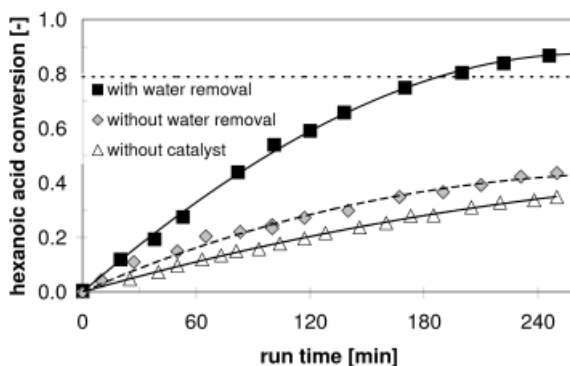


Fig. 8.27. Conversion of hexanoic acid in countercurrent operation with liquid recycle (2 m column length, 5 cm diameter, 160 °C, 5 bar_{abs}, liquid flow 25 kg h⁻¹, nitrogen flow 500 Nm³ h⁻¹).

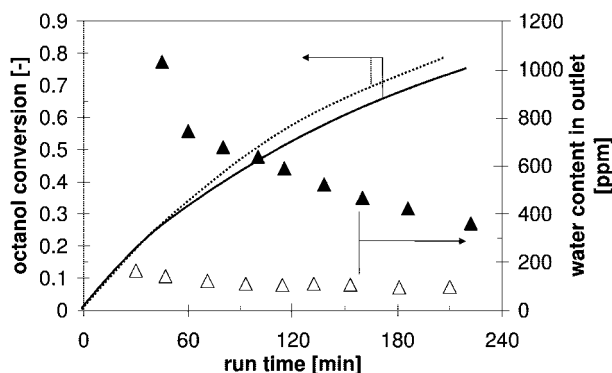


Fig. 8.28. Conversion of octanol and outlet water contents in countercurrent (Δ, dotted line) versus co-current (▲, solid line) operation with liquid recycle (1 m of DX® packings, 5 cm diameter, 160 °C, 5 bar_{abs}, liquid flow 25 kg h⁻¹, nitrogen flow 500 Nm³ h⁻¹).

8.3.3.3 Selectivity

Due to side reactions, in most of the experiments a higher octanol conversion than acid conversion is found. To investigate this phenomenon, an instantaneous selectivity is defined as the ratio of the rate of ester formation over the rate of 1-octanol-disappearance in one pass through the column:

$$S_{inst} = \frac{r_{ester}}{r_{oct.}} \approx \frac{c_{ester, outlet} - c_{ester, inlet}}{c_{oct., inlet} - c_{oct., inlet}} = \frac{c_{hex.acid, inlet} - c_{hex.acid, outlet}}{c_{oct., inlet} - c_{oct., inlet}} \quad (4)$$

As the selectivity depends on the concentrations of all compounds, the instantaneous selectivity is plotted over octanol inlet conversions to compare different experiments at similar concentrations. Figure 8.29 shows the S_{inst} for five different experiments where only the type of packing was varied. Two striking observations can be made. First, all data points for S_{inst} are on the same curve; and second, this curve starts at around 75 %, runs through a maximum, then at ca. 50 % conversion level through a minimum followed by a second maximum and a final decay to ca. 50 % at very high inlet conversion levels.

The coincidence of the data points for several experiments can be explained by the similar concentrations obtained by the way the data are plotted. However, this implies that the water contents are also similar. As shown in Fig. 8.30, and as expected based on the similar stripping performance of most internals (see Fig. 8.24), the water contents are also comparable.

At low inlet conversions, the single-pass conversions are so high that not all of the water produced in one pass can be stripped. Therefore, at the initial stages of

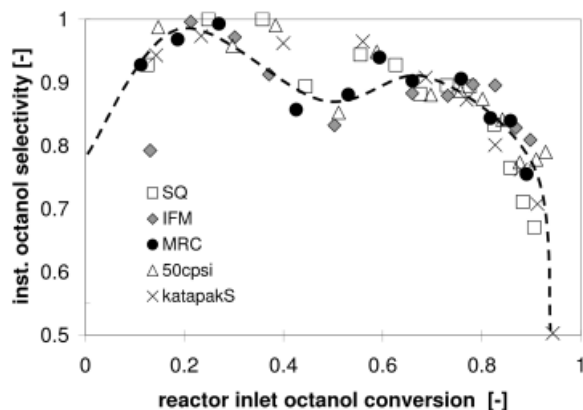


Fig. 8.29. Instantaneous octanol selectivity S_{inst} for different packings plotted over inlet octanol conversion (2 m column length, 5 cm diameter, 160 °C, 5 bar_{abs}, liquid flow 25 kg h⁻¹, countercurrent operation).

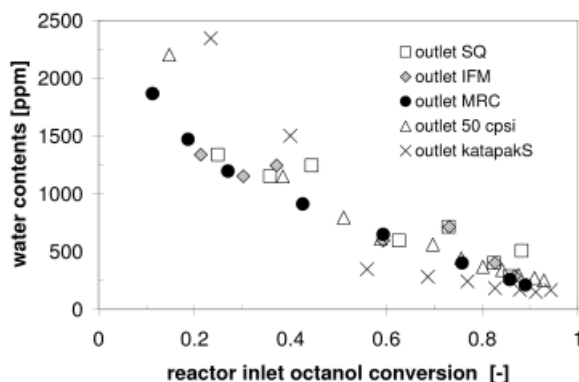


Fig. 8.30. Outlet water concentrations for different packings plotted over inlet octanol conversion (2 m column length, 5 cm diameter, 160 °C, 5 bar_{abs}, liquid flow 25 kg h⁻¹, countercurrent operation).

the experiment the water concentrations are higher at the reactor outlet than at the inlet. Only with decreasing per-pass conversions at higher total conversion levels can the overall water content be decreased.

In order to understand the maxima and the minimum of the instantaneous selectivity S_{inst} , it is useful to plot the predictions of the kinetic model as represented by the two rate Equations (1) and (2). In Fig. 8.31, the S_{inst} expected from the kinetics is plotted depending on the fraction of water stripped from the liquid. All these curves start at around 75 %, increase to near-unity, and then show a sharp drop at high inlet conversion levels. Depending on the fraction of water stripped, the slope of the initial increase and onset of the final drop of S_{inst} differ.

The difference in initial slope is attributed to the different number of catalytic sites involved in the two reactions. If water is stripped from the liquid, coverage of the catalyst surface with water molecules decreases, and in consequence both reactions are running faster. However, the increase of ether formation is proportional to the square of the progress of the esterification, because of the square in the adsorption term in the ether rate expression (3). Therefore, stripping of water increases the rates, but lowers the selectivity at low conversion levels.

If the conversion level increases, the reactant concentrations decrease. As the esterification is of first order in acid, but the etherification of second order in alcohol, the latter suffers more from low reactant concentrations. In consequence, the instantaneous selectivity increases with increasing conversion levels.

The sharp drop at high conversion levels is caused by the equilibrium limitation of the esterification. If the equilibrium is reached, no more ester is formed, whereas the etherification continues. As the equilibrium depends on the water concentration, the drop of S_{inst} to zero occurs at higher conversion levels, if water has been stripped from the liquid.

Fortunately, inlet and outlet concentrations are known, as are the inlet and outlet water contents (Fig. 8.30), and therefore also the maximum possible water content in the middle of the column. This allows plotting “regions” of concentration levels and the corresponding water contents found in the experiments into the graph (shown as circles in Fig. 8.31). At the beginning of the experiments, water contents are so high that the instantaneous selectivity follows the line for stoichiometric water contents. At about 50 % conversion, the effect of the water stripping is evident, and the selectivity drops. As the reaction continues, the selectivity rises again due to the low reactant concentrations until the equilibrium is reached and the selectivity drops finally. Principally, the shape of the S_{inst} -curve is found back and therefore explained from the interaction between kinetics and mass transfer. For a more detailed analysis, modeling/simulation studies are carried out in collaboration with Dortmund University. Results will be published soon.

8.3.3.4 Acid Excess

The selectivity issues discussed in the previous section can easily be avoided by an excess of acid. An optimized process should run in semi-batch operation (continuous feeding of the alcohol to keep its concentration low). In this way, the effective water removal would have the greatest impact on the space–time yield.

To study the influence of the acid concentration, an experiment with an initial hexanoic acid concentration of 20 mol% and 11 mol% initial octanol concentration was carried out. As expected, very high octanol selectivity and octanol conversion are achieved (Fig. 8.32). However, taking the 1.8-fold higher acid concentration into account, enhancement of the single-pass conversions is lower than expected. As the

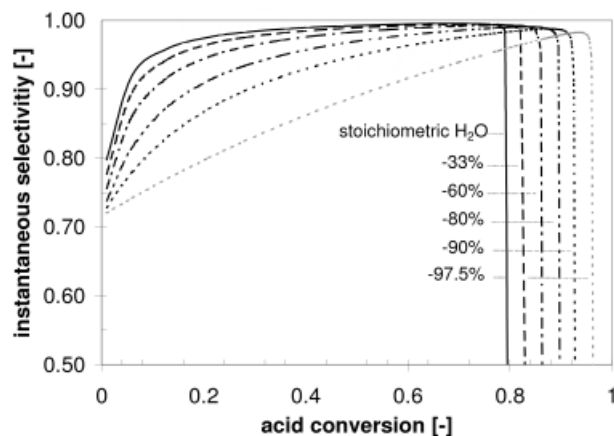


Fig. 8.31. Predicted instantaneous octanol selectivity S_{inst} plotted over inlet octanol conversion for different degrees of water removal. Circles indicate the inlet octanol conversions and the corresponding degrees of water removal found in the experiments shown in Fig. 8.29.

esterification is in first order to the acid concentration, and the acid adsorbs only weakly on the catalyst [29], more than 50 % enhancement could be expected, but only 30 % was found. This can be explained by the high water contents (400 to 3000 ppm), which are almost double the values found at non-elevated acid concentrations (200–1300 ppm).

In a non-reactive stripping experiment, it was found that higher acid concentrations change the GLE and cause higher liquid phase water concentrations. Reaction product mixtures with constant water contents, but of different reactor inlet conversion levels, were fed at 160 °C and 10 bar_g over uncoated IFM-monoliths. Hence, no reaction other than water removal could take place in the column. With increasing reactor inlet conversion levels – and therefore decreasing acid concentrations – the fraction of water stripped out increases. The only reason for this can be a shift of the VLE (Fig. 8.33). This observation is confirmed by flash simulations in Aspen Plus® at Dortmund University [32], which showed increasing equilibrium water contents in the organic liquid for increasing acid concentrations.

8.3.4

Conclusions

The esterification of 1-octanol with hexanoic acid is a good system for studying reactive stripping, as it not only represents many industrial processes, but also illustrates the interdependencies of activity, selectivity, and mass transfer in reactive separations.

Experiments in a pilot-scale plant demonstrated the feasibility of applying coated monoliths and DX® packings or katapak-S® successfully as catalyst carriers in reactive stripping. It was proven that the water removal increases the catalyst activity and permits a “shift” in the equilibrium. In accordance with the kinetics of this

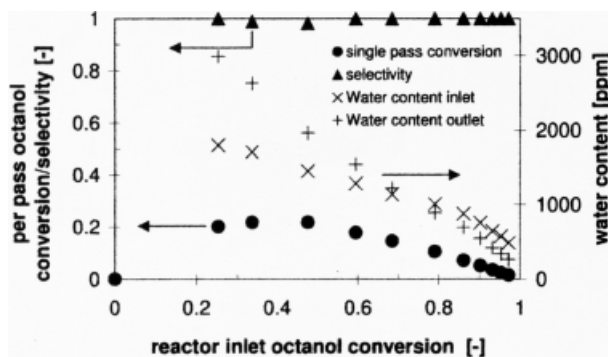


Fig. 8.32. Selectivity, per-pass-octanol-conversion and inlet/outlet water contents for an experiment with increased inlet hexanoic acid concentration (2 m column length, 5 cm diameter, 160 °C, 5 bar_{abs}, liquid flow 25 kg h⁻¹, countercurrent operation).

particular model reaction, the water removal causes a loss in selectivity due to different reaction mechanisms. However, it was shown that acid excess or semi-batch operation mode (continuous feeding of alcohol to keep its concentration low) solves all selectivity issues. In any case, in many other processes or reaction systems, an improved mass transfer may have a positive influence on the selectivity.

8.4

Comparison of Different Internals

In this section, the effects on reactor performance caused by different flow patterns or geometries of the packings investigated are discussed. The first section examines the influence of different monolith channel geometries, whilst in the second section monoliths and distillation packings are compared.

8.4.1

Film-flow Monoliths

Four different types of BEA-coated monoliths were used for reactive stripping experiments [28]: 25 cpsi square, 50 cpsi square, finned (IFM) and more rounded corners (MRC). To allow a direct comparison, in Fig. 8.34, the octanol conversions per single pass (i.e., the difference in overall conversion between inlet and outlet of the reactor), normalized to 100 g of catalyst, are shown, plotted over the octanol conversion at the reactor inlet. The increase in single-pass conversions for low inlet conversions is caused by the strong decrease of the initially high water concentrations due to the stripping. At inlet conversions above 25 %, a decrease in single-pass conversions can be observed, which can be explained by the decreasing concentrations of acid and alcohol.

However, no significant differences in the performance of the three monolith types are observed. As shown in Fig. 8.30, the water contents for all four monolith

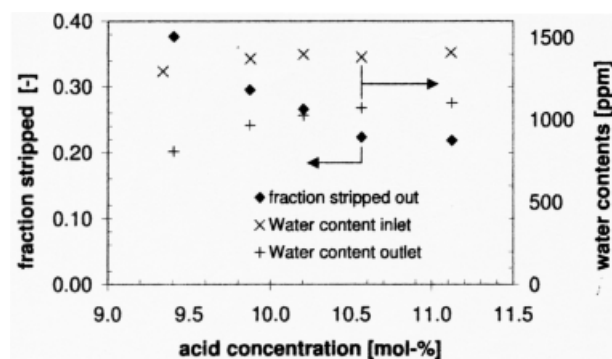


Fig. 8.33. Stripping performance depending on hexanoic acid concentration (2 m column length, 5 cm diameter, 160 °C, 5 bar_{abs}, liquid flow 25 kg h⁻¹, countercurrent operation).

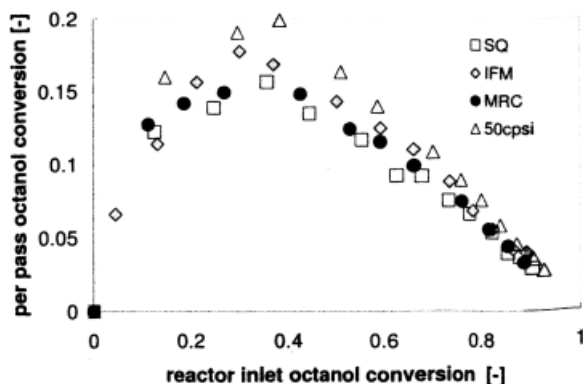


Fig. 8.34. Per-pass-octanol-conversion for different monolith types plotted over inlet octanol conversion (2 m column length, 5 cm diameter, 160 °C, 5 bar_{abs}, liquid flow 25 kg h⁻¹, countercurrent operation).

types are also quite similar, and this was expected on the basis of the non-reactive stripping experiments (see Fig. 8.24). Most probably, wetting of the catalyst layers is more uniform due to the low surface tension of the organic liquid. Another reason might be the dominance of the entrance effects, which may mask differences in mass transfer performance for completely developed laminar films in different channel geometries.

8.4.2

Monoliths versus DX® and katapak-S®

8.4.2.1 Activity

If the conversion of octanol is plotted over the run time for katapak-S®, DX® and a typical monolith experiment (Fig. 8.35), katapak-S® shows clearly the highest, and DX-packings the lowest, space–time yield.

However, catalyst hold-up was very different among the experiments, ranging from 34 g of BEA-coating for the 1 m-long bed of DX over 91 g for 2 m coated monoliths to 262 g BEA-extrudates in the beds of katapak-S® (2 m). The conversions per single pass through the column are shown in Fig. 8.36, but normalized to 100 g of catalyst. Now, the picture is inverted. The high activity of the coated DX-packings can be explained with the extraordinarily low water contents (<300 ppm) in the only 1 m-long bed of DX-packings. As the catalyst activity and water contents are similar for katapak-S and monoliths, a similar normalized conversion was expected. The slightly lower activity of the katapak-S might be explained with some stagnant zones being present in this type of packing at very low liquid loads [22]. Another explanation might be minor catalyst deactivation, as the packings had already been used and calcined several times. Nonetheless, it is remarkable that the higher amount of water produced in katapak-S® by the larger catalyst hold-up did not accumulate.

Thus, it can be concluded that, in monoliths as well as in katapak-S®, the mass transfer performance is limiting, but is reasonable compared to catalyst hold-up. A comparison with the DX-packings should perhaps be made by modeling/simulation, as the shorter column greatly improves the stripping performance.

8.4.2.2 Selectivity

The overall selectivity (i.e., total amount of ester produced divided by the total amount of octanol reacted) for the three experiments is presented in Fig. 8.37. Due to the high water contents in the experiment with katapak-S, the etherification was suppressed to the highest extent, and this resulted in the highest overall selectivity.

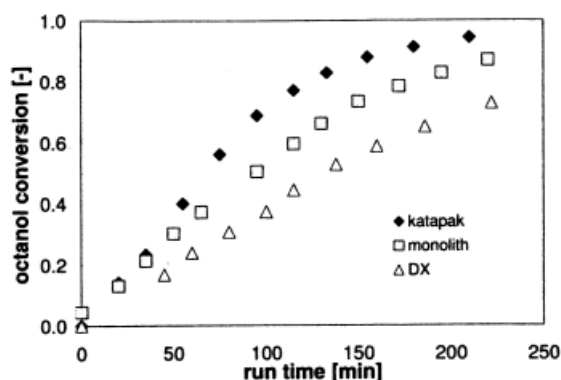


Fig. 8.35. Octanol conversion for different packings plotted over the run time (2 m katapak-S®, 2 m monoliths, 1 m DX®, 160 °C, 5 bar_{abs}, liquid flow 25 kg h⁻¹, countercurrent operation).

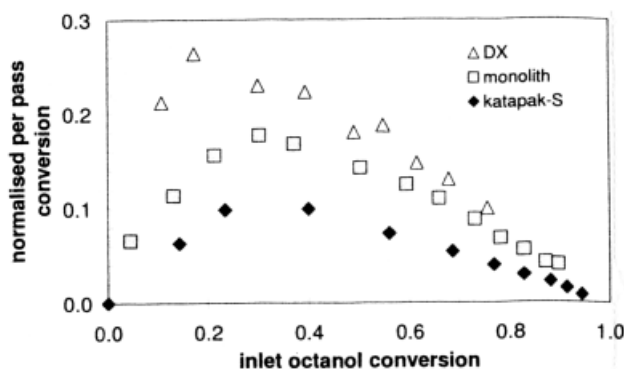


Fig. 8.36. Per-pass-octanol-conversion for different packings, normalized to 100 g catalyst hold-up plotted over inlet octanol conversion (2 m katapak-S®, 2 m monoliths, 1 m DX®, 160 °C, 5 bar_{abs}, liquid flow 25 kg h⁻¹, countercurrent operation).

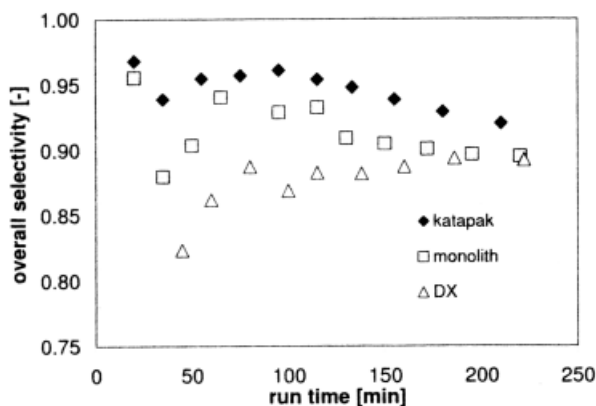


Fig. 8.37. Overall selectivity for different packings plotted over the run time (2 m katapak-S®, 2 m monoliths, 1 m DX®, 160 °C, 5 bar_{abs}, liquid flow 25 kg h⁻¹, countercurrent operation).

On the other hand, the short column of DX-packings favored the stripping and therefore the side reaction (etherification).

8.5

Conclusions and Future Trends

Reactive stripping has its own importance, in addition to reactive distillation. Several situations exist in which reactive stripping becomes more interesting; for example, in the production of high-boiling esters and ethers, especially, when reactants or products are temperature-sensitive, and also in gas–liquid–solid processes, where product inhibition may play a role.

The potential of structured packings as catalyst carriers for reactive stripping, film-flow-monoliths, Sulzer DX®-packings, both coated with zeolite BEA, and katapak-S®, filled with BEA-particles, was explored in cold-flow experiments and under reactive stripping conditions in a pilot-scale plant.

All packings show generally a low pressure drop (compared to a trickle flow in a bed of particles). The onset of flooding in countercurrent operation occurs at similar conditions for all packings; however, the ongoing development of improved monolith stacking and inlet/draining devices shifts the flooding limits for monoliths towards higher capacities.

The flow pattern in DX and katapak-S® (and also Montz Multipak® or katapak-SP®) is characterized by frequent remixing and disturbance of the liquid films, whereas fully developed laminar flow dominates in long monoliths. The latter leads to high early peaks and long tailing in the RTD and fair mass transfer performance, whereas continuous remixing of the fluid in distillation packings leads to a narrower RTD and higher mass transfer rates. However, an improvement is expected from remixing the laminar film flow in stacked monoliths. On the other hand, monoliths

with fully developed laminar flow may have an advantage in gas–liquid contacting of highly viscous fluids.

All reactive stripping experiments showed that reducing the water content level (due to better stripping performance) increases the per-pass conversions, but has a negative effect on selectivity in the chosen model reaction system. Nonetheless, the water contents are the result of a balance between stripping efficiency and catalyst hold-up. As a consequence, the space–time yield was highest for katapak-S®, whereas in DX®-packings, the excellent separation efficiency optimized the use of catalyst, but decreased the selectivity. For industrial applications, the choice will always depend on the balance between mass transfer performance, the kinetics, the activity of the catalyst, and the process economics.

In principle, a higher catalyst hold-up in monoliths is possible, but then the mass transfer performance should also be adapted. For this purpose, the remixing of laminar layers in monoliths by intelligent stacking shows promising preliminary results, although this has still to be demonstrated in reactive stripping experiments.

Acknowledgments

The authors gratefully acknowledge financial support from the EU project “Intelligent Column Internals for Reactive Separations (INTINT)” GRD1 CT1999 10596, by the EU TMR Grant ERBFMGE-CT-950066 (access to EU large scale facility Wageningen NMR Centre), and from Grant No. HPRI-CT-1999-00085 (EU programme Access to Research Infrastructure). The monolithic structures were supplied by Corning, and packings by Sulzer Chemtech. The authors also thank T.A. Nijhuis, A.E.W. Beers, I. Hoek, M. Behrens, M. Kloecker, and H. Kahnis for their support and valuable discussions.

Symbols

$a, S/V$	geometric surface area [$\text{m}^2 \text{m}^{-3}$]
c	concentration [mol dm^{-3}]
c_{catalyst}	catalyst concentration [g dm^{-3}]
$d_{\text{hydraulic}}$	hydraulic diameter [mm]
ε	voidage [$\text{m}^3 \text{m}^{-3}$]
k	kinetic parameter [$\text{dm}^3 \text{g}_{\text{cat}}^{-1} \text{min}^{-1}$, $\text{mol g}_{\text{cat}}^{-1} \text{min}^{-1}$]
K	adsorption constant [$\text{dm}^3 \text{mol}^{-1}$]
K_{eq}	equilibrium constant [$\text{mol}^2 \text{mol}^{-2}$]
k_{La}	volumetric mass transfer coefficient [s^{-1}]
l	length [m]
r	reaction rate [mol min^{-1}]
r_{corner}	corner radius [mm]
S_{inst}	instantaneous selectivity [mol mol^{-1}]
u_{LS}	superficial liquid velocity [$\text{m}^3 \text{m}^2 \text{s}^{-1}$]

References

1. F. M. Dautzenberg and M. Mukherjee, *Chem. Eng. Sci.*, **2001**, 56, 251–267.
2. A. Stankiewicz, *Chem. Eng. Proc.*, **2003**, 42, 137–144.
3. R. Taylor and R. Krishna, *Chem. Eng. Sci.*, **2000**, 55, 5183–5229.
4. R. S. Huss, F. Chen, M. F. Malone, et al., *Comp. Chem. Eng.*, **2003**, 27, 1855–1866.
5. R. S. Hiwale, N. V. Bhate, Y. S. Mahajan, et al., *Int. J. Chemical Reactor Engineering*, **2004**, Vol. 2: R1.
6. G. Schembecker and S. Tlatlik, *Chem. Eng. Proc.*, **2003**, 42, 179–189.
7. U. Kunz, U. Hoffmann, European Patent 0 859 653 (96 945 840.5-2113).
8. S. Yu, A. Zhou and Q. Tan, *Comp. Chem. Eng.*, **1997**, 21, 409–415.
9. B. W. van Hasselt, P. J. M. Lebens, H. P. A. Calis, et al., *Chem. Eng. Sci.*, **1999**, 54, 4791–4799.
10. P. J. M. Lebens, Development and design of a monolith reactor for gas-liquid countercurrent operation, PhD Thesis, TU Delft, 1999.
11. M. Kreutzer, Hydrodynamics of Taylor flow in Capillaries and Monolith Reactors, PhD Thesis, TU Delft, 2003.
12. A. Cybulski, R. Edvinsson, S. Irandoust, et al., *Chem. Eng. Sci.*, **1993**, 48, 3463–3478.
13. T. C. Thulasidas, M. A. Abraham, R. L. Cerro, *Chem. Eng. Sci.*, **1995**, 50, 183–199.
14. J. J. Heiszwolf, L. B. Engelvaart, M. G. van den Eijnden, et al., *Chem. Eng. Sci.*, **2001**, 56, 805–812.
15. A. K. Heibel, F. J. Vergeldt, H. van As, et al., *AIChE J.*, **2003**, 49, 3007–3017.
16. A. K. Heibel, T. W. J. Scheenen, J. J. Heiszwolf, et al., *Chem. Eng. Sci.*, **2001**, 56, 5935–5944.
17. A. K. Heibel, J. A. Jamison, Patent WO03040847.
18. I. Mazzarino, *Chem. Eng. Sci.*, **1999**, 54, 3677–3682.
19. M. Piironen, H. Haario, I. Turunen, *Chem. Eng. Sci.*, **2001**, 56, 859–864.
20. M. I. Urseanu, J. Ellenberger, R. Krishna, *Catalysis Today*, **2001**, 69, 105–113.
21. J. M. van Baten, J. Ellenberger, R. Krishna, *Chem. Eng. Sci.*, **2001**, 56, 813–821.
22. P. Moritz and H. Hasse, *Chem. Eng. Sci.*, **1999**, 54, 1367–1374.
23. A. K. Heibel, J. A. Jamison, P. Woehl, et al., 2004, submitted.
24. A. K. Heibel, P. J. M. Lebens, J. W. Middelhoff, et al., 2004, submitted.
25. C. Noeres, A. Hoffmann, A. Górak, *Chem. Eng. Sci.*, **2002**, 57, 1545–1549.
26. A. Kolodziej, M. Jaroszynski, I. Bylica, *Chem. Eng. Proc.*, **2004**, 43, 457–464.
27. A. Kolodziej, M. Jaroszynski, A. Hoffmann, et al., *Catalysis Today*, **2001**, 69, 75–85.
28. T. J. Schildhauer, F. Kapteijn, J. A. Moulijn, *Chem. Eng. Proc.*, 2004, accepted.
29. T. A. Nijhuis, A. E. W. Beers, F. Kapteijn, et al., *Chem. Eng. Sci.*, **2002**, 57, 1627–1632.
30. I. Hoek, T. A. Nijhuis, A. Stankiewicz, et al., *Appl. Cat. A*, **2004**, 266, 109–116.
31. T. A. Nijhuis, A. E. W. Beers, Th. Virgins, et al., *Catal. Rev.-Sci. Eng.*, **2001**, 43, 345–380.
32. M. Kloeker, Universität Dortmund, Lehrstuhl für Thermische Verfahrenstechnik, Private communication.

9 Reactive Absorption

Eugeniy Y. Kenig and Andrzej Górak

9.1 Introduction

The main purposes of *absorption processes* are the removal of one or more components from the gas phase, the production of particular substances in the liquid phase, and gas mixture separation [1]. Industrial absorption operations are usually realized by combining absorption and *desorption* units.

An example given in Fig. 9.1 illustrates this combination of two processes. In an absorber, one or several gas components are absorbed by a lean solvent, either physically or chemically. A rich solvent, after preheating in heat exchangers H_1 and H_3 , is transported to the top of a desorption unit which usually operates under a pressure lower than in absorber. Part of the gas absorbed by the rich solvent is desorbed due to flashing and heating. The other part has to be desorbed in the stripper with the

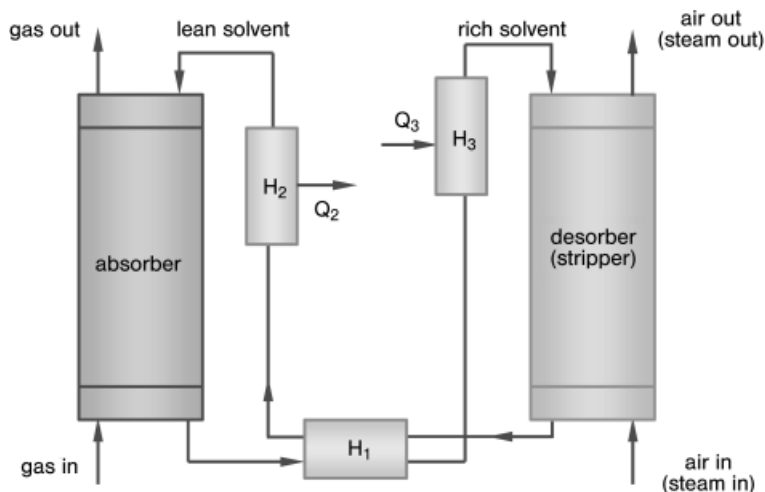


Fig. 9.1. Scheme of an absorber-desorber link (adapted from Ref. [1]).

inert gas or steam. The lean solvent then flows through the heat exchanger H_1 to recover heat necessary for heating the reach solvent, passes the heat exchanger H_2 to cool down to a desired temperature and finally enters the absorber [1].

Usually, a small amount of fresh solvent should be added to the column in order to equalize the solvent loss due to evaporation in the desorber or underwent irreversible chemical reaction occurring in the whole system [1].

Reactive absorption represents a process in which a selective solution of gaseous species by a liquid solvent phase is combined with chemical reactions. As compared to purely physical absorption, reactive absorption does not necessarily require elevated pressure and high solubility of absorbed components: because of the chemical reaction, the equilibrium state can be shifted favorably, resulting in enhanced solution capacity [2]. Most of the reactive absorption processes involve reactions in the liquid phase only, but in some of them both liquid and gas reactions occur [3, 4].

Usually, the effect of chemical reactions in reactive absorption processes is advantageous only in the region of low gas-phase concentrations due to limitations by the reaction stoichiometry or equilibrium [5]. Further difficulties of reactive absorption applications may be caused by the reaction heat through exothermic reactions and by relatively difficult solvent regeneration [6, 7]. Most of the reactive absorption processes are steady-state operations, either homogeneously catalyzed or auto-catalyzed. Recently, an application of a reactive absorption process based on using secondary amine groups on solid supports as immobilized activators has been reported [8].

Reactive absorption processes are predominantly used for the production of basic chemicals, e.g., sulfuric or nitric acids, and for the removal of harmful substances such as H_2S from gas streams. Absorbers or scrubbers in which reactive absorption is performed are often considered as gas-liquid reactors [9]. If more attention is paid to the mass transport, these apparatus are treated rather as absorption units. Some important industrial applications of reactive absorption are given in Tab. 9.1.

Reactive absorption can be realized in a variety of equipment types. The process is characterized by independent flow of both phases and permits both co-current (down-flow and up-flow) and countercurrent regimes.

Reactive absorption is essentially an old process which has been known since the foundation of modern industry. This is also a very important process, being the basic operation in many technological chains. More recently, the role of reactive absorption as a key environmental protection process has grown up significantly, and today the process appears to be the most widely applied reactive separation operation.

Despite the clear importance of reactive absorption, its behavior is still not properly understood. This can be attributed to a very complex combination of process thermodynamics and kinetics, with intricate reaction schemes including ionic species, reaction rates varying over a wide range, and complex mass transfer-reaction coupling. As compared to distillation, reactive absorption is a fully rate-controlled process and it occurs definitely far from the equilibrium state. Therefore, both practitioners and theoreticians are highly interested to establish a proper understanding and description of this process.

Table 9.1. Industrial applications of reactive absorption.

Aim of the process	Examples	Application area	References
Removal of harmful substances	<ul style="list-style-type: none"> • Coke oven gas purification • Carbon dioxide removal by amines/ amine blends/ hot potassium carbonate solutions • NO_x removal 	Gas purification	63, 89, 91, 105–107
Retrieval/regeneration of valuable substances or non-reacted reactants	<ul style="list-style-type: none"> • Solvent regeneration 	Gas separation	108
Production/preparation of particular products	<ul style="list-style-type: none"> • Sulfuric and nitric acid manufacture • Formaldehyde preparation 	Chemical synthesis	4, 26, 86
Water removal	<ul style="list-style-type: none"> • Water removal from natural gas • Air drying 	Gas drying	109, 110
Conditioning of gas streams	<ul style="list-style-type: none"> • Synthesis gas conditioning 	Gas separation/ gas purification	108
Separation of substances	<ul style="list-style-type: none"> • Olefin/paraffin separation 	Separation of organic components	111

This chapter provides a comprehensive overview of reactive absorption and discusses in detail the following issues:

- important industrial applications
- reactive absorption equipment
- modeling basics and different modeling concepts
- model parameter estimation
- four different industrial case studies, namely
 - NO_x absorption
 - coke gas purification
 - CO₂ absorption by amines
 - SO₂ absorption into aqueous NaHCO₃/Na₂CO₃ solutions

9.2

Reactive Absorption Equipment

Reactive absorption is usually carried out in apparatus providing a continuous flow of both contacting phases. Reactive absorption units can be best classified if one considers which of the phases is in a continuous form, and which is in a disperse form. Using this criterion, the classification of the reactive absorption equipment is represented in Tab. 9.2 (see Ref. [1]).

Most often, reactive absorption is carried out in packed or plate columns. The structure of such columns and different internals are shown schematically in Fig. 9.2.

Packed columns are commonly used in reactive absorption operations [10, 11]. They represent cylindrical or rectangular columns up to several meters in diameter

Table 9.2. Reactive absorption units.

Unit group criterion	Unit type
Both phases in a continuous form	<ul style="list-style-type: none"> packed columns thin-film contactors wetted-wall columns contactors with flat surface laminar jet absorber disc (sphere) columns
A disperse gas phase and a continuous liquid phase	<ul style="list-style-type: none"> plate columns plate columns with packing bubble columns packed bubble columns mechanically agitated columns jet absorbers
A disperse liquid phase and a continuous gas phase	<ul style="list-style-type: none"> spray columns venturi scrubbers

and up to 60 meters high. In packed columns, the desired large specific contact area is achieved when a liquid flows down a packing surface, whereas a gas streams along the packing free surface, either countercurrently or co-currently.

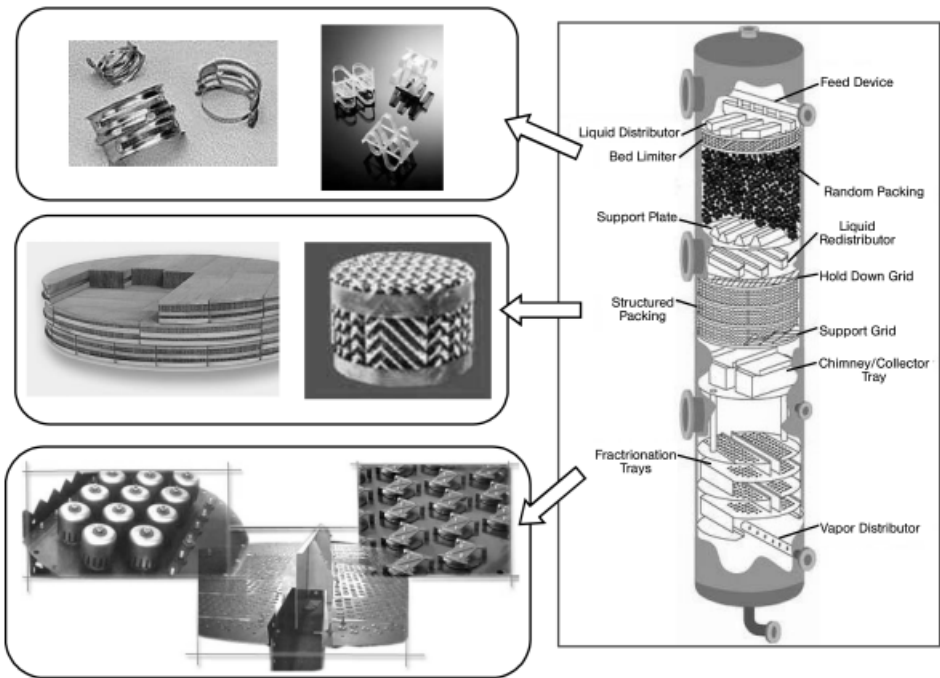


Fig. 9.2. Schematic representation of a reactive absorption column and different column internals.

Packings can be subdivided into two classes: dumped (random) packings and structured ones. Within the first class, one can distinguish between three generations: elements with closed structure (e.g., Rasching rings); those with more open structure (e.g., Pall rings, Berl saddles, Intalox saddles); and low pressure-drop elements (e.g., Nutter-Ring, FLEXIRING, Raschig Super-Ring).

Two “areas of choice” of structured packing are low pressure-drop applications and increasing the capacity of existing columns. Among the modern structured packings are gauze wire packings Sulzer BX and Montz-Pak A-series, sheet packings Sulzer Mellapak and Montz-Pak B-Series, lamella packing RomboPak, etc. [12].

Plate columns represent another basic type of equipment widely used for reactive absorption operations. These consist of a shell and a number of plates placed one above the other (cf. Fig. 9.2). The diameter and height of the column can reach 10 and 50 m, respectively, although they are usually much smaller. The phases generally flow countercurrently, however on each given plate a cross-flow is usually established. The plates are usually made of steel sheets, and there are three basic plate types, namely cross-flow plates (e.g., bubble cap, sieve and valve trays), countercurrent plates (e.g., baffle plates), and less widespread plates, which provide gas and liquid flow through the same orifices in the plate. The latter type does not require downcomers. There are numerous plate designs, and details of their description can be found elsewhere [13]. In cases when the gas phase contains dust particles or some deposit may precipitate, additional light packing elements placed on the plates are advantageous in preventing column blocking.

Bubble columns are used very widely for reaction absorption applications. In bubble columns, the gas phase flows in the form of bubbles, either countercurrently or co-currently. Bubble columns provide significant liquid hold-up and sufficient liquid residence time. The column diameter sometimes exceeds 5 m, and its height reaches 10 m or more.

There are several other types of apparatus used for reactive absorption, though these are less widespread. In *mechanically agitated bubble columns* it can be assumed that both phases are ideally mixed, whereas in the *jet absorber*, the gas stream breaks on a liquid surface and is dispersed in the liquid. In *spray towers* and *venturi scrubbers*, liquid is sprayed as fine droplets. *Thin-film contactors*, in which liquid film is scrapped from the walls by impellers, are applied for reactive absorption in viscous liquids. Some units, such as *wetted-wall columns*, *contactor*, *laminar jet absorber* and *disc (sphere) column* are used mainly in laboratory.

Distributors and collectors of liquid provide uniform wetting of the packings area and the withdrawal of phases from the packing. The best-known distributor types are: orifice-riser, perforated-pipe, spray-nozzles, and through distributors.

9.3

Modeling Concept

9.3.1

General Aspects

Optimal functioning of reactive absorption processes depends primarily on relevant process design, properly selected column internals as well as sufficient understanding of the process behavior. To describe such phenomena adequately, specially developed mathematical models capable of simultaneously taking into consideration column hydrodynamics, mass transfer resistances and reaction kinetics are required [14].

Reactive absorption processes present essentially a combination of transport phenomena and reactions taking place in a two-phase system with an interface. Because of their multicomponent nature, reactive absorption processes are affected by a complex thermodynamic and diffusional coupling which, in turn, is accompanied by simultaneous chemical reactions [14–16]. Generally, the reaction has to be considered both in the bulk and in the film region. Modeling of hydrodynamics in gas–liquid contactors includes an appropriate description of axial dispersion, liquid hold-up and pressure drop.

In order to model large industrial reactive separation units, a proper sub-division of a column apparatus into smaller elements is usually necessary. These elements (the so-called *stages*) are identified with real trays or segments of a packed column. They can be described using different theoretical concepts, with a wide range of physico-chemical assumptions and accuracy (Fig. 9.3).

9.3.2

Equilibrium Stage Model

In recent decades, modeling and design of reactive absorption processes has usually been based on the equilibrium stage model. Since 1893, when the first equilibrium stage model was published by Sorel [17], thousands of publications discussing various aspects of model development, application and solution have appeared in the literature [18]. The equilibrium stage model assumes that each gas/vapor stream leaving a tray or a packing segment is in thermodynamic equilibrium with the corresponding liquid stream leaving the same tray or segment. In the case of reactive separation processes, the chemical reaction has to be additionally taken into account, either via reaction equilibrium, or via rate expressions integrated into the mass and energy balances.

The Hatta-number represents the ratio of maximal possible reaction and mass transfer rates and helps to specify different absorption regimes. Depending on the Hatta-number value, it is possible to discriminate between very fast, fast, average and slow chemical reactions, in respect to physical mass transport [19, 20].

If a very fast reaction is considered, the reactive separation process can be satisfactorily described assuming reaction equilibrium. Here, a proper modeling approach is based on the non-reactive equilibrium stage model, extended by simultaneously

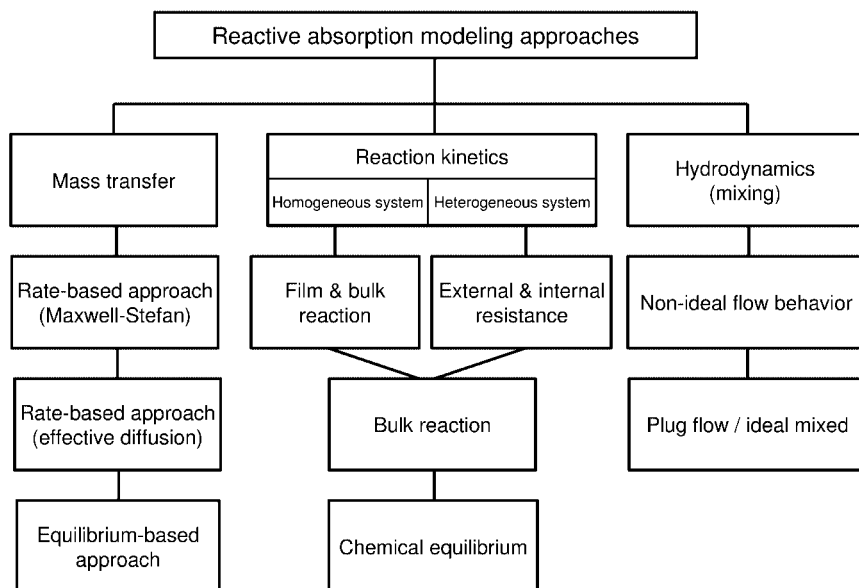


Fig. 9.3. Modeling approaches for reactive absorption.

using the chemical equilibrium relationship and tray efficiency. If the reaction rate with respect to the mass transport is lower, the influence of the reaction kinetics increases and becomes a dominating factor of the process. Taking this tendency into account, the reaction kinetics has to be integrated into the mass and energy balances. This approach is widely used today (see, e.g., Refs. [21, 22]).

In real reactive absorption processes, the thermodynamic equilibrium can seldom be reached. Therefore, some correlation parameters such as tray efficiencies or *HETP-values* (Height Equivalent to One Theoretical Plate) are introduced to adjust the equilibrium-based theoretical description to the reality. However, reactive absorption always occurs in multicomponent mixtures, for which this simplified concept often fails [16, 23, 24].

9.3.3

HTU/NTU-concept and Enhancement Factors

A simple approach to account for the mass transfer kinetics was suggested by Chilton and Colburn for the physical absorption of one component. This is called the HTU/NTU method, as it allows the column height to be determined as a product of two values, HTU (Height of a Transfer Unit) and NTU (Number of Transfer Units) [25]. The NTU-value can be determined either graphically or numerically by integrating an inverse of the mass transfer driving force over the column height. It does not depend on the column internals used. The HTU-value depends on the column load, internals-related geometric parameters and empirical mass transfer

correlations. To simplify the calculations, the total mass transfer resistance is often referred to one of the contacting phases [2].

The acceleration of mass transfer due to chemical reactions in the interfacial region is often accounted for via the so-called *enhancement factors* [19, 26, 27]. These parameters are defined as a relationship between the mass transfer rate with reaction and mass transfer rate without reaction, assuming the same mass transfer driving force.

The enhancement factors are either obtained by fitting experimental results or are derived theoretically on the grounds of simplified model assumptions. They depend on reaction character (reversible or irreversible) and order, as well as on the assumptions of the particular mass transfer model chosen [19, 26]. For very simple cases, analytical solutions are obtained, for example, for a reaction of the first or pseudo-first order or for an instantaneous reaction of the first and second order. Frequently, the enhancement factors are expressed via Hatta-numbers [26, 28]. They can be used in combination with the HTU/NTU-method or with a more advanced mass transfer description method. However, it is generally not possible to derive the enhancement factors properly from binary experiments, and a theoretical description of reversible, parallel or consecutive reactions is based on rough simplifications. Thus, for many reactive absorption processes, this approach appears questionable.

9.3.4

Rate-based Stage Model

A more physically consistent way to describe a column stage is known as *the rate-based approach* [29, 30]. This approach implies that actual rates of multicomponent mass and heat transfer and chemical reactions are taken into account directly.

Mass transfer at the gas/vapor–liquid interface can be described using different theoretical concepts [14, 16]. Most often, the *two-film model* [31] or the *penetration/surface renewal model* [26, 32] are used, whereas the model parameters are estimated from empirical correlations. In this respect, the two-film model is advantageous since there is a broad spectrum of correlations available in the literature, for all types of internals and systems.

In the two-film model (Fig. 9.4), it is assumed that all of the resistance to mass transfer is concentrated in thin films adjacent to the phase interface, and that transfer occurs within these films by steady-state molecular diffusion alone. Outside the films, in the fluid bulk phases, the level of mixing is so high that there is no composition gradient at all. This means that in the film region we have one-dimensional diffusion transport normal to the interface.

Multicomponent diffusion in the films is described by the Maxwell–Stefan equations which can be derived from the kinetic theory of gases [33]. The Maxwell–Stefan equations connect diffusion fluxes of the components with the gradients of their chemical potential. In a generalized form, these equations can also be used for the description of real gases and liquids [16]:

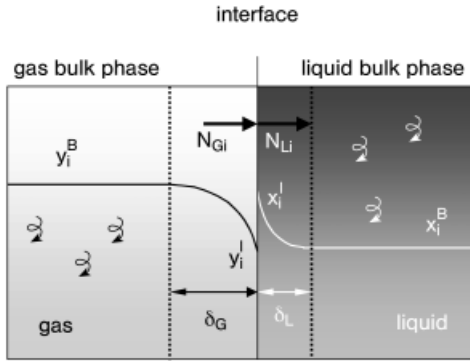


Fig. 9.4. Two-film model.

$$d_i = \sum_{j=1}^n \frac{x_i N_{Lj} - x_j N_{Li}}{c_{Lt} \bar{D}_{ij}}; \quad i = 1, \dots, n \quad (1)$$

where d_i is the generalized driving force:

$$d_i = \frac{x_i}{\mathcal{R}T} \frac{d\mu_i}{dz}; \quad i = 1, \dots, n \quad (2)$$

Similar equations can also be written for the gas phase. Thus, the gas–liquid mass transfer is modeled as a combination of the two-film model presentation and Maxwell–Stefan diffusion description. In this stage model, the thermodynamic equilibrium is assumed only at the phase interface.

The film thickness represents a model parameter which can be estimated using mass transfer coefficient correlations. These correlations govern the mass transport dependence on physical properties and process hydrodynamics and are available from the literature (see, e.g., Refs. [2, 16]).

9.3.4.1 Balance Equations

The component mass balance equations of the traditional multicomponent rate-based model (see, e.g., Refs. [15, 16]) are written separately for each phase. As chemical reactions take place in the fluid phases, the steady-state balance equations should include the reaction source terms:

$$0 = -\frac{d}{dl} (Lx_i^B) + (N_{Li}^B a^I + R_{Li}^B \phi_L) A_c; \quad i = 1, \dots, n \quad (3)$$

$$0 = \frac{d}{dl} (Gy_i^B) - (N_{Gi}^B a^I - R_{Gi}^B \phi_G) A_c; \quad i = 1, \dots, n \quad (4)$$

Equations (3) and (4) represent the component mass balances for continuous systems (packed columns). For discrete systems (tray columns), the differential terms transform to finite differences, and the balances are reduced to algebraic equations.

If chemical reactions take place in the liquid phase only (this is valid for most reactive absorption processes), the gas-phase balances simplify to

$$0 = \frac{d}{dt}(G y_i^B) - N_{Gi}^B a^I A_c; \quad i = 1, \dots, n \quad (5)$$

The bulk-phase balances are completed by the summation equation for the liquid and gas/vapor bulk mole fractions:

$$\sum_{i=1}^n x_i^B = 1 \quad (6)$$

$$\sum_{i=1}^n y_i^B = 1 \quad (7)$$

The volumetric liquid hold-up ϕ_L depends on the gas and liquid flows in the column and is calculated via empirical correlations (e.g., [34]). For the determination of axial temperature profiles, differential energy balances are formulated including the product of the liquid molar hold-up and the specific enthalpy as energy capacity. The energy balances written for continuous systems are as follows:

$$0 = -\frac{d}{dt}(L h_L^B) + (Q_L^B a^I - R_L^B \phi_L \Delta H_{RL}^0) A_c \quad (8)$$

$$0 = \frac{d}{dt}(G h_G^B) - (Q_G^B a^I - R_G^B \phi_G \Delta H_{RG}^0) A_c \quad (9)$$

If the dynamic process behavior has to be considered, Eqs. (3)–(5), (8)–(9) become partial differential equations including derivatives of the hold-up with respect to time (see more details in Section 9.5.2.6).

9.3.4.2 Mass Transfer and Reaction Coupling in the Fluid Film

The component fluxes N_i^B entering into Eqs. (3)–(5) are determined based on the mass transport in the film region. As the key assumptions of the film model result in one-dimensional mass transport normal to the interface, the differential component balance equations including simultaneous mass transfer and reaction in the film are as follows:

$$\frac{dN_{Li}}{dz} - R_{Li} = 0; \quad i = 1, \dots, n \quad (10)$$

Equations (10) are generally valid for both liquid and gas phases if reactions take place there. They represent nothing but a differential mass balance for the film region with the account of the source term due to the reaction. To link this balance to the process variables like component concentrations, some additional relationships – often called *constitutive relations* (see Ref. [16]) – are necessary. For the component fluxes N_i , these constitutive relations result from the multicomponent diffusion description (Eqs. (1), (2)); for the source terms, from the reaction kinetics description. The latter strongly depends on the specific reaction mechanism [27]. The reaction rate expressions R_i usually represent nonlinear dependencies on the mixture composition and temperature of the corresponding phase.

Equations (10) are completed by the boundary conditions relevant to the film model. These conditions specify the values of the mixture composition at both film boundaries and are applicable to both phases. For example, for the liquid phase:

$$x_i(z=0) = x_i^I, \quad x_i(z=\delta_L) = x_i^B; \quad i = 1, \dots, n \quad (11)$$

By combining Eqs. (10) with the boundary conditions (11) written in a vector form and using the constitutive relations like Eqs. (1),(2), one obtains a vector-type boundary value problem which permits the component concentration profiles to be obtained as functions of the film coordinate. These concentration profiles, in turn, allow to determine the component fluxes. Thus, the boundary value problem describing the film phenomena has to be solved in conjunction with all other model equations.

The composition boundary values in Eqs. (11) represent external values for Eqs. (10). With some further assumptions concerning the diffusion and reaction terms, this allows an analytical solution of the boundary value problem (Eqs. (10), (11)) in a closed matrix form; (see Refs. [15, 35]). On the other hand, the boundary values need to be determined from the total system of equations describing the process. The bulk values in both phases are found from the balance relations, Eqs. (3), (4). The interfacial liquid-phase concentrations are related to the relevant gas-phase concentrations y_i^I by the thermodynamic equilibrium relationships and by the continuity condition for the molar fluxes at the interface [16, 35].

Due to the chemical conversion in the liquid film, the molar fluxes at the interface and at the boundary between the film and the bulk of the phase differ. The system of equations is completed by the conservation equations for the mass and energy fluxes at the phase interface and the necessary linking conditions between the bulk and film phases [14, 16].

Generally, all of these considerations are also valid for the gas film phase, provided that reactions occur there [35]. Both the analytical and numerical solution of the coupled diffusion-reaction film problem is analyzed at full length in Ref. [36], their particular applications are considered in the Sections 9.5.1 and 9.5.2.

9.4

Model Parameters

The accuracy of the simulation results obtained by application of the above-mentioned model equations strongly depends on the model parameters used. Thus, a rigorous modeling should be based on high-quality model parameters. This means that the parameter accuracy has to be improved with growing modeling depth. This requires a substantial effort concerning both the experimental technique and the theoretical description.

9.4.1

Thermodynamic Equilibrium

Reactive absorption processes occur mostly in aqueous systems, with both molecular and electrolyte species. These systems demonstrate substantially non-ideal behavior. The electrolyte components represent reaction products of absorbed gases or dissociation products of dissolved salts. There are two basic models applied for the description of electrolyte-containing mixtures, namely the *Electrolyte NRTL* model and the *Pitzer model*. The Electrolyte NRTL model [37–39] is able to estimate the activity coefficients for both ionic and molecular species in aqueous and mixed solvent electrolyte systems based on the binary pair parameters. The model reduces to the well-known NRTL model when electrolyte concentrations in the liquid phase approach zero [40].

The expression for the excess Gibbs energy is built up from the usual NRTL equation normalized by infinite dilution activity coefficients, the Pitzer–Debye–Hückel expression and the Born equation. The first expression is used to represent the local interactions, whereas the second describes the contribution of the long-range ion–ion interactions. The Born equation accounts for the Gibbs energy of the transfer of ionic species from the infinite dilution state in a mixed-solvent to a similar state in the aqueous phase [38, 39]. In order to become applicable to reactive absorption, the Electrolyte NRTL model must be extended to multicomponent systems. The model parameters include pure component dielectric constants of non-aqueous solvents, Born radii of ionic species and NRTL interaction parameters (molecule–molecule, molecule–electrolyte and electrolyte–electrolyte pairs).

Another basic method for the gas–liquid equilibrium calculation is given by the Pitzer model [41, 42], which constitutes a further development of the model by Guggenheim [43]. This model can be used for aqueous electrolyte systems up to ionic strength of 6 mol kg⁻¹. It is, however, applicable exclusively to aqueous solvents [44]. This model considers the “hard-core” effects in the Debye–Hückel theory and suggests a general expression for the excess Gibbs energy including an electrostatic term (responsible for the hard-core interactions), a term describing the short-range forces between two solutes and a term covering the triple solute collisions.

This model also requires different parameters, which are, however, pure interaction parameters, namely binary interaction parameters (molecule–molecule, molecule–electrolyte and electrolyte–electrolyte) and ternary parameters (either two

cations and one anion or two anions and one cation). In order to extend the area of validity to higher electrolyte concentrations, the original Pitzer equation [42] has been modified in [41, 45] and extended in Ref. [46].

The calculation methods for the gas solubility are largely based on the Henry constant, which gives a relationship between the liquid-phase concentration of a physically dissolved gas and its partial pressure. The determination of such coefficients in presence of chemical reactions becomes complicated and, therefore, different estimations based on chemically inert systems are often applied. One of these methods uses the Henry coefficients of similar, but chemically inert, species in order to estimate the solubility of a reactive component. An example is represented by the N_2O analogy for the determination of CO_2 solubility in amine solutions [47].

Equilibrium calculations must involve the non-ideality of both liquid electrolyte phase and gas phase. In order to realize that, a modification of the Henry coefficient with a correction term can be applied. Another way is to include activity and fugacity coefficients into the calculations. In the first method, the correction term integrates the ionic strength and a parameter responsible for all contributions of electrolyte species in the solution and gas-phase components [26]. In the second method, the correction depends both on the calculation procedure for the activity coefficients in the liquid phase (cf. above) and on the description of the gas phase. Here, the equations of state are largely used, e.g. the Soave–Redlich–Kwong equation or the Peng–Robinson equation (see Ref. [40]). An alternative way is to use a single equation of state describing both phases. Such an approach is applied in Ref. [48].

9.4.2

Chemical Equilibrium

Chemical equilibrium state corresponds to the minimum value of the Gibbs free energy. Hence, the chemical equilibrium composition and the reaction direction can be predicted from the dependence of the Gibbs free energy on the reaction extend. For the reaction



the chemical equilibrium constant is defined as [27]

$$K^{eq} = \frac{a_P^{\nu_P} a_Q^{\nu_Q} \dots}{a_A^{\nu_A} a_B^{\nu_B} \dots} \quad (13)$$

For the description of gas-phase reactions, the activities in Eqn. (13) are substituted by the respective partial pressures of reagent and product components. In the case of

non-ideal gases, it is necessary to proceed with the fugacities [49]. The temperature dependence of the equilibrium constant is described via the van't Hoff equation:

$$\frac{d \ln K^{eq}}{dT} = \frac{\Delta H_R^0}{RT^2} \quad (14)$$

From Eqn. (14) it follows that with an exothermic reaction – and this is the case for most reactions in reactive absorption processes – K^{eq} decreases with increasing temperature. The electrolyte solution chemistry involves a variety of chemical reactions in the liquid phase, for example, complete dissociation of strong electrolytes, partial dissociation of weak electrolytes, reactions among ionic species, and complex ion formation. These reactions occur very rapidly, and hence, chemical equilibrium conditions are often assumed. Therefore, for electrolyte systems, chemical equilibrium calculations are of special importance. Concentration or activity-based reaction equilibrium constants as functions of temperature can be found in the literature [50].

9.4.3

Physical Properties

To estimate the Maxwell–Stefan and effective diffusion coefficients, diffusion data for binary mixtures is necessary. For gas systems under low pressure, the model of Fuller et al. is used most frequently [51]. The method of Wilke and Lee [40] is also valid for low pressures. Both of these methods generally agree with experimental data with an accuracy of up to 10 %, although discrepancies of about 20 % cannot be excluded [40].

For diffusion coefficients in systems under high pressure, the method of Dawson–Khoury–Kobayashi (see Ref. [52]) suggests a relevant pressure correction factor. To estimate the molar volumes, some reliable equations of state should be applied, whereas the necessary binary diffusivities at 1 atm can be determined with one of the methods described above.

Liquid-phase diffusion coefficients are a few orders of magnitude smaller than those of gases. This is explained by a denser molecular packing resulting in more intensive interactions. A theoretical consideration of the diffusion process results in the Stokes–Einstein relationship (see Ref. [44]). For the estimation of effective diffusion coefficients of molecular species in the liquid phase, the equation of Wilke and Chang is often used, which represents an empirical modification of the Stokes–Einstein relationship with an average deviation of about 10 % [53]. Here, it is assumed that the molecules diffuse in infinitely diluted mixture, and hence, no interaction of the molecules of the same species occurs. For many engineering applications, this assumption is supposed to be valid up to concentrations of 10 mol%. Another method for diffusion coefficients under infinite dilution in aqueous solutions is suggested by Hayduk and Minhas [40]; here, deviations of about 10 % are possible.

Since reactive absorption systems often contain electrolyte species, the calculation of relevant diffusion coefficients is crucial. The effective diffusion coefficients for electrolyte components can be obtained from the Nernst–Hartley equation (see

Ref. [44]), but this equation is valid only for dilute solutions. At higher electrolyte concentrations, another, empirical equation by Gordon (see Ref. [44]) should be applied, which takes the influence of the liquid phase viscosity into account.

Due to the lack of a reliable description, the diffusion of an ionic species in a molecular species is usually represented by the effective ionic diffusivity in the liquid phase [52]. The calculation of the diffusion coefficient for an ionic component in another ionic species is reduced to the arithmetical mean of both effective ionic diffusivities [52].

The method of Blanc [16] permits calculation of the gas-phase effective multicomponent diffusion coefficients based on binary diffusion coefficients. A conversion of binary diffusivities into effective diffusion coefficients can be also performed with the equation of Wilke [54]. The latter equation is frequently used in spite of the fact that it has been deduced only for the special case of an inert component. Furthermore, it is possible to estimate the effective diffusion coefficient of a multicomponent solution using a method of Burghardt and Krupiczka [55]. The Vignes approach [56] can be used in order to recalculate the binary diffusion coefficients at infinite dilution into the Maxwell–Stefan diffusion coefficients. An alternative method is suggested by Kojiman and Taylor [57].

Generally, diffusion coefficients strongly depend on viscosities and densities as well as molar volumes. The surface tension represents another important factor in calculations of mixture properties and mass transport correlations. Thus, possibly accurate determination methods are required.

The calculation of viscosities of electrolyte mixtures can be accomplished with the method of Andrade (see Ref. [40]) extended with the electrolyte correction by Jones–Dole [44]. First, the pure component viscosities of molecular species are determined by the three-parametric Andrade equation, which allows a mixing rule to be applied and the mixture viscosity of an electrolyte-free liquid phase to be obtained. The latter is transformed into the viscosity of the liquid phase using the electrolyte correction term of Jones and Dole [44], whereas the ionic mobility and conductivity are used as model parameters.

The determination of molar volumes of molecular species in the liquid phase can be performed with the Rackett equation [58], requiring critical temperature, pressure and volume as well as a further fitting parameter. It is possible to calculate the molar volumes of electrolyte species using the two-parameter equation of Clarke (see Ref. [52]).

The surface tension is important for the calculation of mass transfer coefficients and the specific contact area (see Section 9.4.4). Depending on the availability of necessary parameters, the surface tension for a molecular species can be determined either with the simplest method of Hakim–Steinberg–Stiel or with a more complex DIPPR-method (see Ref. [52]). The mixture surface tension can be obtained via a mixing rule. A further extension to cover electrolyte mixtures is realized by the method of Onsager and Samaras (see Ref. [44]). The latter uses an additive term which can be estimated using the dielectric constant of the mixture and molar volumes of electrolytes.

9.4.4

Mass Transport and Fluid Dynamics Properties

In the two-film model applications, the film thicknesses of both liquid-side and gas-side films are of crucial importance. These thicknesses depend strongly on the flow pattern in the column, on the column internals type and on the physical properties such as surface tension, diffusivities and viscosities. The same is valid for another model parameter, the specific contact area, which can deviate from the geometric surface of the column internals. In several cases, it is possible that, at moderate liquid loads, the geometric packing surface is not completely covered, and thus, mass transfer occurs through a smaller surface than the geometric one. The opposite situation in which the phase interface is larger than the geometric surface is also possible.

The above values are most often determined via correlations, which allow a scale-up (or down) to different operating states. Along these lines, the liquid and gas phase mass transfer coefficients are usually related to Sherwood number (Sh) as a function of Reynolds number (Re), Schmidt number (Sc) and other dimensionless process characteristics [3, 59–61]. It is important that the correlations are applied within the same parameter range in which they are determined as only there can their reliability be assured.

Further parameters related to the correlations are the liquid hold-up on the relevant column internals and the pressure drop caused by the flow resistance in the column. The liquid hold-up is necessary both for the liquid-phase reaction description and for the estimation of the gas-phase hold-up in the case of gas-phase reactions. The pressure drop can primarily influence the phase equilibrium and hold-up. These parameters also depend on the operating conditions, column internals type and physical properties. In some cases, hold-up and pressure drop are coupled and, therefore, cannot be calculated explicitly. They should rather be determined by iterations (see, e.g., [59]). Usually, different equations describe different loading regions, as both hold-up and pressure drop depend strongly on hydrodynamic interactions, and there is a discrimination between a region below the loading point and that between the loading and flooding points.

The selection of a proper correlation is mostly a question of user experience. Basically, the mass transfer correlations must be compared and validated with experimental data because the application of different correlations can lead to different simulation results (e.g., axial concentration profiles). Some correlations which – according to our experience – demonstrated their suitability for reactive absorption processes can be found in [60–62].

9.4.5

Reaction Kinetics

Although reactions in reactive absorption processes are fast, the assumption of instantaneous reactions is usually not justified. Figure 9.5 demonstrates substantial differences in the gas phase concentration profiles of CO_2 in a sour gas absorption

by a mixture of monoethanolamine (MEA) and methyldiethanolamine (MDEA) (see Section 9.5.3.1). If reactions are regarded as instantaneous for this system, the CO_2 absorption rates are too high, and consequently the gas-phase concentrations are too low, which leads to an underestimation of the required column height. Thus, it is necessary to differentiate between finite-rate (kinetically controlled) and instantaneous reactions. Reaction kinetics parameters also proved to have a significant influence in other sour gas absorption processes [63–65]. This is especially relevant for reactions including CO_2 as reagent.

The reaction rate of a homogeneous kinetically controlled reaction



is usually represented by

$$r = k_{\text{for}} c_A^{\nu_A} c_B^{\nu_B} - k_{\text{rev}} c_P^{\nu_P} c_Q^{\nu_Q} \quad (16)$$

whereas the reaction rate constant of the forward reaction is determined by the Arrhenius law:

$$k_{\text{for}} = k_0 \cdot e^{-\frac{E_A}{RT}} \quad (17)$$

and the reaction rate constant of the reverse reaction via the chemical equilibrium:

$$k_{\text{rev}} = \frac{k_{\text{for}}}{K^{eq}} \quad (18)$$

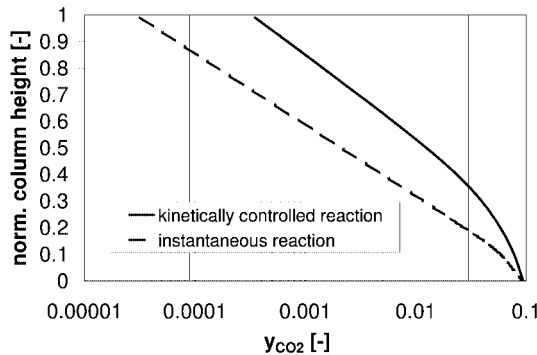


Fig. 9.5. CO_2 gas-phase concentration profile in a monoethanolamine (MEA)/methyldiethanolamine (MDEA) absorption process for different reaction descriptions.

Measurements of kinetic parameters of liquid-phase reactions can be performed in apparatus without phase transition (rapid-mixing method [66], stopped-flow method [67], etc.) or in apparatus with phase transition of the gaseous components (laminar jet absorber [68], stirred cell reactor [69], etc.). In experiments without phase transition, the studied gas is dissolved physically in a liquid and subsequently mixed with the liquid absorbent to be examined, in a way that ensures a perfect mixing. Afterwards, the reaction conversion is determined via the temperature evolution in the reactor (rapid mixing) or with an indicator (stopped flow). The reaction kinetics can then be deduced from the conversion. In experiments with phase transition, additionally, the phase equilibrium and mass transport must be taken into account as the gaseous component must penetrate into the liquid phase before it reacts. In the laminar jet absorber, a liquid jet of a very small diameter passes continuously through a chamber filled with the gas to be examined. In order to determine the reaction rate constant at a certain temperature, the jet length and diameter as well as the amount of gas absorbed per time unit must be known.

Our own dynamic experiments for the determination of the gas–liquid-reaction kinetics have been performed in a stirred-cell reactor (Fig. 9.6). After thermodynamic equilibrium is reached inside the reactor, the gas is introduced rapidly and the pressure decrease recorded as a function of time. From this course, the reaction rate constant at the respective temperature can be obtained.

Simulation studies based on different kinetic descriptions of the monoethanolamine carbamate reaction (see Section 9.5.3.4) using aqueous solutions of MEA and MDEA lead to deviations in the calculated column height of up to 15 % (Fig. 9.7). This demonstrates the importance of a proper kinetics measurement and description.

9.5

Case Studies

In this section, four examples illustrating the application of the rate-based modeling approach discussed above are presented. First three reactive absorption processes – namely absorption of NO_x , coke gas purification and CO_2 absorption by aqueous

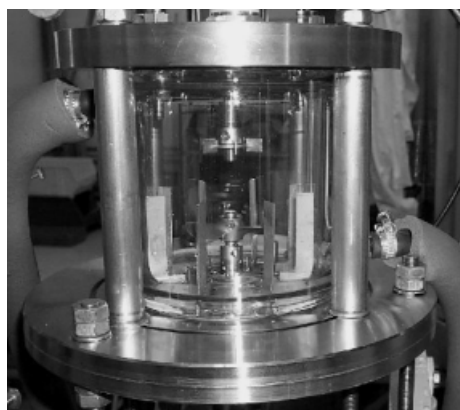


Fig. 9.6. Stirred-cell reactor.

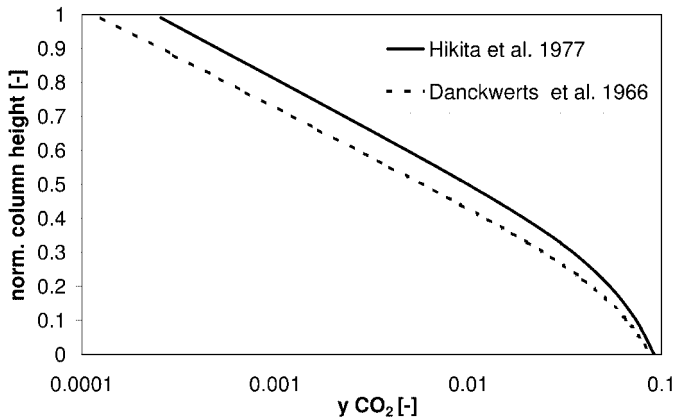


Fig. 9.7. CO₂ gas-phase concentration profile in a MEA/MDEA absorption process for different reaction kinetics.

amine solutions – represent the authors' own studies, whereas the last process, SO₂ absorption into aqueous NaHCO₃/Na₂CO₃ solutions, is taken from Ebrahimi et al. [70]. The process chemistry and set-up, modeling peculiarities, model parameters and the simulation results are discussed for all examples.

9.5.1

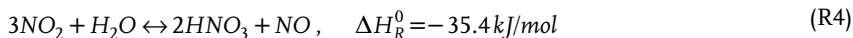
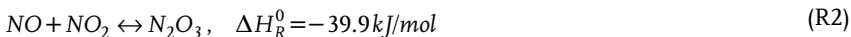
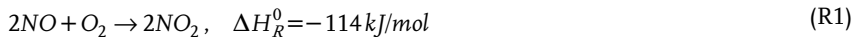
Absorption of NO_x

9.5.1.1 Chemical System

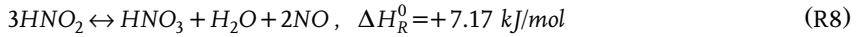
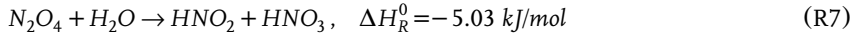
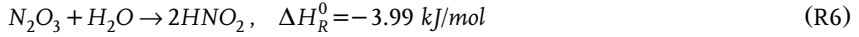
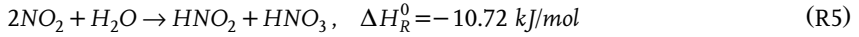
The reactive system considered is the basic one used in the production of nitric acid, as well as in some other industrial processes [4]. It consists of ten main components including air (N₂, O₂), water (H₂O), oxyacids of nitrogen (HNO₂, HNO₃) and nitrogen oxides (NO, NO₂, N₂O, N₂O₃, N₂O₄). The components are involved in simultaneous, parallel and consecutive reactions occurring in both phases. The reactions are of high orders and most of them are exothermic.

The basics of the reaction scheme are given in Ref. [71] and modified for the case considered [72]. The final scheme involves eight reactions and can be regarded as the most extensive reaction system so far.

The gas-phase reactions are governed by the following equations:



whereas the corresponding equations for the liquid phase are:



The liquid-phase reactions are valid for nitric acid concentrations below 34 wt%. In the case of higher nitric acid concentrations, reactions (R5) to (R7) become reversible. The oxidation of NO (R1) is the slowest reaction in this system. Therefore, the total gas-phase hold-up in absorbers can be determined using the kinetic data of this reaction [73]. The other gas-phase reactions are reversible instantaneous reactions.

9.5.1.2 Process Set-up

Measurements have been carried out for an industrial NO_x absorption process [74]. The absorption plant (Fig. 9.8) represents a sequence of four units used for the removal of nitrogen oxides from the waste gas of an adipin acid factory. Each unit is separated into two sections, thus, there are altogether eight columns of 2.2 m diameter and 7 m height each, which are connected countercurrently. To enhance the mass transport in the columns, 35 mm INTALOX ceramic saddles with a packed bed height of 3.2 m are used. The plant is operated at atmospheric pressure.

To cool the liquid phase, columns 1 to 7 are connected with a pump-around. The liquid feeds entering columns 7 and 8 are low-concentration nitric acids. The liquid product has a HNO_3 concentration of about 35 wt%, whereas the gas feed concentration of NO_x is about 60 000 vppm, with one-quarter of the NO_x being NO and the rest NO_2 .

9.5.1.3 Modeling Peculiarities

The boundary value problem (Eqs. (10), (11)) is usually solved numerically. However, it is also possible to use another approach employing a linearization of this second-order, non-linear problem and a subsequent analytical treatment. The analytical solution of the *linearized boundary value problem* in the film region is obtained in [15]:

$$\begin{aligned} \mathbf{x} = & \sinh\{[\Psi](\delta_L - z)\} \sinh^{-1}\{[\Psi] \delta_L\} \mathbf{x}^I \\ & + \sinh\{[\Psi] z\} \sinh^{-1}\{[\Psi] \delta_L\} \mathbf{x}^B \end{aligned} \quad (19)$$

with

$$[\Psi] = ([D]^{-1}[K])^{0.5} \quad (20)$$

Matrix $[D]$ results from the transformation of the Maxwell–Stefan equations (1) to the form of the generalized Fick's law [23]. This matrix is generally a function of the mixture composition and is assumed constant along the diffusion path [23]. The direct expressions for the elements of the diffusion matrix $[D]$ can be found, for example, in Ref. [16].

Matrix $[K]$ follows from the linear approximation suggested by Wei and Prater [75]:

$$\mathbf{R} \cong -[K]\mathbf{x} \quad (21)$$

Equation (21) represents one of the best approaches to the modeling of complex reaction systems providing a satisfactory representation for many rate processes (see, e.g., Refs. [19, 76–78]). It has gained widespread acceptance in various chemical and reactor engineering areas [79], and is also recommended for use in the modeling of reactive separation operations [14, 78]. For the design of large industrial reactive separation units, the analytical solution (Eqs. (19), (20)) can be considered as a useful simplification as compared to numerical methods.

Differentiation of Eqn. (19) gives simple analytical expressions for the component fluxes with regard to the homogeneous reaction in the fluid films (see Ref. [35]). The methods of determination of the reaction matrix $[K]$ have also been detailed [36, 75, 77, 78, 80].

9.5.1.4 Model Parameters

The multicomponent diffusion matrices $[D]$ in both phases are determined via the binary diffusivities. The latter can be estimated using different correlations summarized in Tab. 9.3. The film thicknesses which represent important model parameters (cf. Section 9.4.4) are estimated via the mass transfer coefficients [16, 23].

The correlations of Onda et al. [60] and Billet [10] are valid for various mixtures and packing types. The correlation of Kolev [61] represents a further development of the model by Onda et al. [60], with an extended validity area for the liquid-phase viscosity.

The thermodynamic equilibrium is calculated with the Henry coefficients corrected for the electrolyte influence. As nitric acid is a strong electrolyte, the solubilities of nitrogen oxides in water [81] must be recalculated according to [20] to account for the non-ideal electrolyte behavior.

Table 9.3. Binary diffusion and mass transfer coefficients.

Phase	Binary diffusion coefficients	Mass transfer correlations
Gas	Fuller et al. [51]	Onda et al. [60] Billet [10] Wehmeier (see Ref. [85])
Liquid	Siddiqi and Lucas [112]	Onda et al. [60] Billet [10] Kolev [61] Mika [113]

The chemical equilibrium is calculated in terms of liquid-phase activities. The local composition model of Engels [82] based on the UNIQUAC model is used for the calculation of vapor pressures and activity coefficients of water and nitric acid. Multicomponent diffusion coefficients in the liquid phase are corrected for the non-ideality, as suggested in Ref. [16].

9.5.1.5 Results

The sensitivity analysis performed in Ref. [83] proves that the suggested model provides qualitatively correct behavior of the concentration profiles. The simulations of the industrial absorption process shown in Fig. 9.8 are carried out using the rate constant of reaction (R1) (the slowest and hence the most important reaction in the system) according to [84]:

$$k_{p1} = 217347.9 - 1041.156 \cdot T + 1.3605 \cdot T^2 \quad (22)$$

the liquid-side mass transfer coefficient according to [61] and the gas-side mass transfer coefficient according to Wehmeier (see Ref. [85]).

Figure 9.9 shows a comparison of the simulated and measured gas-phase concentrations of NO and NO₂ throughout the whole absorption plant. The zigzag form of the simulated concentration profiles results from switching different sections of each single column (see Ref. [35]). Good agreement between experimental and simulation results can be definitely observed here.

In Fig. 9.10, the experimental and simulated liquid-phase concentrations of HNO₃ and HNO₂ throughout the absorption plant are demonstrated. They also match each other. Only for the first two columns one observes larger deviations between the experiments and simulated results. This can be attributed to the fact that at high concentration of HNO₃ reactions (R5) to (R7), which are assumed to be irreversible, convert to reversible ones, but data on their rate constants are lacking.

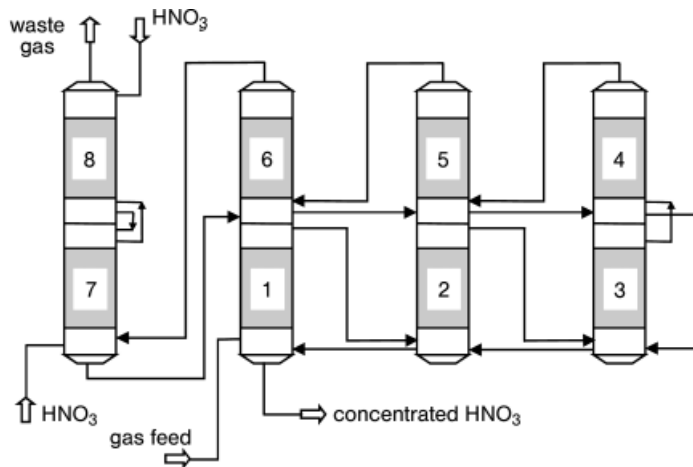


Fig. 9.8. Absorption plant consisting of four units (eight columns).

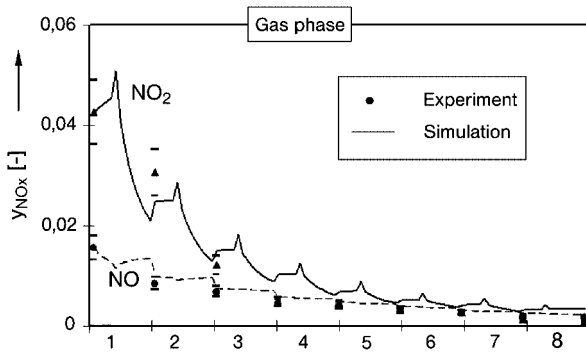


Fig. 9.9. Experimental and simulated gas-phase concentrations of NO and NO₂ throughout the absorption plant.

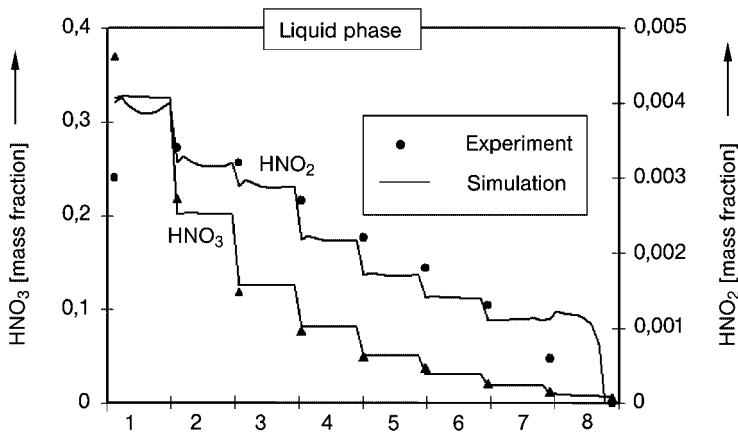


Fig. 9.10. Experimental and simulated liquid-phase concentrations of HNO₃ and HNO₂ throughout the absorption plant.

9.5.2

Coke Gas Purification

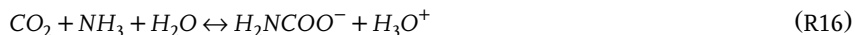
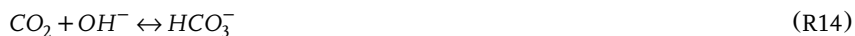
9.5.2.1 Chemical System

Coke oven gas mainly consists of a mixture of carbon monoxide, hydrogen, methane, and carbon dioxide. It is contaminated with a variety of organic and inorganic compounds which must be separated in absorption columns before its further use as a synthesis gas. The selective absorption of coke plant gas contaminants results from a complex system of parallel liquid phase reactions. All reactions are reversible, some of them being instantaneous (a proton transfer) and other being finite-rate reactions.

Instantaneous reversible reactions:



Finite-rate reversible reactions:



Considering pH-values of the process under study, the dissociation reaction of hydrogen sulfide (HS^-) into sulfide ions (S^{2-}) can be neglected.

The reactions including CO_2 obey first- and second-order kinetics, whereas the other reversible reactions result from a simple proton transfer and are, therefore, regarded as instantaneous by the corresponding mass action law equations. The formation of bicarbonate ions (HCO_3^-) takes place via two different mechanisms. The rate of the direct reaction between carbon dioxide and hydroxyl ions (OH^-) is determined according to Ref. [86].

Usually, the reaction between CO_2 and water is very slow and hardly contributes to the total carbon dioxide reaction rate. Nevertheless, for the sake of completeness, it has been considered as a reaction of the first order with respect to the CO_2 , since the reaction kinetics depends on the carbonation ratio (see Ref. [87]).

The absorption rate of carbon dioxide increases with growing concentration of ammonia. Therefore, the reaction kinetics of NH_3 and CO_2 must also be considered in the model equations. The rate constant, as a function of the temperature, has been determined according to Ref. [87]. The coefficients necessary for the calculation of the chemical equilibrium constants in this system of volatile weak electrolytes are taken from Ref. [88].

The CO_2 absorption is hindered either by slow chemical reactions in which the dissolved gas molecules are converted into the more reactive ionic species, or by low

base reagent concentrations. Therefore, when gases containing H_2S , NH_3 and CO_2 contact with water, H_2S and ammonia are absorbed much faster than CO_2 and this selectivity can be accentuated by optimizing the operating conditions [89]. Nevertheless, all chemical reactions are coupled by hydronium ions and additional CO_2 absorption leads to the desorption of hydrogen sulfide and decreases the scrubber efficiency.

9.5.2.2 Process Set-up

Today's coke plant gas purification processes are mostly carried out under atmospheric pressure, employing a circulated ammonia-based absorbent. The consumption of the external solvent is reduced using ammonia available in the coke gas [90]. An example of innovative purification processes is the *Ammonia Hydrogen Sulfide Circulation Scrubbing* (ASCS) (Fig. 9.11), in which the ammonia contained in the raw gas dissolves in the NH_3 -absorber, after which the absorbent saturated with ammonia passes through the H_2S -absorber to selectively absorb the components H_2S and HCN from the coke gas. The next step is thermal regeneration of the absorbent with steam in a two-step desorption plant, while a part of the deacidified water is fed back into the H_2S -absorber [91].

Pilot-plant experiments have been carried out at real process conditions in the coke plant "August Thyssen" (Duisburg, Germany). The DN 100 pilot column (Fig. 9.11) was made from stainless steel and equipped with about 4 m of structured packing (Sulzer MELLAPAK® 350Y), three liquid distributors, and a digital control system. Several steady-state experiments have been compared with the simulation results and supported the design optimization of the coke gas purification process [91].

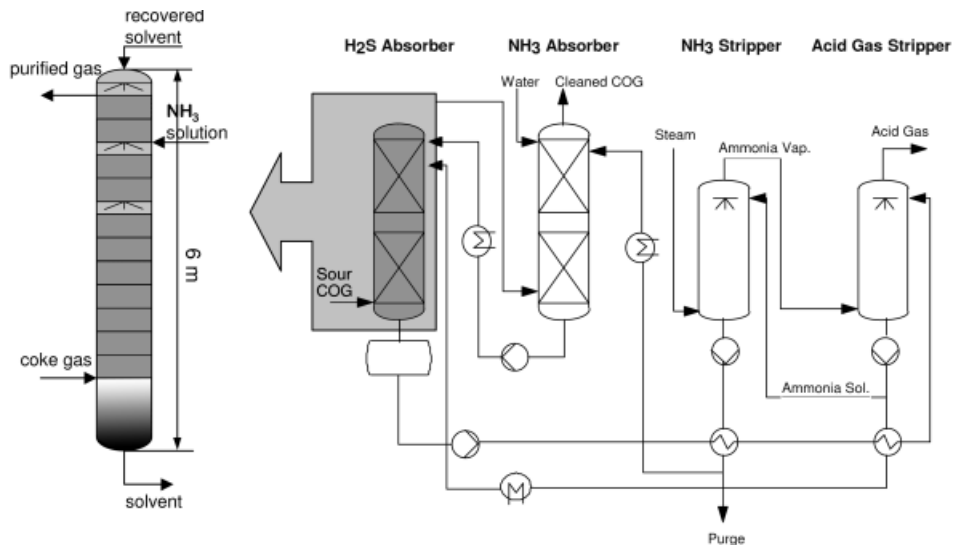


Fig. 9.11. Right: Ammonia-hydrogen sulfide circulation scrubbing process for the coke oven gas purification. Left: H_2S absorber. COG = coke oven gas.

9.5.2.3 Modeling Peculiarities

A purely numerical approach to the solution of this complex reactive absorption problem has been suggested in Ref. [92]. The liquid film is considered as an additional balance region in which reaction and mass transfer occur simultaneously. Therefore, the reactions are considered both in the differential film balances, Eq. (10), and in the liquid bulk phase, Eq. (3).

In order to describe the presence of electrolytes in the system, the driving force due to electrical potential difference needs additionally to be taken into account [16]. Therefore, the gradient of the electrical potential is introduced into the generalized driving force d_i :

$$d_i = \frac{x_i}{\Re T} \frac{1}{\delta_L} \frac{d\mu_i}{d\eta} + x_i z_i \frac{F}{\Re T} \frac{1}{\delta_L} \frac{d\varphi}{d\eta}; \quad i = 1, \dots, n \quad (23)$$

In dilute electrolyte systems, the diffusional interactions can usually be neglected, and the generalized Maxwell–Stefan equations are reduced to the Nernst–Planck equations:

$$N_{Li} = -\frac{c_{Li} D_{Li,eff}}{\delta_L} \left(\frac{dx_i}{d\eta} + x_i z_i \frac{F}{\Re T} \frac{d\varphi}{d\eta} \right) + x_i N_{Ln}; \quad i = 1, \dots, n \quad (24)$$

where n is the solvent index. In electrolyte systems, the *electroneutrality condition* has to be met in each point of the liquid phase:

$$\sum_{i=1}^n x_i z_i = 0 \quad (25)$$

9.5.2.4 Model Parameters

Thermodynamic non-idealities are considered both in the transport equations and in the equilibrium relationships at the phase interface. If electrolytes are present, the liquid-phase diffusion coefficients should be corrected to account for the specific transport properties of electrolyte systems.

The thermodynamic equilibrium at the gas–liquid interface is described as follows (see also Section 9.4.1):

$$\gamma_i^I = K_i x_i^I; \quad i = 1, \dots, n \quad (26)$$

It should be noted that distribution coefficients K_i comprise both fugacities in the gas phase and activity coefficients in the liquid phase. These coefficients are determined by the three-parametric Electrolyte-NRTL method. The latter is based on the local composition concept and satisfactorily represents physical interactions of this multicomponent electrolyte system [46].

The liquid-phase diffusion coefficients are found with the Nernst–Hartley equation (cf. Section 9.4.3). The gas-phase diffusion coefficients are estimated according

to the Chapman–Enskog–Wilke–Lee model (see Ref. [40]). The mass transport properties of the packing type are described with the correlations suggested in Ref. [62].

9.5.2.5 Results

Several steady-state simulations have been performed with the aim of analyzing the influence of numerical and physico-chemical parameters, beginning with a single stage and ending with a column simulation. Different film and packing section discretizations, several mass transfer and hydrodynamic correlations, and different driving forces and diffusion models have been thoroughly tested (Fig. 9.12).

The most sensitive components appeared to be those involved in finite-rate reactions, especially CO_2 . Furthermore, the impact of electrical forces enhances the absorption of the strong electrolytes H_2S and HCN by 3–5 %, while the CO_2 absorption rate is dominated by the reaction in the film [92, 93]. Significant changes in the concentration profiles and the component absorption rates due to the film reaction have been established [65, 94].

Single-stage simulations reveal that the intermolecular friction forces do not lead to reverse diffusion effects, and thus the molar fluxes calculated with the effective diffusion approach differ only slightly from those obtained by the Maxwell–Stefan equations without the consideration of generalized driving forces. This result is as expected for dilute solutions and allows to reduce the model complexity for the process studied [95].

As a further model simplification, a linearization of the film concentration profiles has been studied. This causes no significant changes in the simulation results and, at the same time, reduces the total number of equations by half and stabilizes the numerical solution [94]. The assumption of chemical equilibrium in the liquid bulk

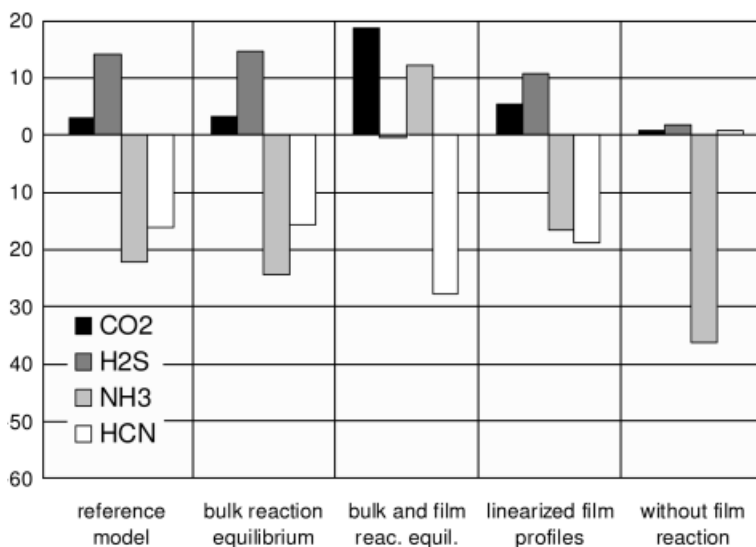


Fig. 9.12. Absorption rates calculated with different model assumptions concerning reaction consideration.

phase does not change the absorption rates significantly, which indicates fast conversion. Therefore, neglecting the film reaction unrealistically reduces the absorption rates. On the other hand, neglecting the reaction kinetics within the film results in completely different orders of magnitude for the calculated absorption degree. As a consequence, the reactions of CO_2 should not be regarded instantaneous although the corresponding Hatta number of about 7 characterizes the reaction as very fast [1].

The model optimized in respect to the numerical parameters and physico-chemical properties has been validated against experimental data, whereas the axial concentration and temperature profiles for both phases demonstrated a good agreement (Fig. 9.13). It has also been found that the simulations of the scrubber based on the equilibrium stage model extended by the chemical reaction kinetics yield results completely inconsistent with the experimental studies, namely, the selectivity towards H_2S and HCN absorption cannot be reflected (Fig. 9.13). In this case, the film reaction constitutes an essential element of the rate-based approach which must be considered in the model. In this respect, the only feasible simplification is represented by a linearization of the film concentration profiles, including the implementation of the average reaction kinetics in the liquid film region [95].

9.5.2.6 Dynamic Issues

Steady-state modeling is not sufficient if one faces various operation disturbances (e.g., feed variation) or tries to optimize the start-up and shut-down phases of the process. In this case, a knowledge of dynamic process behavior is necessary. Further areas where dynamic information is crucial are the process control, as well as safety

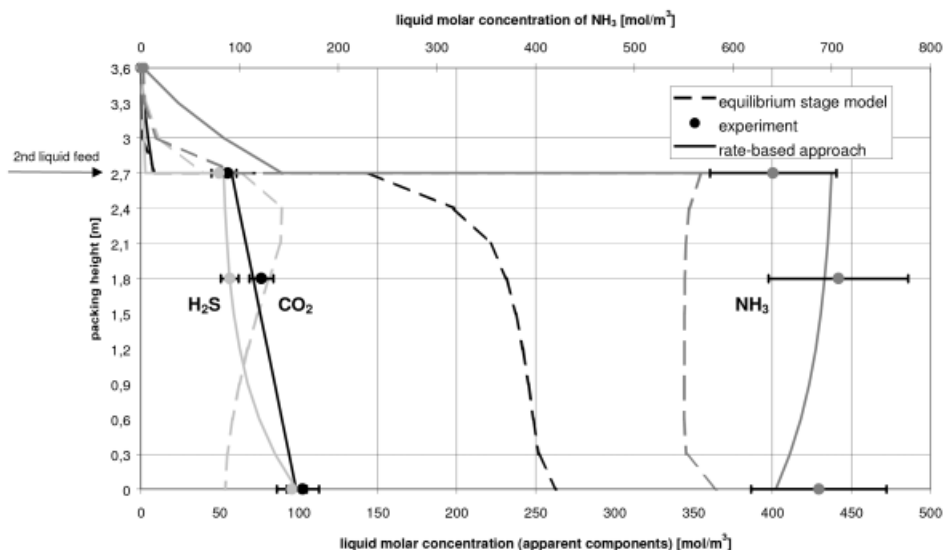


Fig. 9.13. Liquid phase axial concentration profiles for the H_2S scrubber: comparison between experimental and simulation results based on different model approaches.

issues and factory staff training. Dynamic modeling can also be considered as the next step towards the deep process analysis which follows steady-state modeling and is based on its results.

In the dynamic rate-based stage model, molar hold-up terms must be implemented into the mass balance equations, whereas the change of both, the specific molar component hold-up and the total molar hold-up, are taken into account. For the liquid phase, these equations are as follows:

$$\frac{\partial}{\partial t} U_{Li} = -\frac{\partial}{\partial t} (Lx_i^B) + (N_{Li}^B a^I + R_{Li}^B \phi_L) A_c ; \quad i = 1, \dots, n \quad (27)$$

$$U_{Li} = x_i^B U_{Lt} ; \quad i = 1, \dots, n \quad (28)$$

The gas hold-up can often be neglected due to the low gas-phase density, and the component balance equation reduces to Eqn. (4) (see Ref. [92]).

The dynamic formulation of the model equations requires a careful analysis of the whole system in order to prevent high index problems during the numerical solution [96]. As a consequence, a consistent set of initial conditions for the dynamic simulations and a suitable description of the hydrodynamics must be introduced. For example, pressure drop and liquid hold-up must be correlated with the gas and liquid flows.

The model optimized based on the steady-state analysis allows for a dynamic real-time simulation of the entire absorption process. As the dynamic behavior is mainly determined by process hydraulics, it is necessary to consider those elements of the column periphery which lead to larger time constants than the column itself. Therefore, major elements of the column periphery such as distributors, stirred tanks and pipelines have been additionally implemented into the dynamic model.

The dynamic behavior of the coke gas purification process has been investigated systematically [92, 93, 97]. For example, local perturbations of the gas load and its composition have been analyzed. A significant dynamic parameter is represented by the liquid hold-up. Figure 9.14 illustrates the changes in solvent composition after a decrease of the gas flow rate from $67 \text{ m}^3 \text{ h}^{-1}$ to $36.4 \text{ m}^3 \text{ h}^{-1}$ and a simultaneous small increase of the liquid flow rate.

The liquid hold-up of the packing section decreases, and this leads to a lower conversion of the kinetically controlled reactions of CO_2 and a reduction of the CO_2 absorption rate. As a consequence, the solvent molar fractions of HS^- and carbamate decreases, whereas the relative fraction of (HS^-) increases. Selectivity of the absorption process towards the H_2S and HCN reduction is enhanced by minimizing the liquid hold-up of the column. At the same time, a larger interfacial area improves the performance of the plant. Therefore, modern industrial sour gas scrubbers should be equipped with structured packings.

Figure 9.15 illustrates the system response after a sudden increase of the gas flow by 20 % and its H_2S load by 100 %. As expected, the H_2S load increases everywhere

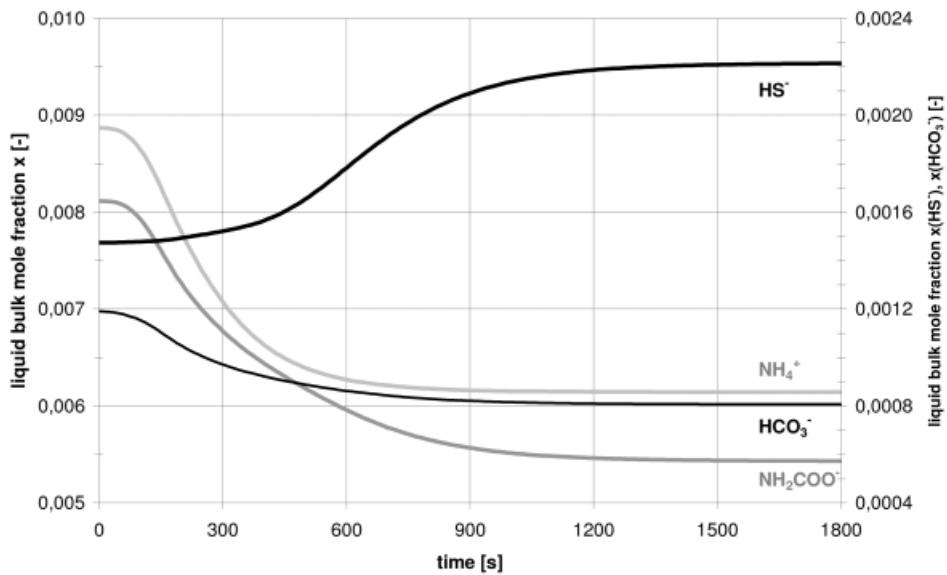


Fig. 9.14. Dynamic change of solvent composition after a sudden significant decrease in the gas flow rate and a simultaneous small increase of the liquid flow rate.

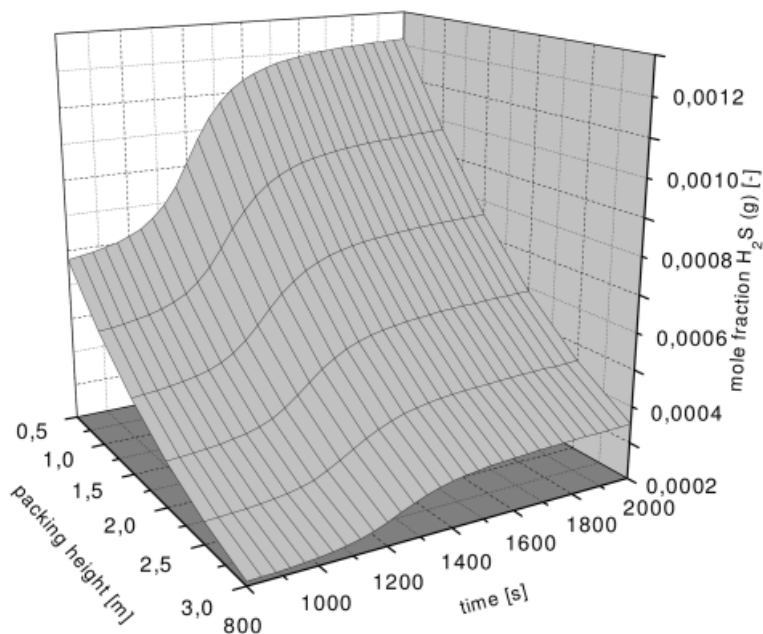


Fig. 9.15. Dynamic change of the H_2S gas phase concentration along the column after a sudden increase of the gas flow rate and its H_2S load.

along the column height in the gas phase. The change is more significant in the lower part of the absorber than at the top because some additional hydrogen sulfide is absorbed. The new steady state is achieved after only 30 minutes, which justifies the implementation of dynamic models for the column periphery.

9.5.3

CO₂ Absorption by Aqueous Amine Solutions

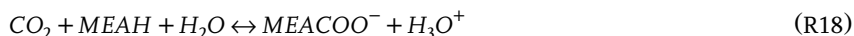
9.5.3.1 Chemical System

Amine solvents are widely used for sour gas removal, in syngas, fertilizer and natural gas plants. They are mainly used to withdraw the sour components CO₂ and H₂S from process gas streams, and the process is usually carried out in packed-bed columns. Depending on the specifics of a particular process, either aqueous primary (e.g., monoethanolamine, MEA), secondary (e.g., diethanolamine, DEA), tertiary (e.g., methyldiethanolamine, MDEA) amines or aqueous amine blends are employed.

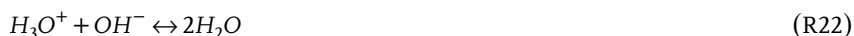
As no chemical reaction between CO₂ and tertiary amines occurs, the latter (e.g., MDEA) are used in selective scrubbing of H₂S. To absorb CO₂, primary or secondary amines in the aqueous phase are required, which can react with CO₂ directly yielding carbamate ions.

The example to be considered concerns the removal of CO₂ from a natural gas stream free of H₂S using an aqueous MEA-solution [98]. Amine gas treating processes follow a basic liquid-phase reaction system. All reactions are reversible; however instantaneous (a proton transfer) and finite-rate reactions should be differentiated here again (cf. Section 9.5.2.1).

Finite-rate reversible reactions:



Instantaneous reversible reactions:



Since the solvent is a base, the reaction between CO_2 and H_2O is neglected. The reactions involving CO_2 obey second-order kinetics, while all other reactions are described as instantaneous reactions by application of the respective mass action law. The CO_2 in the liquid phase participates in two different reactions mechanisms, (R17) and (R18). The reaction rate constant of (R17) is determined as a function of temperature according to Ref. [86]. The data necessary for the description of the instantaneous reactions (R19)–(R22) for the electrolyte system under study are taken from Ref. [50].

In this reaction system, CO_2 absorption takes place at moderate liquid-phase loads mainly via (R18). This can be explained as follows: in spite of the fact that reaction (R17) is faster than (R18), the MEA concentration is much higher than that of OH^- -ions.

9.5.3.2 Process Set-up

To investigate amine gas-treating processes, a column reducing CO_2 content of a natural gas stream using an aqueous MEA solution is modeled and simulated. The column (Fig. 9.16), which is made of stainless steel, has a diameter of 1.9 m and is equipped with 50-mm Pall rings placed into three sections, with the total packing bed height of 14.1 m. Natural gas consists mainly of a mixture of low alkanes (C1-C4) and nitrogen. Carbon dioxide represents a contaminant to be withdrawn, before the purified gas can be applied further. As solvent, an aqueous MEA solution providing high CO_2 solubilities at low partial pressures [98] is used.

9.5.3.3 Modeling Peculiarities

Similar to the case of coke gas purification (see Section 9.5.2), this complex reactive absorption problem is solved by a purely numerical method. The liquid film is

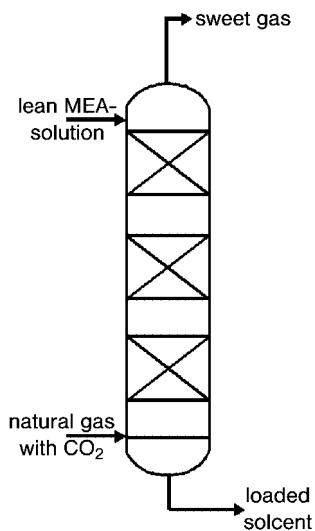


Fig. 9.16. CO_2 -absorber in an amine scrubbing process.

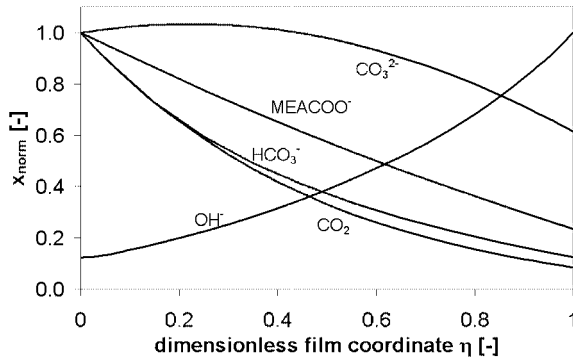


Fig. 9.17. Concentration profiles in the liquid film in a MEA absorption process.

subdivided into additional balance segments in which simultaneous reactions and mass transfer take place. This discretization permits the calculation of film concentration profiles, which become curvilinear, due to the reaction influence (Fig. 9.17).

As electrolyte species are available in the system considered, the driving forces caused by the electrical potential differences must be taken into account [16]. The migration is described through the Nernst–Planck equation (Eq. (24)). This implies that the electroneutrality condition, Eq. (25), is satisfied.

9.5.3.4 Model Parameters

Thermodynamic non-idealities are taken into account while calculating necessary physical properties such as densities, viscosities, and diffusion coefficients. In addition, non-ideal phase equilibrium behavior is accounted for. In this respect, the Electrolyte-NRTL model (see Section 9.4.1) is used and supplied with the relevant parameters from Ref. [50]. The mass transport properties of the packing are described via the correlations from Refs. [59, 61]. This allows the mass transfer coefficients, specific contact area, hold-up and pressure drop as functions of physical properties and hydrodynamic conditions inside the column to be determined.

For the studied system consisting of monoethanolamine, CO₂ and water, experiments for the determination of reaction kinetics in a stirred-cell reactor have been carried out (see Section 9.4.5). These experiments yield the following Arrhenius expression for the second-order reaction (R18) (Fig. 9.18):

$$k_{for} = 4,4947 \cdot 10^{11} \cdot e^{-\frac{44940}{RT}} \quad (29)$$

Figure 9.18 demonstrates significant deviations between the kinetics proposed in Ref. [66] and the measurements taken from other works [87] (see Section 9.4.5). Our experiments show a good agreement with the kinetics reported by Hikita et al. [66].

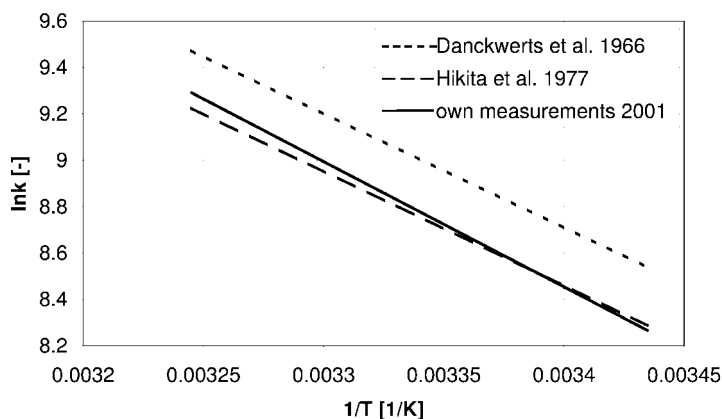


Fig. 9.18. Arrhenius diagram for the reaction between CO_2 and MEA.

9.5.3.5 Results

From the sensitivity analysis of individual segments, it is possible to obtain the required number and scaling type of the discretization points in the liquid film for the amine system. By varying the number of discretized points, significant changes of the concentration profiles – and consequently absorption rates of the individual species – are obtained. The increase in the number of discretized points is related to a growing model complexity, which can lead to a significantly longer calculation time. A reduction of the number of grid points, without any loss in the model accuracy, can be achieved with a corresponding grid point scaling. Thus, one arrives at a numerical optimization problem, the solution of which should provide both a minimal number of grid points and minor deviations of the results from those obtained with a finer discretization.

Furthermore, steady-state simulations have been carried out in order to investigate the influence of numerical and physico-chemical parameters, starting from a single segment up to the total column. Different segment heights and different driving force descriptions, as well as different mass transfer and hydrodynamic correlations, have been thoroughly analyzed. The specific contact area and liquid-phase mass transfer coefficient have been found to be the most sensitive parameters. An additional result of this study is that the film reaction consideration is indispensable.

The model optimized with regard to numerical and physico-chemical parameters has been tested with experimental data from a pilot plant, and used to evaluate industrial operation data. Here, a good agreement between experimental and simulated values is established, both for the gas-phase concentration of CO_2 (Fig. 9.19) and for the temperature in the liquid phase (Fig. 9.20).

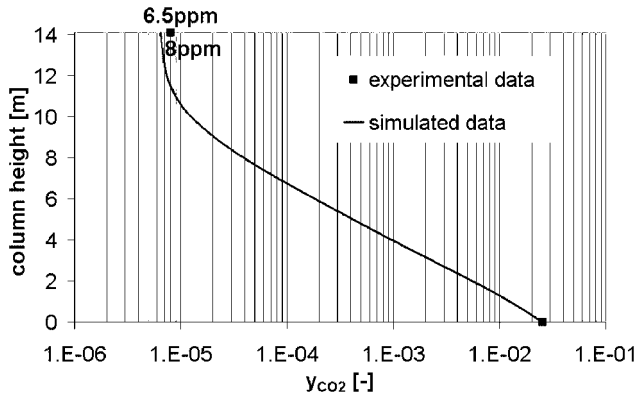


Fig. 9.19. Concentration profile of CO_2 in the gas phase.

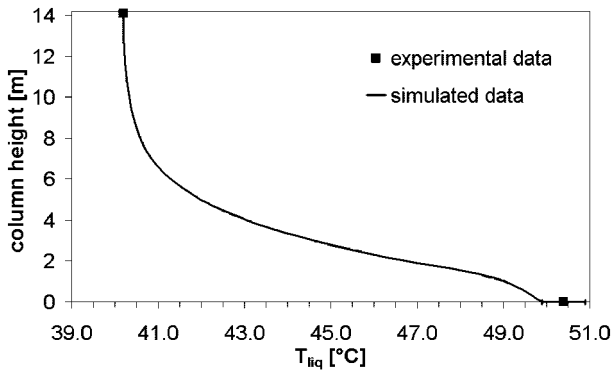


Fig. 9.20. Temperature profile in the liquid phase.

9.5.4

SO_2 Absorption into Aqueous $NaHCO_3/Na_2CO_3$ Solutions

9.5.4.1 Chemical System

Sulfur dioxide is generated in flue gas as a result of combustion of fossil fuel in, for example, thermal plants. Although the sulfur dioxide content in the flue gas is usually small, namely below about 0.1–0.4 vol.% [86], the volume of the produced gas is so large that considerable amounts of sulfur dioxide contaminate the atmosphere, and therefore proper desulfurization becomes important. Here, absorption of SO_2 by the sodium method is considered as part of the combined chemical/biological process shown in Fig. 9.21. The process includes SO_2 removal, $NaHCO_3$ recovery, and elemental sulfur production [70].

When diluted sulfur dioxide is absorbed into aqueous $NaHCO_3/Na_2CO_3$ solutions, the following reactions should be considered [70]:

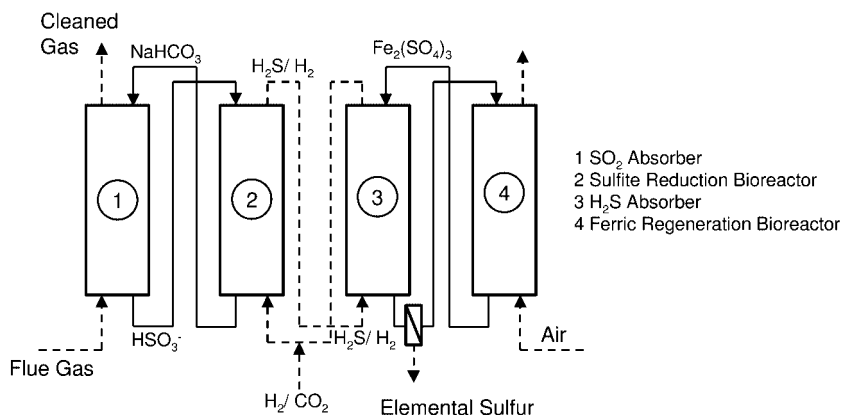
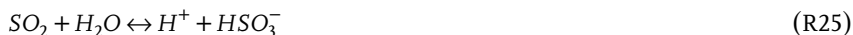


Fig. 9.21. Process scheme of chemo-biological SO₂ removal.

Finite-rate reversible reactions:



Instantaneous reversible reactions:



The hydrolysis of CO₂ is a slow reaction [26]. Forward reaction (R23) obeys pseudo-first-order kinetics, whereas forward reaction (R24) has second-order kinetics. The reaction rates for (R23) and (R24) are defined in Refs. [86, 99].

In any solution of pH ≥ 10, the CO₂ reaction rate according to (R24) will be more than 30-fold higher than that of (R23). However, at pH values below 8, as in the process considered here, reaction (R23) is faster than (R24) [26, 86].

9.5.4.2 Process Set-up

A gas mixture containing SO₂ is fed at the bottom of the column, as shown schematically in Fig. 9.22, whilst a liquid containing the absorbing reactant flows from the top. This set-up is common for reactive absorption processes (cf. Figs. 9.11 and

9.16). The flue gas from a 600-MW power plant contains 1000 ppm SO_2 (0.1 vol%) and has an inlet flow rate of $2 \times 10^6 \text{ Nm}^3 \text{ h}^{-1}$. The temperature is 110°C and the total pressure is 0.14 bar. The liquid phase is an aqueous $\text{NaHCO}_3/\text{Na}_2\text{CO}_3$ solution.

The design studies are made for a packed column filled with 35-mm Pal rings. The height of the column is determined for 95 % removal of SO_2 when 0.05 kmol m^{-3} bicarbonate solution is used as absorbent. The column diameter choice is based on 60 % of flooding condition.

For the validation purpose, the data from Ref. [100] are used. In this study, absorption experiments were carried out using a baffled vessel operated batch-wise with respect to liquid, and the experimental results were compared with an approximate analytical solution based on the Leveque model. The authors proposed a two-reaction-plane model and achieved a good agreement between theoretical and experimental absorption rates (see Section 9.5.4.5).

9.5.4.3 Modeling Peculiarities

Similar to the two previous cases (see Sections 9.5.2 and 9.5.3), the problem is solved numerically, whereas the liquid film region is discretized in a spatially uniform grid. The process is considered as an isothermal operation, assuming plug flow of both phases and constant flow rate values of both gas and liquid phases due to low solute concentrations [70]. In the bulk liquid, reaction equilibrium condition is used as a boundary condition for the film region. In order to describe film diffusion, the simple Fick's law is applied.

It has been shown that the impact of any electric potential gradient on the flux of ions may be disregarded under flue gas desulfurization conditions, as long as the mass flux equations are combined with a flux charge equation [99]. Therefore, the mass balances must be combined with a flux of charge balance as the potential gradient is neglected [70].

9.5.4.4 Model Parameters

The gas-phase diffusion coefficients are calculated using the equation given in Ref. [40]. The liquid-phase diffusion coefficients of components at infinite dilution in

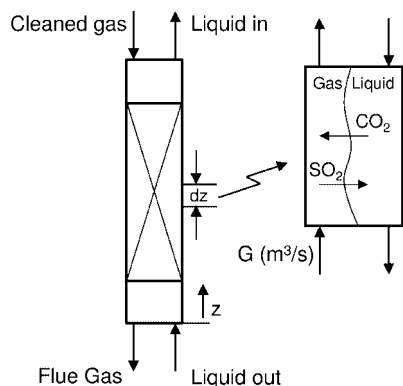


Fig. 9.22. Schematic of the packed column for SO_2 -absorption.

water at 25 °C were taken from Ref. [101] and extrapolated from 25 °C to 55 °C using the Stokes–Einstein equation:

$$\frac{D_A \mu_v}{T} = \text{constant} \quad (30)$$

Correlations for the determination of the dissociation equilibrium constants and solubility values for SO₂ and CO₂ as functions of temperature as well as the equations for activity coefficients are given in Ref. [70]. Thermodynamic non-idealities are taken into account depending on whether species are charged, or not. For uncharged species, a simple relationship from Ref. [102] is applied, whereas for individual ions, the extended Debye–Hückel model is used according to Ref. [103].

Mass transfer coefficients and specific contact area are calculated with the correlations of Onda et al. [60]. In order to determine the liquid film thickness, the diffusion coefficient for SO₂ is used.

9.5.4.5 Results

To validate the model, the pH and concentration profiles for all species are calculated in Ref. [70], using the same parameters and conditions as those from Ref. [100]. The concentration profiles clearly demonstrate the rapid depletion of SO₂ near the gas–liquid interface, and agree with the existence of two reaction planes suggested elsewhere [100].

The predictions of the analytical model [100] and the calculations performed in Ref. [70] using the rate-based model described above are compared with experimental data in Fig. 9.23. It can be seen that the theoretical results obtained with both

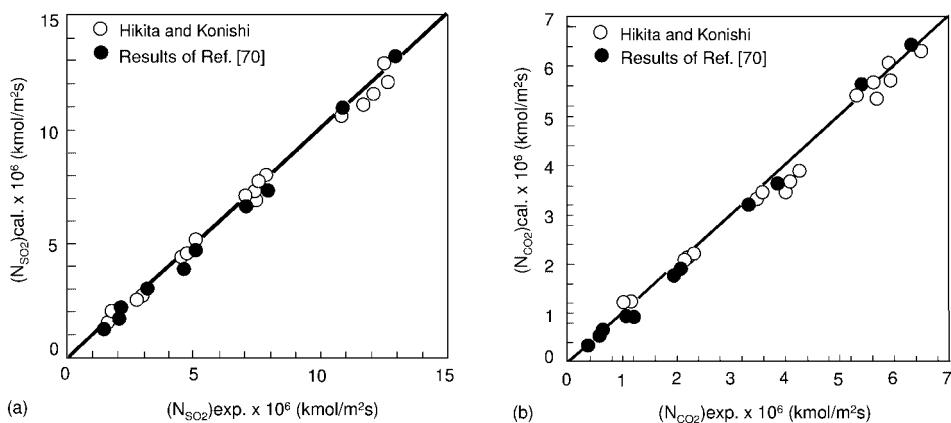


Fig. 9.23. Comparison of simulated absorption/desorption rates with experimental data of Hikita and Konishi [100] for SO₂ absorption into aqueous Na₂CO₃ solutions (adapted from Ref. [70]). (a) SO₂ absorption rate; (b) CO₂ desorption rate.

models are in good agreement with the measured absorption rate. However, it cannot be expected that at high concentrations of Na_2CO_3 the two-reaction-plane model proposed in Ref. [100] will still be valid, as, for example, an assumption of zero concentrations for specific components will not be realistic any longer. The significance of the rate-based model developed in Ref. [70] is therefore clear.

Based on calculated pH and concentration profiles for the various chemical species in the liquid film, the process behavior can be understood. In particular, SO_2 depletion close to the interface due to the very fast reactions causes a high enhancement of SO_2 transfer. In addition, two different reaction regions can be discriminated in the liquid film.

The film phenomena influence the process variables along the column. The partial pressures of SO_2 and CO_2 are shown in Fig. 9.24. It can be seen that CO_2 is absorbed in the fresh alkaline solution at the column top. Then, as the pH decreases from the top to the bottom due to SO_2 absorption, the CO_2 concentration increases, and the direction of the CO_2 flux at the interface changes (see Fig. 9.25). CO_2 desorption also occurs when the concentration in the reaction plane is higher than that at the interface, even if in the bulk it may be lower [70]. The co-existence of absorption and desorption phenomena shown in Figures 9.24 and 9.25 is similar to the phenomena discussed elsewhere [104]. Further sensitivity studies regarding the effect of the buffer concentration and SO_2 gas concentration can also be found [70].

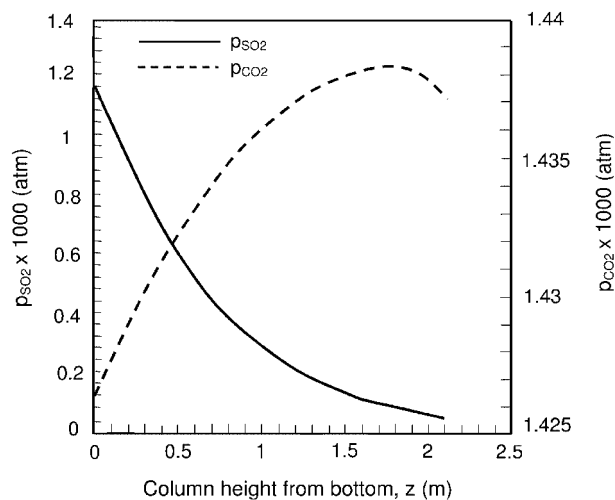


Fig. 9.24. Partial pressure of SO_2 and CO_2 in the flue gas along the column (adapted from Ref. [70]).

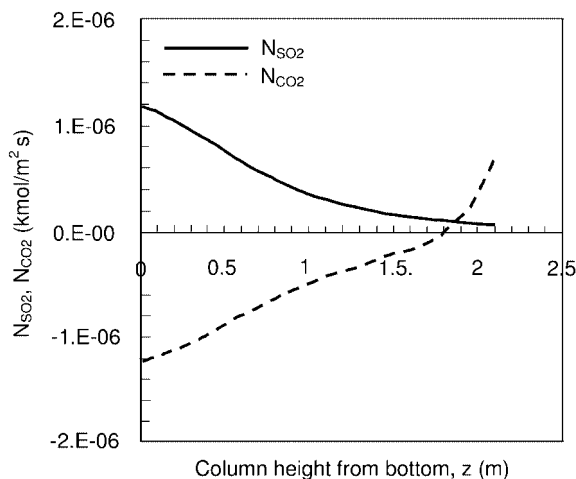


Fig. 9.25. Mass transfer fluxes of SO_2 and CO_2 in the flue gas along the column (adapted from Ref. [70]).

9.6

Conclusions and Outlook

This chapter presents an overview of reactive absorption, which is one of the most important industrial reactive separation operations. Industrially relevant systems and equipment are highlighted, the modeling basics and peculiarities are detailed, and the methods of model parameter estimation are discussed. Both steady-state and dynamic modeling issues are addressed. The implementation of the theoretical description is illustrated with a number of up-to-date applications and validated against laboratory-, pilot- and industrial-scale experiments.

Reactive absorption occurs in multiphase multicomponent fluid systems, and a single modeling approach for all – in part very different – processes, is desirable. Such an approach is suggested here, whereby an application of a reactive rate-based model as a suitable and accurate method is recommended. This method employs a kinetic description of diffusion and reaction steps.

A comprehensive discussion of the most important model parameters covers phase equilibrium, chemical equilibrium, physical properties (e.g., diffusion coefficients and viscosities), hydrodynamic and mass transport properties, and reaction kinetics. The relevant calculation methods for these parameters are explained, and a determination technique for the reaction kinetics parameters is represented. The reaction kinetics of the monoethanolamine carbamate synthesis is obtained via measurements in a stirred-cell reactor. Furthermore, the importance of the reaction kinetics with regard to axial column profiles is demonstrated using a blend of aqueous MEA and MDEA as absorbent.

The peculiarities of specific processes and different solution strategies considered within the discussion of the case studies govern mass and heat transfer phenomena

and chemical reactions as well as their coupling, both for steady-state and dynamic cases.

The suggested modeling strategy is illustrated with NO_x absorption, coke gas purification, CO₂ absorption by amines and SO₂ absorption into aqueous NaHCO₃/Na₂CO₃ solutions. The first example handles the reaction and mass transfer coupling in the film analytically, whereas three other examples employ a purely numerical method. The simulation results are compared with experimental data from an industrial absorption plant consisting of eight columns with countercurrent pump-around (NO_x absorption), a pilot plant for ammonia, hydrogen sulfide circulation scrubbing (coke gas purification), an industrial plant for CO₂ reduction (amine scrubbing process), and a batch-wise operated baffled agitated vessel (SO₂ absorption). For the coke gas purification, both steady-state and dynamic operations are studied.

All results demonstrate a good agreement between the simulations and experiments. The simulation studies warn of equilibrium stage model application, which appears to be completely inappropriate for the case of finite rate reactions. The film reaction consideration is found to be crucial.

Despite highly developed computer technologies and numerical methods, the application of new-generation rate-based models requires a high computational effort, which is often related to numerical difficulties. This is a reason for the relatively limited application of modeling methods described above to industrial problems. Therefore, a further study in this field – as well as in the area of model parameter estimation – is required in order to bridge a gap and to provide process engineers with reliable, consistent, robust and user-friendly simulation tools for reactive absorption operations.

Acknowledgments

The authors are grateful to all project partners involved in this research investigation, and especially to BASF AG, Bayer AG, Thyssen Still Otto Anlagentechnik GmbH, Institut für Prozess- und Anlagentechnik (TU Berlin). They also thank the Volkswagen-Foundation (Project No. I/70 875, 876, 877) for financial support.

Symbols

A_c	cross-sectional column area	m ²
a	activity	
a^I	specific contact area	m ² m ⁻³
c	molar concentration	kmol m ⁻³
d	mass transport driving force	m ⁻¹
\bar{D}	Stefan–Maxwell diffusivity	m ² s ⁻¹
D_A	diffusion coefficient of component A	m ² s ⁻¹
D_{eff}	effective diffusivity	m ² s ⁻¹
E_A	activation energy	kJ kmol ⁻¹
F	Faraday's constant	9.65 × 10 ⁴ C mol ⁻¹

G	gas phase molar stream	kmol s^{-1}
ΔH_R^0	reaction enthalpy	kJ kmol^{-1}
h	molar enthalpy	kJ kmol^{-1}
k	second order reaction rate constant	$\text{m}^3 (\text{kmol}^{-1} \text{s}^{-1})$
k_0	pre-exponential factor (Eq. (17))	$\text{m}^3 (\text{kmol}^{-1} \text{s}^{-1})$
K_i	distribution coefficient	
K_i^{eq}	equilibrium constant of reaction i	
$[K]$	reaction matrix (Eqs. (20), (21))	s^{-1}
l	axial co-ordinate	m
L	liquid-phase molar stream	kmol s^{-1}
n	number of components	
N	molar flux	$\text{kmol m}^{-2}\text{s}^{-1}$
Q	heat flux	kW m^{-2}
r	specific reaction rate of reaction	$\text{kmol m}^{-3}\text{s}^{-1}$
R	reaction rate of component	$\text{kmol m}^{-3}\text{s}^{-1}$
\mathbf{R}	vector with elements R_i	$\text{kmol m}^{-3}\text{s}^{-1}$
\mathfrak{R}	gas constant	$8.3144 \text{ kJ kmol}^{-1} \text{K}^{-1}$
t	time	s
T	temperature	K
U	specific molar hold-up	kmol m^{-1}
x	component liquid-phase mole fraction	kmol kmol^{-1}
\mathbf{x}	vector with elements x_i	kmol kmol^{-1}
y	component gas-phase mole fraction	kmol kmol^{-1}
z	normal co-ordinate	m
z	ionic charge	

Greek letters

δ	film thickness	m
ϕ	volumetric hold-up	$\text{m}^3 \text{m}^{-3}$
φ	electrical potential	V
η	dimensionless film coordinate	
ν	stoichiometric coefficient	
μ	chemical potential	kJ kmol^{-1}
μ_v	dynamic viscosity	$\text{Pa} \cdot \text{s}$

Subscripts

f	forward reaction
G	gas phase
i, j	component or reaction index
L	liquid phase
n	solvent
rev	reverse reaction
t	mixture property

Superscripts

<i>B</i>	bulk phase
<i>I</i>	interface

References

1. R. Zarzycki, A. Chacuk, *Absorption: Fundamentals and Applications*, Pergamon Press, Oxford, 1993.
2. T. K. Sherwood, R. L. Pigford, C. R. Wilke, *Mass Transfer*, McGraw-Hill, New York, 1975.
3. T. K. Sherwood, R. L. Pigford, *Absorption and Extraction*, McGraw-Hill, New York, 1952.
4. R. M. Counce, J. J. Perona, *Designing Packed-Tower Wet Scrubbers: Emphasis on Nitrogen Oxides*, in: *Handbook of Heat and Mass Transfer*, N. P. Chermisinoff (Ed.), Gulf Publ. Comp. Book Division, Houston, 1986, 953–966.
5. K. Sattler, *Thermische Trennverfahren*, VCH, Weinheim, 1988.
6. S. Strelzoff, Choosing the optimum CO₂-removal system, *Chem. Eng.*, 1975, 82 (18), 115–120.
7. J. Falbe, *Chemierohstoffe aus Kohle*, Georg-Thieme-Verlag, Stuttgart, 1977.
8. S. Schubert, M. Grünwald, D. W. Agar, Enhancement of carbon dioxide absorption into aqueous methyl-diethanolamine using immobilised activators, *Chem. Eng. Sci.*, 2001, 56, 6211–6216.
9. W. J. Hatcher, *Reaction and Mass Transport in Two-Phase Reactors*, in: *Handbook of Heat and Mass Transfer*, N. P. Chermisinoff (Ed.), Gulf Publ. Comp. Book Division, Houston, 1986, 837–868.
10. R. Billet, *Packed Towers*, 1st edn., VCH, Weinheim, 1995.
11. V. M. Ramm, *Absorption of Gases*, Israel Program for Scientific Translations, Jerusalem, 1968.
12. S. Pelkonen, *Multicomponent Mass Transfer in Packed Distillation Columns*, PhD Thesis, University of Dortmund, 1997.
13. N. P. Lieberman, E. T. Lieberman, *Working Guide to Process Equipment*, 2nd edn., McGraw-Hill, 2002.
14. E. Y. Kenig, *Modeling of Multicomponent Mass Transfer in Separation of Fluid Mixtures*, VDI-Verlag, Düsseldorf, 2000.
15. E. Y. Kenig, A. Górak, A film model based approach for simulation of multicomponent reactive separation, *Chem. Eng. Process.*, 1995, 34, 97–103.
16. R. Taylor, R. Krishna, *Multicomponent Mass Transfer*, Wiley, New York, 1993.
17. E. Sorel, *La rectification de l'alcool*, Gauthiers - Villais et fils, Paris, 1893.
18. E. J. Henley, J. D. Seader, *Equilibrium Stage Separation Operations in Chemical Engineering*, Wiley, New York, 1981.
19. L. L. Doraiswamy, M. M. Sharma, *Heterogeneous Reactions: Analysis, Examples and Reactor Design*, Wiley, New York, 1984.
20. D. W. van Krevelen, P. J. Hoftijzer, Kinetics of gas-liquid reactions – Part I: General theory, *Recl. Trav. Chim. Pays-Bas*, 1948, 67, 563–586.
21. H. Holma, J. Sohlo, A mathematical model of an absorption tower of nitrogen oxides in nitric acid production, *Computers Chem. Eng.*, 1979, 3, 135–141.
22. G. Carta, Scrubbing of nitrogen oxides with nitric acid solutions, *Chem. Eng. Commun.*, 1986, 42, 157–170.
23. H. L. Toor, Solution of the linearized equations of multicomponent mass transfer, *AIChE J.*, 1964, 10, 448–455, 460–465.
24. A. Górak, *Simulation thermischer Trennverfahren fluider Vielkomponentengemische*, in: *Prozeßsimulation*, G. Schuler (Ed.), VCH Verlag, Weinheim, 1995, 349–408.
25. R. E. Treybal, *Mass Transfer Operations*, McGraw-Hill, New York, 1980.

26. P. V. Danckwerts, *Gas-Liquid Reactions*, McGraw-Hill, New York, 1970.
27. K. R. Westerterp, W. P. M. van Swaaij, A. A. C. M. Beenackers, *Chemical Reactor Design and Operation*, 2nd. edn., Wiley, Chichester, 1984.
28. L. Kucka, *Modellierung und Simulation der reaktiven Absorption von Sauer gasen mit Alkanolaminlösungen*, PhD Thesis, University of Dortmund, 2003.
29. J. D. Seader, The rate-based approach for modeling staged separations, *Chem. Eng. Prog.*, **1989**, 85 (10), 41–49.
30. S. S. Katti, Gas-liquid-solid systems: An industrial perspective, *Trans. Inst. Chem. Engrs.*, **1995**, 73 Part A, 595–607.
31. W. K. Lewis, W. G. Whitman, Principles of gas absorption, *Ind. Eng. Chem.*, **1924**, 16, 1215–1220.
32. R. Higbie, The rate of absorption of a pure gas into a still liquid during short periods of exposure, *Trans. Am. Inst. Chem. Engrs.*, **1935**, 31, 365–383.
33. J. O. Hirschfelder, C. F. Curtiss, R. B. Bird, *Molecular Theory of Gases and Liquids*, Wiley, New York, 1964.
34. J. Mackowiak, *Fluiddynamik in Kolonnen mit modernen Füllkörperpackungen und Packungen für Gas/Flüssigkeitssysteme*, Sauerländer, Frankfurt am Main, 1991.
35. E. Y. Kenig, U. Wiesner, A. Górák, Modeling of reactive absorption using the Maxwell-Stefan equations, *Ind. Eng. Chem. Res.*, **1997**, 36, 4325–4334.
36. E. Y. Kenig, F. Butzmann, L. Kucka, et al., Comparison of numerical and analytical solutions of a multicomponent reaction-mass transfer problem in terms of the film model, *Chem. Eng. Sci.*, **2000**, 55, 1483–1496.
37. C.-C. Chen, H. I. Britt, J. F. Boston, et al., Local compositions model for excess Gibbs energy of electrolyte systems. Part I: Single solvent, single completely dissociated electrolyte systems, *AIChE J.*, **1982**, 28, 588–596.
38. C.-C. Chen, L. B. Evans, A local composition model for the excess Gibbs energy of aqueous electrolyte systems, *AIChE J.*, **1986**, 32, 444–459.
39. B. Mock, L. B. Evans, C.-C. Chen, Thermodynamic representation of phase equilibria of mixed-solvent electrolyte systems, *AIChE J.*, **1986**, 32, 1655–1664.
40. R. Reid, J. M. Prausnitz, B. E. Poling, *The Properties of Gases and Liquids*, 4th. edn., McGraw-Hill, New York, 1987.
41. K. S. Pitzer, G. Mayorga, Thermodynamics of electrolytes. II. Activity and osmotic coefficients for strong electrolytes with one or both ions equivalent, *J. Phys. Chem.*, **1973**, 77, 2300–2308.
42. K. S. Pitzer, Thermodynamics of electrolytes. I. Theoretical basis and general equations, *J. Phys. Chem.*, **1973**, 77, 268–277.
43. E. A. Guggenheim, J. C. Turgeon, Specific interaction of ions, *Trans. Faraday Soc.*, **1955**, 51, 747–761.
44. A. L. Horvath, *Handbook of Aqueous Electrolyte Solutions*, Ellis Horwood, Chichester, 1985.
45. K. S. Pitzer, J. J. Kim, Thermodynamics of electrolytes. IV. Activity and osmotic coefficients for mixed electrolytes, *J. Am. Chem. Soc.*, **1974**, 96, 5701–5707.
46. T. J. Edwards, J. Maurer, J. Newman, et al., Vapor-liquid equilibria in multicomponent aqueous solutions of volatile weak electrolytes, *AIChE J.*, **1978**, 24, 966–976.
47. G. F. Versteeg, L. A. J. van Dijk, W. P. M. van Swaaij, On the kinetics between CO₂ and alkanolamines both in aqueous and non-aqueous solutions. An overview, *Chem. Eng. Commun.*, **1996**, 144, 113–158.
48. G. Kuranov, B. Rumpf, G. Maurer, et al., VLE modelling for aqueous systems containing methyldiethanolamine, carbon dioxide and hydrogen sulfide, *Fluid Phase Equil.*, **1997**, 136, 147–162.
49. O. A. Hougen, K. M. Watson, R. A. Ragatz, *Chemical Process*

- Principles I, Material and Energy Balances*, 2nd edn., Wiley, New York, 1962.
50. D. M. Austgen, G. T. Rochelle, X. Peng, et al., Model of vapor-liquid equilibria for aqueous acid gas-alkanolamine systems using the electrolyte NRTL equation, *Ind. Eng. Chem. Res.*, **1989**, 28, 1060–1073.
 51. E. N. Fuller, P. D. Schettler, J. C. Giddings, A new method for prediction of binary gas-phase diffusion coefficients, *Ind. Eng. Chem.*, **1966**, 58, 19–27.
 52. *Aspen Properties. Physical Property Methods and Models. Version 10.2*, 10.2 ed., Aspen Technology, Inc., Cambridge, MA, USA, 2000.
 53. C. R. Wilke, P. Chang, Correlation of diffusion coefficients in dilute solutions, *AIChE J.*, **1955**, 1, 264–270.
 54. C. R. Wilke, Diffusional properties of multicomponent gases, *Chem. Eng. Progress*, **1950** (46), 95–104.
 55. A. Burghardt, R. Krupiczka, Wnikanie masy w układach wieloskładnikowych – Teoretyczna analiza zagadnienia i okreslenia współczynników wnikania masy, *Inz. Chem.*, **1975**, 5, 487–510.
 56. A. Vignes, Diffusion in binary solutions, *Ind. Eng. Chem. Fundam.*, **1966**, 5, 189–199.
 57. H. A. Kooijman, R. Taylor, Estimation of diffusion coefficients in multicomponent liquid systems, *Ind. Eng. Chem. Res.*, **1991**, 30, 1217–1222.
 58. H. G. Rackett, Equation of state for saturated liquids, *J. Chem. Eng. Data*, **1970**, 15, 514–517.
 59. R. Billet, M. Schultes, Prediction of mass transfer columns with dumped and arranged packings, *Trans. Inst. Chem. Engrs.*, **1999**, 77 Part A, 498–504.
 60. K. Onda, H. Takeuchi, Y. Okumoto, Mass transfer coefficients between gas and liquid phases in packed columns, *J. Chem. Eng. Japan*, **1968**, 1, 56–62.
 61. N. Kolev, Wirkungsweise von Füllkörperschüttungen, *Chem. Ing. Techn.*, **1976**, 48, 1105–1112.
 62. J. A. Rocha, J. L. Bravo, J. R. Fair, Distillation columns containing structured packings - 2. Mass transfer model, *Ind. Eng. Chem. Res.*, **1996**, 35, 1660–1667.
 63. B. Ohlmeier, *Validierung der Simulation reaktiver Absorptions- und Desorptionsprozesse*, PhD Thesis, University of Essen, 2001.
 64. R. Schneider, *Modelloptimierung für die dynamische Simulation der reaktiven Absorption und Rektifikation*, PhD Thesis, University of Dortmund, 2001.
 65. R. Schneider, A. Górak, Model optimisation for the dynamic simulation of reactive absorption processes, *Chem. Eng. Technol.*, **2001**, 24, 979–989.
 66. H. Hikita, S. Asai, H. Ishikawa, et al., The kinetics of reactions of carbon dioxide with monoethanolamine, diethanolamine and triethanolamine by a rapid mixing method, *Chem. Eng. Journal*, **1977**, 13, 7–12.
 67. D. Barth, C. Tondre, J. J. Delpuech, Stopped-flow investigations of the reaction kinetics of carbon dioxide with some primary and secondary alkanolamines in aqueous solution, *Int. J. Chem. Kin.*, **1986**, 18, 445–457.
 68. E. J. Cullen, J. F. Davidson, Absorption of gases in liquid jets, *Trans. Faraday Soc.*, **1957**, 53, 113–120.
 69. S. S. Laddha, P. V. Danckwerts, Reaction of CO₂ with ethanolamines: Kinetics from gas-absorption, *Chem. Eng. Sci.*, **1981**, 36, 479–482.
 70. S. Ebrahimi, C. Picioreanu, R. Kleerebezem, et al., Rate-based modelling of SO₂ absorption into aqueous NaHCO₃/Na₂CO₃ solutions accompanied by the desorption of CO₂, *Chem. Eng. Sci.*, **2003**, 58, 3589–3600.
 71. N. J. Suchak, K. R. Jethani, J. B. Joshi, Modeling and simulation of NO_x absorption in pilot-scale packed columns, *AIChE J.*, **1991**, 37, 323–339.
 72. U. Wiesner, *Mathematische Modellierung der Absorption nitroser Gase in Füllkörperkolonnen*, PhD Thesis, University of Dortmund, 1997.

73. K. Ulrichs, W. Laue, H.-D. Renovanz, *Salpetersäure und salpetrige Säure, Stickstoffoxide, Nitrate, Nitrite*, in: *Ullmanns Encyklopädie der technischen Chemie*, VCH, Weinheim, 1981, 305–362.
74. U. Wiesner, A. Górak, E. Y. Kenig, et al., Modelling of absorption of nitrous waste gases, *ICHEME Symp. Ser.*, **1997**, 142 (1), 323–333.
75. J. Wei, C. D. Prater, The structure and analysis of complex reaction systems, *Adv. Catal.*, **1962**, 13, 203–392.
76. H. Hikita, S. Asai, Gas absorption with (m, n)-th order irreversible chemical reactions, *Int. Chem. Eng.*, **1964**, 4, 332–340.
77. H. L. Toor, Dual diffusion-reaction coupling in first order multicomponent systems, *Chem. Eng. Sci.*, **1965**, 20, 941–951.
78. G. B. DeLancey, Multicomponent film-penetration theory with linearized kinetics – I. Linearization theory and flux expressions, *Chem. Eng. Sci.*, **1974**, 29, 2315–2323.
79. G. Astarita, S. I. Sandler, *Kinetic and Thermodynamic Lumping of Multicomponent Mixtures*, Elsevier, Amsterdam, 1991.
80. E. Y. Kenig, L. P. Kholpanov, Analysis of formulation and solution of multicomponent reaction-diffusion problems, *Theor. Found. Chem. Eng.*, **1992**, 26, 510–521.
81. S. E. Schwartz, W. H. White, *Solubility Equilibria of the Nitrogen Oxides and Oxyacids in Dilute Aqueous Solutions*, in: *Advances in Environmental Science and Engineering*, J. R. Pfafflin and E. N. Zeigler (Eds.), Gordon and Breach Science Publ., New York, 1981.
82. H. Engels, *Anwendung des Modells der lokalen Zusammensetzung auf Elektrolytlösungen*, PhD Thesis, RWTH Aachen, 1985.
83. U. Wiesner, M. Wittig, A. Górak, Design and optimization of a nitric acid recovery plant from nitrous waste gases, *Computers Chem. Eng.*, **1996**, 20, S1425–S1430.
84. V. V. Kafarov, E. A. Shestopalov, E. A. Novikov, et al., Mathematical model of absorption of NO_x in production of weak nitric acid, *Soviet Chem. Ind.*, **1975**, 7, 1224–1226.
85. H. Brauer, *Stoffaustausch einschließlich chemischer Reaktionen*, Sauerländer, Aarau, 1971.
86. G. Astarita, D. W. Savage, A. Bisio, *Gas Treating with Chemical Solvents*, Wiley, New York, 1983.
87. P. V. Danckwerts, M. M. Sharma, The absorption of carbon dioxide into solutions of alkalis and amines (with some notes on hydrogen sulfide and carbonyl sulfide), *The Chemical Engineer*, **1966**, July–August, 244–280.
88. G. Maurer, On the solubility of volatile weak electrolytes in aqueous solutions, *ACS Symp. Ser.*, **1980**, 133, 139–172.
89. A. L. Kohl, F. C. Riesenfeld, *Gas Purification*, 4th. edn., Gulf Publ. Comp. Book Division, Houston, 1985.
90. K. Tippmer, Progress in the desulphurization of coke oven gas and utilization of H₂S-Still Otto's SOLOX process, *Coke Making Int.*, **1994**, 6, 32–43.
91. H. Thielert, *Simulation und Optimierung der Kokereigaswäsche*, PhD Thesis, Technical University of Berlin, 1997.
92. R. Schneider, E. Y. Kenig, A. Górak, Dynamic modeling of reactive absorption with the Maxwell-Stefan approach, *Trans. Inst. Chem. Engrs*, **1999**, 77 Part A, 633–638.
93. E. Y. Kenig, R. Schneider, A. Górak, Rigorous dynamic modelling of complex reactive absorption processes, *Chem. Eng. Sci.*, **1999**, 54, 5195–5203.
94. R. Schneider, E. Y. Kenig, A. Górak, *Complex reactive absorption processes: model optimisation and dynamic column simulation*, in: *Proceedings ESCAPE-11 European Symposium on Computer Aided Process Engineering*, Kolding, Denmark, Elsevier, 2001.
95. E. Y. Kenig, R. Schneider, A. Górak, Reactive absorption: Optimal process design via optimal modelling, *Chem. Eng. Sci.*, **2001**, 56, 343–350.

96. C. C. Pantelides, The consistent initialization of differential-algebraic systems, *SIAM J. Sci. Stat. Comp.*, **1988**, 9, 213–231.
97. R. Schneider, E. Y. Kenig, A. Górák, Dynamische Simulation reaktiver Absorptionsprozesse am Beispiel einer Sauer gaswäsche: Modellentwicklung, -analyse und -optimierung, *Chem. Ing. Techn.*, **2000**, 72, 1224–1229.
98. T. Pintola, P. Tontiwachwuthikul, A. Meisen, Simulation of pilot plant and industrial CO₂-MEA absorbers, *Gas Sep. & Purif.*, **1993**, 7, (1), 47–52.
99. C. Brogren, H. T. Karlsson, Modeling the absorption of SO₂ in a spray scrubber using the penetration theory, *Chem. Eng. & Technol.*, **1997**, 52, 3085–3099.
100. H. Hikita, K. Konishi, The absorption of SO₂ into aqueous Na₂CO₃ solutions accompanied by the desorption of CO₂, *Chem. Eng. J.*, **1983**, 27, 167–176.
101. P. Vanysek, *CRC Handbook of Chemistry and Physics*, 82 ed., CRC Press LLC, Boca Raton, 1999.
102. P. Gerard, G. Segantini, J. Vanderschuren, Modeling of dilute sulfur dioxide absorption into calcium sulfite slurries, *Chem. Eng. Sci.*, **1996**, 51, 3349–3358.
103. D. L. Parkhurst, C. A. J. Appelo, *User's guide to PHREEQC (Version 2)*, U.S. Geological Survey, Denver, CO, 1999.
104. E. Y. Kenig, Mass transfer-reaction coupling in two-phase multicomponent fluid systems, *Chem. Eng. J.*, **1995**, 57, 189–204.
105. W.-C. Yu, G. Astarita, Selective absorption of hydrogen sulphide in tertiary amine solutions, *Chem. Eng. Sci.*, **1987**, 42, 419–424.
106. M. R. Rahimpour, A. Z. Kashkooli, Enhanced carbon dioxide removal by promoted hot potassium carbonate in a split-flow absorber, *Chem. Eng. Process.*, **2004**, 43, 857–865.
107. J. B. Joshi, V. V. Mahajani, V. A. Juvekar, Absorption of NO_x gases, *Chem. Eng. Commun.*, **1985**, 33, 1–92.
108. A. Kobus, *Ein heuristisch-numerischer Ansatz zum systematischen Entwurf und Design von Absorptionsverfahren*, PhD Thesis, Ruhr-Universität Bochum, 1999.
109. E. Y. Kenig, L. P. Kholpanov, L. I. Katysheva, et al., Calculation of two-phase non-isothermal absorption in a liquid film in downward co-current flow, *Theor. Found. Chem. Eng.*, **1985**, 19, 97–102.
110. P. Gandhidasan, *Heat and Mass Transfer in Solar Regenerators*, in: *Handbook of Heat and Mass Transfer*, N. P. Cheremisinoff (Ed.), Gulf Publ. Comp. Book Division, Houston, 1986, 1475–1499.
111. D. J. Safarik, R. B. Eldridge, Olefin/paraffin separations by reactive absorption: a review, *Ind. Eng. Chem. Res.*, **1998**, 37, 2571–2581.
112. M. A. Siddiqi, K. Lucas, Correlations for prediction of diffusion in liquids, *Can. J. Chem. Eng.*, **1986**, 64, 839–843.
113. V. Mika, Model of packed absorption column. I. Physical absorption, *Coll. Czech. Chem. Commun.*, **1967**, 32, 2933–2943.

10

Reactive Extraction: Principles and Apparatus Concepts

Hans-Jörg Bart

10.1

Introduction

Extraction processes have their history in “life-science” applications with the recovery of perfumes, waxes or pharmaceutically active substances. An extraction pot dating back to 3500 BC was found 250 km north of Baghdad (Fig. 10.1), and extraction instructions were documented by a Summerian text of 2100 BC. The next technological milestone was in the mediaeval age, when ethanol was used as a new solvent, and mineral acids or amalgams were used for metal extraction and refinement. The next major step was in the 19th century, when Peligot [1] first applied reactive extraction when using diethylether as a solvent for uranyl nitrate. Additionally, the distribution law by Nernst (1891) was formulated and the first liquid–liquid extraction column was patented by Pfleiderer (1898) which incorporated all the features (counterflow of phases, stirrer, inlet distributor, coalescence aids) of modern columns [2]. The reactive extraction of metals was first industrialized within the “Manhattan” project during the 1940s, with the extraction of uranium. Niche applications were then identified with Nb/Ta or Zr/Hf separations, until during the 1960s when Cu/Fe separation provided the breakthrough for a broad commercial application. In this process, LIX (Liquid Ion eXchanger) chemicals [3], as size-selective extractants, allowed the recovery of copper from low-grade ores. Today, the use of liquid ion exchangers has expanded to include the recovery, enrichment or separation of ionic or neutral solutes in the hydrometallurgical, environmental, petrochemical, chemical and biochemical fields [4–8].

10.1.1

Physical Extraction

Liquid extraction systems consist either of pure solvents and mixtures, but may also contain additives. The application of single solvent or simple mixtures is well-known in classical physical extractions when using bulk organic chemicals (toluene, butanol, etc.) to extract a solute. Today, a new class of solvents is that of ionic liquids [10], which are low-melting organic salts where the cation is, for example, from

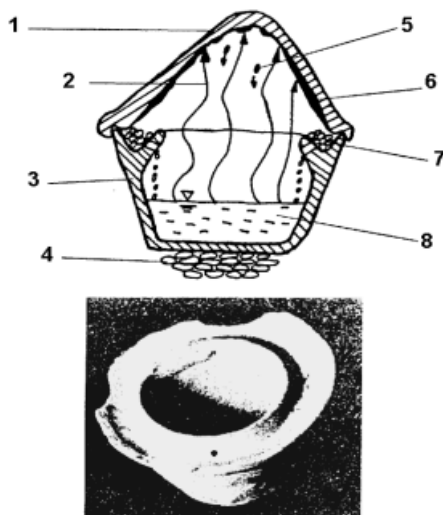


Fig. 10.1. Extraction pot (1 cooling cap, 2 vapor, 3 extraction pot, 4 heating, 5 condensate droplet, 6 condensate film, 7 feed material, 8 solvent (oil or water). (From Ref. [9]).

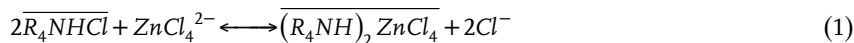
nitrogen ions (e.g., quaternary ammonium, quinolinium, pyridinium, imidazolium). These are liquid at room temperature, and have negligible vapor pressure and varying water miscibility due to the anion. Typical anions promoting water miscibility are Cl^- , NO_3^- and CF_3CO_2^- , while immiscibility is with PF_6^- , $\text{N}(\text{SO}_2\text{CF}_3)_2^-$. Generally, thermodynamic data are scarce (physico-chemical properties, solubilities, etc.), but commercial applications have been reported. BASF were able to reduce a 8-m³ batch reactor to a 5-mL continuous tube reactor in their BASIL® process when using ionic liquids based on imidazoles. This was due to the simpler process when extracting products, which shifted the equilibria towards higher yields, in addition to employing the catalytic activity of the ionic liquid [11, 12].

10.1.2

Reactive Extraction

A reactive extraction system usually consists of a liquid ion exchanger diluted in solvent. The latter is used to adjust rheological or physico-chemical properties, since most of the ion exchangers are highly viscous or even solid. The solvent should be non-miscible with water and with a high boiling point (e.g., ~ 500K) to avoid losses. If kerosene-like solvents are used, a modifier (e.g., isododecanol) is sometimes necessary in order to prevent the formation of a third phase and so to help to solubilize the ion exchanger-solute complex. The regeneration and re-extraction of the extract phase is with a chemical shift as discussed below. This is in contrast to physical extraction, where stripping is performed by distillation.

The practical handling and design of a reactive solvent extraction process is given in appropriate handbooks [4–8], but a short review on the principles involved is provided here. Liquid ion exchangers are available as either anion, cation, or solvating exchangers. An example of an anion exchange is:

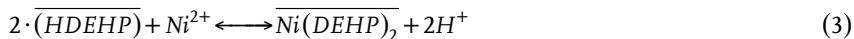


The quaternary R_4 -alkyl-substituted ammonium chlorides are commercially available, and can be stripped with a surplus of chloride, hydroxide, etc.; thus, the solute is regenerated in the re-extraction or stripping step. The quaternary compound has the advantage of being able to be used in alkaline media compared to the frequently used ternary amines. Primary, secondary (both are water-soluble, less used) and tertiary amines are only stable in acidic aqueous media, as hydroxide destroys the ammonium complex:



Volatile anions such as acetate and formate can also be removed and stripped by a temperature swing, which yields the free tertiary amine, R_3N , similar to Eq. (2). The change in counter ion concentration and temperature gives rise to a reversible extraction process according to Eq. (1). Generally, the selectivity of anion exchangers is not always good, and there are many developments of new host–guest–ligands which take advantage of the different sizes of the solutes [13].

The cation exchange mechanism is as follows:



Here, nickel is extracted with a di(2-ethylhexyl) phosphoric acid in its H-form (HDEHP) and two protons are set free. This causes a pH-shift during extraction, which can be avoided if the ion exchanger is, for example, in the Na-form. Typical extraction isotherms are depicted in Fig. 10.2. At the indicated pH-value no nickel, but more than 80 % cobalt, can be extracted in one equilibrium stage. During cobalt

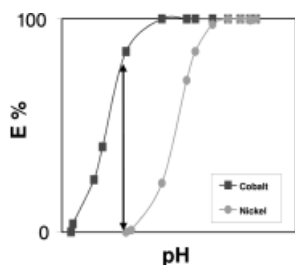


Fig. 10.2. Typical pH-dependency of Co/Ni isotherms.

extraction similar to Eq. (3), the pH-value will shift and, as can be seen from Fig. 10.2, the extraction efficiency of cobalt will be reduced. Exchange of Co versus Na will avoid this. However, a problem with sodium is the occurrence of microemulsion systems, which will be discussed below. Re-extraction is usually with strong mineral acids (preferable H_2SO_4). In addition to the alkylated phosphoric compounds, phosphonic and phosphinic acids and their thio-forms are also available. The latter compounds are strong extractants, and although di-thiophosphoric acids are difficult to strip they can be used at a feed pH-value lower than 1. Carboxylic acid-based ion exchangers are seldom used due to their high water solubility, whilst aryl-substituted compounds also have limited applications for steric reasons. Most liquid ion exchangers have branched alkyl substituents as n-alkyls tend to crystallize and are not liquid. From a chemical point of view, both the solute–anion exchanger or solute–cation exchanger complex are ionic liquids or liquid organic salts.

As mentioned above, the breakthrough with reactive solvent systems was obtained with chelating ion exchangers for copper recovery. A size-specific host–guest complexation in addition to ion exchange separates copper from impurities such as iron. As can be seen in Fig. 10.3, the nitrogen chelates the copper ion, developing a new six-ring structure only stable with copper as solute. A typical process flowsheet is depicted in Fig. 10.4. In the center is the extraction circuit where copper is extracted and two protons are set free; these are then consumed in the leaching circuit. The re-extraction is with strong sulfuric acid, and the stripping solution is fed to the electrowinning station. Here, copper is deposited, whilst on the anode water is transformed to protons and oxygen is set free. In literal terms, as a current is applied, new sulfuric acid is produced which, via the extraction cycle, is transported to the leaching section countercurrent to the solute copper. This self-sustaining copper extraction unit (the primary requirements are only water and current) proved to be successful when built in remote areas such as deserts. As can be seen, the copper extraction circuit is a very comprehensive and compact scheme that normally includes three extraction and two re-extraction stages. If a separation factor (e.g., selectivity) is poor, then reflux of the product or scrubbing section might help to improve separation (Fig. 10.5). Extra steps to regenerate the ion exchanger in order to formulate a sodium or ammonium salt of the ion exchanger may be incorporated, as was discussed above with the Co/Ni separation. Aqueous phase microdroplets entrained in the organic phase can be removed by using an extra washing step, especially when there is a switch between different aqueous media (sulfate, nitrate, chloride, etc.) during the extraction, regeneration and stripping stages. For more complex separation tasks (e.g., the Co/Ni separation detailed above), these stages may be a scrub (reflux), followed by extraction, stripping and regeneration, with a possible intermediate one-stage water scrub when extraction is from chloride and re-extraction is from a sulfuric acid medium.

An example of coordinative extraction with solvating agents is shown in Eq. (4). The difference with physical extraction is that the capacity and extraction power of the liquid neutral ion exchanger is much higher than with any bulk organic solvent (toluene, xylene, butanol, etc.) used in physical extraction. Alkyl-substituted

phosphates, phosphonates and phosphine oxides (e.g., tri-octyl phosphine oxide) are widely used.

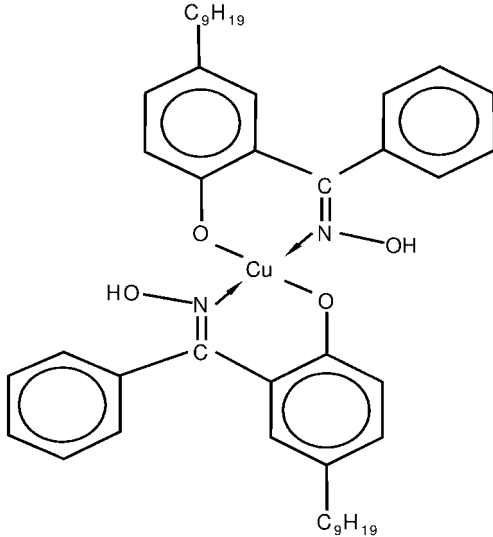


Fig. 10.3. Copper chelate structure.

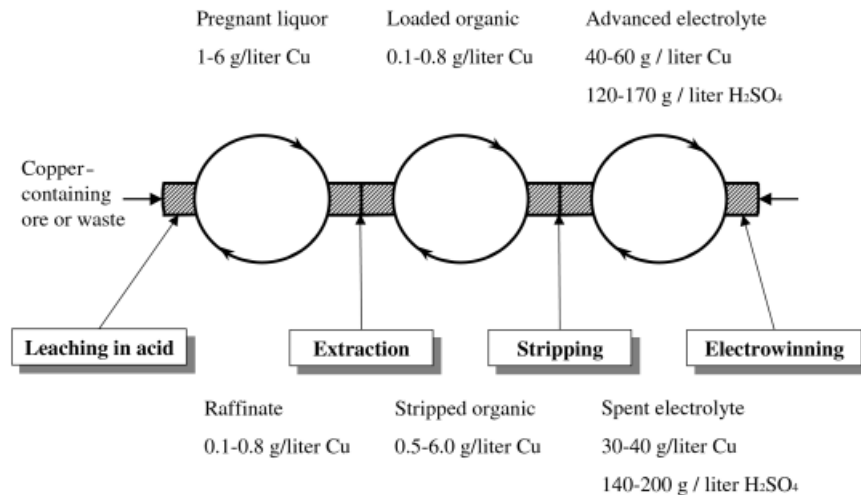


Fig. 10.4. Circuits with copper recovery. (left: leaching, middle: extraction, right: electrowinning).

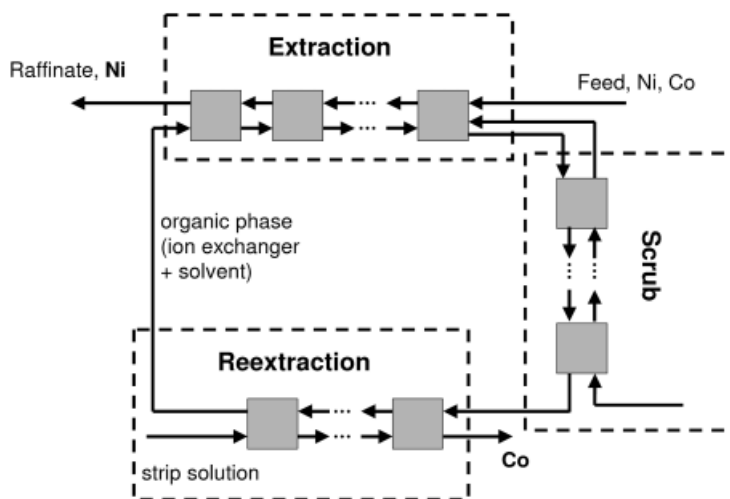
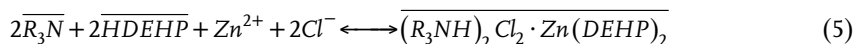


Fig. 10.5. Process flowsheet for Co/Ni separation.

Tri-butyl-phosphate (TBP) has a very high solvating power for neutral substances (e.g., undissociated acids or salts), and will extract them. Elevated temperatures and low ionic strength (pure water) will achieve re-extraction. Most of the solvating exchangers can be used undiluted due to appropriate physical properties. Carbon-based compounds (e.g., ketones, ethers) suffer from lower capacity and higher water solubility, and the stoichiometry in Eq. (4) is determined by the coordination number x . They can be regenerated by distillation which otherwise is limited due to high boiling points.

Liquid ion exchangers can be mixed together in order to create synergistic effects. This means that the effect of a mixture provides a non-linear improvement with regard to the single systems. Basically, the effect results from an improvement in solvation of the new ion exchanger–solute complex. Such synergistic behavior has also been reported with extraction kinetics, when Henkel improved their first commercial copper extraction reagent LIX64 with an admixture of a small amount of LIX63. This markedly enhanced the kinetics of the new reagent LIX64N [14], which proved to be a milestone and the commercial beginnings of a process to extract base metals on a large scale. Generally, numerous references can be found to synergistic effects, and reviews are available in many solvent extraction textbooks.

An equimolar mixture of cation and anion exchanger gives a “mixed” extraction system [15] which can extract salts or acids according to Eq. (5). Re-extraction is then either by shift of temperature, aqueous ionic strength, or acidity/basicity.



Selection of the correct reactive solvent phase is the key to a successful separation process, and a list of various solvent-selection criteria is provided in following. Some of these are essential for separation, while others are simply desirable properties that will improve a separation and/or make it more economical. Solvent selectivity, recoverability and a large density difference with the raffinate are essential. Some of the requirements of physical or reactive solvent phases will conflict, and a compromise may be necessary.

In general, the requirements for reactive solvent extraction phases are similar to those of physical extraction phases. Typically, the viscosity should be lower than $2 \text{ mPa} \cdot \text{s}$, the boiling point range in the region of 420 to 520 K, and densities from 750 to 900 kg m^{-3} . The flash point should be at least 25 K higher than the working temperature, and a value higher than 330 K is recommended. Aromatic diluents with equivalent molecular weight as aliphatic ones are more polar and thus more water-soluble. The higher price and greater toxicity of aromatic diluents leads to a preference for aliphatic diluents in industrial practice. Degradation of the diluent is usually negligible in comparison to that of the ion exchanger. The latter can be chemically, thermally and radiochemically degraded, and also can be “poisoned” by an irreversibly extracted compound. “Crud” (Chalk River Unidentified Deposit) [G.M. Ritcey, personal communication, 1998] is the term used to describe the pollutant phase containing mineral or biological solids that tends to build up at the phase interfaces in the solvent extraction plant. Colloidal and dissolved substances (especially silica) precipitate at high shear rates, and humic acids promote this behavior, as reported in hydrometallurgical applications [16].

10.1.3

Additives

Additives are usually amphiphilic in nature, and thus are either ionic or neutral surfactants or even polymers. The role of surfactants in solvent extraction is ambiguous. Usually, they should be avoided as they lower the interfacial tension, which may lead to emulsion formation in an agitated extractor. However, every metal-loaded ion exchanger is amphiphilic, and can adsorb at the interface or aggregate in the bulk phase. This occurrence is well known with sodium or other metals [17], and above a critical surfactant concentration (cmc, critical micelle concentration) micellar aggregates are formed. A dimensionless geometric parameter is decisive for the structure of the associates, according to Fig. 10.6:

$$\frac{v}{a_0 \cdot l} \quad (6)$$

where v is the molecular volume, a_0 the surface and l the length of the surfactant.

When the value $v/a_0 \cdot l < 1/3$, spherical micelles will be found, whilst up to a value of $1/2$ the micelles are rod-like, followed by lamellar phases. Inverted micelles are then found at a value > 1 . At values between 1 and 2 the structures are rod-like, and

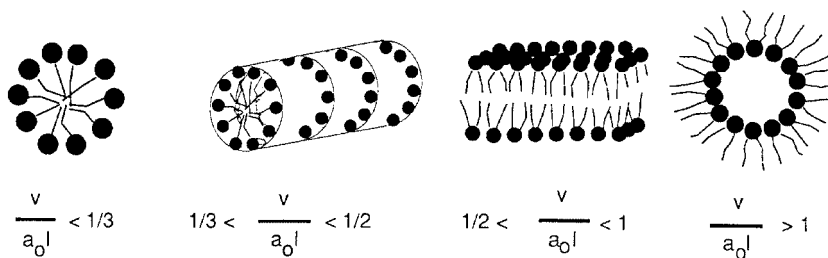


Fig. 10.6. Possible micellar aggregates.

above 2 they are spherical. The phase boundaries for this structure is based on a classification deduced by P.A. Winsor [18, 19]. The classification relies on four classes containing surfactant, co-surfactant, oil, and water. The Winsor I system consists of an organic oil phase in equilibrium with an oil-in-water microemulsion, while Winsor II is an aqueous phase in equilibrium with a water-in-oil microemulsion. Winsor III consists of three phases of oil, water, and microemulsion, while Winsor IV is an isotropic microemulsion phase (Fig. 10.7). The microemulsion is translucent, as the small micelles (5 to 50 nm diameter) will not refract light. Bias et al. [20] describe this phase equilibria with Gibbs excess energies. Paatero [21] evaluated the phase diagrams for NaOH/Cyanex 272/*n*-hexane systems. The existence of one-, two-, and three-phase regions, and even of liquid crystalline phases, was identified. The same effect was seen to be true with Escald 120 (Fig. 10.8).

Here, we find up to four phases. The liquid phases (L) are translucent after centrifugation, but the gel phase (G) remains turbid and has a honey-like to solid consistency. A correct solvent extraction operation is with only one organic phase. As can

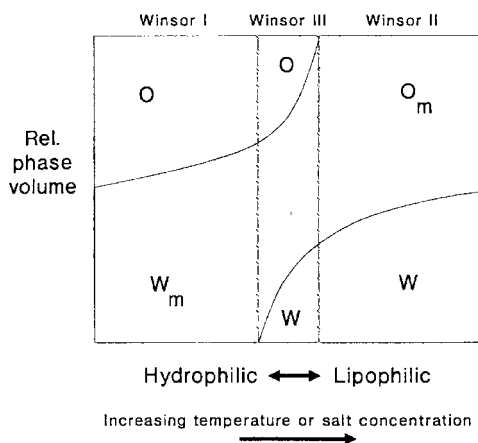


Fig. 10.7. Microemulsion classes according to Winsor.

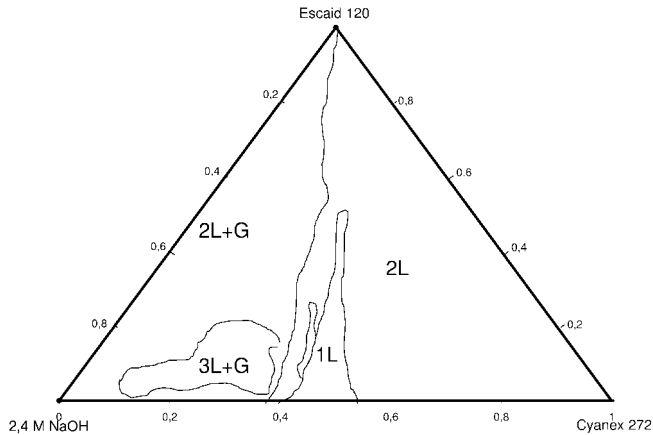


Fig. 10.8. Phase equilibria of Cyanex 272/NaOH/Escaid 120 at 293 K.

be seen, this is only a small region, when about 50 % of the ion exchanger is neutralized with 2.4 M NaOH. Figure 10.9 depicts samples of the single- to four-phase regions. On the far left is a single phase, while in the second-left sample the interface of the two-phase region is not easily visible and is indicated by a bar. In the second-right sample there are two liquid phases (2L) with a gel phase (G) in between, while on the extreme right is a 3L and G phase arrangement. It should be noted that the water content in all these samples is approximately 40 % by mass, and this point must be considered in process design.

10.2

Phase Equilibria

Several sources of liquid–liquid equilibria (LLE) are available, including the DECHEMA databank and others [22–26]. Their use is recommended since vapor–liquid (VLE) data provides less accurate predictions. There are implemented in



Fig. 10.9. Phase behavior of Escaid 120/2.4M NaOH/Cyanex 272 at 293 K.

commercial flowsheet simulators (e.g., ASPEN®, ChemSep®, HYSIM®, ChemCad®). In reactive extraction the aqueous phase is often composed of ions. The aqueous non-ideality of electrolyte solutions can be simulated with a modified Pitzer model [27], which is applicable up to 6 molar ionic strength for weak and strong electrolytes. The organic non-ideality can be treated with different concepts [28]. The regular solution theory of Hildebrand and Scott [29] is suitable for non-polar mixtures of molecules which are not too different in size. The molar volumes of the solute should not differ more than 50 % in respect to that of the solvent. The extraction of Zn zinc with the cation exchanger di(2-ethylhexyl) phosphoric acid, (RH), is according to the following equation:



The ion exchanger is known to be in dimeric form in aliphatic diluents [30], and the stoichiometry in Eq. (7) was found with classical slope analysis at low concentrations and FTIR-analysis even at high concentrations [31, 32]. A compilation of all thermodynamic parameters is given in <http://dechema.de/Extraktion/>, as this system is a recommended test system for reactive extraction studies by the European Federation of Chemical Engineering (EFCE). The predictability of the model is quite good, as is depicted in Fig. 10.10, where zinc extraction from chloride media is predicted from sulfate media [33].

For molecules which differ in size or shape interactions between the surface of the molecules, different Gibbs excess models, such as NRTL [34] or UNIQUAC [35], are recommended, respectively. The predictive group contribution method UNIFAC [36] will fail if several polar groups compose a solvent or solute molecule. As a

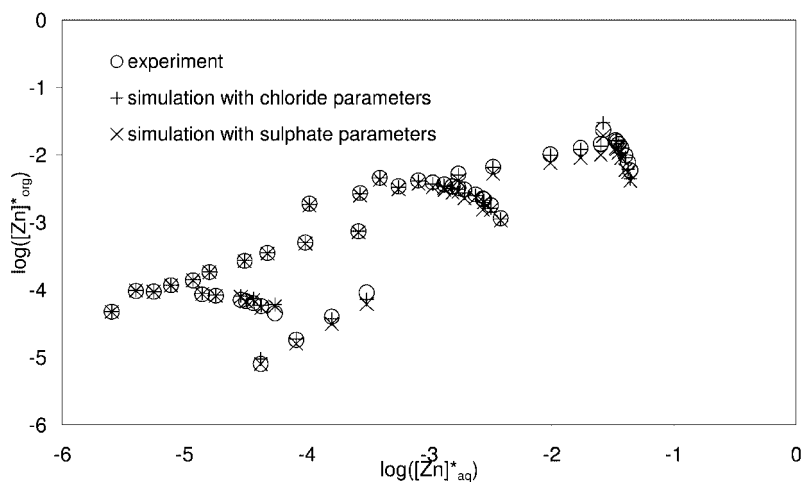


Fig. 10.10. Comparison of experiments with simulated zinc equilibria from chloride or sulfate parameters.

consequence, complex solvents such as sulfolane are then best treated as single group. If the compounds involved are highly polar and even form hydrogen bonds, then solvatochromic models are appropriate.

The standard molar Gibbs energy of solvation can also be derived from pure component data using spectroscopic information for determining solvatochromic parameters in respect of activity, basicity, polarity, etc. There exists a number of linear solvatochromic scales, the most widely used of which is the linear solvation energy relationship (LSER) devised by Kamlet and Taft [37, 38]. The Nernst distribution of solute i according to Kamlet is:

$$\log D_i^\infty = C_0 + C_1 V_i + C_2 \delta_i + C_3 \pi_i^* + C_4 \alpha_i + C_5 \beta_i \quad (8)$$

Here, V_i is the molar volume of the solute (as a measure of the size of the cavity to accommodate the solute i in the solvent), δ_i is an empirical parameter which takes also account for polarizability π^* , α_i and β_i characterize respectively the acidity or basicity which in general represents the ability to form hydrogen bonds, and the C 's are solvent characteristics independent of the solute. Meyer and Maurer [39] used this equation for 30 systems (371 substances, 947 experimental distribution coefficients) to evaluate generalized solvent C_j parameters.

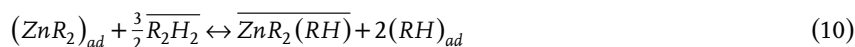
This equation is quite accurate in comparison with group contributing methods [40] or other predictive LSER methods [41]. For compounds where the solvatochromic parameters are known, the mean absolute error in $\log D_{ij}$ is about 0.16. It is usually less than 0.3 if solvatochromic parameters of the solute and solvent must be estimated according to empirical rules [42]. In contrast to the prediction of gas–liquid distribution coefficients, which is usually easier, the LSER method allows a robust estimation of liquid–liquid distribution coefficients. However, these equations always involve empirical terms, despite their being physico-chemically founded thermodynamic models. However, this is considered due to the fundamental character of the solvatochromic scales.

One promising predictive method based on statistical thermodynamics and quantum chemistry is that of COSMO-RS. Thermodynamic parameters, even of complex molecules, can be derived using eight general COSMO-RS inherent parameters, a single radius and one dispersion constant per chemical element [43, 44]. To date, the system has been tested (www.cosmologic.de) with vapor–liquid binary phase diagrams, activity coefficients, excess properties, isomeric effects, temperature dependency and applications in life science (water solubility, blood–brain partitioning, intestinal absorption). However, the accuracy of the method is relatively poor, and few reports have been made with liquid ionic solutions.

10.3 Reactive Mass Transfer

The mass transfer at the liquid–liquid interface is composed of diffusional, kinetic and convective elements. Most of these applications are concerned with the extraction

of ionic species that are primarily not soluble in the organic phase. After complexation by the liquid ion exchanger, the complex formed is rendered soluble in organic media. This is why complexation or chemical reaction takes place at the interface. A prerequisite to that is that the ion exchanger is available at the interface. Most of them have an amphiphilic behavior, and their adsorption isotherms can easily be estimated when measuring the interfacial tension arising from different bulk concentrations [31]. In general, the assumption is that the adsorbed ion exchanger reacts with the solute, and in a second step is replaced by a fresh one while the complex is been released to the bulk. According to a model of Klocker et al. [45], this reads:



Here, *ad* denotes the adsorbed species and the bars indicate bulk organic species. The resulting governing kinetics equation is then [31]:

$$-\frac{d[\text{Zn}^{2+}]}{dt} = \frac{\kappa_f \cdot [\overline{\text{R}_2\text{H}_2}]^{1.5} \cdot [\text{Zn}^{2+}] - \kappa_r \cdot [\text{H}^+]^2 \cdot [\overline{\text{ZnR}_2(\text{RH})}]}{[\overline{\text{R}_2\text{H}_2}]^{1.5} + C_1 \cdot [\text{H}^+]^2} \cdot \left(\frac{\sqrt{[\overline{\text{R}_2\text{H}_2}]}}{C_2 + \sqrt{[\overline{\text{R}_2\text{H}_2}]}} \right)^2 \quad (11)$$

The equation has three kinetic parameters, (see: <http://dechema.de/Extraction/>), since the forward, κ_f , or the reward reaction constant κ_r , can be substituted by the equilibrium constant (see Eq. (7)) according to

$$K_{1,3} = \frac{\kappa_f}{\kappa_r} \quad (12)$$

The parameter estimation is made in a stirred Lewis-type cell (Fig. 10.11) where, in the plateau region, chemical reaction prevails. With increasing stirring speed the initial mass transfer rates will increase as diffusional effects are diminished and a plateau is reached where mass transfer is independent of diffusion, as discussed elsewhere [31, 46]. A further increase in stirrer speed will disrupt the planar interface, leaving the operating area for determining the kinetics parameters.

The usual mass transfer geometry for reactive extraction is not planar but is spherical, due to dispersions produced in mixer-settlers, extraction columns or centrifuges. Rigid spheres can be found with small droplet diameters, whereas with increasing droplet diameters (usually 1 to 6 mm) there is an onset of circulations until large oscillating droplets are disrupted into smaller new ones. In these small droplets, instationary diffusion from the surface to the center prevails. In general, with reactive extraction we normally find bulky organic constituents, which is the

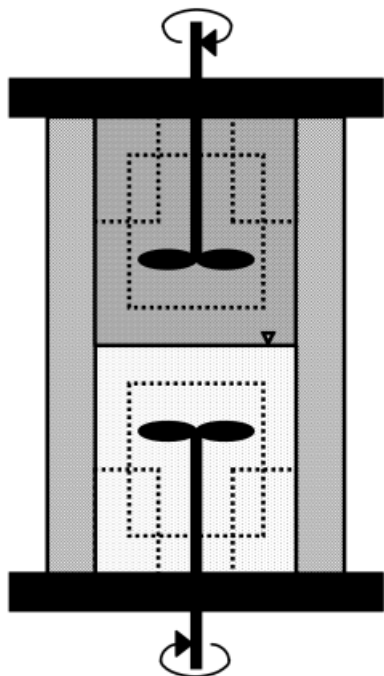


Fig. 10.11. Stirred Lewis cell with two independent stirrers and a planar interphase.

ion exchanger and the ion exchanger–solute complex. Their molecular mass is higher than that of the solute in the aqueous phase. Additionally, the higher viscosity of the organic phase makes it more likely that diffusion resistance is predominant in the organic phase in respect to the aqueous phase. A correct description is then to model diffusion inside the droplet with the Maxwell–Stefan diffusion law [47], where the chemical potential – and not the concentration differences – represent the driving force. However, a problem until now has been to obtain information in respect of an exact value of the cross-diffusion coefficients. These represent frictional coupling of the fluxes of the species involved, and can be neglected only in very dilute systems.

Bosse [48] proposed a new model to predict binary Maxwell–Stefan diffusion coefficients \mathcal{D}_{ij} , based on Eyring's absolute reaction rate theory [49]. A correlation from Vignes [50] which was shown to be valid only for ideal systems of similar-sized molecules without energy interactions [51] was extended with a Gibbs-excess energy term

$$\ln\left(\frac{\mathcal{D}_{12}}{\lambda_m^2}\right) = x_1 \ln\left(\frac{\mathcal{D}_{12}^\infty}{\lambda_1^2}\right) + x_2 \ln\left(\frac{\mathcal{D}_{21}^\infty}{\lambda_2^2}\right) + \frac{g^E}{RT} \quad (13)$$

where the mean distance parameter is as

$$\lambda_m = x_1 \lambda_1 + x_2 \lambda_2 \quad (14)$$

and the individual λ_i may be estimated from the cubic root of the molecular or the van der Waals volumes. The g^E parameters can be taken from isotherm VLE or LLE data using UNIQUAC, COSMO-RS or any other g^E model. The quality of these parameters is then decisive for the model predictions. A bad choice may produce up to 30 % error compared to 5 % in the best case.

Modern measurement techniques based on Raman spectroscopy [52] are under way for rapid data evaluation with technically acceptable accuracy. It is clear from theory that in circulating droplets diffusion no longer prevails, as in the case of rigid droplets. This is depicted in Fig. 10.12, where a Laser-Lichtschnitt of a 3-mm toluene droplet using laser-induced fluorescence (LIF) is depicted. The fluorescence signal of the solute in the continuous phase, responding to wake and interfacial tension effects affecting mass transfer, can be clearly seen. This is why it is difficult to recommend mass transfer correlations, and direct measurements in rising/falling droplet or venturi tubes should be preferred. In that respect, the venturi tube (Fig. 10.13) allows arbitrary residence times in respect of the chemical reaction kinetics involved. With regard to the Zn/HDEHP EFCE test system, a correlation proposed by Steiner [53] for single droplets in combination with the above derived kinetics model (see Eq. (11)) gave satisfying results. A better representation of the experimental data was with models having adjustable parameters, such as the stagnant cap model of Slater [54] or the model of Henschke and Pfennig [55], but the contribution of the chemical reaction to the overall mass transfer kinetics could never be neglected, as has been discussed elsewhere [28, 56]. It is well known that amphiphilic substances will adsorb at liquid–liquid interfaces (see Section 10.1.3). Humic acids, impurities and even the solute–ion exchanger complex act in that respect. As a result, during the droplet rise the surfactants adsorbed will be swept to the rear of the droplet, where they build into a stagnant cap (Fig. 10.14) followed by a wake in the continuous phase. Thus, part of the droplet is then mobile or rigid, and the ratio may be determined experimentally using the model of Slater [54].

In extraction columns, it is possible to find droplet swarms where the local velocities near the droplet surface are higher, this being due to the lower free area available for the countercurrent flowing continuous phase. Wake and Marangoni influences make the prediction of a physical mass transfer coefficients difficult. With reactive extraction the influence of interfacial kinetics on overall mass transfer is generally not negligible. In any case, a combination of reactive kinetics with any eddy mass transfer model is recommended, whereas the latter could rely on correlations derived for specific column geometries.

A practical approach is to use the venturi tube (see Fig. 10.13) with a swarm of representative droplets of a certain diameter to estimate an effective mass transfer coefficient, including diffusional and reactive resistances. The value obtained would be

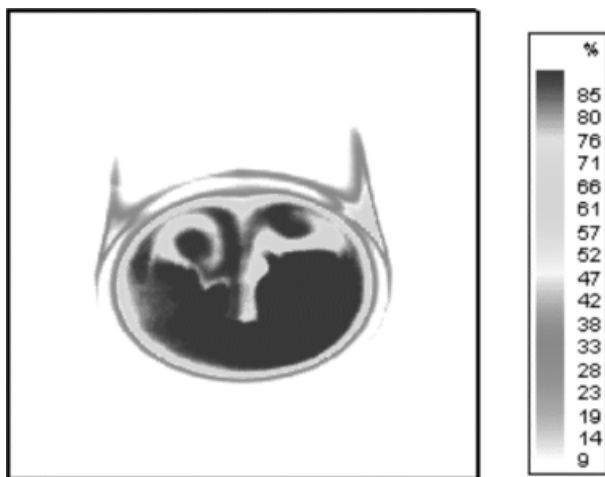


Fig. 10.12. Laser-induced fluorescence picture of a toluene droplet (100 % is 0.1 mmol L^{-1} Rhodamine 6G).

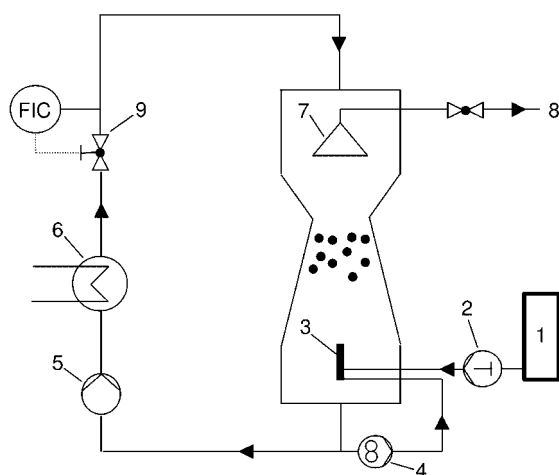


Fig. 10.13. Venturi tube (1 feed, 2 metering pump, 3 nozzle, 4 rotary gear pump, 5 pump, 6 heat exchanger, 7 funnel, 8 sample valve, 9 valve).

of limited use to extrapolate to other conditions, but fairly well reflects the system behavior. An advantage here is that only small amounts of process liquids have to be used to obtain the decisive information.

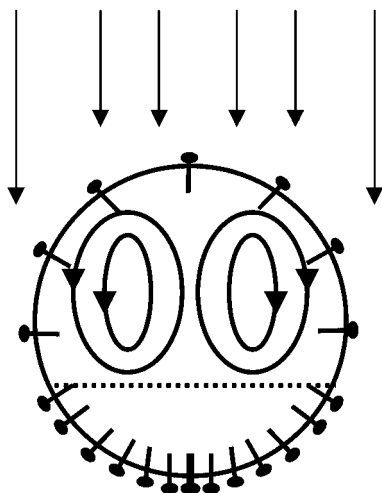


Fig. 10.14. Stagnant cap model.

10.4

Hydrodynamics

The choice of an apparatus for reactive extraction is similar to physical extraction [57]. If longer residence times are needed, mixer settlers are easily adapted. However, modern liquid ion exchangers will reach reaction equilibria in many cases in less than 1 minute, even with the slow chelating reagents for copper extraction. This has led to the use of extraction columns in the mining industries, following a trend set in the chemical and pharmaceutical industries, mainly for reasons of cost. For example, Western Mining Corporations, Olympic Dam operations in South Australia recently installed pulsed Batman columns to treat $800 \text{ m}^3 \text{ h}^{-1}$ of uranium solutions. These columns were shown to be able to reduce evaporation losses, entrainment and solvent inventory when compared to mixer settlers. The Alamine 336/kerosene anion exchanger phase in this case has relatively rapid extraction kinetics, and the extraction is controlled by diffusion process, likewise physical extraction. Other examples where large columns are being considered are in INCO's Ni/Co extraction process plant currently being built at Goro in New Caledonia.

Predictions of the column height required for any given separation can be obtained by using either a staged approach or a transfer unit approach. The plug flow models for determining the height of a column are of limited value due to the effect of axial dispersion, which is caused by

- molecular and turbulent diffusion in axial and radial directions;
- carrying of continuous phase in the wake of a droplet; and
- entrainment of smaller drops.

The state of the art for column simulations is with the dispersion or back-mixing model, where one parameter reflects all hydrodynamic non-idealities [5, 7, 8]. A step

forward is with droplet populance models (DPM) [58, 59], which take into account the coalescence and break-up of droplets, and thus provide a better physical picture and more reliable simulation results. Equation (15) gives the droplet density distribution $P(t,z,d)$ as a function of convection (w_d), back-mixing ($D_{d,ax}$), breakage ($S_{B,P}$) and coalescence ($S_{C,P}$) of the dispersed phase. For the concentration profile of the solute in Eq. (16), a mass transfer term is included. For the solute profile of the continuous phase, the mass transfer must be integrated with respect to all droplet classes (see Eq. (17)).

$$\frac{\partial P(t,z,d)}{\partial t} = w_d \frac{\partial P(t,z,d)}{\partial z} + D_{d,ax} \frac{\partial^2 P(t,z,d)}{\partial z^2} + S_{B,P}(t,z,d,P) + S_{C,P}(t,z,d,P) \quad (15)$$

$$\begin{aligned} \frac{\partial Q(t,z,d,P)}{\partial t} = w_d \frac{\partial Q(t,z,d,P)}{\partial z} + D_{d,ax} \frac{\partial^2 P(t,z,d,P)}{\partial z^2} + k \frac{6P(t,z,d)}{d} (\gamma - m \cdot x(d)) \\ + S_{B,Q}(t,z,d,P) + S_{C,Q}(t,z,d,P) \end{aligned} \quad (16)$$

$$\frac{\partial R(t,z,P)}{\partial t} = -w_c \frac{\partial R(t,z,P)}{\partial z} + D_{c,ax} \frac{\partial^2 R(t,z,P)}{\partial z^2} + \int_0^{d_{max}} k \frac{6P(t,z,d)}{d} (\gamma - m \cdot x(d)) \partial d \quad (17)$$

The local hold-up is obtained from an integration of all droplet classes:

$$\varphi(t,z,d) = \int_{d_{min}}^{d_{max}} P(t,z,d) \partial d \quad (18)$$

The source term for breakage is according to:

$$S_{B,P}(t,z,d,P) = \int_{d_0}^{d_{max}} \beta(d_0,d) g(t,z,d) P(t,z,d) \partial d_0 - g(t,z,d) P(t,z,d) \quad (19)$$

where $g(t,z,d)$ is the breakage frequency and $\beta(d_0,d)$ is the daughter droplet distribution. The same parameters are then valid to describe the concentration distribution within the droplet swarm:

$$S_{B,Q}(t,z,d,Q) = \int_{d_0}^{d_{max}} \beta(d_0,d) g(t,z,d) Q(t,z,d,P) \partial d_0 - g(t,z,d) Q(t,z,d,P) \quad (20)$$

The positive part in the integral is due to the increase in the number in a given class gained from a higher class of bigger droplets and the negative part is due to the loss into a lower class of smaller droplets. The integral terms for coalescence can be

developed in analogy. Here, it is assumed that only two droplets with diameter d_1 respectively d_2 will react (no multilateral effects). The coalescence probability $\omega(d_1, d_2)$ is the determining parameter for the probability density functions of droplets

$$S_{C,P}(t, z, d, P) = \frac{V(d)}{2} \int_{d_0}^{d_{\max}} \omega(d_1, d_2) \frac{P(t, z, d_1)}{V(d_1)} \frac{P(t, z, d_2)}{V(d_2)} \left(\frac{d}{d_2} \right)^2 \partial d_1 - P(t, z, d) \int_0^{\sqrt[3]{d_{\max}^3 - d^3}} \omega(d_1, d_2) \frac{P(t, z, d_1)}{V(d_1)} \partial d_1 \quad (21)$$

and of solutes

$$S_{C,Q}(t, z, d, Q) = \int_d^d \omega(d_1, d_2) Q(t, z, d_1) \frac{P(t, z, d_2)}{V(d_2)} \left(\frac{d}{d_2} \right)^2 \partial d_1 - Q(t, z, d) \int_0^{\sqrt[3]{d_{\max}^3 - d^3}} \omega(d_1, d_2) \frac{P(t, z, d_1)}{V(d_1)} \partial d_1 \quad (22)$$

The breakage frequency and daughter droplet distribution must be determined in the geometry under consideration [60], as is depicted in Fig. 10.15 for Rotating Disc Contactor (RDC) geometry. The daughter droplet distribution is usually according to a decay function which is a β -distribution, starting with a maximum value which is the mother droplet d_0 . The breakage probability is correlated to a modified Weber number taking viscosity and surface tension for a certain droplet diameter into consideration. The coalescence parameters are then evaluated in a similar cell, comprising five column compartments for statistical reasons. In this differential contactor the inverse droplet population balance is solved, considering droplet-breakage but neglecting dispersion effects [61]. Basically, the experiments can be carried out

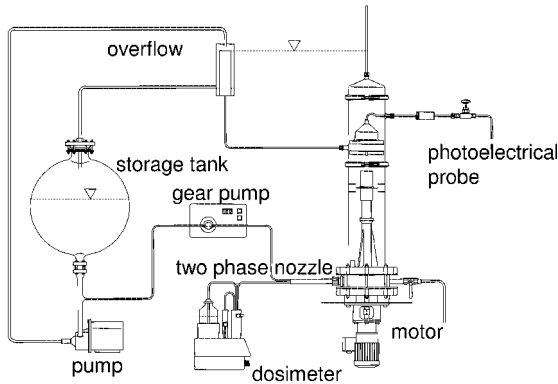


Fig. 10.15. Breakage cell.

simultaneously under mass transfer conditions when estimating the coalescence probability. The saturated phase in equilibrium can then be used for break-up experiments under conditions that are non-critical with regard to coalescence. Since mass transfer is usually rapid, not the initial but the final conditions (altered solute concentration and thus, for instance, interfacial tension) are decisive for the daughter droplet distribution and breakage probability.

The DPM demands knowledge of the dispersion coefficients. At high throughputs and turbulence (i.e., high stirring speed), the dispersion coefficient of both phases become similar, when otherwise the dispersed phase coefficients are three- to six-fold higher [62]. If no correlations are available from the literature, the use of CFD methods is a valid tool for the estimation of residence time distributions of fluid elements and Bodenstein numbers in agitated extraction columns. Figure 10.16 confirms the correlation of Steiner [63], developed on a 150-mm diameter Kühni column used to scale-down the performance of a small scale miniplant Kühni extraction column [64] at a certain compartment height, H_c , rotor diameter, D_R , and rotor speed, N :

$$\frac{1}{Bo_c} = \frac{D_{ax,c}}{u_c \cdot H_c} = A + B \cdot \frac{D_R \cdot N}{u_c} \cdot G \quad (23)$$

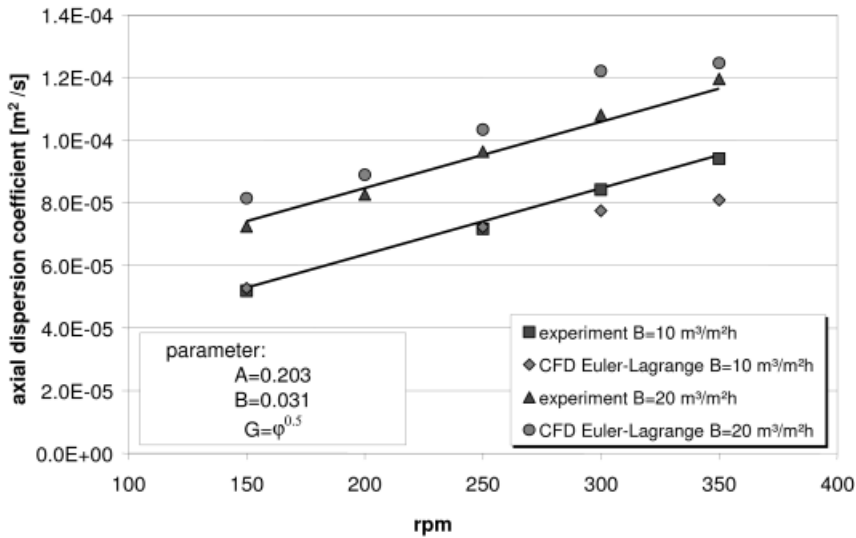


Fig. 10.16. Axial dispersion coefficients (solid line: correlation, points: CFD and experimental data).

The last remaining parameter in the DPM is the individual rising velocity of a dispersed phase droplet in a certain apparatus geometry. The velocities of both phases are related to the two-layer model [65] which is expressed as:

$$w_d(t, z, d, \varphi) = w_r(t, z, d, \varphi) + w_c(t, z, \varphi) \quad (24)$$

with w_c the continuous phase, w_d the dispersed phase and w_r the relative velocity of a drop of diameter d relative to the surrounding continuous phase. It can be obtained from the single drop terminal velocity w_T by the following correlation:

$$w_r(d, \varphi) = k_v(d) w_T (1 - \varphi) \quad (25)$$

where $k_v(d)$ is the slowing coefficient taken by definition values between 0 and 1. The value of $k_v(d)$ depends on the type of the extraction column [66].

For a RDC a correlation from literature has been proposed as follows [67]:

$$k_v(d) = 1 - 1.037(N^3 D_R^5)^{0.12} - 0.62 \left(\frac{d}{D_S - D_R} \right)^{0.44} \quad (26)$$

with N the rotor speed, D_S and D_R as the stator and rotor diameters, respectively.

Figure 10.17 illustrates graphically a comparison of experimental and predicted mean Sauter diameters, d_{23} , from different-sized RDC columns [68, 69] with (from continuous to dispersed phase and vice versa) and without mass transfer. The simulated column values are based on parameter estimations from the above-discussed small laboratory-scale units. There is a good agreement between experimental and simulated Sauter diameters, despite the fact that in the column simulations with the DPM concept there is no adjustable parameter. The dispersion coefficients and rising velocities were taken from above correlations. The break-up probability and daughter droplet distribution were obtained from laboratory-scale experiments (see Fig. 10.15), although appropriate correlations exist [60]. Only the coalescence probability cannot be estimated beforehand and must be experimentally determined [61, 69]. It could be shown that even column behavior under mass transfer conditions could be correctly predicted, assuming an axial linear surface tension gradient arising from mass transfer.

10.5

Conclusions

Reactive extraction is, in many aspects, quite similar to physical extraction. Modern liquid ion exchangers with fast kinetics allow the use of columns for solute recovery. Complex feed mixtures can be efficiently handled in respect to the given selectivity due to the selective chemical reaction involved and the set-up of a process schema, including scrubbing and regeneration steps. Reactive equilibria and mass transfer

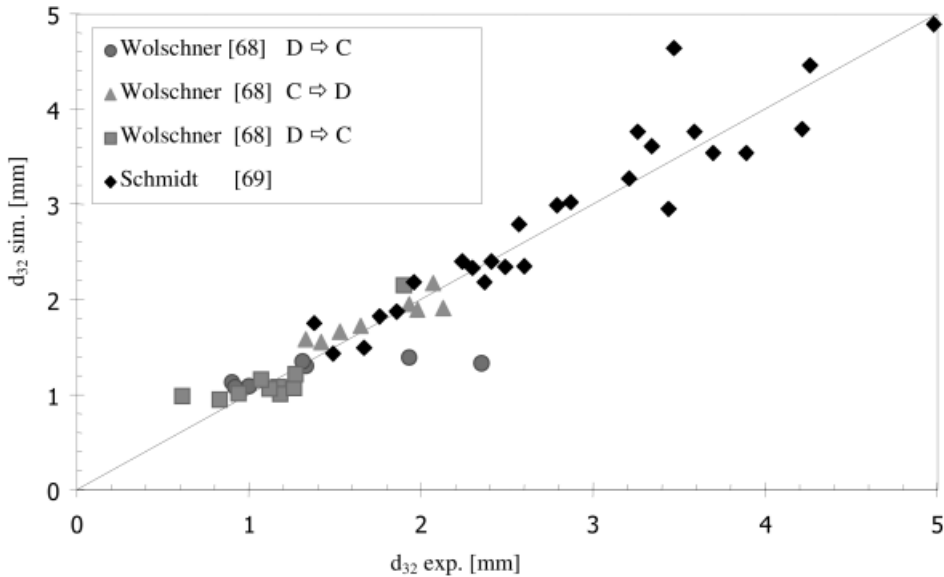


Fig. 10.17. Simulated and experimental Sauter diameters in RDC columns with ($C \rightarrow D$; $D \rightarrow C$) and without mass transfer (system: toluene/acetone/water at 298 K).

concepts are well established in that field, whereas for the latter areas effective mass transfer models with adjustable parameters await improvements.

In the future, the design of reactive extraction columns in general should rely on DPM concepts, since the background is a physically more rigid description of what actually happens in a column. All hydrodynamic and mass transfer parameters required could be estimated in small-scale laboratory units, where only small amounts of process liquors are required. Indeed, when predicting column behavior solely on the basis of physico-chemical data, correlations may also be used, though chemical kinetics and coalescence frequency cannot be determined beforehand. In many industrially relevant cases the kinetics is rapid and the systems have hindered coalescence and thus, at first glance, may be neglected. This provides a means of obtaining reliable estimates of column performance and product recovery before costly attempts are made to validate a process in a pilot or mini-plant operation.

Acknowledgments

The author thanks the DFG (Deutsche Forschungsgemeinschaft), Bonn and AiF (Arbeitsgemeinschaft industrieller Forschungsvereinigungen Otto-von-Guericke e.V.), Düsseldorf and BMWi (Bundesministerium für Wissenschaft und Technologie), Berlin and KTI (Kommission für Technologie und Innovation), Bern for supporting these studies.

References

1. E. Peligot, *Ann. Chim. Phys.*, **1842**, 5 (1).
2. E. Blaß, T. Liebl, M. Häberl, Extraktion – ein historischer Rückblick. *Chem. Ing. Techn.*, **1997**, 69, 431–437.
3. K. L. Power, *Operation of the First Liquid Ion-Exchange and Electrowinning Plant*. in *Proceedings ISEC '71*. 1971, The Hague. L. Chem. Soc. Ing. Ind., (ed.). pp. 1409–1415.
4. G. M. Ritcey and A. W. Ashbrook, *Solvent Extraction Principles and Applications to Process Metallurgy*. Vol. 1–2. 1979, New York: Elsevier.
5. J. D. Thornton, *Science and Practice of Liquid-Liquid Extraction.*, Vol. 1–2. 1992, Oxford: Oxford University Press.
6. J. Rydberg, C. Musikas, G. R. Choppin, *Principles and Practices in Solvent Extraction*. 2002, 2nd edn. New York: Marcel Dekker.
7. T. C. Lo, M. H. I. Baird and C. Hanson, *Handbook of Solvent Extraction*. 1983, New York: J. Wiley & Sons.
8. C. Hanson, *Neuere Fortschritte der Flüssig-Flüssig-Extraktion*. 1971, Aarau: Sauerländer.
9. E. J. Holmyard, *Alchemy*. 1957, London: Pelican Books, A348.
10. P. Wasserscheid and W. Keim, Ionische Flüssigkeiten – neue Lösungen für die Übergangsmetallkatalyse. *Angewandte Chemie*, **2000**, 112 (21), 3926–3945.
11. M. Masse and K. Massone, *Ionische Flüssigkeiten – ein neuartiges Konzept für die Katalyse und die Stofftrennung*. in: *DECHEMA/GVC Jahrestagung*. 16./18.09.2003, Mannheim.
12. M. Masse, K. Massone, K. Halbritter, et al., *Method for the separation of acids from chemical reaction mixtures by means of ionic liquids*, in: *Int. Pat PCT/EP03/00545 (WO 03/062171 A2)*, 21.01.2003.
13. K. Gloe, H. Granbaum, M. Wüst, et al., Macrocyclic and open-chain ligands with the redox switchable trithiadiazapentalene unit: synthesis, structures and complexation phenomena. *Coord. Chem. Rev.*, **2001**, 222, 103.
14. G. A. Kordosky, *The Chemistry of Metals Recovery Using LIX-Reagents*. 1973, Mines Branch: General Mills.
15. G. Schmuckler and G. Harel, in: *Ion Exchange and Solvent Extraction*, J. A. Marinsky and Y. Marcus, (eds.). Vol. 13. 1997, Marcel Dekker: New York. pp. 1–30.
16. G. M. Ritcey, in *Value Adding Through Solvent Extraction*, R. P. D. C. Shellcross, L. M. Prvcic, (ed.). 1996, The University of Melbourne: Melbourne. pp. 17–24.
17. E. Paatero and J. Sjöblom, Phase behaviour in metal extraction systems. *Hydrometallurgy*, **1990**, 25, 231–256.
18. P. A. Winsor, Hydrotrophy, Solubilisation and Related Emulsification Processes, Parts I – IV. *Transaction of the Faraday Society*, **1947**, 44, 376–398.
19. P. A. Winsor, Solubilisation with amphiphilic compounds. *Chemistry and Industry*, **1960**, 4, 632–644.
20. J. Biaies, B. Clin and P. Lalanne, *Phase diagrams and pseudophase assumption*, in: *Microemulsions: Structure and Dynamics*, S. E. Friberg and P. Bothorel, (eds.). 1987, CRC Press, Inc.: Cleveland. pp. 1–31.
21. E. Paatero, P. Ernola, J. Sjöblom, et al., *Formation of microemulsions in solvent extraction systems containing Cyanex 272*, in: *ISEC '88*. 1988, Moskau. Nauka, (ed.). pp. 124–127.
22. J. Wisniak and A. Tamir, *Liquid-Liquid Equilibrium and Extraction*. Phys. Sci. Data. Vol. 7., 1980, New York: Elsevier.
23. J. M. Sorensen, T. Magnussen, P. Rasmussen, et al., *Liquid-Liquid Equilibria Data: Their Retrieval, Correlation and Prediction, Part II: Correlation*. Fluid Phase Equilibria, 1979., 3: pp. 47–82.
24. J. M. Sorensen and W. Arlt, *Liquid-Liquid Equilibrium Data Collection*. Chem. Data Series. 1979–1980, Frankfurt: DECHEMA.

25. H.-J. Bart, R. Berger, T. Misek, et al., *Recommended Systems for Liquid Extraction Studies*, in: *Liquid-Liquid Extraction Equipment*, J. C. Godfrey and M. J. Slater, (eds.). 1994, J. Wiley & Sons: London. pp. 1–43.
26. Y. Marcus, *Solvent Mixtures*. 2002, New York: Marcel Dekker.
27. T. J. Edwards, G. Maurer, J. Newman, et al., Vapor Liquid Equilibria in Multicomponent Aqueous Solutions of Volatile Weak Electrolytes. *AIChE J.*, **1978**, *24*, 966–976.
28. H. J. Bart and G. Stevens, *Reactive Solvent Extraction*, in: *Ion Exchange and Solvent Extraction*, Y. Marcus and A. K. SenGupta, (eds.). Vol. 16. 2004, Marcel Dekker: New York. pp. 37–83.
29. J. M. Hildebrand and R. L. Scott, *The Solubility of Nonelectrolytes*. 3rd edn. 1950, New York: Reinhold.
30. Z. Kolarik, Critical Evaluation of some Equilibrium Constants Involving Acidic Organophosphorous Extractants. *Pure Appl. Chem.*, **1982**, *54* (12), 2593–2674.
31. H.-J. Bart, *Reactive Extraction*. Series: Heat and Mass Transfer, D. Mewes and D. M. F. Mayinger (ed.). 2001, Berlin: Springer.
32. C. I. Sainz-Diaz, H. Klocker, H. J. Bart, et al., New Approach in the Modelling of the Extraction Equilibria of Zinc with Bis(2-ethylhexyl) phosphoric acid. *Hydrometallurgy*, **1996**, *42*, 1–11.
33. M. Mörters and H. J. Bart, Extraction Equilibria of Zinc with Bis(2-ethylhexyl) phosphoric acid. *J. Chem. Eng. Data*, **2000**, *45* (1), 82–85.
34. H. Renon and J. M. Prausnitz, Local Compositions in Thermodynamic Excess Functions for Liquid Mixtures. *AIChE J.*, **1968**, *14*, 135–144.
35. D. S. Abrahams and J. M. Prausnitz, Statistical Thermodynamics of Liquid Mixtures: A New Expression for the Excess Gibbs Energy of Partly or Completely Miscible Systems. *AIChE J.*, **1975**, *21*, 116–128.
36. A. Fredenslund, R. L. Jones, J. M. Prausnitz, Group-Contribution Estimation of Activity Coefficients in Nonideal Liquid Mixtures. *AIChE J.*, **1975**, *21* (6), 1086–1099.
37. M. J. Kamlet, J. L. M. About, R. W. Taft, An Examination of Linear Solvation Energy Relationship. *Prog. Phys. Org. Chem.*, **1981**, *13*, 485–630.
38. M. J. Kamlet, J. L. M. About, M. H. Abraham, et al., LSER 23, A Comprehensive Collection of the Solvatochromic Parameters π^* , α , β and some Methods for Simplifying the Generalized Solvatochromic Equation. *J. Org. Chem.*, **1983**, *48*, 2877–2887.
39. P. Meyer and G. Maurer, Correlation and Prediction of Partition Coefficients of Organic Solutes Between Water and an Organic Solvent with a Generalized Form of the LSER. *Ind. Eng. Chem. Res.*, **1995**, *34*, 373–381.
40. P. Meyer and G. Maurer, Correlation of Partition Coefficients of Organic Solutes Between Water and an Organic Solvent. An Application of the LSER. *Ind. Eng. Chem. Res.*, **1993**, *32*, 113–131.
41. Y. Marcus, LSER Correlation and Prediction of the Distribution of Organic Solutes Between Water and Immiscible Organic Solvents. *J. Phys. Chem.*, **1991**, *95*, 8886–8891.
42. M. J. Kamlet, R. M. Doherty, M. H. Abraham, et al., LSER 46 An Improved Equation for Correlating and Prediction of Octanol/Water Partition Coefficients of Organic Nonelectrolytes (Including Strong Hydrogen Bond Donor Solutes. *J. Phys. Chem.*, **1988**, *92*, 5244–5255.
43. F. Eckert, A. Klamt, Fast Solvent Screening Via Quantum Chemistry: COSMO-RS Approach. *AIChE J.*, **2002**, *48*, 369.
44. A. Klamt, F. Eckert, COSMO-RS: A Quantum Chemistry based Alternative to Group Contribution Methods for the Prediction of Activity Coefficients in Multi-Component Mixtures. *Fluid Phase Equilibria*, **2000**, *172*, 43.

45. H. Klocker, H.-J. Bart, R. Marr, et al., Mass Transfer Based on Chemical Potential Theory: $\text{ZnSO}_4/\text{H}_2\text{SO}_4/\text{D2EHPA}$. *AIChE J.*, **1997**, 43 (10), 2479–2487.
46. W. Nitsch, in *Transportprozesse und chemische Reaktionen an fluiden Phasengrenzen*, Dechema, (ed.). Vol. 114. 1989, VCH: Weinheim. pp. 285–302.
47. R. Taylor and R. Krishna, *Multicomponent Mass Transfer*. 1993, New York: J. Wiley & Sons.
48. D. Bosse, H.-J. Bart, *Vorausberechnung von Diffusionskoeffizienten in fluiden Systemen*, in: *GVC-Fachausschuss "Fluidverfahrenstechnik"*. 2004, Leipzig.
49. S. Glasstone, K. Laidler, H. Eyring, *The Theory of Rate Processes.*, 1941, New York: McGraw-Hill.
50. A. Vignes, Diffusion in Binary Solutions. *Ind. Eng. Chem. Fundam.*, **1966**, 5 (2), 189–199.
51. R. J. Bearman, On the Molecular Basis of some current Theories of Diffusion. *J. Phys. Chem.*, **1961**, 65, 1961–1968.
52. A. Pfennig, *Multicomponent Diffusion*, in: *Int. Workshop "Transport in Fluid Multiphase Systems: From Experimental Data to Mechanistic Models"*. 2004, Aachen.
53. L. Steiner, Mass Transfer Rates from Single Drops and Drop Swarms. *Chem. Eng. Sci.*, **1986**, 41 (8), 1979–1986.
54. M. J. Slater, A Combined Model of Mass Transfer Coefficients for Contaminated Drop Liquid-Liquid Systems. *Can. J. Chem. Eng.*, **1995**, 73, 462–469.
55. M. Henschke and A. Pfennig, Mass Transfer Enhancement in Single-Drop Extraction Experiments. *AIChE J.*, **1999**, 45 (10), 2079–2086.
56. M. Mörters and H. J. Bart, Mass Transfer into Droplets in Reactive Extraction. *Chem. Engng. and Processing*, **2003**, 42, 1251–1269.
57. L. A. Robins and R. W. Cusack, *Liquid-Liquid Extraction Operations and Equipment*, in: *Perry's Chemical Engineers' Handbook*, R. H. Perry and D. W. Green, (eds.). 1997, McGraw Hill: New York. pp. 15/1–15/47.
58. M. M. Attarakih, H.-J. Bart and N. M. Faqir, Numerical solution of the two dimensional population balance equation describing the hydrodynamics of interacting liquid-liquid dispersions. *Chem. Eng. Sci.*, **2004**, 59 (12), 2567–2592.
59. M. M. Attarakih, H.-J. Bart and N. M. Faqir, Solution of the droplet breakage equation for interacting liquid-liquid dispersions: A conservative discretisation approach. *Chem. Eng. Sci.*, **2004**, 59 (12), 2547–2565.
60. M. Simon, S. A. Schmidt, H.-J. Bart, The Droplet Populance Model - Estimation of Breakage and Coalescence. *Chem. Ing. Techn.*, **2003**, 26, 745–750.
61. S. A. Schmidt, M. Simon, L. Lagar García, et al., *Estimation of Populance Parameters in Liquid-Liquid Extraction Columns.*, in: *2nd Int. Conf. Population Balance Modelling*. 2004, Valencia, Spain.
62. G. Goldmann, *Ermittlung und Interpretation von Kennlinienfelder in einer gerührten Extraktionskolonne*. Dissertation, 1986, TU München: München.
63. L. Steiner, A. Kumar, S. Hartland, Determination and correlation of axial-mixing parameters in an agitated liquid-liquid extraction column. *Can. J. Chem. Eng.*, **1988**, 66, 241–247.
64. P. Kolb, H.-J. Bart, Bart, L. Fischer, Entwicklung einer Miniplant-extraktionskolonne. *Chem. Ing. Techn.*, **2002**, 74, 243–247.
65. R. Gayler, N. W. Roberts, H. R. C. Pratt, Liquid-Liquid Extraction. A further Study of Hold-up in Packed Columns. *Trans. Am. Inst. Chem. Eng.*, **1953**, 31, 57.
66. T. Misek, General Hydrodynamic Design Basis for Columns, in: *Liquid-Liquid Extraction Equipment*, J. C. Godfrey and M. J. Slater (eds.). 1994, J. Wiley & Sons: London, pp. 95–113.

67. G. Modes, *Grundsätzliche Studie zur Populationsdynamik von Extraktionskolonnen auf Basis von Einzeltropfenuntersuchungen*. 2000, Aachen: Shaker.
68. B. Wolschner, *Konzentrationsprofile in Drehscheibenextraktoren*. Dissertation, 1980, Dissertation TU Graz: Graz.
69. S. A. Schmidt, H.-J. Bart, *Bestimmung der Tropfeninteraktionen in gerührten Extraktionskolonnen auf der Basis von Einzeltropfenuntersuchungen*, in: Vortrag am DECHEMA/GVC-Fachausschuss "Extraktion", 2004, Aachen.

11

Development of Reactive Crystallization Processes

*Christianto Wibowo, Vaibhav V. Kelkar, Ketan D. Samant,
Joseph W. Schroer and Ka M. Ng*

11.1

Introduction

A large number of products ranging from basic chemicals to pharmaceuticals are produced by reactive crystallization. Examples include terephthalic acid from the air oxidation of *p*-xylene [1], and bisphenol A by means of adductive crystallization of phenol and bisphenol A [2], among others. Also, almost all crystallization products involving ionic species such as inorganics produced from salt lakes belong to this category. The development of such a reactive crystallization process is rather involved. In plant design, the crystallizer as well as the entire plant needs to be considered. In equipment design, both equilibrium thermodynamics and crystallization must be taken into account.

This chapter describes in a step-by-step manner a generic strategy that we have been using for the development of various industrial processes. The chapter begins with a discussion of the overall workflow for process development, followed by a description of the way in which a process is synthesized, which relies heavily on the use of phase diagrams. The deviation from equilibrium behavior is accounted for using a model-based approach. This is illustrated with an example on the asymmetric transformation of an enantiomer.

11.2

Workflow in Process Development

The very nature of process development necessitates the contributions of all members of a typical development team. Thus, reaction engineers determine reaction kinetics and select the best reactor type, while filtration experts measure the filter cake resistance and washing efficiency. To reduce development time, it is crucial that all of these activities be performed in a coordinated manner. Proper workflow automates such a development process, in whole or part, during which documents, information, or tasks are passed from one participant to another for action, according to a set of procedural rules.

Figure 11.1 shows four main tasks in the development of a reactive crystallization process. The central column shows the tasks to be tackled. The rectangles on the left indicate the data required for the corresponding tasks. Experiments are necessary because, contrary to what some people might believe, the state of the art simply does not allow reliable predictions of a number of common engineering parameters. For example, while it is possible to predict SLE (solid–liquid equilibrium) for ideal simple eutectic systems, it is difficult or impossible for complex molecules with complicated phase behaviors such as the presence of solvates, hydrates and compounds. Washing efficiency must also be measured because it can have considerable impact on the cost of solvent recycling. Similarly, it is difficult to predict the occurrence of agglomeration and breakage which depend not only on the material properties, but also on the processing history of the particles. Solid–liquid equilibrium, and nucleation and growth kinetics data were often not measured in a project because of time constraints. It is not uncommon that these quantities are not known, even for an active commercial plant. However, in the past few years a number of industrial laboratories have been set up to measure the relevant quantities on a routine basis. A similar situation existed for reaction kinetics, although systematization of those measurements is much further advanced.

The rounded rectangles on the right in Fig. 11.1 indicate the techniques, design procedures, and basic sciences required for the corresponding tasks. Thus, a good understanding of high-dimensional reactive SLE phase diagrams is helpful for the synthesis of separation schemes. Transport phenomena and population balance

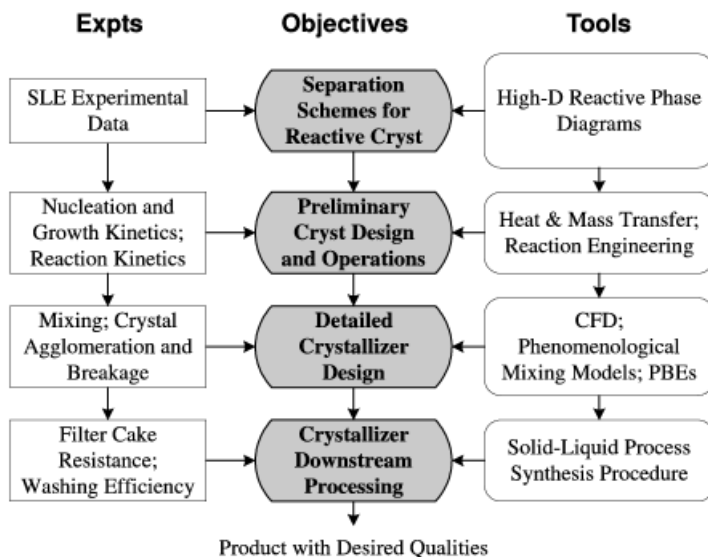


Fig. 11.1. Overall workflow for the development of a reactive crystallization process.

equations (PBEs) are essential for the design of crystallizers. Since the capital and operating costs for the filtration, washing, and deliquoring of the crystals can be more expensive than that for the crystallizers, it is equally important to have a firm grasp of the downstream system.

To integrate conceptual design, modeling and experimentation, it is necessary to assemble a team with the requisite technical skills, and to identify what is achievable based on the available time, technological limit, and both human and monetary resources. Figure 11.2 shows the RAT²IO concept for workflow; the acronym stands for objective, information, tools, time, activities, and resources. Thus, for each step of the workflow, the objective of the task as well as the input and output information should be defined.

The appropriate tools such as software, experimental equipment, and instruments for executing the task should be identified. The activities to meet the objective such as computer simulation, modeling and experimentation are defined. To meet the project deadline, it is also necessary to estimate the time needed to complete the tasks. Proper allocation of human and monetary resources to perform the activities is also essential [3].

11.3

Process Synthesis

Let us consider synthesis of the separation system. Visualization is an effective way of understanding the functional relationships among variables in systems derived from multivariate problems and multicomponent mixtures, which are ubiquitous in chemical engineering. A case in point is the graphical representation of the phase behavior of a system in the form of a phase diagram. Regions where the system exists as a single phase or a mixture of multiple phases are shown in the composition space. To completely represent the phase behavior of a c -component system, we need to use a phase diagram in a $(c + 1)$ -dimensional space, where the axes represent temperature, pressure, and $(c - 1)$ mole fractions. However, since pressure does not have a significant effect on solid–liquid phase behavior, it is generally sufficient to consider isobaric SLE phase diagrams, the dimensionality of which is equal to the number of components (c).

Because of its high dimensionality, it is difficult – or even impossible – to view the phase diagram of a multicomponent system in its entirety. For example, an isobaric phase diagram for four components would involve a four-dimensional space. To

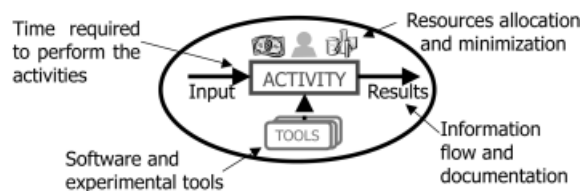


Fig. 11.2. The RAT²IO concept for workflow.

overcome this problem, the only practical approach is to reduce the dimensionality so that entities of dimensions four or higher can be viewed in lower dimensions. This can be achieved by taking projections and cuts. Consider the following familiar low-dimensional example. The T - x diagram for a three-component system is conveniently represented using a 3-D triangular prism (Fig. 11.3). The vertical axis is temperature, while the base is a ternary diagram. We can visualize this 3-D diagram in 2-D by looking at a polythermal projection or a series of isothermal cuts.

The use of phase diagrams to represent thermodynamic relationships such as phase and reaction equilibria has been the foundation for synthesis procedures for distillation processes, crystallization-based separations, extractive reaction processes, and hybrid systems. Graphical methods for synthesizing separation processes depend on the capability to track composition changes on the phase diagram, creating the so-called “process paths”. When the phase diagram is plotted in mole fraction coordinates, material balance lines are always linear and the lever rule is always valid. It is desirable to preserve this feature when taking a projection, so that the process path can still be constructed in the same way on the resulting plot in canonical coordinates (see below). Linear projection is preferable for this purpose, since linearity is preserved.

Figure 11.4 illustrates an example where SLE phase diagram is used for generating a flowsheet alternative for separating *p*- and *m*-cresol from a 50:50 mixture [4]. Crystallization is an attractive technique because *p*-cresol (*A*) and *m*-cresol (*B*) are close boilers (both having a boiling point of 202 °C), while their melting points differ quite significantly (35 °C for *p*-cresol and 10.9 °C for *m*-cresol). The binary system of

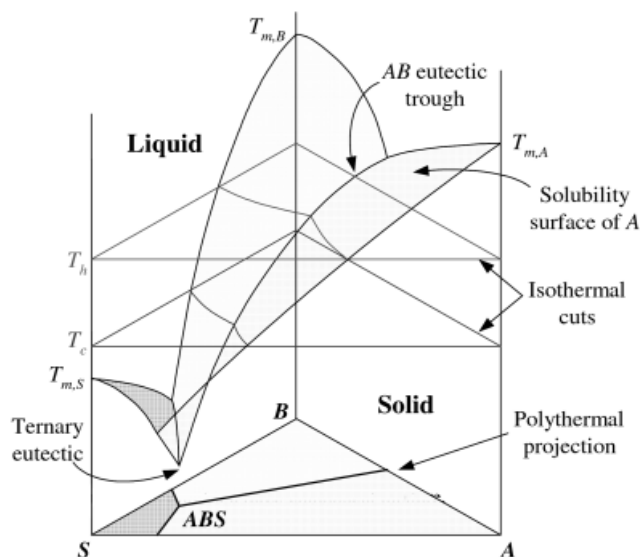


Fig. 11.3. Solid-liquid phase diagram for a three-component mixture.

these isomers forms a compound (AB_2) with a congruent melting point at 33.3 % A. The two eutectics are located at 12.5 % and 60 % A. Tare and Chivate [5] proposed the use of *t*-butyl alcohol (S), as a solvent to enable separation. This component forms an adduct with both isomers, as can be seen from the polythermal phase diagram in Fig. 11.4.

Since it is desired to separate pure A and B from the mixture, two crystallizers are needed (Fig. 11.4(a)). To achieve the separation objective, one must visit compartments A and B. By inspection of the phase diagram, it is found that the feed (located in compartment AB_2) can be brought to compartment A by adding S (Fig. 11.4(b)). This implies that A should be separated first, and B recovered next. However, it is not possible to move from compartment A to B, because the two compartments are not adjacent to each other. One option to deal with this problem is to crystallize AS, which is an adduct that can be easily separated using distillation. Instead of A, the adduct AS is recovered in the first crystallizer (Fig. 11.4(c)). Solvent removal is then used to cross from compartment AS to B, followed by crystallization of B. The final mother liquor (point 4) is recycled (Fig. 11.4(d)). To complete the flowsheet, two units are added: a dissolver to introduce solvent S to the feed, and a distillation column to recover A from the adduct (Fig. 11.4(e)). S is recycled back to the dissolver. Cooling-type crystallizers are used for both C1 and C2, since the boiling point of

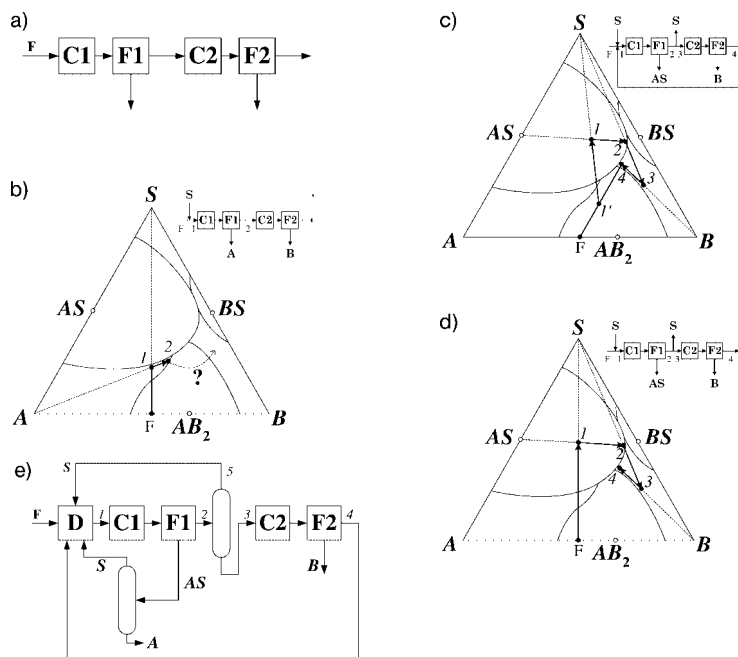


Fig. 11.4. Process synthesis using phase diagram (after Ref. [4]).

t-butyl alcohol (82.9 °C) is substantially higher than the melting points of A and B, prohibiting the use of an evaporative crystallizer.

11.4

Reactive Phase Diagrams

As demonstrated in the previous section, it is advantageous to obtain a deeper understanding of how to perform projections and cuts for multicomponent reactive systems. A single projection or cut captures only part of the system under consideration. However, the user can form a mental picture of the phase diagram in its entirety by making a sequence of such projections and cuts [6].

11.4.1

Projections and Canonical Coordinates

An m -dimensional subspace within the original n -dimensional space can be represented as the intersection of $(n - m)$ hyperplanes of dimension $(n - 1)$,

$$\mathbf{q}_i \cdot \mathbf{y} = 0; \quad i = 1, 2, \dots, n - m, \quad (1)$$

where \mathbf{q}_i is the normal vector to each hyperplane and \mathbf{y} is a position vector. In other words, the subspace is defined by a set of normal vectors $\{\mathbf{q}_1, \mathbf{q}_2, \dots, \mathbf{q}_{n-m}\}$ which are linearly independent. To describe objects lying entirely in an m -dimensional subspace, it is both redundant and inconvenient to use the original set of $(n + 1)$ coordinates. Instead, we can use a set of $(m + 1)$ coordinates $\{Y_1, Y_2, \dots, Y_m, Y_0\}$, which are referred to as the *canonical coordinates*. Once the relationship between the canonical and original coordinates is known, it is straightforward to plot the cut or projection of the original system using the new coordinates.

The most convenient way to plot a projection of an n -dimensional system in an m -dimensional linear projective subspace is to use *multiple orthogonal projection*, in which the directions of projection rays are parallel to the normal vectors $(\mathbf{q}_1, \mathbf{q}_2, \dots, \mathbf{q}_{n-m})$ defining the projective subspace. Under this projection, a point is first projected in the direction of \mathbf{q}_1 , then of \mathbf{q}_2 , and so on. A convenient set of canonical coordinates describing the projective subspace is given by

$$Y_i = y_i - \boldsymbol{\theta}_i^T \mathbf{Q}_{ref}^{-1} \mathbf{y}_{ref}; \quad i = 0, 1, 2, \dots, m \quad (2)$$

where

$$\boldsymbol{\theta}_i = [\mathbf{q}_{1,i} \quad \mathbf{q}_{2,i} \quad \dots \quad \mathbf{q}_{n-m,i}]^T; \quad i = 0, 1, 2, \dots, m \quad (3)$$

$$\mathbf{Q}_{ref} = \begin{bmatrix} q_{1,m+1} & q_{2,m+1} & \cdots & q_{n-m,m+1} \\ q_{1,m+2} & q_{2,m+2} & \cdots & q_{n-m,m+2} \\ \vdots & \vdots & \ddots & \vdots \\ q_{1,n} & q_{2,n} & \cdots & q_{n-m,n} \end{bmatrix} \quad (4)$$

$$\mathbf{Y}_{ref} = [y_{m+1} \quad y_{m+2} \quad \cdots \quad y_n]^T \quad (5)$$

Here, q_{ij} represent the j -th element of vector \mathbf{q}_i .

A special case of orthogonal projection in homogeneous space is the frequently used Jänecke projection, where one reference component is neglected and the composition of the remaining species are renormalized. As a special case of multiple orthogonal projection, we define *multiple Jänecke projection*, where the dimensionality is reduced directly to m . If components $(m+1)$ to $(C-1)$ are taken to be the reference components, the elements of the projection ray vectors $\{\mathbf{q}_1, \mathbf{q}_2, \dots, \mathbf{q}_{C-m-1}\}$ are given by

$$q_{j,i} = \begin{cases} 1, & \text{if } i = j + m \text{ or } i = 0 \\ 0, & \text{otherwise} \end{cases} \quad (6)$$

This projection is equivalent to neglecting components $(m+1)$ to $(C-1)$, and normalizing the remaining mole fractions.

Another special case is the *reactive projection*. When chemical reactions are present, possible compositions are confined to a lower dimensional subspace. Consider a system involving C components and R independent reactions described as

$$\nu_{1j} A_1 + \nu_{2j} A_2 + \cdots + \nu_{Cj} A_C = 0; j = 1, 2, \dots, R \quad (7)$$

where ν_{ij} is the stoichiometric coefficient of component i in reaction j , which has a negative value for reactants and positive for products. Changes in composition due to these reactions are described by a set of equations

$$n_i = n_{i,0} + \sum_{j=1}^R \nu_{ij} \xi_j; i = 1, 2, \dots, C \quad (8a)$$

$$n_{TOT} = n_{TOT,0} + \sum_{j=1}^R \nu_{TOT,j} \xi_j \quad (8b)$$

where ξ_j is the molar extent of reaction j . It can also be written as

$$\mathbf{n} = \mathbf{n}_0 + \xi_1 \mathbf{q}_1 + \xi_2 \mathbf{q}_2 + \cdots + \xi_R \mathbf{q}_R \quad (9)$$

where

$$\mathbf{q}_j = \begin{bmatrix} v_{1,j} & v_{2,j} & \cdots & v_{C-1,j} & v_{TOT,j} \end{bmatrix}^T; j = 1, \dots, R. \quad (10)$$

Equation (9) describes a linear *stoichiometric variety* of dimension R . A reactive projection is defined as a multiple orthogonal projection from a C -dimensional space to a $(C - R - 1)$ -dimensional subspace, where the directions of the R projection rays follow the directions of $\{\mathbf{q}_1, \mathbf{q}_2, \dots, \mathbf{q}_R\}$ defined in Eq. (10). Such projection causes the stoichiometric variety to disappear, leaving a reaction-invariant projection. The set of canonical coordinates defining the projective subspace can be found by substituting Eq. (10) into Eqs. (2)–(4) [7].

11.4.2

High-Dimensional Phase Diagrams

With the generic framework for making projections and cuts, we are in the position to plot high-dimensional phase diagrams. Consider a simple eutectic system of five components: A , B , C , D , and E . A complete representation of the polythermal phase diagram requires a four-dimensional diagram ($c = 5$). Figure 11.5(a) is a 3-D cut taken at $x_E = \text{constant}$, which is formed by stacking together cuts at different values of x_D and that particular value of x_E . In a similar way, one can generate similar 3-D cuts at different values of x_E , and combine them to recover the complete 4-D phase diagram. Another view of the phase diagram is shown in Fig. 11.5(b), where the entire phase diagram is projected onto a 2-D space. Clearly, both figures only provide partial view of the phase diagram, but nonetheless provide an idea of the higher dimensional system.

The plotting of such a phase diagram allows the visualization of saturation varieties, which are regions where one or more components are saturated and can crystallize out of the solution. For example, the region bounded by A_E , AB_E , ABC_E , AC_E , ACD_E , AD_E , and ABD_E in Fig. 11.5(a) is the saturation variety of A , where component A can be crystallized out in a pure form. Identification of this region is useful for determining conditions of a crystallizer for separating A .

Figure 11.6 shows an example of the phase diagram for a reactive system, in which a compound C is formed from components A and B . An isothermal cut and the polythermal projection are also shown. Such a phase diagram can be obtained via a reaction invariant projection of a higher-dimensional simple eutectic phase diagram. AS and BS are binary nonreactive eutectics, since their presence is not affected by the reaction, while ACS_B and BCS_A are ternary reactive eutectics. Similar

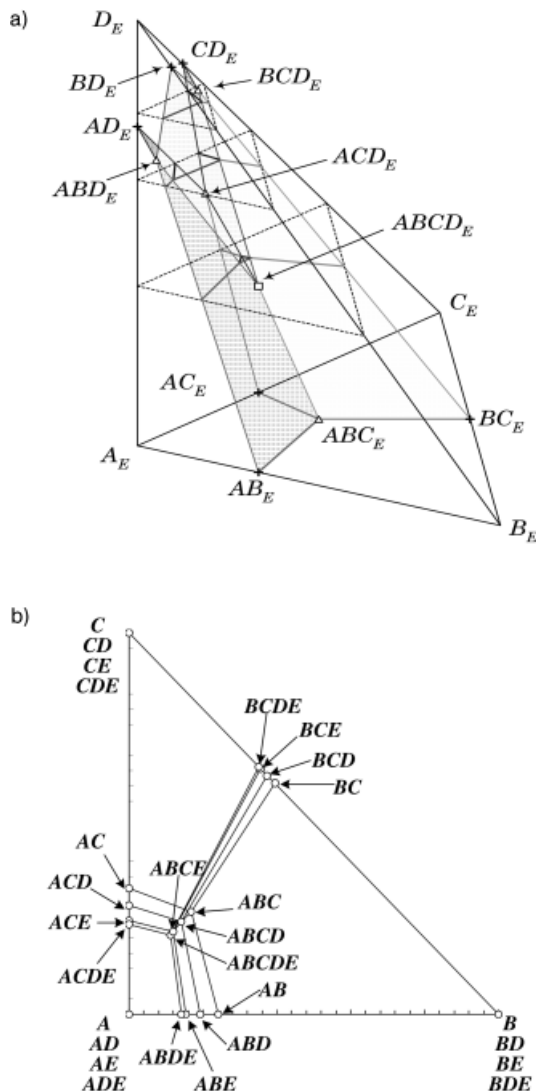


Fig. 11.5. (a) Three-dimensional cut of the five-component polythermal solid-liquid equilibrium (SLE) phase diagram. (b) Projection of the five-component SLE phase diagram to the normalized mole fraction space (after Ref. [4]).

to the nonreactive phase diagram, crystallization regions corresponding to each component can be identified.

Figure 11.7 shows a ternary system consisting of components A, B and a compound C. The presence of the reaction confines the feasible composition to the reaction equilibrium surface. Projection of the intersection between the solubility

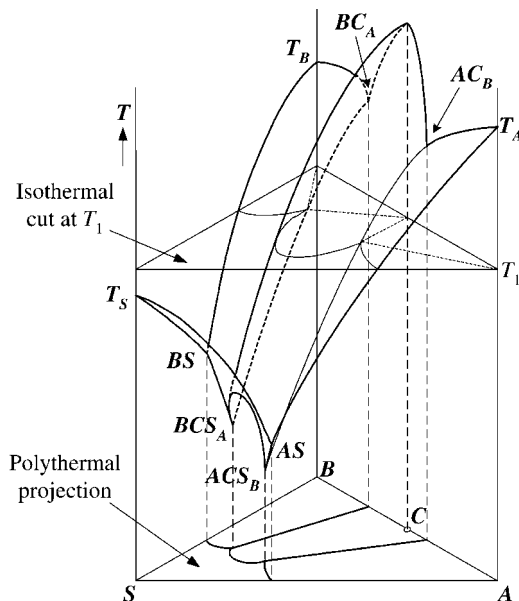


Fig. 11.6. Ternary phase diagram for a system with compound formation.

surfaces and the reaction equilibrium surface results in the familiar temperature-composition diagrams of congruent (Fig. 11.7(a)) and incongruent (Fig. 11.7(b)) compounds. Note that the composition axis is in terms of a transformed coordinate [8].

Figure 11.8 is an example of a high-dimensional ionic system phase diagram [9]. Consider an aqueous solution containing two cations (A^+ , B^{2+}) and three anions (X^- , Y^{3-} , Z^{2-}). The ions can form six simple salts, that is, AX , A_3Y , A_2Z , BX_2 , B_3Y_2 , and BZ . For simplicity, these salts are referred to as K , L , M , N , O , and P , respectively. The isobaric isothermal phase diagram of this system can be represented in a four-dimensional space. Taking a Jänecke projection with respect to the solvent vertex, we obtain a 3-D diagram (Fig. 11.8(a)). Each rectangular face of the prism represents a quaternary conjugate salt system comprising of both cations as well as two of the three anions (X^- and Y^{3-} , X^- and Z^{2-} , or Y^{3-} and Z^{2-}). Each triangular face represents a system of three salts with a common cation (A^+ or B^{2+}). There are nine vertices with two saturated salts lying on the edges of the prism, and eight vertices with three saturated salts lying on the faces (two each on the three rectangular faces and one each on the two triangular faces). There are also three vertices with four saturated salts lying in the interior of the prism, shown as squares. These vertices define the saturation variety of the salts. For example, the saturation variety of salt AX is the volume bounded by vertices K , KL , KLM , KM , KMN , KN , KLN , and $KLMN$. Figure 11.8(b) shows a 2-D projection of the phase diagram obtained by neglecting the concentration of ion Z^{2-} . Two more projections are required to completely represent this system.

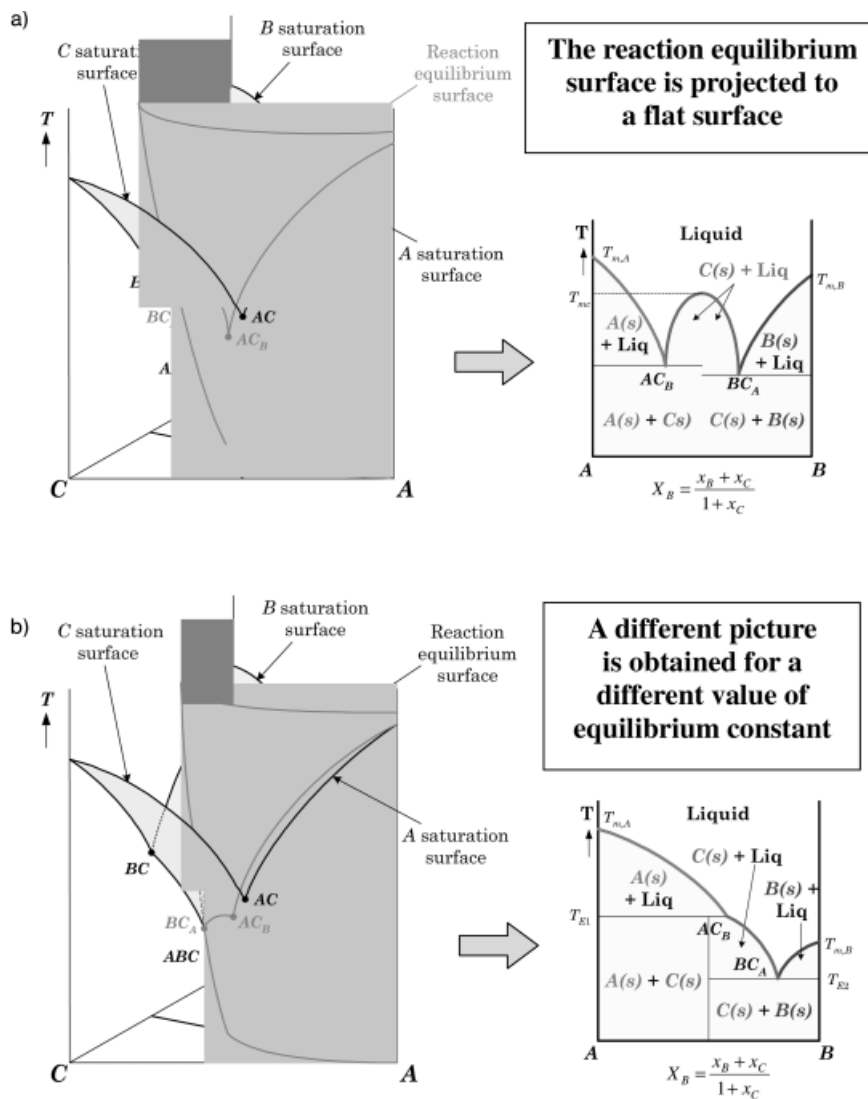


Fig. 11.7. Isobaric phase diagram of a binary system where the following reaction takes place: $A + B \rightarrow C$ resulting in (a) a congruent melting compound and (b) an incongruent melting compound.

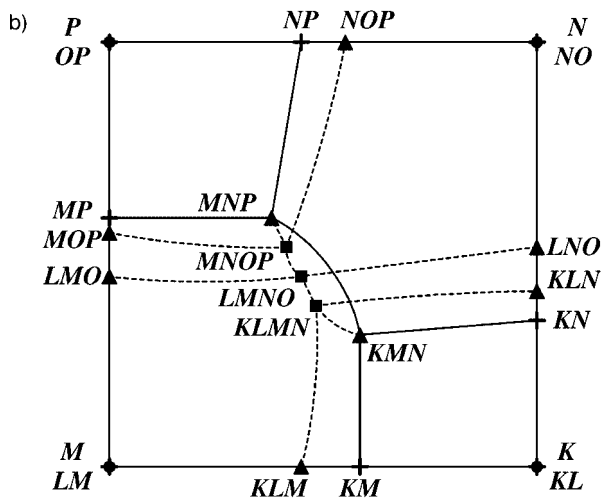
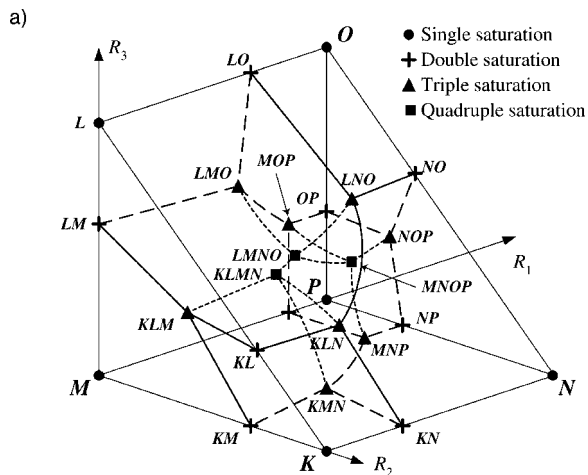


Fig. 11.8. Isobaric isothermal phase diagram for a six-salt simple ionic system: (a) 3-D diagram; (b) 2-D projection.

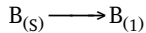
11.5 Kinetic Effects

The equilibrium-based design of reactive crystallization systems provides a starting point for the incorporation of the following kinetics and mass transfer effects. Supersaturation of the dissolved compound is created due to reaction, leading to the formation of crystal nuclei. Incorporation of the solute into the crystal lattice leads to crystal growth, but this can be hindered by mass transfer effects. This scenario can be further complicated by a gas–liquid reaction where gas–liquid mass transfer represents an additional step. Similarly, the dissolution rate of a solid agent can be the rate-limiting step in salting-out crystallization. Each of the above steps is characterized by a characteristic time, the ratios of which determine the relative rates of the different mechanisms. This is illustrated below using a salting-out reactive crystallization system [10].

11.5.1

Reactive Crystallization with a Solid Reactant

Consider a liquid feed stream containing reactant species A entering an MSMPR crystallizer at a volumetric flow rate F . A solid reactant B is also charged continuously at a molar flow rate W . The solid reactant B dissolves, and reacts with A in the liquid phase in the presence of an inert solvent S. The reaction rate can be generally given as a function of the concentrations of the reactant species, $\Phi(\mathbf{c})$. An amount of product P in excess of the solubility limit precipitates out of the solution as a solid product.



The material balances for the reactant and product species:

Balance for species A

$$F(C_A^f - C_A) - V\Phi = 0 \quad (12)$$

Balance for species B

Liquid phase

$$V k_{sA} (C_B^* - C_B) - V\Phi - FC_B = 0 \quad (13)$$

Solid phase

$$W - W \left(\frac{r}{r_0} \right)^3 - V k_S a_S (C_B^* - C_B) = 0 \quad (14)$$

Balance for species P

Liquid phase

$$F(C_P^f - C_P) + V\Phi - V k_S a_T (C_P - C_P^S) - V(k_v \rho_m L_0^3) J_n = 0 \quad (15)$$

Liquid-crystal interface

$$V k_S a_T (C_P - C_P^S) - V(a_T/2) \rho_m G = 0 \quad (16)$$

Here, C_P is the concentration of the dissolved solute in the bulk of the liquid, C_P^S is the concentration of the solute at the liquid–crystal interface, and C_P^* is the solubility. Note that the nucleation rate (J_n) and the linear growth rate (G) have been transformed into molar units by using appropriate multiplying factors. It should be emphasized that, while these equations capture the phenomena under consideration, to be correct, they should be expressed in terms of activities instead of concentrations.

Examination of Eqs. (12) to (16) reveals five distinct rate steps: dissolution of B; the reaction between A and B; the generation of P nuclei in the liquid phase; the mass transfer of dissolved P to the growing P crystals; and the surface integration of the solute P into the crystal lattice (i.e., the crystal growth step). The relative importance of each of these steps can be characterized by a dimensionless number. For a reaction which is second order overall, and for nucleation and growth kinetics which can be represented by conventional power law expressions, we have

$$\Phi = k_2 \left(C_A C_B - \frac{C_P^2}{K} \right) \quad (17)$$

$$J_n = k_n (C_P - C_P^*)^n \quad (18)$$

$$G = k_g (C_P^S - C_P^*)^g \quad (19)$$

Comparison of the individual steps results in the following dimensionless numbers:

Reaction

$$Da_R = \frac{\text{Reaction Rate}}{\text{Reactor Throughput}} = k_2 C_A^f \tau \quad (20)$$

Dissolution

$$Da_D = \frac{\text{Reaction Rate}}{\text{Dissolution Rate}} = \frac{k_2 C_A^f}{k_S a_S} \quad (21)$$

Mass transfer

$$Da_M = \frac{\text{Reaction Rate}}{\text{Mass Transfer Rate from Bulk to Crystal Face}} = \frac{k_2 C_A^f}{k_S a_T} \quad (22)$$

Nucleation

$$N_{Nu} = \frac{\text{Nuclei Generation Rate}}{\text{Reaction Rate}} = \frac{(k_v \rho_m I_0^3) k_n C_p^{n-1}}{k_2 C_A^f} \quad (23)$$

Crystal Growth

$$N_{Gr} = \frac{\text{Surface Integration Rate}}{\text{Mass Transfer Rate from Bulk to Crystal Face}} = \frac{(a_T/2) \rho_m k_g C_p^{n-1}}{k_S a_T} \quad (24)$$

These dimensionless numbers can also be combined. For example, the ratio Da_R/Da_D compares the dissolution rate to the reactor throughput while the product $Da_R N_{Nu}$ compares the nucleation rate with the reactor throughput. The exact form of the dimensionless numbers would change as the reaction kinetics, the growth rate expressions, etc. change, but the meanings would remain the same.

11.6**Asymmetric Transformation of Enantiomers**

The impact of kinetics on the equilibrium-based design is now illustrated using a asymmetric transformation process for resolution of a racemic mixture in a batch crystallizer. The effects of crystal nucleation and growth, seeding, and the racemization reaction are illustrated independently by starting from a simple base case and building up to the full process models. The nucleation and crystal growth rate parameters in the rate laws are the same for both enantiomers. The model parameters for the base case scenario are given by Schroer and Ng [11]. The inputs for the process are typical of the racemization kinetics and crystallization kinetics.

11.6.1**Base Case (BC)**

Figure 11.9 shows the process paths for different cases and operating conditions. This base case examines an unseeded crystallization without racemization reaction.

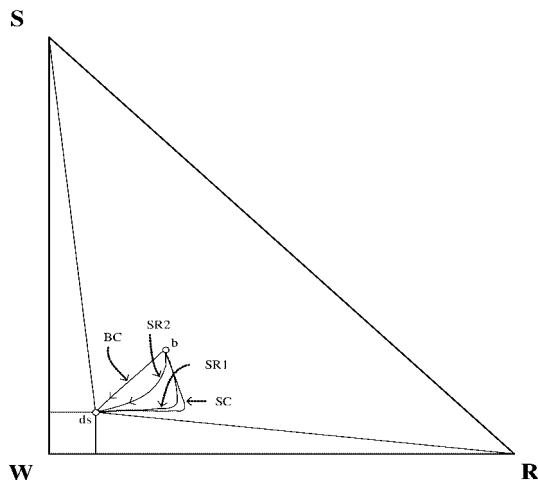


Fig. 11.9. Isobaric isothermal ternary phase diagram containing process paths for an asymmetric transformation example. The two enantiomers are labeled R and S, and the solvent is labeled W. Process paths begin at point b and terminate at the double saturation point, ds (after Ref. [11]).

Both enantiomers nucleate and crystallize. The process path starts from point b which represents an equimolar mixture of R and S enantiomers and proceeds towards the double saturation point (labeled ds), which is the equilibrium point. The linearity of the process path indicates that an equal amount of R and S crystals are being formed.

11.6.2

Seeded Crystallization (SC)

The second case considered is that of a seeded crystallization with racemization. An amount of S crystal seeds that is 2.5 % of the number of moles of S present is added to the mixture. The seeding enhances the crystallization rate of S, and initially the process path moves away from the S vertex with the product at short crystallization times significantly enriched in the S isomer. However, as the nucleation of the R isomers begin to kick in, the path turns towards the double saturation point, resulting in a drop in purity of the solid product. This can be seen in Fig. 11.10, which plots the fraction of the crystallized solid consisting of S crystals, z_S . The left axis in Fig. 11.10 is the mole fraction scale and the right axis is the purity expressed as the percent enantiomeric excess. Toyokura et al. [12] found a similar result in experimental studies on the selective seeding crystallization of S-carboxymethyl-L-cysteine (L-SCMC) from a solution containing its racemate. After a period of desupersaturation of the L-SCMC enantiomer, the concentration of D-SCMC would decrease due to its nucleation and crystal growth. The purity drop with resolution time of racemic mixtures has also been discussed in detail [13]. Figure 11.11 shows the amounts of

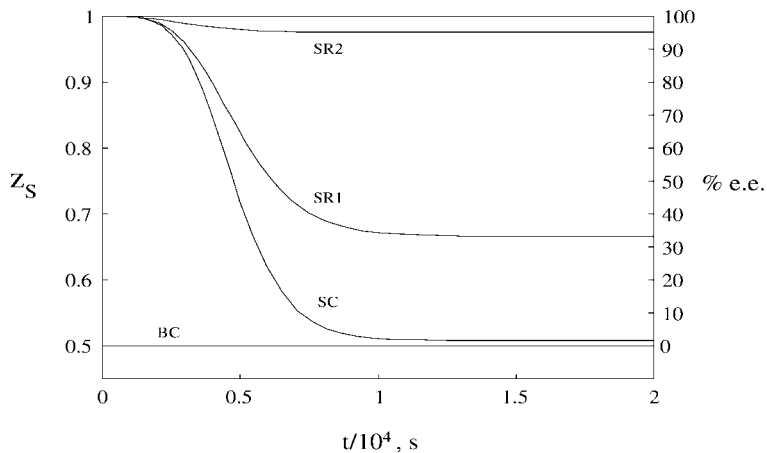


Fig. 11.10. Crystal product purity versus time (after Ref. [11]).

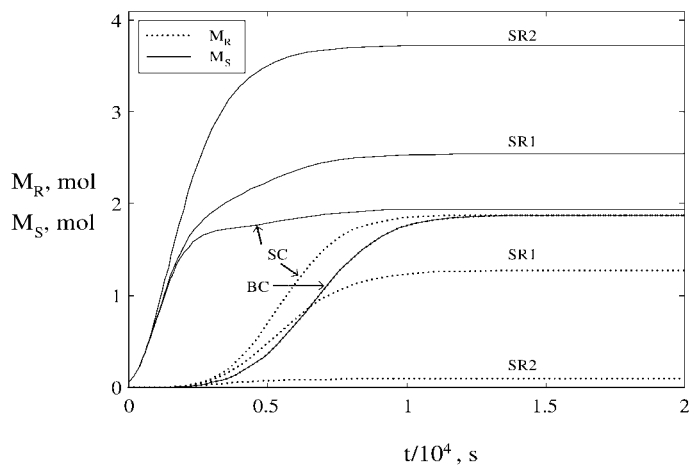


Fig. 11.11. Cumulative amounts of each solid enantiomer versus time (after Ref. [11]).

solids *R* and *S* plotted against time. There is a single curve for both *R* and *S* in the unseeded case (BC), and the amount of *R* enantiomer is less than that of *S* enantiomer in the seeded case (SC). Thus, some enrichment in the *S* enantiomer may be obtained if the crystallization is stopped before reaching equilibrium.

11.6.3

Seeded Crystallization with Racemization (SR)

We now consider seeding of the *S* enantiomer along with the racemization reaction for two values of racemization constant, $1 \times 10^{-4} \text{ s}^{-1}$ (SR1) and $1 \times 10^{-3} \text{ s}^{-1}$ (SR2). As can be seen in Fig. 11.9, racemization holds the path closer to a composition of a 50:50 mixture. In addition, the product purity at the end of the batch is significantly higher than in the other cases (Fig. 11.10). Although some of the undesired *R* enantiomer still crystallizes out, the ratio of the amounts of *S* to *R* is significantly higher than the SC case. This is particularly so for the case with fast racemization from *R* to *S*.

Figure 11.12 shows the relative effects of racemization and seeding on the product purity at the end of the batch. At this time, the supersaturation is depleted and the process path is close to the equilibrium double saturation point on the phase diagram. The results are corrected for the amount of seed used. That is:

$$z'_S = \frac{M_S^f - M_S^0}{M_R^f + M_S^f - M_S^0} \quad (25)$$

In general, purity increases with the amount of seeding and rate of racemization. However, the product purity encounters a plateau when the amount of seeding is in excess of 4 mol% of the amount of *S* in the mother liquor. These results are for a uniform seed size, and are expected to depend on the particle size distribution of the seed crystals used, although the general trends will remain the same.

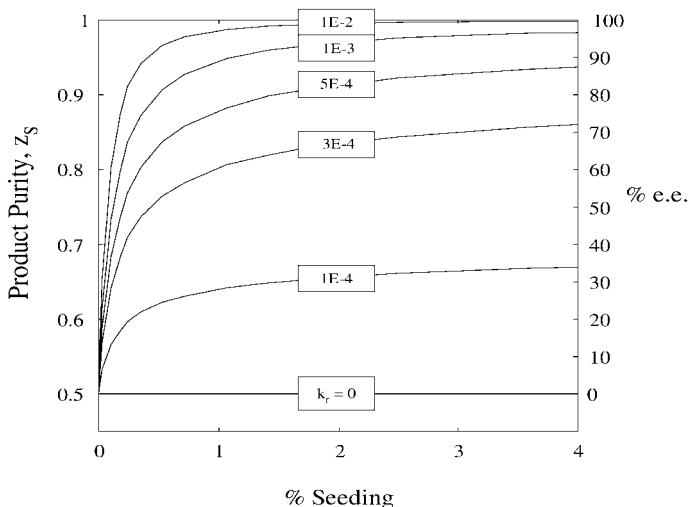


Fig. 11.12. Product purity at the end of the batch versus amount of seeding and racemization reaction rate (after Ref. [11]).

11.7

Conclusions

A strategy is proposed for the development of reactive crystallization processes. First, the strategy emphasizes workflow which helps to identify what operations must be carried out, and how this is achieved from a management viewpoint. Second, process synthesis – which is a key element of such a development effort – shows that, for multicomponent reactive systems, the availability of reactive phase diagrams can greatly facilitate process synthesis. In crystallizer design, reaction and crystallization kinetics can be captured in the form of process paths that show the extent of departure from equilibrium conditions. The strategy also calls for the inclusion of downstream process synthesis [14], although this point is not discussed in the present chapter.

Acknowledgments

The authors gratefully acknowledge financial support from the Research Grant Council HIA02/03.EG02.

References

1. A. G. Bemis, J. A. Dindorf, B. Horwood, et al., Phthalic Acids, in: *Kirk Othmer Encyclopedia of Chemical Technology*, Vol. 17, 3rd edn., p. 732. John Wiley & Sons, New York, 1982.
2. A. K. Mendiratta, Ion Exchange Catalyzed Bisphenol Process, U.S. Patent 4, 391, 997, 1983.
3. K. M. Ng, MOPSD: A Framework Linking Business Decision-Making to Product and process Design, in: *Process Systems Engineering 2003*, Ed. B. Chen and A. W. Westerberg, p. 63, Elsevier, 2003.
4. C. Wibowo and K. M. Ng, Unified Approach for Synthesizing Crystallization-Based Separation Processes, *AIChE J.*, **2000**, *46*, 1400.
5. J. P. Tare and M. R. Chivate, Separation of Close Boiling Isomers by Adductive and Extractive Crystallization, *AIChE Symp. Ser.* No. 143, 1976, 72, 95.
6. K. D. Samant, D. A. Berry, K. M. Ng, Framework for Representation of High-Dimensional, Molecular Solid-Liquid Phase Diagrams, *AIChE J.*, **2000**, *46*, 2435.
7. C. Wibowo and K. M. Ng, Visualization of High Dimensional Systems via Geometric Modeling with Homogeneous Coordinates, *Ind. Eng. Chem. Res.*, **2002**, *41*, 2213.
8. C. Wibowo, K. D. Samant, K. M. Ng, High-Dimensional Solid-Liquid Phase Diagrams Involving Compounds and Polymorphs, *AIChE J.*, **2002**, *48*, 2179.
9. K. D. Samant and K. M. Ng, Representation of High-Dimensional Solid-Liquid Phase Diagrams for Ionic Systems, *AIChE J.*, **2001**, *47*, 861.
10. V. V. Kelkar and K. M. Ng, Design of Reactive Crystallization Systems Incorporating Kinetics and Mass Transfer Effects, *AIChE J.*, **1999**, *45*, 69.
11. J. W. Schroer and K. M. Ng, Process Paths of Kinetically Controlled Crystallization: Enantiomers and Polymorphs, *Ind. Eng. Chem. Res.*, **2003**, *42*, 2230.

12. K. Toyokura, M. Kurotani, Fujinawa, J., Concentration Change of L-SCMC S-(Carboxymethyl)-L-cysteine. in a Supersaturated Solution of DL-SCMC with Suspended L-SCMC Seeds in a Batch Operation, in: *ACS Symposium Series; American Chemical Society*: Washington DC, 1997, Vol. 667, p. 46.
13. M. Matsuoka, Purity Drop in Optical Resolution of Racemic Mixtures, in: *ACS Symposium Series; American Chemical Society*: Washington, DC, 1997, Vol. 667, p. 59.
14. W. C. Chang and K. M. Ng, Synthesis of the Processing System Around a Crystallizer, *AIChE J.*, **1998**, *44*, 2240.

12

Analysis and Experimental Investigation of Catalytic Membrane Reactors

Andreas Seidel-Morgenstern

12.1

Introduction

In this chapter, the possibility will be discussed of using membranes to improve the performance of chemical reactors compared to conventional reactor concepts.

Membrane reactors have, for a long time, been the focus of intensive research, and a variety of membrane reactor configurations have either been developed or suggested. The state of the art with regard to this broad field has been the subject of several excellent reviews [1–10], while comprehensive summaries have recently been provided by Sanchez Marcano and Tsotsis [11] and Dixon [12]. Modern developments were reported on a regular basis during the *International Congresses on Catalysis in Membrane Reactors – ICCMR* [13].

As such reviews are readily available, the discussion below will focus on two experimental case studies conducted recently in the author's laboratory. These studies were related to two different areas where membrane reactors might be applied successfully:

- the selective withdrawal from the reactor of specific reaction products of reversible reactions; and
- the optimized dosing of a specific reactant into the reactor to enhance product selectivity.

In both cases, reactions were considered that require elevated temperatures, and consequently inorganic membranes were utilized in the reactors.

Before introducing the two examples and describing the experiments performed, selected basics of chemical reaction engineering will be summarized. These should be valuable to the reader in identifying the position of membrane reactors among the arsenal of rival concepts.

12.2

Basic Aspects of Chemical Reaction Engineering

Basic aspects of the analysis and optimization of various types of reactors and their operating regimes have been discussed in detail in classical textbooks of chemical

reaction engineering [e.g., Refs. 14, 15]. More specific aspects related to the frequently applied catalytic fixed-bed reactors were treated, for example, by Eigenberger [16].

12.2.1

Reaction Rates

In order to quantify chemical reactions and to describe the performance of chemical reactors, reaction rates are the key information required.

The rate of a single reaction in which N components are involved is defined as:

$$r_{\text{Scale}} = \frac{1}{\text{Scale}} \frac{1}{\nu_i} \frac{dn_i}{dt} \quad i = 1, N \quad (1)$$

The use of the stoichiometric coefficient ν_i guarantees that the reaction rate does not depend on the concrete component i considered. There are several possibilities regarding the selection of an appropriate scale. Frequently, the reaction volume V_R is used leading to a reaction rate r_V which has the dimension $[\text{mol m}^{-3} \text{s}]$.

In heterogeneous catalysis, the mass or surface area of the catalyst, m_{Cat} or A_{Cat} , are often more useful scaling quantities leading to r_M in $[\text{mol g}^{-1} \text{s}]$ or r_A in $[\text{mol m}^{-2} \text{s}]$. Since, typically, the main goal is to describe properly the molar changes dn_i/dt , it is necessary to use only r_{Scale} and the chosen scaling quantity consistently. If different scales are of relevance (e.g., “a” and “b”), it must obviously hold that:

$$\text{Scale}_a r_{\text{Scale}_a} = \text{Scale}_b r_{\text{Scale}_b} \quad (2)$$

Assuming that the scale is the reaction volume V_R and this is constant, for the reaction rate holds:

$$r_V = \frac{1}{\nu_i} \frac{dc_i}{dt} \quad \text{with} \quad c_i = \frac{n_i}{V_R} \quad i = 1, N \quad (3)$$

In principle, the reaction rates might depend on temperature and on all concentrations, i.e.:

$$r_V = r_V(T, c_1, c_2, \dots, c_N) \quad (4)$$

If only one reaction occurs, a single key component is enough to describe the development of the concentrations of all components. If reactant A is chosen as the key component, its conversion defined as:

$$X_A = \frac{c_A^0 - c_A}{c_A^0} \quad (5)$$

can be conveniently used as a dimensionless concentration. The concentration c_A^0 stands here for the initial or inlet concentration. Clearly, Eq. (4) can be reformulated:

$$r_V = r_V(T, c_A^0, X_A) \quad (6)$$

The temperature dependence can be typically described successfully using the Arrhenius equation [e.g., Refs. 14,15].

With regard to the concentration dependence, r_V can be split into a constant factor r_V^0 (related to the initial or inlet concentration) and a conversion dependent function $f(X_A)$ depending on the rate law of a specific reaction:

$$r_V = r_V^0(c_A^0) f(X_A) \quad (7)$$

12.2.2

Conversion as a Function of Rate Laws and Feed Composition

One of the simplest models used to describe the performance of tubular reactors is the well-known isothermal one-dimensional plug flow tubular reactor (PFTR) model. The mass balance of this model for steady-state conditions, the simultaneous occurrence of M reactions and a constant volumetric flow rate \dot{V} is:

$$\frac{dc_i}{dz} = \frac{A_R}{\dot{V}} \sum_{j=1}^M \nu_{ij} r_{Vj} \quad i = 1, N \quad (8)$$

In Eq. (8), the ν_{ij} are the elements of the stoichiometric matrix, A_R represents the cross-section area of the tube, and z is the axial coordinate. This system of ordinary differential equations can be integrated numerically for arbitrary rate laws, provided that appropriate initial conditions $c_i^0 = c_i(z=0)$ are provided.

If only one reaction needs to be considered, and conversion X_A is chosen to be the state variable of interest, using Eqs. (5) and (7), the mass balance of the PFTR, Eq. 8, can be expressed as follows:

$$\frac{(-\nu_A) r_V^0}{c_A^0} \frac{A_R}{\dot{V}} dz = \frac{dX_A}{f(X_A)} \quad (9)$$

Integration from 0 to the reactor length L and from 0 to $X_{A(L)}$ leads to the well-known dimensionless mass balance of the PFTR:

$$Da = \int_0^{X_{A(L)}} \frac{dX_A}{f(X_A)} \quad (10)$$

In this equation, Da is the Damköhler number [14]

$$Da = \frac{(-\nu_A)I_V^0}{c_A^0} \tau \quad (11)$$

and τ is the residence time

$$\tau = \frac{A_R L}{\dot{V}} = \frac{V_R}{\dot{V}} \quad (12)$$

The Damköhler number is a ratio of the characteristic times for convection and reaction.

The dimensionless mass balance Eq. (10) can be solved analytically for various rate laws, providing instructive $X_A(Da)$ -profiles.

If for example a first-order reaction $A \rightarrow C$ ($r = kc_A$) is analyzed, the dimensionless balance provides (with $r_V^0 = kc_V^0$ and $f(X_A) = 1 - X_A$):

$$X_A = 1 - e^{-Da} \quad (13)$$

In contrast, for a second-order reaction with the rate $r = kc_A^2$ holds:

$$X_A = \frac{Da}{1 + Da} \quad (14)$$

In case of a bimolecular reaction of the type $\nu_A A + \nu_B B \rightarrow \text{Products}$, the composition of the feed mixture is an important free parameter. This can be conveniently expressed using a stoichiometric feed ratio λ defined as follows:

$$\lambda = \frac{\nu_B c_A^0}{\nu_A c_B^0} \quad (15)$$

If component B is introduced in excess, i.e., if $0 < \lambda < 1$, holds:

$$X_A = \frac{e^{Da(1-\lambda)} - 1}{e^{Da(1-\lambda)} - \lambda} \quad (16)$$

Besides considering the order of a reaction and its effect on conversion, another important aspect is to understand effects related to reversibilities.

Formally, the overall rate of a first-order reversible reaction $A \rightleftharpoons B$ can be expressed as:

$$r_v = k_f (c_A - c_B/K_e) \quad (17)$$

where K_e is the reaction equilibrium constant for which holds

$$K_e = \frac{k_f}{k_b} \quad (18)$$

with k_f and k_b being the reaction rate constants of the forward and backward reactions, respectively.

Solving the coupled mass balances of components A and B (Eq. (10)) leads to

$$X_A = \frac{K_e}{1 + K_e} - \frac{e^{-Da(1+1/K_e)}}{1 + 1/K_e} \quad (19)$$

For high Da numbers, the following equilibrium conversion is clearly reached:

$$X_{A,eq} = \frac{K_e}{1 + K_e} \quad (20)$$

The different functions described by Eqs. (13), (14), (16) and (19) are illustrated in Figures 12.1 and 12.2.

The curves shown in Figures 12.1 and 12.2 reveal well-known and important facts:

1. An excess of a reactant increases the conversion of the other reactant (this means that dilution of a reactant increases its conversion).

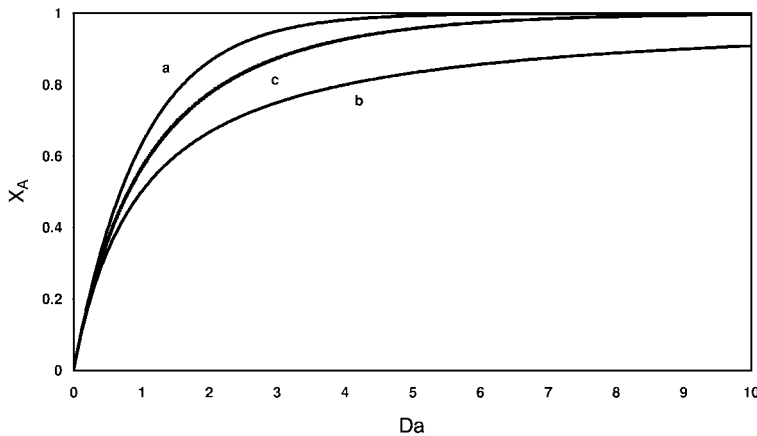


Fig. 12.1. Dependence of conversion on Damköhler number for: a) a first-order reaction (Eq. (13)); b) a second-order reaction (Eq. (14)); and c) a second-order reaction with two reactants and a nonstoichiometric feed composition (Eqs. (15) and (16), here for $\lambda = 0.5$).

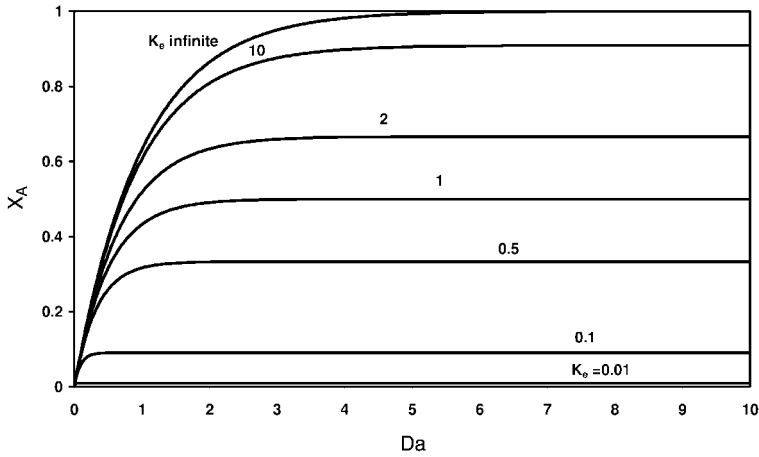


Fig. 12.2. Conversion as a function of Damköhler number for a reversible reaction $A \rightleftharpoons B$ (Eq. (19)) using different values for the equilibrium constant K_e .

2. Higher reaction orders require higher Da numbers (larger residence times) in order to reach the same conversion.

Note that, in particular, aspect (1) is relevant for the evaluation of the potential of membrane reactors aiming to withdraw products via permeable walls.

12.2.3

Selectivity and Yield

Frequently, several reactions proceed simultaneously, and consequently selectivity and yield in networks of parallel and series reactions with respect to a certain desired target component D are essential quantities.

The integral selectivity of a desired component D, S_D , is related to the corresponding consumption of a reactant A. Considering molar fluxes of components at the inlet and outlet of a continuously operated reactor, S_D is defined as follows:

$$S_D = \frac{\dot{n}_D}{(\dot{n}_A^0 - \dot{n}_A)} \frac{(-\nu_A)}{\nu_D} \quad (21)$$

Of more practical relevance is often the related yield of component D, Y_D , which is

$$Y_D = \frac{\dot{n}_D}{\dot{n}_A^0} \frac{(-\nu_A)}{\nu_D} = S_D X_A \quad (22)$$

If we consider a desired reaction $A + B \rightarrow D$ and an undesired consecutive reaction $D + B \rightarrow U$ the following rate laws could be postulated:

$$r_D = k_D c_A c_B \quad (21)$$

$$r_U = k_U c_D c_B \quad (22)$$

The selectivity and the yield with respect to D depend strongly on the ratio k_D/k_U . Typical results obtained solving numerically the mass balance equations of the PFTR model (Eq. (8)) are shown in Fig. 12.3.

The courses of $S_D(X_A)$ -curves depend strongly on the concrete concentration dependencies of the reactions involved – that is, on the reaction orders. An adequate description of the rates of heterogeneously catalyzed reactions is very difficult and often requires complex functions [17] which, in general, can only be determined experimentally [18].

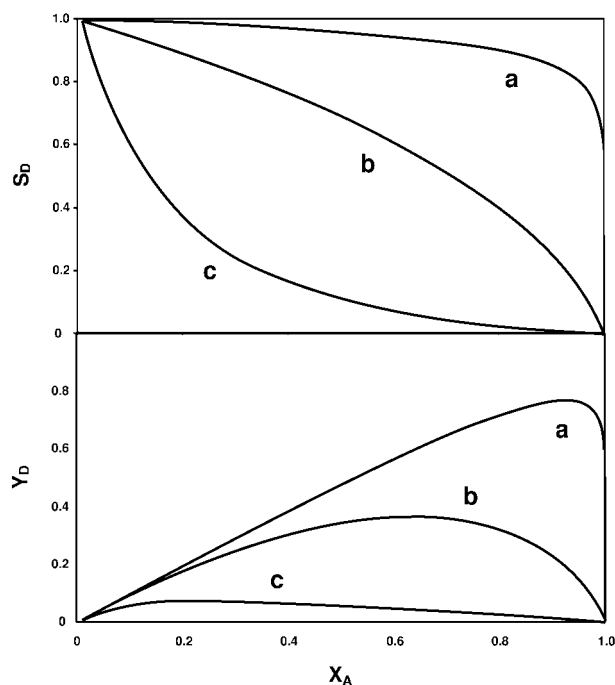


Fig. 12.3. Selectivity S_D and Yield Y_D as a function of conversion X_A for the two consecutive reactions $A + B \rightarrow D$ and $D + B \rightarrow U$ calculated with the PFTR model (Eq. (8)) fixing the residence time and varying the feed composition in a wide range. The reaction rates were described with Eqs. (21) and (22)). Three different ratios of the rate constants of the desired and the undesired reaction were considered: a) $k_D/k_U = 10$; b) $k_D/k_U = 1$; c) $k_D/k_U = 0.1$.

Clearly, it is highly desirable to operate in the upper right corner of the plot shown in Fig. 12.3, where both conversion and selectivity are high. This “corner” is the main target of the numerous intensive activities devoted to the development of more selective catalysts. A demonstration that reaction engineering concepts render this “corner” more accessible will be presented in Chapter 12.6.

12.3

Mass Transfer through Membranes

The reasoning behind developing different membrane reactor concepts is based on the realization of selective transport processes. Typically, certain components should be brought into – or removed selectively from – a reaction zone. Thus, an essential requirement for the successful operation of membrane reactors is to understand, and quantify, these transport processes correctly.

Currently, there is a great deal of activity in the development of various types of new membrane materials, both polymeric and inorganic. As many industrially relevant reactions require higher temperatures to achieve and maintain economic performance, temperature-resistant inorganic membranes are of especial interest. Indeed, many excellent reviews are currently available describing these materials and future trends in their development [e.g., Refs. 19–22].

An example of highly sophisticated new porous membranes with excellent performance is given e.g. in [23]. The current state regarding dense membranes is given in [10] for metal membranes and in [24] for ionic and electron conducting materials. A comprehensive overview of the significant progress made in the last years was provided at the last two *International Conferences on Inorganic Membranes – ICIM* [25].

Comprehensive monographs are also available detailing the analysis of mass transfer through porous and dense membranes. Standard textbooks [e.g., Refs. 26, 27] provide the basis for discriminating between various possible transport mechanisms and the selection of models capable of describing the processes in quantitatively.

In order to predict correctly the fluxes of multicomponent mixtures in porous membranes, simplified models based solely on Fick’s law should be used with care [28]. Often, combinations of several mechanisms control the fluxes, and more sophisticated models are required. A well-known example is the Dusty Gas Model which takes into account contributions of molecular diffusion, Knudsen diffusion, and permeation [29]. This model describes the coupled fluxes of N gaseous components, J_i , as a function of the pressure and total pressure gradients with the following equation:

$$\sum_{\substack{j=1 \\ j \neq i}}^N \frac{x_j J_i - x_i J_j}{(\varepsilon/r) D_{ij}^o} + \frac{J_i}{D_{K,i}^e(K_0)} = -\frac{p}{RT} \nabla x_i - \frac{x_i}{RT} \left(1 + \frac{B_0}{\eta D_{K,i}^e} p \right) \nabla p \quad i = 1, N \quad (23)$$

The free parameters of this model are the ratio of porosity to tortuosity, ε/τ , the binary molecular diffusivities, D_{ij}^0 , the Knudsen coefficient, K_0 (which determines specific effective Knudsen diffusivities, $D_{k,i}^e$) and the permeability constant, B_0 .

More complicated and realistic models which allow the prediction of transport processes in porous media have been suggested, and have been validated in recent years. For example, it was realized that there might be significant contributions to the overall flux by components which are adsorbed at pore walls but possess a certain mobility [30]. To quantify such surface diffusion processes, a Generalized Stefan–Maxwell equation has been proposed [28]:

$$\sum_{\substack{j=1 \\ j \neq i}}^N \frac{q_j J_i^S - q_i J_j^S}{q_{\text{sat}} D_{ij}^S} + \frac{J_i^S}{D_i^S} = -\frac{1-\varepsilon}{RT} q_i \nabla \mu_i^S \quad i = 1, N \quad (24)$$

In Eq. (24) the gradient of the surface chemical potential, μ_i^S , is assumed to be the driving force. The surface phase concentrations, q_i and q_{sat} , and the surface diffusivities, D_{ij}^S and D_i^S , must be known in order to predict the surface fluxes, J_i^S .

Based on classical concepts [31], several significant activities are currently devoted to describing in detail the mass transport processes in porous media, notably by applying more complex network models.

A description of the transport in highly selective dense membranes is easier, provided there are no defects which need to be taken into account. Transport in metallic membranes can be often described successfully by the solution diffusion model (Sievert's law), and a comprehensive overview of hydrogen transport in palladium membranes was recently provided [10]. The aspect of incorporating the presence of membrane defects into a description of mass transfer has been discussed [e.g., Ref. [32]]. Classical Wagner theory is usually adopted to calculate oxygen fluxes through mixed ionic and electron-conducting dense membranes as a function of the oxygen chemical potential gradient, according to the following expression [24]:

$$J_{\text{O}_2} = -\frac{1}{16F^2} \frac{\sigma_{\text{el}} \cdot \sigma_{\text{ion}}}{\sigma_{\text{el}} + \sigma_{\text{ion}}} \nabla \mu_{\text{O}_2} \quad (25)$$

In this equation, σ_{el} and σ_{ion} are the partial conductivities of oxygen ions and electrons, respectively, and F is Faraday's constant.

An important problem which arises when quantifying transport processes in membranes is the fact that they typically possess a composite structure. Although one layer is usually the main resistor to transport, effects caused by other layers can generally not be completely neglected (e.g., Ref. [33]). For this reason, integral descriptions of composite membranes should be applied carefully, as they cannot explain observed direction-dependences of fluxes [34].

12.4

Kinetic Compatibility in Membrane Reactors

In order to achieve a significant effect for a membrane introduced into a reactor compared to a conventional reactor operation, there should be compatibility between fluxes passing the membrane and amounts consumed or produced during the chemical reactions. The specific amounts related to the simultaneous occurrence of M chemical reactions can be expressed, based on Eq. (1) as:

$$\left. \frac{dn_i}{dt} \right|_{\text{Reaction}} = \text{Scale} \sum_{j=1}^M \nu_{ij} r_{\text{Scale},j} \quad i = 1, N \quad (26)$$

As mentioned earlier, different scales might be appropriate to quantify the reaction rates. With regard to transport through membranes, the membrane area A_M is the appropriate scaling parameter. Thus, it holds that:

$$\dot{n}_i \big|_{\text{Membrane}} = A_M J_i \quad i = 1, N \quad (27)$$

In the above, J_i represents the overall flux that might be composed for porous media out of different contributions (see for example Eqs. (23) and (24)).

Provided that the required information is available, based on Eqs. (26) and (27) several important questions can be answered in an early development stage – for example, how much membrane area must be provided per scale of the reaction zone and, more generally, whether a more detailed investigation of the coupling reaction and mass transfer through the membrane considered is justified.

Based on this approach, a useful estimation was provided recently [35]. With regard to the reaction aspect, achievable space–time yields (STY) of currently operated catalytic reactors were considered, whereupon Weisz defined the following “window of reality” [36]:

$$\text{STY} = \frac{\dot{n}_{\text{Prod}}}{V_R} \approx 1 - 10 \frac{\text{mol}}{\text{m}^3 \text{s}} \quad (28)$$

The achievable fluxes through membranes, J , were designated in [35] as area time yields (ATY, in $\text{mol m}^{-2} \text{s}$). Figure 12.4 provides an estimation of the current state regarding the possibility of matching the two processes. For a wide range of membranes under consideration, the required ratios of membrane area to reactor volume (A_M/V_R) are between 10 and 100 m^{-1} . These values allow to estimate that the diameter of applicable cylindrical tubular reactors should be between 0.04 and 0.4 m. These appear to be reasonable values for industrial applications, and indicate that matching of the two processes under consideration is achievable with currently available membranes.

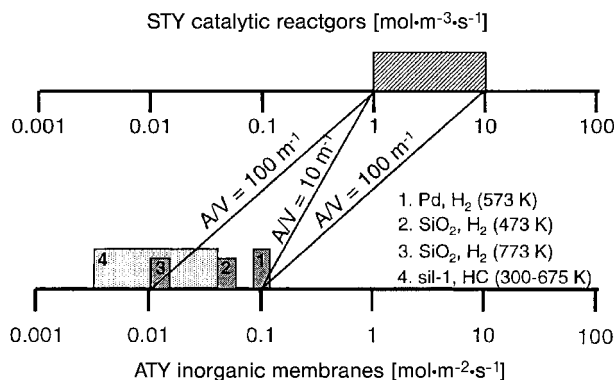


Fig. 12.4. Comparison of the space-time yield (STY) of catalytic reactors with the area time yield (ATY) of several inorganic membranes. (Reprinted from Ref. [35], Fig. 11; copyright 1999, with permission of Elsevier.)

12.5

Example 1: Product Removal with Membranes ("Extractor")

Removal of the products of reversible reactions was the area where, initially, the most intensive efforts related to the development of membrane reactors were undertaken. The simple principle, which is based on removing one of the products of a desired reaction via a membrane from the reaction zone is illustrated in Fig. 12.5.

The starting point of systematic research activities was, in particular, the attempt to remove hydrogen formed in dehydrogenation reactions [37]. Significant contributions to develop highly H_2 -selective Pd and its alloys were made in the former Soviet Union [38] and in Japan [39]. Several dehydrogenation reactions have been investigated in the meantime in membrane reactors applying different porous and dense membranes and catalysts. Examples of this are the dehydrogenations of benzene to cyclohexane [e.g., 40], of ethane [e.g., 41], of propane [e.g., 42, 43], of butane [e.g., 44], and of ethyl benzene [e.g., 45, 46].

In most of the studies mentioned, it was possible to demonstrate positive effects related to the presence of the membrane. Results of reactor simulations were

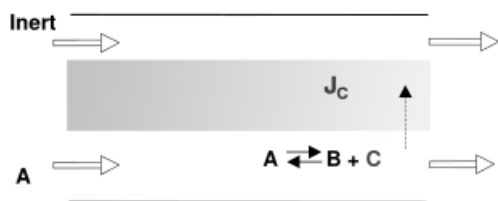


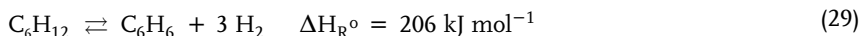
Fig. 12.5. Schematic representation of a membrane reactor aiming to withdraw selectively a product C formed in a reversible reaction.

presented in several reports, although considering the importance of the reaction rates (outlined in Section 12.3.1), their careful determination in the systems under investigation was rarely assessed adequately. For this reason, in the present investigations two laboratory studies were conducted which were devoted to two types of membrane reactors. First, a product extractor aiming to shift the equilibrium of a reversible reaction was investigated, and the results obtained are reported in Section 12.5.1 to 12.5.6. Subsequently, a reactant distributor was considered which aimed to enhance selectivity with respect to an intermediate product. The corresponding results are presented in Section 12.6. In both cases the reaction rates of the model reactions investigated were measured carefully for the specific catalysts applied. This information was then used to describe and analyze the two membrane reactor concepts investigated.

12.5.1

Model Reaction, Procedures and Set-up

The dehydrogenation of cyclohexane to benzene was studied at the laboratory scale.



To catalyze the reaction, 1 wt% Pt on a g-Al₂O₃ support (Degussa, F221 XH/D 1 %) was used. The BET surface area of this catalyst was 215 m² g⁻¹, and pellet sizes of 2–4 mm and crushed material were used.

Due to a high selectivity and moderate temperatures required to perform this endothermic reaction it is well suited to serve as a model reaction [40].

The membrane used was a Vycor glass tube (Corning Inc., code 7930), the dimensions of which were $d_{\text{inner}} = 7.8 \text{ mm}$, $d_{\text{outer}} = 10 \text{ mm}$, and $L = 100 \text{ mm}$. Vycor glass possesses a narrow pore size distribution, with a mean pore diameter of approximately 4 nm.

Four types of measurements were made:

- (i) The rates of the reaction were determined experimentally using a gradient-less reactor.
- (ii) Fixed-bed reactor experiments were performed in order to validate the determined reaction rates and to deliver reference data.
- (iii) The mass transfer through the membrane was quantified using a combination of steady-state and transient experiments.
- (iv) The performance of the membrane reactor was investigated using the set-up illustrated in Fig. 12.6.

12.5.2

Reaction Rates

In preliminary experiments the performance of the applied Micro-Berty reactor (Autoclave Engineers, $V_{\text{R}} = 12 \text{ cm}^3$ [18]) was tested. The catalyst mass introduced in this reactor was $m_{\text{Cat}} = 2.1 \text{ g}$. In preliminary runs, by varying the stirring rate it

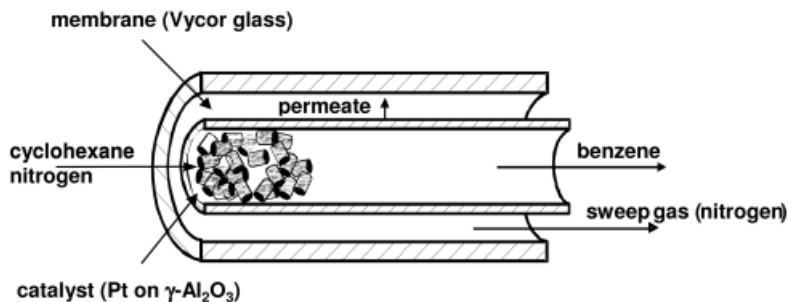


Fig. 12.6. Illustration of the system investigated and the membrane reactor set-up used to withdraw selectively hydrogen from the reaction zone.

was found that gradientless conditions could be achieved above 4500 min^{-1} . Based on standard correlations [15, 18], it was also found that heat and mass transfer limitations do not influence the results significantly [47].

Mass-related reaction rates, r_M , were determined at normal pressure for the following ranges of operating conditions: $T = 473$ to 503 K , $x_{\text{C}_6\text{H}_{12}}^0 = 2\text{--}6 \text{ vol\%}$, normal pressure conditions at both membrane sides, gas hourly space velocity (GHSV): $400\text{--}1000 \text{ h}^{-1}$. The composition of the effluent was measured under steady-state conditions using gas chromatography (GC).

The potential of several models with regard to their ability to analyze the rate data measured was compared [47], and the following model, considering the reversible adsorption of benzene, was found to be the most satisfactory:

$$r_M = k_M \frac{P_{\text{C}_6\text{H}_{12}} - P_{\text{C}_6\text{H}_6} P_{\text{H}_2}^3 / K_{p,e}}{1 + K_{\text{C}_6\text{H}_6} P_{\text{C}_6\text{H}_6}} \quad (30)$$

The reaction equilibrium constant $K_{p,e}$ could be determined a priori based on classical thermodynamic concepts. Thus, four free parameters were determined in attempting to match the observed and predicted rates. The following values were obtained:

$$k_M = 7 \cdot 10^{-6} \cdot \exp(-44600/RT) \quad \left[\frac{\text{mol}}{\text{g}_{\text{Cat}} \text{sPa}} \right] \quad (31)$$

$$K_{\text{C}_6\text{H}_6} = 1 \cdot 10^{-8} \cdot \exp(39900/RT) \quad \left[\frac{1}{\text{Pa}} \right] \quad (32)$$

The quality of the agreement between the observed rates and the predictions of Eq. (30) is shown as a parity plot in Fig. 12.7.

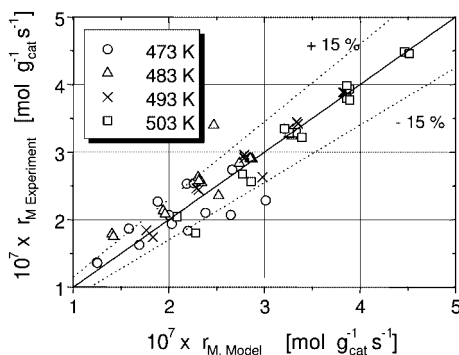


Fig. 12.7. Experimentally determined reaction rates r_M of the dehydrogenation of cyclohexane on a supported Pt-catalyst versus predictions based on Eqs. (30)–(32).

Figure 12.7 illustrates that, with the applied catalyst, reaction rates of up to $r_M \approx 4 \times 10^{-7} \text{ mol g}_{\text{cat}}^{-1} \text{ s}^{-1}$ could easily be achieved. This corresponds (with an apparent density of the catalyst of 1.2 g cm^{-3}) to a STY of ca. $0.5 \text{ mol m}^{-3} \text{ s}$ (which is close to the value given in Eq. (28)).

12.5.3

Fixed-bed Reactor Experiments

In order to validate the reaction rate equation, additional experiments were performed in a fixed bed ($d_{\text{inner}} = 7 \text{ mm}$, $L = 100 \text{ mm}$) filled with 3.1 g of the same catalyst.

Typical results are shown in Fig. 12.8. They demonstrate the expected tendency that increasing the temperature and residence time leads to higher conversions, with equilibrium conversion being reached at sufficient residence time. Figure 12.8 also illustrates the fact that a higher conversion of cyclohexane can be achieved if the feed is more diluted – a finding which is in agreement with the predictions of Eq. (16) (see Fig. 12.1).

To describe the reactor behavior, a simplified isothermal dispersed plug-flow reactor model was used. The well-known mass balance of this model for steady-state conditions can be formulated as [14, 15]:

$$0 = -\frac{p}{RT A_R} \frac{d(\dot{V} x_i)}{dz} + D_{ax} \frac{p}{RT} \frac{d^2 x_i}{dz^2} + \frac{m_{\text{Cat}}}{V_R} \nu_i r_M \quad i = 1, N \quad (33)$$

The axial dispersion coefficient D_{ax} was estimated from conventional residence time analysis for nonreacting conditions [14, 47]. The lines shown in Fig. 12.8 demonstrate that essential features of the reactor behavior are well represented. This also indicates a certain reliability of the derived kinetic equation Eq. (30).

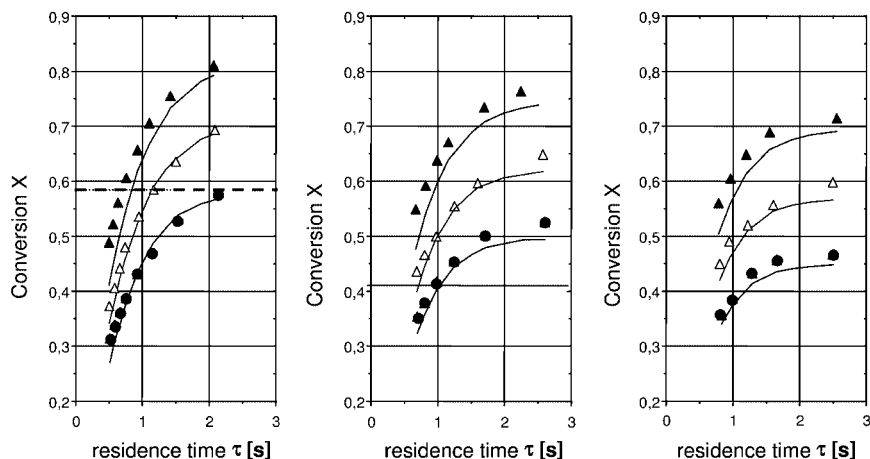


Fig. 12.8. Comparison between measured conversions of cyclohexane and predicted values (based on solving Eq. (33)) as a function of the residence time for different temperatures (\blacktriangle , 493 K; \triangle , 483 K; \bullet , 473 K) and cyclohexane feed concentrations (left, 3.7 vol%; center, 4.9 vol%; right, 5.8 vol%). The dashed line in the left figure indicates the equilibrium conversion at 473 K.

12.5.4

Mass Transfer through the Membrane

In order to study mass transfer through the Vycor glass membrane, systematic measurements were performed with single gases and gas mixtures under steady-state and transient conditions [30, 47]. The results showed that, for many gases, Knudsen diffusion is the most important mechanism, and under the conditions studied permeation plays only a minor role. The two mechanisms could be well described using the Dusty Gas Model (Eq. (23)). The essential free parameters of this model were found for Vycor glass to be: $K = 6.6 \times 10^{-11}$ m, $B_0 = 11 \times 10^{-20}$ m² and $\varepsilon/\tau = 0.03$. With regard to the transport of benzene, a certain contribution of surface diffusion was identified. The surface diffusivity of the Generalized Stefan–Maxwell model (Eq. (24)) was estimated as $D_{C_6H_6}^s = 1.45 \times 10^{-9}$ m² s⁻¹ [47].

In general, the Vycor glass membrane can be considered to be a membrane of the Knudsen type. Thus, the selectivity of transport of two gases i and j is approximately related to their molecular weights [27] according to:

$$S_{M,ij} = \sqrt{\frac{M_j}{M_i}} \quad (34)$$

A comparison is shown in Fig. 12.9 of the transient pressure difference between the two sides of the membrane after introducing a feed composition change at one side [30]. The good agreement between the predicted and measured

data demonstrates the general applicability of applied transport model and the parameters determined.

By using the parameters detailed above, it could be estimated that for a partial pressure difference of 1 bar, hydrogen fluxes through the Vycor glass of ca. $J_{H_2} \approx 5 \times 10^{-7} \text{ mol cm}^{-2} \text{ s}$ could be achieved.

Thus, in order to achieve interaction between the reaction process and the transport process the required membrane area per mass of catalyst must be in the following range:

$$\frac{A_M}{m_{\text{Cat}}} = \frac{r_M}{J_{H_2}} = \frac{4 \cdot 10^{-7} \text{ mol/g}_{\text{Cat}}\text{s}}{5 \cdot 10^{-7} \text{ mol/cm}_M^2} = 0.8 \frac{\text{cm}_M^2}{\text{g}_{\text{Cat}}} \quad (35)$$

12.5.5

Membrane Reactor Experiments and Modeling

The Vycor glass tube used in the membrane reactor experiments was filled with 3.2 g of catalyst. As the accessible area was ca. 30 cm^2 , the ratio of membrane area to catalyst mass is in the range specified by Eq. (35). Consequently, there should be sufficient membrane area available to remove significant amounts of hydrogen and, therefore, to have an effect on the reaction process.

The experiments were performed at a temperature of 473 K, with three different feed compositions being investigated. For each composition the ratio between the sweep flow rate, \dot{V}_s , and the feed flow rate, \dot{V}_f , was altered over a wide range. This sweep (or dilution) ratio, γ , was defined as:

$$\gamma = \frac{\dot{V}_s^0}{x_{f,C_6H_{12}}^0 \dot{V}_f^0} \quad (36)$$

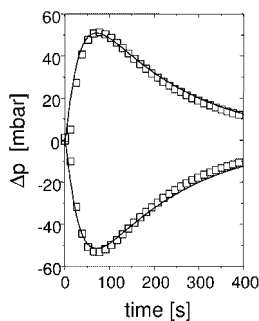


Fig. 12.9. Results of two complementary transient diffusion experiments with a tubular Vycor glass membrane. The figure shows development of the pressure difference between the two sides of the membrane after exchanging

at one side of the membrane 7.5 vol% C_6H_6 in helium against pure helium (and vice versa). The predictions are based on the Dusty Gas Model and the Generalized Stefan–Maxwell equation (Eqs. (23), (24)) [30, 47].

The results of the experimental investigation are summarized in Fig. 12.10. Given is the achieved conversion defined as follows:

$$X_{C_6H_{12}} = \frac{\Delta \dot{n}_{f,C_6H_{12}}}{\dot{n}_{f,C_6H_{12}}^0} = \frac{\dot{n}_{C_6H_{12}}}{\dot{n}_{f,C_6H_{12}}^0} = \frac{x_{f,C_6H_{12}} \dot{V}_f + x_{s,C_6H_{12}} \dot{V}_s}{x_{f,C_6H_{12}}^0 \dot{V}_f^0} \quad (37)$$

It is clear that the cyclohexane conversion increases with an increasing sweep ratio γ —that is, with increasing driving forces for mass transfer through the membrane. In addition, the introduction of a more diluted feed leads to an enhanced conversion. Proof of an effect of the realized product removal via the Vycor glass membrane was the fact that the achieved conversions exceeded the equilibrium conversions (shown as dotted lines in Fig. 12.10).

In addition to these experiments, a simplified isothermal 1-D dispersed plug-flow reactor model of the membrane reactor was used to carry out theoretical studies [47]. The model used consisted of the following mass balance equations for the feed and sweep sides:

$$0 = -\frac{p_f}{RT} \frac{1}{A_{R,f}} \frac{d(\dot{V}_f x_{f,i})}{dz} + D_{axf} \frac{p_f}{RT} \frac{d^2 x_{f,i}}{dz^2} - \frac{2\pi r_{inner}}{A_{R,f}} J_i \Big|_{r=r_{inner}} + \frac{m_{Cat}}{V_{R,f}} \nu_{iRM} \quad i = 1, N \quad (38)$$

$$0 = -\frac{p_s}{RT} \frac{1}{A_{R,s}} \frac{d(\dot{V}_s x_{s,i})}{dz} + D_{axs} \frac{p_s}{RT} \frac{d^2 x_{s,i}}{dz^2} + \frac{2\pi r_{outer}}{A_{R,s}} J_i \Big|_{r=r_{outer}} \quad i = 1, N \quad (39)$$

The $A_{R,f}$ and $A_{R,s}$ represent the cross-sectional areas of the feed and sweep sides, respectively.

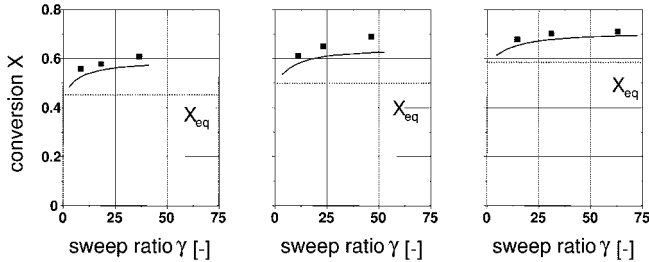


Fig. 12.10. Comparison between experimentally determined and predicted conversions of cyclohexane in the membrane reactor (Eq. (37)) as a function of the sweep (dilution) ratio (Eq. (36)) at 473 K for three different cyclohexane feed concentrations (right, 3.7 vol%; center, 4.9 vol%; left, 5.8 vol%). The corresponding equilibrium conversions, X_{eq} , are indicated by dashed lines.

Compared to Eq. (33), in Eq. (38) an additional term was included which represents the transport through the membrane. In addition, the balance for the membrane was considered:

$$0 = \frac{1}{r} \frac{\partial}{\partial r} (r J_i) \quad i = 1, N \quad (40)$$

In Eq. (40) the flux model validated for Vycor glass [47] was incorporated in order to quantify the J_i as a function of the driving forces.

The set of Eqs. (38)–(40), together with appropriate boundary conditions, was solved numerically using a combination of a finite difference method and a Newton–Raphson iteration [47].

The results shown in Fig. 12.10 indicate that both the simplified model and the measured parameters of reaction rates and mass transport describe the general trends identified during the experiments. Clearly, these predictions do systematically underestimate the conversions achievable. This may be in particular due to deviations from isotherm conditions occurring in the reactor.

12.5.6

Evaluation of the Extractor-type of Membrane Reactor

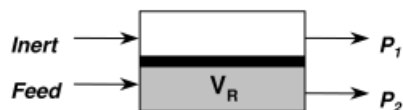
In order to interpret and further analyze the results obtained for the membrane reactor it is expedient to perform a comparison with the conventional fixed-bed reactor. Following studies conducted by Reo et al. [49, 50], the three possible configurations illustrated in Fig. 12.11 could be compared.

Besides considering the membrane reactor and the conventional fixed-bed reactor, in this context it is instructive to take into account a “diluted fixed-bed reactor”. In

conventional fixed bed reactor



membrane reactor



„diluted“ fixed bed reactor

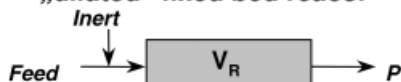


Fig. 12.11. Schematic representation of three rivaling operating modes.

this reactor the additional amount of sweep gas introduced into the membrane reactor is premixed with the feed of the conventional fixed-bed reactor.

For all three reactor configurations the conversion could be expressed as a function of the Damköhler number (defined relative to the forward reaction):

$$Da = \frac{k_M P_{C_6H_{12}}^0 m_{Cat}}{\dot{n}_{C_6H_{12}}^0} \quad (41)$$

The results of a systematic parametric study using the reaction and mass transport rates determined above are summarized in Fig. 12.12.

In Fig. 12.12, curve (a) corresponds to the conventional fixed-bed reactor and is characterized by the typical finite equilibrium conversion which is reached for high Da numbers. The achievable conversion is in agreement with that shown in Fig. 12.10 approximately 0.5.

In contrast, curve (b) in Fig. 12.12 demonstrates the dependence for the "diluted" fixed-bed reactor in which a higher equilibrium conversion can be achieved (cf. Figs. 12.1 and 12.10). For lower Da numbers, due to the lower rates of the forward reaction, the conversion falls in the "diluted" fixed-bed reactor below the corresponding value in the conventional reactor.

The membrane reactor has an additional degree of freedom allowing to optimize the amount of the product removed. This can be conveniently described by a dimensionless Peclet number which relates convective flow through the reactor to transport through the membrane [50]. For each Da number there exists an optimal Pe number maximizing the conversion. For a given membrane material the Pe number is directly related to the membrane thickness. Curve (b) in Fig. 12.12 represents the theoretical behavior of a membrane reactor optimized with respect to membrane thickness. For low Da numbers the membrane should be very thick in order to keep the reactants in the reactor, and in this respect the membrane reactor is identical to the conventional fixed-bed reactor. In contrast, for high Da numbers the membrane reactor should possess a very thin wall for

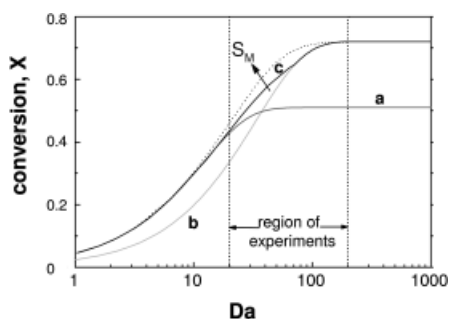


Fig. 12.12. Calculated dependence of cyclohexane conversion (Eq. (37)) as a function of the Damköhler number (Eq. (41)) for: a) the conventional fixed-bed reactor; b) the "diluted" fixed-bed reactor; and c) the membrane reactor with an optimized thickness of Vycor glass membrane (the dashed line corresponds to a hypothetically higher membrane selectivity, S_M). The range in which the membrane reactor experiments were performed is also indicated. Parameters: $T = 473$ K, $x_{f,C_6H_{12}}^0 = 4.9$ vol%, $p_f = 1$ bar, sweep ratio $\gamma = 20$ (Eq. (36)). The catalyst mass was assumed to be the same as in the membrane reactor experiments in all three cases.

the effective removal of reaction products. Clearly, this then attains the performance of the “diluted” fixed-bed reactor. For intermediate Da numbers there may be a potential for improvement using the membrane reactor. As illustrated in Fig. 12.12 for the concrete system under investigation, this potential is quite small, mainly due to the fact that the selectivity of the applied Vycor glass membrane is relatively low (due to the prevailing Knudsen mechanism). If a membrane with a higher permselectivity were to be used, the benefit window for the membrane reactor could be increased (as shown by the dashed line in Fig. 12.12). This window could also be altered by adjusting the sweep ratio γ , as discussed in Ref. [50]. Increasing γ clearly increases the driving force for transport through the membrane, but this can also be achieved by using on the sweep side a reactive gas that consumes the permeated product of the main reaction. Couplings between dehydrogenation and hydrogenation reactions in membrane reactors have been investigated previously (e.g., Refs. [32, 48, 51]).

From the above it may be concluded that a careful analysis should be performed prior to substituting a fixed-bed reactor by a membrane reactor in order to perform reversible reactions. If conversion is the essential objective function, then a “diluted” fixed-bed reactor might be a simple alternative.

12.6

Example 2: Reactant Dosing with Membranes (“Distributor”)

In the field of chemical reaction engineering considerable efforts are devoted to tackling the problem of limited selectivities with which intermediates can be produced in coupled parallel-series reactions. Typical and important examples are partial oxidations where the formation of undesired side products or total oxidation products significantly reduces process efficiencies. Despite the progress achieved in the field of catalysis, many important industrial reactions still suffer from not satisfying conversion-selectivity relationships [52].

It is well known that in parallel-series reaction networks, optimal local reactant concentrations are essential for a high selectivity towards a certain target product [14, 15]. If undesired consecutive reactions can occur it is usually advantageous to avoid back-mixing, and this is one of the main reasons why partial hydrogenations or oxidations are performed preferentially in tubular reactors. Typically, all reactants enter such reactors together at the reactor inlet (co-feed mode). Thus, in order to influence the reaction rates along the reactor length, essentially the temperature remains as the sole parameter that could be influenced. The realization of defined temperature modulation in a tubular reactor is not straightforward, however. An alternative and attractive possibility which is capable of influencing the course of complex reactions in tubular reactors is to abandon the co-feed mode and to install more complex dosing regimes. It is possible to add one or several of the reactants to the reactor in a locally distributed manner. This concept, which is illustrated in Fig. 12.13, obviously offers a large variety of options that differ mainly in the positions at which one or several components are dosed.

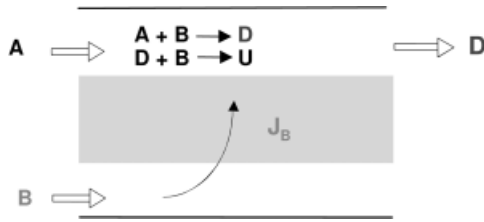
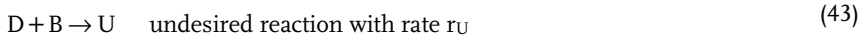
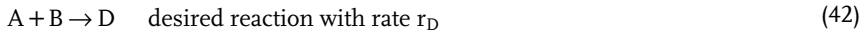


Fig. 12.13. Schematic representation of a membrane reactor aiming to dose one reactant which participates in several reactions of a network.

To answer the question whether a certain dosing strategy is useful requires a detailed knowledge of how the reaction rates depend upon the concentrations. It may therefore be instructive to consider (as in Section 12.2.3) a simple scheme for a desired reaction and an undesired consecutive reaction:



If the rates of these two equations are described by power laws based on the partial pressures:

$$r_D = k_D p_A^\alpha p_B^{\beta_1} \quad (44)$$

$$r_U = k_U p_D^\delta p_B^{\beta_2} \quad (45)$$

for the differential selectivity with respect to D follows:

$$S_D = \frac{r_D - r_U}{r_D} = 1 - \frac{k_U p_D^\delta}{k_D p_A^\alpha} p_B^{\beta_2 - \beta_1} \quad (46)$$

Equation (46) reveals that an improved selectivity S_D can be achieved if:

- (i) a temperature is chosen which minimizes k_U/k_D ;
- (ii) the partial pressure of D is kept low (i.e., low conversion of A and/or a product removal, e.g., with a membrane reactor of the above described extractor type);
- (iii) the partial pressure of A is kept high (i.e., low conversion and no back-mixing, the latter fact obviously favors tubular reactors compared to stirred-tank reactors); and
- (iv) a low (for $\beta_2 > \beta_1$) or high (for $\beta_2 < \beta_1$) partial pressure of B is realized (in the first case a distributed feeding of B is attractive).

Clearly, the distributor type of membrane reactor is focussed on point (iv) above. Systematic theoretical studies explaining in the more detail the significance of reaction orders with regard to the selection of the component that should be dosed are available [53–55].

Besides dosing one or several components at discrete positions into a fixed-bed reactor (Fig. 12.14, top), there exists also the possibility of implementing a continuous distributed feeding over the reactor wall (center). This can be conveniently achieved by applying membranes. Possible extensions of the concept consist of implementing stagewise arrangements, as also illustrated in Fig. 12.14 (bottom).

Several profound theoretical and experimental studies performed on the laboratory scale have been reported which focus on the use of various configurations of membrane reactors as a reactant distributor in order to improve selectivity-conversion performances. In particular, several industrially relevant partial oxidations have been investigated, including the oxidative coupling of methane [56], the oxidative dehydrogenations of propane [57], butane [58], methanol [59, 60], the epoxidation of ethylene [61], and the oxidation of butane to maleic anhydride [62].

12.6.1

Model Reaction, Set-ups and Procedures

As in previous investigations [63, 64], the oxidative dehydrogenation of ethane to ethylene was chosen as a model reaction for an experimental study on the laboratory scale. A $\text{VO}_x/\gamma\text{-Al}_2\text{O}_3$ catalyst with 1.4 % V was used, and prepared using standard techniques described in Ref. [65]. The particle size of the support was 1.8 mm.

Two types of reactors were utilized: 1) a conventional (co-feed) fixed bed reactor; and 2) a tubular membrane reactor. Both reactors were filled with the catalyst particles. A schematic illustration of the configurations used is shown in Fig. 12.15.

A specific feature of the membrane reactor is the fact that a “dead” end configuration regarding the shell side was implemented. This means that all gas

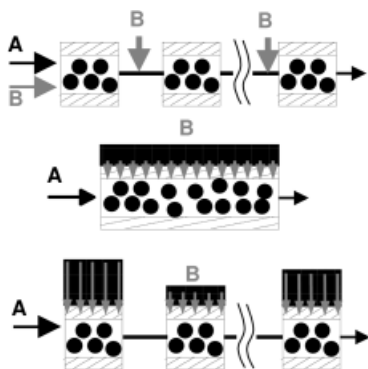


Fig. 12.14. Illustration of possible dosing concepts: top, discrete dosing; center, continuous dosing in a single stage; bottom, continuous dosing in several stages.

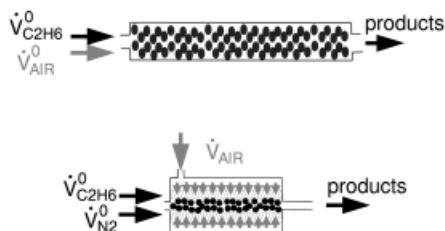


Fig. 12.15. Illustration of the two configurations used in an experimental study of the oxidative dehydrogenation of ethane to ethylene.

supplied to the shell side was forced by convection to enter the tube side. In this way, the amounts dosed could be controlled precisely in the experiments. A tubular ceramic composite membrane was applied consisting of a stable α - Al_2O_3 support (average pore diameter 3 μm), three α - Al_2O_3 layers (pore diameters: 1 μm , 0.2 μm , 60 nm, thicknesses: each 25 μm) and a final γ - Al_2O_3 layer (pore diameter: 6 nm, thickness: 2 μm) (Hermesdorfer Institut für technische Keramik, Germany). The whole tube had a length of 300 mm, and both ends were vitrified, leaving a permeable zone of $L = 60$ mm. Further dimensions were: $d_{\text{inner}} = 7$ mm and $d_{\text{outer}} = 10$ mm. Additional experimental details are provided in Refs. [66, 67].

The performance of the membrane used was investigated in detail [33]. However, as it acts in this study simply as a distributor, and controlled convection is the essential transport mechanism, no specific knowledge is required to predict fluxes. A membrane suitable for the purpose described does not need to possess a special permselectivity.

The operating parameters covered in this study were as follows: $p = 1$ bar, $T = 673\text{--}923$ K, $x_{\text{O}_2}^0 = 0\text{--}0.203$, $x_{\text{C}_2\text{H}_6}^0 = 0\text{--}0.01$, gas hourly space velocity (GHSV): 6000–38 000 h^{-1} . The composition of the effluent was measured under steady-state conditions using GC.

Three types of measurements were performed:

- (i) In preliminary investigations systematic measurements were performed in the fixed-bed reactor under low conversion conditions in order to understand the reaction network and to estimate kinetic parameters.
- (ii) In order to deliver reference data, more fixed-bed reactor experiments were performed at elevated conversion levels.
- (iii) Experiments with the membrane reactor set-up were carried out.

12.6.1

Reaction Rates

For various types of catalyst there are results of kinetic investigations for the oxidative dehydrogenation of ethane available (e.g., for a magnesium oxide catalyst doped with samarium oxide, lithium nitrate and ammonium chloride [64] or a $\text{V}_2\text{O}_5/\gamma\text{-Al}_2\text{O}_3$ catalyst [68]). In another study with a $\text{Sr}_{1.0}\text{La}_{1.0}\text{Nd}_{1.0}\text{O}_x$ catalyst, investigations were reported of noncatalytic reactions, which were found to be significant at temperatures above 700 $^\circ\text{C}$ [69].

By analyzing the experimental data collected over a wide range of operating parameters, the reaction scheme illustrated in Fig. 12.16 was established. By using this scheme it was possible to explain the observations made in the most consistent manner [65].

The five reactions were analyzed using simple power law expression of the type of Eqs. (44) and (45):

$$r_j = k_j p_C^{\alpha_j} p_B^{\beta_j} \quad j = 1, 5 \quad (47)$$

with C being the carbon-containing component. The determined reaction orders of the five reactions with respect to oxygen are also shown in Fig. 12.16 [70]. These orders are rather low, a situation which is in agreement with that reported in Ref. [68]. By applying the arguments given above, and noting that the desired reaction possesses the smallest order with respect to oxygen ($\beta_1 = 0.02$), there should be a potential to dose oxygen over the wall in the membrane reactor compared to the conventional co-feed fixed-bed reactor operation.

12.6.2

Fixed-bed and Membrane Reactor Experiments

A selection of the experimental data obtained is provided in Fig. 12.17. The figure illustrates initially the achieved conversions of ethane as a function of temperature in the fixed-bed reactor, and in the membrane reactor for the highest space velocity investigated (GHSV: 38 000 h⁻¹) and a relatively low oxygen concentration in the dosed gas stream ($X_{O_2}^0 = 0,004$). The slightly higher ethane conversion seen in the membrane reactor compared to the fixed-bed reactor was mainly due to differences in the residence time behavior of ethane (due to the fact that oxygen is only dosed gradually, and there is initially a lower flow rate in the membrane reactor). This effect becomes more pronounced for oxygen-excess conditions [66, 67].

The center section of Fig. 12.17 indicates the expected and observed increases of ethylene selectivity in the membrane reactor. This increase is related to the sequence of reaction orders with respect to oxygen, as was discussed above.

The improvement achievable in such a type of membrane reactor is finally illustrated in the selectivity versus conversion plot. The results show that, for the same catalyst, by simply changing the concentration and residence time

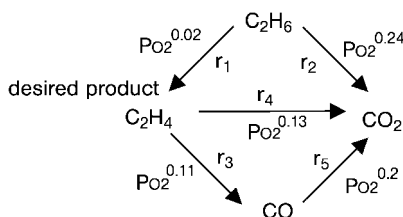


Fig. 12.16. Reaction network of the oxidative dehydrogenation of ethane [65]. Reaction r_1 is the desired reaction. The individual reaction orders with respect to oxygen, determined experimentally, are indicated [70].

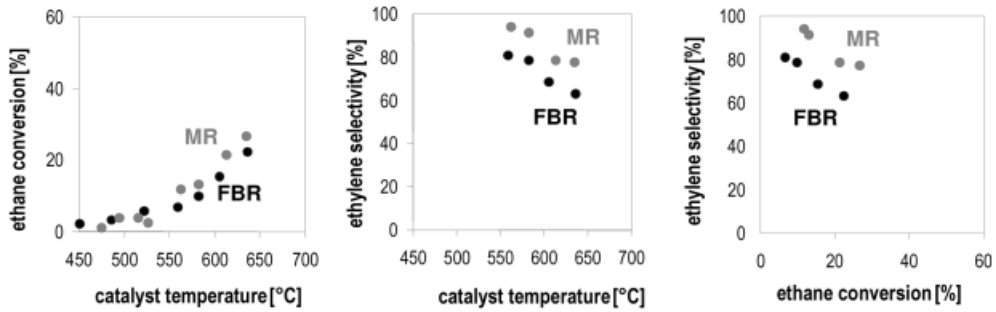


Fig. 12.17. Comparison between experimental results obtained in a conventional (co-feed) fixed-bed reactor (FBR) and in a membrane reactor (MR) where the oxygen was dosed from the shell side over the membrane wall in a dead-end configuration. Conditions: $x_{O_2}^0 = 0.004$; $x_{C_2H_6}^0 = 0.007$; GHSV = 38 000 h⁻¹.

conditions there is a potential to progress further into the “corner of desire”. It should be noted that the results shown in Fig. 12.17 do not represent optimized situations for both reactors.

Additional experimental data not presented here are summarized in Refs. [66, 67]. As was pointed out also in Ref. [64], these results highlight the important point that in membrane reactors, besides differences in local concentration profiles, different residence time distributions occur that lead to specific reactor behavior. Others [71] have also suggested that the flexibility of this type of “distributor” membrane reactors allows a certain target component to be produced efficiently within a complex reaction network. In the present example, there exist certain operating conditions under which the membrane reactor outperforms the conventional reactor in terms of the production of CO or CO₂ (if these are considered as target products instead of ethylene).

12.6.3

Theoretical Analysis

Several profound theoretical studies are available with regard to the “distributor” type of membrane reactor available. A thorough analysis of this situation has been presented in [72]. Later reports [53–55] deliver further instructive insight.

Again, the simple isothermal 1-D plug-flow reactor model provides a good basis for quantitative descriptions. This model allows to explore the potential of using series connections of several membrane reactor segments. The corresponding mass balance for a component i and a segment k can be formulated as follows:

$$\frac{d\dot{n}_i^k}{dz^k} = A_R \sum_{j=1}^M \nu_{ij} r_V + P_R J_i^k \quad i = 1, N \quad k = 1, N_{\text{seg}} \quad (48)$$

In the above equation, P_R represents the perimeter of the tube. For complex reaction networks and transport laws and most boundary conditions, Eq. (48) can be solved only numerically. However, there are several special cases of interest which allow to derive instructive analytical solutions [73, 74].

Provided that the reaction kinetics are known, the available models can be used to determine optimal dosing profiles for single units and for multistage arrangements. Typical results that can be obtained by solving Eq. (48) numerically and applying a sequential quadratic programming (SQP) optimizer are shown in Fig. 12.18 [66].

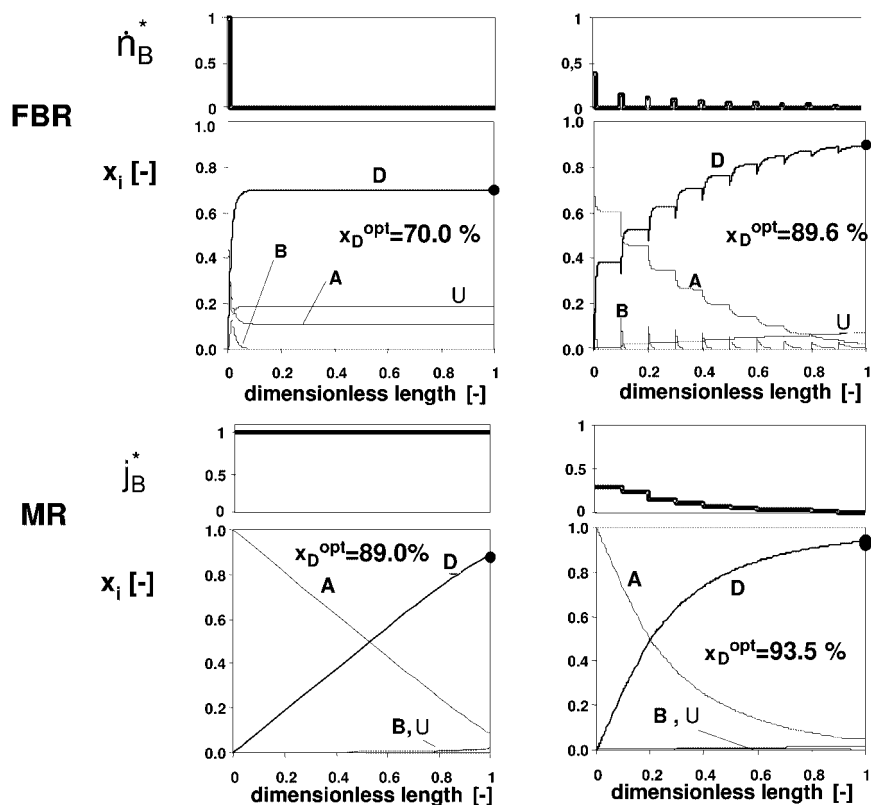


Fig. 12.18. Comparison of the optimized reduced amounts that should be dosed and the corresponding internal compositions for a fixed-bed reactor (discrete dosing, top) and a membrane reactor (continuous dosing, bottom). A triangular network of parallel and series reactions was analyzed using an adapted plug-flow reactor model, Eq. 48. One stage (left) and 10 stages connected in series (right) were considered. All reaction orders were assumed to be 1, except for those with respect to the dosed component in the consecutive and parallel reactions (which were assumed to be 2) [66].

In Fig. 12.18, a comparison is provided between the fixed-bed reactor and the membrane reactor for a conventional triangular reaction network where component B is consumed in all three reactions (e.g., oxygen). For given kinetic parameters in both cases the optimal amount of component B that should be dosed was determined in order to maximize the fraction of the desired component at the reactor outlet, X_D . The figure shows the corresponding axial composition profiles. For the single-stage units there is clearly a significant improvement applying the distributed dosing with regard to the achievable amount of D (an increase from 0.7 to 0.89 compared to the fixed-bed reactor). The results for ten stages are summarized on the left side of the figure. The membrane reactor arrangement is also superior in this situation. It is instructive to note that for this reactor and the conditions studied, there is no significant further improvement between one and ten stages (indicating the attractive feature, that with a low number of stages most of the potential might already be available).

When evaluating these results, the immense importance of reaction rates for the results of such studies should again be highlighted. Indeed, other reaction orders can change the trends discussed here to a significant degree.

12.7

Summary and Conclusions

In the present chapter, only a narrow view of the broad and active field of membrane reactors has been presented. Many important aspects could not be discussed. Finally, a few more points should be shortly mentioned.

One subject not considered above was the large field of membrane bioreactors, despite their frequent and successful use in a variety of industrial processes where soluble catalysts must be retained in the reactor. However, excellent reviews are available on this subject [75–77].

Another area where membrane reactors have now reached the industrial scale is in pervaporation-based hybrid processes using various types of polymer membranes (for an informative review, see Ref. [78]).

Related to the experimental studies performed in our laboratory, in this review packed-bed membrane reactors were discussed. It should be mentioned that there are significant investigational activities devoted to study catalytically active membranes where the catalyst is deposited in either the membrane pores or on the inner or outer surface of the tubes [11]. Another similarly interesting and promising principle is based on using the “Contactor” type of membrane reactors, where the reactants are fed from different sides and react within the membrane [79]. Significant efforts have been made to exploit this principle for heterogeneously catalyzed gas–liquid reactions (three-phase membrane reactors) [80, 81].

Finally, there is intensive and widespread activity on the development of electrochemical membrane reactors. Recent results of these investigations have been presented in [82–86].

In general, there remain many problems which must be solved in order to initiate a broader use of membrane reactors in industry. One critical aspect of this is

related to reactor safety, and in particular possible membrane breakage must be incorporated into design concepts. Currently, more realistic 2-D nonisothermal mathematical models also available [87–90] that could be applied to analyze concrete configurations in more detail. Another issue which until now has been only rarely investigated is that of the dynamics of membrane reactors [91]. Also from the catalytic viewpoint there remains room for significant improvement. Recently, it was emphasized that the optimal catalyst for a membrane reactor might differ significantly from that used in conventional fixed-bed operation [92].

Some conclusions which might be drawn from the concrete results reported in this chapter include:

1. When withdrawing the products of equilibrium-limited reactions, the amounts of sweep gas required must be included in the process evaluation.
2. Highly selective and still sufficiently permeable membranes are required for the efficient use of extractor-type membrane reactors.
3. Dosing profiles in distributor-type membrane reactors should be adjusted carefully in accordance with the reaction rates.
4. A multistage membrane reactor configuration appears to be attractive for the enhancement of yields.

Considering the significant potential for further improvement, the prognosis regarding the development of high-temperature membrane reactors which was suggested in 1996 by Burggraaf and Cot [20] and is shown in Fig. 12.21 appears to be somewhat behind schedule, though still a very realistic evaluation.

Acknowledgments

The author wishes to thank for substantial contributions and excellent cooperation: Dr. A. Tuchlenski, Dr. O. Schramm, Dr. S. Thomas, Dr. F. Klose, Dr. T. Wolff, C. Hamel, M. Joshi, and A. Tota. The numerous discussions with Prof. J. Caro, Dr. R. Dittmeyer and with colleagues in the project “Membrane assisted reaction engineering”, were also extremely enjoyable and helpful. Finally, the financial support of Deutsche Forschungsgemeinschaft, German Ministry of Education and Research, Max-Buchner-Forschungsförderung and Fonds der Chemischen Industrie is gratefully acknowledged.

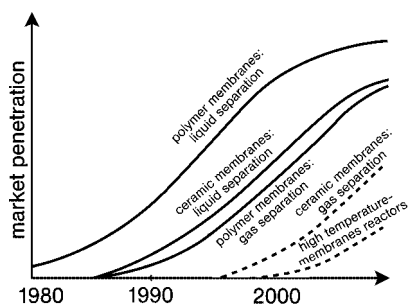


Fig. 12.19. Quantitative scheme of expected market penetration as a function of time for different groups of membrane applications. (Reprinted from Ref. [20], p. 10, Fig. 1.2; copyright 1996, with permission of Elsevier.)

References

1. V. T. Zaspalis, A. J. Burggraaf, *Inorganic membrane reactors to enhance the productivity of chemical processes*, in: *Inorganic membranes: synthesis, characteristics and applications*, Ed. R. R. Bhavé, Reinhold, New York, 1991.
2. H. P. Hsieh, *Catal. Rev.-Sci. Eng.*, **1991**, 33, 1.
3. T. T. Tsotsis, R. G. Minet, A. M. Champagnie, et al., *Catalytic membrane reactors*, in: *Computer aided design of catalysts*, Eds.: E. R. Becker, C. J. Pereira, Marcel-Dekker, New York, 1993.
4. G. Saracco, G. F. Versteeg, W. P. M. van Swaaij, *J. Membrane Sci.*, **1994**, 95, 105.
5. J. N. Amor, *Catalysis Today*, **1995**, 25, 2129.
6. H. P. Hsieh, *Inorganic membranes for separation and reaction*, Vol. 3, Membrane Science and Technology, Elsevier, Amsterdam, 1996.
7. G. Saracco, H. W. J. P. Neomagnus, G. F. Versteeg, et al., *Chem. Eng. Sci.*, **1999**, 54, 1997.
8. J. A. Dalmon, *Catalysis in membrane reactors*, in: *Handbook of heterogeneous catalysis*, Eds.: G. Ertl, H. Knözinger, J. Weitkamp, Wiley-VCH, Weinheim, Chapter 9.3, 1997.
9. A. G. Dixon, *Innovations in inorganic catalytic membrane reactors*, in: *Specialist periodical reports: Catalysis*, Vol. 14, Ed.: J. J. Spivey, Royal Society of Chemistry, London, 1999, 40.
10. R. Dittmeyer, V. Höllein, K. Daub, *J. Molecular Catalysis A: Chemical*, **2001**, 173, 135.
11. J. G. Sanchez Marcano, T. T. Tsotsis, *Catalytic membranes and membrane reactors*, Wiley-VCH, Weinheim, 2002.
12. A. G. Dixon, *Int. J. Chem. Reactor Engng.*, **2003**, 1, Review R6.
13. *Proceedings of the International Congresses on Catalysis in Membrane Reactors (ICCMR)*: 1) Villeurbanne (1994); 2) Moscow (1996); 3) Copenhagen (1998); 4) Zaragoza (Catalysis Today, 2000, 56); 5) Dalian (Catalysis Today, 2003, 82); 6) Lahnstein (Catalysis Today, 2005, in preparation).
14. O. Levenspiel, *Chemical Reaction Engineering*, 3rd edn., Wiley, New York, 1999.
15. H. S. Fogler, *Elements of chemical reaction engineering*, 3rd edn., Prentice-Hall, Upper Saddle River, New Jersey, 1999.
16. G. Eigenberger, *Catalytic fixed-bed reactors*, in: *Handbook of heterogeneous catalysis*, Eds.: G. Ertl, H. Knözinger, J. Weitkamp, Vol. 3, Wiley-VCH, Weinheim, 1997.
17. R. Mezaki, H. Inoue, *Rate equations of solid-catalyzed reactions*. University of Tokyo Press, 1991.
18. J. M. Berty, *Experiments in catalytic reaction engineering*, Elsevier, Amsterdam, 1999.
19. R. R. Bhavé, Ed., *Inorganic membranes: synthesis, characteristics and applications*, Reinhold, New York, 1991.
20. A. J. Burggraaf, L. Cot, Eds., *Fundamentals of inorganic membrane science and technology*, Elsevier, 1996.
21. H. Verweij, *J. Mater. Science*, **2003**, 38, 4677.
22. A. Julbe, D. Farrusseng, C. Guizard, *J. Membrane Sci.*, **2001**, 181, 3.
23. R. M. de Vos, H. Verweij, *Science*, **1998**, 279, 1710.
24. H. J. M. Bouwmeester, *Catalysis Today*, **2003**, 82, 141.
25. *Proceedings of the International Conferences on Inorganic Membranes (ICIM)*: ICIM-7 (Dalian, 2002), ICIM-8 (Cincinnati, 2004).
26. B. B. Bird, W. E. Stewart, E. N. Lightfoot, *Transport phenomena*, Wiley, New York, 2002.
27. J. A. Wesselingh, R. Krishna, *Mass transfer in multicomponent mixtures*, Delft University Press, 2000.
28. R. Krishna, *Chem. Eng. Sci.*, **1993**, 48, 845.
29. E. A. Mason, A. P. Malinauskas, *Gas transport in porous media*:

- The Dusty Gas Model*, Elsevier, Amsterdam, 1983.
30. A. Tuchlenski, P. Uchytel, A. Seidel-Morgenstern, *J. Membrane Sci.*, **1998**, 140, 165.
 31. F. Sahimi, *Flow and transport in porous media and fractured rock: from classical methods to modern approaches*, VCH, Weinheim, 1995.
 32. O. Schramm, A. Seidel-Morgenstern, *Chem. Eng. Sci.*, **1999**, 54, 1447.
 33. S. Thomas, R. Schäfer, J. Caro, A. Seidel-Morgenstern, *Catalysis Today*, **2001**, 68, 205.
 34. P. Uchytel, O. Schramm, A. Seidel-Morgenstern, *J. Membrane Sci.*, **2000**, 170, 215.
 35. J. M. van de Graaf, M. Zwiep, F. Kapteijn, et al., *Appl. Catal. A: General*, **1999**, 178, 225.
 36. P. B. Weisz, *CHEMTECH*, **1992**, July, 424.
 37. W. C. Pfefferle, U.S. Patent App. 3290406, 1966.
 38. V. M. Gryaznov, *Platinum Met. Rev.*, **1986**, 30, 68.
 39. E. Kikuchi, *CATTECH*, **1997**, 67.
 40. N. Itoh, Y. Shindo, K. Haraya, et al., *J. Chem. Eng. Japan*, **1988**, 21, 399.
 41. A. M. Champagnie, T. T. Tsotsis, R. G. Minet, et al., *Chem. Eng. Sci.*, **1990**, 45, 2423.
 42. Z. D. Ziaka, R. G. Minet, T. T. Tsotsis, *J. Membrane Sci.*, **1993**, 77, 221.
 43. R. Schäfer, M. Noack, P. Kölsch, et al., *Catalysis Today*, **2003**, 82, 15.
 44. V. T. Zaspalis, W. van Praag, K. Keizer, et al., *Appl. Cat.*, **1991**, 74, 223.
 45. B. K. Abdalla, S. S. Elnashaie, *J. Membrane Sci.*, **1993**, 85, 229.
 46. R. Dittmeyer, V. Höllein, P. Quicker, et al., *Chem. Eng. Sci.*, **1999**, 54, 1431.
 47. A. Tuchlenski, *Charakterisierung poröser Membranen und ihre Charakterisierung in Membranreaktoren*, Logos Verlag Berlin, 1998 (ISBN 3-89722-145-4) and Ph.D. thesis (1998, Otto-von-Guericke-Universität Magdeburg)
 48. O. Schramm, *Zur Durchführung reversibler Reaktionen in Membranreaktoren*, Logos Verlag Berlin, 2000 (ISBN 3-89722-412-7) and Ph.D. thesis (2000, Otto-von-Guericke-Universität Magdeburg)
 49. C. M. Reo, L. A. Bernstein, C. R. F. Lund, *Chem. Eng. Sci.*, **1997**, 52, 3075.
 50. C. M. Reo, L. A. Bernstein, C. R. F. Lund, *AIChE J.*, **1997**, 43, 495.
 51. E. Gobina, R. Hughes, *Chem. Eng. Sci.*, **1996**, 51, 3045.
 52. B. K. Hodnett, *Heterogeneous Catalytic Oxidation: Fundamental and Technological Aspects of the Selective and Total Oxidation of Organic Compounds*; John Wiley & Sons, 2000.
 53. Y. L. Lu, A. G. Dixon, W. R. Moder, et al., *Chem. Eng. Sci.* **1997**, 52, 1349.
 54. Y. L. Lu, A. G. Dixon, W. R. Moder, et al., *Catalysis Today*, **1997**, 35, 443.
 55. Y. L. Lu, A. G. Dixon, W. R. Moder, et al., *Ind. Eng. Chem. Res.*, **1997**, 36, 559.
 56. J. Coronas, M. Menendez, J. Santamaria, *Chem. Eng. Sci.*, **1994**, 49, 2015.
 57. M. J. Alfonso, A. Julbe, D. Farrusseng, et al., *Chem. Eng. Sci.*, **1999**, 54, 1265.
 58. C. Tellez, M. Menendez, J. Santamaria, *AIChE J.*, **1997**, 43, 777.
 59. V. Diakov, A. Varma, *Chem. Eng. Sci.*, **2003**, 58, 801.
 60. V. Diakov, A. Varma, *Ind. Eng. Chem. Res.*, **2004**, 43, 309.
 61. M. A. Al-Juaied, D. Lafarga, A. Varma, *Chem. Eng. Sci.*, **2001**, 56, 395.
 62. R. Mallada, M. Menendez, J. Santamaria, *Catal. Today*, **2000**, 56, 191.
 63. J. Coronas, M. Menendez, J. Santamaria, *Ind. Eng. Chem. Res.*, **1995**, 34, 4229.
 64. A. L. Y. Tonkovich, J. L. Zilka, D. M. Jimenez, et al., *Chem. Eng. Sci.*, **1996**, 51, 789.
 65. F. Klose, M. Joshi, C. Hamel, et al., *Appl. Cat. A*, **2004**, 260, 101.
 66. S. Thomas, *Kontrollierte Eduktzufuhr in Membranreaktoren zur Optimierung der Ausbeute gewünschter Produkte in Folge- und Parallelreaktionen*, Logos Verlag Berlin, 2004 (ISBN 3-8325-0535-0) and Ph.D. thesis (2003,

- Otto-von-Guericke-Universität
Magdeburg)
67. F. Klose, T. Wolff, S. Thomas, et al., *Catalysis Today*, **2003**, 82, 25.
 68. T. Waku, M. D. Argyle, A. T. Bell, et al., *Ind. Eng. Chem. Res.*, **2003**, 42, 5462.
 69. S. A. R. Mulla, O. V. Buyevskaya, M. Baerns, *Applied Cat. A: General*, **2002**, 2226, 73.
 70. A. Tota, C. Hamel, S. Thomas, et al., *Transactions Inst. Chem. Eng., Chem. Eng. Res. and Design*, **2004**, 82, 236.
 71. F. Klose, T. Wolff, S. Thomas, et al., *Appl. Cat. A*, **2004**, 257, 193.
 72. M. P. Harold, V. T. Zaspalis, K. Keizer, et al., *Chem. Eng. Sci.*, **1993**, 48, 2705.
 73. C. Hamel, S. Thomas, K. Schädlich, et al., *Chem. Eng. Sci.*, **2003**, 58, 4483.
 74. S. Thomas, S. Pushpavanam, A. Seidel-Morgenstern, *Ind. Eng. Chem. Res.*, **2004**, 43, 969.
 75. M. Cheyran, A. Mehaaia, *Membrane Bioreactors*, in: W. C. McGregor, Ed., *Membrane Separation in Biotechnology*, Marcel Dekker, New York, 1986, p. 255.
 76. U. Kragl, D. Gyax, O. Ghisalba, et al., *Angew. Chem. Int. Ed. Engl.*, **1991**, 30, 827.
 77. U. Kragl, C. Dreisbach, *Membrane Reactors in Homogeneous Catalysis*, in: B. Cornils, W. A. Herrmann, Eds., *Applied Homogeneous Catalysis with Organometallic Compounds*, 2nd edn., Wiley-VCH Weinheim, 2002, p. 941.
 78. F. Lipnitski, R. F. Field, P.-K. Ten, *J. Membrane Sci.*, **1999**, 153, 183.
 79. S. Miachon, V. Perz, G. Crehan, et al., *Catal. Today*, **2003**, 82, 75.
 80. R. Dittmeyer, M. Reif, *Catalysis Today*, **2003**, 82, 3.
 81. M. Vospernik, A. Pintar, G. Bercic, et al., *J. Membrane Sci.*, **2003**, 223, 157.
 82. P. N. Dyer, R. E. Richards, S. L. Russek, et al., *Solid State Ionics*, **2000**, 134, 21.
 83. M. Stoukides, *Catal. Rev.-Eng.*, **2000**, 42, 1.
 84. F. T. Akin, Y. S. Lin, *AIChE J.*, **2002**, 48, 2298.
 85. H. Wang, Y. Cong, W. Yang, *Catalysis Today*, **2003**, 82, 157.
 86. Y. Ye, L. Rihko-Struckmann, B. Munder, et al., *Ind. Eng. Chem. Res.*, **2004**, 43, 4551.
 87. K. Hou, R. Hughes, R. Ramos, et al., *Chem. Eng. Sci.*, **2001**, 56, 57.
 88. A. G. Dixon, *Catal. Today*, **2001**, 67, 189.
 89. U. Kürten, M. van Sint Annaland, J. A. M. Kuipers, *Ind. Eng. Chem. Res.*, **2004**, 43, 4753.
 90. U. Kürten, M. van Sint Annaland, J. A. M. Kuipers, *Int. J. Chem. Reactor Engng.*, **2004**, 2, Review A24.
 91. V. Diakov, A. Varma, *Chem. Eng. Sci.*, **2002**, 57, 1099.
 92. S. Miachon, J. A. Dalmon, *Topics in Catalysis*, **2004**, 29, 59.

Part III

Integration of Mechanical Operations and Chemical Reactions

13

Reactive Extrusion for Solvent-Free Processing: Facts and Fantasies

Leon P. B. M. Janssen

Abstract

Reactive extrusion has emerged from a scientific curiosity to an industrial process. Various types of extruders can be used, all with their specific advantages and disadvantages. Further development suffers from lack of kinetic and rheological data at high conversions and from uncertainties about heat transfer and reactor stability. Nonlinear effects in the process can give rise to instabilities that are of thermal, hydrodynamical or chemical origin.

13.1

Introduction

The possibility of using an extruder as a polymerization reactor was recognized as early as 1950, when Stober and Amos filed a patent for the Dow Chemical Company [1] describing the use of a single-screw extruder as a main polymerizing device. Following a pre-polymerization stage in a stirred-tank reactor with a residence time of 90 hours, a screw conveyor was used as a polymerization reactor in which a residence time of 18 hours was necessary for the thermal polymerization of styrene. The first polymerizations described in the open literature were the polymerization of nylon [2] and several polycondensation reactions (e.g., Ref. [3]). The first theoretical considerations concerning reactive extrusions appeared during the mid-1970s, when Meyuhas et al. [4] stated that an extruder is a good plug-flow reactor for viscous materials, though some distribution in molecular weight of the polymer formed could not be prevented. In this study, a pre-polymerization is advised to avoid low viscous material to be fed to the extruder. Much later [5], it was shown that this also adds greatly to the stability of the reactive extrusion process. Pioneering studies were conducted by Mack and Herter [6], who proposed twin-screw technology for reactive extrusion because of difficulties in scaling up single-screw extruders, that could be avoided in twin-screw extruders. Residence times of half an hour were possible in self-wiping, twin-screw machines.

During the past few decades, the mechanisms for reactive extrusion have become much better understood, and the residence times needed for complete conversion have come within reasonable limits. A large variety of polymerization reactions have been investigated in different types of extruders, and reactive extrusion has been implemented on an industrial scale [7].

13.2

Advantages and Disadvantages

Due to its specific properties, the extruder has certain advantages as a reactor for polymerization and modification reactions:

- The extruder is a stable pump for highly viscous media; this guarantees a constant throughput, which is vital for its operation as a continuous reactor.
- No solvent (or only a small amount) has to be used in an extruder-polymerization process; therefore no expensive extra separation steps are needed. Due to the absence of volatile solvents the process is also more environmentally friendly, which is important as legislation is expected to increase strongly in this area.
- The process is continuous.
- The mixing can be adjusted to the requirements by using a judicious screw design.
- Devolatilization of the reaction product in the extruder makes it possible to remove and recycle unreacted components.

However, there are also certain restrictions to the use of extruders as polymerization reactors, and also to the type of extruder that can be used:

- As the extruder is a reactor with a relatively expensive volume, the residence time needed for the reaction should be short. Therefore, the reaction kinetics must be sufficiently fast to acquire an economically feasible process.
- There is a limitation to the reactions that can be performed in extruders based on the heat of reaction and the viscosity reached. If the reaction enthalpy is very large, the temperature rise in the extruder is too large to control. Moreover, the viscosity of the reaction product must be sufficiently high to be able to obtain a stable transport of the material and to make the use of an extruder profitable.
- On scaling-up the equipment, the surface-to-volume ratio decreases, which limits the heat removal in production machines. Moreover, in production-size machines thermal inhomogeneities may occur that do not exist in laboratory equipment. This requires a careful design of the experiments on laboratory scale in order to assure a reliable scale-up procedure.
- Due to the large viscosity changes that arise during most polymerizations, instabilities may occur, resulting in very low conversions or fluctuating throughput. These instabilities can be dependent on the scale of the equipment, and therefore they pose extra restrictions to the scaling up of the process.

13.3

Main Reactions in Extruders

Reactions involving polymers which have been performed in extruders can generally be divided into five categories [8], as indicated in Tab. 13.1.

From a processing point of view, all reactions can be divided into two main groups: single component and multi-component.

Single-component reactions can occur throughout the bulk of the material. At the start of the reaction only one single component, monomer or prepolymer, is present or the components used are well miscible and premixed. For this group of reactions the temperature of the mixture plays an important role, as well as macro-mixing over the length of the extruder, which is related to the residence time distribution. Both parameters determine the progress of the reaction.

Multi-component reactions, on the other hand, occur predominantly between immiscible components. Because the reaction proceeds mainly at the interface between the components, micro-mixing plays an important role. Normally, this type of reaction becomes diffusion-limited as the reaction progresses due to the build-up of reaction products at the interface between the components. To overcome this diffusion limitation, extensive micro-mixing is necessary. In addition to micro-mixing, these reactions are, of course, also influenced by temperature and macro-mixing.

Table 13.1. Reactions performed in extruders.

Type of polymerization	End product
Step polymerization (condensation reactions)	polyetheramide, polyesters, polyethylterephthalate (PET), polybutylterephthalate (PBT), polyamide 6.6, polyarylate, polyurethanes, polyamide 6
Chain polymerization (addition reactions)	polyoxymethylene, polymethyl methacrylate (PMMA), acrylic polymers, polystyrene and styrene copolymers, water-soluble polyamide
Graft reactions and functionalization reactions	Graft copolymer of polystyrene and maleic anhydride graft copolymer of polyolefines and vinylsilanes graft copolymers of polyolefines and (meth)acrylic monomers, graft copolymer of EVA with acrylic acid graft copolymer of polyolefines and maleic anhydride halogenation of polyolefines or EVA
Interchain copolymer formation	Copolymers of reactive polystyrene and polymers with amide, mercaptan, epoxy, hydroxy, anhydride or carboxylic acid groups, copolymer of polypropylene grafted with maleic anhydride and nylon-6, copolymer of polyolefines and polystyrene, copolymer of EVA grafted with methacrylates and grafted polystyrene
Coupling reactions	Coupling of PBT with diisocyanate and polyepoxide or polycarbodiimide, coupling of PET with bis(2-oxazoline)
Degradation reactions	Degradation of polypropylene by shear-heating, degradation of PET with ethylene glycol

13.4

Extruder Types

Although there exists a variety of different types of extruders, a main division can be made between single-screw and twin-screw forms. The transport mechanism is the most important difference between those two types of machine. A single-screw extruder consists of one screw rotating in a closely fitting barrel; the transport mechanism is based on friction between the polymer and the walls of the channel. If the polymer slips at the barrel wall, it is easy to envisage that the material will rotate with the screw, but without being pushed forward. This makes this type of machines strongly dependent on the frictional forces at the wall and the properties of the material processed. Generally, these machines are less suitable for reactive extrusion processes where large viscosity differences occur. An exception to this is the co-kneader, in which the screw consists of elements with interrupted flights and rotates in a barrel with stationary pins. Due to the rotation and a superimposed axial oscillation, a good mixing action is achieved.

All twin-screw extruders consist of two screws, placed in an 8-shaped barrel. In the case of intermeshing extruders, the flights of one screw sticks in the channel of the other screw. Because of this, the polymer cannot rotate with the screw, irrespective of the rheological characteristics of the material. This indicates the most important advantage of intermeshing twin screw-extruders – that the transport action depends on the characteristics of the material to a much lesser degree than in the case of a single-screw extruder. There are various ways of classifying extruders, and the main types are shown diagrammatically in Fig. 13.1.

- The single screw extruder (a) is most common in polymer processing. Its working characteristics are strongly dependent on the material properties. In reactive extrusion single-screw extruders can only be used if the viscosity changes of the material are limited and if there are no strong requirements to micro-mixing.
- Co-kneaders (b) have one single screw, whilst the barrel is equipped with kneading pins. The screw rotates and oscillates, giving a very good mixing action. The pins can also be used for monitoring the temperature, or as injection points. Moreover, the pins prevent the material from rotating with the screw and therefore ensure a more stable operation than can be provided in an ordinary single-screw extruder. Pressure build-up is rather poor in this type of machine.
- Tangential twin-screw extruders (c and d) are not closely intermeshing; they can be envisaged as a parallel connection of two single-screw extruders with mutual interaction. The screws can be arranged in two different ways, a mixing mode (c) or a transport mode (d). All commercial tangential twin screw-extruders are counter-rotating. This type of machine is particularly popular in the USA for modification reactions.
- The closely intermeshing twin-screw extruders, both counter-rotating (e) and co-rotating (f), can best be modeled as series of C-shaped chambers. Due to the rotation of the screws these chambers transport the material from hopper to die, while interactions between the chambers occur via leakage flows. Due to the large resistance to back-flow through the narrow gaps, these extruders possess a

strong positive conveying character and their process stability in reactive extrusion is large.

- The screws and the barrel of closely intermeshing twin-screw extruders can also be conical (g). This has advantages for the feeding process if the material has a low bulk density. While passing through the extruder the chambers gradually decrease in size and compress the material. Moreover, conical screws provide a larger space for the bearings of the screws, and they can easily be removed from the barrel.
- Self-cleaning, co-rotating, twin-screw extruders (h) are very popular for reactive extrusion, and they generally have modular screws with different types of mixing elements. This provides a large flexibility in screw design. They rotate at high speed and are able to provide intensive micro-mixing at large throughput. To ensure sufficient residence times in reactive extrusion, the screws are generally quite long (L/D ratio = 30 to 40).

If a twin-screw extruder is stopped and opened, several zones can be clearly distinguished [9]. Depending on whether the extruder is fed with a solid or a liquid material, two different situations occur. In the case of a solid feed (a polymer or solid monomer), the channels near the feed hopper are more or less filled with solids. This material melts, resulting in a zone where the channels are only partly filled. At the end of the screw, close to the die, a zone exists where the channels are completely filled with polymer. If the extruder is fed with a liquid monomer, the first part does not necessarily need to be partly empty but, as will be explained later, for reasons of stability it is advisable to create a zone where the channels are not fully filled. In particular, the fully filled zone is very important for correct functioning of the extruder. In this zone the pressure is built up, the mixing and kneading mainly

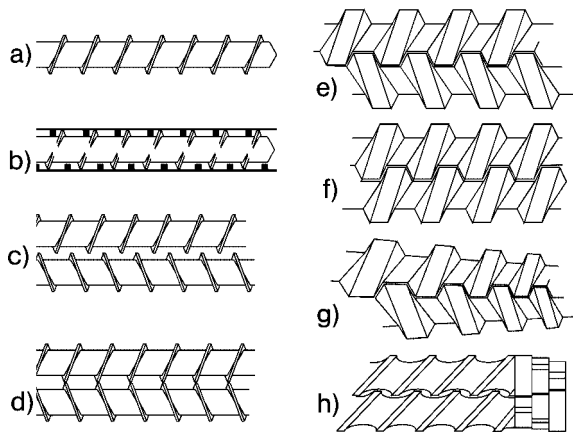


Fig. 13.1. Different types of extruders. a) single screw; b) co-kneader; c) non-intermeshing, mixing mode; d) non-intermeshing, transport mode; e) counter-rotating, closely intermeshing; f) co-rotating, closely intermeshing; g) conical counter-rotating; h) self-wiping, co-rotating.

takes place, and the major influence of viscous dissipation also occurs. In order to explain the existence of the fully filled zone, it must be realized that the different zones in a twin-screw extruder cannot be viewed separately, but are interconnected. The throughput of a twin-screw extruder is determined by the feeding zone. Because the channels are only partially filled no pressure can be built up in this zone, and the hydrodynamics will be limited to drag flow only. Under normal circumstances, the throughput of this zone is therefore independent of pressure at the die end of the extruder. In the last part of the extruder, where the pressure required to squeeze the polymer through the die is built up, a pressure gradient is present and considerable back-flow will occur.

A fixed pressure is built up at the die of the extruder, which depends only on throughput, viscosity and die geometry. With a given screw geometry the pressure gradient in the screw is fixed; therefore, within reason, there will be a point in the extruder at which the actual pressure becomes zero (Fig. 13.2). Between this point and the die there is a pressure gradient, and this will result in a back-flow and the channels being completely filled with polymer. Between this point and the feed hopper, there is no pressure gradient and the channel is only partly filled with material. For good processing, the length of the completely filled zone is one of the most important factors, while for good process control, knowledge of the different parameters that influence the length of the completely filled zone is indispensable. Details of these influence are shown schematically in Tab. 13.2. If, for example, in an iso-viscous situation the resistance of the die is doubled, the pressure in front of the die will also double, because the output remains constant. However, the leakage flow is not influenced by the die pressure, so that the pressure gradient in the extruder remains constant. Ergo, the completely filled length increases, as indicated in Fig. 13.2(b). If the viscosity is not constant, as in reactive extrusion, the ability to build up pressure is proportional to the viscosity. If a monomer is polymerized by reactive extrusion, hardly any pressure can be built up in the region where conversion is low. Small fluctuations in die pressure result in large fluctuations in filled length, which requires for an appreciable buffer zone where the channel is not fully filled with material.

13.5

Kinetic Considerations

In order to describe reactive extrusion it is important to understand the kinetics in all stadia of the reactions, from diluted solutions to concentrated melts. Unfortunately, most of the kinetic experiments which have been reported are performed only in strongly diluted systems, whereas in extrusion polymerization the polymer concentration changes in time between zero and approximately 100 %. This implies that for the first stage of the polymerization reaction, where the polymer forms a diluted solution in its monomer conventional kinetics can be used. The second stage of the reaction occurs when the polymer molecules interact with each other and entangle. At this stage the kinetics is still fairly conventional, although the viscosity increases dramatically with the progress of the reaction. The third stage, which is much less documented, is reached when the conversion passes a certain critical

Table 13.2. Influence of extrusion parameters on the filled length.

Influence of:	Q	P	ΣQ_I	dp/dx	filled length
die resistance	0	+	0	0	+
rotation speed	+	+	+	+	0
filling degree	+	+	–	–	++
wall temperature	0	0	0	–	+
die temperature	0	–	0	0	–
gap size	0	0	0	–	+

point. During polymerization the reaction system has become increasingly viscous, and this leads to a limitation in the mobility of the polymer chains. In chain radical-polymerization the consequence is that at these high viscosity levels the termination reaction is controlled by diffusion, and this results in a reduced termination constant. On the other hand, because the diffusion of the small monomer molecules is not restricted until very high conversions are reached, the propagation rate does not decrease significantly. Due to the reduced termination velocity the amount of active polymer radicals increases, which results in an abrupt rise in the propagation velocity and of the momentary degree of polymerization (Fig. 13.3) [10]. This phenomenon is known as the “Trommsdorff effect” or “gel effect” [11, 12] and results in a higher molecular weight and higher conversion than would be expected from conventional kinetics.

Another complication, which generally is not encountered in conventional solution polymerization, is the occurrence of a ceiling temperature. Many polymer-

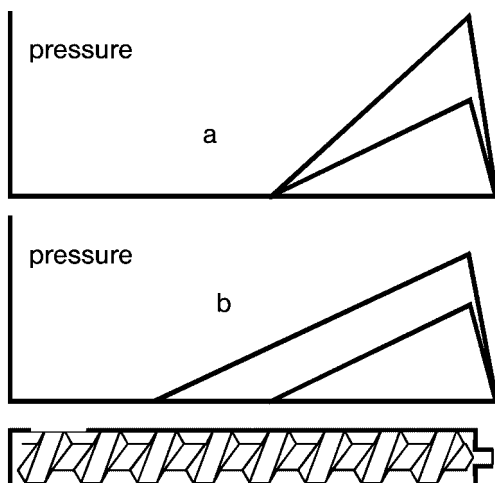


Fig. 13.2. Pressure build up. a) Changing rotational speed; b) changing die resistance.

izations are equilibrium reactions that shift towards increased monomer concentrations at higher temperatures. Dainton and Ivin [13] first established that above a certain temperature depropagation may occur, and that this may lead to an appreciable decrease in final conversion. The temperature, where propagation and depropagation are in equilibrium is referred to as the “ceiling temperature”, T_c , and it follows from the Gibbs energy equation:

$$\Delta G = \Delta H_p - T\Delta S_p$$

where ΔG is the Gibbs free energy, ΔH_p the polymerization enthalpy, ΔS_p the polymerization entropy and T the absolute temperature. Only if ΔG for the polymerization is less than zero the reaction can take place. The temperature at which ΔG equals zero is termed the ceiling temperature, and for a polymer–monomer mixture this can be written as:

$$T_c = \frac{\Delta H_p}{\Delta S_p} = \frac{\Delta H_p}{\Delta S_p^0 + R \cdot \ln\left(\frac{[M]}{[M]^0}\right)}$$

where ΔS_p^0 is the polymerization entropy at the monomer concentration $[M]^0$ and R the gas constant. Generally, for polymers, ΔH_p and ΔS_p have negative values. This means that the higher the conversion, the lower the monomer concentration and consequently the lower the ceiling temperature. For pure methylmethacrylate the ceiling temperature is 220 °C [14] and the polymerization enthalpy is $-55.5 \text{ kJ mol}^{-1}$ at 74.5 °C. Ceiling temperatures of similar materials can be derived because the

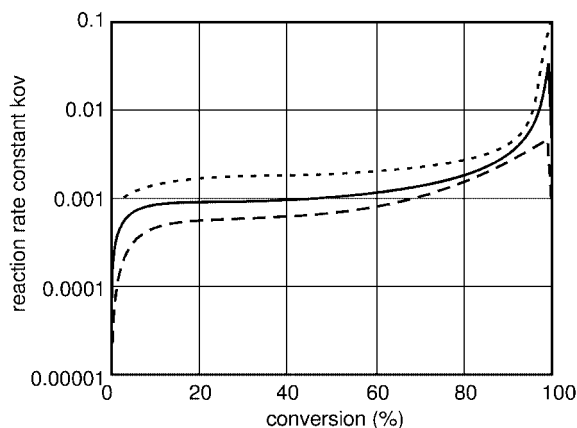


Fig. 13.3. Reaction rate constant for *n*-butyl methacrylate at three different temperatures (110, 120 and 130 °C).

standard molar entropy for the polymerization of liquid monomer to condensed amorphous polymer is virtually independent of the constitution in the case of compounds with olefinic double bonds [15]. Differences in ceiling temperature are therefore generally caused by polymerization enthalpy only.

13.6

Heat Transfer and Thermal Instabilities

The most important heat resistance in extrusion occurs between the polymer and the barrel wall. The oldest model for this heat transfer is based on the theory of a scraped heat exchanger, and was suggested in 1953 by Jephson [16]. In this mechanistic model the extruder is considered as a scraped heat exchanger, where the passing screw flight acts as scraper. After a flight has passed, a layer of fresh polymer is deposited against the barrel wall, and penetration of heat into this layer occurs, forming a thermal boundary layer. This model leads to an expression for the heat transfer coefficient:

$$\langle \alpha \rangle = \frac{1}{t_e} \int_0^{t_e} \alpha dt = \sqrt{\frac{4}{3}} \lambda \rho C_p m N$$

or, in terms of dimensionless numbers:

$$\frac{\langle \alpha \rangle D}{\lambda} = 1.15 \sqrt{\frac{D^2}{at_e}} \quad \text{or:} \quad \langle Nu \rangle = 1.15 \cdot \langle Fo_{rot} \rangle^{-1/2}$$

where Fo_{rot} is the Fourier number related to the revolution time

The heat transfer coefficient according to Jephson is proportional to the rotational speed, to the square root of the number of screw flights and is independent of viscosity and screw diameter.

An alternative heat transfer model was published by Todd [17], based on a correlation of heat transfer data over a Reynold's number range from 10^{-3} to 10:

$$\langle Nu \rangle = 0.94 Re^{0.28} Pr^{0.33} (\mu_b / \mu_w)^{0.14}$$

where μ_b and μ_w represent the viscosities in the bulk and at the wall, respectively. The heat transfer coefficient according to Todd is much less dependent on rotational speed ($N^{0.28}$) than the Jephson model, is approximately inversely proportional to the square-root of the diameter ($D^{-0.44}$), and depends only slightly on bulk viscosity ($\mu_b^{0.05}$). The dependence on the number of screw flights is not given. Both expressions lead to a heat transfer coefficient that varies for practical situations between 300 and 700 W m⁻²K.

A special complication is formed by thermal inhomogeneities. The polymer follows a circular path in the cross-channel direction, which implies that only a certain amount of polymer passes the thermal boundary layer where it is cooled directly. Therefore, for deep cut channels the heat of reaction in the middle of the channel is difficult to remove. Janeschitz Kriegl [18] compared the thickness of the thermal boundary layer with the channel depth, and identified a criterion for thermal homogeneity in a single-screw extruder. This can be adapted to twin-screw extruders with m thread starts per screw. It may be concluded that thermal inhomogeneities become important if:

$$\frac{mNH^2}{a} > 150$$

where N is the rotational speed, H is the channel depth, and a is the thermal diffusivity. It can also be seen that thermal inhomogeneities increase strongly for larger scale extruders, where the channels are deeper cut. This is especially the case for continuous channels, for example in self-wiping, co-rotating machines operating with materials with a large heat of reaction. Local high temperatures can reduce the conversion considerably due to a ceiling temperature. Moreover, a reliable scale-up, in terms of thermal homogeneity is only possible if at regular intervals mixing elements are used to homogenize the radial temperature differences.

If the overall temperature rise is too large to be accepted, some classical solutions can also be applied to reactive extrusion:

- Part of the polymer formed may be fed back and mixed with or desolved into the monomer. This will decrease the heat of reaction per unit throughput. An extra advantage of desolving some polymer into the monomer is the viscosity rise at the feed end of the extruder, which stabilizes the process.
- If an inert material has to be added this also decreases the reaction heat per kilogram throughput.
- Devolatilization of part of the monomer (or of an inert material) will decrease the effective heat by the phase change enthalpy of the volatiles removed.
- Several side feeds of deep cooled monomer will lower the base temperature to which the adiabatic temperature rise has to be added. A fraction of the monomer is fed at the beginning of the extruder and has to be heated to the starting temperature of the reaction; hence successive side feeds can be metered at much lower temperatures.

13.7

Instabilities

The large variations in viscosity during reactive extrusion can lead to process instabilities as a result of competition between die effects and pressure build-up abilities of the screws. In general, two stable working points can be distinguished – one at low conversion with a short, fully filled length, and one at high conversion with a

long, fully filled length. Figure 13.4 illustrates a sudden drop in conversion for a radical styrene polymerization if the die resistance decreases below a certain value [19].

In the transition region between the two stable working points, severe oscillations in throughput and conversion may occur [20] (Fig. 13.5). These oscillations can be explained by assuming an initial situation where the reaction comes to completion in the vicinity of the die, thereby resulting in a high local viscosity at the die and a lower viscosity in the rest of the extruder. Due to the resultant low throughput, the extruder fills itself while the reaction proceeds; the viscosity continues to build up until the extruder is capable of emptying itself. The resulting short residence time after this period leads again to low viscosities in the extruder and a higher viscosity in the melt. A more stable operation can be achieved if a certain amount of high-viscosity material is permanently present at the end of the screws, thereby assuring a good pumping ability at all times. The same conclusions follow from a more rigid mathematical derivation of the stability regions [21].

Instabilities, resulting in a sudden transition from an operating mode with high conversions to low conversion, vice versa, or in severe oscillations during the process can have three possible sources of instabilities: of thermal origin; of hydrodynamic origin; and of chemical origin [7]. This can be illustrated by an interaction diagram for reactive extrusion, as shown in Fig. 13.6.



Fig. 13.4. Transition from state of high conversion to state of low conversion at decreasing die resistance.

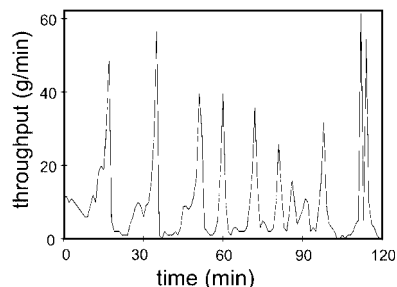


Fig. 13.5. Instabilities in throughput for reactive extrusion of styrene.

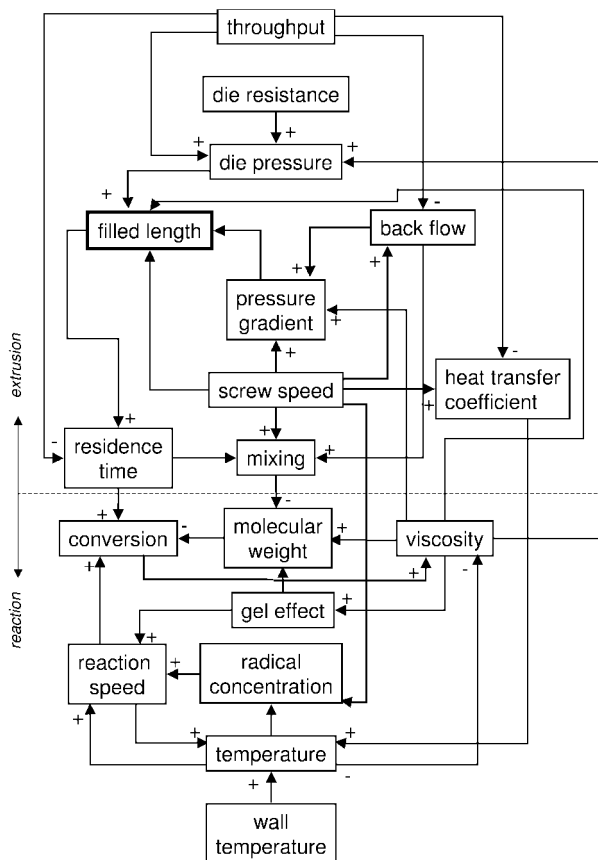


Fig. 13.6. Interaction diagram for a radical polymerization reaction in a twin-screw extruder.

In this diagram, a plus sign (+) indicates a positive correlation between the parameters, while a minus sign (–) stands for a negative correlation [22]. If only the extruder part of the diagram is considered and, for the time being the reaction part is neglected, four dependencies of the fully filled length can be distinguished:

1. An increase in die resistance demands for a larger pressure build-up in the extruder, which leads to a longer fully filled length.
2. An increase of the screw rotation rate at constant throughput increases the back-flow and therefore decreases the filled length.
3. An increase of throughput increases the die pressure and decreases the back-flow, both leading to an increase of the filled length.
4. An increase in viscosity both increases the die pressure and the pressure build-up abilities of the extruder. In the simplified case of an iso-viscous process, the filled length remains constant. In reactive extrusion, where the material is generally far from iso-viscous, the filled length may increase or decrease, depending on the viscosity changes along the screw.

In the total interaction diagram of Fig. 13.6, as the system yields for reactive extrusion, several positive feedback loops can be distinguished, due to which a disturbance in a process parameter can be amplified which may lead to an unstable operation. In this way, three different possible sources of instabilities can be distinguished:

1. Thermal instability, where an increase in temperature leads to an acceleration of the reaction which, for exothermic reactions, again leads to an extra increase in temperature.
2. Hydrodynamic instability, where a small increase in die pressure leads to a larger local residence time, which in turn, through conversion, results in a larger viscosity. This viscosity increase will successively increase the die pressure even further. The positive feedback will be counterbalanced by the back-flow, because an increased viscosity also increases the pressure build-up ability of the extruder. An influence on the stability may be expected if the interaction parameters and the local viscosities are such that the positive feedback dominates.
3. A chemical instability which can be distinguished based on the gel effect or Trommsdorff effect, or on the ceiling effect. The influence of the gel effect on stability depends on its location. For example, if it occurs entirely within the screws, the increases in viscosity and reaction rate will stabilize the process, but if it occurs close to the die it will mainly affect viscosity in the die, which leads to destabilization. The ceiling effect will generally decrease the reaction speed, and therefore it will be negative for the stability of the process.

13.8

Conclusions

Reactive extrusion is a new tool in polymer reaction engineering. From an environmental viewpoint, the need for only small quantities of volatile solvents, and consequent reduced cost, are positive aspects. From an economical point of view, the expensive extrusion equipment is compensated by there being no need to separate the polymer from the solvent. The process is largely complicated by the occurrence of various nonlinear effects that may introduce instabilities into the process, these being of thermal, hydrodynamic, and chemical origin.

Thermal considerations teach us that most extrusion polymerization processes occur under local runaway conditions. This point is especially the case for large-sized equipment, and should be considered when designing an experimental program. Experiments on a small scale may easily lead to results that cannot be scaled up successfully. If the barrel wall is heated electrically, then small temperature changes may be enhanced by the reaction, leading to severe fluctuations in the filled length and residence time. Large radial thermal inhomogeneities can build up especially in large-scale equipment.

Hydrodynamic considerations lead to the contention that there are two stable operating points in reactive extrusion – one with a large, fully filled length and a high conversion, and one with a small, fully filled length and a low conversion. Severe

oscillations in throughput and conversion may also occur. The stability and, as a consequence, the maximum attainable throughput at high and stable conversion, can be improved by increasing the reaction speed, by increasing the viscosity build-up in the screws, and by increasing the residence time.

Chemical considerations lead to two effects that influence the stability of reactive extrusion – the gel effect and the ceiling temperature. Gel effects increase the conversion by an “autocatalytic” behavior. If the gel effect occurs completely in the screws it stabilizes the process, but if it occurs near or in the die it may have a destabilizing effect. The occurrence of a ceiling temperature slows down the reaction and so has a direct, negative influence on hydrodynamic stability.

References

1. K. E. Stober, J. L. Amos, Dow Chemical Co. U.S. Patent no. 2,530,409 (1950).
2. G. Illing, *Modern Plast.*, **1969**, 46, 70–76.
3. W. A. Mack, *Chem. Engng.*, **1972**, 79, 99–102.
4. G. S. Meyuhas, A. Moses, Y. Reibenbach, et al., *J. Polymer Sci., Pol. Let. Ed.*, **1973**, 11, 103–111.
5. L. P. B. M. Janssen, *Polym. Engng. Sci.*, **1998**, 38, 2010.
6. W. A. Mack and R. Herter, *Chem. Eng. Prog.*, **1976**, 72, 64–70.
7. L. P. B. M. Janssen, *Reactive Extrusion Systems*, Marcel Dekker, New York (2004).
8. S. B. Brown, C. M. Orlando, Reactive extrusion, in: *Encyclopedia of Polymer Science and Engineering*, Vol. 14, p. 169, John Wiley, New York (1988).
9. L. P. B. M. Janssen, *Twin screw extrusion*, Elsevier, Amsterdam, 1978.
10. H. A. Jongbloed, Thesis, University of Groningen, 1996.
11. E. Trommsdorff, H. Hohle, P. Lagally, *Macromol. Chem.*, **1947**, 1, 196.
12. J. N. Cardenas, K. F. O'Driscoll, *J. Polymer Sci. Chem. Ed.*, **1976**, 14, 883.
13. F. S. Dainton and K. J. Irvin, *Q. Rev.*, **1958**, XII, 61.
14. G. Odian, *Principles of Polymerization*, McGraw-Hill, New York, 1970.
15. H. G. Elias, *Macromolecules, part 2: synthesis, Materials and Technology*, 2nd edn., Plenum Press, New York, 1984.
16. C. H. Jephson, *Ind. Ind. Eng. Chem.*, **1953**, 45, 992.
17. D. B. Todd, *Soc. Plast. Eng. ANTEC Tech. Pap.*, **1988**, 34, 54.
18. H. Janeschitz-Kriegl and J. Schijf, *Plastics and Polymers*, **1969**, 37, 523.
19. A. J. van der Goot, S. A. Klaasens, L. P. B. M. Janssen, *Polym. Eng. Sci.*, **1997**, 37, 519–528.
20. A. J. van der Goot, R. Hettema, L. P. B. M. Janssen, *Polym. Eng. Sci.*, **1997**, 37, 511–518.
21. L. P. B. M. Janssen, P. F. Rozendal, H. W. Hoogstraten, et. al., *Int. Polymer Proc.*, **2003**, 18, 277–284.
22. K. J. Ganzeveld and L. P. B. M. Janssen, *Can. J. Chem. Eng.*, **1993**, 71, 411–418.

14

Reactive Comminution

Ulrich Hoffmann, Christian Horst and Ulrich Kunz

14.1

Introduction

Reactive comminution is a field of long tradition in human mankind, and a short history of mechanochemistry can be found in Refs. [1–3]. Very early applications are the lighting of fire with flint, pyrite and steel, the use of matches, the preparation of gunpowder, or the welding of silver and platinum in South America. During the early 20th century, contributions from for example Tamman [4] extended the view on pressure-induced phase transformations and solid-state reactions. The initiation of explosions during milling gave rise to the theory of “hot spots” in mechanical activated solids and liquids, as mentioned by Bowden and Yoffe [5]. The mechanical activation of solids and mechanochemical reactions are a field of prolonged research which has been conducted since the classification of Ostwald [6, 7] and his findings about the so-called Ostwald ripening. Many small crystals form in a system initially but slowly disappear, except for a few that grow larger. The formation of smaller crystals is kinetically favored and lowers the supersaturation of the solution. The larger crystals are thermodynamically favored because of the smaller surface energy. The morphology, structure and energy state of mechanically treated substances have been examined by many authors. Thiessen et al. [8], Schmalzried [9], and Heinicke et al. [10] were among the first to compile these earlier studies into books about tribochemistry. Boldyrev and Meyer [11], Heegn [12] and Tkacova [13] showed the positive influence of mechanical treatment on minerals and other materials. Fundamental ideas about the description of mechanochemical reactions have also been presented by Heegn [14, 15]. The theory of fracture mechanism and stressed single particles has been originated by Schönert [16].

The utilization of mechanical energy in solid transformations can be divided into four clusters:

- mechanical comminution: the size reduction of solids by mechanical means;
- mechanical activation: the use of mechanical energy to alter the behavior of solids in a subsequent process;
- mechanical alloying: the use of mechanical energy to cause dissolution or dispersion of different solid materials; and

- reactive comminution: the use of mechanical energy to induce a chemical reaction, simultaneous mechanical treatment and chemical reaction (tribochemistry or mechanochemistry).

14.2

Mechanical Comminution of Solids

Most of the technical raw materials used in solid reactions are polycrystalline, and these – when in solid form – undergo a range of modifications during milling. The first observation is the fracture of the solid into smaller pieces. The fracture mechanics are a topic of discussion, and fracture can be divided into two steps, namely “crack formation” and “crack propagation”. Depending on the ability of the material to undergo plastic deformation before fracture, either brittle or ductile fracture can be defined:

- Ductile fracture is present if the solid undergoes plastic deformation in the crack tip and can be observed in most metals. The plastic deformation quenches energy and leads to stable cracks.
- Brittle fracture is accompanied by very little plastic deformation and is predominant in ceramics and inorganic material. Mostly, a very rapid propagation of the crack is observed.

The ductile fracture can be mediated by dislocations which accumulate and form a cavity perpendicular to the applied stress. Brittle fracture can be transgranular with fracture of crystallites or intergranular with fracture along grain boundaries. Typically, the fracture strength of a material should be approximately one-tenth of Young’s modulus, E . Practical values are orders of magnitude smaller, this being due to the action of defects which act as stress raisers. A second possible mechanism is the fatigue fracture in dynamic loading. This is initiated by the formation of a crack, the incremental crack propagation, and finally by a brittle-like failure.

Steinicke and Linke [17] refer to several microscopic and macroscopic states of mechanically stressed solids. Short time effects can be described by stochastic means or nonequilibrium thermodynamics. Long-lasting effects can be measured by calorimetry. The chemical potential and activity of the stressed solid can be measured depending on the induced defects. These defects include:

- Zero-dimensional point defects, such as Schottky and Frenkel defects.
- One-dimensional line defects, such as step and screw dislocations.
- Two-dimensional area defects, such as stacking faults, grain boundaries, twin boundaries and contact areas with other phases.
- Three-dimensional volume defects such as amorphous regions, pores, other phases and metastable regions.

Line defects in crystals such as screw or edge dislocations are quite common in solid substances. The typical length of all dislocation in 1 m³ of annealed material amounts to 10¹⁰ m (10 km in 1 cm³). The so-called dislocation density is defined as:

$$\rho = \frac{\text{total length of dislocation lines}}{\text{volume}}$$

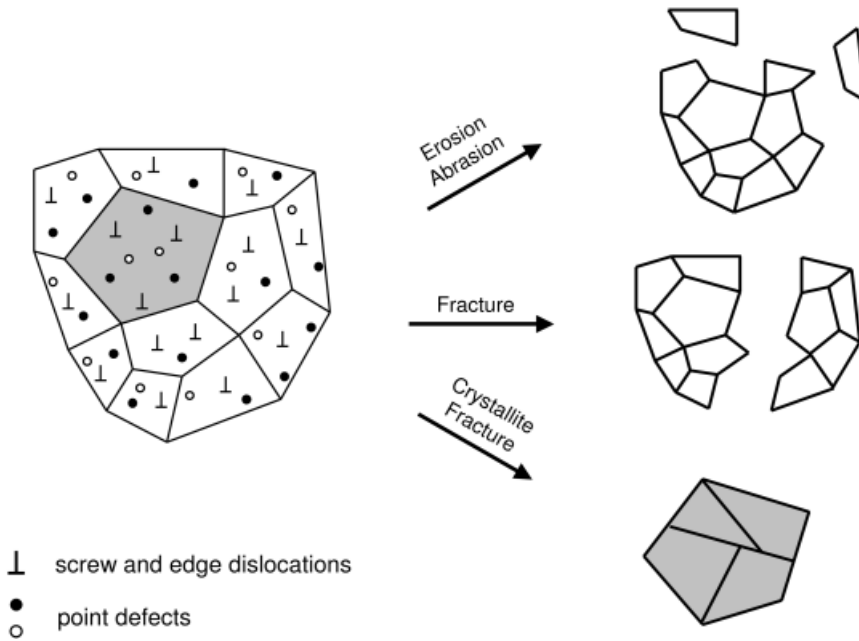


Fig. 14.1. Modifications in polycrystalline solids during processes with particle size changes.

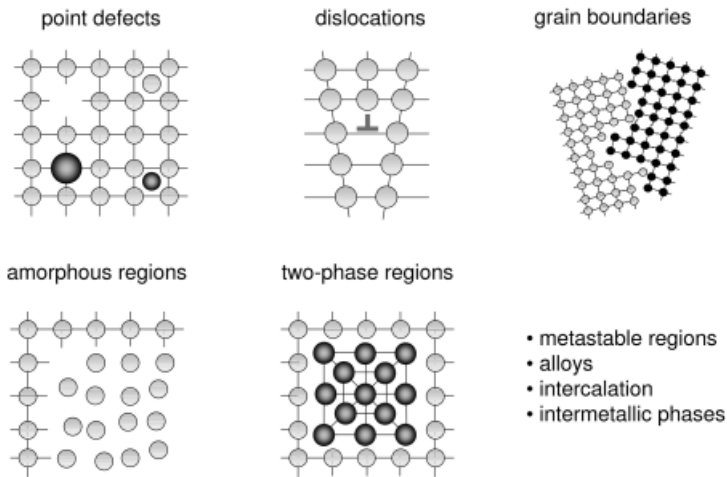


Fig. 14.2. Defects introduced by mechanical processing in solid substances.

During the cold hardening of material the dislocation density rises from 10^{10} m m^{-3} to values of 10^{14} m m^{-3} . The stored strain energy is released during recrystallization.

During milling, the fragmentation of polycrystalline material and primary crystallites proceeds until the fragmentation limit is reached. The particles undergo mainly plastic deformations and accumulate defects, which leads to an amorphization of the solid.

The amount of additional free energy in a solid ranges from 5 kJ mol^{-1} in calcite to 20 kJ mol^{-1} in quartz and 350 kJ mol^{-1} in kaolinite [12].

Typical quantities for the description of stresses in polycrystalline material are:

- specific surface area
- diameter of the primary crystallites
- crystallinity
- lattice distortion

Most of these quantities can be measured by using either BET (Brunauer, Emmett, Teller surface area measurement) or X-ray diffraction methods. The fact that the necessary amount of energy to comminute solids depends on the particle size, the size reduction ratio and the solid can be expressed by empirical formulas. According to Beddow [18] three of the most common types are the equations by:

1. Rittinger's law

$$W_m = C \cdot \left(\frac{1}{D_1} - \frac{1}{D_0} \right)$$

2. Kick's law

$$W_m = C \cdot \left(\ln \left(\frac{1}{D_1} \right) - \ln \left(\frac{1}{D_0} \right) \right)$$

3. Bond's law

$$W_m = C \cdot \left(\frac{2}{\sqrt{D_1}} - \frac{2}{\sqrt{D_0}} \right)$$

all of which allow calculation of the specific energy consumption W_m depending on the difference between initial particle size D_0 and final particle size D_1 and a solid-specific constant C . Figure 14.3 shows typical energy demands for the comminution of different materials.

The Bond working index W_i is the most common description for comminution tasks, and is measured routinely in small-scale laboratory mills:

$$W_m = \left(\frac{10W_i}{d_{80,P}^{0.5}} \right) \left(1 - \frac{d_{80,P}^{0.5}}{d_{80,F}^{0.5}} \right)$$

where $d_{80,F}$ and $d_{80,P}$ are in units of μm . The Bond working index ranges between $W_i = 8 \text{ kWh t}^{-1}$ (gypsum) and 20 kWh t^{-1} (granite).

According to Rumpf [19] and Schönert and Steier [20] the mechanical energy must be transferred to the treated solid, and this can be accomplished by four basic load modes: compression; shear; impact; and impingement. In milling equipment, one of these modes is generally predominant. Hard and brittle material is readily fragmented by compression, ductile, plastic-elastic, and visco-elastic materials are best milled by impact, and soft material can only be cut. The main criteria for the fragmentation [15] are the loading velocity, intensity, frequency, and the thickness of the grinding stock. The loading frequency depends on the type of apparatus. In tumbling mills, vibration mills, stirred media mills or planetary mills, the product of rotational speed and residence time determine the number of single load events. Rotary impact mills have a mean loading frequency depending on the internals, but approximately 10 single events per pass can be expected. The loading velocity depends on the acceleration and the free path of the particles or the grinding media or the rotation velocity and the diameter. Tumbling mills operate at velocities of the grinding media of only a few meters per second (fall in gravity field), whereas for

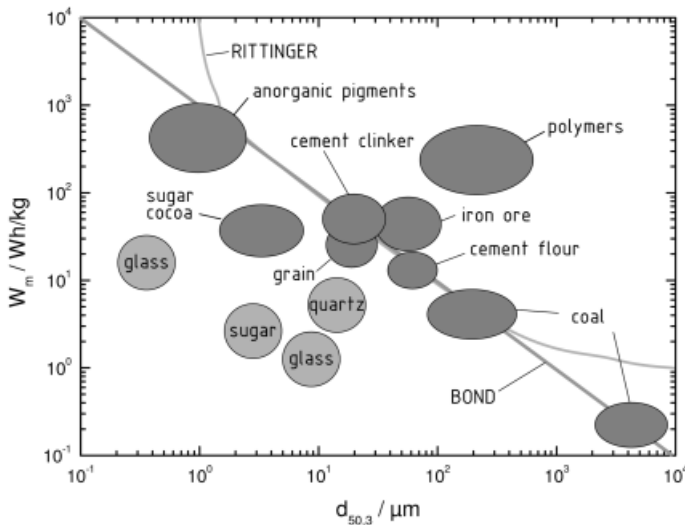


Fig. 14.3. Energy consumption in typical milling application with polydisperse (ellipses) and monodisperse solids (spheres).

vibration mills, planetary mills and grinding media mills, values of between 5 and 15 m s⁻¹ are common. Rotary impact mills reach 300 m s⁻¹, whereas jet mills operate at supersonic velocity of the driving gas. The loading energy is a composed quantity. The number of single load events N and the kinetic energy of the grinding media E_{kin} are referred to the mass m_S of the grinding stock

$$W_{th} = \frac{N \cdot E_{kin}}{m_S} \left[\frac{\text{kWh}}{\text{t}} \right]$$

and the kinetic energy of the grinding stock is determined by the loading velocity v_M and the mass m_M of the grinding media

$$E_{kin} = \frac{1}{2} m_M v_M^2$$

and can be interpreted as the loading intensity if multiplied with the loading frequency.

A typical task is the milling of minerals in the μm -range with power consumption of approximately 50 Wh kg⁻¹. A tumbling ball mill would need 1 hour of milling time at a specific power input of 50 W kg⁻¹ for the comminution, a stirred media mill would need 2 min at 1400 W kg⁻¹, a vibration mill 40 s at 4500 W kg⁻¹, and a planetary mill 5 s at 36,000 W kg⁻¹ (Fig. 14.4).

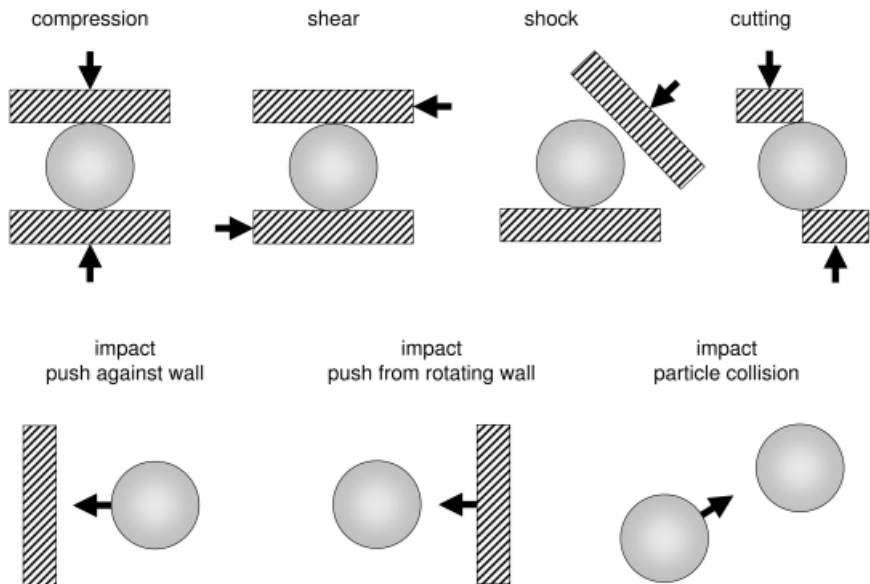


Fig. 14.4. Fundamental load modes in milling equipment.

Energy-efficient milling can be achieved when the transmitted force, loading mode and energy in a single fragmentation event are high enough to overcome the strength of the material. Excess energy is lost in waste heat. Impact and impingement stress leads to increased specific surface areas and a deep destruction of crystal structure. Compression and shear stress leads to increased surface areas without major structure alteration. Wet grinding leads to higher surface areas with less structure destruction than dry grinding.

Other milling parameters are, for example, the impact energy E_B of a single ball

$$E_B = \frac{1}{2} m_B v_B^2$$

and the milling intensity I of the impact frequency

$$I = f_I \cdot E_B$$

the energy dose D

$$D = I \cdot t$$

and specific dose

$$D_m = \frac{D}{m_s}$$

The erosion of metals by solid and liquid impact has been investigated (e.g., [21]).

$$I_E = P_I \cdot R_I \cdot f_I \quad \left[\text{W/m}^2 \right]$$

A review on the energetics, stresses and strains in different devices has also been compiled [22].

14.2.1

Reactivity of Mechanically Activated Solids

The primary effect of milling a solid is to increase its specific surface area. Most reactions between a solid and another phase are proportional to the extent of specific surface area being in contact. This includes outer surfaces as well as the inner surfaces of pore systems and primary crystallites. Intensive milling decreases the size of the primary crystallites which tend to lower the energy by recrystallization. Therefore, a limiting crystallite size can be reached for a given experimental set-up. Most of the crystallite surface is not accessible for fluid reactants, but changes in the pore system and the outer surface allow for an increased reaction rate.

Other mechanisms which are related to enhanced reaction rates under mechanical treatment include:

- short-lived, highly excited states during impact (impact plasma);
- states initiated by energy dissipation such as hot-spots, high crack-tip temperatures; and
- states which are caused by lattice defects with relatively high life-times.

Early explanations about the effect of mechanical energy on the reactivity of solids are the 'hot-spot-model' [23] and the 'magma-plasma-model' [8]. The generation of 'hot-spot' may be used to explain the initiation of a self-sustained reaction such as explosion, deflagration, or decomposition. Temperatures of over 1000 K on surfaces of about $1 \mu\text{m}^2$ for 10^{-4} to 10^{-3} s can be created. These temperatures can also be found near the tip of a propagating crack [24]. Typically nonequilibrium thermodynamics are used to describe these phenomena. The 'magma-plasma-model' allows for local nonequilibrium states on the solid surface during impact; however, due to the very short time scale of 10^{-7} s of these states only statistical thermodynamics can describe the behavior.

Long-lived states including defects and dislocations have been analyzed by equilibrium thermodynamics [14]. Mechanically activated solids have an actual free energy content G which is higher than the equilibrium free energy G^* :

$$G = G^* + G^E$$

the excess free enthalpy is made up of the contributing defects and their disturbance enthalpy

$$G^E = \sum_i c_i H_i^* + T k_b N A \sum_i c_i \ln c_i$$

with major contributions from:

- step and screw dislocations;
- outer specific surface;
- particle size of primary crystallites; and
- amorphous regions and different phases.

Knowledge of the concentration of defects and molar disturbance enthalpies would permit calculation of the actual free energy of the solid, and also the chemical potential. These can be measured by using either solution calorimetry or differential scanning calorimetry. An example of the excess energy was given as $20\text{--}30 \text{ kJ mol}^{-1}$ in mechanically activated quartz. Different types of reactions demand different defect types. For example, Boldyrev et al. [25] state a classification and provide examples for solid reactions with different mechanisms and necessary solid alterations. Often, reaction rates in solids depend strongly on the mass transport of matter. Lidiard [26] and Schmalzried [27] each provide reviews on transport properties in mechanically treated solids. The increased amount of defects allows a faster transport of ions and atoms in the solid structure.

14.3 Equipment and Processes

Reactive comminution is a multistep phenomenon with simultaneous fragmentation, mixing of reactants, and mechanical activation, and is carried out in modified milling devices. Thorough classifications of grinding equipment have been published [28–30]. Crushers operate with high forces and low specific energy on feed particle size greater than 100 mm, whilst mills operate with low forces and high specific energy with a product size smaller than 10 mm. Often, particle diameters of 1 μm result. The mills can be further categorized as roller and ring-roller mills, cutting mills, grinding media mills, impact mills, and jet mills, with most types being capable of operation in either dry or wet milling. A typical criterion is the fineness (Tab. 14.1) of the resulting particles, the hardness of the material (Fig. 14.5), and available combinations of these criteria (Fig. 14.6).

14.3.1

Milling Designs

14.3.1.1 Crushers

Crushers of different designs are large-scale machines for coarse grinding. They have throughputs of up to 3500 t h^{-1} , with a specific comminution work of $0.15\text{--}2.2 \text{ kWh t}^{-1}$. The product particle size lies between 5 and 250 mm.

14.3.1.2 Cutting Mills

Cutting mills, like shredders, are able to chop material which is too soft for milling; examples of such materials include plastic, paper or leather. Industrial applications can be found in the paper and pulp industry, or in the recycling sector.

14.3.1.3 Roller and Ring-roller Mills

Roller mills apply stress to single solid particles between two rotating rollers. The diameter of the rollers is between 0.5 and 1.5 m, and the minimum gap width allows only fine milling. A second type of roller mills operates at higher roller pressures and treats a bed of solids. These high-compression roller mills can be used for ultrafine milling.

Table 14.1. Classification of mills by final particle size range.

Size range [μm]	Milling term
$10^6\text{--}10^5$	Coarse crushing
$10^5\text{--}10^4$	Fine crushing
$10^3\text{--}50$	Fine milling
50–5	Ultrafine milling
5–0.5	Microfine milling
< 0.5	Nanofine milling

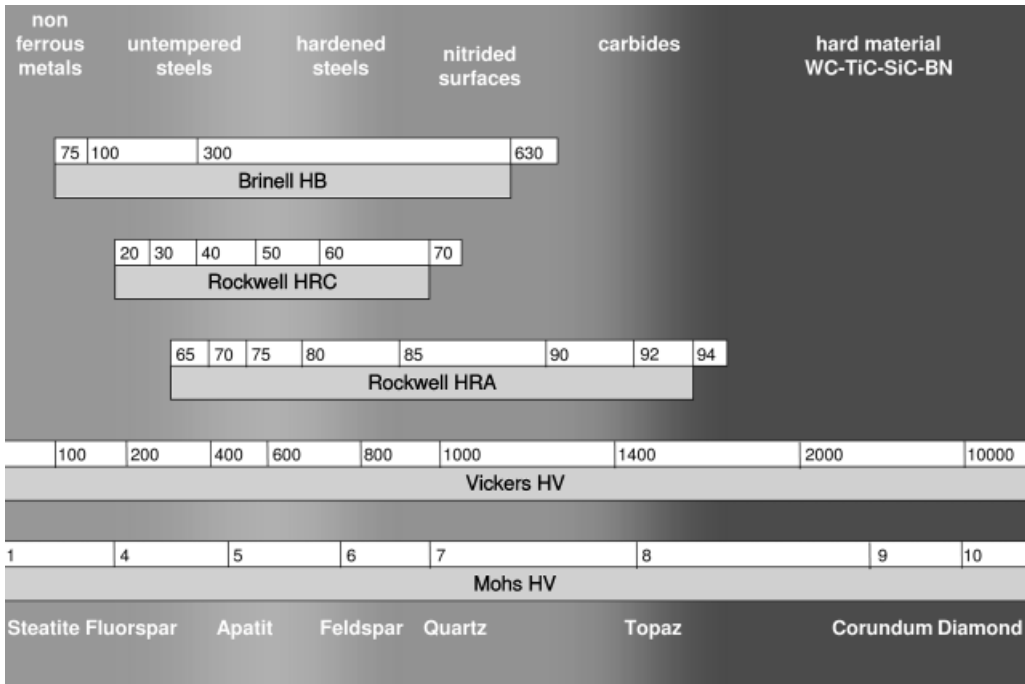


Fig. 14.5. Hardness of typical grinding stocks, grinding media and construction materials.

Ring-roller mills operate with a layer of solid material on a screen which is treated by a roller. The oldest type of a ring-roller mill is known from the milling of cereal. The solid bed is compressed, and a resulting fineness of less than 30 µm is possible. The Szego mill is a common type of ring-roller mill used in wet grinding. Roller frames with gaps of 20 µm are used in the ink industry, or in the production of chocolate.

14.3.1.4 Disk Attrition Mills

This type of mill is used in wet nanofine grinding. The gap between the conical rotor and the stator of an attrition mill can be varied from 30 to 500 µm. Velocities of up to 35 m s⁻¹ and throughputs of up to several tonnes per hour are possible. Colloid mills are used for the homogenization of liquid–liquid or liquid–solid dispersions. Teeth or abrasive coatings are the main grinding tools.

14.3.1.5 Grinding Media Mills

Mills with grinding media include tumbling mills such as ball mills, rod mills, or autogeneous mills. Other designs are planetary mills where the grinding drum is moved on a rotating disk. Vibration mills utilize an eccentric drive to actuate an oscillator consisting of the milling chamber, springs, and a bracket. Centrifugal mills are special planetary mills with a grinding drum between two eccentric bearings.

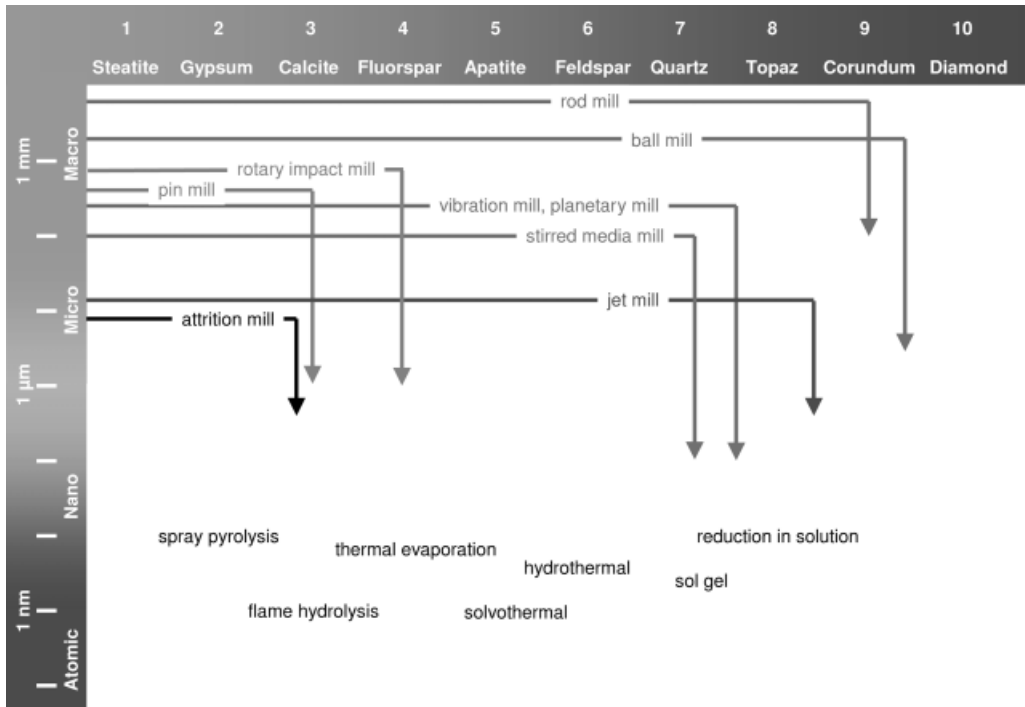


Fig. 14.6. Length scale, Mohs hardness and applicability of different mills.

Tumbling mills are commonly used in industry for grinding large quantities. There are three distinct types, each with different application areas:

- Ball mills are operated with cylpebs or balls, and often employ a conical shape or compartments for better milling characteristics; they can also be used for microfine milling.
- Rod mills rods of up to 6 m in length as the grinding media, and can be used for fine milling.
- Autogeneous mills use the grinding stock itself as grinding media, but can only be used for fine crushing. They have the lowest length to diameter (L/D) ratio of 0.25, whereas rod and ball mills can have a L/D ratio up to 6.

The motion of the grinding media depends on the rotation speed, and can be cascading at low speeds (Fig. 14.7), cataracting at medium speed, and centrifugal at higher speeds. The volume fraction of the grinding media amounts to 0.3, while the mass fraction of the grinding stock is typically less than 0.2 of the total mass.

Planetary mills operate at higher stress intensities than tumbling mills. Grinding drums are placed on a rotating bracket and rotate at about 400 rpm such that accelerations of 60 g and over are possible. These mills are used for nanofine milling in batch mode (Fig. 14.8).

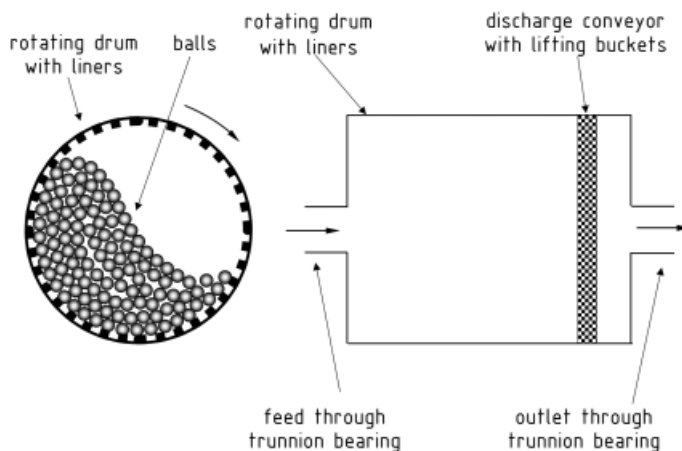


Fig. 14.7. Schematic of a ball mill with discharge conveyor in cascading mode.

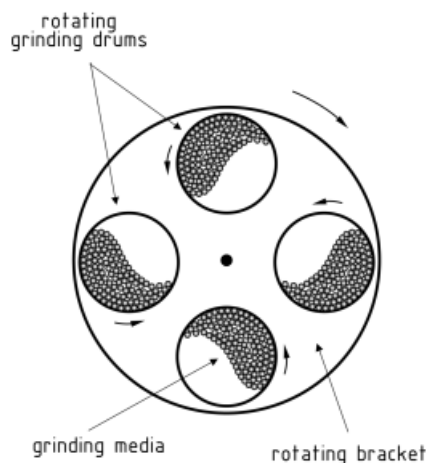


Fig. 14.8. Schematic of a four-drum planetary mill.

Vibration mills are filled with 60–80 % spheres, cylpebs® or rods. The grinding drum is attached to a frame on springs and is driven by an eccentric drive at a frequency of 1000–1500 rpm and amplitudes of approximately 10 mm. The tubes can be up to 4 m in length, with diameters of up to 0.65 m. The continuous operation is performed without classifier at throughputs of up to 15 tonnes per. Vibration mills are used for the microfine grinding of hard material (Fig. 14.9).

Centrifugal mills are a special design of vibration mill with a fixed amplitude (Fig. 14.10).

Stirred media mills or *agitated ball mills* are used mainly in wet microfine and nanofine milling. They are filled to 80 % capacity with grinding media (glass beads,

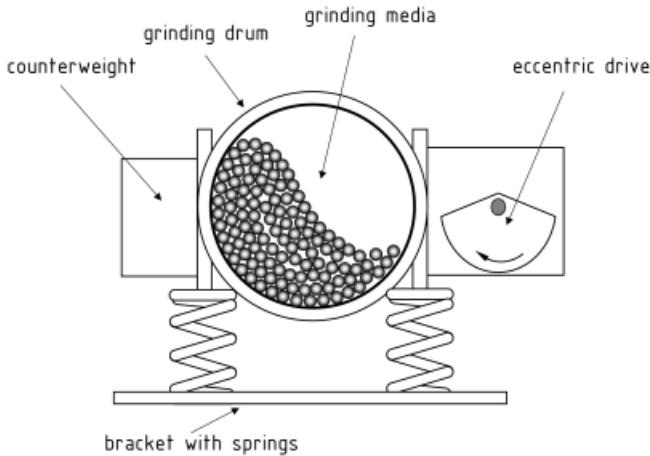


Fig. 14.9. Schematic of an eccentric vibration mill.

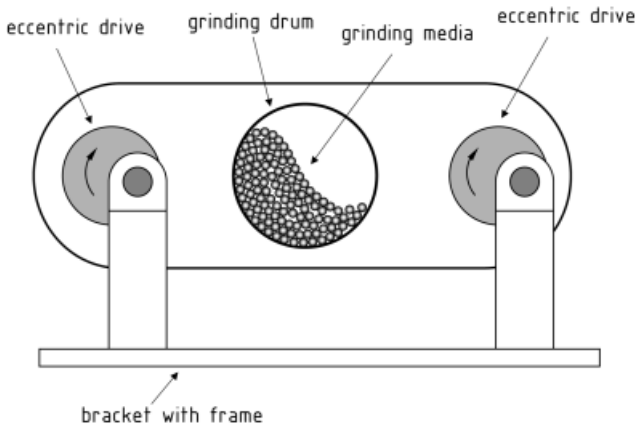


Fig. 14.10. Schematic of a centrifugal mill.

steel balls, ceramic powder ranging from 0.1 mm to several millimeters). A stirrer with velocities controllable between 2 and 40 m s⁻¹ agitates the plates, disks or pins, whereas other designs locate the grinding media and the grinding stock in a conical or cylindrical gap. Very high energy densities can be achieved, with special types of rotary ball mills being operated in a horizontal position (e.g., Simoloyer from Zoz GmbH, Germany). Low-velocity mills are sometimes referred to as Attritor®.

14.3.1.6 Impact Mills

Impact mills are commonly used in industry, and utilize the collision of particles on surfaces for fragmentation. Because of the impact of solid particles on high-velocity parts of the mill, only soft and brittle solids with hardness below 4 Mohs can be used. The design type is mostly a rotary impact mill with different impactors.

Depending on the design of the impactor, these mills can be divided into subclasses such as pinned disc mills, baffle plate mills, beater mills, hammer mills or swing hammer mills.

Beater mills, hammer mills, baffle plate mills, pin mills and universal mills consist of a horizontal shaft with a rotor and, optionally, an impact surface (Fig. 14.12). Impact bar mills and impact hammer mills with vertical shafts are also used.

14.3.1.7 Jet Mills

The impact of accelerated solid particles with walls or other particles is used in jet mills (Fig. 14.13). Velocities of 500 to 1200 m s⁻¹ are reached in a driving gas or vapor jet [31]. In a spiral jet mill, particles are sucked through an injector into a

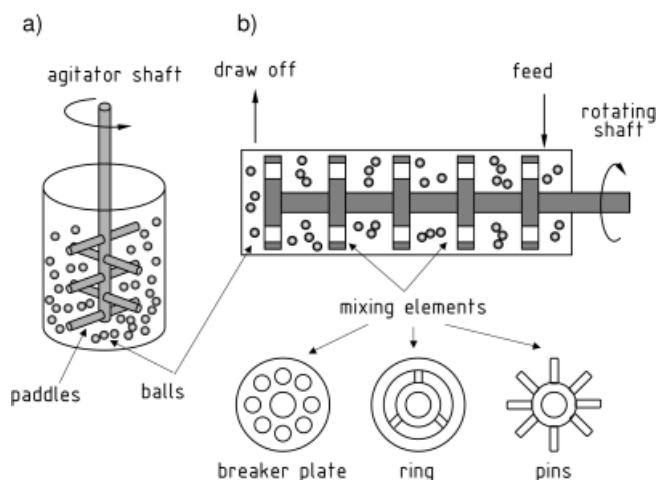


Fig. 14.11. Schematic of different stirred media mills. (a) Batch stirred mill; (b) stirred ball mill.

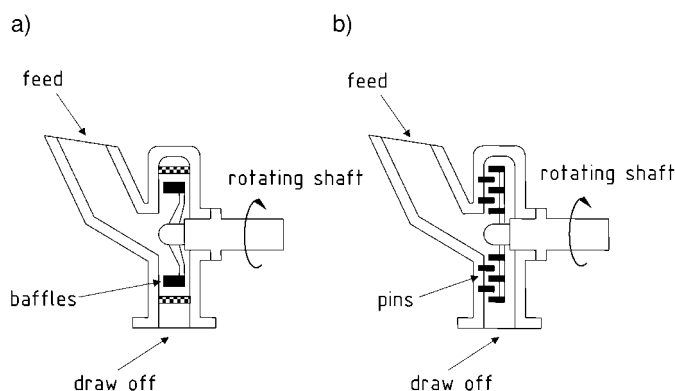


Fig. 14.12. Schematic of rotary impact mill. (a) Baffle plate mill; (b) pin mill.

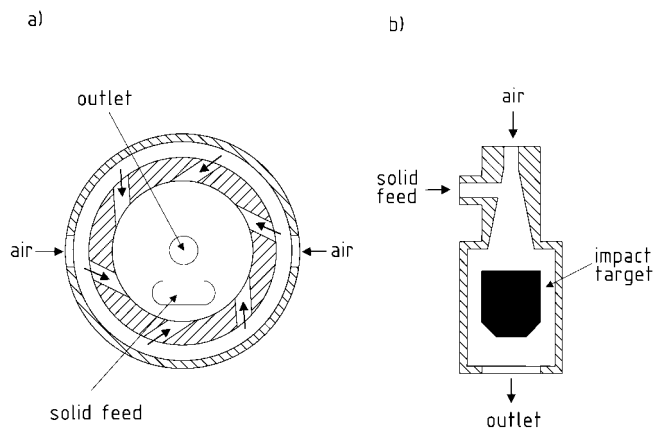


Fig. 14.13. Schematic of a spiral jet mill (a) and a target mill (b).

spiral chamber, and the gas jets are introduced into the chamber via gaps. In the oval jet mill, particles are accelerated in the chamber and are broken up as the result of particle–particle collisions. The fines are removed by the classifying effect of the spiral flow. Particles can also be accelerated in a two-phase injector, in which two injectors are used in the opposed jet mill. Fluidized-bed jet mills use only gas nozzles to maintain a fluidized bed, with the particle–particle collisions leading to abrasion. Target mills use heavy, armored targets for accelerated particle jets in order to increase the possibility of particle impact.

14.3.1.8 Pressure and Shear Devices

The first diamond anvil cell was constructed by Bridgman in the mid-1900s [32], and cells of this type are commonly used to generate high static pressures. The surfaces comprise 8- or 16-sided polygons with areas in the range of 0.01 to 0.5 mm² (0.1 to 0.8 mm width between opposing sides), while the back surface of the anvil – the so-called table – has a surface which is 25- to 1000-fold larger. This in turn is mounted in a metallic component of even much larger cross-section. Thus, with a moderate force acting on the back of this metallic component, very high pressures can be achieved in the sample, which is still much smaller than the cullet surface of the diamonds. By rotating the cell, very high shear forces can be applied in addition to the static pressure.

14.3.1.9 Special Milling and Activation Devices

Solids are sometimes fragmented in shock tubes by the action of shock waves in liquids or gases. The breakdown of kidney stones – known as lithotripsy – by shock waves is an example of this type of apparatus. Typically, shock tube applications are limited to laboratory experiments.

Ultrasound reactors are used quite often for the low-intensity treatment of solids in liquids. Examples of industrial-scale ultrasound reactors are the ‘Reveratory Ultrasonic Mixer’ with 16 kW total power input and 0.2 m³ min^{−1} flow rate, the

'Vibrating Tray' with 2 kW total power input operating with 40 tons of slurry per hour at $1 \text{ m}^3 \text{ min}^{-1}$ flow rate, or the 'Ultrasound Gap Reactor' with 4 kW total power input used in the production of 1 ton per day of organometal compounds. An introduction into the field of ultrasound reactors has been produced by Hoffmann et al. [33]. One special type of milling device is the 'Vibrating Bar Reactor', which consists of a magnetically driven bar which weighs 3 tons, is 4.1 m long, has a diameter of 34 cm, and vibrates at 100 Hz. According to Mason [34], this device is used to treat solid slurries.

Electrical discharge-assisted mills use ball milling with high voltage in spark-milling or glow-milling conditions. This type of mill is used to prepare nanomaterials [35].

14.3.1.10 Dry and Wet Grinding

Normally, milling is performed with dry or only slightly moist solids. Wet grinding is used when the feed or the product form a suspension, or the material tends to explode. Another reason for wet grinding is the achievable lower particle size and the deagglomeration of sticky powder. Wet grinding stocks do not cover the grinding media and allow therefore a finer size reduction. All of the above-mentioned designs except for crushers, impact mills and jet mills, can be used in wet grinding.

14.3.1.11 Machine Wear

Both machine parts and the grinding media are exposed to great stress during the milling process, and this leads in general to a severe mass loss of these parts. Typical values for machine wear are 0.5 to $5 \text{ g kWh} \cdot \text{t}^{-1}$ for dry grinding, and 10 to $80 \text{ g kWh} \cdot \text{t}^{-1}$ for wet grinding of hard material [29]. This very low mass loss is normally of no importance, unless this material is poisoning the product sample. Residues from machine parts can be avoided by the use of polymeric linings, and grinding media can be chosen to be inert under all conditions.

14.3.1.12 Energy Efficiency

The ideal process of particle fragmentation is defined as a multistage sequence in which stress is applied to single particles. This can be described by a mathematical model which requires experimental determination of the breakage function, the breakage fraction, and the energy required to comminute the various particle sizes under different loads. Knowledge of the necessary energy for a typical milling procedure and the actual energy input into the milling device can be used to define a energy efficiency, η . Standard values for the efficiency of size-reduction equipment are very unequal for different equipment. Schubert [30] discriminates between:

- Jaw and roll crushers $\eta = 0.7\text{--}0.9$
- Impact crushers $\eta = 0.3\text{--}0.4$
- Roller-ring mills $\eta = 0.007\text{--}0.15$
- Ball mills $\eta = 0.05\text{--}0.1$
- Impact mills $\eta = 0.1$

The poor values for roller-ring and ball mills are due to the fact that stress is applied to a bed of particles. Furthermore, in ball mills the stress is applied stochasti-

cally and with a wide variation in intensity. Roller-ring mills require energy for extensive internal circulation of the feed. Impact mills are not very efficient because of the energy needed for ventilation and the limited loading attainable in fine grinding.

14.3.1.13 Solid Guidance

The movement of solids in the milling equipment is a very considerable aspect of the process. Depending on the raw material used, pre-milling to the actual particle size in the reactive comminution device might be necessary. Rotary vane feeders, treadmills or lock chambers must be employed to feed the solids. The movement inside the mill is typically determined by cross fall, hydraulic or pneumatic transport, as well as guided movement by internal baffles. The solids are held back in the reaction chamber by slot screens, sieves, gratings or gaps. Large particles leaving the reactor are typically recycled to the feed of the milling chamber, such that this internal or external loop amounts up to six-fold the feed mass. Hydrocyclones, cyclones or other classifying devices are used to separate coarse fractions for recycling purposes.

14.4 Applications

The combination of the two unit operations comminution and reaction can be distinguished into several application fields:

- increase in specific surface area during the reaction;
- mechanical activation of solids prior to a subsequent reaction;
- mechanical alloying of distinct solids; and
- simultaneous comminution and reaction.

A review on the subject of application has been published by McCormick and Froes [36].

14.4.1

Surface Area Creation

The simple effect of enhanced surface area after milling cannot be disregarded. Ellern [37] mentions the influence of the specific surface area of metallic powders in pyrotechnical applications. Beside the spherical particles of magnesium and aluminum made by the so-called atomizing process, iron, nickel and cobalt can be prepared by pyrolysis of carbonyls. Other, less-easily vaporizable metals can be prepared by grinding in an inert atmosphere. The increase in specific surface area is directly proportional to the reaction rate and leads to enhanced conversions. Reactions which generate insoluble products are also appropriate because the constant removal of product layers allows faster reactions and higher solid conversions (Fig. 14.14). Finely dispersed alkali and alkaline earth metals in high-boiling solvents have a broad application in organometal reactions.

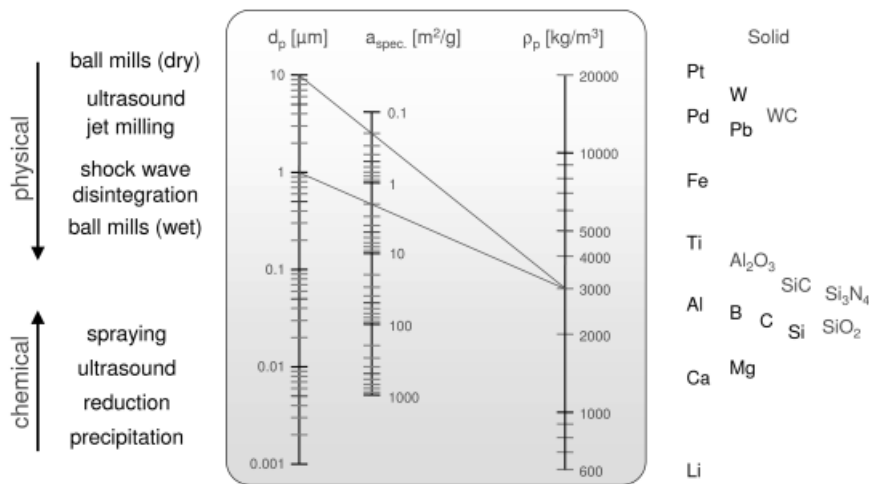


Fig. 14.14. Surface areas for different materials and available particle diameters by the corresponding particle preparation methods.

14.4.2

Mechanical Activation

The term “mechanical activation” should only be used for processes where a solid is pretreated prior to a subsequent reaction. The mechanical activation of solids is often used on an industrial scale to effect the calcination times of ceramics, or the solubility of ores. For a review of hydrometallurgical applications, see Ref. [38].

14.4.2.1 Phase Transitions

The transformation of solids with different phases is often thermally initiated, but it can be shifted to lower temperatures by milling. Fernández-Bertran [39] describes the phase transformation of low-pressure forms into high-pressure phases for CaCO_3 calcite-aragonite, Sb_2O_3 : senarmonite-valentinite, and SiO_2 : quartz-coesite. The transformation of quartz into cristobalite at 1200 °C [40] results in a drastic decrease in the necessary activation energy of the pre-milled solid. This was interpreted as a breakage of Si–O bonds and therefore a facilitated reordering of the crystal structure. Phase changes of $\gamma\text{-Al}_2\text{O}_3$ to $\alpha\text{-Al}_2\text{O}_3$ have been reported [41]. A disordering of the solid lattice is often observed in addition to the change into stable phases. Metastable phases can be created as described by Begin-Colin et al. [42], who investigated the preparation of metastable rutile phases formed from anatase TiO_2 by wet grinding. Amorphous phases can also be prepared and measured by X-ray diffraction. For example Koch [43] described the formation of amorphous phases during milling, and explained the amorphization by an increase in grain boundaries and defect density. In the raw materials industry, the pretreatment of solid materials is a common method for reducing the calcination temperature. Examples for the

partial amorphization of SiO_2 , the cement clinker formation, the sintering of ceramics, and the thermal decomposition of carbonates have been reported [38].

14.4.2.2 Enhanced Solubility of Minerals

The mechanical activation of minerals is a well-known method for enhancing the solubility of natural ores. These two key processes of hydrometallurgy – namely, milling of the solid and leaching of the valuable metal – can be combined in a simultaneous process. The increased dissolution of ilmenite (FeTiO_3 , the source of TiO_2) after milling in a ball mill has been reported [44], the acid-leaching process being four- to five-fold faster than normal. The same group [46] also used carbon as the reducing agent for the conversion of ilmenite to rutil after or during milling. Boldyrev [46a] cites the mechanical activation of phosphate rocks for fertilizers. Tricalcium phosphate in phosphate rocks cannot be dissolved readily in soil, and typically a chemical conversion to “superphosphate” under wet acidic situation is required. A commercial product, Tribophos®, was prepared by mechanical activation of natural phosphates. Tungsten-containing minerals are leached by sodium carbonate solutions [2]. An example of selective leaching has also been identified [47] where the reaction between CuFeS_2 and CuO results in the formation of CuSO_4 which can be removed easily with water. The leaching of mixed copper iron sulfides has been investigated [48] where acid leaching of ore was easy with finely milled material. Corrosion of magnesium alloys has been investigated as an example for the dissolution of metals [49].

14.4.2.3 Surface Cleaning

The reactivity of solids is sometimes reduced by the existence of unreactive (passivating) surface layers that are easily removed by mechanical energy. In this way the reactivity of hydrogenation catalysts such as nickel or platinum has been greatly increased. The use of metals and nonmetals in synthetic reactions under mechanical surface cleaning has been reviewed [50].

14.4.3

Mechanical Alloying

The repeated deformation, fracture and welding of metallic and non-metallic powders allows the preparation of very interesting materials. The thermodynamic basis of mechanical alloying is reviewed by Bormann [51], while others [52] regard mechanical alloying nowadays to be a key step in powder metallurgy. This technique originated during the late 1960s, when dispersion-strengthened alloys of nickel or iron alloys (Inconel) were prepared from powders [53]. Other materials have been investigated and the preparation of metallic glasses, raw materials for powder metallurgy, mixed oxides, and ceramic–metal composites is an active topic in research, based on the plethora of evidence presented at a recent congress on reactive comminution, the 4th INCOME in Braunschweig 2003. (The proceedings of this congress are to be published in the *Journal of Materials Science*.) The process has been considered as an effective tool for the synthesis of metastable materials, supersaturated

solid solutions, amorphous alloys, and nanocrystalline materials. These metastable materials can be used as precursors.

Cocco et al. [54] discuss the preparation of metallic glass, while copper–titanium, aluminum–titanium, and palladium–titanium systems in particular are prepared under a controlled atmosphere with hydrogen and argon. Components of Nb–Ni and Nb–Y have also been described [55]. Amorphous Ni–Ti alloys have been prepared by Schwarz et al. [56], while Ni–Ga, Ni–Ge, Ni–In, and Ni–Sn has been synthesized in supersaturated solid solutions [57]. Fe, Co, Ni–Ta-alloys are described by Lee and Yang [58], while FeSi₂ doped with Co or Al for thermoelectric material is also mentioned [59].

14.4.4

Simultaneous Reaction and Comminution

The simultaneous reaction and comminution of solid reactants can lead to synergetic effects. A better size reduction by reaction, or a faster reaction due to the simultaneous grinding, are possible. Both processes are quite difficult to describe and must be investigated separately, and also in combination. Until now, very few systems have been modeled and the quality of scale-up calculations is only approximate.

14.4.4.1 Solid–Solid Reactions

Solid–solid reactions are often limited by the diffusion of solid reactants. The product layer forms a barrier against diffusion of the two reactants such that, with increased conversion the diffusion lengths become larger. Milling offers the opportunity to create fresh surfaces without product layers, and hence an increased contact area due to fragmentation. Schmalzried [60] describes the reaction of binary solid system on the basis of thermodynamic models and experiments. According to others [61], two main procedures are observed in mechanically activated solid–solid reactions. The reaction proceeds only at distinct areas, and the product is formed in separated zones, or the reaction is self-supporting and a combustion is initiated. Depending on the solid–solid system analyzed, distinct types of mechanical activation routes are possible, and different reaction types demand different comminution strategies.

Displacement reactions are typical examples for solid–solid reactions. The reduction of magnetite by aluminum for example is mentioned in Takacs [62]. Reactions of CuO and Ag₂O with several metals during milling are also described [63–65]. Schaffer and McCormick [66] observed the mechanical alloying of CuO and ZnO together with Ca which resulted in the formation of brass. An interesting approach for the control of fast reactions has been investigated by Pardavi-Horvath and Takacs [67], who were able to suppress the reaction between magnetite and aluminum by dosing inert solids such as Al₂O₃. The preparation of hematite powder from milling FeCl₃ and CaO/Ca(OH)₂ and subsequent thermal decomposition has been discussed [69]; barium or strontium hexaferrite powders (BaFe₁₂O₁₉) have been prepared in a like-wise manner [69]. Other reactions for the reduction of metal oxides sometimes lead to mixed metal alloys [70]. The simultaneous reduction and grinding of metal oxides

with aluminum leads, in the case of tungsten, to the pure metal. Titanium oxide and nickel oxide can be reduced by Al, but produce the corresponding alloys TiAl and NiAl. The reduction of chlorides of rare earth elements for magnets with calcium or sodium was also used [71–73]. For example, Tsuzuki and McCormick [74] used reactive comminution to prepare niobium pentoxide Nb_2O_5 nanoparticles from the reaction of NbCl_5 with Na_2CO_3 or MgO . Iron nanoparticles have been synthesized from FeCl_3 and Na [75], and the reduction of TiCl_4 with Mg to Ti-powder has also been utilized [76]. This reaction occurs at low temperatures when the TiCl_4 is in the solid phase.

Mixed oxides have a widespread application as magnets, catalysts, and ceramics. Often, nonstoichiometric mixtures with unusual properties can be prepared; for example, Fe_2O_3 and ZnO have been milled for the production of zinc ferrite [40], while mixed oxides of $\text{Ca}(\text{OH})_2$ and SiO_2 were described by Kosova et al. [77]. Piezoceramic material such as BaTiO_3 from BaO and anatase TiO_2 has been prepared [78], while ZnO and Cr_2O_3 have been treated by Marinkovic et al. [79] and calcium silicate hydrates from calcium hydroxide and silica gel by Saito et al. [80]. The thermal dehydroxylation of $\text{Ni}(\text{OH})_2$ to NiO or $\text{NiO-Ni}(\text{OH})_2$ nanocomposites has also been investigated [81].

Reactions of metal oxides with elementary carbon or sulfur produce the carbides and sulfides. The reaction of FeTiO_3 with carbon releases Fe and TiC, and the reaction with CaWO_4 produces Ca and WC. These hard materials are used for mechanical purposes [70].

Solid-state reactions are currently used to evaluate the possibility of solvent-free organic synthesis. Normally, solid products are produced by the dissolution/evaporation of solid starting materials, a reaction in the gas or liquid phase, and a drying or crystallization step. The reaction in the solid phase would permit synthesis in a one-step process [46b]; indeed, the synthesis of sodium salicylate [2] is mentioned as an example for the solvent-free synthesis of material by milling solid sodium bicarbonate and salicylic acid at production rates of 100 kg h^{-1} . Fernandez-Bertran et al. [82] obtained ammonium salts by grinding organic acids and amines under proton transfer. Phosphorus ylides and phosphonium salts have also been prepared [83a], while others [84b] use high-energy ball milling to obtain imines from the condensation of *p*-hydroxybenzaldehyde with *p*-aminobenzoic acid. Organic reactions which run to completion and do not require purification steps are prone to be produced by milling of the solid reactants.

Topochemically controlled solid reactions are governed by the crystal structure of the solid. Even if the intrinsic reactivity allows for a reaction, the topochemical restrictions circumvent a conversion. The photodimerization of solid anthracene was observed electron microscopically at dislocations [85]. The reason for this is the possibility of molecule rotation at the dislocation, and not only the high pressure.

14.4.4.2 Catalyst Preparation

The structure and the morphology of solids determine their use in catalytic reactions. Several examples for the preparation and reactivation of solid catalysts by

reactive comminution have been reported. Hashimoto [86] provides a survey of catalysts and electrocatalysts prepared from metastable materials.

The preparation of Cu/ZnO catalysts and precursors for the methanol synthesis reaction have been described [87, 88], while others [89] used a mixture of Pt, Ru and a leachable metal such as Al to prepare catalysts for CO-tolerant catalysts for fuel cells.

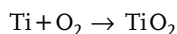
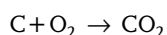
Janot et al. [90] described the increased hydrogen adsorption of ball-milled Mg₂Ni alloys and interpreted their findings with the removal of oxide layers. A Pd-Mg catalyst precursor used for the synthesis of methyl isobutyl ketone was prepared by milling PdO with Mg [91]. Dehydration and dehydrogenation reactions of 4-methylpentan-2-ol over ball-milled catalysts such as CuM (M = Ti, Zr, Hf) have also been investigated [92].

Zeolites and inorganic ion-exchange catalysts have been treated in reactive milling to alter their properties. For example, the amorphization of Zeolite A has been described by Kosanovic et al. [93]; these authors observed a loss of crystallinity, a decrease of cation-exchange capacity, and an increase of solubility of A and Y zeolites which was caused by breaking of Si–O–Si and Si–O–Al bonds in the zeolite.

Intercalation reactions were referred to by Chatakondur et al. [94], who observed the deposition of *n*-hexylamine in TaS₂. Mechanically activated Al(OH)₃ shows enhanced dissolution rates in acids, and can also be used as a host material for foreign molecules. The use of the layers of hydrargillite as a selective sorption medium for small ions such as Li can be enhanced by a mechanical pretreatment [2], and this can also be used in the electrolysis of bauxite. The use and preparation of clay minerals and kaolinite has been reviewed by Yariv and Lapides [95].

14.4.4.3 Solid–Gas Reactions

The first mechanochemical gas–solid reactions, which were identified almost by accident, include the oxidation of carbon and titanium, the reactions being explosive under certain conditions.



Other solid–gas reactions are limited by the low reactivity of the solid and the occurrence of passivating layers. An extensive overview of solid–gas reactions was provided by Roa and Gopalakrishnan [70].

The synthesis of carbonyls by the reaction of Ni, Fe or Mo with carbon monoxide is possible under low-temperature and low-pressure conditions. The apparent activation energy is reduced under milling conditions. The difference between non-activated solid, pretreated solid and simultaneous reaction and milling is depicted in Fig. 14.15 [10]. At normal temperatures, a distinct decrease in activation energy and frequency factor can be seen; this higher reactivity is derived from a high dislocation density. Below a critical temperature, the solid alters the breakage behavior from

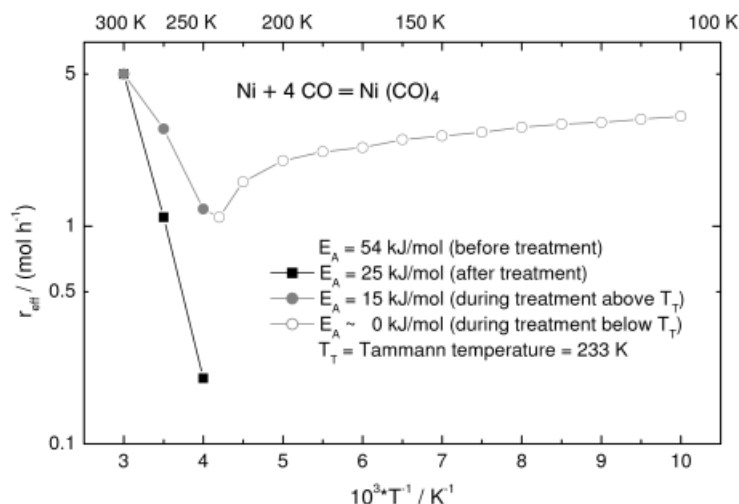


Fig. 14.15. Preparation of nickel carbonyl at different temperatures and milling conditions according to Heinicke et al. [10].

ductile to brittle, this point occurring at -40°C for Ni. Below this temperature a change in the reaction behavior can be observed because of the local action of hot-spots and magma states. Other examples of gas–solid reactions are the treatment of Fe with NH_3 which has been described in Chen and Williams [96], yielding phase transformations and nitrides. Hydrides of magnesium, magnesium alloys, TiFe and LaNi_5 from the reaction with hydrogen are described by Konstanchuk et al. [97]; likewise, the hydrogenation of carbon monoxide to methane with alloys in hydrogen atmosphere has also been investigated [54], the postulated mechanism being hydride formation. Metals can be converted directly to the corresponding nitrides, chlorides and sulfides in the correct gas atmosphere. An industrially important example of gas–solid reactions is the conversion of Si with HCl, wherein the simultaneous removal of surface coatings and the fracture allows synthesis to be performed at lower temperatures than usual. This leads to an increased selectivity towards the desired SiHCl_3 compared to SiCl_4 which is favored in the normal high-temperature reaction. Bade et al. [98] and Uhde and Hoffmann [99] describe the mechanical, chemical and theoretical investigations of a novel vibration mill (Fig. 14.16). Activation energies, synthesis temperatures and selectivity are greatly enhanced by the simultaneous milling and reaction.

14.4.4.4 Solid–Liquid Reactions

Few data are available on the subject of the simultaneous reaction and comminution in solid–liquid systems. This field is occupied by ultrasound applications and synthetic methods, as summarized previously [50, 101]. Of the few applications in milling devices the reduction of liquid TiCl_4 with Mg to Ti-powder has been

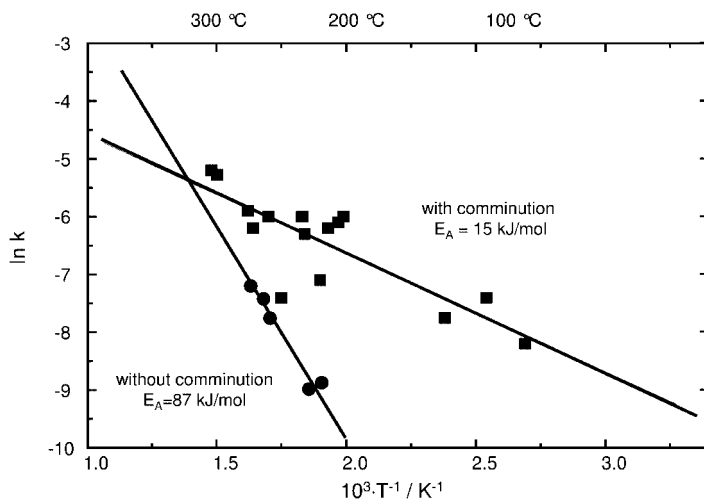


Fig. 14.16. Preparation of chlorosilanes from FeSi and HCl in a vibration mill (after Ref. [100]).

mentioned [76]. Organometal reactions between magnesium and several organic chlorides have been investigated in a vibration mill [102].

Kaupp et al. [84a] mineralized organic wastes such as chlorinated hydrocarbons or tin compounds by milling sand, metallic sodium or magnesium in ethanol, while others used CaO to remove organochlorines such as polychlorinated biphenyl and dichlorodiphenyltrichloroethane during milling [47]. Monagheddu et al. [103] treated hexachlorobenzene with different metals to destroy the organic molecule.

14.4.4.5 Depolymerization Reactions

Polymers are very soft materials which are not easily milled under normal conditions. The mastication of natural rubber is the reduction of molecular weight by milling or cutting, the process being invented by Thomas Hancock as early as 1820. Even today this is a major industrial process in the tire and rubber industry. Other polymers are milled under reduced temperature or even in liquid nitrogen to achieve a controlled molecular mass. The degradation of several polymers has been investigated by Dimitrov et al. [104].

Other applications of simultaneous milling and reaction in polymer systems include the blending of different immiscible polymers, the blending of polymers with ceramics and metals, the coating of material with polymers and the radical copolymerization of block and graft co-polymers. One group has described the preparation of co-polymers and polymer blends by cryogenic milling [105, 106a,b], using the breakage and recombination of polymer bonds for the synthesis of block and graft co-polymers. Mechanochemical modifications of different polymers are described by Butyagin and Radzig [107], while Janke et al. [108] use a vibration mill to prepare co-polymers and functionalized polymers.

14.5

Conclusions

Processes with simultaneous comminution and reaction represent a field of increasing importance. Milling is a key process in industry which has a huge impact on the global energy demand, and the combination of the necessary milling with subsequent process steps will lead to a better utilization of resources. The modification of existing mills for use as reaction mills, together with a more fundamental understanding of the mechanisms, are necessary to employ reaction mills with the same degree of implicitness as other unit operations.

In the future, it is likely that reactive comminution will be used as a tool for the preparation of novel materials and precursors for catalysts, membranes, high-performance ceramics, hydride storage media, raw material for powder metallurgy, and nanoparticles. The emerging applications in organic synthesis reactions and environmental protection will undoubtedly also lead to broader applications.

References

1. L. Takac, Quicksilver from Cinnabar: The First Documented Mechanochemical Reaction?, *JOM*, **2000**, 52, 12.
2. V. V. Boldyrev, Mechanical Activation and Its Application in Technology, *Materials Science Forum Vols.*, 1998, 269–272, 227.
3. V. V. Boldyrev, K. Tkacova, Mechanochemistry of Solids: Past, Present, and Prospects, *Journal of Materials Synthesis and Processing*, **2000**, 8 (3–4), 121.
4. G. Tamman, *Lehrbuch der Metallkunde*, 4th edn.; Voss: Leipzig, 1932.
5. F. P. Bowden, A. Yoffe, *Initiation and Growth of Explosions in Liquids and Solids*; Cambridge University Press: Cambridge, 1952.
6. W. Ostwald, *Grundriss der allgemeinen Chemie*; Engelmann: Leipzig, 1900.
7. W. Ostwald, Studien über die Bildung und Umwandlung fester Körper, *Z. Phys. Chem.*, **1897**, 22, 289.
8. P.-A. Thiessen, K. Meyer, G. Heinicke, *Grundlagen der Tribochemie*; Akademie-Verlag: Berlin, 1967.
9. H. Schmalzried, *Solid state reactions*, in: *Materials science and technology*; Verlag Chemie: Weinheim, 1974.
10. G. Heinicke, H.-P. Henning, E. Linke, et al., *Tribochemistry*; Carl Hanser: München, 1984.
11. V. Boldyrev, K. Meyer, Festkörperchemie, in: *Beiträge aus Forschung und Praxis*; Dt. Verl. für Grundstoffindustrie: Leipzig, 1973.
12. H. Heegn, *Veränderung der Festkörpereigenschaften bei mechanischer Aktivierung und Feinzerkleinerung*, PhD thesis; AdW der DDR: Freiberg, 1985.
13. K. Tkacova, Mechanical Activation of Minerals, in: *Developments in Mineral Processing*; Elsevier Science: Amsterdam, 1990, Vol. 11.
14. H. Heegn, On the Connection between Ultrafine Grinding and Mechanical Activation of Minerals, *Aufbereitungs-Technik*, **1989**, 30 (10), 635.
15. H. Heegn, Mechanische Aktivierung von Festkörpern, *Chem.-Ing.-Tech.*, **1990**, 62 (6), 458.

16. K. Schönert *Einzelkorn-Druckzerkleinerung und Zerkleinerungskinetik: Untersuchungen an Kalkstein-, Quarz-, und Zementklinkerkörnern des Größenbereiches 0,1 bis 3 mm*, PhD thesis; Techn. Hochsch.: Karlsruhe, 1966.
17. U. Steinicke, E. Linke, Die Rolle von Anregungszuständen und Strukturdefekten bei mechanisch aktivierten Festkörperreaktionen, *Z. für Chemie*, **1982**, 22 (11), 397.
18. J. K. Beddow, *Particulate Science and Technology*; Chemical Publishing Co., Inc.: New York, 1980.
19. H. Rumpf, Zur Entwicklungsgeschichte der Physik der Brucherscheinungen, *Chemie-Ingenieur-Technik*, **1959**, 31, 697.
20. K. Schönert, K. Steier, Die Grenze der Zerkleinerung bei kleinen Korngrößen, *Chemie-Ingenieur-Technik*, **1971**, 43, 773.
21. A. Thiruvengadam, The Concept of Erosion Strength, in: *Erosion by Cavitation or Impingement*, ASTM STP 408; American Society for Testing and Materials, 1967, pp. 22–41.
22. F. Kh. Urakaev, V. V. Boldyrev, Mechanism and Kinetics of Mechanochemical Processes in Comminuting Devices, *Powder Technol.*, **2000**, 107 (1–2), 93.
23. F. P. Bowden, D. Tabor, *The Friction and Lubrication of Solids*, Reissued as an Oxford Science Classic in 1986 and re-printed in 1996; Clarendon Press: Oxford, 1950.
24. R. Weichert, K. Schönert, Heat Generated at the Tip of a Moving Crack, *J. Mech. Phys. Solids*, **1978**, 26, 151.
25. V. V. Boldyrev, M. Bulens, B. Delmon, The Control of the Reactivity of Solids, in: *Studies in Surface Science and Catalysis*; Elsevier Scientific Publishing Company: Amsterdam, 1979, Vol. 2.
26. A. B. Lidiard, Atomic Transport in Solids: Models and their Parametrization, *Solid State Ionics*, **1997**, 101–103, 299.
27. H. Schmalzried, *Chemical Kinetics of Solids*; VCH: Weinheim, 1995.
28. K. Schönert, K. Bauckhage, Zerteilprozesse, in: *Handbuch der Mechanischen Verfahrenstechnik*; Schubert, H., Ed.; Wiley-VCH: Weinheim, 2003, Vol. 1, Chapter 5, pp. 299–382.
29. S. Bernotat, K. Schönert, Size Reduction, in: *Ullmann's Encyclopedia of Industrial Chemistry*; Wiley-VCH: Weinheim, 2002.
30. H. Schubert, *Aufbereitung fester mineralischer Rohstoffe*, 4th edn.; VEB Deutscher Verlag für Grundstoffindustrie: Leipzig, 1964.
31. R. Nied, Die Dichtbettstrahlmühle – eine neue Interpretation der bekannten Spiralstrahlmühle, *Aufbereitungstechnik*, **2002**, 8, 52.
32. P. W. Bridgman, *The Physics of High Pressure*; Bell and Sons: London, 1949.
33. U. Hoffmann, C. Horst, U. Wietelmann, et al., Sonochemistry, in: *Ullmann's Encyclopedia of Industrial Chemistry*, 7th edn.; Wiley-VCH, 2004.
34. T. J. Mason, Sonochemistry: current uses and future prospects in the chemical and processing industries, *Phil. Trans. R. Soc. Lond. A*, **1999**, 357, 355.
35. A. Calka, D. Wexler, Mechanical milling assisted by electrical discharge, *Nature*, **2002**, 419, 147.
36. P. G. McCormick, F. H. Froes, The Fundamentals of Mechanochemical Processing, *JOM*, **1998**, (11), 61.
37. H. Ellern, *Military and Civilian Pyrotechnics*; Chemical Publishing Company: New York, 1968.
38. P. Balaz, Mechanical Activation in Hydrometallurgy, *Int. J. Mineral Processing*, **2003**, 72 (1–4), 341.
39. J. F. Fernández-Bertran, Mechanochemistry: An Overview, *Pure Appl. Chem.*, **1999**, 71 (4), 581.
40. U. Steinicke, K. Tkacova, Mechanochemistry of Solids – Real Structure and Reactivity, *J. Mater. Synth. Processing*, **2000**, 8 (3–4), 197.

41. B. B. Bokhonov, I. G. Konstanchuk, V. V. Boldyrev, Structural and Morphological Changes during the Mechanical Activation of Nano-Size Particles, *Mater. Res. Bull.*, **1995**, 30 (10), 1277.
42. S. Begin-Colin, T. Girott, G. le Caer, et al., *Optimisation of the Elaboration of a Nanocrystalline Metastable TiO₂ Phase via Mechanochemistry Followed by Wet Grinding*, ECCE 2, 2nd European Congress of Chemical Engineering, 5.–7. October 1999.
43. C. C. Koch, Mechanical Milling and Alloying, in: *Materials Science and Technology – A Comprehensive Treatment, Volume 15, Processing of Metals and Alloys*; R. W. Cahn, P. Haasen, E. J. Kramer, Eds.; Wiley: Chichester, 1996.
44. Y. Chen, J. S. Williams, S. J. Campbell, G. M. Wang, Increased Dissolution of Ilmenite Induced by High-Energy Ball Milling, *Mater. Sci. Eng. A*, **1999**, 271 (1–2), 485.
45. Y. Chen, T. Hwang, J. S. Williams, Ball milling induced low-temperature Carbothermic Reduction of Ilmenite, *Mater. Lett.*, **1996**, 28, 55.
- 46a. V. V. Boldyrev, Reactivity of Solids and New Technology, in: *Chemistry for the 21st Century, Reactivity of Solids: Past, Present and Future*; V. V. Boldyrev, Ed.; Blackwell Science: Oxford, 1996a, Chapter 12, pp. 267–285.
- 46b. V. V. Boldyrev, Mechanochemistry and Mechanical Activation, *Mater. Sci. Forum*, **1996b**, 225–227, 511.
47. S. A. Rowlands, A. K. Hall, P. G. McCormick, et al., Destruction of toxic materials, *Nature*, **1994**, 267, (6460), 223.
48. S. Nasher, N. Y. Roslyn, F. A. Forward, US Patent 3,034,864, 1962.
49. E. M. Gutman, Ya. Unigovski, A. Eliezer, et al., Mechanoelectrochemical Behavior of Pure Magnesium and Magnesium Alloys Stressed in Aqueous Solutions, *J. Mater. Synth. Processing*, **2000**, 8 (3–4), 133.
50. J.-L. Luche, *Synthetic Organic Sonochemistry*; Plenum Press: New York, 1998.
51. R. Bormann, *Mechanical alloying: fundamental mechanisms and applications*; GKSS 94 E 3: Geesthacht, 1994.
52. E. Ivanov, C. Suryanarayana, Materials and Process Design through Mechanochemical Routes, *J. Mater. Synth. Processing*, **2000**, 8 (3–4), 235.
53. J. S. Benjamin, C. B. Raymond, Nickel-Based Dispersion-Strengthened Alloys, in: *Mechanical Properties of Metallic Composites*; Ochiai, S., Ed.; Marcel Dekker, 1993.
54. G. Cocco, G. Mulas, L. Schiffini, Mechanical Alloying Processes and Reactive Milling (Overview), *Mater. Trans., JIM*, **1995**, 36 (2), 150.
55. Y. G. Chen, B. X. Liu, Different Driving Force for Metallic Glass Formation Nb-Ni and Nb-Y Systems by Ion Mixing and Solid-State Reaction, *Mater. Lett.*, **1997**, 33, 167.
56. R. B. Schwarz, R. R. Petrich, C. K. Saw, The Synthesis of Amorphous Ni-Ti Alloy Powders by Mechanical Alloying, *J. Non-Crystalline Solids*, **1985**, 76 (1), 281.
57. T. F. Grigorieva, A. P. Barinovam, V. V. Boldyrev, et al., The Influence of Structural Relationship on Extended Solid Solubility at Mechanical Alloying, *Solid State Ionics*, **1997**, 101–103, 17.
58. P.-Y. Lee, J.-L. Yang, Solid-State Amorphization in Ta-based alloy system by mechanical alloying technique, *Mater. Sci. Eng.*, **1997**, A226–228, 43.
59. S. G. Mamylov, E.-Yu. Belyaev, O. I. Lomovskii, Thermoelectric Power of Doped β -FeSi₂ Materials Prepared by Mechanochemical Synthesis, *Inorg. Mater.*, **1998**, 34 (7), 683.
60. H. Schmalzried, Chemical Kinetics at Solid-Solid Interfaces, *Pure Appl. Chem.*, **2000**, 72 (11), 2137.
61. L. Takacs, Nanocomposite Formation and Combustion Induced by Reaction Milling, *Mater. Res. Soc. Symp. Proc.*, **1993**, 286, 413.

62. L. Takacs, Reduction of Magnetite by Aluminium: A Displacement Reaction Induced by Mechanical Alloying, *Mater. Lett.*, **1992**, 13, 119.
63. G. B. Schaffer, P. G. McCormick, Anomalous Combustion Effects During Mechanical Alloying, *Metallurgical Trans. A*, **1991**, 22, 3019.
64. K. Tokumitsu, Reduction of Metal Oxides by Mechanical Alloying Method, *Solid State Ionics*, **1997**, 101–103, 25.
65. L. Takacs, Combustion Phenomena Induced by Ball Milling, *Mater. Sci. Forum*, **1998**, 269–272, 513.
66. G. B. Schaffer, P. G. McCormick, Reduction of Metal oxides by Mechanical Alloying, *Appl. Physics Lett.*, **1989**, 55 (1), 45.
67. M. Pardavi-Horvath, L. Takacs, Iron-Alumina Nanocomposites Prepared by Ball Milling, *IEEE Trans. Magn.*, **1992**, 28, 3186.
68. J. Ding, T. Tsuzuki, P. G. McCormick, Hematite Powder Synthesized by Mechanochemical Processing, *NanoStructured Mater.*, **1997**, 8 (6), 739.
69. J. Ding, W. F. Miao, P. G. McCormick, et al., High-Coercivity Ferrite Magnets Prepared by Mechanical Alloying, *J. Alloys Compounds*, **1998**, 281, 32.
70. C. N. R. Roa, Gopalakrishnan, *New Directions in Solid State Chemistry*, in: *Cambridge Solid State Science Series*; Cambridge University Press: Cambridge, 1986.
71. P. G. McCormick, Mechanical Alloying and Mechanically Induced Chemical Reactions, in: *Handbook on the physics and chemistry of rare earths*; Gschneidner Jr., K.A., L. Eyring, Eds., 1997, Vol. 24, Chapter 160.
72. P. G. McCormick, G. B. Schaffer, US Patent 5,328,501, 1994.
73. T. Tsuzuki, W. T. A. Harrison, P. G. McCormick, Synthesis of Ultrafine Gadolinium Powder by Mechanochemical Processing, *J. Alloys Compounds*, **1998**, 281, 146.
74. T. Tsuzuki, P. G. McCormick, Mechanochemical Synthesis of Niobium Pentoxide Nanoparticles, *Mater. Trans.*, **2001**, 42 (8), 1623.
75. J. Ding, W. F. Miao, P. G. McCormick, et al., Mechanochemical Synthesis of Ultrafine Fe Powder, *Appl. Physics Lett.*, **1995**, 67, (25), 3804.
76. F. H. Froes, The Production of Low-Cost Titanium Powders, *JOM*, **1998**, 50 (9), 41.
77. N. V. Kosova, A. Kh. Khabibullin, V. V. Boldyrev, Hydrothermal Reactions under Mechanochemical Treating, *Solid State Ionics*, **1997**, 101–103, 53.
78. Q.-S. Wu, S.-J. Gao, S.-M. Zhang, et al., Nano-Crystalline BaTiO₃ Synthesized by Mechanochemistry, *Wuji Cailiao Xuebao/J. Inorganic Mater.*, **2002**, 17 (4), 719.
79. B. A. Marinkovic, Z. V. Zakula, T. Sreckovic, et al., The Influence of Tribophysical Activation on Solid-State Reaction during Thermal Treatment of ZnO-Cr₂O₃, *Cryst. Res. Technol.*, **1999**, 34 (7), 881.
80. F. Saito, G. Mi, M. Hanada, Mechanochemical Synthesis of hydrated calcium silicates by room temperature grinding, *Solid State Ionics*, **1997**, 101–103, 37.
81. G. J. C. Carpenter, Z. S. Wronski, Nanocrystalline NiO and NiO-Ni(OH)₂ Composite Powders prepared by Thermal and Mechanical Dehydroxylation of Nickel Hydroxide, *Nanostructured Mater.*, **1999**, 11 (1), 67.
82. J. Fernandez-Bertran, J. C. Alvarez, E. Reguera, Proton Transfer in the Solid State: Reactions of Organic Acids and Amines, *Solid State Ionics*, **1998**, 106, (1–2), 129.
- 83a. V. P. Balema, J. W. Wiench, M. Pruski, et al., Mechanically induced Solid-State Generation of Phosphorus Ylides and the Solvent-free Wittig Reaction, *J. Am. Chem. Soc.*, **2002a**, 124, 6244.
- 83b. V. P. Balema, J. W. Wiench, M. Pruski, et al., Solvent-free Mechanochemical Synthesis of Phosphonium Salts, *Chem. Commun.*, **2002b**, 2002 (7), 724.
- 83c. V. P. Balema, J. W. Wiench, M. Pruski, et al., Solvent-free Mechanochemical Synthesis of two Pt-Complexes: cis(Ph₃P)₂PtCl₂ and cis(Ph₃P)₂PtCO₃,

- Chem. Commun.*, **2002c**, 2002, (15), 1606.
- 84a. G. Kaupp, M. R. Naimi-Jamal, H. Ren, et al., Environmentally Protective Reactive Milling, *Chemie Technik*, **2002a**, 31, 206.
 - 84b. G. Kaupp, J. Schmeyers, M. R. Naimi-Jamal, et al., Reactive Milling with the Simuloyer: Environmentally Benign Quantitative Reactions without Solvents and Wastes, *Chem. Engng. Sci.*, **2002b**, 57, 763.
 85. J. O. Williams, J. M. Thomas, Photochemical reactions inside the electron microscope: preferred dimerization of anthracene at dislocations, *Mol. Cryst. Liq. Cryst.*, **1972**, 16, 371–375.
 86. K. Hashimoto, Recent Advantages in the Catalytic Properties of Metastable Materials, *Mater. Sci. Eng.*, **1997**, A226–228, 891.
 87. L. Huang, G. J. Kramer, W. Wieldraaijer, et al., Methanol Synthesis over Cu/ZnO Catalysts prepared by Ball Milling, *Catalysis Lett.*, **1997**, 48, 55.
 88. U. Kunz, C. Binder, U. Hoffmann, Preparation of fine particles as catalysts and catalyst precursors by the use of ultrasound during precipitation, in: *Preparation of Catalysts VI*; Elsevier, 1995, Vol. 91, pp. 869–879.
 89. M. C. Denis, G. Lalande, D. Guay, et al., High Energy Ball-Milled Pt and Pt-Ru catalysts for Polymer Electrolyte Fuel Cells and Their Tolerance to CO, *J. Appl. Electrochem.*, **1999**, 29, 951.
 90. R. Janot, L. Aymard, A. Rougier, et al., Fast Hydrogen Sorption Kinetics for Ball-Milled Mg₂Ni Alloys, *J. Physics Chem. Solids*, **2004**, 65 (2–3), 529.
 91. G. Mulas, M. Varga, I. Bertoti, et al., Characterization of Pd-Mg Catalyst Precursors Prepared by Ball Milling and Comparison with Cu-Mg, *Mater. Sci. Forum*, **2001**, 377, 57.
 92. G. Mulas, M. Monagheddu, G. Cocco, et al., Conversion of 4-methylpentan-2-ol over Powder Catalysts Prepared by Ball Milling, *J. Mater. Synthesis Processing*, **2000**, 8 (5–6), 385.
 93. C. Kosanovic, J. Bronic, B. Subotic, et al., Mechanochemistry of Zeolites: Part 1. Amorphization of Zeolites A and X and Synthetic Mordenite by Ball Milling, *Zeolites*, **1993**, 45 (13), 261.
 94. K. Chatakondur, M. L. H. Green, M. E. Thompson, et al., Enhancement of Intercalation Reactions by Ultrasound, *J. Chem. Soc., Chem. Commun.*, **1987**, 900.
 95. S. Yariv, I. Lapides, The Effect of Mechanochemical Treatments on Clay Minerals and the Mechanochemical Adsorption of Organic Materials onto Clay Minerals, *J. Mater. Synthesis Processing*, **2000**, 8 (3–4), 223.
 96. Y. Chen, J. S. Williams, High-Energy Ball-Milling-Induced Non-Equilibrium Phase Transformations, *Mater. Sci. Eng.*, **1997**, A226–228, 38.
 97. I. G. Konstanchuk, E. Yu. Ivanov, V. V. Boldyrev, Interaction of Alloys and Intermetallic Compounds obtained by Mechanochemical method with hydrogen, *Russian Chem. Rev.*, **1998**, 67 (1), 69.
 98. S. Bade, U. Hoffmann, K. Schöner, Mechano-chemical reaction of metallurgical grade silicon with gaseous hydrogen chloride in a vibration mill, *Int. J. Miner. Process*, **1996**, 44–45, 167.
 99. G. Uhde, U. Hoffmann, Noncatalytic Gas-Solid Reactions: Modelling of Simultaneous Reaction and Formation of Surface with a Nonisothermal Crackling Core Model, *Chem. Eng. Sci.*, **1997**, 52, 1045.
 100. S. Bade, *Einsatz einer Reaktions-schwingmuehle zur simultanen Zerkleinerung und chemischen Reaktion von Ferrosilicium mit Chlorwasserstoff*, PhD thesis; TU Clausthal, 1995.
 101. J. Lindley, T. J. Mason, Sonochemistry Part 2 – Synthetic Applications, *Chem. Soc. Rev.*, **1987**, 16, 275.
 102. M. Veit, *Einsatz einer Reaktionsmühle zur Verbesserung der Verfahrensführung nichtkatalytischer heterogener Flüssig-Fest-Umsetzungen*, PhD thesis,

- TU Clausthal; Papierflieger e.V.: Clausthal-Zellerfeld, 1998.
103. M. Monagheddu, S. Doppiu, G. Cocco, MSR Reduction of Hexachlorobenzene, *J. Mater. Synthesis Processing*, **2000**, 8 (5–6), 295.
 104. M. Dimitrov, T. Pazonyi, F. Tuedoes, Mechanochemischer Abbau von Polymeren durch Zerkleinerung, *Plaste Kautsch.*, **1969**, 16 (8), 577.
 105. A. P. Smith, H. Ade, S. D. Smith, et al., Polymer Blends Prepared by Cryogenic Mechanical Alloying: New Insights and Opportunities, in: *Advanced Materials Processing*; D. L. Zhang, K. L. Pickering, X. Y. Xiong, Eds.; Institute of Materials Engineering Australasia Ltd.: New Zealand, 2000, pp. 199–204.
 - 106a. A. P. Smith, H. Ade, C. C. Koch, et al., Copolymer to Polymer blends Produced by Cryogenic Mechanical Alloying, *Macromolecules*, **2000**, 33, 1163.
 - 106b. A. P. Smith, H. Ade, C. C. Koch, et al., Temperature-induced Morphological Evolution in Polymer Blends Produced by Cryogenic Mechanical Alloying, *Macromol. Mater. Eng.*, **2000**, 274, 1.
 107. P. Yu. Butyagin, W. A. Radzig, Mechanochemische Umwandlungen in Polymeren, *Plaste Kautsch.*, **1972**, 19 (2), 81.
 108. G. Janke, A. Frendel, G. Schmidt-Naake, Polymer Modification in a Mill, *Chem. Eng. Technol.*, **1999**, 22, 997.

15

Reactive Filtration

Thomas Rieckmann and Susanne Völker

15.1

Introduction

The term “reactive filtration” may be used in a variety of applications. A simple search of the internet provides results such as reactive filter paper [1], adsorption filters for removing heavy metals from water [2], solid matrices used in organic synthesis [3], membranes for wastewater treatment, or even dialysis machines, filters for deep-frying pans and devices for the dechlorination of shower water by reaction with vitamin C. Most of the applications termed reactive filtration would be named heterogeneous catalysis or adsorption from a chemical engineer’s point of view.

In the context of integrated chemical processes however, reactive filtration should be specified as the combination of the solids handling unit operation “filtration device” and the unit operation “chemical reactor”. This comprises the separation of solids or aerosols from a fluid stream and the chemical conversion of undesired compounds carried by the stream in one instead of two unit operations. The chemical reaction can proceed either continuously during the separation or stepwise after a certain amount of solids or aerosols has been deposited. Two general cases for the application of a reactive filtration unit may be distinguished:

- the removal of inert solids and of reactive volatiles; and
- the removal of reactive solids.

The first case covers for example flue-gas treatment, which requires the filtration of fly-ash and the reduction of NO_x , or gasification processes, where particulates and high-boiling tars have to be removed. An example of the second case is that of combustion processes, where incomplete combustion leads to the emission of carbonaceous particulates. The most relevant topic in this category is the reduction of diesel particulate emissions (“diesel soot”) by catalytic filtration. A more “exotic” example is the reaction cyclone for the thermal conversion of biomass, which also combines chemical reactions and separation in one apparatus, though its separation mechanism is not filtration.

The chemical conversion in the reactive filter can be achieved either by simply altering the reaction environment through the deposition of material, or with the help of catalysts. The alteration of the reaction environment may lead to higher concentrations of reactive species or to different heat transfer conditions. The reactions

of volatiles and/or solids may be accelerated by catalysts or may be initialized by additives, which decompose into radicals at low temperatures. A stepwise reaction of deposited solids may also be promoted by periodically heating the filter.

The question remains, why should a chemical engineer try to convert a filter, which is a simple unit operation, into a much more complex apparatus? It can be expected that the combination of the two unit operations in the reactive filter results in synergetic effects such as energy and space savings or a reduction in investment and operation costs. In some cases – for example, the diesel particulate abatement for passenger cars – the reactive filter seems to be the only option. In other cases, such as the production of bio-oil by the pyrolysis of biomass, the reaction cyclone is a promising option to guarantee a very short gas residence time, together with a longer particulate residence time. Besides, reactive filters show a unique dynamic behavior, which poses challenges to the understanding, modeling and control of these systems and makes them an interesting field for chemical engineering research.

In the following sections, the different types of reactive filters, together with their typical applications, will be presented. The separation and catalytic combustion of diesel soot is the most important and furthest investigated application. Consequently, this type of reactive filtration, with its practical and theoretical aspects, will form the main focus of this chapter.

15.2

Separation of Particulates and Catalytic Reaction of Volatiles

15.2.1

Flue-gas Treatment

Flue-gas from boilers fired with liquid or solid fuels contains fly-ash and gaseous contaminants such as CO, NO_x, SO₂, or volatile organic compounds (VOCs). Emission regulations require their removal, which is achieved by a sequence of after-treatment processes. The after-treatment usually comprises a filter to remove solid particulates operated at approximately 150 °C, a wet scrubber for the removal of SO₂ with an alkaline solution operated at approximately 50 °C, and finally a selective catalytic reduction (SCR) unit, which converts NO_x to N₂ with the help of NH₃ at approximately 370 °C (Fig. 15.1) [4]. During this process, the flue gas is cooled down and then heated up again, which requires additional heat transfer equipment, with its inherent energy losses.

In order to avoid the unfavorable process conditions, different flue-gas treatment processes for combustion plants based on catalytic filters were developed, which combine fly-ash removal with SCR of NO_x with NH₃ [4–8]. The advantages of these processes are space and treatment-cost savings, reduced internal and external mass transfer resistances compared to honeycomb SCR catalysts, heat recovery from off-gases with good efficiency, and low corrosion problems due to the removal of both dust and NO_x at high temperatures.

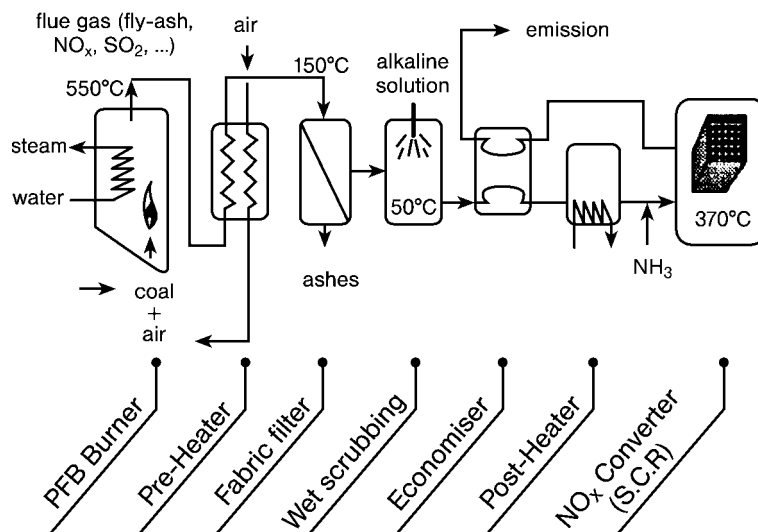


Fig. 15.1. Flue-gas treatment by a conventional process comprising a fabric filter for fly-ash removal, a wet scrubber for SO_2 reduction and a selective catalytic reduction unit for NO_x treatment (from Ref. [4]).

Catalytic filters should possess the following properties: 1) high thermal, chemical, and mechanical stability; 2) high dust separation efficiency attained by cake filtration (no penetration of particulates into the filter structure); 3) low cost; 4) high catalytic activity (operation at high superficial velocities); and 5) low pressure drop.

Saracco et al. tested several filter types and catalysts, and reported their best filter to be a candle filter made from porous $\alpha\text{-Al}_2\text{O}_3$ with an average pore size of $15\ \mu\text{m}$ and a catalytically active surface coating of V_2O_5 and TiO_2 (anatase) [6]. This functions as a “cake filter” for fly-ash removal with periodic cleaning by countercurrent jet pulsing and as a catalyst for the abatement of gaseous pollutants (NO_x , VOCs). The group proposed a flue-gas treatment comprising the following sequence: The first process step is dry scrubbing of the hot flue gas with $\text{Ca}(\text{OH})_2$, which reacts with SO_2 to CaSO_4 . Then, NH_3 is added to the flue gas, which reacts in the second process step with NO_x on the surface of the catalytic filter. The catalytic filter also removes the solid CaSO_4 . In the last process step, a pre-heater transfers residual heat from the flue gas to the inlet air for the combustion process (Fig. 15.2).

The theoretical advantages of this integrated system seem to be challenged by real world problems related to ash removal from the surface of the catalytic filter. Alvin et al. reported field experiences of the company Westinghouse Electric in 1998 [9]. Failure and performance limitations resulted from ash-related issues such as bridging, filter bowing, inner wall blinding, inner pore plugging, wedging of fines between the ceramic filter flange and metal holder mount, auto-ignition of char, and membrane debonding in alkali-laden systems. Nevertheless, in 2003 laboratory tests for

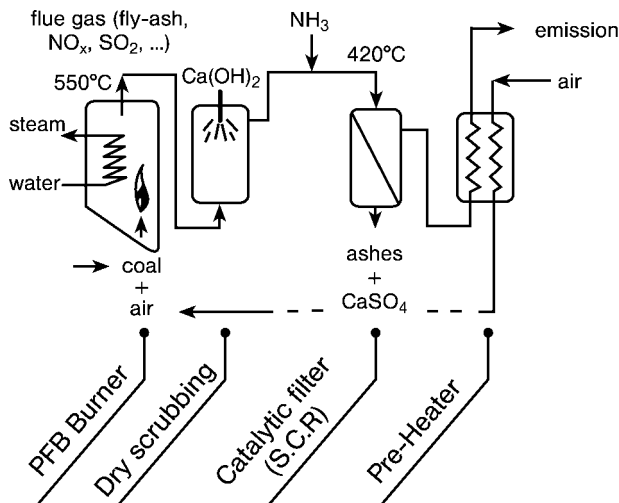


Fig. 15.2. Flue-gas treatment by dry scrubbing and catalytic filtration (from Ref. [4]).

the combined reduction of SO₂, NO_x, and particulates in power plants were under investigation again by GE Power Systems. Different sorbents for SO₂ were tested and blended with different coals for NO_x reduction. Field experiences with this new approach have not yet been reported [10].

15.2.2

Biomass Gasification

The major challenge for the utilization of biomass as renewable energy source in combined gasification/gas turbine plants is the efficient removal of tar and particulates from the feed gas of the gas turbine [11]. This is another promising application of the concept of catalytic filtration, but the technical development is still in the laboratory state.

Nickel-based steam reforming catalysts are very efficient for the decomposition of tars and ammonia in biomass gasification gas. Ceramic candle filters can be applied to remove particles at high temperature. It is proposed to use nickel-activated alumina candle filters for the simultaneous removal of tar, ammonia and particles from biomass gasification gas [12].

Engelen et al. prepared a novel catalytic nickel-calcium-coated alumina candle filter for the combined removal of tar and particulates from hot biomass gasification gas [13]. Special attention was paid to the improvement of the catalyst's resistance against H₂S poisoning. Deactivation tests were performed with benzene and naphthalene as tar model compounds in a simulated dust-free gasification gas. The filter did not change the H₂S content in the gas. Naphthalene showed a higher conversion (96–98 % at 100 ppm H₂S) than the less problematic benzene. Both compounds

were converted to CO, CO₂ and H₂ only. A long-time test over 180 h revealed constant conversion of naphthalene, an increased conversion of benzene after a sharp drop, and no problems with carbon deposition. These results are very promising for further development.

15.3

Separation of Particulates and Reaction of Solids

15.3.1

Diesel Soot Abatement

The most promising technical application for reactive filtration is the removal of reactive solids from effluent gases of internal combustion engines such as diesel engines. Diesel exhaust gas contains volatile pollutants, such as hydrocarbons and NO_x together with particulate matter. Diesel particulate is a carcinogenic matter comprising small carbon particles and inorganic compounds. The soot particulates result from incomplete combustion and consist of primary particulates ranging in size from 20 to 60 nm, which aggregate to form secondary aggregates [14]. Some 90 % of these secondary particulates are smaller than 300 nm in size. On the surface of the diesel particulates there is adsorbed a huge variety of hydrocarbons. The EPA reported the presence of more than 10,000 identified chemical compounds, most of which are more or less volatile and harmful to health. Special interest is given to adsorbed polycyclic aromatic hydrocarbons (PAH), most of which are classified as being either mutagenic or carcinogenic [15–17].

Diesel soot emissions can be reduced by two different end-of-pipe technologies:

- off-line exchange-filter systems with external filter regeneration; and
- in-line filters, which regenerate during operation by direct soot combustion on the filter surface.

As an example of the performance of such a diesel particulate trap, a spontaneous filter regeneration is shown in Fig. 15.3.

The pressure drop over the filter increases continuously with time until the moment, when a critical soot load has accumulated on the filter surface. Self-ignition of the soot then occurs, which in addition depends on the exhaust gas temperature, the filter temperature, the oxygen concentration, the type and amount of the volatiles adsorbed onto the carbonaceous soot matrix, and the packing density of the soot on the filter surface. The soot-laden filter burns free, the pressure drop decreases and the loading/regeneration cycle repeats itself again, as shown in Fig. 15.4.

Diesel soot self-ignites at temperatures of approximately 600 °C. This is well above the average temperature of a diesel exhaust system, which is in the range of 150 to 400 °C. To overcome this problem, it is possible to: 1) increase the exhaust temperature by engine management measures; or 2) increase the soot reactivity or reduce the ignition temperature, respectively. Published engineering solutions [19] include the use of an open flame (e.g., by means of a diesel burner), electrical heating, additives sprayed onto the soot surface, fuel additives, catalytic generation of NO₂, which

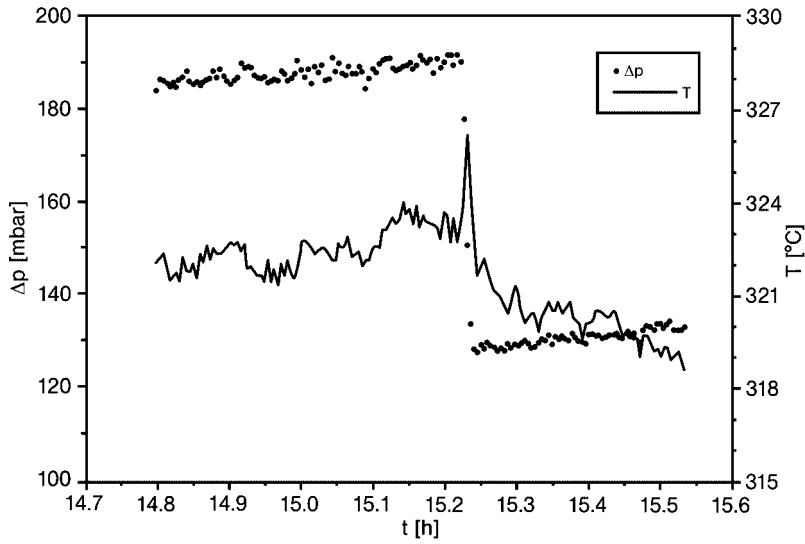


Fig. 15.3. Pressure drop over an experimental diesel particulate trap versus time, showing a spontaneous filter regeneration event (from Ref. [18]).

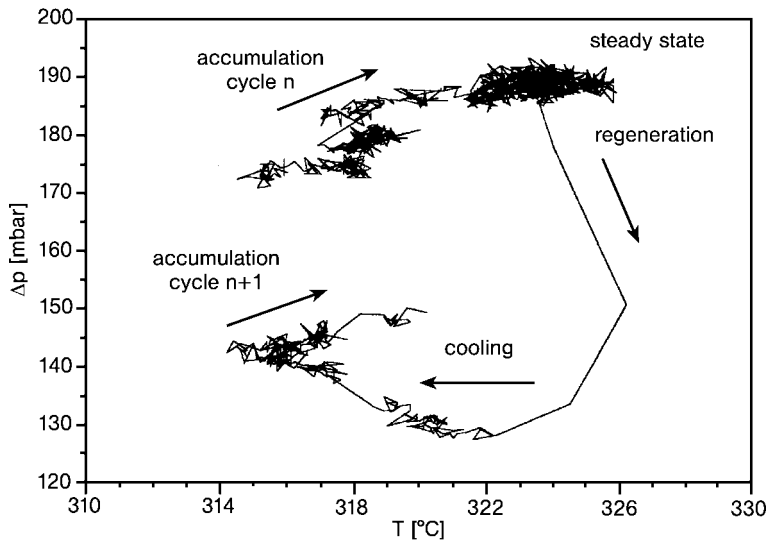


Fig. 15.4. Loading and regeneration cycle of a diesel particulate trap in the exhaust system of a 1.6 L Volkswagen test rig engine (from Ref. [18]).

reacts with the diesel soot, or catalytic combustion of the diesel soot on the filter surface, which requires an intense contact between soot and catalyst. The mechanisms of catalytic diesel soot combustion are: 1) catalytic combustion of the adsorbed hydrocarbons and co-combustion of the carbonaceous soot matrix; and 2) catalytic combustion of the carbonaceous soot matrix, which is in direct contact to the catalyst-coated filter surface.

Reactive filters and fuel additives for the reduction of diesel soot emissions have been the subject of scientific efforts for many decades. Investigations into fuel additives have been published since 1979 [20], on filter systems since 1980 [21], and on catalytic filters since 1982 [22]. The working group of Hoffman built a laboratory test rig for investigations on the catalytic combustion of real diesel soot during the late 1980s, and the first thesis and papers were published by this working group in 1989 [23] and 1990 [24]. In 1993, by running test rigs and test engines, the diesel soot community had already learned much about:

- the use of additives sprayed onto the filter surface;
- the performance and stability of many different catalytic coatings, such as Pt and Pd and the oxides of Ca, Ce, Co, Cr, Cu, Fe, Ni, Mn, V, and Zn;
- the performance of different filter designs, such as foam ceramic filters, sintered ceramic filters, packed-bed filters, and fiber filters made from different materials, such as CeO_2 , SiC, ZrO_2 , Al_2O_3 , TiO_2 , and stainless steel; and
- the use of fuel additives.

Today, in 2004, the reactive diesel soot filter finally seems to have become a state-of-the-art technology (Tabs. 15.1 and 15.2).

The question remains – why did it take so long from the laboratory to the market? The answer comprises three reasons:

1. End-of-pipe technology is not attractive – both technically and economically.
2. The reduction of diesel soot emissions measured as a soot deposit on a filter paper was achieved more easily by improved fuel injection and engine control technique.
3. The European regulations did not require lower soot emission levels.

By using improved fuel injection and engine control techniques, the concentration of soot particles in the exhaust gas was reduced (less gray filter paper), but the number of soot particles was increased and their average size was reduced, which made the diesel engine emissions even more harmful. So, everyone was back to square one – and the unfavored end-of-pipe technology for the reduction of diesel soot emissions came back to life again!

15.3.1.1 Filter Types and Catalyst Performance

The particulate filter must perform equally well in different areas. High mechanical and thermal stability, together with a high surface area, high filter efficiency, and low pressure drop, are the main requirements. The design and geometry must ensure a close contact between the filter surface and the deposited soot [25, 26]. The soot should be packed on the filter surface as densely as possible, thus ensuring high local concentrations for a maximized combustion rate [27]. Only if the contact

Table 15.1. Diesel cars available on the German market with diesel soot abatement. Data taken from the web, ADAC Germany, spring 2004.

Make	Type	Availability
Audi	A4, A6, A8	mid 2004
BMW	5	beginning 2004
Citröen	C5, C8	can be ordered
Fiat/Alfa	Ulysse	can be ordered
Ford	Focus C-Max, Mondeo	2004
Jaguar	X-Type	2004
Mazda	diverse	2004
Mercedes	C-, E-Class, 200 and 220 CDI	can be ordered
Opel	Vectra, Signum, Astra	2004
Peugeot	307, 406, 607, 807	can be ordered
Renault	Vel Satis, Espace, Laguna	2004
Toyota	Avensis D4D D-Cat (limousine)	can be ordered
Volvo	diverse	mid 2004
VW	Passat 2.0 TDI	can be ordered

Table 15.2. Different methods of diesel soot abatement: the state of the art.

Provider	Technology
Peugeot	Fuel additive, ignition temperature ~ 450 °C. Increase of exhaust temperature by exhaust port injection. Filter material: silicon carbide
HJS	Fuel additive, ignition temperature ~ 200 °C. Assisted regeneration by electrical heating. Filter material: sinter metal
Toyota	DPNR = Diesel Particulate NO _x -Reduction. No fuel additive, NO oxidation forming NO ₂ . BaO as intermediate buffer for NO ₂
Bosch	Based on HJS technology. Sinter ceramic filter with catalytic coating
Greenpeace	Using a Peugeot filter and a primary catalyst with high loads of Pd resulting in high NO ₂ levels. Self-generation by reaction of NO ₂ with diesel soot

between soot and catalyst can be increased can the catalytic coatings have a major impact on diesel soot combustion [28].

Many different filter designs have been the subject of experimental studies on diesel soot combustion. In the early investigations, structured honeycomb filters made from cordierite, such as those applied for the three-way catalyst for the reduction of spark ignition engine gas emissions, were the focus of the experimental studies [29–39]. The experimental results with these filters were not promising, because the cordierite honeycomb filter did not withstand the thermal stress. Temperature peaks of almost 1200 °C were measured, after which the ceramic structure was partly melted or totally destroyed [29, 40].

To overcome this challenge, other filter designs and construction materials were tested, such as packed-bed filters [41], foam ceramic filters [39, 42–44], sintered ceramic filters [18, 45, 46], candle-type filters made from metal or ceramics [22, 47], or honeycomb structures made from steel [48]. Among the construction materials, the performance of high-temperature ceramics, such as SiC, ZrO₂, or SiO₂, was investigated [18, 45, 46, 49].

To accelerate the combustion of diesel soot deposited on the filter surface, a huge variety of different single, binary, and ternary catalyst systems comprising metal oxides from all over the periodic table of the elements, such as the oxides of Al, Ca, Ce, Co, Cu, Cr, Fe, K, La, Mn, Ni, Si, Ti, V, and Zr, together with noble metals such as Pd or Pt, were tested in laboratory experiments on real diesel soot [24, 46, 49–54]. Besides a high activity for diesel soot combustion, those catalyst must withstand high temperatures without aging, and must also resist poisoning by water or sulfur dioxide.

More recent investigations have been conducted into NO_x-assisted soot oxidation [55, 56]. NO₂ was suggested as an oxidation agent to assist the combustion of particulate matter in the presence of oxygen in the exhaust gas [57]. NO₂ can be produced by catalytic oxidation of NO prior to the catalytic filter.

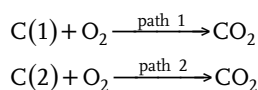
15.3.1.2 Formal Kinetics and Modeling

Many working groups have modeled the performance of diesel particulate traps during the past few decades. Concentrated parameter models (CSTR assumption) have been applied for the evaluation of formal kinetic models and model parameters. The formal kinetic parameters lump the heat and mass transfer effects with the reaction kinetics of the complicated reaction network of diesel soot combustion. Those models and model parameters were used for the characterization of the performance of different filter geometries and filter materials, as well as of the performance of a variety of catalytically active coatings and fuel additives [58].

The pressure drop over a soot filter and the concentration versus time function gained from an experiment in a closed gas-loop system are shown in Fig. 15.5. The inflection point of the oxygen respectively the carbon dioxide concentration (maximum of the respective first deviations) is often referred to as the “ignition temperature”, which is commonly used as a simple measure for benchmarking work on catalyst activity or filter performance.

Regeneration curves for different diesel particulate trap geometries and materials are shown in Fig. 15.6.

The regeneration curves are often derived from CO₂ generation data in closed-loop laboratory systems. It is assumed that the formal kinetics of soot combustion may be described by the oxidation of carbon with oxygen. A typical formal kinetic model comprises two parallel reactions of *n*-th order:



The set of formal kinetic parameters is then evaluated by a LSQ-fitting procedure.

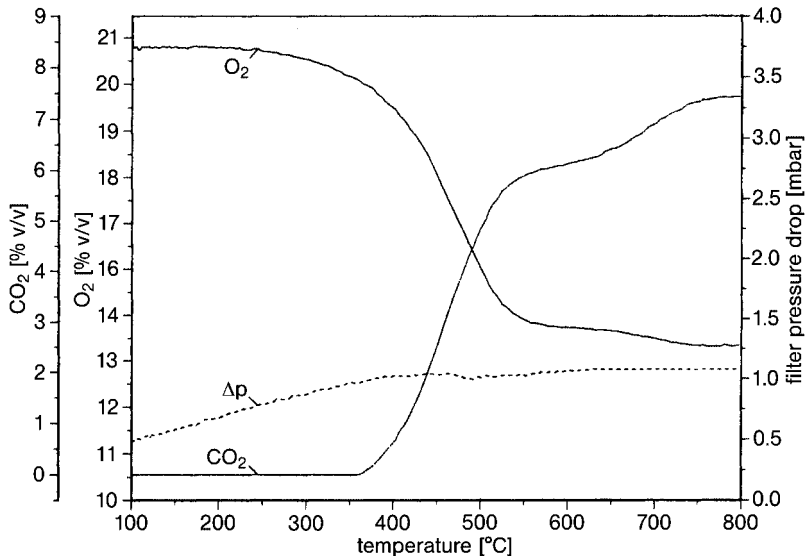


Fig. 15.5. Typical pressure drop and concentration–time curves of a diesel particulate trap in a closed gas-loop experiment with constant heating rate for the characterization of catalyst or filter performance for the combustion of diesel soot. Sintered SiC ceramic filter, without catalyst coating or fuel additive (from Ref. [46]).

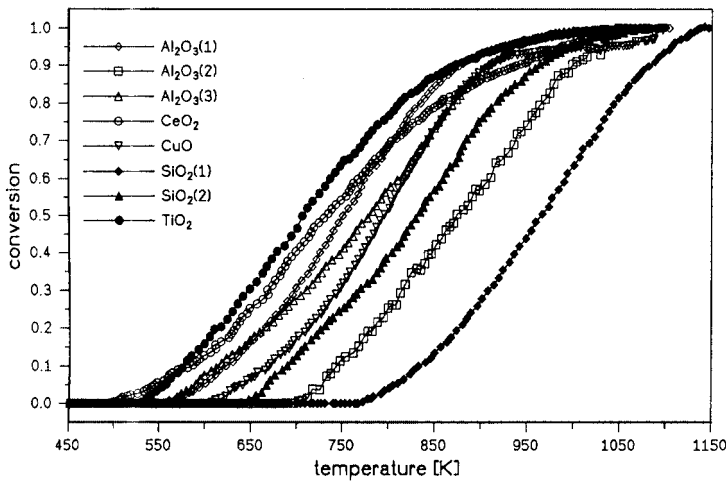


Fig. 15.6. Standardized burn-off curves of different packed-bed filter materials. Without fuel additive, filter without catalytic coating (from Ref. [46]).

Most commonly, distributed parameter models are applied to describe the performance of diesel particulate traps, which are a part of the diesel engine exhaust system. Those models are one- or two-dimensional, non-isothermal plug-flow reactor models with constant convection terms, but without diffusion/dispersion terms. They include a mass balance of particulate on the trap pore walls and a mass balance of the major gas phase compounds, such as CO, CO₂, O₂, and N₂. A pseudohomogeneous enthalpy balance with thermal conductivity of the trap is used to cover the description of temperature changes [57–64] or to calculate the thermal stress of a honeycomb-structured wall flow diesel particulate filter [65]. Haralampous et al. added a diffusion term to cover the effect of NO₂ back-diffusion, which is responsible for higher reaction rates than expected at low temperatures [66].

Some mathematical models have been developed to predict the behavior of the pressure drop over the diesel particulate trap with time during the loading/regeneration cycles [62, 67–69], to calculate the effect of filter-medium properties on filter performance of fibrous filters [70] or to describe the flow and filtration process [71] and the regeneration process [72–75]. An illustrative example for the performance of such a pressure drop model is provided in Fig. 15.7.

15.3.2

Filtration Combustion of Solid Fuels

Some interesting modeling studies have been carried out on the combustion of gaseous or solid fuels in porous ceramic reactors, which is referred to as “filtration combustion” (FC). This covers a wide range of combustion processes having a common mechanism of front propagation. The main feature of this mechanism is the delivery of gaseous reactant to the combustion front by filtration through a porous solid. FC refers to chemically heterogeneous systems, where the reactants gas and solid fuel

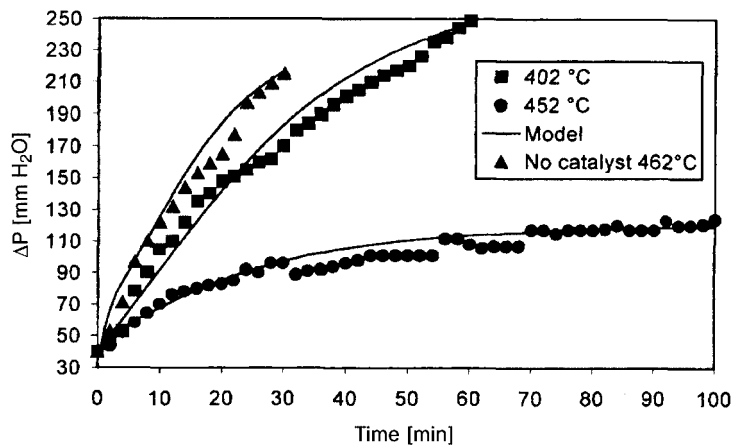


Fig. 15.7. Modeling and experimental results of the pressure drop of a catalytic diesel particulate trap (from Ref. [68]).

are initially separated and the reaction is controlled either by the chemical kinetics or by the mass transport of the gas. Co-flow filtration refers to the fact that the gaseous reactant flows to the reaction site through the product region and transfers stored heat to the reaction site and, even more importantly, to the unburned fuel region. A strong overheating of the reaction zone results, where the temperature far exceeds the thermodynamic combustion temperature. This is called the “superadiabatic effect” [76, 77].

15.3.3

Reaction Cyclone

The cyclone is a standard solids-handling apparatus for the separation of particulates from flowing liquids or gases. For the separation of particulates from gases, the cyclone is a suitable separation device for particle sizes in the range of $1\text{ }\mu\text{m}$ to $1000\text{ }\mu\text{m}$. It is characterized by high separation efficiencies, a low pressure drop, simple operation, no clogging and easy scale-up, together with low investment and operation costs. One of the unique features of cyclones is an unusual residence time distribution, which leads to much longer residence times for particulates than for gases. This makes the cyclone an interesting reactor for fast heterogeneous reactions with time constants in the range of milliseconds. The cyclone reactor is best qualified for reactions where solids are converted to volatile products, and where the volatile products should be removed immediately from the reaction zone, thus avoiding back-reactions or secondary reactions of the volatiles. Additionally, longer residence times of the solids ensure a higher conversion.

The fast pyrolysis (flash pyrolysis) of biomass to bio-oil, which has gained attention as a renewable source for fuels or chemicals [78], is such a case (Fig. 15.8).

The desired primary liquid products of biomass pyrolysis react readily in secondary cracking reactions, shifting the product yield from liquids to gases. Those cracking reactions are assisted by contact of the volatiles to the remaining solids, which can be reduced significantly by running the fast pyrolysis in a reaction cyclone [79, 80]. A simplified flow sheet of such a laboratory plant for the fast pyrolysis of biomass is shown in Fig. 15.9.

The manner of heat transfer is unusual, as this reaction cyclone is solar-heated. In any other cases, the carrier gas (e.g., nitrogen or product gas from the fast pyrolysis) must be preheated, because the heat transfer by direct contact of the particles to the cyclone wall is poor and only sufficient to keep the reactor at adiabatic conditions. Lédé built two different cyclone reactors for experiments on the fast pyrolysis of

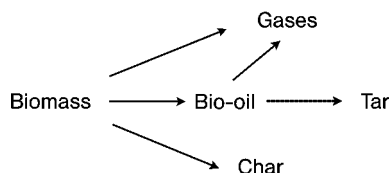


Fig. 15.8. Overall reaction pathways for the thermal conversion of biomass by fast pyrolysis

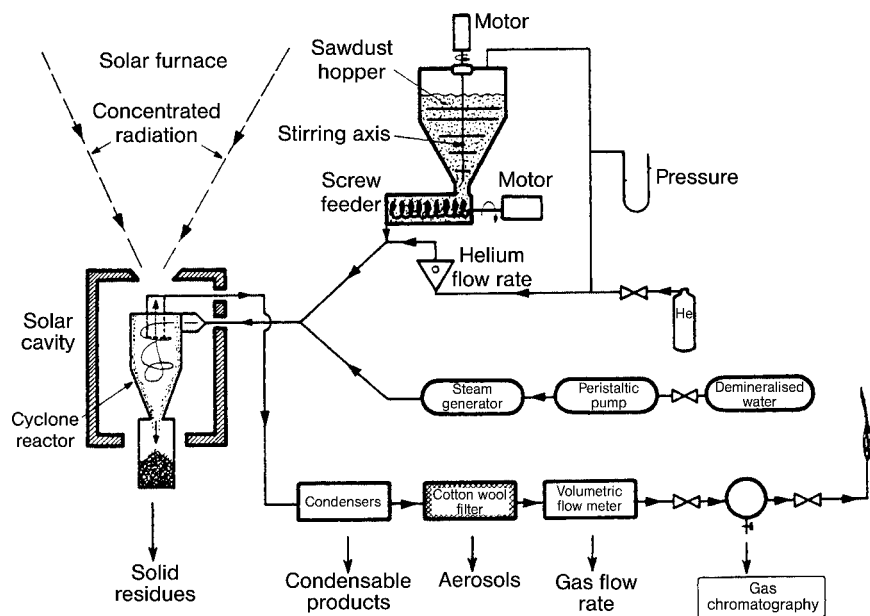


Fig. 15.9. Pyrolysis of biomass in a solar-heated reaction cyclone (from Ref. [79]).

wood sawdust. The cyclone appears to be a very efficient multifunctional reactor for either liquefaction or gasification of biomass [80].

Gabra et al. made use of a reaction cyclone for experiments on the gasification of bagasse and cane trash with steam and air to produce a combustible gas with low particle and alkali content suitable for use in gas turbines. The bagasse and the cane trash were gasified in a two-stage process, where the first stage was a cyclone acting as a combined gasification reactor and separator for the residual particles [81, 82].

An inverted cyclone gasifier and secondary cyclone combustor have been developed for use in a biomass fired, small-scale cogeneration plant. The gasifier exhaust gas is suitable for direct firing into the secondary cyclone combustor without any complex hot-gas cleaning systems. The cyclone combustor produces a strong swirling flow with good mixing and burnout patterns, creating stable combustion conditions [83].

15.4

Conclusions

Reactive filters for the removal of inert solids and of reactive volatiles are not yet a proven and reliable technique on an industrial scale. The cleaning of flue gases by reactive filtration is a tempting and elegant engineering concept with high potential energy savings due to the immense number of power plants and steam plants, which operate world-wide on the basis of fossil fuels. The application of reactive

filtration to the removal of tar from fuel gas derived by biomass gasification is also a very encouraging development, because simple and efficient gas cleaning is one of the main requirements for the commercialization of biomass gasification processes.

Reactive filters for the removal of reactive solids (i.e., diesel soot) have already passed through the test rig state. For the reactive filtration of diesel soot, industrially manufactured devices are available, but improved reaction kinetics and models predicting accurately the loading and regeneration cycles are yet to be produced.

The reaction cyclone is a promising integrated system for cases where a residence time of gases in the order of magnitude of milliseconds and an efficient separation of solids (feed or product) from the gaseous reaction products is essential for good performance. A preheated gas or heating by radiation is necessary, because the heat transfer coefficients between the wall and the reacting solids are not sufficient. Promising applications include the thermal conversion of biomass by fast pyrolysis or gasification.

The reactive filtration concept is waiting for new applications!

References

1. A. M. Dessouki, M. El-Tahawy, H. El-Boohy, et al., *Radiation Phys. Chem.*, **1999**, *54*, 627–635.
2. U. Förstner, P. Jacobs, F. v.d. Kammer, *Fresenius J. Anal. Chem.*, **2001**, *371*, 652–659.
3. J. A. Tripp, J. A. Stein, F. Svec, et al., *Org. Lett.*, **2000**, *2*, 195–198.
4. G. Saracco, V. Specchia, *Chem. Eng. Sci.*, **1995**, *50*, 3385–3394.
5. G. Saracco, S. Specchia, V. Specchia, *Chem. Eng. Sci.*, **1996**, *51*, 5289–5297.
6. G. Saracco, V. Specchia, ECCE-1, Florenz, May 4–7, 1997, Proceedings, 397–400.
7. G. Saracco, V. Specchia, Chapter 15, in: *Structured catalysts and reactors*, Eds. J. A. Moulijn, A. Cybulski, Marcel Dekker, New York 1997.
8. W. Duo, J. R. Grace, C. J. Lim, et al., *Ind. Eng. Chem. Res.*, **1999**, *38*, 260–269.
9. M. A. Alvin, *Fuel Processing Technol.*, **1998**, *56*, 143–168.
10. A. Ergut, Y. A. Levensis, G. A. Simons, *Combust. Sci. Technol.*, **2003**, *175*, 579–617.
11. Ph. Hasler, R. Buehler, Th. Nussbaumer, “Biomass for Energy and Industry”, Proc. 10th Int. Conf., Würzburg, Germany, 8–11 June 1998, 272–275.
12. H. Zhao, D. J. Draelants, G. V. Baron, *Catalysis Today*, **2000**, *56*, 229–237.
13. K. Engelen, Y. Zhang, D. J. Draelants, et al., *Chem. Eng. Sci.*, **2003**, *58*, 665–670.
14. B. S. Haynes, H. Gg. Wagner, *Prog. Energy Combust. Sci.*, **1981**, *7*, 229–273.
15. T. J. A. Ålander, A. P. Leskinen, T. M. Raunemaa, et al., *Environ. Sci. Technol.*, **2004**, *38*, 2707–2714.
16. S. D. Shah, D. R. Cocker III, J. W. Miller, et al., *Environ. Sci. Technol.*, **2004**, *38*, 2544–2550.
17. A. K. K. Virtanen, J. M. Ristimäki, K. M. Vaaraslahti, et al., *Environ. Sci. Technol.*, **2004**, *38*, 2551–2556.
18. U. Hoffmann, Th. Rieckmann, K. Schädlich, *Erdöl, Erdgas, Kohle*, **1994**, *5*, 227–232.
19. J. H. Johnson, S. T. Bagley, L. D. Gratz, et al., *SAE Techn. Paper Ser.* 1994, 940233.
20. G. Spengler, G. Haupt, *MTZ*, **1979**, *31* (3).

21. L. P. Tessier, H. F. Sullivan, G. M. Bragg, et al., *SAE Techn. Paper Ser.* 1980, 800338.
22. B. E. Enga, M. F. Buchman, I. E. Lichtenstein, *SAE Techn. Paper Ser.* 1982, 820184.
23. J. Ma, Thesis, Technical University Clausthal, 1989.
24. U. Hoffmann, J. Ma, *Chem. Eng. Technol.*, **1990**, 13, 251–258.
25. A. Löwe, C. Mendoza-Frohn, *Chem. Ing. Techn.*, **1990**, 62, 759–762.
26. J. P. A. Neeft, M. Makkee, J. A. Moulijn, *Appl. Catal. B: Environm.*, **1996**, 8, 57–78.
27. Th. Rieckmann, U. Hoffmann, *Dechema Annual Meetings*, 1993, May 26–28, Nuremberg, Germany.
28. J. P. A. Neeft, O. P. van Pruissen, M. Makkee, et al., *Appl. Catal. B: Environm.*, **1997**, 12, 21–31.
29. F. Indra, *VDI Berichte*, **1988**, 714, 327–351.
30. Z. N. Mogaka, V. W. Wong, S. M. Shahed, *SAE Techn. Paper Ser.* 1982, 820272.
31. N. Higushi, S. Mocida, M. Kojima, *SAE Techn. Paper Ser.* 1983, 830078.
32. P. Öser, U. Thomas, *SAE Techn. Paper Ser.* 1983, 830087.
33. V. D. Rao, J. E. White, W. R. Wade, et al., *SAE Techn. Paper Ser.* 1985, 850014.
34. Y. Niura, K. Okhubo, K. Yagi, *SAE Techn. Paper Ser.* 1986, 860290.
35. M. Arai, S. Miyashita, K. Sato, *SAE Techn. Paper Ser.* 1987, 870012.
36. E. D. Dainty, T. P. Kreuzer, B. H. Engler, *SAE Techn. Paper Ser.* 1987, 870014.
37. H. Berendes, H. Eickhoff, *VDI Berichte*, **1989**, 765, 559–569.
38. F. Shadman, *Combust. Sci. Tech.*, **1989**, 63, 183–191.
39. O. Shinozaki, E. Shinojama, K. Saito, *SAE Techn. Paper Ser.* 1990, 900107.
40. H. O. Hardenberg, H. L. Daudel, H. J. Erdmannsdörfer, *SAE Techn. Paper Ser.* 1987, 870016.
41. B. Wiedemann, U. Doerges, W. Engeler, et al., *SAE Techn. Paper Ser.* 1983, 830086.
42. G. W. Schweimer, *VDI-Berichte*, **1984**, 178, 447–463.
43. J. J. Tutko, H. F. Sullivan, G. M. Bragg, et al., *SAE Techn. Paper Ser.* 1984, 840073.
44. Y. Kiyota, K. Tsuji, S. Kume, et al., *SAE Techn. Paper Ser.* 1986, 862094.
45. U. Hoffmann, Th. Rieckmann, K. Schädlich, *Erdöl, Erdgas, Kohle*, **1994**, 4, 163–170.
46. U. Hoffmann, Th. Rieckmann, *Chem. Eng. Technol.*, **1994**, 17, 149–160.
47. K. Schnitzlein, A. Löwe, *Chem. Eng. Sci.*, **1990**, 45, 2671–2678.
48. C. Knab, A. Messerer, R. Nießner, et al., *Chem. Ing. Techn.*, **2004**, 76, 1092–1096.
49. D. Fino, G. Saracco, V. Specchia, *Industrial Ceramics*, **2002**, 22, 37–43.
50. R. E. Marinangeli, E. H. Homeier, F. S. Molinaro, *Stud. Surf. Sci. Catal.*, **1987**, 30, 457–467.
51. P. Ciambelli, P. Parrella, S. Vaccaro, *Catalysis and Automotive Pollution Control II, Proceedings*, Elsevier, 1991, 685.
52. J. van Doorn, J. Varlout, P. Mériadeau, *Appl. Catal. B*, **1992**, 1, 117–127.
53. P. G. Harrison, I. K. Ball, W. Daniell, et al., *Chem. Eng. J.*, **2003**, 95, 47–55.
54. S. Kureti, K. Hizbullah, W. Weisweiler, *Chem. Eng. Technol.*, **2003**, 26, 1003–1006.
55. K.-H. Choi, Y. Korai, I. Mochida, *Combust. Flame*, **2004**, 137, 255–260.
56. A. Setiabudi, M. Makkee, J. A. Moulijn, *Appl. Catal. B: Environmental*, **2003**, 42, 35–45.
57. G. C. Koltsakis, A. M. Stamatelos, *Ind. Eng. Chem. Res.*, **1997**, 36, 4155–4165.
58. U. Hoffmann, Th. Rieckmann, J. Ma, *Chem. Eng. Sci.*, **1991**, 46, 1101–1113.
59. E. J. Bissett, *Chem. Eng. Sci.*, **1984**, 39, 1233–1244.
60. H. Aoki, K. Asano, K. Kurazono, et al., *SAE Techn. Paper Ser.* 1993, 930364, 155–161.
61. A. G. Konstandopoulos, M. Kostoglou, P. Housiada, *SAE Techn. Paper Ser.* 2001, 2001-01-0908, 111–122.
62. D. Fino, G. Saracco, V. Specchia, *Chem. Eng. Sci.*, **2002**, 57, 4955–4966.
63. O. A. Haralampous, G. C. Koltsakis, *Chem. Eng. Sci.*, **2002**, 57, 2345–2355.

64. M. Kostoglou, P. Housiada, A. G. Konstandopoulos, *Chem. Eng. Sci.*, **2003**, 58, 3273–3283.
65. Y. Miyairi, S. Miwa, F. Abe, et al., *SAE Techn. Paper Ser.* 2001, 2001-01-0912, 161–176.
66. O. A. Haralampous, G. C. Koltsakis, *Ind. Eng. Chem. Res.*, **2004**, 43, 875–883.
67. G. Saracco, C. Badini, V. Specchia, *Chem. Eng. Sci.*, **1999**, 54, 3035–3041.
68. G. Saracco, N. Russo, M. Ambrogio, et al., *Catalysis Today*, **2000**, 60, 33–41.
69. M. Ambrogio, G. Saracco, V. Specchia, *Chem. Eng. Sci.*, **2001**, 56, 1613–1621.
70. S. H. Oh, S. McDonald, G. L. Vaneman, et al., *SAE Techn. Paper Ser.* 1981, 810113.
71. C. N. Opris, J. H. Johnson, *SAE Techn. Paper Ser.*, 1998, 980545, 149–175.
72. K. Schnitzlein, *Chem. Eng. Technol.*, **1997**, 20, 317–325.
73. K. Schnitzlein, T. Ratte, *Chem. Eng. Technol.*, **1998**, 21, 179–186.
74. K. Schnitzlein, *Chem. Eng. Technol.*, **2001**, 24, 1281–1287.
75. P. Versaavel, H. Colas, C. Rigauddau, et al., *SAE Techn. Paper Ser.* 2000, 2000-01-0477, 129–139.
76. A. P. Aldushin, I. E. Rumanov, B. J. Matkowsky, *Combust. Flame*, **1999**, 118, 76–90.
77. C. Lu, Y. C. Yortsos, *Ind. Eng. Chem. Res.*, **2004**, 43, 3008–3018.
78. S. Czernik, A. V. Bridgwater, *Energy Fuels*, **2004**, 18, 590–598.
79. J. Lédé, F. Verzarro, B. Antoine, et al., *Chem. Eng. Proc.*, **1986**, 20, 309–317.
80. J. Lédé, *Ind. Eng. Chem. Res.*, **2000**, 39, 893–903.
81. M. Gabra, E. Pettersson, R. Backman, et al., *Biomass Bioenergy*, **2001**, 21, 351–369.
82. M. Gabra, E. Pettersson, R. Backman, et al., *Biomass Bioenergy*, **2001**, 21, 371–380.
83. C. Syred, W. Fick, A. J. Griffiths, et al., *Fuel*, **2004**, 83, 2381–2392.

16

Reaction-Assisted Granulation in Fluidized Beds

*Matthias Ihlow, Jörg Drechsler, Markus Henneberg,
Mirko Peglow, Stefan Heinrich and Lothar Mörl*

16.1

Introduction

The intensive heat and mass transfer in fluidized-bed spray granulation has been reported in many publications. As described in Section 16.1.2, this characteristic of fluidized-bed spray granulation is one of the reasons why this process covers a broad operational area in process engineering. Fluidized bed spray granulation is an evolutionary application where the drying process, shaping and homogenization, as well as thermal treatment processing, for granular solids are coupled. The objective of these studies was to model processes during the removal of sulfur dioxide in liquid sprayed fluidized beds by injection of a calcium hydroxide suspension, and a reactive absorption with a high conversion of the absorbed gas component on the wetted surface of the fluidized particles. The process of dissolution of the gaseous components in a liquid is termed “absorption”. Therefore, it would be possible to realize the process of absorption, chemical reactions, drying and granulation in a single step. In this chapter, a model is developed for the semi-dry flue gas desulfurization in a fluidized bed as an example of reaction-assisted granulation in fluidized beds [41, 42].

The pollutant sulfur dioxide is a product by the oxidation of sulfur during combustion. Besides carbon dioxide and water, many pollutants are produced by the combustion of fossil energy sources (e.g., hydrocarbons (C_mH_n), carbon monoxide (CO), nitrogen oxides (NO_x)) as well as sulfur dioxide (SO_2), and these cause the majority of environmental damage. For example, over 60 % of forests in Germany are affected by acid rain, and about 20 % of them are heavily damaged [11]. Moreover, for decades the continuing decay of historical buildings as well as the human health endangerment has been caused by air pollution.

16.1.1

Gas Cleaning

Product disposal and/or utilization, the investment and the operating costs, the space requirement for the plant, the possible wastewater accumulation and the material conversion are all important criteria for the selection of a desulfurization plant.

Flue-gas desulfurization processes can be arranged into primary and secondary processes. In primary processes, the desulfurization takes place directly in the combustion chamber. These processes are technically easily feasible, but they have many disadvantages – for example, there is no usability of the produced solid, lime consumption is high, and desulfurization is low. Secondary desulfurization processes do not suffer these disadvantages because they are carried out in downstream plants. The most well-known secondary processes are detailed in Ref. [41]. Another classification into dry, semi-dry and wet flue gas desulfurization processes has been proposed, whereby semi-dry and wet desulfurization are technically important. After Schultes [82], the advantages of the semi-dry processes are the effective material conversion at low temperatures, the unproblematic separation of the reaction product, and no wastewater production. One disadvantage which contrasts with wet gas cleaning is that the reaction products of the dry and semi-dry desulfurizations are not usable, or are usable only after a secondary treatment. In general, a common problem of the semi-dry processes is treatment of the dust. The final classification describes regenerative and non-regenerative processes.

At present, almost 200 fossil-fuelled power plants with flue gas desulfurization are in operation, and the total electrical power produced is over 53,000 MW. The different process variants, together with their market shares, are listed in Tab. 16.1.

Thus, 87 % of power plants in Germany operate on the basis of wet-chemical processes with calcium. Here, the process involves limestone cleaning or a variant, the Saarberg Hölter process. The spray absorption process equates to only 8 % of the market, but if all calcium-based desulfurization plants were to be combined, the market share would increase to 97 %. One reason for this is the high affinity between calcium and sulfur dioxide, coupled with the almost inexhaustible availability of limestone. The critical points for using this technology include total investment and operating costs, in addition to agreement with all legal regulations.

Table 16.1. Classification of the gas desulfurization processes in Germany [84].

Processes	Electrical power	
	[MW]	[%]
Fluidized bed	500	0.94
Ca dry process	200	0.38
Ca semi-dry process	4,400	8.26
Ca wet process	46,535	87.4
– coal	25,780	
– brown coal	18,950	
– gas and oil	1,805	
Na wet process	1,000	1.88
Na-Ca wet process (two-stage)	270	0.51
Activated coke process (simultaneous NO _x -separation)	240	0.45
Miscellaneous	100	0.19
Sum	53,245	100

16.1.2

Application of the Gas-solid Fluidized Bed

Fluidized-bed technology was founded in 1922 by Winkler [99] for coal gasification, but has since been extended into many areas of applications which require different constructions of fluidized-bed apparatus. Typical examples of these are described in Refs. [7] and [93].

Technical fluidized-bed plants can fundamentally be divided into those for physical processes and chemical processes. Fluidized beds used for physical processes have applications in mixing, drying, coating, granulation, agglomeration, adsorption, heating and cooling of bulk materials. The plants for combustion, gas cleaning, water purification, catalytic reactions and gas–solid reactions belong to chemical fluidized-bed processes.

It is also possible to use fluidized beds for the horizontal or vertical transport [95] of bulk materials. Fluidized beds can also be used as mixer reactor with an immersed agitator [95] to improve mixing behavior, or as a separator of components of a bulk mixture. The separation occurs due to the different densities or diameters of the components, an example being the separation from ores. This process is described by Reboux [76] as a dry flotation process. Further examples are found in agriculture, for example separating potatoes and stones [97], and in the woodworking industry [44].

Fluidized-bed granulators and agglomerators are very common. Using this process, atomizable liquids (e.g., suspensions, solutions, emulsions or melts) can be converted into free-flowing granular solids. Fluidized-bed granulation and agglomeration finds application in a wide range of industries, including pharmaceuticals, foodstuffs, fertilizers, detergents, mineral processing, and specialty chemicals. Overviews of these processes are available in Refs. [3, 91, 93]. Other important examples of fluidized bed use in reactive granulation are the production of sodium percarbonate [8, 45] and the neutralization of tensides [73]. Another use is the coating of fabric or paper drains, and the coating of hot metals by immersion into the powder-like bed. A continuous plant for the coating of fabric drains is described in Ref. [7].

Fluidized bed technology has prevailed for the heating, cooling, drying and adsorption of porous materials due to a high heat transfer between the fluidization gas and the bed material. Examples are the preheating unit for the tempering process of cement in a rotary kiln [94] and the continuous cooling of particles in rectangular fluidized-bed channels or multi-stage cylindrical apparatuses [58]. Fluidized-bed dryers permit a drying process of thermal-resistant and fluidizable, powdered or granular materials. It is also possible to use superheated steam as fluidizing gas to achieve an inert atmosphere. For industrial applications, the superheated steam cycle offers a series of energy-saving and plant safety advantages [29, 33, 64, 65]. In continuous fluidized-bed adsorption plants, the adsorber can be combined with the desorber, the main problem being the strong attrition of the adsorbent due to the fluidization. Ermenc [21] described a multistage adsorption process for the humidity removal of gases using silica gel.

Combustion plants are classical chemical fluidization plants. The stationary and circulating fluidized bed combustions must be differentiated one from another. The

advantages of fluidized-bed combustion plants are the intensive heat and mass transfer, the low combustion temperature, the long residence times, and the renouncement of REA- and DENOX plants [6]. For optimal operation, the temperature must be between 750 °C and 950 °C. According to Kaltschmitt and Hartman [46], the disadvantage of this technique is the heating-up time (which depends on the installed power) and the high pressure drop in the fluidized bed. Furthermore, this process is characterized by high specific investment and operating costs. The major problem is the attrition of the apparatus wall by inert and combustion materials. One publication from 1968 highlights the fact that combustion in fluidized beds is a very dated technique [77].

A further example of using chemical fluidized-bed processes is that of plants where fluidizable solids are used as a heat transfer medium. Willing [98] describes the use of this process for the cracking of oil arrears, but fluidized-bed plants are also suitable for catalytic or gas–solid reactions. The easy controllability of the reactor temperature is emphasized by Baranek et al. [7], wherein the heat of reaction can be used by immersed coolers to generate steam. The isothermal behavior, and the possibility of both supplying and removing heat, are further advantages.

Experiments were conducted at the University of Magdeburg to examine the partial oxidation of ethane to ethylene by dosing oxygen into the fluidized bed of porous catalysts using immersed sintered metal and ceramic membranes. These studies were related to a DFG (German Research Association) research group (DFG-Nr. FOR 447/1-1) “Membrane supported reaction engineering” in the subproject “Fluidized-bed membrane reactor”.

16.1.3

Modeling and Experimental Set-up

Simultaneous execution of reactive absorption and granulation is the most recent application of the liquid-sprayed gas–solid fluidized bed. Hence, although no models have been published for the computation and interpretation of such a process, several different models describing subprocesses are available. Indeed, the absorption of spray drops has been the subject of many investigations over several years.

Danckwerts [16] showed, on the basis of the absorption of sulfur dioxide in water and of carbon dioxide in solution, that absorption increases by dissociation processes.

The effect of solid particles in the gas–liquid phase boundary on absorption was investigated by Ramachandran and Sharma [74], who showed the absorption process to be strengthened by chemical reaction between the absorbed component and the solid in solution.

Uchida and Wen [92] also proposed a mathematical model for absorption by dividing the concentration profiles of the absorbed gas and migration of the solid into solution in six classical cases, including the boundary conditions.

Sada et al. [79] experimented with stirred vessels to determine the absorption of CO₂ and SO₂ in calcium hydroxide suspensions, and found their results to be comparable with others [74, 92]. These authors concluded that an increase in the solid

concentration in suspension leads to an improved absorption of gases; moreover, the gas absorption when overlaid with the chemical reaction in suspension could be computed using the model of Uchida and Wen.

Several other groups [9, 10, 72, 80, 83, 96] investigated the classical concentration profiles at absorption introduced by Uchida and Wen and, as an alternative to the film theory and describing processes at the phase boundary, postulated the penetration theory.

Von Getler et al. [23] were the first to consider these processes during spray absorption drying when they examined the material system of SO_2 and $\text{Ca}(\text{OH})_2$. In the opinion of these authors, the absorption of sulfur dioxide is limited either by the dissolution of solid or by the gas-phase mass transfer in the first drying period of the drop. The product of this reaction causes substantial diffusion resistance for the absorbed sulfur dioxide and thus obstructs further reactions as the calcium hydroxide remains in the core.

Chang and Rochelle [12–15] investigated some aspects of SO_2 absorption in an agitated cell filled with aqueous solution or suspension, and compared their measurements with those of other authors with simulated absorbed mass flows, based on enhancement factors from the film and surface renewal theory. The results showed that mass transfer, when corrected by an enhancement factor from the surface renewal theory, agreed clearly with the measurements.

Krishnamurthy and Taylor [51] developed a so-called “non-equilibrium stage model”, the characteristics of which were the balance of mass and energy for each component in the two phases. These are coupled over the energy and mass flows in the boundary layers and are at equilibrium at the phase boundary.

Experimental investigations and theoretical computations of SO_2 absorption in a spray drier [47] showed that, with an excess of calcium hydroxide absorption is limited only by the gas-phase mass transfer. In addition, the flow in a spray drier could be described by the model of an ideal stirred vessel. Newton et al. [70] considered the subprocesses of mass transfer of SO_2 from the gaseous phase to the drop surface, the absorption, the dissociation of SO_2 , the diffusion of the produced species and the dissolution of calcium hydroxide particles in the drop.

The mathematical models of Partridge et al. [71] and Dantuluri et al. [17] referred to a liquid-phase transport resistance for SO_2 and the calcium hydroxide solution. These authors assume a reduction of the distance between calcium particles during the drying process of the drop. As a result, a decrease of the liquid-phase mass transfer for the SO_2 occur. They concluded that the gas-phase mass transfer limits absorption at the end of drying.

Korischem and Werner [49, 50] simulated the procedures of flue-gas scrubbing of an industrial waste combustion plant. Their model considered the mass and heat transfer process between gas and liquid phase by neglecting the solids present in the suspension.

Luckas and Lucas [62] also investigated the thermodynamic processes of wet flue-gas scrubbing, while others [52–61, 63] dealt extensively the description and computation of phase and reaction equilibrium for many materials. Hill [40] deduced experimental and theoretical values for SO_2 separation from flue gases in a spray

drier, and noted that "... careful drying conditions lead to a large absorption factor". A number of additional parameters were examined, including the drop diameter, the stoichiometric ratio and water vapor content. Ultimately, the model developed provided an excellent description of the process during spray absorption.

Schultes presented an absorption model for packed columns including simulations [81], while Eden [18] developed a non-equilibrium stage model describing the absorption of electrolytes in co-current and countercurrent scrubbers. The simultaneous view of phase and reaction equilibrium and the existence of solids in the liquid phase were emphasized in these reports.

In addition to knowledge of absorption, mass and heat transfer, drying processes and possibly also the bubble behavior of fluidized beds, particle growth is also of interest in the development of a suitable model. The performance of bubbling fluidized beds is influenced by, and may also be limited by, the distribution and mixing of fluid and solids in the bed, and by transport phenomena. Particle-to-fluid heat and mass transfer coefficients which appear to be much smaller than respective values for single particles are a well-recognized expression of this effect. Indeed, too-low values of the transfer coefficients could be explained on the basis of suspension gas back-mixing, while the performance of fluidized-bed evaporators and dryers could be predicted accurately, without any fitting [27].

Mörl [67, 68] provided the basis for future studies on the computation of height-dependent air humidity, air temperature and degree of wetting in liquid-sprayed fluidized beds. Also based on measurements of temperature dependency on height, Trojosky and Mörl [88–90] stated that a rapid fall in air temperature could not be attributed to evaporation of the liquid at the particles; rather, this was due to the heat transfer of hot air to the cool particles. These results led to the proposal of a new mathematical model which describes the temperature and humidity in liquid-sprayed fluidized beds by introducing an axial dispersion coefficient for solid mixing. The model was validated for different fluidized bed plants, but was later extended to the radial dispersion of solids to compute temperature and humidity distribution in liquid-sprayed fluidized beds [30–32, 34–39]. Likewise, a three-dimensional model for humidity, temperature and concentration fields was also proposed [28] and used to compute the humidity and temperature of air, the degree of particle wetting, liquid film temperature on the particles, particle temperature, local liquid loading and locally evaporated water mass flow for different operating parameters and/or measured variables. Stationary spatial air temperature distributions were measured using a specially prepared probe in both a semi-industrial (diameter 400 mm) and an industrial fluidized-bed plant (diameter 1500 mm) of the IAUT, and the data obtained were compared with simulation results. The results confirmed the dependency of substantial temperature gradients in the bed on the position and number of nozzles employed.

In many reports, the terms of granulation and agglomeration are often used equivocally, but in the present studies "granulation" is used to indicate the onion-like growth of particles. In contrast, the sticking together of particles to form a blackberry-like structure is termed "agglomeration".

Mörl [67, 68] assumed in his growth model that the solid in the suspension would deposit itself onto the particles, depending on the size of its surface. Hence, small particles would receive less solid than large particles, such that the growth rate (i.e., the change of diameter over time) would be identical for both large and small particles. Consequently, and as a result of a constant particle surface over the time, a growth in linear diameter will occur. Smith and Nienow [86] used this model to describe the growth process and validate the model on the basis of their own experimental data, and found a good agreement between model and measured data. Physically justified conceptions to describe the granulation, the coating and the drying in fluidized beds has been derived [2, 19, 20, 43]. For nonporous, wetted surface particles, a viscous Stokes' number, which relates relative kinetic energy (capillary dissipation) between colliding particles and viscous dissipation of the binder liquid is given by:

$$St_V = \frac{8\rho_p r_p w_p}{9\eta_{susp}}, \quad (1)$$

where ρ_p , r_p , w_p , η_{susp} , is the particle density, the particle radius, the relative particle collision velocity and the dynamic viscosity of the binder liquid, respectively. A critical viscous Stokes' number is used as a boundary condition

$$St_V^* = \left(1 + \frac{1}{e}\right) \ln\left(\frac{\Delta f}{s_R}\right), \quad (2)$$

where e is the coefficient of restitution, Δf is the thickness of the liquid surface layer (liquid film thickness), and s_R is the characteristic height of surface asperities. The model predicts that collisions will result in coalescence when the viscous Stokes' number is less than the critical viscous Stokes' number. Therefore, more agglomeration takes place with increasing particle diameter, particle collision velocity and particle density. On the other hand, increasing the binder viscosity decreases the rate of granule consolidation. Studies conducted by Link [59, 60] were also based on the surface-proportional particle growth. These investigations, which were related to the wettability and properties of granulates were carried out as single particle levitator experiments. The degree of separation of droplets onto particles, and the growth of the particles, can be understood as a function of adhesion efficiency and impact efficiency. Impact efficiency increases with increasing velocity of the drops. However, adhesion efficiency falls, starting from a certain velocity and thus the product of both quantities, the separation efficiency, will attain a maximum. Furthermore, an improvement in wettability was determined with higher particle moistures due to smaller gas inlet temperatures. A higher particle moistures leads to improved capillary liquid transport and, thus, to wettability. The capillary liquid transport of the pore saturation is limited by a moist surface. Besides reducing adhesion efficiency and growth rate, the reflection and destruction of the drops is also possible. This

means, with respect to fluidized-bed spray granulation drying, that an average surface moisture of the particles must be adjusted, and this can be varied via the injection rate as well as by changing the ratio of drying time to spraying time due to different fluidizing air temperatures, nozzle arrangements, bed masses and particle circulation rates. A further possibility to improve wetting is to reduce the surface tension by adding tensides. As mentioned earlier, the growth rate increases progressively with increasing solid concentration, this being due to an increase in adhesion efficiency via an increase in viscosity and a decrease in surface tension expressed by the capillary number. Becher [5] also suggested that in addition to the necessary particle–particle impacts, a sufficiently large particle moisture must exist for liquid bridges to form and, in turn, for successful coalescence. Starting from a critical liquid mass flow, agglomerate formation in the fluidized bed increases strongly.

Mörl [67, 68] reported a similar behavior with the degree of wetting. Likewise, the agglomeration mechanism could be confirmed with the help of this model by raising liquid mass flows, gas inlet temperatures and gas mass flows.

Turton et al. [91] suggested a further growth model. According to their concept, two cases could be differentiated – namely, that either each particle stays at the same position for a very long period in the spray of the nozzle, or a circulation time could be computed, depending upon the size of the particles. Subsequently, larger particles circulate more frequently and thus receive a thicker granulate layer than smaller particles. The different approach of Turton et al. should be recognized as being analogous to surface-proportional growth.

Further experimental investigations [100] showed that granulates growth increases if the suspension mass flow increases, and the bed temperature or the gas mass flow is reduced. An increase of throughput in atomization air leads to smaller drops, which in turn results in reduced growth. These findings confirmed those of other authors.

Zank and colleagues [101, 102] investigated growth processes in continuously operated fluidized-bed granulators. On the basis of their installed configuration, they defined a circulation time for particles in the fluidized-bed granulator, and assumed that the diameter changed by Δd within a circulation. A size-dependent particle growth was identified within the examined diameter range.

Many reports have been made on experimental and theoretical investigations in the area of liquid sprayed-fluidized beds by Heinrich [30], who dealt comprehensively with the modeling of heat and mass transfers, as well as with particle populations in the fluidized beds.

16.2 Modeling

The granulator with coupled reactive absorption is modeled in such a way that simultaneous computation of the conversion of the component removed from gas and granulates growth is considered. A balance area from the bottom to the top of the fluidized bed, including the apparatus wall, has been considered. The gas fluidizes particles above the air distribution plate, whilst liquid injection is possible from all directions by using either one-component or multi-component nozzles in the

form of drops. Part of the drops is deposited onto the particles and is distributed through spreading. This wetted particle area is the mass transfer surface for the absorption process. The process of dissolution of gaseous components in a liquid is termed “absorption”. In principle, the physical absorption is different from the chemical absorption. Physical absorption is the dissolution of a gas component in a pure liquid. During chemical or reactive absorption, the gas component to be absorbed reacts with the reactant contained within the liquid. Physical absorption in the gas–solid fluidized bed is not meaningful due to the constant drying process of the liquid on the particles. Furthermore, the solubility of most gases is limited in pure liquids, such that chemical gas cleaning is frequently used with technical absorption processes [87]. In time, the dissolved gas is removed stepwise by means of a chemical reaction from the absorption equilibrium. This offers the possibility of obtaining higher separation rates and/or conversions.

Investigations of absorption in liquid-sprayed gas–solid fluidized beds in the context of these investigations are limited to the material system of sulfur dioxide, air, and calcium hydroxide suspension. Here, the calcium hydroxide represents the reactants necessary in the liquid for the shifting of the equilibrium.

16.2.1

Model Assumptions

These are many-fold, and include the following:

- The gas flows as ideal plug.
- Fluidization of the fluidized bed is homogeneous, i.e., the porosity of the bed is constant.
- The liquid and/or suspension load of the fluidizing material is locally independent.
- The basis for the description of evaporation is the film theory. All resistances are in the gas-phase boundary film. A liquid-phase mass transfer is not considered.
- The phase and dissociation balances are instantaneous.
- Fluidized-bed reactors are often rotationally symmetrical, and spraying takes place at different positions (uniform distribution of the sprayed liquid). Thus, a one-dimensional approach is used.
- The fluidized bed material is mono-disperse and has the form of an ideal sphere.
- The liquid on the particles forms a coherent film of thickness Δ_{film} .
- The fluidized-bed material is non-porous; hence, diffusion processes in the pores are not considered.
- The gas mixture contains dry air as the inert component and the components SO_2 and water vapor.
- The reactions and/or dissociation processes take place only in the liquid; there are no reactions in the gas phase.
- There is no transport resistance in the gas–liquid phase boundary surface.
- The BIOT-number of the solid particles is so small that the unsteady heat conduction in the particle is neglected.

- Heat conduction in the liquid film and in the apparatus wall is also not considered.
- Any non-converted reactant of the suspension and the reaction product are deposited on fluidized-bed material after the drying process, and can be removed from the bed material by attrition. The dust due to the attrition is elutriated with the gas flow from the fluidized bed.
- The hold-up material and the sprayed solid with the suspension have same densities.
- Agglomeration and breakage processes are not considered.
- The granulation process follows the surface-proportional growth.
- The attrition process is described with a surface-proportional attrition coefficient.
- There is no particle discharge due to hydrodynamic processes.
- The residence time of the dust feeding from outside of the granulator is negligibly small.
- The Reynolds number at the fluidizing point is computed according to Goroschko [26].
- The computation of the relative void volume is also calculated according to Goroschko [26].
- The heat and mass transfer coefficients between gas and particle are computed according to Gnielinski [25].
- The computation of the heat losses from the apparatus wall to the environment is done with the equations proposed by Kast and Klan [48].
- The steam pressure of the water vapor in the model is determined by the method of Baehr [4].
- The description of the surface proportional growth of granulates follows according to Mörl [67, 68].
- The description of the surface proportional attrition of granulates is taken from Rangelova [75].

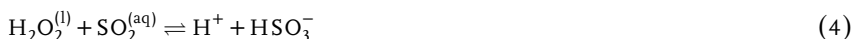
16.2.2

Phase and Reaction Equilibrium

The phase equilibrium of SO_2 and the dissociation and reaction equilibrium form the basis of the model. The gaseous sulfur dioxide is in equilibrium with the molecular dissolved sulfur dioxide in the suspension



The molecular dissolved sulfur dioxide reacts with the water to form a hydrogen sulfate ion and a hydrogen ion.



The hydrogen sulfate ion dissociates into a hydrogen and a sulfate ion.



Moreover, the calcium hydroxide dissociates into its ions.



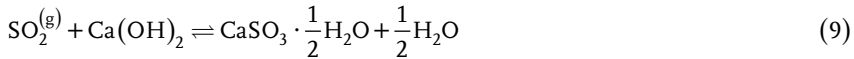
The calcium ion reacts with the sulfate ion and a half water molecule to form a calcium sulfate-hemihydrate.



The hydroxyl ions form water with the hydrogen ions



According to Hill [40], analyses of reaction products during the spray absorption drying shows that the reaction of the calcium hydroxide with the sulfur dioxide leads to calcium sulfate hemihydrate. The main reaction equation can be formulated as follows:



16.2.3

Mass and Energy Flows

Consider a differential volume element dV , all mass and energy balances can be represented as shown in Fig. 16.1.

Figure 16.2 shows the components of the system at the phase boundary.

16.2.3.1 Gas Balance

Mass balance of the sulfur dioxide

The temporal change of the molar quantity within the differential balance area (Fig. 16.1a) is affected by inflow and outflow as well as by transferred mole flux into the volume element

$$\frac{\partial n_{\text{SO}_2}^{\text{G}}}{\partial t} = -\frac{\partial \dot{n}_{\text{SO}_2}^{\text{G}}}{\partial z} dz - d\dot{n}_{\text{SO}_2}^{\text{S,G}} \quad (10)$$

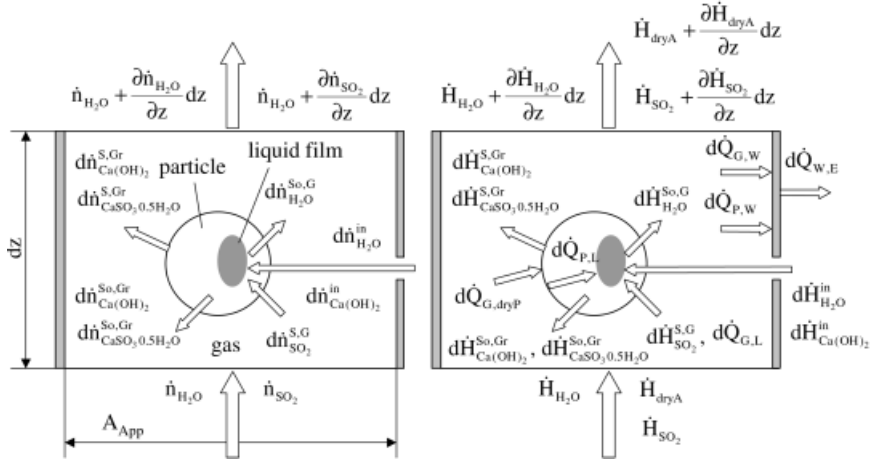


Fig. 16.1. Mass (left) and energy balances (right).

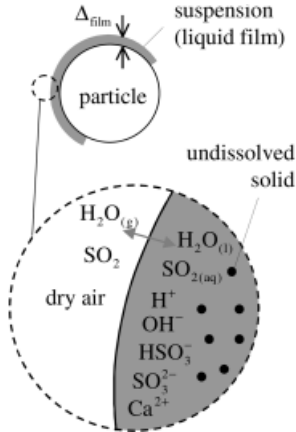


Fig. 16.2. Components at the phase interface gas-liquid film.

The molar loading is introduced now to gain the molar quantity of the inert component dry air

$$n_{SO_2}^G = n_{dryA}^G \tilde{Y}_{SO_2} \quad (11)$$

Inserting the value from Eq. (11) into the Eq. (10), we get

$$\frac{\partial \tilde{Y}_{SO_2}}{\partial t} = -\frac{\dot{n}_{dryA}^G}{n_{dryA}^G} \frac{\partial \tilde{Y}_{SO_2}}{\partial z} dz - \frac{1}{n_{dryA}^G} \dot{n}_{SO_2}^{S,G} \quad (12)$$

With the knowledge of a suitable driving force for the mass transfer in the gaseous phase, Eq. (12) becomes

$$\frac{\partial \tilde{Y}_{\text{SO}_2}}{\partial t} = -\frac{\dot{n}_{\text{dryA}}^G}{\text{dn}_{\text{dryA}}^G} \frac{\partial \tilde{Y}_{\text{SO}_2}}{\partial z} dz - \beta_{\text{SO}_2}^G \frac{A_{\text{P,tot}} \phi \rho_{\text{dryA}}}{\text{dn}_{\text{dryA}}^G M_{\text{dryA}}} (\tilde{Y}_{\text{SO}_2} - \tilde{Y}_{\text{SO}_2}^{\text{PG}}) \frac{dz}{H_{\text{bed}}} \quad (13)$$

For the computation of the mass flow of sulfur dioxide between the gaseous phase and the film, the averaged value of loading of SO_2 over the height is needed, thus

$$\bar{\tilde{Y}}_{\text{SO}_2} = \frac{1}{H_{\text{bed}}} \int_0^{H_{\text{bed}}} \tilde{Y}_{\text{SO}_2} dz \quad (14)$$

Mass balance of water vapor

The mass balance of water vapor is effected in the similar way as sulfur dioxide and leads to the following partial differential equation

$$\frac{\partial \tilde{Y}_{\text{H}_2\text{O}}}{\partial t} = -\frac{\dot{n}_{\text{dryA}}^G}{\text{dn}_{\text{dryA}}^G} \frac{\partial \tilde{Y}_{\text{H}_2\text{O}}}{\partial z} dz - \beta_{\text{H}_2\text{O}}^G \frac{A_{\text{P,tot}} \phi \rho_{\text{dryA}}}{\text{dn}_{\text{dryA}}^G M_{\text{dryA}}} (\tilde{Y}_{\text{H}_2\text{O}}^{\text{PG}} - \tilde{Y}_{\text{H}_2\text{O}}) \frac{dz}{H_{\text{bed}}} \quad (15)$$

In order to compute the average vapor mass flow over the fluidized-bed height, the following approximation is introduced

$$\bar{\tilde{Y}}_{\text{H}_2\text{O}} = \frac{1}{H_{\text{bed}}} \int_0^{H_{\text{bed}}} \tilde{Y}_{\text{H}_2\text{O}} dz \quad (16)$$

Energy balance of gas

The energy of the gas is influenced by the enthalpy flow of the gas, the enthalpy flow of the absorbed sulfur dioxide, the enthalpy flow of the water vapor, the heat flow of the gas to the dry part of the particles, the heat flow of the gas to the liquid film and the heat flow of the gas to the apparatus wall

$$\frac{\partial H_G}{\partial t} = -\frac{\partial \dot{H}_G}{\partial z} dz - d\dot{H}_{\text{SO}_2}^{\text{S,G}} - d\dot{H}_{\text{H}_2\text{O}}^{\text{So,G}} - d\dot{Q}_{\text{G,dryP}} - d\dot{Q}_{\text{G,L}} - d\dot{Q}_{\text{G,W}} \quad (17)$$

The enthalpy of the gas mixture consists of the terms for the enthalpy of dry air, the water vapor and the sulfur dioxide. The temporal change of the enthalpy of the gas can be calculated accordingly to the following equations

$$\frac{\partial H_G}{\partial t} = \text{dn}_{\text{dryA}} \frac{\partial \left[\tilde{c}_{\text{P,dryA}} \vartheta_G + \tilde{Y}_{\text{H}_2\text{O}} \left(\tilde{c}_{\text{P,H}_2\text{O}}^{\text{vap}} \vartheta_G + \tilde{r}_0 \right) + \tilde{Y}_{\text{SO}_2} \tilde{c}_{\text{P,SO}_2} \vartheta_G \right]}{\partial t} dz \quad (18)$$

$$\begin{aligned}
\frac{\partial H_G}{\partial t} = & \text{dn}_{\text{dryA}} \tilde{c}_{\text{P,dryA}} \frac{\partial \vartheta_G}{\partial t} + \text{dn}_{\text{dryA}} \tilde{c}_{\text{P,H}_2\text{O}}^{\text{vap}} \left(\tilde{Y}_{\text{H}_2\text{O}} \frac{\partial \vartheta_G}{\partial t} + \vartheta_G \frac{\partial \tilde{Y}_{\text{H}_2\text{O}}}{\partial t} \right) + \\
& + \text{dn}_{\text{dryA}} \tilde{r}_0 \frac{\partial \tilde{Y}_{\text{H}_2\text{O}}}{\partial t} + \text{dn}_{\text{dryA}} \tilde{c}_{\text{P,SO}_2} \left(\tilde{Y}_{\text{SO}_2} \frac{\partial \vartheta_G}{\partial t} + \vartheta_G \frac{\partial \tilde{Y}_{\text{SO}_2}}{\partial t} \right)
\end{aligned} \quad (19)$$

Similar to the previous Eq. (19), the local change of enthalpy can be formulated. The driving force for the heat flow together with these equations leads to the following Eq. (20)

$$\begin{aligned}
\frac{\partial \vartheta_G}{\partial t} = & \frac{1}{\left(\tilde{c}_{\text{P,dryA}} + \tilde{c}_{\text{P,H}_2\text{O}}^{\text{vap}} \tilde{Y}_{\text{H}_2\text{O}} + \tilde{c}_{\text{P,SO}_2} \tilde{Y}_{\text{SO}_2} \right) \text{dn}_{\text{dryA}}} \times \\
& \times \left[- \left(\tilde{c}_{\text{P,H}_2\text{O}}^{\text{vap}} \vartheta_G + \tilde{r}_0 \right) \text{dn}_{\text{dryA}} \frac{\partial \tilde{Y}_{\text{H}_2\text{O}}}{\partial t} - \text{dn}_{\text{dryA}} \tilde{c}_{\text{P,SO}_2} \vartheta_G \frac{\partial \tilde{Y}_{\text{SO}_2}}{\partial t} - \right. \\
& - \left(\tilde{c}_{\text{P,dryA}} + \tilde{c}_{\text{P,H}_2\text{O}}^{\text{vap}} \tilde{Y}_{\text{H}_2\text{O}} + \tilde{c}_{\text{P,SO}_2} \tilde{Y}_{\text{SO}_2} \right) \dot{n}_{\text{dryA}} \frac{\partial \vartheta_G}{\partial z} dz - \\
& - \left(\tilde{c}_{\text{P,H}_2\text{O}}^{\text{vap}} \vartheta_G + \tilde{r}_0 \right) \dot{n}_{\text{dryA}} \frac{\partial \tilde{Y}_{\text{H}_2\text{O}}}{\partial z} dz - \dot{n}_{\text{dryA}} \tilde{c}_{\text{P,SO}_2} \vartheta_G \frac{\partial \tilde{Y}_{\text{SO}_2}}{\partial z} dz - \\
& - \alpha_{\text{G,P}} A_{\text{P,tot}} (1 - \phi) (\vartheta_G - \vartheta_p) \frac{dz}{H_{\text{bed}}} - \alpha_{\text{G,P}} A_{\text{P,tot}} \phi (\vartheta_G - \vartheta_F) \frac{dz}{H_{\text{bed}}} - \\
& \left. - \dot{n}_{\text{SO}_2}^{\text{S,G}} \tilde{c}_{\text{P,SO}_2} \vartheta_G + \dot{n}_{\text{H}_2\text{O}}^{\text{So,G}} \left(\tilde{c}_{\text{P,H}_2\text{O}}^{\text{vap}} \vartheta_G + \tilde{r}_0 \right) - \alpha_{\text{G,W}} A_{\text{W,tot}} (\vartheta_G - \vartheta_W) \frac{dz}{H_{\text{bed}}} \right]
\end{aligned} \quad (20)$$

The transferred mass flows can be calculated by Eq. (13) and Eq. (15). After some simplifications, the final differential equation for the temporal and local change of the gas temperature is

$$\begin{aligned}
\frac{\partial \vartheta_G}{\partial t} = & - \frac{\dot{n}_{\text{dryA}}}{\text{dn}_{\text{dryA}}} \frac{\partial \vartheta_G}{\partial z} dz - \\
& - \alpha_{\text{G,P}} \frac{A_{\text{P,tot}} dz}{\text{dn}_{\text{dryA}} \left(\tilde{c}_{\text{P,dryA}} + \tilde{c}_{\text{P,H}_2\text{O}}^{\text{vap}} \tilde{Y}_{\text{H}_2\text{O}} + \tilde{c}_{\text{P,SO}_2} \tilde{Y}_{\text{SO}_2} \right) H_{\text{bed}}} \times \\
& \times \left[(1 - \phi) (\vartheta_G - \vartheta_p) + \phi (\vartheta_G - \vartheta_L) \right] - \\
& - \alpha_{\text{G,W}} \frac{A_{\text{W,tot}} dz}{\text{dn}_{\text{dryA}} \left(\tilde{c}_{\text{P,dryA}} + \tilde{c}_{\text{P,H}_2\text{O}}^{\text{vap}} \tilde{Y}_{\text{H}_2\text{O}} + \tilde{c}_{\text{P,SO}_2} \tilde{Y}_{\text{SO}_2} \right) H_{\text{bed}}} (\vartheta_G - \vartheta_W)
\end{aligned} \quad (21)$$

The gas temperature integral averaged over the height is

$$\bar{\vartheta}_G = \frac{1}{H_{\text{bed}}} \int_0^{H_{\text{bed}}} \vartheta_G dz \quad (22)$$

16.2.3.2 Suspension Balance

Mass balance of the suspension

This balance computes the adjusting mass transfer surface. The suspension loading depends on the liquid in the bed and the evaporation of this liquid from the particles. Moreover, mass of the suspension on the fluidized-bed particles depends on the solid mass in the suspension and of the solid leaving the suspension by accumulation at the fluidized-bed material. Under stationary conditions, the evaporated mass will correspond to the sprayed solid mass at the fluidized-bed particles. For simplicity, the suspension consists only of water, undissolved calcium hydroxide (Ca(OH)_2) and product ($\text{CaSO}_3 \times 1/2 \text{H}_2\text{O}$). The mass balance has the following form

$$\frac{dn_{\text{susp}}}{dt} = (\dot{n}_{\text{H}_2\text{O}}^{\text{in}} + \dot{n}_{\text{Ca(OH)}_2}^{\text{in}})(1 - k_{\text{OS}}) - \left(\dot{n}_{\text{Ca(OH)}_2}^{\text{So,Gr}} + \dot{n}_{\text{CaSO}_3, \frac{1}{2}\text{H}_2\text{O}}^{\text{So,Gr}} \right) - \dot{n}_{\text{H}_2\text{O}}^{\text{So,G}} + \dot{n}_{\text{SO}_2}^{\text{S,G}} \quad (23)$$

A problem presents the description of the solid ($\dot{n}_{\text{Ca(OH)}_2}^{\text{Q,Gr}}$ and $\dot{n}_{\text{CaSO}_3, \frac{1}{2}\text{H}_2\text{O}}^{\text{Q,Gr}}$) deposited on the particles. Here, it is assumed that the mass of the deposited solid to the sprayed solid is in the same relationship as the evaporated to the sprayed water mass. Also, like suspension, the deposited solid consists of the non-converted Ca(OH)_2 and the product $\text{CaSO}_3 \times 1/2 \text{H}_2\text{O}$.

The equilibrium of the reactive processes in the film supplies the ratio of the raw material to the product. It is also assumed that this relationship is equal for the film and the deposited solid. Thus, the coupling with the equilibrium leads to

$$\begin{aligned} &= (\dot{n}_{\text{H}_2\text{O}}^{\text{in}} + \dot{n}_{\text{Ca(OH)}_2}^{\text{in}})(1 - k_{\text{OS}}) - \frac{\dot{n}_{\text{Ca(OH)}_2}^{\text{in}} M_{\text{Ca(OH)}_2} \dot{n}_{\text{H}_2\text{O}}^{\text{So,G}}}{\dot{n}_{\text{H}_2\text{O}}^{\text{in}} \left(\tilde{z}_{\text{Ca(OH)}_2} M_{\text{Ca(OH)}_2} + \tilde{z}_{\text{CaSO}_3, \frac{1}{2}\text{H}_2\text{O}} M_{\text{CaSO}_3, \frac{1}{2}\text{H}_2\text{O}} \right)} - \\ &- \dot{n}_{\text{H}_2\text{O}}^{\text{So,G}} + \dot{n}_{\text{SO}_2}^{\text{S,G}} \end{aligned} \quad (24)$$

$$\begin{aligned} \frac{dn_{\text{susp}}}{dt} &= \dot{n}_{\text{H}_2\text{O}}^{\text{in}} (1 - k_{\text{OS}}) + \dot{n}_{\text{Ca(OH)}_2}^{\text{in}} \left[1 - k_{\text{OS}} - \right. \\ &- \frac{M_{\text{Ca(OH)}_2} \beta_{\text{SO}_2}^{\text{G}} A_{\text{tot}} \phi \frac{\rho_{\text{dryA}}}{M_{\text{dryA}}} (\tilde{Y}_{\text{SO}_2}^{\text{PG}} - \bar{\tilde{Y}}_{\text{H}_2\text{O}})}{\dot{n}_{\text{H}_2\text{O}}^{\text{in}} \left(\tilde{z}_{\text{Ca(OH)}_2} M_{\text{Ca(OH)}_2} + \tilde{z}_{\text{CaSO}_3, \frac{1}{2}\text{H}_2\text{O}} M_{\text{CaSO}_3, \frac{1}{2}\text{H}_2\text{O}} \right)} \left. \right] - \\ &- \beta_{\text{H}_2\text{O}}^{\text{G}} A_{\text{tot}} \phi \frac{\rho_{\text{dryA}}}{M_{\text{dryA}}} (\tilde{Y}_{\text{H}_2\text{O}}^{\text{PG}} - \bar{\tilde{Y}}_{\text{H}_2\text{O}}) + \beta_{\text{SO}_2}^{\text{G}} A_{\text{tot}} \phi \frac{\rho_{\text{dryA}}}{M_{\text{dryA}}} (\bar{\tilde{Y}}_{\text{SO}_2} - \tilde{Y}_{\text{SO}_2}^{\text{PG}}). \end{aligned} \quad (25)$$

Subsequently, the molar quantity of suspension is expressed by the density, the molar mass, the mass transfer surface and the film thickness

$$n_{\text{susp}} = \frac{\rho_{\text{susp}}}{M_{\text{susp}}} V_{\text{Film}} = \frac{\rho_{\text{susp}}}{M_{\text{susp}}} A_{\text{tot}} \Delta_{\text{film}} \quad (26)$$

Assuming that the density and the molar mass of the suspension in the fluidized bed are time-independent, there is a possibility of the computation of the mass transfer surface with the following differential equation

$$\begin{aligned} \frac{dA_{\text{tot}}}{dt} = & -\frac{M_{\text{susp}}}{\rho_{\text{susp}} \Delta_{\text{film}}} \left\{ \dot{n}_{\text{H}_2\text{O}}^{\text{in}} (1 - k_{\text{OS}}) + \dot{n}_{\text{Ca(OH)}_2}^{\text{in}} \left[1 - k_{\text{OS}} - \right. \right. \\ & \left. \left. - \frac{M_{\text{Ca(OH)}_2} \beta_{\text{SO}_2}^{\text{G}} A_{\text{tot}} \phi \frac{\rho_{\text{dryA}}}{M_{\text{dryA}}} \left(\tilde{Y}_{\text{SO}_2}^{\text{PG}} - \bar{\bar{Y}}_{\text{H}_2\text{O}} \right)}{\dot{n}_{\text{H}_2\text{O}}^{\text{in}} \left(\tilde{Z}_{\text{Ca(OH)}_2} M_{\text{Ca(OH)}_2} + \tilde{Z}_{\text{CaSO}_3, \frac{1}{2}\text{H}_2\text{O}} M_{\text{CaSO}_3, \frac{1}{2}\text{H}_2\text{O}} \right)} \right] - \right. \\ & \left. - \beta_{\text{H}_2\text{O}}^{\text{G}} A_{\text{tot}} \phi \frac{\rho_{\text{dryA}}}{M_{\text{dryA}}} \left(\tilde{Y}_{\text{H}_2\text{O}}^{\text{PG}} - \bar{\bar{Y}}_{\text{H}_2\text{O}} \right) + \beta_{\text{SO}_2}^{\text{G}} A_{\text{tot}} \phi \frac{\rho_{\text{dryA}}}{M_{\text{dryA}}} \left(\bar{\bar{Y}}_{\text{SO}_2} - \tilde{Y}_{\text{SO}_2}^{\text{PG}} \right) \right\}. \end{aligned} \quad (27)$$

If the mass transfer surface A_{tot} is described by the degree of wetting ϕ , then the formulation leads to the Eq. (28). The temporal change of the particle surface must be considered due to growth and attrition during the formulation of the mass transfer surface with the help of the degree of wetting

$$\begin{aligned} \frac{d\phi}{dt} = & -\frac{M_{\text{susp}}}{\rho_{\text{susp}} \Delta_{\text{film}} A_{\text{P,tot}}} \left\{ \dot{n}_{\text{H}_2\text{O}}^{\text{in}} (1 - k_{\text{OS}}) + \dot{n}_{\text{Ca(OH)}_2}^{\text{in}} \left[1 - k_{\text{OS}} - \right. \right. \\ & \left. \left. - \frac{M_{\text{Ca(OH)}_2} \beta_{\text{SO}_2}^{\text{G}} A_{\text{P,tot}} \phi \frac{\rho_{\text{dryA}}}{M_{\text{dryA}}} \left(\tilde{Y}_{\text{SO}_2}^{\text{PG}} - \bar{\bar{Y}}_{\text{H}_2\text{O}} \right)}{\dot{n}_{\text{H}_2\text{O}}^{\text{in}} \left(\tilde{Z}_{\text{Ca(OH)}_2} M_{\text{Ca(OH)}_2} + \tilde{Z}_{\text{CaSO}_3, \frac{1}{2}\text{H}_2\text{O}} M_{\text{CaSO}_3, \frac{1}{2}\text{H}_2\text{O}} \right)} \right] - \right. \\ & \left. - \beta_{\text{H}_2\text{O}}^{\text{G}} A_{\text{P,tot}} \phi \frac{\rho_{\text{dryA}}}{M_{\text{dryA}}} \left(\tilde{Y}_{\text{H}_2\text{O}}^{\text{PG}} - \bar{\bar{Y}}_{\text{H}_2\text{O}} \right) + \beta_{\text{SO}_2}^{\text{G}} A_{\text{P,tot}} \phi \frac{\rho_{\text{dryA}}}{M_{\text{dryA}}} \left(\bar{\bar{Y}}_{\text{SO}_2} - \tilde{Y}_{\text{SO}_2}^{\text{PG}} \right) \right\} \\ & - \frac{\phi}{A_{\text{P,tot}}} \frac{dA_{\text{P,tot}}}{dt} \end{aligned} \quad (28)$$

Mass balance of the element sulfur

The temporal change of the molar quantity of the element sulfur in the film on a fluidized-bed particle is caused by inflow and outflow of the material. This mass balance is needed only once, since the fluidized-bed particles and, thus, the liquid films on the particles are regarded as ideally mixed. The condition of the ideal mixing leads to the fact that with the mass and energy balance of the film, the average variables of state of the gas in the respective driving force approximations find the following form

$$\frac{\partial n_S}{\partial t} = \beta_{SO_2}^G \pi d_{32}^2 \phi \frac{\rho_{dryA}}{M_{dryA}} \left(\bar{Y}_{SO_2} - \bar{Y}_{H_2O}^{PG} \right) - n_{CaSO_3 \cdot \frac{1}{2}H_2O}^{So,Gr} \quad (29)$$

Mass balance of the element calcium

In this model, the temporal change of the molar quantity of the element calcium is due to the temporal change of the molar quantity on the fluidized-bed material. With a constant liquid film thickness, this problem reduces to the temporal change of the wetted surface:

$$\frac{\partial n_{Ca}}{\partial t} = \frac{\dot{n}_{Ca(OH)_2}^{in}}{\dot{n}_{H_2O}^{in} + \dot{n}_{Ca(OH)_2}^{in}} \frac{\rho_{susp} \Delta_{film}}{M_{susp}} \left(\phi \frac{dA_{P,tot}}{dt} + A_{P,tot} \frac{d\phi}{dt} \right) \quad (30)$$

Dissociation and reaction equilibrium

In the liquid film, there are five dissociation equilibria for the modeling. The description of these equilibria is provided by the assistance of equilibrium correlations. Initially, equilibrium correlations for dissociation are given with Eq. (4) and Eq. (5)

$$K_{Req2}(T) = \frac{\bar{m}_H + \bar{m}_{HSO_3^-}}{\bar{m}_{SO_2^{(aq)}} \frac{\bar{m}_{H_2O^{(l)}}}{\sum_{i=1} \bar{m}_i}} \frac{\gamma_{H^+}^{iddS^*} \gamma_{HSO_3^-}^{iddS^*}}{\gamma_{SO_2^{(aq)}}^1 \gamma_{H_2O}^1} = \exp \left(\frac{\mu_{pure,H_2O}^1 + \mu_{SO_2^{(aq)}}^{iddS^*} - \mu_{H^+}^{iddS^*} - \mu_{HSO_3^-}^{iddS^*}}{RT} \right) \quad (31)$$

$$K_{Req3}(T) = \frac{\bar{m}_H + \bar{m}_{SO_3^{2-}}}{\bar{m}_{HSO_3^-}} \frac{\gamma_{H^+}^{iddS^*} \gamma_{SO_3^{2-}}^{iddS^*}}{\gamma_{HSO_3^-}^{iddS^*}} = \exp \left(\frac{\mu_{HSO_3^-}^{iddS^*} - \mu_{H^+}^{iddS^*} - \mu_{SO_3^{2-}}^{iddS^*}}{RT} \right) \quad (32)$$

In connection to Eq. (6) and Eq. (7), the two further equilibrium correlations are

$$\begin{aligned} K_{Req4}(T) &= \frac{\bar{m}_{Ca^{2+}} (\bar{m}_{OH^-})^2}{\bar{m}_{Ca(OH)_2}} \frac{\gamma_{Ca^{2+}}^{iddS^*} (\gamma_{OH^-}^{iddS^*})^2}{\gamma_{Ca(OH)_2}^s} \frac{1}{\bar{m}_{Ca^{2+}}^{iddS^*} (\bar{m}_{OH^-}^{iddS^*})^2} = \\ &= \exp \left(\frac{\mu_{pure,Ca(OH)_2}^s - \mu_{Ca^{2+}}^{iddS^*} - 2\mu_{OH^-}^{iddS^*}}{RT} \right) \end{aligned} \quad (33)$$

$$\begin{aligned}
K_{\text{Req5}}(T) &= \frac{\bar{m}_{\text{CaSO}_3 \cdot \frac{1}{2}\text{H}_2\text{O}} \gamma_{\text{CaSO}_3 \cdot \frac{1}{2}\text{H}_2\text{O}}^s}{\bar{m}_{\text{Ca}^{2+}} \bar{m}_{\text{SO}_3^{2-}} \left(\frac{\bar{m}_{\text{H}_2\text{O}^{(l)}}}{\sum_{i=1} \bar{m}_i} \right)^{0.5} \gamma_{\text{Ca}^{2+}}^{\text{iddS}^*} \gamma_{\text{SO}_3^{2-}}^{\text{iddS}^*} \left(\gamma_{\text{H}_2\text{O}}^1 \right)^{0.5}} \frac{\bar{m}_{\text{Ca}^{2+}}^{\text{iddS}^*} \bar{m}_{\text{SO}_3^{2-}}^{\text{iddS}^*}}{1} = \\
&= \exp \left(\frac{\mu_{\text{Ca}^{2+}}^{\text{iddS}^*} + \mu_{\text{SO}_3^{2-}}^{\text{iddS}^*} + 0.5 \mu_{\text{pure, H}_2\text{O}}^1 - \mu_{\text{pure, CaSO}_3 \cdot \frac{1}{2}\text{H}_2\text{O}}^s}{RT} \right).
\end{aligned} \quad (34)$$

The last equilibrium is the formation of the water and considered by the formation of H^+ and OH^- ions

$$K_{\text{Req6}}(T) = \bar{m}_{\text{OH}^-} \bar{m}_{\text{H}^+} \quad (35)$$

Boundary conditions

For the determination of the unknown quantities in the liquid film, three further secondary conditions are needed. So, it is necessary to divide the molar masses of the sulfur and the calcium resulting from the mass balances in the film. A sulfur atom is bonded in hydrogen sulfite ion, molecular diluted sulfur dioxide, sulfite ion and calcium sulfite hemihydrate

$$n_{\text{S}} = 1 \left(n_{\text{HSO}_3^-} \right) + 1 \left(n_{\text{SO}_2^{(\text{aq})}} \right) + 1 \left(n_{\text{SO}_3^{2-}} \right) + 1 \left(n_{\text{CaSO}_3 \cdot \frac{1}{2}\text{H}_2\text{O}} \right) \quad (36)$$

$$n_{\text{Ca}} = 1 \left(n_{\text{CaSO}_3 \cdot \frac{1}{2}\text{H}_2\text{O}} \right) + 1 \left(n_{\text{Ca}(\text{OH})_2} \right) + 1 \left(n_{\text{Ca}^{2+}} \right) \quad (37)$$

Additionally, the secondary condition of the electrical neutrality is to be accomplished

$$0 = 1 \left(n_{\text{H}^+} \right) + 2 \left(n_{\text{Ca}^{2+}} \right) - 1 \left(n_{\text{HSO}_3^-} \right) - 1 \left(n_{\text{OH}^-} \right) - 2 \left(n_{\text{SO}_3^{2-}} \right) \quad (38)$$

Energy balance of the suspension

The temperature of the suspension depends on heat and enthalpy flows. Thus, the enthalpy of the film is influenced by the absorbed mass of sulfur dioxide, the evaporated water mass, the injected mass of the suspension as well as the masses of product and non-converted material in the film at the particle. The heat flow from the gas and from the particle to the film must also be considered. The changes of the molecular structure of the involved components arising due to chemical reactions

can also lead to energetic effects in the liquid film. These changes of enthalpy – the so-called reaction enthalpies – are considered in the model. The energy balance is

$$\begin{aligned} \frac{dH_{\text{susp}}}{dt} = & \dot{Q}_{P,L} + \bar{Q}_{G,L} + \bar{H}_{\text{SO}_2}^{S,G} - \bar{H}_{\text{H}_2\text{O}}^{S,G} + \dot{H}_{\text{H}_2\text{O}}^{\text{in}}(1 - k_{\text{OS}}) + \dot{H}_{\text{Ca(OH)}_2}^{\text{in}}(1 - k_{\text{OS}}) - \\ & - \dot{H}_{\text{Ca(OH)}_2}^{\text{So,Gr}} - \dot{H}_{\text{CaSO}_3 \cdot \frac{1}{2}\text{H}_2\text{O}}^{\text{So,Gr}} - \dot{n}_{\text{SO}_2}^{S,G} \tilde{\Delta h}_R \end{aligned} \quad (39)$$

The enthalpy of the suspension can be expressed in terms of the mass, the specific thermal capacity, and the temperature of the suspension

$$\begin{aligned} \frac{d(A_{P,\text{tot}} \phi \Delta_{\text{film}} \rho_{\text{susp}} c_{P,\text{susp}} \vartheta_{\text{film}})}{dt} = & \dot{Q}_{P,L} + \bar{Q}_{G,L} + \bar{H}_{\text{SO}_2}^{S,G} - \bar{H}_{\text{H}_2\text{O}}^{S,G} + \dot{H}_{\text{H}_2\text{O}}^{\text{in}}(1 - k_{\text{OS}}) + \\ & + \dot{H}_{\text{Ca(OH)}_2}^{\text{in}}(1 - k_{\text{OS}}) - \dot{H}_{\text{Ca(OH)}_2}^{\text{So,Gr}} - \dot{H}_{\text{CaSO}_3 \cdot \frac{1}{2}\text{H}_2\text{O}}^{\text{So,Gr}} - \dot{n}_{\text{SO}_2}^{S,G} \tilde{\Delta h}_R. \end{aligned} \quad (40)$$

Neglecting the temporal changes of the density and the specific heat capacity of the suspension as well as the film thickness, the differential equation for the temporal change of the suspension temperature takes the following form (with $\vartheta_L = \vartheta_{\text{film}}$)

$$\begin{aligned} \frac{\partial \vartheta_{\text{film}}}{\partial t} = & \alpha_{G,P} \frac{f_\alpha}{\Delta_{\text{film}} \rho_{\text{susp}} c_{P,\text{susp}}} (\vartheta_p - \vartheta_{\text{film}}) + \alpha_{G,P} \frac{1}{\Delta_{\text{film}} \rho_{\text{susp}} c_{P,\text{susp}}} (\bar{\vartheta}_G - \vartheta_{\text{film}}) + \\ & + \beta_{\text{SO}_2}^G \frac{\rho_{\text{dryA}}}{M_{\text{dryA}} \Delta_{\text{film}} \rho_{\text{susp}} c_{P,\text{susp}}} (\bar{Y}_{\text{SO}_2} - \tilde{Y}_{\text{SO}_2}^{\text{PG}}) (\tilde{c}_{P,\text{SO}_2} \bar{\vartheta}_G - \tilde{\Delta h}_R) - \\ & - \beta_{\text{H}_2\text{O}}^G \frac{\rho_{\text{dryA}}}{M_{\text{dryA}} \Delta_{\text{film}} \rho_{\text{susp}} c_{P,\text{susp}}} (\tilde{Y}_{\text{H}_2\text{O}}^{\text{PG}} - \bar{Y}_{\text{H}_2\text{O}}) (\tilde{c}_{P,\text{H}_2\text{O}}^{\text{vap}} \bar{\vartheta}_G - \tilde{t}_0) + \frac{\dot{n}_{\text{H}_2\text{O}}^{\text{in}} (1 - k_{\text{OS}}) \tilde{c}_{P,\text{H}_2\text{O}} \vartheta_{\text{susp}}^{\text{in}}}{A_{P,\text{tot}} \phi \Delta_{\text{film}} \rho_{\text{susp}} c_{P,\text{susp}}} + \\ & + \frac{\dot{n}_{\text{Ca(OH)}_2}^{\text{in}} (1 - k_{\text{OS}}) \tilde{c}_{P,\text{Ca(OH)}_2} \vartheta_{\text{susp}}^{\text{in}}}{A_{P,\text{tot}} \phi \Delta_{\text{film}} \rho_{\text{susp}} c_{P,\text{susp}}} - \frac{\dot{n}_{\text{Ca(OH)}_2}^{\text{Q,Gr}} \tilde{c}_{P,\text{Ca(OH)}_2} \vartheta_{\text{film}}}{A_{P,\text{tot}} \phi \Delta_{\text{film}} \rho_{\text{susp}} c_{P,\text{susp}}} - \\ & - \frac{\dot{n}_{\text{CaSO}_3 \cdot \frac{1}{2}\text{H}_2\text{O}}^{\text{So,Gr}} \tilde{c}_{P,\text{CaSO}_3 \cdot \frac{1}{2}\text{H}_2\text{O}} \vartheta_{\text{film}}}{A_{P,\text{tot}} \phi \Delta_{\text{film}} \rho_{\text{susp}} c_{P,\text{susp}}} - \frac{\vartheta_{\text{film}}}{A_{P,\text{tot}}} \frac{dA_{P,\text{tot}}}{dt} - \frac{\vartheta_{\text{film}}}{\phi} \frac{d\phi}{dt} \end{aligned} \quad (41)$$

16.2.3.3 Gas–Liquid Phase Boundary

After balancing the masses in the gaseous phase for the components sulfur dioxide and water vapor, the question arises as to which quantities are still unknown for solution of the differential equations. Knowledge of the gaseous phase balance conditions ($\tilde{Y}_{\text{SO}_2}^{\text{PG}}, \tilde{Y}_{\text{H}_2\text{O}}^{\text{PG}}$) is missing in both of the equations. The following section is concerned in detail with the determination of these phase balances. The consideration of the thermodynamic effects with the help of the represented coefficients must be decided depending on the concentrations.

Equilibrium of the water vapor

Computation of the phase balance is made by equating the chemical potential of the gas component

$$\mu_i^G(T, P) = \mu_{\text{pure}, i}^{iG}(T, P^0) + RT \ln \tilde{\gamma}_i^G + RT \ln \phi_i^G + RT \ln \frac{P}{P^0} \quad (42)$$

The chemical potential of the liquid is obtained by the following correlation

$$\mu_i^l(T, P) = \mu_{\text{pure}, i}^{iG}(T, P) + RT \ln(\tilde{x}_i^l \gamma_i^l) + RT \ln \left(\frac{\phi_{\text{pure}, i}^{\text{Sat}} P_{\text{pure}, i}^{\text{Sat}}}{P} \right) + \int_{P_{\text{pure}, i}^{\text{Sat}}}^P \tilde{v}_{\text{pure}, i}^l dP \quad (43)$$

Thus, the subcritical component water results to the following relationship

$$\phi_{\text{H}_2\text{O}}^G \tilde{\gamma}_{\text{H}_2\text{O}}^{\text{PG}} P = \tilde{x}_{\text{H}_2\text{O}}^{\text{PG}} \gamma_{\text{H}_2\text{O}}^l \phi_{\text{pure}, \text{H}_2\text{O}}^{\text{Sat}} P_{\text{pure}, \text{H}_2\text{O}}^{\text{Sat}} e^{\frac{1}{RT} \int_{P_{\text{pure}, \text{H}_2\text{O}}^{\text{Sat}}}^P \tilde{v}_{\text{pure}, \text{H}_2\text{O}}^l dP} \quad (44)$$

Neglecting the volume dependency of the liquid on the pressure, the integral can be solved and the exponent has the following form

$$\phi_{\text{H}_2\text{O}}^G \tilde{\gamma}_{\text{H}_2\text{O}}^{\text{PG}} P = \tilde{x}_{\text{H}_2\text{O}}^{\text{PG}} \gamma_{\text{H}_2\text{O}}^l \phi_{\text{pure}, \text{H}_2\text{O}}^{\text{Sat}} P_{\text{pure}, \text{H}_2\text{O}}^{\text{Sat}} e^{\frac{\tilde{v}_{\text{pure}, \text{H}_2\text{O}}^l (P - P_{\text{pure}, \text{H}_2\text{O}}^{\text{Sat}})}{RT}} \quad (45)$$

The exponential term is also known as the Poynting factor $\text{Poy}_{\text{H}_2\text{O}}$ [24]. This factor describes the change of the fugacity by expansion or by compression of the pure liquid related to the standard behavior in dependence of the saturation vapor pressure and the absolute system pressure. Neglecting the Poynting correction and considering the gaseous phase as ideal, the preceding equation leads to the following form

$$P_{\text{H}_2\text{O}}^{\text{PG}} = \tilde{\gamma}_{\text{H}_2\text{O}}^{\text{PG}} P = \tilde{x}_{\text{H}_2\text{O}}^{\text{PG}} \gamma_{\text{H}_2\text{O}}^l \phi_{\text{pure}, \text{H}_2\text{O}}^{\text{Sat}} P_{\text{pure}, \text{H}_2\text{O}}^{\text{Sat}} \quad (46)$$

The mole content can be expressed in terms of molar quantity

$$P_{\text{H}_2\text{O}}^{\text{PG}} = \tilde{\gamma}_{\text{H}_2\text{O}}^{\text{PG}} P = \frac{n_{\text{H}_2\text{O}}^{\text{PG}}}{\sum_{i=1} n_i^{\text{PG}}} \gamma_{\text{H}_2\text{O}}^l \phi_{\text{pure}, \text{H}_2\text{O}}^{\text{Sat}} P_{\text{pure}, \text{H}_2\text{O}}^{\text{Sat}} \quad (47)$$

With the assumption that the mass transfer of the water vapor is described with the mole loadings, the mole content in equilibrium Eq. (47) must be converted into a loading

$$\tilde{Y}_{\text{H}_2\text{O}}^{\text{PG}} = \frac{1 + \tilde{Y}_{\text{SO}_2}^{\text{PG}}}{\frac{1}{\tilde{Y}_{\text{H}_2\text{O}}^{\text{PG}}} - 1} \quad (48)$$

Equilibrium of the sulfur dioxide

According to Eq. (42), equating the chemical potentials of the gaseous and the liquid phase of the supercritical component SO_2

$$\mu_i^{\text{l}}(T, P) = \mu_{\text{pure}, i}^{\text{iG}}(T, P^0) + RT \ln \left(\frac{\bar{m}_i}{\bar{m}_i^{\text{iddS}^*}} \gamma_i^{\text{iddS}^*} \right) + RT \ln \left(\frac{H_i^{\text{m}}(T, P)}{P^0} \right) \quad (49)$$

leads to the possibility of the computation of the phase balance

$$\phi_{\text{SO}_2}^{\text{G}} \tilde{Y}_{\text{SO}_2}^{\text{PG}} P = \bar{m}_{\text{SO}_2}^{\text{PG}} \gamma_{\text{SO}_2}^{\text{iddS}^*} H_{\text{SO}_2}^{\text{m}} \quad (50)$$

Assuming that the gaseous phase behaves ideally, Eq. (50) can be further simplified

$$P_{\text{SO}_2}^{\text{PG}} = \tilde{Y}_{\text{SO}_2}^{\text{PG}} P = \bar{m}_{\text{SO}_2}^{\text{PG}} \gamma_{\text{SO}_2}^{\text{iddS}^*} H_{\text{SO}_2}^{\text{m}} \quad (51)$$

The Henry constant is still unknown, but can be calculated using Eq. (49) for the molecular dissolved components in the real state

$$\mu_i^{\text{l}}(T, P) = \mu_i^{\text{iddS}^*}(T, P^0) + RT \ln \left(\frac{\bar{m}_i}{\bar{m}_i^{\text{iddS}^*}} \right) + RT \ln \gamma_i^{\text{iddS}^*} + \int_{P^0}^P v_i^{\infty} dp \quad (52)$$

Moreover, using the fact that the chemical potential of the components of liquid mixtures calculated from different methods must result in same value for the potential

$$H_{\text{SO}_2}^{\text{m}}(T, P) = \frac{P^0}{\bar{m}_{\text{SO}_2}^{\text{iddS}^*}} \exp \left(\frac{\mu_{\text{SO}_2}^{\text{iddS}^*}(T, P^0, \bar{m}_{\text{SO}_2}^{\text{iddS}^*}) - \mu_{\text{pure}, \text{SO}_2}^{\text{iG}}(T, P^0)}{RT} \right) \quad (53)$$

The Poynting correction is also neglected here. Finally, the following relationship results for the equilibrium of SO_2 at the gas–liquid phase boundary

$$\tilde{y}_{\text{SO}_2}^{\text{PG}} P = \frac{\frac{n_{\text{SO}_2}^{\text{PG}}}{n_{\text{H}_2\text{O}}^{\text{PG}} M_{\text{H}_2\text{O}}}}{\bar{m}_{\text{SO}_2}^{\text{iddS}^*}} \gamma_{\text{SO}_2}^{\text{iddS}^*} P^0 \exp \left(\frac{\mu_{\text{SO}_2}^{\text{iddS}^*}(T, P^0, \bar{m}_{\text{SO}_2}^{\text{iddS}}) - \mu_{\text{pure, SO}_2}^{\text{iG}}(T, P^0)}{RT} \right) \quad (54)$$

With the assumption that the mass transfer of the sulfur dioxide is also described with the mole loadings, the mole content in equilibrium Eq. (54) must be converted into a loading

$$\tilde{Y}_{\text{SO}_2}^{\text{PG}} = \frac{1 + \tilde{Y}_{\text{H}_2\text{O}}^{\text{PG}}}{\frac{1}{\tilde{Y}_{\text{SO}_2}^{\text{PG}}} - 1} \quad (55)$$

16.2.3.4 Particle Balance

Population balance of the particles

The particle diameter changes during the unsteady start-up phase at batch or at continuous granulation process due to growth of the particles by layering of injected solid in the suspension onto the particles, due to attrition of the particles as a result of particle–particle collisions and particle–wall collisions, as well as due to the feeding and discharge of particle fluxes from the granulator (Fig. 16.3).

In practice, so-called “overspray” occurs; this characterizes the non-deposited liquid drops. In the model, a factor k_{OS} considers the overspray, as a ratio of the mass flux of the overspray and the injected solid mass flux. The efficiency of the separator (filter, cyclone) is considered by a factor k_{sep} , which describes the ratio of the re-fed mass flux to the granulator to the fed mass flux into the separator. The factor k_{growth} describes the ratio of the mass flux which comes from the separator and is used for the layering and growth (continuous phase) and the mass flux which comes from the separator (dust) and is used as new internal seeds (disperse phase).

Knowledge of the temporal change of the number and mass particle size distribution is important for the calculation the product properties, hydrodynamic behavior of the fluidized bed, heat and mass transfer.

In this model the diameter is the distributed property of the particle population:

$$\frac{\partial N}{\partial t} = - \frac{\partial \dot{N}}{\partial d_p} dd_p + d\dot{N}^{\text{So}} - d\dot{N}^{\text{S}} \quad (56)$$

The growth rate G is the temporal change of the particle diameter and the particle flux \dot{N} is the temporal change of the number of particles. By this definition, the differential rate of change of particles leads to the following equations

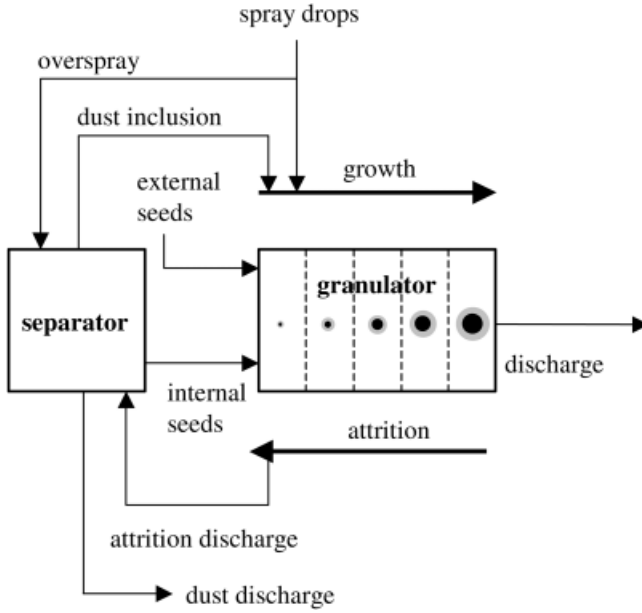


Fig. 16.3. Modeling of the particle population.

$$\frac{\partial N_p}{\partial t} = -\frac{\partial \frac{dN_p}{dt}}{\partial d_p} dd_p + d\dot{N}_p^{So} - d\dot{N}_p^S \quad (57)$$

$$\frac{\partial N_p}{\partial t} = -\frac{\partial \frac{dN_p}{dd_p} G}{\partial d_p} dd_p + d\dot{N}_p^{So} - d\dot{N}_p^S \quad (58)$$

If the number of particles within the differential length dd_p can be expressed in terms of the entire number of particles and the number density, then the population balance results to

$$\frac{\partial (N_{p,tot} q_0)}{\partial t} = -\frac{\partial (N_{p,tot} q_0 G)}{\partial d_p} + \dot{N}_{p,tot}^{So} q_0^{So} - \dot{N}_{p,tot}^S q_0^S \quad (59)$$

In the population balance, the knowledge of kinetics is needed for modeling of the growth rate of the particles. The description of the growth is according to the model of surface-proportional growth proposed by Mörl [67, 68]. If the attrition process is understood as a negative growth, then growth can be summarized with attrition kinetics. Surface-proportional attrition kinetics is used according to Rangelova [75].

Both models are combined to formulate an expression for the rate of change of mass of particles:

$$\frac{dm_p}{dt} = \frac{A_p}{A_{p,tot}} \dot{m}^{So,Gr} - R_{att} A_p \quad (60)$$

The mass flux $\dot{m}^{So,Gr}$ is the sum of the reaction product deposited on the liquid film and non-converted material flux, of the dust deposited on the particles coming from separator into granulator and of the attrition mass flux coming from separator into granulator, which leads to the growth of particles.

According to the simplification from the section detailing the mass balance of suspension and the modeling of the re-fed fluxes it follows that

$$\dot{m}^{So,Gr} = \frac{\dot{m}_{Ca(OH)_2}^{in} \dot{m}_{H_2O}^{So,G}}{\dot{m}_{H_2O}^{in}} + \dot{m}_{Ca(OH)_2}^{in} k_{OS} k_{sep} k_{growth} + R_{att} A_{p,tot} k_{sep} k_{growth} \quad (61)$$

By replacing the mass of particles by the density and the diameter, the growth rate can be obtained in the following equation

$$G = \frac{dd_p}{dt} = 2 \left(\frac{\dot{m}^{So,Gr}}{\rho_p A_{p,tot}} - \frac{R_{att}}{\rho_p} \right) \quad (62)$$

The result of the population balance is the surface area

$$A_{p,tot} = \pi \int_{d_p=0}^{d_p=\infty} d_p^2 N_{tot} dd_p = \pi N_{tot} \int_{d_p=0}^{d_p=\infty} d_p^2 q_0 dd_p \quad (63)$$

and the bed mass

$$m_{p,tot} = \frac{\pi}{6} \rho_p \int_{d_p=0}^{d_p=\infty} d_p^3 N_{tot} dd_p = \frac{\pi}{6} \rho_p N_{tot} \int_{d_p=0}^{d_p=\infty} d_p^3 q_0 dd_p \quad (64)$$

For the computation of the heat and mass transfer coefficients, the Sauter diameter d_{32} is used

$$d_{32} = d_p = \frac{6m_{p,tot}}{\rho_p A_{p,tot}} \quad (65)$$

Energy balance of the particles

The particle temperature depends on the heat flux from the gas to the particle, the particle to the liquid film, and the particle to the apparatus wall. Further, the enthalpy flow of the deposited and attrited solids, as well as entering or leaving solid fluxes (seeds and product), also influence the temperature of the bed material. The energetic balance has the following form

$$\frac{\partial H_P}{\partial t} = \bar{Q}_{G,P} + \dot{H}^{So,Gr} - \dot{Q}_{P,L} - \dot{Q}_{P,W} - \dot{H}^{S,Gr} + \dot{H}_{sep} + \dot{H}_{seeds} - \dot{H}_{product} \quad (66)$$

With $H_P = m_P c_{P,P} \vartheta_P$ and the heat fluxes follows

$$\begin{aligned} \frac{\partial \vartheta_P}{\partial t} = & \alpha_{G,P} \frac{A_{P,tot}(1-\phi)}{m_{P,tot} c_{P,P}} (\bar{\vartheta}_G - \vartheta_P) + \frac{\dot{m}_{P,tot}^{So,Gr}}{m_{P,tot}} \vartheta_{film} - \\ & - \alpha_{G,P} \frac{A_{P,tot} f_{\alpha} \phi}{m_{P,tot} c_{P,P}} (\vartheta_P - \vartheta_{film}) - \alpha_{P,W} \frac{A_{W,tot}}{m_{P,tot} c_{P,P}} (\vartheta_P - \vartheta_W) - \\ & - \frac{R_{att} A_{P,tot}}{m_{P,tot}} \vartheta_P + \frac{(\dot{m}^{So,Gr} + R_{att} A_{P,tot}) k_{OS} (1 - k_{growth})}{m_{P,tot}} \vartheta_{sep} + \frac{\dot{m}_{seeds}}{m_{P,tot}} \vartheta_{seeds} - \\ & - \left[\dot{m}_{Ca(OH)_2}^{in} + \dot{m}_{seeds} - (k_{OS} \dot{m}_{Ca(OH)_2}^{in} + R_{att} A_{P,tot}) (1 - k_{sep}) \right] \frac{1}{m_{P,tot}} \vartheta_P \end{aligned} \quad (67)$$

16.2.3.5 Apparatus Wall Balance

Energy balance of the apparatus wall

The enthalpy of the wall can be expressed in terms of mass, specific heat capacity and the temperature of the wall

$$\frac{\partial H_W}{\partial t} = \frac{d(m_W c_{P,W} \vartheta_W)}{dt} = \bar{Q}_{G,W} + \dot{Q}_{P,W} - \dot{Q}_{W,E} \quad (68)$$

The balance leads to the time-dependency of the apparatus wall temperature

$$\frac{\partial \vartheta_W}{\partial t} = \frac{A_{W,tot}}{m_W c_{P,W}} \left[\alpha_{G,W} (\bar{\vartheta}_G - \vartheta_W) + \alpha_{P,W} (\vartheta_P - \vartheta_W) - \alpha_{W,E} (\vartheta_W - \vartheta_E) \right] \quad (69)$$

16.2.3.6 Solution of the Equations

A system of differential and algebraic equations (DAE system) is obtained from the model balances. The developed set of equations consists of the ordinary differential equations of first order and of partial differential equations. An analytical solution of the coupled equations is not possible. Therefore, a numeric procedure is used.

The independent variable in ordinary differential equations is time t . The partial differential equations includes the local coordinate z (height coordinate of fluidized bed) and the diameter d_p of the particle population. An idea for the solution of partial differential equations is the discretization of the continuous domain. This means discretization of the height coordinate z and the diameter coordinate d_p . In addition, the frequently used finite difference methods are applied, where the derivatives are replaced by central difference quotient based on the Taylor series. The idea of the Taylor series is the value of a function $f(z)$ at $z + \Delta z$ can be expressed in terms of the value at z .

$$f|_{z+\Delta z} = f|_z + \frac{\partial f}{\partial z}\bigg|_z \Delta z + \frac{\partial^2 f}{\partial z^2}\bigg|_z \frac{\Delta z^2}{2!} + \frac{\partial^3 f}{\partial z^3}\bigg|_z \frac{\Delta z^3}{3!} \dots \quad (70)$$

By simple adjustment, the following results

$$\frac{f|_{z+\Delta z} - f|_z}{\Delta z} = \frac{\partial f}{\partial z}\bigg|_z + \frac{\partial^2 f}{\partial z^2}\bigg|_z \frac{\Delta z}{2!} + \frac{\partial^3 f}{\partial z^3}\bigg|_z \frac{\Delta z^2}{3!} \dots \quad (71)$$

In the similar way, the function value at $z - \Delta z$ becomes

$$f|_{z-\Delta z} = f|_z - \frac{\partial f}{\partial z}\bigg|_z \Delta z + \frac{\partial^2 f}{\partial z^2}\bigg|_z \frac{\Delta z^2}{2!} - \frac{\partial^3 f}{\partial z^3}\bigg|_z \frac{\Delta z^3}{3!} \dots \quad (72)$$

and, then

$$\frac{f|_z - f|_{z-\Delta z}}{\Delta z} = \frac{\partial f}{\partial z}\bigg|_z - \frac{\partial^2 f}{\partial z^2}\bigg|_z \frac{\Delta z}{2!} + \frac{\partial^3 f}{\partial z^3}\bigg|_z \frac{\Delta z^2}{3!} \dots \quad (73)$$

Neglecting higher-order derivatives and with equidistant discretization, we obtain the following expression for the central difference quotient of first order by the addition of the Eq. (71) and Eq. (73)

$$\frac{\partial f}{\partial z} = \frac{f|_{z+\Delta z} - f|_{z-\Delta z}}{2\Delta z} \quad (74)$$

Using difference quotients, the partial differential equations become ordinary differential equations. The boundary conditions (e.g., inlet and outlet gas temperature of the fluidized bed) can easily be implemented using difference quotient in the entire differential equation system. So, initial/boundary value problems are transferred into initial value problems. Now, the ordinary differential equations of order 1

are coupled with algebraic equations. The general form of differential algebraic set of equations (DAE system) is

$$M\dot{x} = f(t, x) \quad (75)$$

M is a singular Matrix. Zero entries on the main diagonal of this matrix identify the algebraic equations, and all other entries which have the value 1 represent the differential equation. The vector x describes the state of the system. As numeric tools for the solution of the DAE system, MATLAB with the solver *ode15s* was used. In this solver, a Runge Kutta procedure is coupled with a BDF procedure (Backward Difference Formula). An implicit numeric scheme is used by the solver.

16.3 Experiments

16.3.1

Fluidized-bed Plant

The measurements were carried out at a semi-industrial fluidized-bed plant DN 400. The scheme of the process is illustrated in Fig. 16.4, while the plant itself is illustrated in Fig. 16.5.

The plant DN 400 has a cylindrical glass tube of 400 mm diameter. Using a pressure fan ($\dot{V}_{\max} = 4000 \text{ m}^3 \text{ h}^{-1}$), the main air mass flux from the environment is sucked in and heated up by two 60-kW electrical heaters. In the extension chamber DN 800 the air flow velocity is reduced such that a percentage of the elutriated dust particles fall back into the fluidized bed. Light particles are tangentially transported to the cyclone. The particles separated in the cyclone can be re-fed to the fluidized bed by the use of a fan. Along with a pressure fan, the experimental plant also possesses an exhaust radial ventilator ($\dot{V}_{\max} = 4400 \text{ m}^3 \text{ h}^{-1}$).

The liquid injection is realized using a two-fluid nozzle (Co. Schlick, type 943, form 3, ring-shaped beam 20° – 40° , $d_{\text{nozzle}} = 2.3 \text{ mm}$). A adjustable hose pump conveys the liquid from a store tank, and compressed air is used for the better spreading of the liquid. The investigations of Henneberg et al. [38, 39] in an industrial fluidized-bed plant showed that high nozzle injection rates may lead to low particle concentrations near the nozzle, and to overspray.

The plant can be operated either discontinuously or continuously. To characterize the process, the temperature of the gas, pressures and pressure losses in the plant, and the gas and liquid mass flows, as well as the concentration of the component SO_2 (using an Ultramat P22 waste gas analyzer; Siemens Co.) over the bed which can be absorbed are measured.

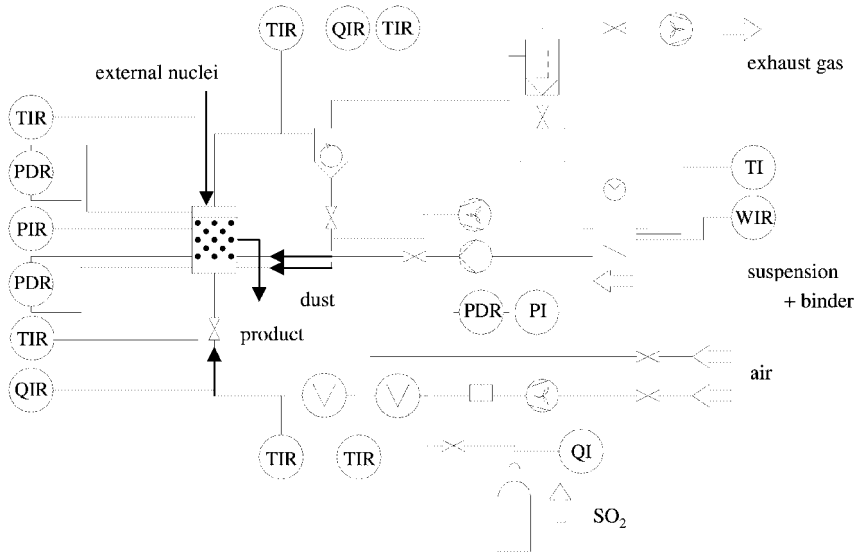


Fig. 16.4. Flow sheet of the fluidized bed plant DN 400 (PD: pressure loss, P: absolute

pressure, T: temperature, Q: quantity, W: weight, I: indication, R: registration).

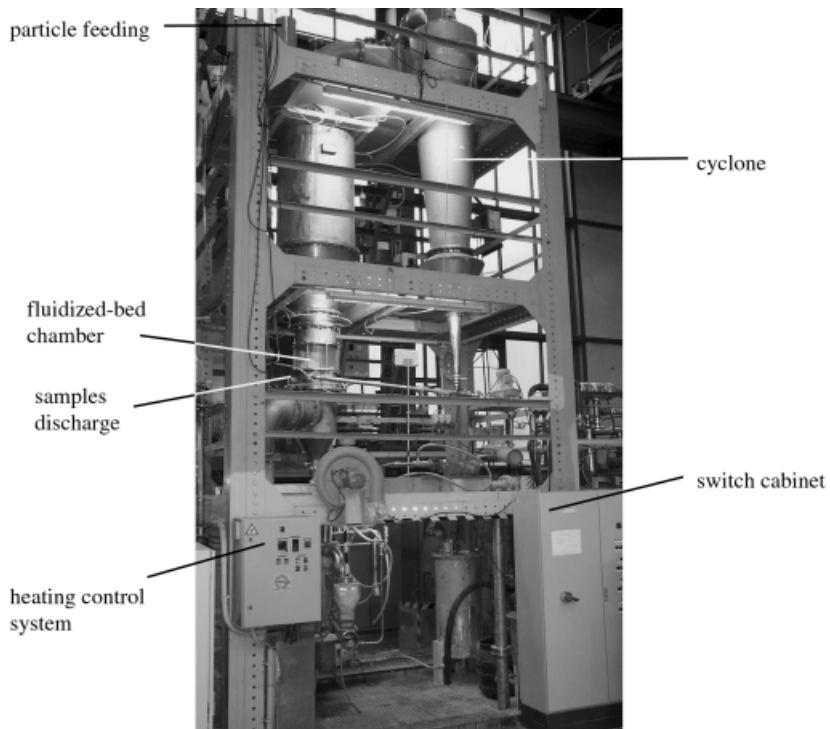


Fig. 16.5. Illustration of the fluidized bed plant DN 400.

16.3.2

Experiments of Absorption without Granulation of Solid (Reactive Absorption)**16.3.2.1 Experimental Realization**

The aim of the experiments was to obtain stationary values for SO₂ separation. Initially, the hold-up was sprayed with water to obtain stationary temperatures after cooling the particles and to conserve the used calcium hydroxide during the unsteady start-up phase. At the steady-state temperature the injection was suddenly switched to suspension. The SO₂-concentration at the outlet then decreased. The suspension consisted of lime hydrate (DIN 1060-CL90, DIN EN 12518) and water. The suspension injection had to be held constant until the SO₂-concentration was constant. After achieving steady state the injection was stopped, and this caused an increase in SO₂-concentration at the outlet up to the initial value. The same procedure was started after a few minutes in order to obtain a new measuring point at a higher suspension injection rate.

16.3.2.2 Influence of the Liquid Injection Rate

The experimental parameters are displayed in Tab. 16.2.

Figure 16.7 shows that an increase of the liquid injection leads to a decrease in gas temperature at the outlet of the fluidized bed, while an improved sulfur dioxide conversion is also documented (see Fig. 16.8).

The separation efficiency is determined by the difference in gas concentration between the inlet and outlet of the fluidized bed. A dimensionless quantity defined by Hill [40] – the so-called absorption factor – can be used in reaction technology at a constant volume flow rate if mole fluxes are replaced by concentrations

$$\Pi = \frac{c_{\text{SO}_2}^{\text{in}} - c_{\text{SO}_2}^{\text{out}}}{c_{\text{SO}_2}^{\text{in}}} \quad (76)$$

In the diagrams (Figs. 16.7 and 16.8), there are two normalized quantities, the normalized liquid mass flow

$$\Omega = \frac{\dot{m}_{\text{H}_2\text{O}}^{\text{in}}}{\dot{m}_{\text{H}_2\text{O}}^{\text{Sat}}} \quad (77)$$

and the normalized outlet temperature

$$\Theta_{\text{out}} = \frac{\vartheta_{\text{G}}^{\text{out}} - \vartheta_{\text{G}}^{\text{Sat}}}{\vartheta_{\text{G}}^{\text{in}} - \vartheta_{\text{G}}^{\text{Sat}}} \quad (78)$$

which are related to the isenthalpic saturation values of gas.

Table 16.2. Parameters of experiment V-17.

Bed material (glass spheres): $d_{32} = 0.00257$ m, $\rho_P = 2470$ kg m ⁻³ , $m_{FB} = 20$ kg			
Parameter			
ϑ_G^{in}	102.06 ± 0.027 °C		
ϑ_E	21 °C		
φ	72 %		
\dot{m}_G	0.37 ± 0.00035 kg s ⁻¹		
$c_{\text{SO}_2}^{\text{in}}$	492.7 ± 5.1 mg Nm ⁻³		
ϑ_L^{in}	13.5 ± 0.79 °C		
Variation			
No.	Ca/S ratio	\dot{m}_{susp}	Composition
Injection rate I	1.19	0.0049 ± 7.2 × 10 ⁻⁴ kg s ⁻¹	$\frac{0.704 \text{ kg}_{\text{Ca(OH)}_2}}{16.89 \text{ kg}_{\text{H}_2\text{O}}}$
Injection rate II	1.35	0.0037 ± 0 kg s ⁻¹	$\frac{0.79 \text{ kg}_{\text{Ca(OH)}_2}}{12.41 \text{ kg}_{\text{H}_2\text{O}}}$
Injection rate III	1.21	0.0014 ± 1.3 × 10 ⁻⁴ kg s ⁻¹	$\frac{0.71 \text{ kg}_{\text{Ca(OH)}_2}}{4.39 \text{ kg}_{\text{H}_2\text{O}}}$
Injection rate IV	1.22	0.0024 ± 1.6 × 10 ⁻⁴ kg s ⁻¹	$\frac{0.715 \text{ kg}_{\text{Ca(OH)}_2}}{7.885 \text{ kg}_{\text{H}_2\text{O}}}$
Injection rate V	1.29	0.004 ± 0 kg s ⁻¹	$\frac{0.76 \text{ kg}_{\text{Ca(OH)}_2}}{13.64 \text{ kg}_{\text{H}_2\text{O}}}$
Injection rate VI	1.29	0.006 ± 2.9 × 10 ⁻⁴ kg s ⁻¹	$\frac{0.76 \text{ kg}_{\text{Ca(OH)}_2}}{20.845 \text{ kg}_{\text{H}_2\text{O}}}$
Injection rate VII	1.21	0.0081 ± 5.8 × 10 ⁻⁴ kg s ⁻¹	$\frac{0.712 \text{ kg}_{\text{Ca(OH)}_2}}{28.57 \text{ kg}_{\text{H}_2\text{O}}}$
Injection rate VIII	1.27	0.0095 ± 0 kg s ⁻¹	$\frac{0.745 \text{ kg}_{\text{Ca(OH)}_2}}{33.46 \text{ kg}_{\text{H}_2\text{O}}}$
Injection rate IX	1.31	0.0075 ± 1.8 × 10 ⁻⁴ kg s ⁻¹	$\frac{0.77 \text{ kg}_{\text{Ca(OH)}_2}}{26.13 \text{ kg}_{\text{H}_2\text{O}}}$

Any increase of the suspension injection, in order to realize an improved separation of the gas component which can be removed, is not possible. The maximum liquid and/or solvent injection into a fluidized bed is limited by the capacity of the fluidization gas. The maximum of the capacity is reached with the state of saturation of the gas. Figure 16.6 illustrates the dependence of the adjusting wetted surface and the absolute humidity on the spraying liquid mass flow. Clearly, a small deviation of

the liquid mass flow leads to a slight change in the mass transfer surface. Within the range of high liquid loads due to the proximity to the saturation point, such a change can have fatal consequences. A minimum rise in the liquid mass flow can lead to a situation where the gas level exceeds its state of saturation. For stable behavior, complete evaporation of the solvent into the gas is necessary.

A physical explanation of the process where the injection rate is changed can be described with help from the mass balance of the liquid within the fluidized bed. For simplicity, the suspension is regarded as a pure liquid. The particle movement follows the model of the ideal mixing, and the liquid on the particles is a thin film of constant thickness. Under these stationary conditions, the degree of wetting can be formulated from the moisture balance around the entire apparatus

$$\phi = -\frac{\dot{n}_{\text{dryA}} M_{\text{dryA}}}{\rho_{\text{H}_2\text{O}}^G A_{\text{P,tot}} \rho_{\text{dryA}}} \ln \left(\frac{\frac{\dot{n}_{\text{H}_2\text{O}}^{\text{in}}}{\dot{n}_{\text{dryA}}} + \tilde{Y}_{\text{H}_2\text{O}}^{\text{in}} - \tilde{Y}_{\text{H}_2\text{O}}^{\text{PG}}}{\tilde{Y}_{\text{H}_2\text{O}}^{\text{in}} - \tilde{Y}_{\text{H}_2\text{O}}^{\text{PG}}} \right) \quad (79)$$

It is clear from the equation that an increase in the liquid injection rate results in a larger degree of wetting. If this surface becomes larger, the gas temperature will decrease above the bed as a result of the increasing evaporation (Fig. 16.7).

The absorption process in the bed is affected, as with all mass transfer processes, by the surface. If no other factors have any strong limiting effect on the process, an increase in mass transfer surface leads to a reduced sulfur dioxide concentration (Fig. 16.8).

Thus, the absorption factor or the conversion increases. The relationship between increased conversion and mass transfer surface can be clarified with a simple model of gas-phase-limited absorption. Integration of Eq. (13) over the height coordinate provides the stationary solution of the component which can be absorbed and also

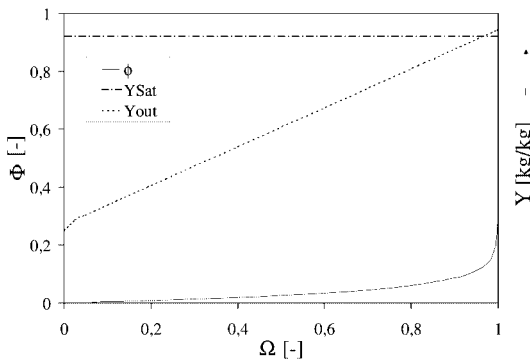


Fig. 16.6. Dependency between liquid injection rate, wetted surface and air humidity.

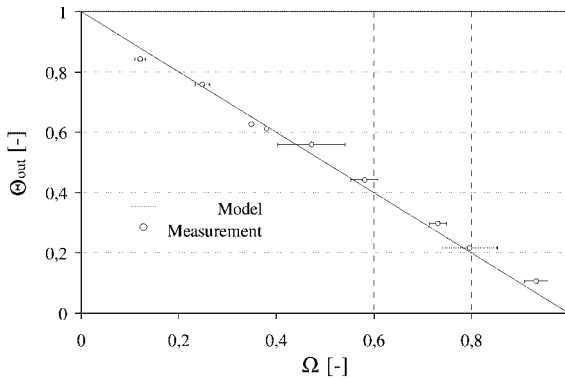


Fig. 16.7. Dependency of outlet temperature on liquid injection rate, experiment V-17.

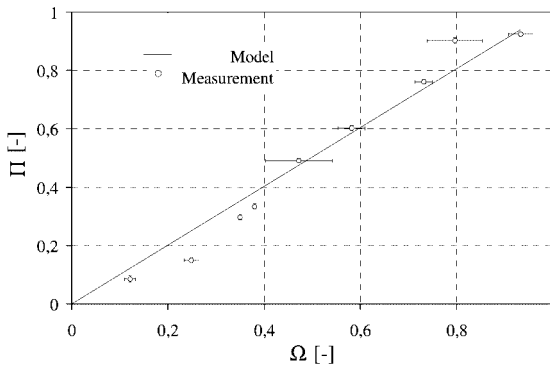


Fig. 16.8. Dependency of conversion on liquid injection rate, experiment V-17.

describes the process of sulfur dioxide loading as a function of the degree of wetting. The quotient

$$NTU_{SO_2} = \frac{\beta_{SO_2}^G A_{P,tot} \phi \rho_{dryA}}{\dot{n}_{dryA}^G M_{dryA}} \quad (80)$$

can be understood as the ratio of the rate of the gas mass transfer to the rate of gas convection, and describes the number of transfer units. An increase in injection rate results in an increase of the mass transfer units, and this explains the increasing conversion (Figs. 16.9 and 16.10).

The model developed is capable of describing the determined behavior of increased conversion due to an increased injection mass flux. The mass balance of the suspension indicates that the mass transfer surface represents one unknown

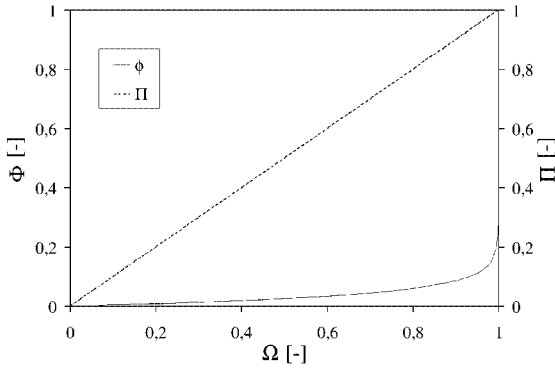


Fig. 16.9. Dependency between liquid injection rate, wetted surface and conversion.

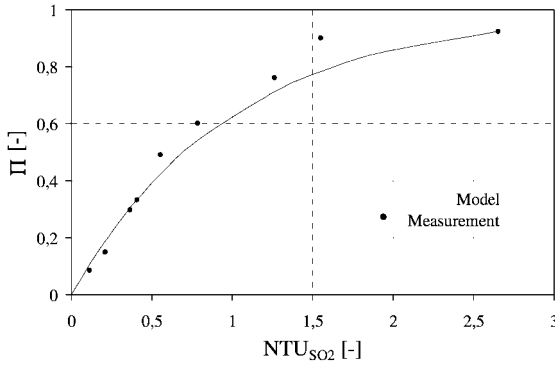


Fig. 16.10. Dependency of conversion on NTU .

quantity and, in contrast to other absorbers, this must be calculated by using a suitable model. One problem is that differential Eq. (23) provides only the liquid mass within the bed, whilst the form of the film on the particles remains unknown. The development of a physically justified model to describe the form of the liquid film is difficult due to the multiplicity of the influences – for example, droplet size of the sprayed liquid, surface tension, and fluidization behavior. Link [60] coupled single particle levitator experiments with granulation in order to scale-up investigations into fluidized-bed granulation. However, the importance of film formation combined with formation of the mass transfer surface in fluidized beds was neglected. Heinrich and Mörl [34] assumed a coherent liquid film on the particle surface with a constant thickness. Only by using these simplifications can the mass balance of the liquid film be used to compute the mass transfer surface. The liquid film thickness is an unknown in the model. In a series of studies, Becher [5] considered the film thickness to be equal to the diameter of the spraying drops. Similarly, Heinrich and Mörl [34] found that the film thickness is only important during the unsteady start-up phase.

The stationary solution of the balance equation with acceptance of computing the gas mass-transfer coefficient depends only on the saturation loading and/or the saturation partial pressure at the gas–liquid phase boundary. To compute this quantity, the temperature at the phase boundary is required, and this corresponds to a uniform liquid film temperature according to the condition for the model. This temperature is the result of a liquid energy balance. If the particle temperature and film temperature is uniform, a jump in temperature will occur at the contact area between particle and film, though this is physically impossible. Nevertheless, in order to utilize this model the thermal conduction between particle and film is approximated by the heat transfer coefficient between gas and particle. Previous investigations concentrated on pure granulations, coating and agglomeration processes, and thus on the spraying of suspensions or solutions, which were only dried. In general, the gas temperature and gas humidity at the outlet (top) and the inlet (bottom) of the fluidized bed were measured by all balanced quantities. An agreement between experimentally determined values for the gas outlet temperature and humidity does not validate the internal balance of the liquid film.

The calculated size of the wetted surface depends on the correct calculation of the liquid film temperature and thus, on the size of the heat transfer particle film described with the factor f_α . The processes can be described with the help of the Mollier diagram. An increase in f_α leads to a higher liquid film temperature. A slight increase of this temperature is due to the small upward gradient of the saturation line with a significant larger saturation loading of the gas in direct proximity of the phase boundary. This increment of the saturation loading entails an increased driving force for the liquid evaporation. The more liquid is evaporated, the mass transfer surface will be smaller. Since the effects of the driving force and the mass transfer surface are moving in opposite directions, the evaporated liquid mass flow remains almost constant. Thus, an incorrect balance of the liquid enthalpy and the liquid mass in the bed will have no measurable effect on temperature and humidity. Evaluation of the quality of the calculated mass transfer surface can be made only by evaluating the conversion of a gas component deviating from the water vapor. The kinetics for the description of this conversion should be limited only by the surface and the gas mass transfer. Sulfur dioxide absorption in the liquid-sprayed fluidized bed may possibly be estimated and the size of the wetted surface controlled (Figs. 16.11 and 16.12). An investigation of the model on the basis of experimental data shows that for a certain bed material (e.g., glass spheres of a certain particle diameter), a f_α value exists which describes all experiments. The experiments with small values for f_α are easily reproducible – a fact which can be proven with the help of a high contact resistance.

Figure 16.13 shows that the surface of calcium hydroxide-coated glass spheres is characterized by a strong porosity and cavities, and this results in a worsened heat transfer.

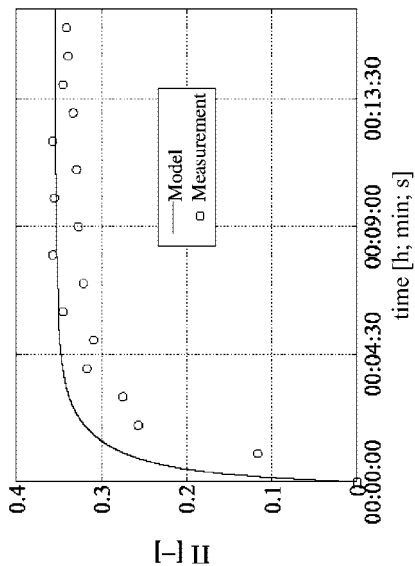


Fig. 16.11. Unsteady progressions of temperature and conversion, experiment V-17 ($\dot{m}_{\text{sup}} = 14.4 \text{ kg h}^{-1}$, $f_{\alpha} = 0.1$, $\Delta_{\text{film}} = 0.0001 \text{ m}$).

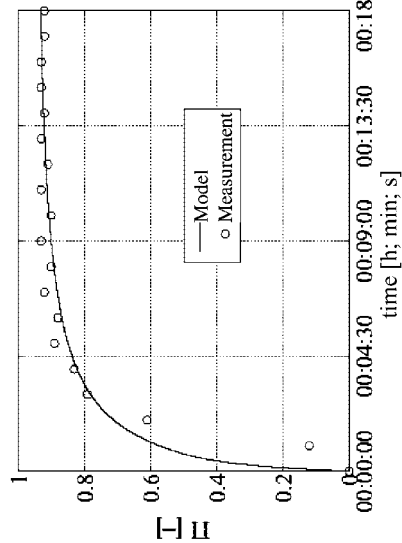
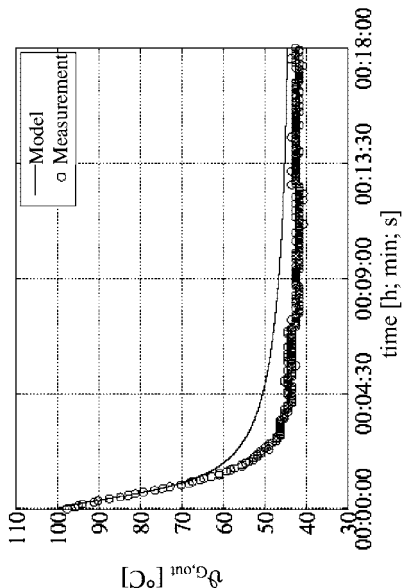
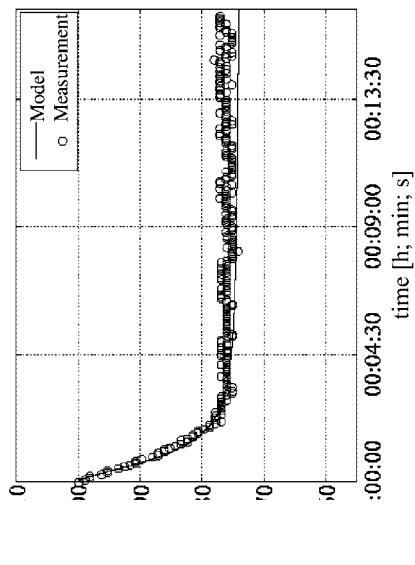


Fig. 16.12. Unsteady progressions of temperature and conversion, experiment V-17 ($\dot{m}_{\text{sup}} = 34.2 \text{ kg h}^{-1}$, $f_{\alpha} = 0.1$, $\Delta_{\text{film}} = 0.0001 \text{ m}$).



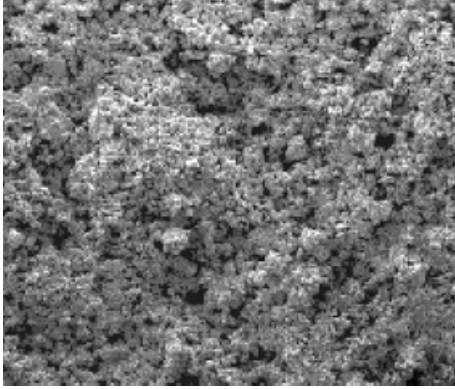


Fig. 16.13. Scanning electron micrograph of the surface of a coated granulate.

16.3.2.3 Influence of Ca/S Ratio

Investigations into the calcium/sulfur ratio represent an important aspect of the evaluation of the economy of this procedure. The influence of the stoichiometric relationship for different spraying mass fluxes has been investigated, and the adjusted experimental conditions are listed in Tabs. 16.3 and 16.4.

The results demonstrate that for liquid mass fluxes, which do not lead into the direct proximity of the state of saturation of air, a stoichiometric relationship does not play an unimportant role. Rather, the mass transfer area of the fluidized bed is the limiting factor of the absorption. Over-stoichiometric operation does not lead to any improved separation of the SO_2 (Figs. 16.14 and 16.15), the reason being the permanent destruction of the liquid film by particle–particle collisions and the consequent production of inactive reactants.

In order to estimate the probability of impact of the moistened part of a particle by surrounded particles in the fluidized bed, a simple model was developed [69]. As an assumption that the fluidized bed is in an homogeneous condition, a certain portion of the relative porosity is assigned to each particle, and the shape of air covering the particle is taken to be a cube (Fig. 16.16). The entire bed consists of stacked cubes containing a particle at their center. The amount of air – and in consequence the distance between the particles – becomes larger; for example, with the same fluidization mass flow the Archimedes' number is decreased. The bed will then expand with a greater fluidization throughput and with a constant Archimedes' number; hence, the distance between the surrounded particles will increase.

A probability of impact P_T depends on the path length a_P between surrounded particles and the relationship of the total projected surface of the surrounded particles $A_{P,\text{surrounded}}^{\text{projected}}$ in relation to the surface of the sphere $A_{Sp,\text{surrounded}}$ with the radius a_P .

Two events occur at this time:

- Event A: impact of particles, $p(A) = \frac{A_{Sp,\text{surrounded}}^{\text{projected}}}{A_{Sp,\text{surrounded}}}$ and
- Event B: no impact of particles, $p(A) = 1 - p(A)$.

Table 16.3. Parameters of experiment V-11.

Bed material (glass spheres): $d_{32} = 0.00257$ m, $\rho_p = 2470$ kg m ⁻³ , $m_{FB} = 23.2$ kg			
Parameter			
ϑ_G^{in}	97.559 ± 0.012 °C		
ϑ_E	20 °C		
φ	55 %		
\dot{m}_G	0.5351 ± 0.00055 kg s ⁻¹		
$c_{\text{SO}_2}^{\text{in}}$	330.92 ± 2.51 mg Nm ⁻³		
ϑ_L^{in}	9.83 ± 0.48 °C		
Variation			
No.	Ca/S ratio	\dot{m}_{susp}	composition
Injection rate I	3.08	0.00906 ± 9.8 × 10 ⁻⁵ kg s ⁻¹	$\frac{0.484 \text{ kg}_{\text{Ca(OH)}_2}}{8.5 \text{ kg}_{\text{H}_2\text{O}}}$
	4.48	0.00903 ± 3.5 × 10 ⁻⁴ kg s ⁻¹	$\frac{0.726 \text{ kg}_{\text{Ca(OH)}_2}}{8.5 \text{ kg}_{\text{H}_2\text{O}}}$
	5.6	0.00868 ± 4.2 × 10 ⁻⁴ kg s ⁻¹	$\frac{0.968 \text{ kg}_{\text{Ca(OH)}_2}}{8.5 \text{ kg}_{\text{H}_2\text{O}}}$
	8.82	0.0096 ± 5.9 × 10 ⁻⁴ kg s ⁻¹	$\frac{1.45 \text{ kg}_{\text{Ca(OH)}_2}}{8.5 \text{ kg}_{\text{H}_2\text{O}}}$
Injection rate II	1.01	0.00297 ± 9.3 × 10 ⁻⁵ kg s ⁻¹	$\frac{0.484 \text{ kg}_{\text{Ca(OH)}_2}}{8.5 \text{ kg}_{\text{H}_2\text{O}}}$
	1.42	0.00287 ± 4.5 × 10 ⁻⁴ kg s ⁻¹	$\frac{0.726 \text{ kg}_{\text{Ca(OH)}_2}}{8.5 \text{ kg}_{\text{H}_2\text{O}}}$
	1.78	0.00277 ± 1.9 × 10 ⁻⁴ kg s ⁻¹	$\frac{0.968 \text{ kg}_{\text{Ca(OH)}_2}}{8.5 \text{ kg}_{\text{H}_2\text{O}}}$
	2.54	0.00277 ± 1.1 × 10 ⁻⁴ kg s ⁻¹	$\frac{1.45 \text{ kg}_{\text{Ca(OH)}_2}}{8.5 \text{ kg}_{\text{H}_2\text{O}}}$
Injection rate III	4.58	0.0135 ± 5.9 × 10 ⁻⁴ kg s ⁻¹	$\frac{0.484 \text{ kg}_{\text{Ca(OH)}_2}}{8.5 \text{ kg}_{\text{H}_2\text{O}}}$
	6.86	0.0138 ± 2.9 × 10 ⁻⁴ kg s ⁻¹	$\frac{0.726 \text{ kg}_{\text{Ca(OH)}_2}}{8.5 \text{ kg}_{\text{H}_2\text{O}}}$
	8.9	0.0138 ± 2.9 × 10 ⁻⁴ kg s ⁻¹	$\frac{0.968 \text{ kg}_{\text{Ca(OH)}_2}}{8.5 \text{ kg}_{\text{H}_2\text{O}}}$
	13.4	0.0146 ± 8.5 × 10 ⁻⁴ kg s ⁻¹	$\frac{1.45 \text{ kg}_{\text{Ca(OH)}_2}}{8.5 \text{ kg}_{\text{H}_2\text{O}}}$

Table 16.4. Parameters of experiment V-12.

Bed material (glass spheres): $d_{32} = 0.00257$ m, $\rho_P = 2470$ kg m ⁻³ , $m_{FB} = 23$ kg			
Parameter			
ϑ_G^{in}	98.83 ± 0.017 °C		
ϑ_E	22 °C		
φ	57 %		
\dot{m}_G	0.479 ± 0.00055 kg s ⁻¹		
$c_{SO_2}^{in}$	348.9 ± 2.58 mg Nm ⁻³		
ϑ_L^{in}	10.8 ± 0.57 °C		
Variation			
No.	Ca/S ratio	\dot{m}_{susp}	composition
Injection rate I	1.83	0.00644 ± 2.3 × 10 ⁻⁴ kg s ⁻¹	$\frac{0.484 \text{ kg}_{Ca(OH)_2}}{10.92 \text{ kg}_{H_2O}}$
	1.38	0.00647 ± 1.4 × 10 ⁻⁴ kg s ⁻¹	$\frac{0.365 \text{ kg}_{Ca(OH)_2}}{11.034 \text{ kg}_{H_2O}}$
	0.943	0.0066 ± 4.2 × 10 ⁻⁴ kg s ⁻¹	$\frac{0.2425 \text{ kg}_{Ca(OH)_2}}{11.157 \text{ kg}_{H_2O}}$
Injection rate II	1.9	0.0032 ± 2.3 × 10 ⁻⁴ kg s ⁻¹	$\frac{0.48 \text{ kg}_{Ca(OH)_2}}{4.92 \text{ kg}_{H_2O}}$
	0.89	0.00297 ± 1.7 × 10 ⁻⁴ kg s ⁻¹	$\frac{0.2425 \text{ kg}_{Ca(OH)_2}}{5.158 \text{ kg}_{H_2O}}$
	0.767	0.0017 ± 2.3 × 10 ⁻⁴ kg s ⁻¹	$\frac{0.365 \text{ kg}_{Ca(OH)_2}}{5.035 \text{ kg}_{H_2O}}$
Injection rate III	1.74	0.0092 ± 2.6 × 10 ⁻⁴ kg s ⁻¹	$\frac{0.48 \text{ kg}_{Ca(OH)_2}}{16.52 \text{ kg}_{H_2O}}$
	0.901	0.00946 ± 2.5 × 10 ⁻⁴ kg s ⁻¹	$\frac{0.2425 \text{ kg}_{Ca(OH)_2}}{16.75 \text{ kg}_{H_2O}}$
	1.45	0.0101 ± 3.8 × 10 ⁻⁴ kg s ⁻¹	$\frac{0.365 \text{ kg}_{Ca(OH)_2}}{16.635 \text{ kg}_{H_2O}}$
Injection rate IV	1.57	0.012 ± 1.3 × 10 ⁻³ kg s ⁻¹	$\frac{0.365 \text{ kg}_{Ca(OH)_2}}{18.535 \text{ kg}_{H_2O}}$

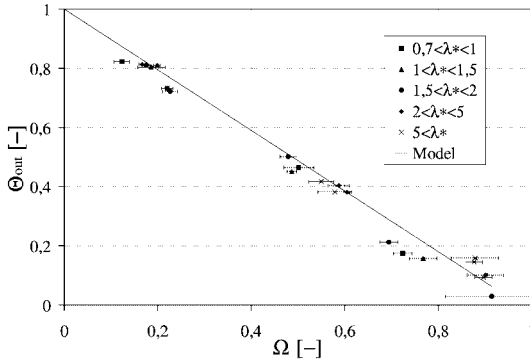


Fig. 16.14. Dependency of outlet temperature on injection rate at different Ca/S-relationships; experiments V-17 and V-12.

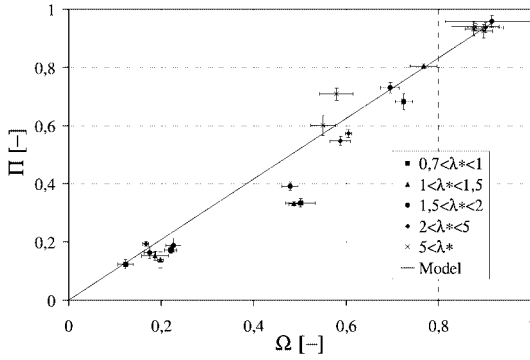


Fig. 16.15. Dependency of conversion on injection rate at different Ca/S-relationships; experiments V-17 and V-12.

The probability for n successful collisions between the particles with the distance a_p and k follows with [22]:

$$P_T(x = k) = \frac{n!}{k!(n-k)!} p(A)^k (1 - p(A))^{n-k} \quad (81)$$

The probability of at least one collision can be calculated with the probability of no collisions

$$P_T(x \geq 1) = 1 - P_T(x < 1) \quad (82)$$

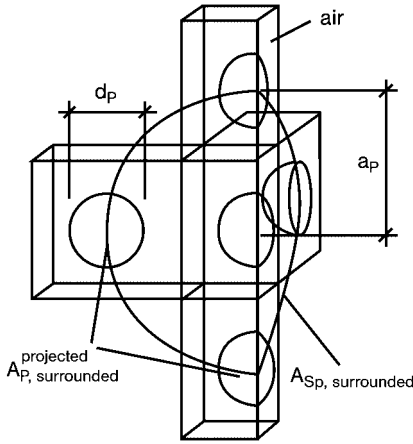


Fig. 16.16. Scheme of the impact probability model.

With the help of the Eqs. (81) and (82), the probability results

$$P_T(x \geq 1) = 1 - (1 - p(A))^n = 1 - \left(1 - \frac{A_{p,surrounded}^{projected}}{A_{Sp,surrounded}} \right)^n \quad (83)$$

The time for the movement of a particle along the distance a_p leads to the time-dependent impact probability

$$P_T(x \geq 1) = 1 - \left(1 - \frac{A_{Sp,surrounded}^{projected}}{A_{p,surrounded}} \right)^{\frac{\Delta t}{t_s}} \quad (84)$$

Uhlemann and Mörl [93] described the calculation of the average particle velocity \bar{w}_p within the fluidized bed. The impact time of a particle can be calculated with the help of particle distance a_p and average particle velocity. Analogous to the previous derivations, the probability of destruction P_φ of the wetted particles surface – and thus of the liquid film – can be calculated by the ratio of the wetted surface to the total surface of the particle.

The probability of impact of particles with the wetted part of their surfaces is the product of both probabilities

$$P_Z(x \geq 1) = P_T \cdot P_\varphi \quad (85)$$

The time-dependent destruction probability P_Z of the wetted particle surface of a particle with typical parameters is illustrated in Fig. 16.17.

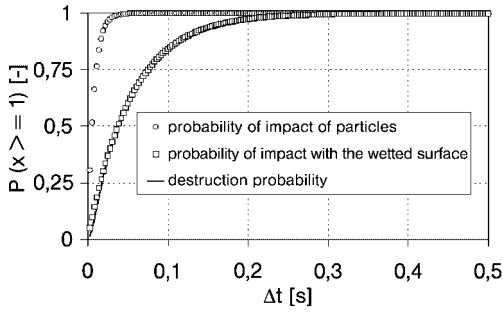


Fig. 16.17. Dependency of destruction probability on time
($Ar = 1.7 \times 10^6$, $Re_p = 663$, $d_{App} = 0.4$ m, $\Phi = 5$ %, $\bar{w}_p = 1$ m s⁻¹).

It is clear that the wetted surface is destroyed within a fraction of a second. Link [60] investigated the residence time of a liquid droplet onto a solid particle, and found that the liquid evaporates within the range of few seconds. The life-time of the film is thus greater than the time taken for the liquid film to be destroyed. The reason for this limitation of absorption by the liquid-phase mass transfer is the permanent destruction of the liquid film.

16.3.2.4 Influence of the Gas Inlet Temperature

The parameters of the experiments for the variation of the gas inlet temperature are displayed in Tabs. 16.5–16.8.

Figures 16.18 and 16.19 present the comparison between measured and calculated steady-state gas outlet temperatures and conversions, depending upon the injection rate at different gas inlet temperatures.

The tendency of the curves for constant gas inlet temperature was described in Section 16.3.2.2. High injection rates lead to smaller outlet concentrations and thus larger conversions. It is also clear that a higher gas inlet temperature leads to a smaller conversion during constant suspension injection. An increase in gas inlet temperature represents an increased driving force for the evaporation process, whilst a high heat flux between the liquid film and the gas leads to an increased liquid film temperature. The associated high contact temperature at the gas/liquid phase boundary leads to an increased saturation humidity of gas in the direct proximity of the phase boundary. As mentioned earlier, this higher humidity produces the high driving forces required for the evaporation process. Figure 16.20 illustrates the connection between NTU and associated increased conversion with increased injection rate. Clearly, at an increased gas temperature, the same conversion can only be obtained by having a high injection rate. A comparison of experimental and theoretical results showed that the model is capable of describe the conversions and outlet temperatures for different inlet temperatures (Fig. 16.21). One assumption made here was the momentary reaction with the complete conversion of sulfur dioxide. As the measured and simulated values were similar, the temperature influenced only the driving force of the drying process.

Table 16.5. Parameters of experiment V-1.

Bed material (glass spheres): $d_{32} = 0.00257$ m, $\rho_p = 2470$ kg m ⁻³ , $m_{FB} = 30$ kg			
Parameter			
ϑ_G^{in}	100.116 ± 0.018 °C		
ϑ_E	19 °C		
ϕ	75 %		
\dot{m}_G	0.296 ± 0.0008 kg s ⁻¹		
$c_{SO_2}^{in}$	966.89 ± 4.22 mg Nm ⁻³		
ϑ_L^{in}	15.7 ± 0.63 °C		
Variation			
No.	Ca/S ratio	\dot{m}_{susp}	composition
Injection rate	1.57	0.00692 ± 2.7 × 10 ⁻⁴ kg s ⁻¹	$\frac{1.45 \text{ kg}_{Ca(OH)_2}}{23.45 \text{ kg}_{H_2O}}$
	1.57	0.00568 ± 1.5 × 10 ⁻⁴ kg s ⁻¹	$\frac{1.45 \text{ kg}_{Ca(OH)_2}}{19.05 \text{ kg}_{H_2O}}$
	1.57	0.00442 ± 1.2 × 10 ⁻⁴ kg s ⁻¹	$\frac{1.45 \text{ kg}_{Ca(OH)_2}}{14.49 \text{ kg}_{H_2O}}$
	1.57	0.00319 ± 1.1 × 10 ⁻⁴ kg s ⁻¹	$\frac{1.45 \text{ kg}_{Ca(OH)_2}}{10.05 \text{ kg}_{H_2O}}$

Although the temperature of the liquid film changes by 10 K due to an increased inlet temperature from 100 °C to approx. 190 °C, the effect of increased solubility of sulfur dioxide (Fig. 16.22) or calcium hydroxide on the conversion plays an insignificant role.

The thermodynamic model of Krissmann [53] was used in the calculations of these experiments, though this was limited by the phase equilibrium (Eq. (3)) and the reaction equilibrium (Eq. (4)). Calculation of the activity coefficients of the H⁺ ions and HSO₃⁻ was performed according to the extended Debye–Hückel theory, using the approximation of Pitzer

$$\ln \gamma_i^{idds^*} = -A_\phi(T) \sqrt{\frac{1000}{M_{LM}}} \left[\frac{z_i^2}{\xi} \ln(1 + \xi \sqrt{I_x}) + \frac{z_i^2 \sqrt{I_x} - 2I_x^{1.5}}{1 + \xi \sqrt{I_x}} \right] \quad (86)$$

The reference condition of the ideal diluted solution and the ion strength I_x is approximated with the mass content

$$I_x = \frac{1}{2} \sum_j x_j z_j^2 \quad (87)$$

Table 16.6. Parameters of experiment V-2.

Bed material (glass spheres): $d_{32} = 0.00257$ m, $\rho_P = 2470$ kg m ⁻³ , $m_{FB} = 30$ kg			
Parameter			
ϑ_G^{in}	130.963 ± 0.0158 °C		
ϑ_E	23 °C		
φ	68 %		
\dot{m}_G	0.297 ± 0.000834 kg s ⁻¹		
$C_{\text{SO}_2}^{\text{in}}$	969.59 ± 4.0 mg Nm ⁻³		
ϑ_L^{in}	13.5 ± 0.45 °C		
Variation			
No.	Ca/S ratio	\dot{m}_{susp}	composition
Injection rate	1.56	$0.00414 \pm 2.45 \times 10^{-4}$ kg s ⁻¹	$\frac{1.45 \text{ kg}_{\text{Ca(OH)}_2}}{13.45 \text{ kg}_{\text{H}_2\text{O}}}$
	1.56	$0.00701 \pm 1.11 \times 10^{-4}$ kg s ⁻¹	$\frac{1.45 \text{ kg}_{\text{Ca(OH)}_2}}{23.75 \text{ kg}_{\text{H}_2\text{O}}}$
	1.56	$0.00824 \pm 1.86 \times 10^{-4}$ kg s ⁻¹	$\frac{1.45 \text{ kg}_{\text{Ca(OH)}_2}}{28.25 \text{ kg}_{\text{H}_2\text{O}}}$
	1.56	$0.00563 \pm 1.12 \times 10^{-4}$ kg s ⁻¹	$\frac{1.45 \text{ kg}_{\text{Ca(OH)}_2}}{18.85 \text{ kg}_{\text{H}_2\text{O}}}$

The activity coefficient of the molecular diluted sulfur dioxide is set to 1. The water activity is

$$\ln a_{H_2O} = M_{H_2O} \left[\frac{2A_\phi(T)I^{1.5}}{1 + b\sqrt{I}} - \sum_{i \neq H_2O} \sum_{j \neq H_2O} \bar{m}_i \bar{m}_j \left(\beta_{ij}^{(0)} + \sum_{n=1}^q \beta_{ij}^{(n)} \exp(-\alpha_n \sqrt{I}) \right) \right] - M_{H_2O} \sum_{i \neq H_2O} \bar{m}_i \quad (88)$$

In this case, the ion strength is described by

$$I_X = \frac{1}{2} \sum_j \bar{m}_j z_j^2 \quad (89)$$

The parameters q , b and a were set to $q = 1$, $b = 1, 2$ and $a = 2.0$ [52]. The interaction parameters $\beta_{ij}^{(0)}$ and $\beta_{ij}^{(n)}$ can be found in tables.

16.3.2.5 Influence of Gas Mass Flow

The parameters for the variation of gas mass flow and thus for the influence of the Re -number onto the conversion of the component SO_2 are displayed in Tabs. 16.9–16.11.

Table 16.7. Parameters of experiment V-3.

Bed material (glass spheres): $d_{32} = 0.00257$ m, $\rho_P = 2470$ kg m ⁻³ , $m_{FB} = 30$ kg			
Parameter			
ϑ_G^{in}	161.611 ± 0.0195 °C		
ϑ_E	22 °C		
φ	65 %		
\dot{m}_G	0.295 ± 0.001065 kg s ⁻¹		
$C_{SO_2}^{in}$	972.217 ± 10.9 mg Nm ⁻³		
ϑ_L^{in}	10.3 ± 0.2 °C		
Variation			
No.	Ca/S ratio	\dot{m}_{susp}	composition
Injection rate	1.57	$0.01243 \pm 1.75 \times 10^{-4}$ kg s ⁻¹	$\frac{1.45 \text{ kg}_{Ca(OH)_2}}{43.35 \text{ kg}_{H_2O}}$
	1.57	$0.00976 \pm 1.11 \times 10^{-4}$ kg s ⁻¹	$\frac{1.45 \text{ kg}_{Ca(OH)_2}}{33.65 \text{ kg}_{H_2O}}$
	1.57	$0.00702 \pm 6.67 \times 10^{-4}$ kg s ⁻¹	$\frac{1.45 \text{ kg}_{Ca(OH)_2}}{23.85 \text{ kg}_{H_2O}}$
	1.57	$0.00282 \pm 9.43 \times 10^{-5}$ kg s ⁻¹	$\frac{1.45 \text{ kg}_{Ca(OH)_2}}{8.65 \text{ kg}_{H_2O}}$

The measurements and simulations in Figs. 16.23 and 16.24 show that a high gas throughputs leads to a lower conversion and higher outlet temperature when the liquid injection is constant. There is a overlap of formation of the mass transfer surface and of mass transfer of the absorbed component. An increase in gas throughput does not yield to a change of the Sh -number and thus to an enhanced heat and mass transfer.

The functional progression dependency of the Sh -number on gas mass flow, expressed by the Re -number, is illustrated for experiment V-9 in Fig. 16.25. The curve has a maximum which is caused by the higher expansion (relative porosity) of the fluidized bed [66]. In contrast to fixed beds, the energy input in fluidized beds is higher because of higher gas throughputs, and consequently the drying is faster.

The higher enthalpy flow of the increased gas mass flow leads to a faster drying, and thus to a decreased liquid loading as well as mass transfer surface. Thus, the conversion is lower at constant conditions.

The steady-state humidity of the gas at the outlet of the fluidized bed follows with:

$$\tilde{Y}_{H_2O}^{out} = \tilde{Y}_{H_2O}^{in} + \frac{\dot{n}_{H_2O}^{in}}{\dot{n}_{dryA}} \quad (90)$$

Table 16.8. Parameters of experiment V-4.

Bed material (glass spheres): $d_{32} = 0.00257$ m, $\rho_P = 2470$ kg m ⁻³ , $m_{FB} = 30$ kg			
Parameter			
ϑ_G^{in}	192.672 ± 0.0179 °C		
ϑ_E	18 °C		
φ	75 %		
\dot{m}_G	0.297 ± 0.001 kg s ⁻¹		
$C_{\text{SO}_2}^{\text{in}}$	958.34 ± 10.41 mg Nm ⁻³		
ϑ_L^{in}	14.1 ± 0.5 °C		
Variation			
No.	Ca/S ratio	\dot{m}_{susp}	composition
Injection rate	1.58	$0.01243 \pm 7.78 \times 10^{-4}$ kg s ⁻¹	$\frac{1.45 \text{ kg}_{\text{Ca(OH)}_2}}{23.65 \text{ kg}_{\text{H}_2\text{O}}}$
	1.58	$0.00976 \pm 9.34 \times 10^{-4}$ kg s ⁻¹	$\frac{1.45 \text{ kg}_{\text{Ca(OH)}_2}}{33.35 \text{ kg}_{\text{H}_2\text{O}}}$
	1.58	$0.00702 \pm 1.43 \times 10^{-5}$ kg s ⁻¹	$\frac{1.45 \text{ kg}_{\text{Ca(OH)}_2}}{43.45 \text{ kg}_{\text{H}_2\text{O}}}$

An analysis of the driving force of evaporation is necessary, as an increase in gas mass flow yields to a lower outlet humidity. An approximation for the evaporated molar mass flux is given by:

$$\dot{n}_{\text{H}_2\text{O}}^{\text{So,G}} = \beta_{\text{H}_2\text{O}}^G A_{P,\text{tot}} \phi \frac{\rho_{\text{dryA}}}{M_{\text{dryA}}} \left(\bar{Y}_{\text{H}_2\text{O}}^{\text{PG}} - \bar{Y}_{\text{H}_2\text{O}} \right) \quad (91)$$

A decreased gas outlet humidity entails a decrease in average gas humidity over the bed height, and an increase in driving force for the evaporation. Thus, it is evident that a driving force rising due to a larger gas throughput must lead to a smaller mass transfer surface. Likewise, the influence of gas throughput on the conversion of sulfur dioxide can be reduced with the theoretical model to NTU . The gradient of the function $NTU_{\text{SO}_2} = f(Re)$ (Fig. 16.26) is larger at high gas throughputs.

16.3.2.6 Influence of the Particle Diameter

Two experiments were carried out at a gas inlet temperature of 130 °C and 160 °C to investigate the influence of the diameter of the bed material on reactive absorption.

The experimental parameters for a gas inlet temperature of 130 °C are summarized in Tabs. 16.6, 16.9 and 16.12.

The parameter values for a gas inlet temperature of 160 °C are listed in Tabs. 16.7, 16.13 and 16.14.

In the investigated diameter range, there were no significant differences between the conversions and outlet temperatures (Figs. 16.27–16.30). An increase in the

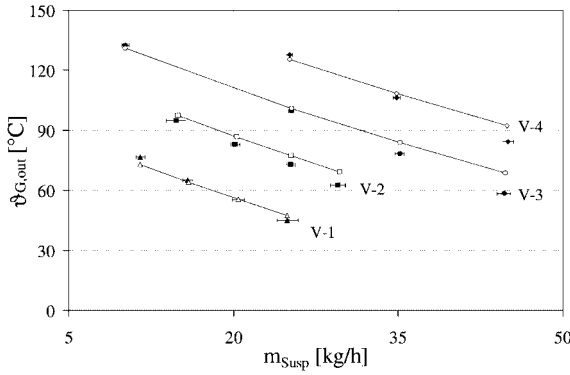


Fig. 16.18. Dependency of outlet temperature on injection rate for different gas inlet temperatures, experiment V-1: $\vartheta_{G,in} = 100$ °C, V-2: $\vartheta_{G,in} = 130$ °C, V-3: $\vartheta_{G,in} = 161$ °C, V-4: $\vartheta_{G,in} = 192$ °C (symbols = experiments; lines = model).

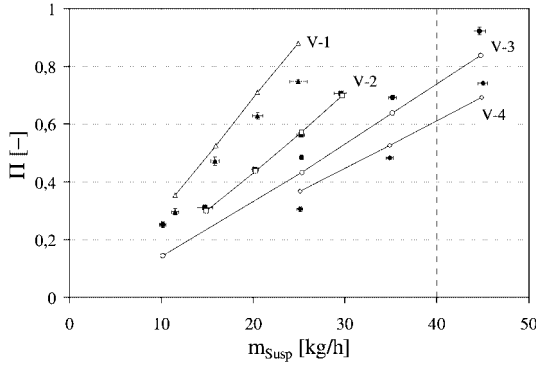


Fig. 16.19. Dependency of conversions on injection rate for different gas inlet temperatures, experiment V-1: $\vartheta_{G,in} = 100$ °C, V-2: $\vartheta_{G,in} = 130$ °C, V-3: $\vartheta_{G,in} = 161$ °C, V-4: $\vartheta_{G,in} = 192$ °C (symbols = experiments; lines = model).

diameter of the bed particles resulted in a larger Re -number at constant gas mass flow

$$Re_p = \frac{w_G d_p}{\nu_G} \quad (92)$$

The larger Re -number is contained in the empirical Sh -approximation for the calculation of the mass transfer coefficient gas-particle. Increases in the Re -number, Ar -number and Sh -number do not provide a large gas mass transfer coefficient, as this will decrease due to diameter growth and thus lead to larger Sh -numbers. This dependency is illustrated by the equation from Rowe [78]

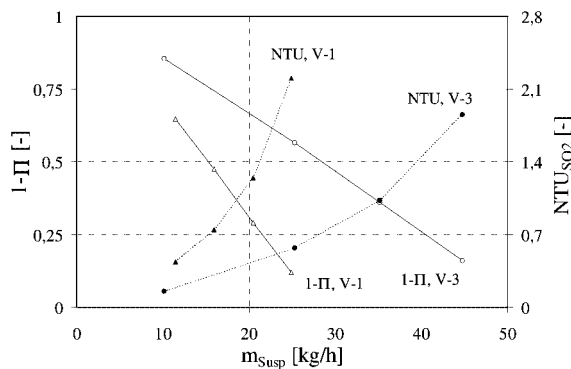


Fig. 16.20. Relationship between injection rate, conversion und NTU ; experiment V-1: $\vartheta_{G,in} = 100\text{ }^{\circ}\text{C}$, V-3: $\vartheta_{G,in} = 161\text{ }^{\circ}\text{C}$.

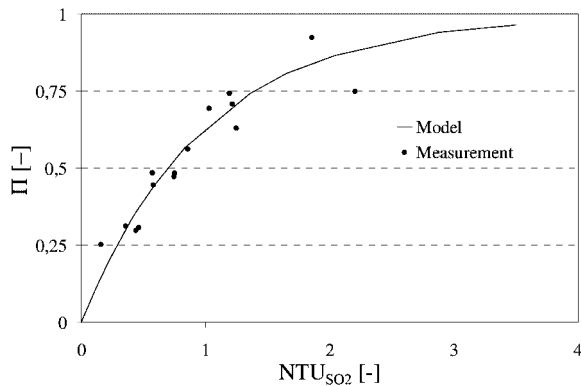


Fig. 16.21. Dependency of conversion on NTU , experiment V-1: $\vartheta_{G,in} = 100\text{ }^{\circ}\text{C}$, V-2: $\vartheta_{G,in} = 130\text{ }^{\circ}\text{C}$, V-3: $\vartheta_{G,in} = 161\text{ }^{\circ}\text{C}$, V-4: $\vartheta_{G,in} = 192\text{ }^{\circ}\text{C}$.

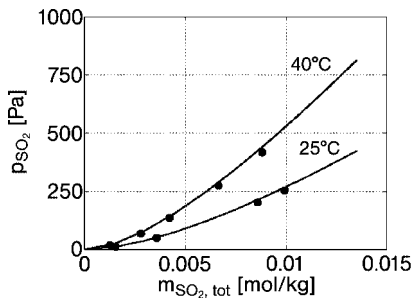


Fig. 16.22. Phase and reaction equilibrium of SO_2 and H_2O (symbols = experiments).

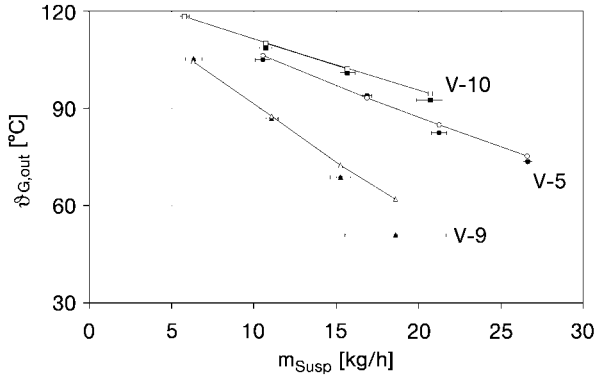


Fig. 16.23. Dependency of outlet temperature on injection rate for different gas mass flows, experiment V-9: $\dot{m}_G = 0.153 \text{ kg s}^{-1}$, V-5: $\dot{m}_G = 0.289 \text{ kg s}^{-1}$, V-10: $\dot{m}_G = 0.392 \text{ kg s}^{-1}$ (symbols = experiments; lines = model).

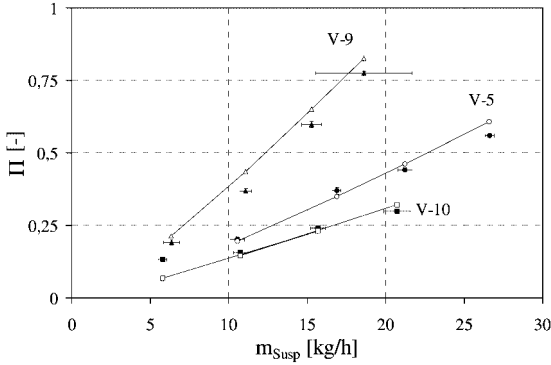


Fig. 16.24. Dependency of conversions on injection rate for different gas mass flows, experiment V-9: $\dot{m}_G = 0.153 \text{ kg s}^{-1}$, V-5: $\dot{m}_G = 0.289 \text{ kg s}^{-1}$, V-10: $\dot{m}_G = 0.392 \text{ kg s}^{-1}$ (symbols = experiments; lines = model).

$$Sh = 2 + 0.72\sqrt{Re}^3\sqrt{Sc} \quad (93)$$

$$\beta^G = \frac{Sh_{G,p}D}{d_p} = \frac{2D}{d_p} + 0.72\sqrt{\frac{w_G}{v_G d_p}} D^3\sqrt{Sc} \quad (94)$$

The transport of sulfur dioxide in the gas phase to the particles, as well as transport of water vapor from the particles, is a convective mass transfer. Both mass transfer coefficients can be described by *Sh*-approximations. Thus, progression of the *Sh*-numbers and the mass transfers coefficients must be qualitatively identical (Fig. 16.31).

Table 16.9. Parameters of experiment V-5.

Bed material (glass spheres): $d_{32} = 0.0015 \text{ m}$, $\rho_P = 2470 \text{ kg m}^{-3}$, $m_{\text{FB}} = 30 \text{ kg}$			
<i>Parameter</i>			
$\vartheta_{\text{G}}^{\text{in}}$	$130.78 \pm 0.045 \text{ }^{\circ}\text{C}$		
ϑ_{E}	$21 \text{ }^{\circ}\text{C}$		
φ	71 \%		
\dot{m}_{G}	$0.289 \pm 0.00113 \text{ kg s}^{-1}$		
$C_{\text{SO}_2}^{\text{in}}$	$920 \pm 6.47 \text{ mg Nm}^{-3}$		
$\vartheta_{\text{L}}^{\text{in}}$	$11.4 \pm 0.5 \text{ }^{\circ}\text{C}$		
<i>Variation</i>			
No.	Ca/S ratio	\dot{m}_{susp}	composition
Injection rate	1.69	$0.00293 \pm 1.26 \times 10^{-4} \text{ kg s}^{-1}$	$\frac{1.45 \text{ kg}_{\text{Ca(OH)}_2}}{9.1 \text{ kg}_{\text{H}_2\text{O}}}$
	1.69	$0.00469 \pm 7.78 \times 10^{-5} \text{ kg s}^{-1}$	$\frac{1.45 \text{ kg}_{\text{Ca(OH)}_2}}{15.45 \text{ kg}_{\text{H}_2\text{O}}}$
	1.69	$0.0059 \pm 1.26 \times 10^{-4} \text{ kg s}^{-1}$	$\frac{1.45 \text{ kg}_{\text{Ca(OH)}_2}}{19.79 \text{ kg}_{\text{H}_2\text{O}}}$
	1.69	$0.00739 \pm 7.78 \times 10^{-4} \text{ kg s}^{-1}$	$\frac{1.45 \text{ kg}_{\text{Ca(OH)}_2}}{25.15 \text{ kg}_{\text{H}_2\text{O}}}$

The increase in diameter during granulation or agglomeration produces, by a decrease in mass transfer coefficient and thus by a worsened drying, to a larger mass transfer surface. The opposite mechanism is the process of absorption, and a decrease in the mass transfer coefficient is the limiting condition. A reduction in the gas phase mass transfer coefficient increases the limitation. A change in particle diameter by either growth or attrition entails two effects for the absorption process. An increase in the mass transfer surface due to particle growth results in a decrease of the gas phase mass transfer coefficient. The question remains as to whether these processes have positive or negative effects on the conversion of the absorbed component, sulfur dioxide.

It is clear from Fig. 16.32 that for the quantitative evaluation of convective mass transfer, the product of the two quantities – mass transfer surface and mass transfer coefficient – is crucial. As a result, a constant product of mass transfer coefficient and mass transfer surface under the conditions of a constant fluidization mass flow has a constant number of transfer units (*NTU*).

If *NTU* is constant, then the conversion cannot change (Fig. 16.33). These theoretical considerations confirm the experimental tendency that the conversion of sulfur dioxide is not dependent upon the diameter of the particles in the examined range.

Table 16.10. Parameters of experiment V-9.

Bed material (glass spheres): $d_{32} = 0.0015$ m, $\rho_P = 2470$ kg m ⁻³ , $m_{FB} = 30$ kg			
Parameter			
ϑ_G^{in}	130.57 ± 0.0626 °C		
ϑ_E	17 °C		
φ	76 %		
\dot{m}_G	0.1528 ± 0.000396 kg s ⁻¹		
$c_{SO_2}^{in}$	1665.25 ± 4.25 mg Nm ⁻³		
ϑ_L^{in}	10.2 ± 0.3 °C		
Variation			
No.	Ca/S ratio	\dot{m}_{susp}	composition
Injection rate	1.46	$0.00176 \pm 1.4 \times 10^{-4}$ kg s ⁻¹	$\frac{1.2 \text{ kg}_{Ca(OH)_2}}{5.2 \text{ kg}_{H_2O}}$
	1.46	$0.00308 \pm 1.04 \times 10^{-4}$ kg s ⁻¹	$\frac{1.2 \text{ kg}_{Ca(OH)_2}}{9.9 \text{ kg}_{H_2O}}$
	1.46	$0.00424 \pm 1.75 \times 10^{-4}$ kg s ⁻¹	$\frac{1.2 \text{ kg}_{Ca(OH)_2}}{14.05 \text{ kg}_{H_2O}}$
	1.46	$0.00517 \pm 8.52 \times 10^{-4}$ kg s ⁻¹	$\frac{1.2 \text{ kg}_{Ca(OH)_2}}{17.4 \text{ kg}_{H_2O}}$

16.3.3

Experiments for Reactive Absorption with Overlapped Granulation of Solid**16.3.3.4 Experimental Realization**

During the experiments, contrary to the pure reactive absorption, a stationary regime is pursued. The solid mass content of the suspension is much higher than is theoretically required for sulfur dioxide absorption. Thus, the process times will be reduced and the granulation effect with overlapped reactive absorption can be achieved within a few hours. In order to achieve a better granulating effect, carboxyl methyl cellulose (CMC) was added to the suspension as a binder.

After filling the apparatus with the hold-up, heating of the particles occurred until constant temperatures were achieved, whereupon injection of the suspension is commenced.

During the batch experiments (no particle discharge), which are conducted mainly at high solid concentrations, the nozzle must be cleaned manually using a cleaning pin in order to obtain a constant injection.

In the non-classifying continuous granulation experiments, a permanent discharge of particles is necessary to keep the bed mass and pressure loss constant; this in turn is dependent on the amount of solid injected, the attrition, and the

Table 16.11. Parameters of experiment V-10.

Bed material (glass spheres): $d_{32} = 0.0015$ m, $\rho_P = 2470$ kg m ⁻³ , $m_{FB} = 30$ kg			
Parameter			
ϑ_G^{in}	129.35 ± 0.0174 °C		
ϑ_E	19 °C		
φ	68 %		
\dot{m}_G	0.3923 ± 0.000532 kg s ⁻¹		
$C_{\text{SO}_2}^{\text{in}}$	778.77 ± 5.71 mg Nm ⁻³		
ϑ_L^{in}	10.7 ± 0.3 °C		
Variation			
No.	Ca/S ratio	\dot{m}_{susp}	composition
Injection rate	1.44	$0.00576 \pm 2.36 \times 10^{-4}$ kg s ⁻¹	$\frac{1.42 \text{ kg}_{\text{Ca(OH)}_2}}{19.3 \text{ kg}_{\text{H}_2\text{O}}}$
	1.44	$0.00161 \pm 7.78 \times 10^{-5}$ kg s ⁻¹	$\frac{1.42 \text{ kg}_{\text{Ca(OH)}_2}}{4.4 \text{ kg}_{\text{H}_2\text{O}}}$
	1.44	$0.00436 \pm 1.3 \times 10^{-4}$ kg s ⁻¹	$\frac{1.42 \text{ kg}_{\text{Ca(OH)}_2}}{14.3 \text{ kg}_{\text{H}_2\text{O}}}$
	1.44	$0.00298 \pm 1.11 \times 10^{-4}$ kg s ⁻¹	$\frac{1.42 \text{ kg}_{\text{Ca(OH)}_2}}{9.3 \text{ kg}_{\text{H}_2\text{O}}}$

continuous feeding of external seeds. Constancy of the bed mass is controlled by the pressure loss.

For the measurement of particle size distribution with time, samples were collected at set time intervals.

16.3.3.2 Batch Experiments

The bed mass loss is caused by elutriated particles (dust) generated by attrition, breakage and non-deposited spray drops (overspray). The overspray depends on the position of the nozzle.

This dust separated by pneumatic filters or cyclones can be recycled and used as internal seeds (disperse phase) for the production of new particles or for the layered growth (continuous phase) of existing particles. One effect of the production of internal seeds is the formation of a wide particle size distribution, while the deposition of the re-fed dust yields to growth of particles.

Validation of the experiment without dust recycle and external seeds

The parameters for the batch granulation experiment without dust recycle and external seeds V-13 are listed in Tab. 16.15. The measured number and mass density particle size distribution (Fig. 16.34) answer the question as to whether particle growth can be modeled as either size-dependent or size-independent in the estimated range.

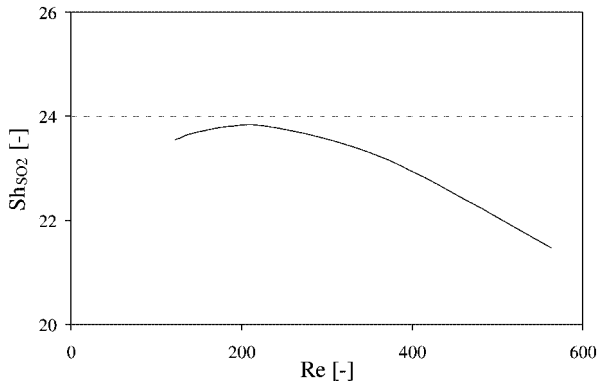


Fig. 16.25. Dependency of the Sherwood number (Sh) on the Reynolds number (Re), experiment V-9.

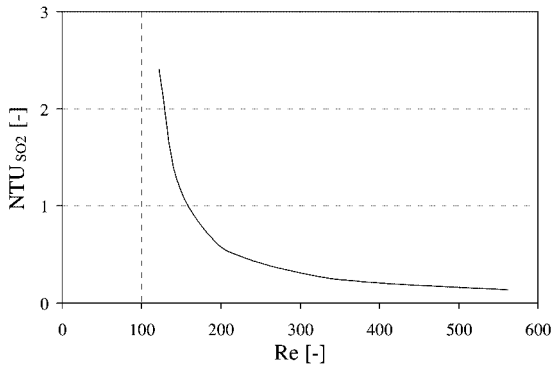


Fig. 16.26. Dependency of NTU on Re , experiment V-9.

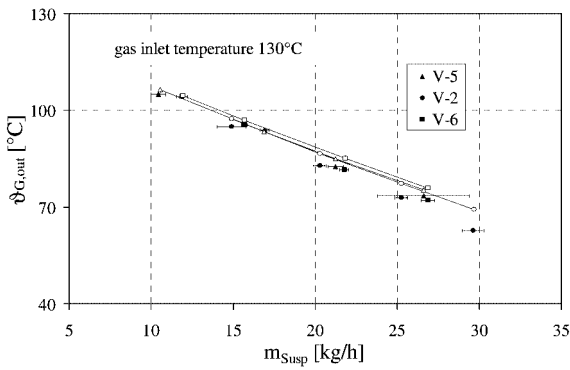


Fig. 16.27. Dependency of outlet temperature on injection rate for different particle diameters and at inlet temperature $T_{G,in} = 130\text{ }^{\circ}\text{C}$, experiment V-5: $d_p = 1.5\text{ mm}$, V-2: $d_p = 2.57\text{ mm}$, V-6: $d_p = 3.29\text{ mm}$ (symbols = experiments; lines = model).

Table 16.12. Parameters of experiment V-6.

Bed material (glass spheres): $d_{32} = 0.00329$ m, $\rho_P = 2470$ kg m ⁻³ , $m_{FB} = 30$ kg			
<i>Parameter</i>			
ϑ_G^{in}	130.619 ± 0.016 °C		
ϑ_E	17 °C		
ϕ	80 %		
\dot{m}_G	0.3 ± 0.0007 kg s ⁻¹		
$C_{\text{SO}_2}^{\text{in}}$	956.25 ± 9.312 mg Nm ⁻³		
ϑ_L^{in}	10.2 ± 0.1 °C		
<i>Variation</i>			
No.	Ca/S ratio	\dot{m}_{susp}	Composition
Injection rate	1.57	$0.00436 \pm 4.9 \times 10^{-5}$ kg s ⁻¹	$\frac{1.45 \text{ kg}_{\text{Ca(OH)}_2}}{13.45 \text{ kg}_{\text{H}_2\text{O}}}$
	1.57	$0.00606 \pm 7.78 \times 10^{-5}$ kg s ⁻¹	$\frac{1.45 \text{ kg}_{\text{Ca(OH)}_2}}{23.75 \text{ kg}_{\text{H}_2\text{O}}}$
	1.57	$0.00746 \pm 1.12 \times 10^{-4}$ kg s ⁻¹	$\frac{1.45 \text{ kg}_{\text{Ca(OH)}_2}}{28.25 \text{ kg}_{\text{H}_2\text{O}}}$
	1.57	$0.00331 \pm 9.81 \times 10^{-5}$ kg s ⁻¹	$\frac{1.45 \text{ kg}_{\text{Ca(OH)}_2}}{18.85 \text{ kg}_{\text{H}_2\text{O}}}$

The batch process is characterized by a constant number of particles. The number and mass density distribution are constant in their form. This confirms the assumption of surface-proportional growth and thus the diameter-independent growth at uniform wetting of particles [30, 67, 68]. Every particle grows at the same rate, and an increase in process time would lead to a permanent reduction in growth rate due to permanent enlargement of the particle surface. In the limiting case of an infinite particle surface, the growth rate will be zero. The comparison between measurement (Fig. 16.34) and simulation (Fig. 16.35) shows a good agreement.

A total mass balance is necessary for qualitative evaluation. A solid mass loss of 1.2 % by depositions of dust on apparatus wall and by elutriation is demonstrated in Tab. 16.16.

The essential objective was investigation of the fluidized bed as a convenient semi-dry absorption reactor for the extensive reduction of dust production by coupling of the granulation. Measurements of sulfur dioxide concentrations (Fig. 16.36) and particle growth (Fig. 16.37) for experiment V-13 confirm for the first time that coupling of the thermal transfer processes of absorption and drying with the mechanical growth process of granulation can be achieved in a single processing step. It is also of interest that at different injection rates the bed mass increases (Fig. 16.37(b)), whilst the particle number remains constant. The Sauter diameter growth is seen to be declining (Fig. 16.37(a)).

Table 16.13. Parameters of experiment V-7.

Bed material (glass spheres): $d_{32} = 0.0015$ m, $\rho_P = 2470$ kg m ⁻³ , $m_{FB} = 30$ kg			
<i>Parameter</i>			
ϑ_G^{in}	161.579 ± 0.05 °C		
ϑ_E	25 °C		
ϕ	61 %		
\dot{m}_G	0.284 ± 0.0012 kg s ⁻¹		
$c_{\text{SO}_2}^{\text{in}}$	940.05 ± 8.01 mg Nm ⁻³		
ϑ_L^{in}	11.7 ± 0.2 °C		
<i>Variation</i>			
No.	Ca/S ratio	\dot{m}_{susp}	composition
Injection rate	1.69	$0.00463 \pm 9.9 \times 10^{-5}$ kg s ⁻¹	$\frac{1.45 \text{ kg}_{\text{Ca(OH)}_2}}{15.19 \text{ kg}_{\text{H}_2\text{O}}}$
	1.69	$0.00768 \pm 7.17 \times 10^{-5}$ kg s ⁻¹	$\frac{1.45 \text{ kg}_{\text{Ca(OH)}_2}}{26.19 \text{ kg}_{\text{H}_2\text{O}}}$
	1.69	$0.01 \pm 1.55 \times 10^{-4}$ kg s ⁻¹	$\frac{1.45 \text{ kg}_{\text{Ca(OH)}_2}}{34.79 \text{ kg}_{\text{H}_2\text{O}}}$
	1.69	$0.0115 \pm 9.84 \times 10^{-5}$ kg s ⁻¹	$\frac{1.45 \text{ kg}_{\text{Ca(OH)}_2}}{40.15 \text{ kg}_{\text{H}_2\text{O}}}$

The different injection rates explain the possibility of process control. This process would be stable at high conversions at constant nozzle operation. The reason for temporal clogging of the nozzle is the high solid content of the suspension and the coarse suspended calcium hydroxide. A cyclic cleaning of the nozzle has been used in later experiments.

Validation of the experiment with dust recycle and without external seeds

Parameters for the batch granulation experiment with dust recycle and without external seeds V-14 are listed in Tab. 16.17. The objective was to investigate the deposition of the recycled dust.

Figures 16.38 and 16.39 demonstrate that the form of the particle size distributions is once again almost constant during the process time, and consequently the pneumatic recycled dust is not used for seed production. Dust is deposited on the particles because the nozzle position is close to the dust recycle tube (uniform wetted dust), and this leads to an enlarged particle growth. The measured time-dependent gas outlet temperature and the measured time-dependent conversion corresponds with simulations (Fig 16.40). The bed mass growth is linear at constant liquid injection rates (Fig. 16.41). The change in particle size distribution value and of the Sauter diameter is, again, declining.

Table 16.14. Parameters of experiment V-8.

Bed material (glass spheres): $d_{32} = 0.00329$ m, $\rho_P = 2470$ kg m ⁻³ , $m_{FB} = 30$ kg			
Parameter			
ϑ_G^{in}	161.609 ± 0.238 °C		
ϑ_E	22 °C		
φ	64 %		
\dot{m}_G	0.305 ± 0.00079 kg s ⁻¹		
$C_{\text{SO}_2}^{\text{in}}$	961.2 ± 5.11 mg Nm ⁻³		
ϑ_L^{in}	9.8 ± 0.3 °C		
Variation			
No.	Ca/S ratio	\dot{m}_{susp}	composition
Injection rate	1.53	$0.00439 \pm 7.78 \times 10^{-5}$ kg s ⁻¹	$\frac{1.45 \text{ kg}_{\text{Ca(OH)}_2}}{14.35 \text{ kg}_{\text{H}_2\text{O}}}$
	1.53	$0.00718 \pm 7.17 \times 10^{-5}$ kg s ⁻¹	$\frac{1.45 \text{ kg}_{\text{Ca(OH)}_2}}{24.45 \text{ kg}_{\text{H}_2\text{O}}}$
	1.53	$0.00968 \pm 7.17 \times 10^{-4}$ kg s ⁻¹	$\frac{1.45 \text{ kg}_{\text{Ca(OH)}_2}}{33.45 \text{ kg}_{\text{H}_2\text{O}}}$
	1.53	$0.0111 \pm 2.58 \times 10^{-5}$ kg s ⁻¹	$\frac{1.45 \text{ kg}_{\text{Ca(OH)}_2}}{38.55 \text{ kg}_{\text{H}_2\text{O}}}$

An analytical solution for the surface proportional growth is given by Eq. (95):

$$\frac{dd_{32}}{dt} = \frac{2\dot{m}_{\text{Solid}}}{\rho_{\text{Solid}}A_{\text{tot}}} = \frac{2\dot{m}_{\text{Solid}}}{\rho_{\text{Solid}}\pi Nd_{32}^2} \quad (95)$$

With integration of the differential equation

$$\int_{d_{32}^{t=0}}^{d_{32}^{t=t}} d_{32}^2 dd_{32} = \frac{2\dot{m}_{\text{Solid}}}{\rho_{\text{Solid}}\pi N} \int_{t=0}^{t=t} t dt \quad (96)$$

follows

$$\left(d_{32}^{t=t}\right)^3 = \left(d_{32}^{t=0}\right)^3 + \frac{6\dot{m}_{\text{Solid}}}{\rho_{\text{Solid}}\pi N} t \quad (97)$$

The function $d_{32} = f(t)$ has no boundary value. The progression of the Sauter diameter of experiment V-14 shows an agreement between measurement and analytical solution (Fig. 16.42). Experiment V-14 shows the achievement of a high conversion of the absorbed gas component sulfur dioxide by simultaneous granulation of the reaction product in a fluidized-bed reactor.

The total mass balance in Tab. 16.18 illustrates that the dust recycle and deposition onto the particles reduces dust formation and assists particle growth.

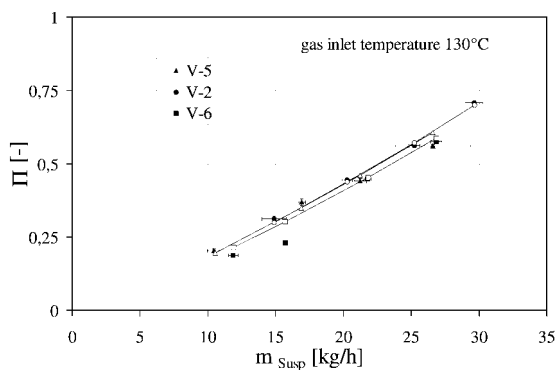


Fig. 16.28. Dependency of conversion on injection rate for different particle diameters and at inlet temperature $\vartheta_{G,in} = 130$ °C,

experiment V-5: $d_p = 1.5$ mm, V-2: $d_p = 2.57$ mm, V-6: $d_p = 3.29$ mm (symbols = experiments; lines = model).

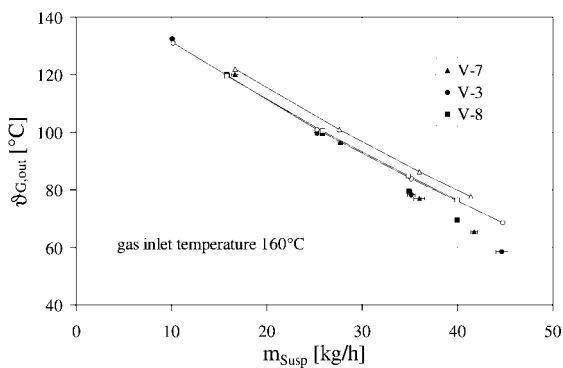


Fig. 16.29. Dependency of outlet temperature on injection rate for different particle diameters and at inlet temperature $\vartheta_{G,in} = 160$ °C,

experiment V-7: $d_p = 1.5$ mm, V-3: $d_p = 2.57$ mm, V-8: $d_p = 3.29$ mm (symbols = experiments; lines = model).

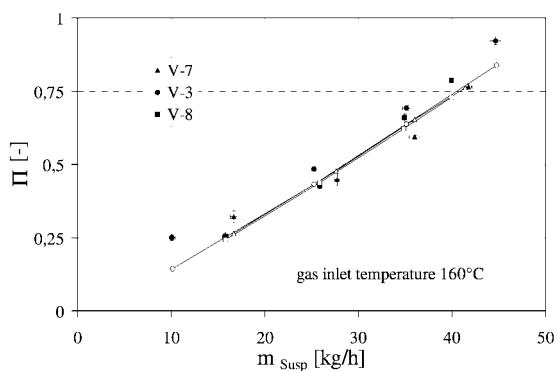


Fig. 16.30. Dependency of conversion on injection rate for different particle diameters and at inlet temperature $\vartheta_{G,in} = 160$ °C,

experiment V-7: $d_p = 1.5$ mm, V-3: $d_p = 2.57$ mm, V-8: $d_p = 3.29$ mm (symbols = experiments; lines = model).

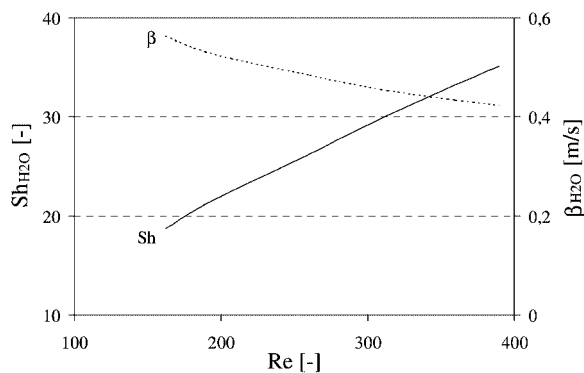


Fig. 16.31. Dependency between Re , Sh and NTU .

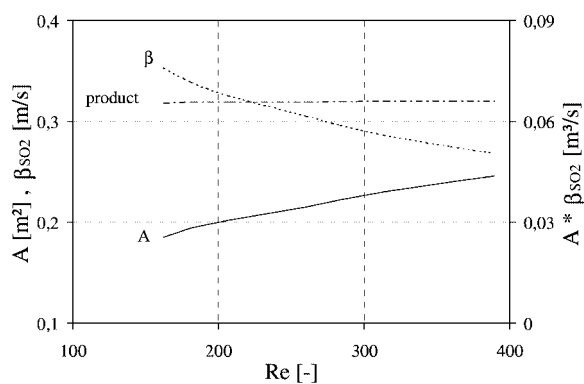


Fig. 16.32. Dependency between Re , A and β .

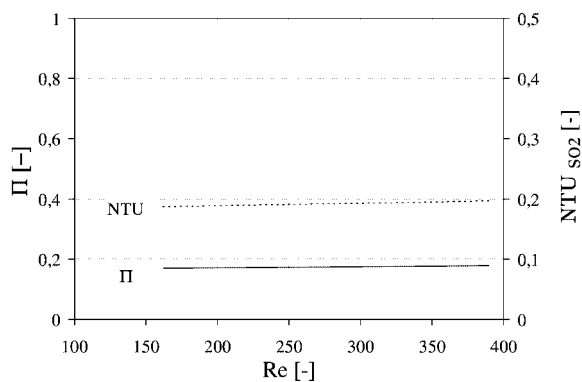


Fig. 16.33. Dependency between Re , conversion and NTU .

Table 16.15. Parameters of experiment V-13.

Bed material (glass spheres): $d_{32} = 0.002682$ m, $\rho_p = 2470$ kg m ⁻³ , $m_{FB} = 20$ kg			
<i>Parameter</i>			
ϑ_G^{in}	100.29 ± 0.018 °C		
ϑ_E	19 °C		
φ	73 %		
\dot{m}_G	0.5613 ± 0.00038 kg s ⁻¹		
$C_{SO_2}^{in}$	353.98 ± 6.77 mg Nm ⁻³		
ϑ_L^{in}	10.1 ± 0.4 °C		
x_{binder}	1.5 mass-%		
<i>Variation</i>			
No.	Ca/S ratio	\dot{m}_{susp}	composition
Injection rate I	4.32	0.00666 ± 9.05 × 10 ⁻⁴ kg s ⁻¹	$\frac{1.45 \text{ kg}_{Ca(OH)_2}}{9.1 \text{ kg}_{H_2O}}$
Injection rate II	8.09	0.01246 ± 4.38 × 10 ⁻⁴ kg s ⁻¹	$\frac{1.45 \text{ kg}_{Ca(OH)_2}}{9.1 \text{ kg}_{H_2O}}$
Injection rate III	6.66	0.01025 ± 1.78 × 10 ⁻⁴ kg s ⁻¹	$\frac{1.45 \text{ kg}_{Ca(OH)_2}}{9.1 \text{ kg}_{H_2O}}$

16.3.3.3 Continuous Experiments

In practice, the power plants operates with continuous downstream desulfurization. The continuous granulation process presents, in contrast to the batch process, the advantage of operating the plant at lower costs under stationary conditions at higher product throughputs. One characteristic of the stationary operation point – in addition to constant mass flows, temperatures and humidity – is a constant granulate spectrum. In order to form this constant granulate spectrum, it is essential to start with injection of the suspension into the fluidized bed, and to have seeds of a certain quantity and size. The seeds can either be fed externally or produced by partial milling of the oversized product and the successive recycle. The steady state is obtained by complete discharge of granulates of the hold-up.

The following experiments were carried out with a non-classifying discharge of particles by an industrial vacuum cleaner.

Validation of the experiment with dust recycle and without external seeds

The constant non-classifying discharge leads to a constant bed mass; this is the central condition of continuous operation.

The parameters listed in Tab. 16.19 represent experiment V-15. The objective was to analyze the influence of absent seeds on the stability of the semi-batch process. Without external seeds, the number of particles will decrease as particles are discharged.

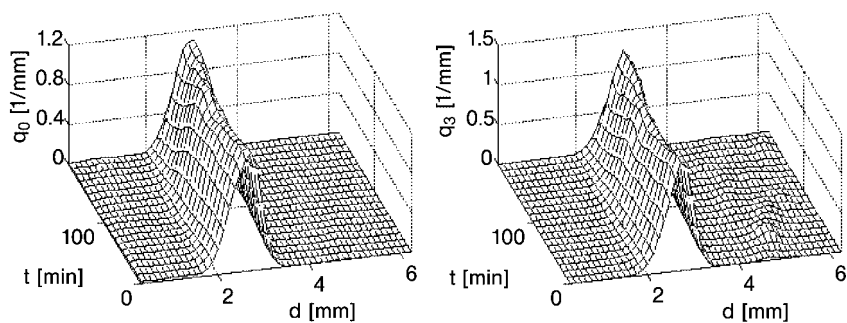


Fig. 16.34. Measured number and mass density distribution, experiment V-13.

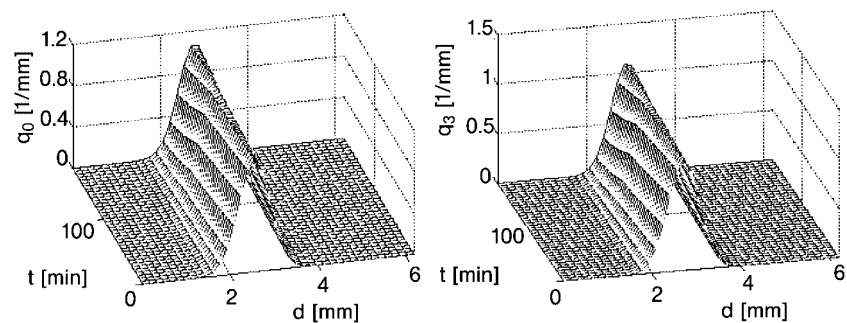


Fig. 16.35. Simulated number and mass density distribution, experiment V-13.

Table 16.16. Solid mass balance, experiment V-13.

<i>Fed solid</i>	
Hold-up:	20 kg
Injection rate I, duration: 1.85 h	5.116 kg
Injection rate II, duration: 0.5 h	2.588 kg
Injection rate III, duration: 0.633 h	2.699 kg
Sum:	30.4 kg
<i>Discharged solid</i>	
Bed mass (end) + samples:	25.56 kg
Cyclone (end):	4.48 kg
Sum:	30.04 kg

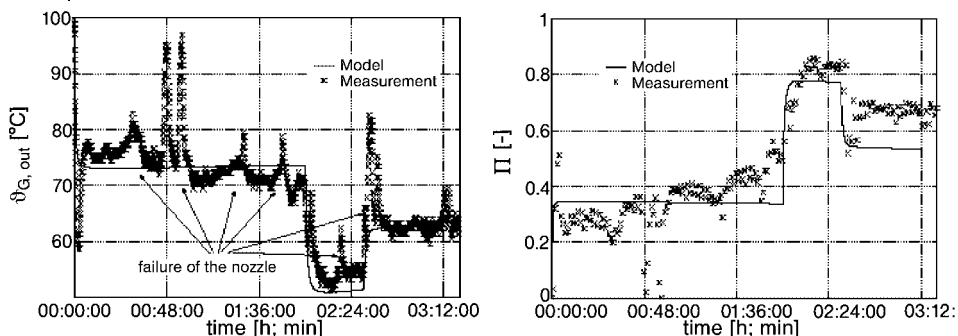


Fig. 16.36. Progression of gas outlet temperature and of conversion over time, experiment V-13.

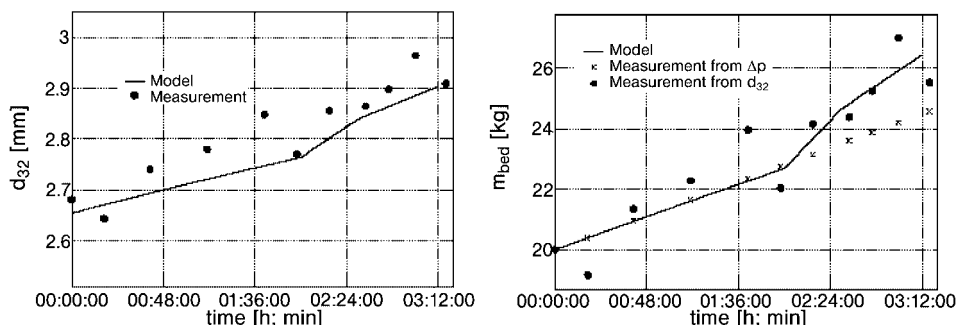


Fig. 16.37. Progression of Sauter diameter and bed mass over time, experiment V-13 (simulation: $R_A = 0.075 \text{ kg m}^{-2} \text{ h}^{-1}$, $k_{OS} = 0 \%$, $k_{\text{growth}} = 100 \%$, $k_{\text{sep}} = 0 \%$).

On the basis of Fig. 16.46, it is clear that the particle diameters change due to granulation, while the coupled mass and heat transfers from gas to particles does not affect the conversion. As all of these experiments show, the crucial criterion is the suspension stored in the bed. Absorption of the gas component can occur only by the mass transfer surface. As a result of the nozzle clogging, the liquid in the granulator begins immediately to dry, and the drying process entails a decrease in mass transfer surface for absorption and a reduction in the conversion. Thus, an increasing concentration and associated conversion of sulfur dioxide can be explained in the case of nozzle failure.

The solid injected with the suspension is constant, and particle growth is enlarged with process time due to the surface-proportional growth. Thus, progression of the Sauter diameter over time (Fig. 16.47) as well as the number and mass of particle size distributions, is progressive (Figs. 16.44 and 16.45). The non-classifying discharge has no influence on the form and width of the particle size distributions. Illustrations of the hold-up particles and the product are shown in Fig. 16.43.

Table 16.17. Parameters of experiment V-14.

Bed material (coated glass spheres): $d_{32} = 0.002916\text{ m}$, $\rho_P = 2470\text{ kg m}^{-3}$, $m_{FB} = 20\text{ kg}$			
Parameter			
ϑ_G^{in}	$100.813 \pm 0.033\text{ }^{\circ}\text{C}$		
ϑ_E	$20\text{ }^{\circ}\text{C}$		
φ	75 \%		
\dot{m}_G	$0.549 \pm 0.0008\text{ kg s}^{-1}$		
$C_{\text{SO}_2}^{\text{in}}$	$384.35 \pm 4.66\text{ mg Nm}^{-3}$		
ϑ_L^{in}	$18.6 \pm 0.37\text{ }^{\circ}\text{C}$		
x_{binder}	1.5 mass-\%		
Variation			
No.	Ca/S ratio	\dot{m}_{susp}	composition
Injection rate I	12.88	$0.015 \pm 7.0 \times 10^{-4}\text{ kg s}^{-1}$	$\frac{16\text{ kg}_{\text{Ca(OH)}_2}}{84\text{ kg}_{\text{H}_2\text{O}}}$

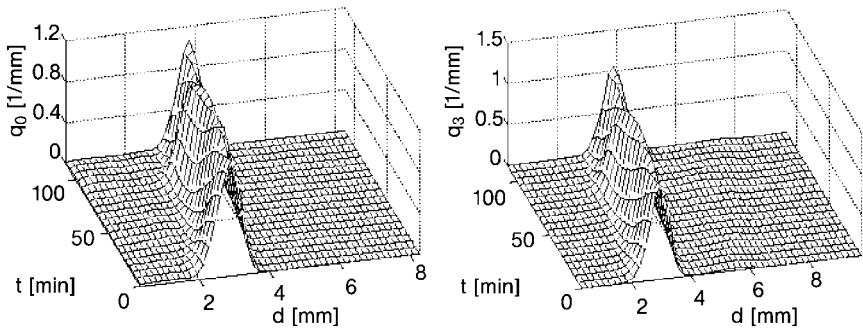


Fig. 16.38. Measured number and mass density distribution, experiment V-14.

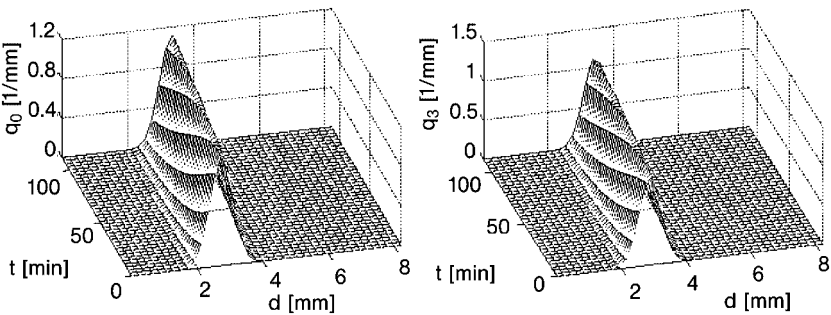


Fig. 16.39. Simulated number and mass density distribution, experiment V-14.

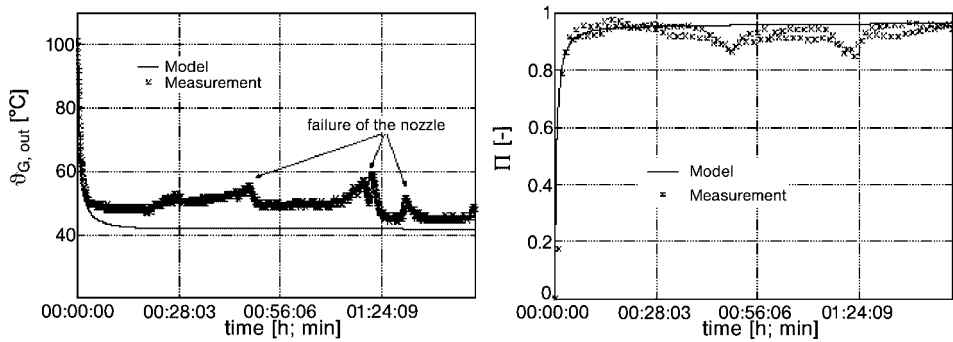


Fig. 16.40. Progression of gas outlet temperature and of conversion over time, experiment V-14.

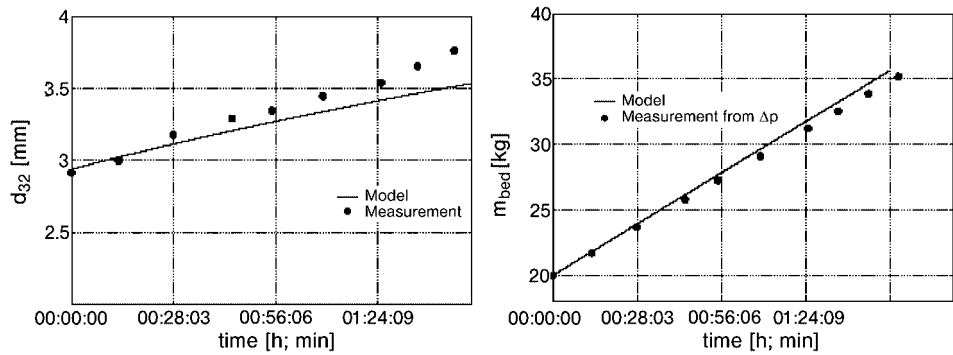


Fig. 16.41. Progression of Sauter diameter and bed mass over time, experiment V-14 (simulation: $R_A = 0.075 \text{ kg m}^{-2} \text{ h}^{-1}$, $k_{OS} = 0 \%$, $k_{growth} = 100 \%$, $k_{sep} = 80 \%$).

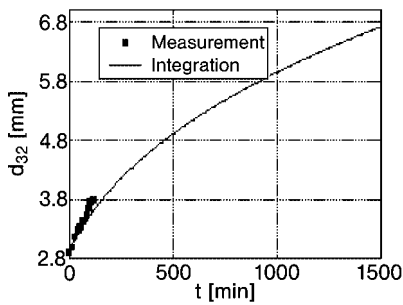


Fig. 16.42. Progression of the Sauter diameter over time – measurement versus analytical solution, experiment V-14.

Table 16.18. Solid mass balance, experiment V-14.

<i>Fed solid</i>	
Hold-up:	20 kg
Injection rate I, duration: 1.85 h	16.16 kg
Sum:	36.16 kg
<i>Discharged solid</i>	
Bed mass (end) + samples:	34.04 kg
Cyclone (end):	0.88 kg
Sum:	34.92 kg

Table 16.19. Parameters of experiment V-15.

Bed material (coated glass spheres): $d_{32} = 0.003756 \text{ m}$, $\rho_P = 2470 \text{ kg m}^{-3}$, $m_{\text{FB}} = 20 \text{ kg}$			
Parameter			
ϑ_G^{in}	$101.167 \pm 0.036 \text{ }^{\circ}\text{C}$		
ϑ_E	$22 \text{ }^{\circ}\text{C}$		
φ	68%		
\dot{m}_G	$0.639 \pm 0.0006 \text{ kg s}^{-1}$		
$c_{\text{SO}_2}^{\text{in}}$	$316.37 \pm 8.6 \text{ mg Nm}^{-3}$		
ϑ_L^{in}	$16.3 \pm 0.48 \text{ }^{\circ}\text{C}$		
x_{binder}	$1.5 \text{ mass-}\%$		
Variation			
No.	Ca/S ratio	\dot{m}_{susp}	composition
Injection rate I	21.25	$0.0167 \pm 7.1 \times 10^{-4} \text{ kg s}^{-1}$	$\frac{24 \text{ kg}_{\text{Ca(OH)}_2}}{80 \text{ kg}_{\text{H}_2\text{O}}}$

The growth rate tends to infinity over a very long process time due to permanent particle discharge and a decrease in the number of particles. The boundary limitation is a decrease of the particle surface near to zero. This is the worst case where fluidization is not possible.

Figure 16.48 presents a comparison of the calculation of bed mass under use of pressure loss and of the Sauter diameter. Although both progressions showed the same tendency, the constant reduction of the particles justified their elutriation and the excessive amount of particles discharged by a industrial vacuum cleaner during the experiments. The total mass balance is listed in Tab. 16.20.

Validation of the experiment with dust recycle and with external seeds

Experiment V-15 shows that seeds are necessary for a continuous process. Thus, experiment V-16 describes a continuous experiment with larger monodisperse glass spheres as hold-up, and with smaller monodisperse glass spheres as external seeds (Fig. 16.49), together with recirculation of the dust. The mass flow of the seeds influences the duration until steady state is attained, whilst the size of the seeds influences the particle size distribution of the product [30].

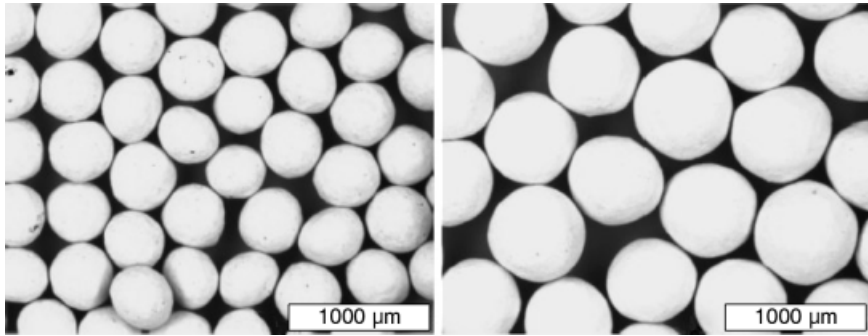


Fig. 16.43. Illustration of hold-up (left) and product (right), experiment V-15.

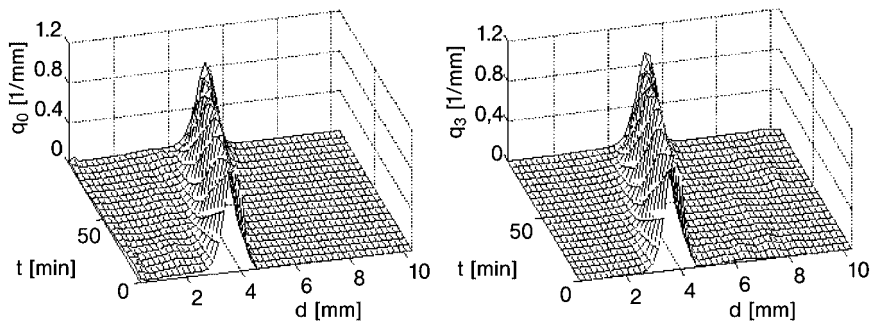


Fig. 16.44. Measured number and mass density distribution, experiment V-15.

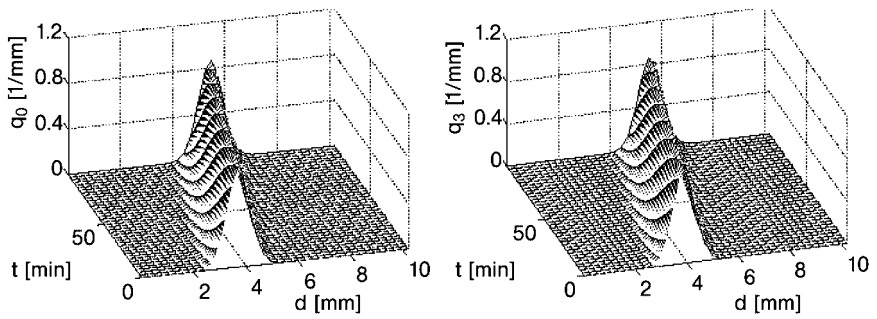


Fig. 16.45. Simulated number and mass density distribution, experiment V-15.

Heinrich [30] reported that a rapid achievement of steady state depends on complete substitution of the hold-up particles by external seeds when the hold-up and seed particles are of the same size, and very small. Otherwise, the unsteady start-up phase is of much longer duration and the particle size distribution of the product is wider.

A high seed mass flow of 4 kg h⁻¹ in relation to a hold-up of 20 kg used to reduce the unsteady start-up phase is shown in Tab. 16.21.

The time-dependent number and mass density distribution shown in Figs. 16.51 and 16.52 is wide, and illustrates the influence of the seeds. The agreement between measurement and simulation is good. The non-classifying discharge results in a bimodal distribution, and the local maximum at larger particle diameters in the mass distribution is characterized by granules of the hold-up, while the left side of the size distribution is dominated by the added external seeds. There is a large number of seeds in the number distribution. Steady state was not reached during the

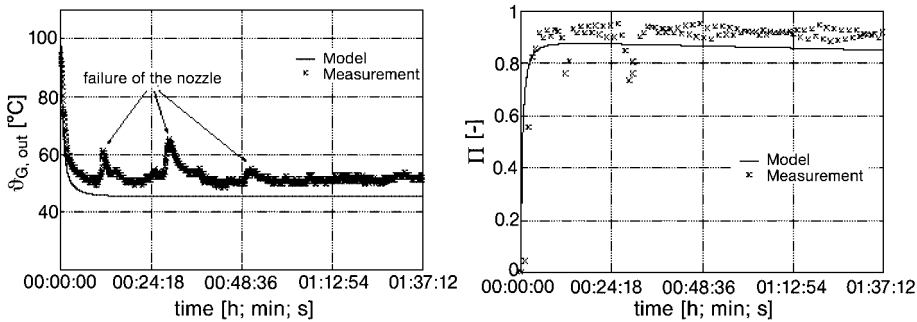


Fig. 16.46. Progression of gas outlet temperature and of conversion over time, experiment V-15.

Table 16.20. Solid mass balance, experiment V-15.

<i>Fed solid</i>	
Hold-up:	20 kg
Injection rate I, duration: 1.58 h	21.95 kg
Sum:	41.95 kg
<i>Discharged solid</i>	
Bed mass (end) + samples:	15.6 kg
Cyclone (end):	4.1 kg
Sample 1 (13 min):	3 kg
Sample 2 (30 min):	3.1 kg
Sample 3 (43 min):	3.2 kg
Sample 4 (59 min):	3.53 kg
Sample 5 (73 min):	3.4 kg
Sample 6 (84 min):	6.67 kg
Sum:	39.6 kg

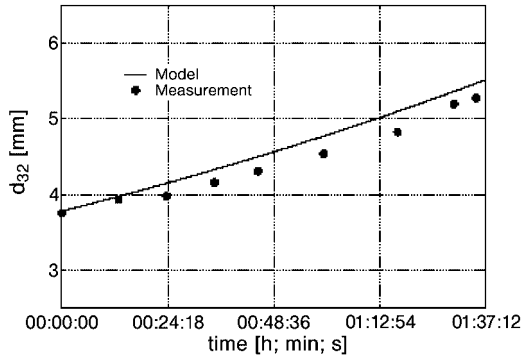


Fig. 16.47. Progression of the Sauter diameter over time, experiment V-15.

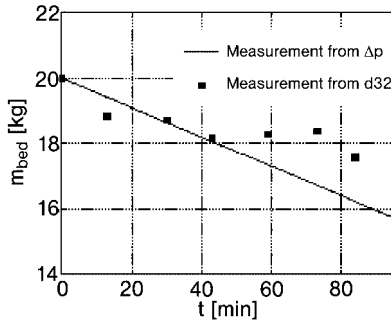


Fig. 16.48. Progression of the bed mass over time, experiment V-15.

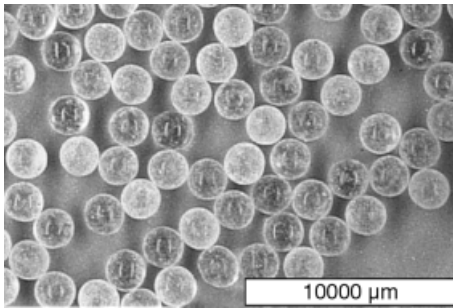


Fig. 16.49. Illustration of external seeds (inert glass spheres, $d_{32} = 1.655$ mm), experiment V-16.

Table 16.21. Parameters of experiment V-16.

Bed material (coated glass spheres): $d_{32} = 0.003297$ m, $\rho_P = 2470$ kg m ⁻³ , $m_{FB} = 20$ kg			
Parameter			
ϑ_G^{in}	101.476 ± 0.021 °C		
ϑ_E	21 °C		
φ	74 %		
\dot{m}_G	0.436 ± 0.0003 kg s ⁻¹		
$C_{\text{SO}_2}^{\text{in}}$	381.03 ± 9.58 mg Nm ⁻³		
ϑ_L^{in}	13.3 ± 0.48 °C		
x_{binder}	1.5 mass-%		
\dot{m}_{seeds}	4 kg h ⁻¹		
$d_{32,\text{seeds}}$	0.001655 m		
Variation			
No.	Ca/S ratio	\dot{m}_{susp}	composition
Injection rate I	21.09	$0.0136 \pm 2 \times 10^{-4}$ kg s ⁻¹	$\frac{42 \text{ kg}_{\text{Ca(OH)}_2}}{140 \text{ kg}_{\text{H}_2\text{O}}}$

experiment because the hold-up was not fully discharged after 200 min. Figure 16.50 confirms that the product still consists of particles of different sizes.

The progression of measurements in Figs. 16.53 and 16.54 shows the feasibility of the continuous process at high conversion.

The total mass balance is summarized in Tab. 16.22.

16.3.4

Comparison between Measurement and Simulation

In this section, we are concerned with gas outlet temperatures and conversions of all reactive absorption measurements. Figures 16.55 and 16.56 show that both the gas outlet temperatures and conversions can be approximated by the proposed model.

It is clear from Fig. 16.57 that the conversions can be realized up to 90 % for small *NTU* of 3 in a liquid-sprayed fluidized bed. It also shows that the assumption of ideal plug flow of gas (PFTR) is more appropriate than the assumption of ideal mixing of the gas (CSTR).

16.3.5

Simplified Stationary Balancing

The increasing efficiency of computational technology, together with associated possibilities of solving complicated differential equations or set of equations, leads to ever-more complex models. Thus, for the practicing engineer the most up-to-date realizations often remain inaccessible. For this reason, in the following sections the

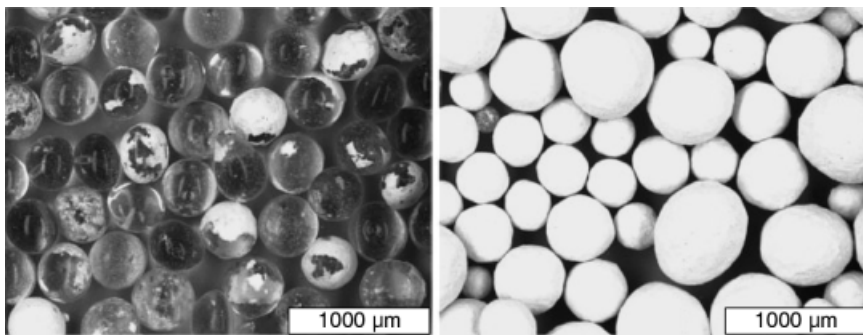


Fig. 16.50. Illustration of partially coated glass spheres as hold-up (left) and calcium hydroxide-coated glass spheres as product (right), experiment V-16.

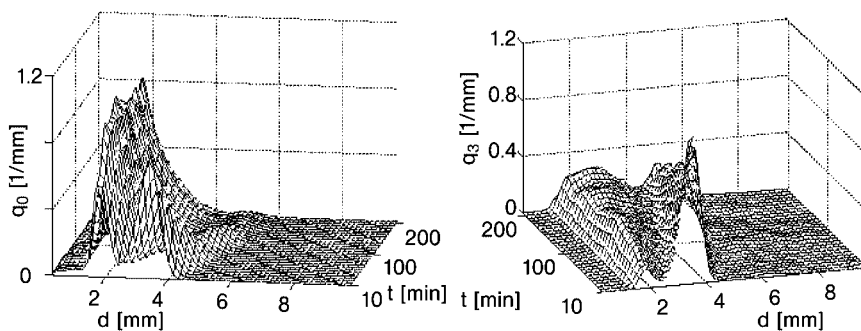


Fig. 16.51. Measured number and mass density distribution, experiment V-16.

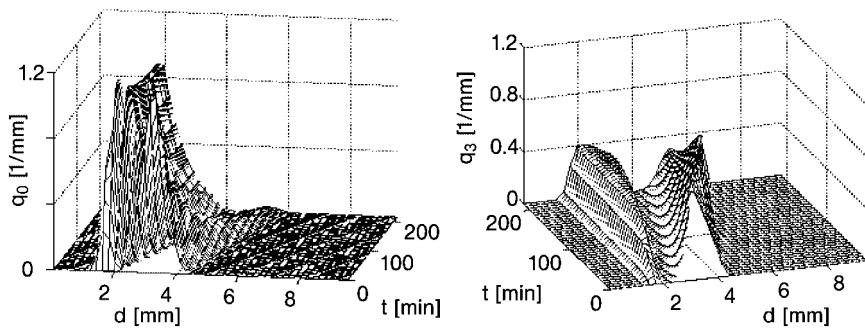


Fig. 16.52. Simulated number and mass density distribution, experiment V-16.

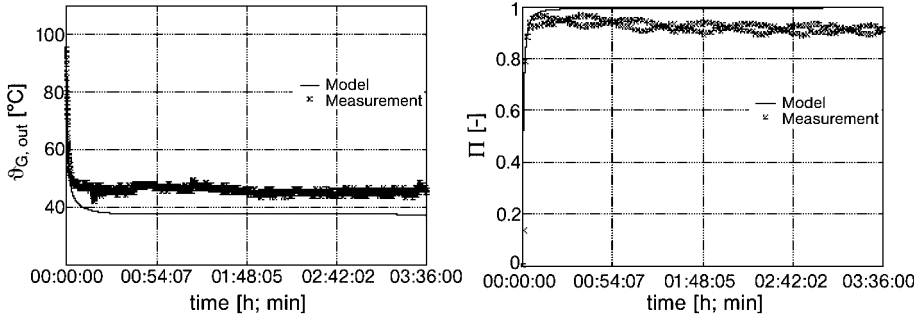


Fig. 16.53. Progression of gas outlet temperature and of conversion over time, experiment V-16.

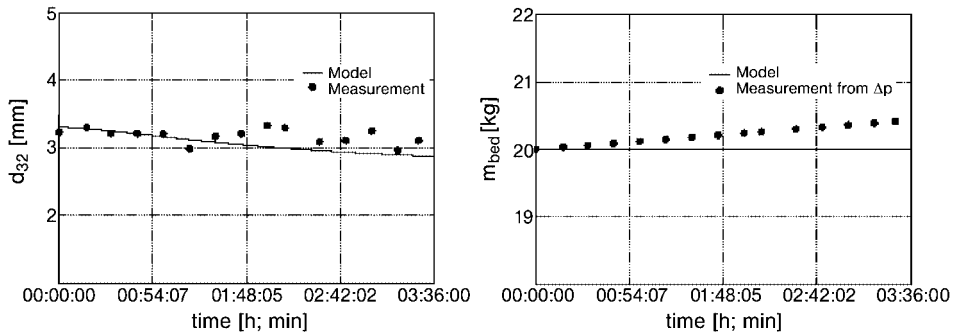


Fig. 16.54. Progression of Sauter diameter and bed mass over time, experiment V-16.

equations are arranged for computation of the stationary values for balance quantities such as outlet humidity, outlet temperature and outlet loading of absorption component, and the Sauter diameter of the product. All mass fluxes entering or leaving both the fluidized bed and the bed mass are assumed to be initial parameters. It is possible to use the inverse simulation procedure to calculate initial conditions at given product parameters. The simplified balances are based on the continuous process with non-classifying particle discharge and feeding of external seeds. The following assumptions are added to the assumptions from Section 16.2.1:

- neglect of heat loss over the apparatus wall (adiabatic condition);
- no dust recycling;
- neglect of non-deposited spray drops (overspray), attrition, agglomeration and breakage;
- consideration of a momentary reaction of the sulfur dioxide with the film, which occurs at the wetted surface;
- a limitation of the conversion of the sulfur dioxide is evoked by the gas phase mass transfer and the mass transfer surface;
- neglect of the water content of the product and of the seeds; and
- the product temperature is equal to the gas outlet temperature.

Table 16.22. Solid mass balance, experiment V-16.

<i>Fed solid</i>	
Hold-up:	20 kg
Injection rate I, duration: 3.7 h	41.8 kg
Seeds:	14 kg
Sum:	75.8 kg
<i>Discharged solid</i>	
Bed mass (end) + samples:	25.1 kg
Cyclone (end):	4 kg
Sample 1 (19 min):	3.5 kg
Sample 2 (33 min):	3.5 kg
Sample 3 (50 min):	3.5 kg
Sample 4 (65 min):	3.5 kg
Sample 5 (79 min):	3.5 kg
Sample 6 (94 min):	3.53 kg
Sample 7 (110 min):	3.27 kg
Sample 8 (125 min):	2.75 kg
Sample 9 (139 min):	3 kg
Sample 10 (154 min):	1.87 kg
Sample 11 (170 min):	3 kg
Sample 12 (185 min):	2.85 kg
Sample 13 (199 min):	3 kg
Sample 14 (215 min):	2.64 kg
Sum:	72.51 kg

The amount of calcium hydroxide required can be calculated at a given gas mass flow, sulfur dioxide concentration and calcium/sulfur ratio:

$$\dot{m}_{\text{Ca(OH)}_2} = \lambda^* \frac{M_{\text{Ca(OH)}_2}}{M_{\text{SO}_2}} c_{\text{SO}_2} \dot{m}_G \frac{\tilde{R}T^0}{P^0 M_L} \quad (98)$$

The stoichiometric ratio λ^* should be minimal 1 for a complete conversion. It is possible to determine the diameter growth of the seeds with the mass flow and the solid content of the suspension and with the average residence time. The residence time is the ratio of the number of bed particles to the seeds flux

$$t_{\text{res}} = \frac{N}{\dot{N}_{\text{seeds}}} \quad (99)$$

The seeds flux can be estimated by seeds mass flow, diameter of the seeds and particle density. By integration of Eq. (95)

$$\int_{d_{\text{seeds}}}^{d_{32}} d_{32}^2 dd_{32} = \frac{2\dot{m}_{\text{solid}}}{\rho_{\text{solid}} \pi N} \int_{t=0}^{t_{\text{res}}} t dt \quad (100)$$

over residence time with the assumption of a constant bed surface (stationary condition) results in the Sauter diameter of the bed

$$d_{32} = d_{\text{seeds}} + \frac{6\dot{m}_{\text{solid}}}{\rho_{\text{solid}}\pi d_{32}^2 N} t_{\text{res}} \quad (101)$$

The gas outlet humidity is described by the total water balance

$$Y_{\text{H}_2\text{O}}^{\text{out}} = Y_{\text{H}_2\text{O}}^{\text{in}} + \frac{\dot{m}_{\text{H}_2\text{O}}}{\dot{m}_{\text{dryA}}} \quad (102)$$

With d_{32} and $Y_{\text{H}_2\text{O}}^{\text{out}}$, the average degree of wetting is approximated by Eq. (103)

$$\phi = \frac{\dot{m}_{\text{dryA}}}{\beta_{\text{H}_2\text{O}}^G \pi d_{32}^2 N \rho_{\text{dryA}}} \ln \left(\frac{Y_{\text{H}_2\text{O}}^{\text{out}} - Y_{\text{H}_2\text{O}}^{\text{sat}}}{Y_{\text{H}_2\text{O}}^{\text{in}} - Y_{\text{H}_2\text{O}}^{\text{sat}}} \right) \quad (103)$$

The mass transfer coefficient $\beta_{\text{H}_2\text{O}}^G$ is calculated accordingly to Gnielinski [25] under the assumption $Sh_{G,P} \approx Sh_{\text{single particle}}$ [66]. The isenthalpic saturation humidity $Y_{\text{H}_2\text{O}}^{\text{sat}}$ is related to the inlet condition of the gas.

The sulfur dioxide outlet loading of the dry air is given by Eq. (104)

$$Y_{\text{SO}_2}^{\text{out}} = Y_{\text{SO}_2}^{\text{in}} \exp \left(- \frac{\beta_{\text{H}_2\text{O}}^G \pi d_{32}^2 N \phi \rho_{\text{dryA}}}{\dot{m}_{\text{dryA}}} \right) \quad (104)$$

The energy balance results to the gas outlet humidity

$$\begin{aligned} \vartheta_G^{\text{out}} = & \frac{1}{\dot{m}_{\text{dryA}} \left(c_{\text{P,dryA}} + c_{\text{P,H}_2\text{O}}^{\text{vap}} Y_{\text{H}_2\text{O}}^{\text{out}} + c_{\text{P,SO}_2} Y_{\text{SO}_2}^{\text{out}} \right) + \dot{m}_{\text{prod}} c_{\text{P,solid}}} \times \\ & \times \left\{ \dot{m}_{\text{dryA}} \left[c_{\text{P,dryA}} \vartheta_G^{\text{in}} + Y_{\text{H}_2\text{O}}^{\text{in}} \left(c_{\text{P,H}_2\text{O}}^{\text{vap}} \vartheta_G^{\text{in}} + r_0 \right) + Y_{\text{SO}_2}^{\text{in}} c_{\text{P,SO}_2} \vartheta_G^{\text{in}} \right] + \right. \\ & \left. + \dot{m}_{\text{susp}} c_{\text{P,susp}} \vartheta_{\text{susp}}^{\text{in}} + \dot{m}_{\text{seeds}} c_{\text{P,solid}} \vartheta_{\text{seeds}}^{\text{in}} - \dot{m}_{\text{dryA}} Y_{\text{H}_2\text{O}}^{\text{out}} r_0 \right\} . \end{aligned} \quad (105)$$

16.4

Conclusions

In the present studies, the possibility of realizing absorption processes with reactive conversion of the absorbed gas component in liquid-sprayed fluidized beds is investigated. The goal of this new technology is the production of a free-floating product and a simultaneous high conversion of the absorbed gas component. The main subject of these studies is the experimental investigation of reactive absorption and

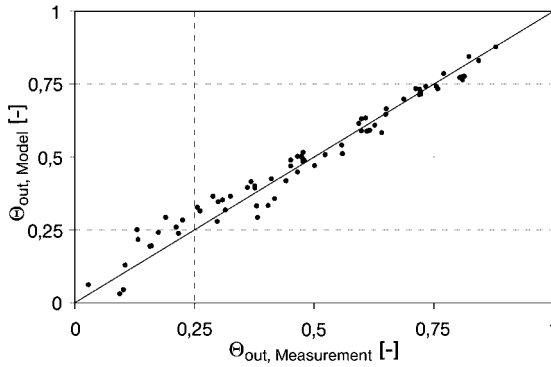


Fig. 16.55. Comparison of the measured and simulated gas outlet temperatures.

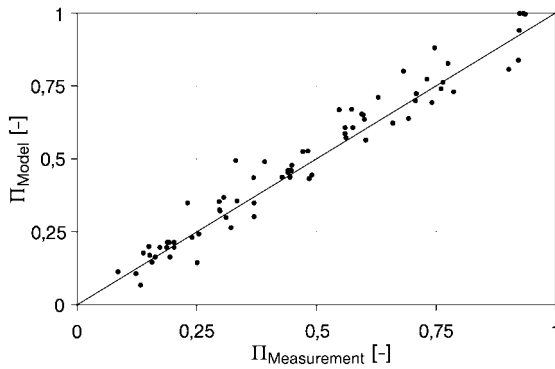


Fig. 16.56. Comparison of measured and simulated sulfur dioxide conversions.

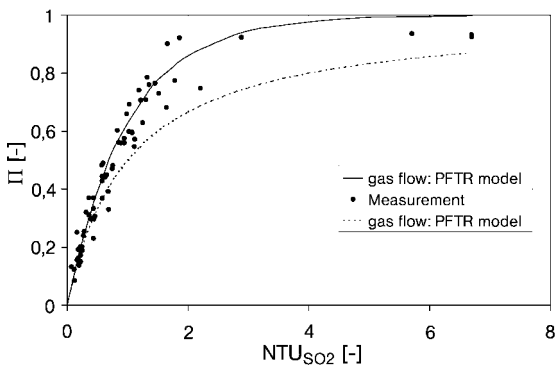


Fig. 16.57. Comparison of measured and simulated sulfur dioxide conversions in dependence of NTU .

granulation, as well as the development of a model to calculate conversion, gas outlet temperature and particle size distribution.

A mixture of humid air and sulfur dioxide forms the model gas for these experiments, as in today's world the removal of sulfur dioxide from exhaust gases is an important gas cleaning process. Calcium hydroxide suspension was injected as a reactant, and the experimental investigations have been subdivided into two parts.

In the first part, the influence of process parameters is investigated. Variation of the injection rate of a suspension shows a substantial influence on the obtained conversion of sulfur dioxide. This is attributed to the mass transfer surfaces produced within the fluidized bed, caused by variations in the liquid injection rate. A high mass flux of sprayed suspension leads to larger mass transfer surfaces and thus, with existing calcium hydroxide, to improved conversions of sulfur dioxide. The increase in suspension injection rate is limited by the receptiveness on solvent (water), and thus by the saturation of gas. An opposite mechanism to prevent agglomeration is a uniform liquid injection, with larger or more heavy particles resp. a higher mass transfer surface (a large number of particles).

Investigations into the relationship between calcium and sulfur have shown that the minimum calcium hydroxide supply is determined by the desired conversion. This seems to be fluidized bed-specific, because investigations with spray absorption dryers have demonstrated clear dependence on the stoichiometric ratio. The conversion increases strongly with increasing reactant in the suspension, the reason being the decreased liquid phase mass transport.

If sufficient calcium hydroxide is present in the spraying drop, then the diffusion of sulfur dioxide is small. In liquid-sprayed fluidized beds the drops or films on the particles are under permanent stresses, and particle-particle impacts lead to constant destruction of the film surface. Thus, no converted calcium hydroxide reaches the film surface to perform the reaction for disposal, and consequently a strongly over-stoichiometric process is not necessary.

The results of investigations into changes in gas inlet temperature show that the influence on sulfur dioxide conversion of the driving force for the drying process can be reduced. An increase in gas inlet temperature leads to a higher evaporation and thus to a lower liquid mass, as well as to a decreased mass transfer surface. The conversion of sulfur dioxide is then reduced. The decrease in solubility of sulfur dioxide at high film temperatures caused by high gas temperatures is not important. From an economic viewpoint, a gas at low temperature is preferred because a lesser amount of liquid is required for equal conversion in comparison to high temperatures. This lower mass flows reduce the consumption of water, of pressurized air for atomization, and of pump/fan power.

For fluidized beds, one essential operating parameter is that of gas throughput; this is necessary for fluidization of the bed material, and depends on the diameter and density of the particles and on the density and viscosity of the gas. These studies highlight the fact that sulfur dioxide conversion is decreased at increased gas flow rate, and thus with higher energy input. As a result, a more rapid drying of the liquid contained in the bed occurs with a coupled decrease in the mass transfer surface.

The average particle diameter which is growing during granulation and agglomeration has no effect on the conversion of sulfur dioxide. An increase in particle diameter leads to higher *Re*-numbers, and thus to an enhanced mass transfer of sulfur dioxide. However, the opposite phenomenon is that the increased mass transfer of the evaporation reduces the mass transfer surface. In addition, these experimental studies illustrate that the liquid-sprayed fluidized bed can be used as a reactive absorber.

The second part of these studies is concerned with the experimental feasibility of a desired high conversion with simultaneous granulation of the reaction product and non-converted raw material due to drying of the suspension and accumulation on these particles in both batch and continuous modes of operation. The dust from attrition and overspray can either be deposited onto the particles or used as internal seeds, while the granulated products are free of dust and easily dosable. Cyclic cleaning of the nozzle leads to optimal operation.

In order to validate these experiments, a simplified model was developed which incorporates the partial mechanisms of the micro-processes.

Symbols and Abbreviations

A	–	activity
A	m	average ion diameter
A	m ²	surface area
A	–	Debye–Hückel constant
A _Φ	–	osmotic coefficient
B	–	Debye–Hückel constant
C	mg Nm ⁻³	concentration
C _P	J kg K ⁻¹	specific heat capacity
\bar{c}_p	J mol K ⁻¹	molar heat capacity
D	m	diameter
D ₃₂	m	Sauter diameter
D	m ² s ⁻¹	diffusion coefficient
E	–	Euler number [= 2.71828 × 10 ⁻¹⁹]
F	–	fugacity
f _α	–	heat transport ratio
g	m s ⁻²	gravity
g	J mol ⁻¹	molar Gibbs energy
G	J	free enthalpy (Gibbs energy)
h	J mol ⁻¹	molar enthalpy
H	J	enthalpy
\dot{H}	W	enthalpy flux
H	m	height
H	Bar	Henry coefficient
H ^m	bar kg mol ⁻¹	Henry coefficient related to molality
I	Mol kg ⁻¹	ionic strength

K	—	equilibrium constant
k_{growth}	—	efficiency of growth
k_{OS}	—	efficiency of overspray
k_{sep}	—	separation efficiency
l	m	length, distance
m	kg	mass
\bar{m}	mol kg^{-1}	molality
\dot{m}	kg s^{-1}	mass flux
M	kg mol^{-1}	molar mass
n	mol	mol quantity
\dot{n}	mol s^{-1}	particle flux
N	—	number
\dot{N}	s^{-1}	number flux
p	Bar	partial pressure
P	Bar	pressure
P_{oy}	—	poynnting factor
P_{T}	—	impact probability
P_{Φ}	—	impact probability particle-film
P_{Z}	—	destruction probability
q_0	mm^{-1}	number density distribution
q_3	kg (kg mm)^{-1}	mass density distribution
\dot{Q}	W	heat flux
r	m	radius
\bar{r}_0	J kmol^{-1}	molar evaporation enthalpy
R	J (kg K)^{-1}	specific gas constant
\bar{R}	J (mol K)^{-1}	universal gas constant
R_{att}	$\text{kg m}^{-2} \cdot \text{s}$	attrition coefficient
St	s	time
T	K	temperature
v	$\text{m}^3 \text{mol}^{-1}$	molar volume
V	m^3	volume
w	m s^{-1}	velocity
x	—	mass content in the liquid
\bar{x}	—	mole content in the liquid
X	—	conversion
y	—	mass content in the gas
\bar{y}	—	mole content in the gas
\bar{Y}	—	mole loading
$\bar{\bar{Y}}$	—	average mole loading
z	—	valence
Z	m	height dependent coordinate
\bar{z}	—	mole content in the solid

Greek letters

α	$\text{W (m}^2 \text{ K)}^{-1}$	heat transfer coefficient
β	m s^{-1}	mass transfer coefficient
γ	–	activity coefficient
Δ	m	thickness
$\Delta \tilde{h}_r$	J mol^{-1}	reaction enthalpy
ε	–	relative porosity of the fluidized bed
Θ	–	normalized temperature
ϑ	$^{\circ}\text{C}$	temperature
κ	–	parameter at Debye–Hückel
λ^*	–	stoichiometric ratio Ca/S
μ	J mol^{-1}	chemical potential
ν	–	stoichiometric ratio
ξ	$\sqrt{\text{kg/kmol}}$	parameter in Pitzer equation (86) [= 14.9]
ξ	mol	extent of reaction
Π	–	absorption factor, conversion
ρ	kg m^{-3}	density
Φ	–	fugacity coefficient
Φ	–	degree of wetting
Ω	–	normalized mass flux

Subscripts

A	air
App	apparatus
Aq	molecular dissolved
Bed	fluidized bed
E	environment
Film	liquid film
G	gas
Out	at outlet
P	particle
Req	reaction equilibrium
S	sulfur
Susp	suspension
Tot	total
Vap	vapor
W	wall

Superscripts

Aq	molecular dissolved
g, G	gas
Gr	granulate
IddS	ideal diluted solution
iddS*	hypothetic ideal diluted solution
IG	ideal gas
In	at inlet
l, L	liquid
Lcomp	liquid component
M	related to molality
PG	particle-gas
S	solid
S	sink
Sat	saturation
So	source
0	standard point

References

1. A. A. Adetayo, B. J. Ennis, Unifying approach to modeling granule coalescence mechanisms, *AIChE J.*, **1997**, 43 (4), 927–934.
2. A. A. Adetayo, J. D. Litster, S. E. Pratsinis, et al., Population balance modeling of drum granulation of materials with wide size distribution, *Powder Technol.*, **1995**, 82, 37–49.
3. M. Banks, M. E. Aulton, Fluidised-bed granulation: A chronology, *Drug Dev. Indust. Pharm.*, **1991**, 17 (11), S1437–S1463.
4. H. D. Baehr, Thermodynamik, 8. Auflage, Springer-Verlag, Berlin-Heidelberg-New York, 1994.
5. R.-D. Becher, Untersuchungen der Agglomeration von Partikeln bei der Wirbelschicht-Sprühgranulation, VDI Fortschritt-Berichte, Reihe 3, Nr. 500, VDI Verlag, Düsseldorf, 1997.
6. W. A. Benesch, 850 C – Theorie und Praxis der Wirbelschichtfeuerung, VDI Berichte, Nr. 1492 (1999), S145–S152.
7. J. Beranek, K. Rose, G. Winterstein, Grundlagen der Wirbelschichttechnik, VEB Deutscher Verlag für Grundstoffindustrie, Leipzig, 1975.
8. B. Bertsch-Frank, H. Jakob, Natriumpercarbonat-Wirbelschichtgranulat und Verfahren zu seiner Herstellung, Deutsches Patent 10048514A1, offengelegt am 11. April 2002, Patentinhaber: Degussa AG, 40474 Düsseldorf.
9. R. Blumhofer, Untersuchungen zur Absorption von Stickoxiden in wässrigen Lösungen von Natriumsulfit und Übergangsmetall-Komplexen, Dissertation, Universität Karlsruhe, 1984.
10. M. Brinkmann, Wechselwirkung von Hydrodynamik, Stofftransport und Chemischer Reaktion im G-L-Strahldüsen-schlaufenreaktor. VDI Fortschritt-Berichte, Reihe 3, Nr. 371, VDI Verlag, Düsseldorf, 1994.
11. Bundesministerium für Ernährung, Landwirtschaft und Forsten.
12. C. S. Chang, G. T. Rochelle, SO₂ absorption into NaOH and Na₂SO₃ aqueous solutions, *Ind. Eng. Chem. Fundam.*, **1985**, 24 (1), 7–11.

13. C. S. Chang, G. T. Rochelle, Mass transfer enhanced by equilibrium reactions, *Ind. Eng. Chem. Fundam.*, **1982**, 21 (4), 379–385.
14. C. S. Chang, G. T. Rochelle, Effect of organic acid additives on SO₂ absorption into CaO/CaCO₃ slurries, *AIChE J.* **1982**, 28 (2), 261–266.
15. C. S. Chang, G. T. Rochelle, SO₂-absorption into aqueous solutions, *AIChE J.*, **1981**, 27 (2), 292–298.
16. P. V. Danckwerts, Gas absorption with instantaneous reaction, *Chem. Eng. Sci.*, **1968**, 23, 1045–1051.
17. S. R. Dantuluri, W. T. Davis, R. M. Counce, et al., Mathematical model of sulfur dioxide absorption into a calcium hydroxide slurry in a spray dryer, *Separation Sci. Technol.*, **1990**, 25, 1843–1855.
18. D. Eden, Simulation von Rauchgassprühwäschern, VDI Fortschritt-Berichte Reihe 3, Nr. 536, VDI Verlag, Düsseldorf, 1998.
19. B. J. Ennis, A micro-level based characterization of granulation phenomena, *Powder Technol.*, **1991**, 65, 257–272.
20. B. J. Ennis, J. Li, G. Tardos, et al., The influence of viscosity on the strength of an axially strained pendular liquid bridge, *Chem. Eng. Sci.*, **1990**, 45 (10), 3071–3088.
21. E. D. Ermenc, Designing a fluidized adsorber, *Chem. Eng.*, **1961**, 29, S87–S94.
22. M. Fisz, Wahrscheinlichkeitsrechnung und mathematische Statistik, VEB Deutscher Verlag der Wissenschaften, Berlin, 1978.
23. J. L. Getler, H. L. Shelton, D. A. Furlong, Modelling the spray absorption process for SO₂-removal, *J. Air Pollution Control Assoc.*, **1979**, 29 (12), 1270–1274.
24. J. Grmehling, B. Kolbe, Thermodynamik, VCH Verlagsgesellschaft mbH, Weinheim-New York-Basel-Cambridge, 1992.
25. V. Gnielinski, Wärme- und Stoffübertragung in Festbetten, *Chem.-Ing.-Tech.*, **1980**, 52, 228–236.
26. W. D. Gorosko, R. B. Rozenbaum, O. M. Todes, *Neft i Gaz*, **1958**, 1, 125.
27. H. Groenewold, E. Tsotsas, Predicting apparent Sherwood numbers for fluidized beds, Proceedings of the 11th International Drying Symposium (IDS '98), Halkidiki, Greece August 19–22. Vol. A (1998), pp. 192–199.
28. S. Heinrich, J. Blumschein, M. Henneberg, et al., Study of dynamic multi-dimensional temperature and concentration distributions in liquid sprayed fluidized beds, *Chem. Eng. Sci.*, **2003**, 58, 5135–5160.
29. S. Heinrich, M. Ihlow, M. Henneberg, et al., An optimization model of the operating costs of a fluidized bed-steam drying plant, *Can. J. Chem. Eng.*, **2002**, 80, 326–333.
30. S. Heinrich, Modellierung des Wärme- und Stoffübergangs sowie der Partikelpopulationen bei der Wirbelschicht-Sprühgranulation, VDI-Fortschrittbericht Nr. 675, Reihe 3, VDI-Verlag, Düsseldorf, 2001.
31. S. Heinrich, J. Blumschein, M. Ihlow, L. Mörl, Unsteady multi-dimensional liquid distribution in fluidized bed spray granulation: numerical solution and optimization aspects, Proceedings, 3rd European Congress of Chemical Engineering ECCE-3, Nuremberg, June 26–28, 2001, *Chem.-Ing.-Tech.*, **2001**, 73 6, S651–S652, Topic 7: Computational.
32. S. Heinrich, L. Mörl, G. Krüger, Modelling and experimental verification of the heat and mass transfer in fluidized bed spray-granulation, Proceedings, 2nd European Congress of Chemical Engineering ECCE-2, Montpellier, October 5–7, 1999, No. 67, vol. 13-1999, Heat, Mass and Momentum Transfer (II), pp. 95–104.
33. S. Heinrich, G. Krüger, L. Mörl, Modelling of the batch treatment of wet granular solids with superheated

- steam in fluidized beds, *Chem. Eng. Proc.*, **1999**, 38 (2), 131–142.
34. S. Heinrich, L. Mörl, Fluidized bed spray granulation-A new model for the description of particle wetting and of temperature and concentration distribution, *Chem. Eng. Proc.*, **1999**, 38 (4-6), 635–663.
 35. S. Heinrich, L. Mörl, Description of the temperature, humidity and concentration distribution in gas-liquid-solid fluidized beds, *Chem. Eng. Technol.*, **1999**, 22 (2), 118–122.
 36. S. Heinrich, L. Mörl, Temperatur- und Konzentrationsverteilung der Wirbelschicht-Sprühgranulation, *Chem.-Ing.-Tech.*, **1998**, 70 (8), S976–S979.
 37. S. Heinrich, L. Mörl, Heat- and mass transfer in liquid-sprayed gas/solid fluidized beds, Proceedings, 11th International Drying Symposium (IDS '98), Halkidiki, Greece, August 19–22, 1998, Vol. A, pp. 414–421.
 38. M. Henneberg, Untersuchung des Flüssigkeitseintrages auf die Temperaturverteilung in Gas/Feststoff-Wirbelschichten, Dissertation Otto-von-Guericke-Universität Magdeburg, 2004.
 39. M. Henneberg, A. Katzarov, S. Heinrich, et al., Messung und Berechnung von dreidimensionalen Temperatur- und Konzentrationsfeldern in einer großtechnischen flüssigkeitsbedüsten Wirbelschicht WSA DN 1500, Proceedings of the Energy Forum 2002, Varna, Bulgaria, June 14–17, 2002, pp. 154–172.
 40. F. F. Hill, Schwefeldioxidabscheidung aus Rauchgasen mit der Sprühabsorptionstrocknung, VDI Fortschritt-Berichte, Reihe 3, Nr. 535, VDI Verlag, Düsseldorf, 1998.
 41. M. Ihlow, Beitrag zur Absorption in flüssigkeitsbedüsten Wirbelschichten, Dissertation Otto-von-Guericke-Universität Magdeburg, 2003.
 42. M. Ihlow, H. Will, L. Mörl, S. Heinrich, Schwefeldioxidentfernung aus Rauchgasen mittels flüssigkeitsbedüster Gas/Feststoff-Wirbelschichten, *Chemische Technik*, **1999**, 51 5, S276–S282.
 43. S. M. Iveson, J. D. Litster, B. J. Ennis, Fundamental studies of granule consolidation – part 1: Effects of binder content and binder viscosity, *Powder Technol.*, **1996**, 88, 15–20.
 44. Jde: Schwebesichter in der Spanplattenindustrie, *Holz*, **1964**, 11, 27–36.
 45. H. Jakob, W. Heßberger, J. Latisch, et al., Verfahren zur Herstellung von Natriumpercarbonat, Deutsches Patent 10140838A1, offengelegt am 06. März 2003, Patentinhaber: Degussa AG, 40474 Düsseldorf.
 46. M. Kalschmitt, H. Hartmann, Energie aus Biomasse Grundlagen, Techniken und Verfahren, Springer-Verlag, Berlin-Heidelberg-New York, 2001.
 47. H. T. Karlsson, J. Klingspor, Tentative modelling of spray-dry scrubbing of SO₂, *Chem. Eng. Technol.*, **1987**, 10, 104–112.
 48. W. Kast, H. Klan, Wärmeübergang durch freie Konvektion an umströmten Körpern, VDI-Wärmeatlas, 7. Auflage, 1994, Fa1–Fa7.
 49. B. Korischem, Modellierung der Rauchgaswäsche einer Industriemüllverbrennungsanlage, VDI Fortschritt-Berichte, Reihe 3, Nr. 361, VDI Verlag, Düsseldorf, 1994.
 50. B. Korischem, U. Werner, Rauchgaswäsche bei der Industriemüllverbrennung, *VGB Kraftwerkstechnik*, **1994**, 74 (6), 537–542.
 51. R. Krishnamurthy, R. Taylor, A nonequilibrium stage model of multicomponent separation processes (Part I, II), *AIChE J.*, **1985**, 31 (3), 449–465.
 52. J. Krissmann, Komplexe Phasen- und Reaktionsgleichgewichte bei der nassen Rauchgasreinigung, VDI Fortschritt-Berichte, Reihe 3, Nr. 598, VDI Verlag, Düsseldorf, 1999.
 53. J. Krissmann, M. A. Siddiqi, K. Lucas, Komplexe Phasen- und Reaktionsgleichgewichte bei der nassen Rauchgasreinigung - Einsatz der UV-spektralphotometrie am Beispiel des SO₂/H₂O-Systems, *Chem. Ing. Tech.*, **1996**, 68 (12), 1598–1602.

54. J. Krissmann, M. A. Siddiqi, K. Lucas, Absorption of sulfur dioxide in dilute aqueous solutions of sulfuric and hydrochloric acid, *Fluid Phase Equilibriums*, **1997**, 141, S221–S233.
55. J. Krissmann, M. A. Siddiqi, K. Lucas, Thermodynamics of SO₂ absorption in aqueous solutions, *Chem. Eng. Technol.*, **1998**, 21, 641–644.
56. J. Krissmann, M. A. Siddiqi, K. Lucas, Thermodynamik der SO₂-Absorption in wässrigen Lösungen, *Chem. Ing. Tech.*, **1997**, 69 (12), 1764–1767.
57. J. Krissmann, M. A. Siddiqi, P. Reters-Gerth, et al., A study of the thermodynamic behaviour of mercury in a wet flue gas cleaning process, *Ind. Eng. Chem. Res.*, **1998**, 37, 3288–3294.
58. W. Lehmann, Zur Auslegung von Gas-Feststoff-Wirbelschichtapparaten speziell in Rinnenform, *Wissenschaftl. Zeitschrift der TH für Chemie Leuna-Merseburg* 11 1969 Heft 4.
59. K. C. Link, E.-U. Schlünder, A new method for the characterization of the wettability of porous solids, *Chem. Eng. Technol.*, **1999**, 19 (5), 432–437.
60. K. Link, Wirbelschichtsprühgranulation: Untersuchungen der Granulatbildung an einer frei schwebenden Einzelpartikel. VDI Fortschritt-Berichte, Reihe 3, Nr. 491, VDI Verlag, Düsseldorf, 1997.
61. M. Luckas, Berechnung und Modellierung komplexer Phasen- und Reaktionsgleichgewichte in wässrigen Elektrolytlösungen, *Chem. Ing. Tech.*, **1996**, 68 (4), 390–398.
62. M. Luckas, K. Lucas, Thermodynamik der nassen Rauchgaswäsche fossilbefeuerter Kraftwerke, *Chem. Ing. Tech.*, **1994**, 66 (10), 1358–1361.
63. M. Luckas, K. Lucas, H. Roth, Computation of Phase and Chemical Equilibriums in Fluid-Gas/Water Systems, *AIChE J.*, **1994**, 40 (11), 1892–1900.
64. E. Machnow, M. Ihlow, M. Henneberg, et al., Fluidized bed steam drying – modelling and experimental studies, *Chem. Eng. Technol.*, **2001**, 24 (9), 884–889.
65. E. Machnow, Modellierung der diskontinuierlichen Wirbelschichttrocknung körniger Güter mit überhitztem Wasserdampf und Heißluft. Dissertation, Universität Magdeburg, 2001.
66. H. Martin, Wärmeübergang in Wirbelschichten, VDI-Wärmeatlas, 7. Auflage 1994, Mf1–Mf8.
67. L. Mörl, Anwendungsmöglichkeiten und Berechnung von Wirbelschichtgranulations-trocknungsanlagen, Dissertation B, TH Magdeburg, 1981.
68. L. Mörl, M. Mittelstraß, J. Sachse, Zum Kugelwachstum bei der Wirbelschicht-trocknung von Suspensionen oder Lösungen, *Chem. Techn.*, **1977**, 29 (10), 540–541.
69. L. Mörl, M. Mittelstraß, J. Sachse, Berechnung der Verteilungsspektren von Feststoffgranulateilchen in Wirbelschichtapparaten mit klassierendem Abzug, *Chem. Techn.*, **1978**, 30 (5), 242–245.
70. G. H. Newton, J. Kramlich, R. Payne, Modelling the SO₂-slurry droplet reaction, *AIChE J.*, **1990**, 36 (12), 1865–1872.
71. G. P. Partridge, W. T. Davis, R. M. Counce, et al., A mechanistically based mathematical model of sulfur dioxide absorption into a calcium hydroxide slurry in a spray dryer, *Chem. Eng. Commun.*, **1990**, 96, 97–112.
72. L. Raible, Untersuchung zur Abscheidung von Stickoxiden und zur Simultanabscheidung von Stickoxiden und Schwefeldioxid in verschiedenen wässrigen Absorbentien unter Einsatz eines Strahldüsenreaktors als Gas/Flüssig-Kontaktapparat. VDI Fortschritt-Berichte, Reihe 3, Nr. 88, VDI Verlag, Düsseldorf, 1984.
73. B. Orlich, H.-F. Kruse, W. Rähse, et al., Tensidgranulate und Verfahren zur Herstellung von Tensidgranulaten, Deutsches Patent 10160319A1, offengelegt am 26. June 2003, Patentinhaber: Henkel KGaA, 40589 Düsseldorf.

74. P. A. Ramachandran, M. M. Sharma, Absorption with fast reaction in a slurry containing sparingly soluble fine particles, *Chem. Eng. Sci.*, **1969**, 24, 1681–1686.
75. J. Rangelova, Abriebsverhalten von Feststoffpartikeln in Wirbelschichten, Dissertation Universität Magdeburg, 2002.
76. P. Reboux, Phenomenes de fluidisation Association de Fluidisation, Paris, 1954.
77. L. Reh, Verbrennung in der Wirbelschicht, *Chem. Ing. Techn.*, **1968**, 40 (11), 509–514.
78. P. N. Rowe, K. T. Claxton, J. B. Lewis, *Transact. Instn. Chem. Engr.*, **1965**, 43, 14.
79. E. Sada, H. Kumazawa, M. A. Butt, Single gas absorption with reaction in a slurry containing fine particles, *Chem. Eng. Sci.*, **1977**, 32, 1165–1170.
80. H.-F. Schneider, Untersuchungen zur Nassabscheidung von Schwefeldioxid. Dissertation, Universität Hannover, 1982.
81. M. Schultes, Absorption of sulfur dioxide with sodium hydroxide solution in packet columns, *Chem. Eng. Technol.*, **1998**, 21, 201–209.
82. M. Schultes, Abgasreinigung, Springer-Verlag, Berlin Heidelberg New York, 1996.
83. M. Schultes, Einfluß der Phasengrenzfläche auf die Stoffübertragung in Füllkörperkolonnen, VDI Fortschritt-Berichte, Reihe 3, Nr. 230, VDI Verlag, Düsseldorf, 1990.
84. M. Schütz, Stand der Rauchgasentschwefelungstechnik, *VGB Kraftwerkstechnik* **1997**, 77, 11.
85. D. Shi, Fluidodynamik und Wärmeübergang in einer zirkulierenden Wirbelschicht, VDI-Fortschritt-Berichte, Reihe 3, Nr. 466, VDI Verlag, Düsseldorf, 1997.
86. P. G. Smith, A. W. Nienow, Particle growth mechanisms in fluidised bed granulation – I. the effect of process variables, *Chem. Eng. Sci.*, **1983**, 38 (8), 1223–1231.
87. K. Sundmacher, Reaktionstechnische Grundlagen der elektrochemischen Absorption mit Gasdiffusionselektroden, VDI Fortschritt-Berichte, Reihe 3, Nr. 564, VDI Verlag, Düsseldorf, 1998.
88. M. Trojosky, L. Mörl, P. Wnukowski, et al., Lufttemperaturmessung in flüssigkeitsbedüsten Gas-Feststoff-Wirbelschichten nichthygroskopischer Partikeln, *Wiss. Z. Techn. Hochsch. Magdeburg*, **1990**, 34 (3), 36–40.
89. M. Trojosky, L. Mörl, Ein mathematisches Modell zur Beschreibung der Temperatur- und Feuchteverläufe in flüssigkeitsbedüsten Gas-Feststoff-Wirbelschichten, *Chem. Techn.*, **1991**, 43 (4), 141–145.
90. M. Trojosky, Modellierung des Stoff- und Wärmetransportes in flüssigkeitsbedüsten Gas/Feststoff-Wirbelschichten, Dissertation, TU Magdeburg, 1991.
91. R. Turton, G. I. Tardos, B. J. Ennis, Fluidized bed coating and granulation, Fluidisation, Solid Handling and Processing, Chapter 7, (W.C. Yang, Ed.) Noyes Publications, Westwood, New Jersey 1999, pp. 331–434.
92. S. Uchida, C. Y. Wen, Rate of gas absorption into a slurry accompanied by instantaneous reaction, *Chem. Eng. Sci.* **1977**, 32, 1277–1281.
93. H. Uhlemann, L. Mörl, Wirbelschicht-Sprühgranulation, Springer-Verlag, Berlin-Heidelberg-New York, 2000.
94. R. Vogel, *Silikattechnik*, **1966**, 17, 173–178.
95. R. Vollheim, Der pneumatische Transport taubförmiger Güter in senkrechten Rohrleitungen in Verbindung mit der Einschleusung durch Wirbelschichten. *Maschinenbautechnik* 16 1967 Heft 5.
96. J. von Velsen, Stoffübergang mit chemischer Reaktion in einer Rührzelle am Beispiel des Abbaus von Phenol und Cyanid durch Ozon, Dissertation, Universität Dortmund, 1977.
97. Ch. von Zabeltitz, Über die Trennung von Körpern verschiedener Dichte

- in einem Fließbett, *VDI-Z.* **1966**, 108 25, S1226.
98. E. Willing, Moderne Verfahren der Mineralölverarbeitung, *Erdöl und Kohle*, **1957**, 10, S20–S23.
99. F. Winkler, Verfahren zum Herstellen von Wasserglas, Patenschrift DE 437 970 1926.
100. C. Y. Yu, Y. K. Xu, X. Z. Wang, Study of fluidized bed spray granulation, *Drying Technology*, **1999**, 17, 1893–1904.
101. J. Zank, Tropfenabscheidung und Granulatwachstum bei der Wirbelschicht-Sprühgranulation, Shaker Verlag, Aachen 2003.
102. J. Zank, M. Kind, E.-U. Schlünder, Particle growth and droplet deposition in fluidised bed granulation, *Powder Technol.*, **2001**, 120, 76–81.

Index

a

absorber 265
 absorption 456
 absorption processes 265
 achiral chromatography 168
 addition reaction 395
 adductive crystallization 339
 adsorptive enhanced reactor 204
 adsorptive reactor 206, 218
 agglomeration 459
 agitated ball mill 418
 annular chromatography reactor
 184, 185
 anode cascade 59
 anode exhaust gas 47, 58, 63, 64
 arheotrope 89, 110, 115, 119,
 126, 137, 144
 Arrhenius equation 197
 Arrhenius' law 54
 asymmetric mode of operation 12
 attainable region 56
 attractor point 58
 attrition kinetics 475
 autothermal reforming (ATR) 29
 axial dispersion coefficient
 195, 196
 azeotrope 88, 92, 98,
 103, 110, 111, 134,
 137, 142, 144–146

b

batch experiment 503
 BEA zeolite 250, 251
 bifurcation analysis 69
 binaphthol separation 168
 biomass gasification 440
 Bodenstein number 331
 Bond working index 411
 Bond's law 410
 brittle fracture 408
 bubble column 269
 1,4-butanediol (1,4-BD) 133, 134–136,
 143–145

Butler-Volmer kinetics 70
 Butler-Volmer reaction kinetics 55

c

calcium hydroxide 461
 calcium/sulfur ratio 488, 522
 canonical coordinates 344
 catalyst activity 233, 234, 258, 260
 catalytic activity 184, 197, 198
 catalytic combustion chamber 47, 53
 catalytic filter 439
 catalytic plate reactor 33
 cathode channel 53
 cathode gas 54
 cathode reaction 47
 cell cascading 58, 61–63
 cell power 55
 centrifugal mill 418
 chemical equilibrium 89, 90, 92, 119,
 123, 130, 277
 chemical equilibrium line 101, 124
 chemical equilibrium surface 96–100,
 102, 134, 138
 chemical fluidized-bed 456
 chemical instability 405
 chromatographic reactor 204
 chromatographic reactors 163
 classification of the gas desulfurization
 process 454
 Claus process 207
 Co/Ni separation 316
 CO₂ absorption 289, 295
 co-current operation 234, 237, 248, 254
 codimension-1-singularity 79
 condensation reaction 395
 constant pattern waves 150, 151, 158
 contactor 385
 continuous distillation 152
 continuous experiment 510
 conversion 233–235, 250,
 252 ff, 360, 361,
 363, 366, 375 ff
 conversion diagram 56

conversion selectivity 378
 corrected molar flow 51, 53
 counter-current operation 234–237,
 244, 248, 254, 262
 coupling of endo- and exothermic
 reactions 13
 coupling reaction 395
 crusher 415
 crystal growth 351, 353, 354
 crystal lattice 351, 352
 crystal nuclei 351, 353

d

Damköhler number 49–51, 55, 90,
 128, 190, 191, 195, 362,
 363, 364, 377, 378
 Deacon process 211
 degradation reaction 395
 degree of wetting 468, 483
 desupersaturation 354
 diesel soot abatement 441
 direct internal reforming (DIR)
 45, 46, 48
 discrete heat sources 19
 disk attrition mill 416
 dislocation density 408
 dispersive waves 150, 152, 158
 displacement desorption 222
 displacement reactions 426
 dissociation and reaction equilibrium
 469
 distributed heat release 18
 distributor 370, 378, 380,
 381, 383, 386
 dosing 359, 379, 384, 386
 droplet distribution 331
 droplet population balance 330
 ductile fracture 408
 dusty gas model 366, 373, 374
 dynamic modeling 293

e

effective diffusion coefficient 278
 efficiency of size-reduction equipment
 422
 electric swing process 221
 electrochemical
 oxidation 45–47
 reduction 47, 55
 electrolyte conductivity 70, 72
 electrolyte solutions 322
 Eley-Rideal mechanism 250

ellipse 93, 95, 140, 142
 enantiomeric excess 354
 enantiomers 168, 353, 355
 enhancement factor 272
 equilibrium constant 363, 364, 371
 equilibrium limitation 233, 250, 256
 equilibrium line 56
 equilibrium stage model 270
 equilibrium theory 149, 188, 189
 ester hydrolysis 166
 esterification 166, 234, 250 ff, 258
 ethanol 153, 175
 eutectic 343
 eutectic carbonate melt 47
 extended Debye-Hückel theory 494
 extent of oxidation reaction 50, 56
 extent of reforming reaction 50, 56
 external reforming 59
 external reforming (ER) 48
 extraction 313
 extractor 369, 370, 376, 379, 386
 extruder 393
 co-kneader 396, 397
 conical counter-rotating 397
 co-rotating 397
 counter-rotating 397
 non-intermeshing 397
 self-wiping 397
 single screw 396, 397
 single-screw 393, 402
 twin-screw 393, 396, 402
 extrusion 401

f

fast pyrolysis 448
 feasibility analysis 87, 127
 feasibility diagram 93, 96, 100, 105
 feasible product 87
 feasible split 106, 108
 film-flow 236, 246, 249, 259
 filter regeneration 441
 filter regeneration curve 445
 filter types 443
 filtration combustion 447
 fixed-bed chromatographic process
 150, 152, 164
 fixed-bed reactor 360, 370, 372, 376 ff
 flameless oxidation (FLOX- burner) 30
 flash cascade 88–89
 flooding behavior 239
 flooding limits 236, 241 ff, 249, 262
 Flory-Huggins model 196, 197

flow pattern 236
 flowsheet simulators 322
 flue gas treatment 437, 438
 catalytic filtration 439
 conventional process 438
 flue-gas desulfurization 454
 fluidized-bed combustion 456
 fluidized-bed dryers 455
 fluidized-bed granulators and
 agglomerators 455
 fluidized-bed plant 479
 fluidized-bed reactor 219
 fluidized-bed spray granulation 453
 folded plate reactor 35
 fuel cell 69
 fuel utilization 50, 55
 functionalization reaction 395

g

galvanostatic operation 78
 gas cleaning 454
 gas recycling 63
 gas-liquid mass transfer 241, 247
 gel effect 399, 405
 graft reaction 395
 granulation 456, 458, 502
 growth kinetics 340, 352
 growth rate 352

h

Hatta number 270, 272
 heat capacity ratio 6
 heat effect in adsorptive reactor 227
 heat integrated processes 4
 heat resistance 401
 heat transfer 401
 heat transfer coefficient 401
 Henry coefficient 190, 191
 high-temperature fuel cell 69
 hodograph space 159
 hold up 242
 hot spot formation 69, 75, 81
 HTU/NTU method 271
 hydraulic diameter 239, 240
 hydrodynamic
 instability 405
 stability 406
 hydrodynamics 328
 hydrogen cyanide synthesis 208
 hyperbola 93, 96, 140, 142
 hypothetical systems 92, 118,
 119, 130
 hysteresis varieties 79

i

impact mill 419
 indirect internal reforming (IIR) 48, 59
 instabilities 402, 403, 405
 instability 69
 chemical 403, 406
 hydrodynamic 403, 405
 thermal 403, 405
 integrated fuel processor (IFP) 33
 integrated heat recovery 13
 interchain copolymer formation 395
 ion exchange 315
 ionic liquids 313
 isola varieties 79
 isomer 343
 isopropyl acetate hydrolysis 103, 104,
 105, 109

j

jet mill 420

k

Kick's law 410
 kinetic arheotrope 127, 133, 134,
 137, 138, 144
 kinetic azeotrope 89, 92, 93, 101,
 134, 137, 145
 kinetic compatibility 368
 kinetics 326
 Knudsen diffusion 129, 134, 142

l

Langmuir isotherm 189, 196
 laser-induced fluorescence (LIF) 326
 latent heat storage 16
 leaching of metal 425
 lever rule 53, 64
 Lewis cell 325
 liquid-liquid 102, 103
 liquid-liquid equilibria (LLE) 321
 liquid-sprayed gas-solid fluidized bed 456
 low order model of a distillation column 175

m

m_2 - m_3 plane 189, 191
 mass transfer 323 ff, 366, 370, 373, 375
 mass transfer coefficient 112, 115-117, 120,
 129-131, 142, 144, 279, 280, 302
 Maxwell-Stefan diffusion 325
 Maxwell-Stefan equation 272
 mean residence time 246, 247
 mechanical activation 424
 mechanical alloying 425

- mechanochemistry 408
 - membrane reactor 359, 364, 366, 368, 382 ff
 - methane steam reforming 36
 - methanol 152, 175
 - micelles 319
 - microemulsion 320
 - migration velocity 183
 - milling intensity 413
 - mixing rule 49, 63
 - mixing rules 52
 - model reduction 174
 - model-based control 174
 - modeling of the granulator coupled with reactive absorption 460
 - modeling of the particle population 475
 - mollier diagram 486
 - molten carbonate fuel cell (MCFC) 45, 46
 - molten electrolyte 70
 - monoliths 248 ff
 - moving-bed chromatographic process 152
 - MSMPR crystallizer 351
 - MTBE 97–100
 - multicomponent mixtures 341
 - multi-component reaction 395
 - multi-component system 341, 357
 - multifunctional reactor with integrated heat recovery 10
 - multiple Jänecke projection 345, 348
 - multiple orthogonal projection 344
- n**
- nitric acid 283
 - nonlinear waves 149
 - normalized heat loss 6
 - nucleation kinetics 340, 352, 354
 - nucleation rate 352, 353
 - number of transfer unit 115, 120, 125
 - number of transfer units 6
- o**
- operation window 234
 - overheating during oxidative coke removal 24
- p**
- packed column 267
 - parabola 93, 141
 - particle size distribution 356
 - pellet microstructuring 223
 - pervaporation 117
 - phase diagram 341, 342, 346, 348
 - high-dimensional 346
 - isobaric 349
 - reactive 344
 - phase plane analysis 74
 - phase splitting 95
 - planetary mill 417
 - plate column 269
 - plug flow tubular reactor 361, 365
 - plug flow tubular reactor (PFTR) 361
 - polycyclic aromatic hydrocarbons 441
 - polymerization 399
 - chain radical 395, 399
 - extrusion 398
 - step 395
 - thermal 393
 - polymerization reactor 393
 - population balance 474
 - population balance equations (PBEs) 340
 - potential singular point surface (PSPS) 88, 91, 137
 - potentiostatic operation 74
 - prediction of wave patterns 157
 - pressure drop 236, 237, 242, 244, 263
 - pressure swing regeneration 220
 - probability of destruction 492
 - probability of impact 488, 492
 - probability of no collisions 491
 - propagating adsorptive reaction zone 203
 - propagation velocity
 - reaction front 19
 - thermal front 19
 - 1-propanol 152, 175
- r**
- racemization 353, 356
 - reactant dosing 378
 - reaction cyclone 437, 448
 - reaction kinetic surface 91
 - reaction rate 360, 363, 368, 370, 376, 379 ff, 385, 386
 - reaction separation process 154, 161
 - reactive absorption 265, 266, 456, 460, 481, 502
 - reactive absorption experiments
 - with granulation 502
 - without granulation 481
 - reactive arheotrope 119, 123–125, 133, 137, 138, 145

reactive azeotrope 88, 94–96,
 103, 110, 119, 137,
 144, 145, 162
 reactive chromatography (see also
 chromatographic reactor) 161,
 183–185
 reactive condenser 87, 89
 reactive crystallization 339, 340, 351
 reactive distillation 87–148, 161,
 233, 234, 236,
 241, 262
 reactive extraction 313
 reactive extrusion 393, 398, 402, 405
 reactive filtration 437
 separation of particulates and reaction
 of solids 441
 of volatiles 438
 reactive projection 345
 reactive regeneration 221
 reactive separation 233, 258, 263
 reactive separation process 89
 reactive stripping 234, 236, 241, 249,
 252, 253, 258 ff
 recuperative heat exchange 10
 recuperative process 27
 recycle ratio 48, 63
 reextraction 318
 reforming concept 48, 59
 regenerative heat exchange 10, 12
 residence time 362, 364, 365,
 372, 373, 382
 residence time distribution 236,
 240, 244, 331
 residue curve map 87
 residue curves 87, 112, 116, 123
 reversible reactions 359, 369, 378
 Rittinger's law 410
 roller mill 415

S

Sauter diameter 476, 510, 523
 seeded crystallization 354, 356
 selectivity 233, 250, 255 ff, 359,
 364, 365 ff, 370, 373, 378 ff
 Sherwood number 280
 side stream injection 20
 simulated moving bed (SMB)
 187–189, 220
 chromatographic process 172
 simulated moving-bed reactor (SMBR)
 184, 188, 189, 191, 196, 197, 199
 single-component reaction 395

single-screw 396
 SLE (solid-liquid equilibrium) 340
 SLE phase diagram 341, 342
 solid oxide fuel cell (SOFC) 45
 solid-liquid equilibrium 340
 solubility 347
 solvent 313
 sorption capacity 184, 197
 sorption selectivity 184, 197
 sorptively enhanced reactor 204
 SO_x absorption 299
 space-time yield 254, 257, 260, 263
 specific contact area 280, 302
 stacking of monoliths 246, 248
 stationary phase 183, 184,
 186–188, 197, 199
 stationary point 57
 steady-state simulation 291
 steam reforming 45
 of methane 36
 of methanol 36
 steam reforming of methane 36
 steam/carbon (S/C) ratio 46, 50
 Stefan–Maxwell 112, 113
 Stefan–Maxwell equation 367, 373
 stirred cell reactor 282
 stirred media mill 418
 stripping efficiency 236, 247, 248,
 253, 258, 263
 sulfur dioxide 461
 Sulzer packing 248, 262
 superficial fluid velocity 196
 sweep gas 110, 111, 117
 symmetric mode of operation 12
 Szego mill 416

T

Taylor-flow 236
 temperature swing regeneration 221
 tetrahydrofuran (THF) 133,
 134–136, 142–144
 thermal wave 19
 thermodynamic equilibrium 276
 transformed concentration variables
 156, 165
 transformed equilibrium function
 162, 165
 transformed variable 87, 92, 98,
 101, 103, 108, 137, 144
 tribochemistry 407
 tri-butyl-phosphate 318
 trickle bed operation 236, 237, 241

Trommsdorff effect 399, 405
true countercurrent (TCC)
185–187, 188
tumbling mill 416
twin-screw 396
two-film model 272, 280, 301
two-layer model 332

u

ultrasound reactor 421
UNIFAC model 196, 197

v

venturi tube 326

vibration mill 418
volumetric solid flow rate 189

w

water gas shift 209
water stripping 249, 257
water-gas shift reaction 46, 47
wave fronts 150
wave phenomena 150
wave solution 158

y

yield 364 ff, 369, 386